NanoBioMedical Center
Adam Mickiewicz Univeristy in Poznań

European Institute for the Membranes
University of Montpellier

Doctoral Thesis:

Development and Characterization of Polydopamine/Semiconductor Laminar Heterostructures for Efficient Photocatalytic Applications

Mgr inż. Jakub Szewczyk

Supervised by

Dr hab. inż. Emerson Coy
University Professor
NanoBioMedical Center
Adam Mickiewicz University in Poznań

Dr Mikhael Bechelany (hDr)
Director of the Research
European Institute for the Membranes
University of Montpellier

Poznań, 2024

Acknowledgements

Podziękowania

First of all, I would like to express the greatest gratitude to my Supervisors.

Dr hab. inż. Emerson Coy, prof. UAM
Joining your team was the best decision I could have made. Your friendly personality and curious attitude as a scientist are extraordinary. You provided everything necessary for the development of my career, but the most important was that I could get inspiration from You. Thanks for Your patience and time, which is of great importance for the quality of this doctoral thesis. I truly appreciate all your accurate tips, I could never count them all. Finally, thank You for believing in me.

Dr Mikhael Bechelany
It is an honor but also a pleasure to work with You. The time I spent at the Institute in Montpellier was truly great. However, whenever I encountered difficulties, Your positive attitude, expertise and determination have helped me to overcome them. You are also a wonderful leader who creates a great and helpful team, thank You for inviting me to join it, it was a great adventure.

Dziękuję najbliższej rodzinie- Rodzicom i Dziadkom. Przede wszystkim za to, że rozumieją drogę, którą wybrałem. Szczególnie podziękowania kieruje do moich sióstr- Aleksandry i Majki- *jesteście skarbem*. Dziękuję Przyjaciołom, którzy od wielu lat są ze mną na dobre i na złe. Za każdy wspólnie spędzony dzień, inspiracje i słowa otuchy. Największe wyrazy wdzięczności przesyłam Szymonowi i Adamowi- *jesteście niezastąpieni.*

Dziękuję Oliwii, za bezgraniczne wsparcie i bezwarunkową miłość. *Jesteś moim największym odkryciem. Tobie dedykuję tę pracę.*

Nad wodą wielką i czystą
Stały rzędami opoki,
I woda tonią przejrzystą
Odbiła twarze ich czarne;

Nad wodą wielką i czystą
Przebiegły czarne obłoki,
I woda tonią przejrzystą
Odbiła kształty ich marne;

Nad wodą wielką i czystą
Błysnęło wzdłuż i grom ryknął,
I woda tonią przejrzystą
Odbiła światło, głos zniknął.

A woda, jak dawniej czysta,
Stoi wielka i przejrzysta.

Tę wodę widzę dokoła
I wszystko wiernie odbijam,
I dumne opoki czoła,
I błyskawice – pomijam.

Skałom trzeba stać i grozić,
Obłokom deszcze przewozić,
Błyskawicom grzmieć i ginąć,
Mnie płynąć, płynąć i płynąć

Adam Mickiewicz
Nad wodą wielką i czystą

Table of Content

Summary

Heterogeneous photocatalysis is a class of chemical transformation of significant interest in the fields of Chemistry and Materials Engineering. It is because sunlight is an abundant energy source, and its utilization fits perfectly into the current trends, including the UN in the Sustainable Development Goals Agenda for 2030. However, to date, no significant progress has been made in the development of large-scale heterogenous photocatalytic systems. In short, the process of heterogeneous photocatalysis is as follows: When a semiconductor is illuminated with photons of energy equal to or higher than Bandgap Energy, the absorption of these photons and the creation of electron-hole charge carriers pairs occurs. These, in turn, can drive the redox reaction on the surface of the photocatalyst, which is desired in a given process (e.g. decomposition of pollutants by their oxidation). The current, most important milestones towards the production of the applicable photocatalysts are the increase of the overall process efficiency, large-scale suitability, improving stability and recyclability. These topics are very willingly taken up by scientists, as evidenced by, among others, a dynamically increasing number of scientific publications on this subject year by year. However, despite these research efforts, existing systems are limited to academic laboratory scales.

In turn, as the TiO_2 photoactivity has been reported since the early part of the 20^{th} century, it is still one of the most widely investigated promising photocatalyst materials, together with another transition metal oxide- ZnO. Their photocatalytic capabilities are being improved in many ways, e.g., by doping them with other elements (e.g. Nitrogen) and creating functional heterojunctions with other semiconductors. These strategies aim primarily to reduce the band gap and limit unfavorable photo-electric effects, such as recombining photo-generated charges. One recent, very promising strategy is the construction of organic/inorganic heterostructures. There are many indications that such systems are the best candidates for large-scale solutions because the ability to obtain polymers on large surfaces is one of their basic advantages. Laminar nanometrically thin heterostructures are an exciting solution because two active materials have a vast interface surface. At the same time, the volume of bulk materials is small enough to transport the photogenerated charge carriers to the surface of the photocatalyst. In this context, free-standing polymer films with a nanometer thickness seem particularly attractive, but they would have to meet extremely stringent requirements regarding mechanical resistance and the ability to adhere to functional surfaces on a large (>1 cm^2) scale.

One prominent candidate is Polydopamine (PDA), a biomimetic polymer with superior adhesive properties. The structural and mechanical properties of PDA nanostructures vary between synthesis strategies. However, a novel synthesis path towards 2D-like layered polydopamine films was presented very recently. It is based on the spontaneous oxidation of PDA at the air/water interface (a/w-PDA). Moreover, polydopamine has interesting semiconductor properties and has been previously used to create core-shell heterojunction nanoparticles with inorganic semiconductors. This all inspired this doctoral project and opened up a possibility for a real application, i.e. obtaining a new class of hybrid organic/inorganic large-scale laminar nanocomposites.

The main goal of this work was to develop a novel, efficient, large-scale, laminar nanocomposite for photocatalysis based on polydopamine and inorganic semiconductors: TiO_2 and ZnO. The project addresses the current limitations in the field of materials for photocatalysis by proposing a new, advanced, and tailored system.

My work here presented, consists of six thematically related scientific articles that were published between 2021 and 2024 in internationally peer-reviewed journals listed in the JCR database, and they garnered a combined impact factor of 43.6 as indicated by the Web of Science Database.

I have formulated four main research theses, which have been confirmed in my research:

(1) *Photocatalytic-relevant properties of the polydopamine make it an attractive candidate for a new hybrid organic/inorganic photocatalyst type. The recent developments in the field of construction of PDA/semiconductor hybrids indicate an early stage of advancement but a great applicational potential. However, current film-production approaches based on electrochemistry are insufficient for large-scale applications in photocatalysis.*

(2) *Polydopamine free-standing films from the air/water interface with layered-like structure possess promise for this work because, provided the synthesis process is highly controllable, they can be obtained on a macro scale and exhibit superior mechanical stability.*

(3) *Effective ex-situ transfer of the large-scale PDA films from the air/water interface to the TiO_2 or ZnO surfaces will lead to the formation of a heterojunction at the organic/inorganic interface, as would be in the case of in-situ deposition of polydopamine films, directly from the solution.*

(4) *The novel approach of ex-situ transferring of the a/w-PDA films onto the semiconductor surfaces enables the formation of advanced architectures, e.g. large-scale multilayer laminar nanostructures.*

Verifying the above theses was completed by 3 work packages, and the subsequent 4^{th} work package was to collect information and write this thesis.

The first package aimed at a comprehensive summary of the current state of the art by collecting the latest developments and studies on novel nanocomposites for photocatalysis based on different semiconductors and polydopamine. Overall, this information was embedded in Review Publications 1 and 2 (P1) and (P2), which provide an in-depth description of the literature research and conclusions and perspectives for the future. The P1 clearly shows that polydopamine has appropriate physicochemical, optical and electrochemical properties that enable its effective use for a new type of nanolaminates for photocatalysis. I also showed that there are already working and highly efficient PDA-based nanocomposites that have great potential for application in the field of heterogeneous photocatalysis; however, they are only available at the laboratory scale. In turn, P2 is not concerning photocatalysis directly, but it enables to understand the limitations resulting from the previously used methods of depositing PDA films. The subsequent Work Packages aimed to apply this knowledge to construct a next-generation large-scale nanometrically thin photocatalyst.

In Work Package 2, I started with the recently reported 2D-like layered PDA films from the air/water interface. To be able to synthesize them on a large scale (> $1cm^2$) with a high quality and precise thickness control, I conducted an extensive study to find the most beneficial synthesis conditions. Moreover, in P3, I studied their formation dynamics and control of the morphology, all to increase their application potential. During this Work Package, it was crucial to investigate the influence of synthesis conditions on a/w-PDA film growth in real-time and preferably *in-situ*. Therefore, in collaboration with experts from the field, I designed (P3) and

later upgraded (P4) the novel type of apparatus for Spectroscopic Reflectometry measurements. Later, within P4, I was able to drive the oxidation path towards a more physically cross-linked polymeric structure using oxidation agents, which resulted in superior elastic properties of the obtained ultra-thin free-standing a/w-PDA films. Overall, work package 2 resulted in the production of tailored high-quality films that could be effectively used to construct new types of organic/inorganic heterostructures on a large scale.

Work Package 3 was implemented in a step-like manner, where P5 was a fundamental study of whether a functional heterojunction could be produced in such an *ex-situ* transferring method, and P6 was intended to propose a new, advanced nanoarchitecture. Starting from P5, an *ex-situ* transfer of the large-scale PDA films onto functional substrates was tested. Transferring procedures were also examined to refine the best method. The effective formation of the PDA/TiO_2 and PDA/ZnO heterojunction was investigated in terms of 1) bandgap shifting, 2) improving the ability to photogenerate charge carriers, 3) increasing their stability and finally, 4) reducing the electron transfer resistance at the electrolyte/photocatalyst interface. This led to more efficient photodegradation of the methylene blue in comparison to bare semiconductors. The exact mechanism was investigated by executing a test with scavengers, and the stability of the obtained nanocomposite was tested during 4 subsequent cycles of photodegradation. In turn, P6 was the culmination of this project, where I showed that it is possible to repeatedly transfer PDA onto semiconductor surfaces to produce nanometrically thin multilayers with very sharp interfaces and excellent quality. Moreover, I discovered a new technique for doping oxide layers with nitrogen during the experiment. Each of the subsequent nanostructures (1, 2 and 3 layers) was characterized by increasingly better photoelectrochemical properties, which proves the unique capabilities of the PDA/semiconductor interface.

In conclusion, based on the results obtained, which were described in publications 1-6, I state that the veracity of the assumed theses was confirmed. Moreover, this project's scope was very broad, but it was possible to expand it even further during the experiments. The obtained multilayered nanocomposites already have significant application potential on a large scale, but it is expected that their further development is possible. At the end of the work, I presented future perspectives that may serve as a guide for other research groups dealing with similar topics.

Streszczenie

Fotokataliza heterogeniczna to klasa przemian chemicznych ciesząca się dużym zainteresowaniem w dziedzinie chemii i inżynierii materiałowej. Dzieje się tak dlatego, że światło słoneczne jest obfitym źródłem energii, a jego wykorzystanie doskonale wpisuje się w panujące trendy, m.in. w Agendę ONZ *Cele Zrównoważonego Rozwoju na rok 2030*. Jednakże, dotychczas nie nastąpił znaczący postęp z wykorzystaniem heterogenicznych systemów fotokatalitycznych na dużą skalę. W skrócie, proces fotokatalizy heterogenicznej można przedstawić następująco: gdy fotony o energii równej lub większej niż energia potrzebna do pokonania pasma wzbronionego padaja na powierzchnie półprzewodnika, następuje absorpcja tych fotonów i utworzenie par nośników ładunku elektron-dziura. Te z kolei mogą uczestniczyć w reakcji redoks na powierzchni fotokatalizatora, która jest pożądana w danym procesie (np. rozkład zanieczyszczeń poprzez ich utlenienie). Obecne, można zdefiniować najważniejsze kamienie milowe w kierunku produkcji odpowiednich fotokatalizatorów, jest to: wzrost ogólnej wydajności procesu, możliwość prowadzenia procesów w dużej skali, poprawa stabilności i możliwości recyklingu. Tematyka ta jest bardzo chętnie podejmowana przez naukowców, o czym świadczy m.in. dynamicznie rosnąca z roku na rok liczba publikacji naukowych na ten temat. Jednak pomimo tych wysiłków badawczych, istniejące systemy ograniczają się do skali laboratoryjnej.

Z kolei, w związku z doniesieniami o fotoaktywności TiO_2, od początków XX wieku jest on jednym z najlepiej zbadanych i najbardziej obiecujących materiałów dla fotokatalizy, podobnie jak inny tlenek metalu– ZnO. Ich właściwości fotokatalityczne są udoskonalane na wiele sposobów, np. poprzez domieszkowanie ich innymi pierwiastkami (np. azotem) i tworzenie funkcjonalnych heterozłączy z innymi półprzewodnikami. Strategie te mają na celu przede wszystkim zmniejszenie energii potrzebnej do pokonania pasma wzbronionego i ograniczenie niekorzystnych efektów fotoelektrycznych, takich jak rekombinacja fotogenerowanych nośników ładunków. Jedną z najnowszych, bardzo obiecujących strategii jest produkcja heterostruktur organiczno/nieorganicznych. Wiele wskazuje na to, że takie układy hybrydowe są najlepszymi kandydatami do rozwiązań wielkoskalowych, gdyż możliwość otrzymywania polimerów na dużych powierzchniach jest jedną z ich podstawowych zalet. Laminarne, nanometrycznie cienkie heterostruktury są ekscytującym rozwiązaniem, ponieważ w takiej konfiguracji, dwa aktywne materiały mają ogromną powierzchnię styku. Jednocześnie objętość takich materiałów jest na tyle mała, że umożliwia transport fotogenerowanych nośników ładunku na powierzchnię fotokatalizatora. W tym kontekście szczególnie atrakcyjne wydają się wolnostojące cienkie warstwy polimerowe o grubości nanometrów, jednak musiałyby one spełniać niezwykle rygorystyczne wymagania dotyczące wytrzymałości mechanicznej i możliwości przylegania do powierzchni funkcjonalnych w dużej skali (>1 cm^2).

Jednym z czołowych kandydatów jest polidopamina (PDA), polimer biomimetyczny o doskonałych właściwościach adhezyjnych. Właściwości strukturalne i mechaniczne nanostruktur PDA różnią się w zależności od strategii syntezy. Jednakże niedawno zaprezentowano nową ścieżkę syntezy cienkich wolnostojących warstw polidopaminowych o strukturze zblizonej do 2D. Niniejsza strategia opiera się na spontanicznym utlenianiu PDA na granicy faz powietrze/woda (a/w-PDA). Ponadto, polidopamina ma ciekawe właściwości półprzewodnikowe i była już wcześniej wykorzystywana do tworzenia heterozłączy z półprzewodnikami nieorganicznymi w formie nanocząstek typu rdzeń-powłoka. To wszystko zainspirowało powstanie niniejszego projektu doktoranckiego i otworzyło możliwość

otrzymania nowej klasy hybrydowych organiczno-nieorganicznych wielkoskalowych nanokompozytów laminarnych dla rzeczywistych zastosowań w fotokatalizie.

Głównym celem pracy było opracowanie nowatorskiego, wydajnego, wielkoskalowego, laminarnego nanokompozytu do fotokatalizy na bazie polidopaminy i półprzewodników nieorganicznych: TiO_2 i ZnO. Projekt uwzględnia obecne ograniczenia w dziedzinie wykorzystywania materiałów półprzewodnikowych do fotokatalizy, proponując nowy, zaawansowany i wysoce modularny system.

Prezentowana tutaj praca składa się z sześciu powiązanych tematycznie artykułów naukowych, które zostały opublikowane w latach 2021–2024 w recenzowanych czasopismach międzynarodowych wymienionych w bazie danych JCR i uzyskały one łączny współczynnik wpływu wynoszący 43.6, jak wskazuje baza danych Web of Science.

Sformułowałem cztery główne tezy badawcze, które znalazły potwierdzenie w wynikach moich badań:

(1) Właściwości fotokatalityczne polidopaminy czynią ją atrakcyjnym kandydatem do opracowania nowego typu hybrydowych fotokatalizatorów organiczno/nieorganicznych. Najnowsze osiągnięcia w dziedzinie konstrukcji hybryd PDA/półprzewodniki wskazują na wczesny etap zaawansowania, ale duży potencjał aplikacyjny. Jednak obecne podejścia do produkcji cienkich warstw PDA oparte na elektrochemii są niewystarczające do zastosowań w fotokatalizie na dużą skalę.

(2) Wolnostojące cienkie warstwy polidopaminowe wytworzone na granicy faz powietrze/woda o warstwowej strukturze są obiecujące dla tej pracy, ponieważ pod warunkiem, że proces syntezy jest w dużym stopniu kontrolowany, można je otrzymać w skali makro i wykazują doskonałą stabilność mechaniczną.

(3) Skuteczny transfer ex-situ wielkoskalowych cienkich warstw PDA z granicy faz powietrze/woda na powierzchnie TiO_2 lub ZnO doprowadzi do powstania heterozłącza na granicy faz organiczna/nieorganiczna, tak jak miałoby to miejsce w przypadku osadzania in-situ powłok z polidopaminy, bezpośrednio z roztworu.

(4) Nowatorskie podejście polegające na przenoszeniu ex-situ cienkich wolnostojących warstw a/w-PDA wprost na powierzchnie półprzewodników umożliwia tworzenie zaawansowanych architektur, m.in. wielkoskalowych wielowarstwowych nanostruktur laminarnych.

Weryfikację powyższych tez przeprowadzono w ramach 3 pakietów zadań, a kolejnym 4 pakietem było zebranie informacji i napisanie niniejszej pracy.

Pierwszy pakiet miał na celu kompleksowe podsumowanie obecnego stanu wiedzy poprzez zebranie najnowszych osiągnięć i badań nad nowatorskimi nanokompozytami do fotokatalizy w oparciu o różne półprzewodniki i polidopaminę. Ogólnie rzecz biorąc, informacje te zostały zawarte w Publikacjach Przeglądowych 1 i 2 (P1) i (P2), które zawierają szczegółowy opis badań literaturowych oraz wnioski i perspektywy na przyszłość. P1 wyraźnie wskazuje, że polidopamina posiada odpowiednie właściwości fizykochemiczne, optyczne i elektrochemiczne, które umożliwiają jej efektywne wykorzystanie do konstrukcji nowego rodzaju nanolaminatów do fotokatalizy. Pokazałem także, że obecnie istnieją działające i wysokowydajne nanokompozyty na bazie PDA, które mają ogromny potencjał zastosowania w dziedzinie fotokatalizy heterogenicznej; są one jednak dostępne tylko w skali laboratoryjnej. Z kolei P2 nie dotyczy bezpośrednio fotokatalizy, ale pozwala zrozumieć ograniczenia

wynikające z dotychczas stosowanych metod otrzymywania cienkich warstw PDA. Celem kolejnych pakietów zadań było zastosowanie tej wiedzy do skonstruowania nowej generacji fotokatalizatorów – wielkoskalowego i nanometrycznie cienkiego.

W pakiecie zadań nr 2, punkt wyjścia stanowiły niedawno zaprezentowane wolnostojące cienkie warstwy PDA z interfejsu powietrze/woda, które posiadają strukturę zblizoną do 2D. Aby umożliwić ich syntezę na dużą skalę (> 1cm^2) przy zachowaniu wysokiej jakości i precyzyjnej kontroli grubości, przeprowadziłem szeroko zakrojone badania w celu znalezienia najkorzystniejszych warunków syntezy. Ponadto w P3 badałem dynamikę ich powstawania i przeprowadziłem kontrolę morfologii, aby zwiększyć ich potencjał aplikacyjny. Podczas tego pakietu zadań, kluczowe było zbadanie wpływu warunków syntezy na formowanie się cienkich warstw a/w-PDA w czasie rzeczywistym (*in-situ*). Dlatego też, we współpracy ze specjalistami w tej dziedzinie, zaprojektowałem (P3) a następnie udoskonaliłem (P4) nowatorską aparaturę do pomiarów reflektometrycznych. Następnie, w ramach P4, udało mi się ukierunkować ścieżkę utleniania w kierunku bardziej korzystnej, usieciowanej struktury polimerowej. Dokonałem tego przy użyciu modyfikatorów utleniania, co zaowocowało lepszymi właściwościami mechanicznymi otrzymanych ultracienkich, wolnostojących warstw a/w-PDA. Ogólnie rzecz biorąc, w ramach pakietu zadań nr 2 wytworzyłem materiały wysokiej jakości, które można skutecznie wykorzystać do konstruowania nowych typów heterostruktur organicznych/nieorganicznych na dużą skalę.

Pakiet zadań nr 3 wdrożono etapowo. P5 stanowiła fundamentalne badanie tego, czy funkcjonalne heterozłącze może zostać otrzymane poprzez przenoszenie wytworzonych warstw polidopaminowych *ex-situ*. Z kolei, P6 miała na celu zaproponowanie nowatorskiej, zaawansowanej nanoarchitektury. Począwszy od P5, testowałem dwie metody transferu *ex-situ* wielkoskalowych cienkich wolnostojących warstw PDA na podłoża funkcjonalne, aby wybrać najbardziej korzystną. Następnie, badałem efektywność utworzenia heterozłącza PDA/TiO_2 i PDA/ZnO pod kątem: 1) przesunięcia energii potrzebnej do pokonania pasma wzbronionego, 2) poprawy zdolności do fotogeneracji nośników ładunku, 3) zwiększenia ich stabilności, 4) zmniejszenia oporu przenikania elektronów na interfejsie elektrolit/fotokatalizator. Doprowadziło to do bardziej wydajnej fotodegradacji błękitu metylenowego w porównaniu z samymi półprzewodnikami TiO_2 oraz ZnO. Dokładny mechanizm zbadałem wykonując test z wychwytywaczami rodników, a także sprawdziłem stabilność otrzymanego nanokompozytu podczas 4 kolejnych cykli fotodegradacji błękitu metylenowego. Z kolei P6 było zwieńczeniem tego projektu, w którym pokazałem, że możliwe jest wielokrotne przeniesienie a/w-PDA na powierzchnie półprzewodników w celu wytworzenia nanometrycznie cienkich wielowarstw o bardzo ostrych interfejsach i doskonałej jakości. Ponadto w trakcie eksperymentu odkryłem nową technikę domieszkowania warstw tlenkowych azotem. Każda z kolejnych nanostruktur (1, 2 i 3 warstwy) charakteryzowała się coraz lepszymi właściwościami fotoelektrochemicznymi, co świadczy o unikalności interfejsu PDA/półprzewodnik.

Podsumowując, na podstawie uzyskanych wyników, które zostały opisane w publikacjach 1-6, stwierdzam, że prawdziwość przyjętych tez została potwierdzona. Co więcej, zakres tego projektu był bardzo szeroki, ale w trakcie eksperymentów udało się go jeszcze bardziej rozszerzyć. Otrzymane wielowarstwowe nanokompozyty mają już znaczny potencjał aplikacyjny w dużej skali, ale oczekuję, że możliwy jest ich dalszy rozwój. Na zakończenie pracy przedstawiłem perspektywy na przyszłość, które mogą posłużyć jako wskazówka dla innych grup badawczych zajmujących się podobną tematyką.

Résumé

La photocatalyse hétérogène représente une catégorie de transformations chimiques d'un intérêt significatif dans les domaines de la chimie et du génie des matériaux. L'utilisation de la lumière solaire comme source d'énergie est particulièrement pertinente dans le contexte des tendances actuelles, notamment celles de l'Agenda des objectifs de développement durable à l'horizon 2030 établi par l'ONU. Toutefois, malgré cette importance, le développement de systèmes photocatalytiques à hétérojonction à grande échelle n'a pas encore connu de progrès significatifs. Pour résumer, le processus de photocatalyse hétérogène implique l'illumination d'un semi-conducteur avec des photons dont l'énergie est égale ou supérieure à l'énergie de bande interdite. Cette illumination entraîne la création de paires de porteurs de charge électron-trou, qui peuvent ensuite déclencher des réactions redox à la surface du photocatalyseur, telles que la décomposition des polluants par oxydation. Les avancées majeures nécessaires pour rendre les photocatalyseurs applicables à grande échelle incluent l'amélioration de l'efficacité globale du processus, l'adaptation à des volumes importants, ainsi que l'augmentation de la stabilité et de la recyclabilité. Ces défis sont activement étudiés par les chercheurs, comme en témoigne la croissance constante du nombre de publications scientifiques sur ce sujet chaque année. Cependant, malgré ces efforts de recherche, les systèmes actuels restent limités à l'échelle des laboratoires universitaires.

Par ailleurs, étant donné que la photoactivité du TiO_2 est signalée depuis le début du 20e siècle, il demeure l'un des matériaux photocatalyseurs les plus prometteurs, aux côtés d'autres oxydes de métaux de transition tels que le ZnO. Leurs capacités photocatalytiques sont sujettes à de multiples améliorations, notamment par le dopage avec différents éléments tels que l'azote, ainsi que par la formation d'hétérojonctions fonctionnelles avec d'autres semi-conducteurs. Ces approches visent principalement à réduire la largeur de la bande interdite et à atténuer les effets photoélectriques indésirables, tels que la recombinaison des charges photo-générées.

Une stratégie récente et prometteuse consiste en la construction d'hétérostructures organiques/inorganiques. De nombreux indicateurs suggèrent que de tels systèmes représentent les meilleurs candidats pour des applications à grande échelle, en raison notamment de la possibilité d'étendre des polymères sur de vastes surfaces, ce qui constitue l'un de leurs principaux avantages. Les hétérostructures laminaires nanométriquement minces sont particulièrement attrayantes, car elles offrent une large interface entre deux matériaux actifs, tout en maintenant un volume suffisamment réduit pour faciliter le transport des porteurs de charge photo-générés jusqu'à la surface du photocatalyseur. Dans ce cadre, les films polymères autoportants d'une épaisseur nanométrique se révèlent particulièrement intrigants, mais leur utilisation nécessite de répondre à des exigences strictes en matière de résistance mécanique et d'adhésion à des surfaces fonctionnelles à grande échelle (>1 cm^2).

Un acteur important dans ce contexte est la polydopamine (PDA), un polymère biomimétique doté de remarquables propriétés adhésives. Les propriétés structurelles et mécaniques des nanostructures PDA varient selon les méthodes de synthèse employées. Cependant, une nouvelle voie de synthèse a récemment été proposée pour obtenir des films de polydopamine en couches de type 2D, basée sur l'oxydation spontanée du PDA à l'interface air/eau (a/w-PDA). En outre, la polydopamine présente des propriétés semi-conductrices intéressantes et a déjà été exploitée pour créer des nanoparticules à hétérojonction cœur-coquille avec des semi-conducteurs inorganiques. Ces caractéristiques ont inspiré le présent projet de doctorat, ouvrant

la voie à une application concrète : la conception d'une nouvelle classe de nanocomposites laminaires hybrides organiques/inorganiques à grande échelle.

L'objectif principal de ce travail était de développer un nouveau nanocomposite laminaire efficace à grande échelle pour la photocatalyse, en utilisant la polydopamine et des semi-conducteurs inorganiques tels que le TiO_2 et le ZnO. Ce projet répondait aux défis actuels dans le domaine des matériaux pour la photocatalyse en proposant un système avancé et sur mesure. Le travail présenté ici se compose de six articles scientifiques thématiquement liés, publiés entre 2021 et 2024 dans des revues internationales à comité de lecture répertoriées dans la base de données JCR. Ces articles ont obtenu un facteur d'impact combiné de 43,6, selon la base de données Web of Science.

J'ai établi quatre thèses de recherche fondamentales, lesquelles ont été corroborées au cours de mes études :

(1) Les propriétés photocatalytiques de la polydopamine en font un candidat attrayant pour un nouveau type de photocatalyseur hybride organique/inorganique. Les progrès récents dans la création d'hybrides PDA/semi-conducteurs indiquent un début de développement mais un potentiel d'application considérable. Néanmoins, les méthodes actuelles de fabrication de films basées sur l'électrochimie se révèlent insuffisantes pour des applications à grande échelle en photocatalyse.

(2) Les films autosupportés de polydopamine, issus de l'interface air/eau et structurés en couches, sont prometteurs pour ce projet. Sous réserve d'une synthèse rigoureusement contrôlée, ils peuvent être obtenus à une échelle macroscopique tout en présentant une stabilité mécanique supérieure.

(3) Un transfert ex situ efficace des films de PDA à grande échelle de l'interface air/eau vers les surfaces de TiO_2 ou de ZnO conduira à la formation d'une hétérojonction à l'interface organique/inorganique, similaire à celle obtenue par le dépôt in situ de films de polydopamine directement à partir de la solution.

(4) La nouvelle approche de transfert ex situ des films a/w-PDA sur les surfaces semi-conductrices permet la formation d'architectures avancées, telles que des nanostructures laminaires multicouches à grande échelle.

La validation de ces thèses a été entreprise à travers trois ensembles de travaux, tandis qu'un quatrième ensemble de travaux a été dédié à la collecte d'informations et à la rédaction de cette thèse.

Le premier ensemble de travaux visait à fournir un résumé exhaustif de l'état actuel de la technique en rassemblant les derniers développements et études sur les nouveaux nanocomposites pour la photocatalyse, basés sur différents semi-conducteurs et la polydopamine. Ces informations ont été intégrées dans les publications de revue 1 et 2 (P1) et (P2), qui ont offert une description approfondie de la recherche documentaire ainsi que des conclusions et perspectives pour l'avenir. Le P1 a clairement démontré que la polydopamine possède des propriétés physicochimiques, optiques et électrochimiques appropriées pour une utilisation efficace dans un nouveau type de nanolaminés pour la photocatalyse. J'ai également présenté des nanocomposites à base de PDA, déjà très fonctionnels et efficaces, avec un grand potentiel d'application dans le domaine de la photocatalyse hétérogène, bien qu'ils ne soient

disponibles qu'à l'échelle du laboratoire. En ce qui concerne P2, bien qu'il ne soit pas directement lié à la photocatalyse, il a permis de comprendre les limitations résultant des méthodes de dépôt de films PDA précédemment utilisées.

Les travaux suivants visaient à appliquer ces connaissances pour construire un photocatalyseur nanométriquement mince à grande échelle dans le cadre du Work Package 2. J'ai commencé avec les films PDA en couches de type 2D récemment obtenus à partir de l'interface air/eau. Pour les synthétiser à grande échelle (> 1 cm^2) avec une qualité élevée et un contrôle précis de l'épaisseur, une étude approfondie a été menée pour identifier les conditions de synthèse les plus bénéfiques. De plus, dans le cadre de P3, j'ai étudié leur dynamique de formation et le contrôle de la morphologie pour augmenter leur potentiel d'application. Les travaux ont également impliqué la conception (P3) et l'amélioration (P4) d'un nouvel appareil pour les mesures de réflectométrie spectroscopique, afin d'étudier l'influence des conditions de synthèse sur la croissance du film a/w-PDA en temps réel. Plus tard, dans P4, j'ai pu améliorer la structure polymère des films a/w-PDA pour obtenir des propriétés élastiques supérieures. Dans l'ensemble, ce lot a permis de produire des films sur mesure de haute qualité qui pourraient être efficacement utilisés pour construire de nouveaux types d'hétérostructures organiques/inorganiques à grande échelle.

Le Work Package 3 a été mis en œuvre par étapes, avec P5 consistant en une étude fondamentale visant à déterminer la possibilité de produire une hétérojonction fonctionnelle dans une méthode de transfert ex situ, et P6 destiné à proposer une nouvelle nanoarchitecture avancée. À partir de P5, un transfert ex situ des films PDA à grande échelle sur des substrats fonctionnels a été testé, avec une analyse des procédures de transfert pour affiner la meilleure méthode. L'efficacité de l'hétérojonction PDA/TiO_2 et PDA/ZnO a été étudiée en termes de déplacement de la bande interdite, d'amélioration de la capacité à photogénérer des porteurs de charge, de stabilité accrue, et de réduction de la résistance de transfert d'électrons à l'interface électrolyte/photocatalyseur. Ces travaux ont conduit à une photodégradation plus efficace du bleu de méthylène par rapport aux semi-conducteurs nus. Enfin, P6 a permis de démontrer la possibilité de transférer de manière répétée du PDA sur des surfaces semi-conductrices pour produire des multicouches nanométriquement minces avec des interfaces très nettes et de grande qualité. En outre, j'ai découvert une nouvelle technique permettant de doper des couches d'oxyde avec de l'azote, renforçant ainsi les propriétés photoélectrochimiques uniques de l'interface PDA/semi-conducteur.

En résumé, en se basant sur les résultats obtenus et décrits dans les publications 1 à 6, je confirme que la validité des thèses proposées a été vérifiée. Les nanocomposites multicouches obtenus démontrent déjà un potentiel d'application significatif à grande échelle, mais leur développement ultérieur reste envisageable. En conclusion de ces travaux, j'ai présenté des perspectives futures qui pourraient guider d'autres groupes de recherche travaillant sur des sujets similaires.

1

Introduction

While sunlight is a crucial and abundant source of energy, only a small fraction of its total power reaching planet Earth is utilized. For most of humankind's history, natural photosynthesis has been the main method utilized for converting solar energy via agriculture and forestry [1]. Then, the era of dynamic photovoltaic technologies growth has arrived, which today is one of the pillars of obtaining clean and renewable electricity [2]. However, the broader perspective analysis (e.g. life-cycle analysis) shows, that photovoltaic systems alone cannot be considered zero-emission solutions due to the potential environmental damage effects e.g. land and water use, the inclusion of hazardous materials, possible noise/visual pollution, the need to maintain the transmission infrastructure and others [3]. Therefore, while photovoltaics is a nearly ideal solution for the direct production of clean electricity, it must be complemented with other technologies, allowing for direct implementation of other key processes for industrial transformation like hydrogen production and environmental remediation [4]. A prime example of the synergy effect is utilizing photocatalysis and photovoltaics, which transform light energy within different application areas [5].

Heterogeneous photocatalysis is one of the most unique and recently progressing classes of chemical transformation [6,7]. Remarkably, the development of this field fits perfectly into today's trends, e.g. those defined by the UN in the Sustainable Development Goals Agenda for 2030. As this plan aims to define the most important challenges of the current era, the basic research and development of technologies that fit well into it is particularly justified. Potential applications of heterogeneous photocatalysis include emerging topics such as sustainable energy production (photocatalytic water splitting) and environmental remediation, i.e., the degradation of pollutants [8]. Regardless of the potential application field, numerous obstacles are encountered that must be overcome by developing new strategies to produce novel classes of functional materials for photocatalysis [9]. This is because the material on the surface on which the process takes place is the pivotal element of the system. An exemplary and very important approach is the ecologically friendly production of photocatalysts, e.g., using biomimetic and bioinspired materials [10]. Other important aspects are enhancing the overall process efficiency, successfully transferring technology from the laboratory scale to the industrial scale, improving stability, and possibly recovering the photocatalyst material.

The above challenges and prospects are addressed currently through advanced engineering of functional materials and progress in chemistry, especially in obtaining new compounds and nanomaterials. There are many strategies for obtaining advanced photocatalysts, but none of them has proven promising enough to move this field beyond the laboratory scale. In order to understand the contemporary directions of development that directly influence the objective of this work, the theoretical foundations and the current state of the art will be discussed later in the introduction section.

1.1. Heterogenous Photocatalysis Principles

Photocatalysis is a subclass of catalysis. Overall, the process can be decomposed into five steps (**Figure 1**), while the major difference between conventional catalysis and photocatalysis is the photonic mode of activation in step 3. When a semiconductor is illuminated with photons of energy equal to or higher than Bandgap Energy ($h\nu \geq E_g$), the absorption of these photons and the creation of electron-hole pairs occurs. Next, these pairs dissociate into photoholes (h^+) in the valence band and photoelectrons (e^-) in the conduction band[11]. Photoholes, as they accept electrons, host an oxidation reaction, while photoelectrons would host a reduction reaction by donating electrons. Schematically, it is shown in **Figure 1.**

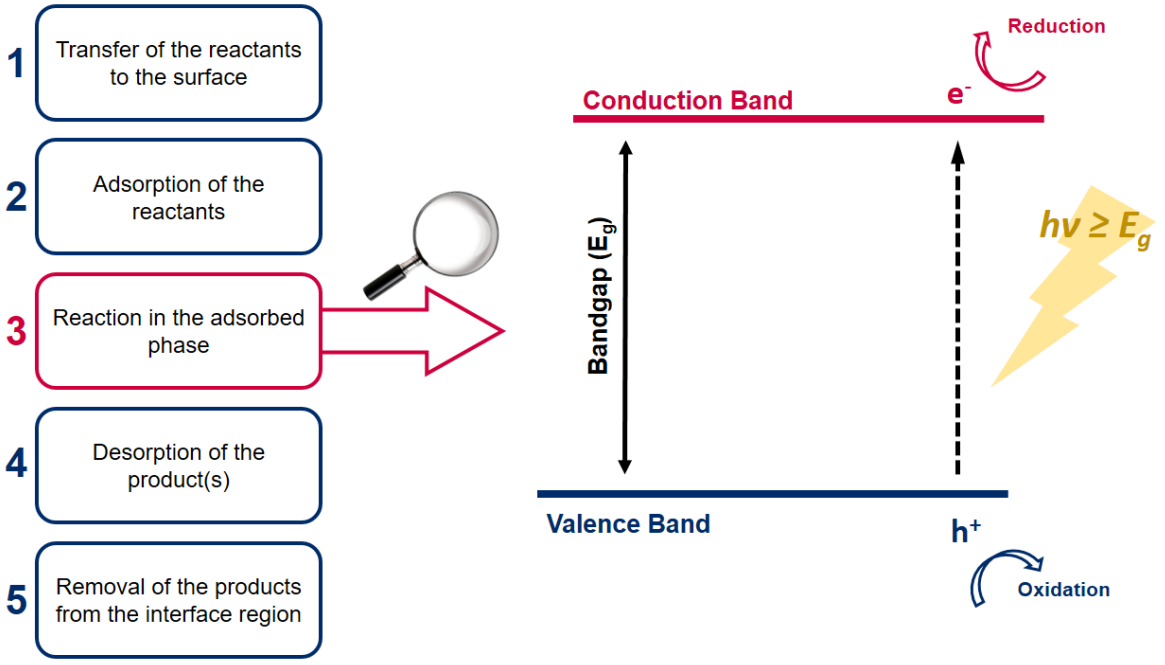

Figure 1. Photocatalytic reaction steps (left) and graphical explanation of step 3 (right).

However, generating photoholes and photoelectrons alone is not sufficient because undesirable effects may occur, reducing the reaction efficiency, such as charge carriers recombination, too short lifetimes (not sufficient to carry out a chemical reaction on the surface), low mobility of charge carriers and others[12]. In order to counteract these effects, various strategies based on advanced materials engineering are used, such as doping the semiconductors, creating heterostructures, providing efficient charge transport layers, and others[13]. We can describe all these activities under the common term band engineering. This will be described in more detail later in this work.

Therefore, the heterogeneous photocatalysis process requires electromagnetic radiation (light) and a semiconductor material with an appropriate band structure on the surface on which the chemical reaction will occur. When it comes to the first of these needs, sunlight can be a virtually unlimited source; this is where current trends are heading[14]. In turn, the dynamic development of functional materials engineering in recent years provides prospects for obtaining and using new classes of semiconductors for photocatalytic processes. Indirect proof that the topic of photocatalysis is being developed in a complementary way both in the field of materials science and in the other fields (environmental chemistry, chemical engineering, energy and others) is the number of scientific publications from the last 30 years in the SCOPUS

database, what was shown in **Figure 2**. The chart shows a dynamic and parallel increase in publications from year to year in both defined categories.

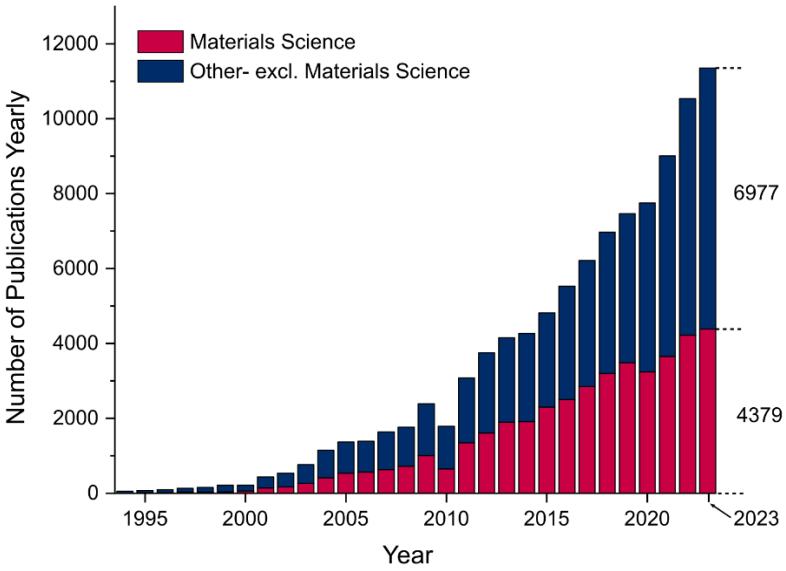

Figure 2. Number of Scientific Publications available in the SCOPUS database from 1993 to 2023, concerning "photocatalysis" (title or keywords or abstract).

Despite the mentioned research efforts, existing heterogeneous photocatalytic systems are limited to academic laboratory scales [7]. These laboratory-scale studies, however, provided answers to many important questions, such as what should characterize a good photocatalyst material [15]. These features include high surface area, homogeneity, efficient light absorption, efficient charge separation, long lifetime and high mobility of photogenerated charge carriers, and selectivity [13]. To date, no single semiconductor material can yield a high-efficiency (industrially acceptable) of the overall photocatalytic reaction [16]. Therefore, hybrid materials with 2 or more components offer a promising alternative. Currently, there are many materials investigated as candidates for the multicomponent systems in the field of heterogeneous photocatalysis (**Table 1)**, they can be categorized based on various criteria, e.g. composition [17] and structure [18], reaction mechanism [7], generation (time of appearance) [19,20], application field [17].

Table 1. The most important groups of heterogenous photocatalyst components

Group	Examples
Transition Metal Oxides (TMOx) [21,22]	Unary Oxides (ZnO, TiO_2), Binary Oxides ($SrTiO_3$, $BiVO_4$), Tertiary Oxides ($Co_xZn_{1-x}Fe_2O_4$), Doped Oxides (N:TiO_2, , GaN:ZnO, Au@SiO_2)
Metal Sulphides [23,24]	ZnS, CdS, CdZnS, SnS, Cu_2ZnSnS_4, Co_3S_4, $ZnInS_4$
Perovskites [25,26]	$LaFeO_3$, $LaMnO_3$, $LaCoO_3$, $SrTiO_3$, $BaTiO_3$, $BiFeO_3$, $CaTiO_3$, $CsPbI_3$, $CsPbBr_3$, $CsSnI_3$, $Cs_2BiAgBr_6$, $AgBi_2I_7$
Nitrides [27–29]	BN, Mo_2N, MoN, CoxN, TiN, Ta_3N_5, Fe_xN, Ni_3N, C_3N_4
Elemental or Metal Nanoparticles (NP) [30,31]	Ag, Cu, C, Au, Al, Pt, Bi, Co, Fe
Organic and other Carbon-based [32–34]	Graphene, Carbon nanotubes, graphene oxide (GO), reduced graphene oxide (rGO), graphene Quantum dots, MXene, Conducting/Semiconducting Polymers, Metal-Organic Frameworks (MOFs), Covalent Organic Frameworks (COFs)

It would seem that since the field of materials for photocatalysis is already well developed, the transition to large-scale should be underway. However, numerous limitations arise, including the large-scale synthesis and deposition of photocatalysts on solid supports, the development of an optimal design, utilizing advanced architectures (characterized by efficient photon absorption), and reactant mass transfer to the interface and from the interface [35]. The following will briefly discuss selected benchmark material groups and recent advances. The focus was on TMOx, carbon-based, and hybrid materials, and the reason these groups were selected will be explained.

1.2. Transition metal oxides (TMOx)

TMOx is a semiconductor, among which the most famous and widely investigated are TiO_2 and ZnO. Historically, this is the group of materials from which the field of heterogeneous photocatalysis originates. TiO_2 photoactivity has been reported since the early part of the 20^{th} century. During that time, it was shown that UV absorption produces reactive oxygen species on the TiO_2 surface, causing the photobleaching of dyes-rich paints. Moreover, it was noticed that TiO_2 itself does not change the photoreaction, indicating that the process is a specific type of catalysis [36]. Since then, despite reports of using other groups of materials (**Table 1**), TMOx is still at the forefront regarding application potential. One big advantage is that they can be produced through various industrial-scale methods, such as hydrothermal, sol-gel, Atomic Layer Deposition (ALD), Sputter coating and others [37]. As these are extremely promising materials, significant progress has been made in their preparation and modification, which translates into increasingly advanced structures. However, they also exhibit several limitations, such as photo-corrosion, rapid charge carriers recombination rate, wide band gap (utilization of the UV spectrum only), and low quantum efficiency [38]. Thus, various strategies were used to modify these materials. Krishnan et al. [21] Proposed the classification of the TMOx-based photocatalyst into 4 generations: 1- single TMOx suspended in solution, 2- doped single TMOx and binary TMOx composites suspended in the solution, 3- same as generation 2, but supported (e.g. on silica), 4- supported many-components composites based on TMOx, doped TMOx, plasmonic materials, polymers, MOFs and others. The 4^{th} generation utilizes many photocatalytic-related properties improvement approaches.

1.3. Doping

This strategy is employed to enhance the optical absorption of TMOx, by introducing the additional energy level into the forbidden band of the semiconductor photocatalyst, which was schematically shown in **Figure 3**. This is because doping atoms (X) cause structural defects (in particular oxygen vacancies or reduced M sites) or the formation of new M-X or M-O-X bonds [39–41]. The most common doping agents are non-metals like nitrogen, sulfur and metals e.g. aluminum, and copper.

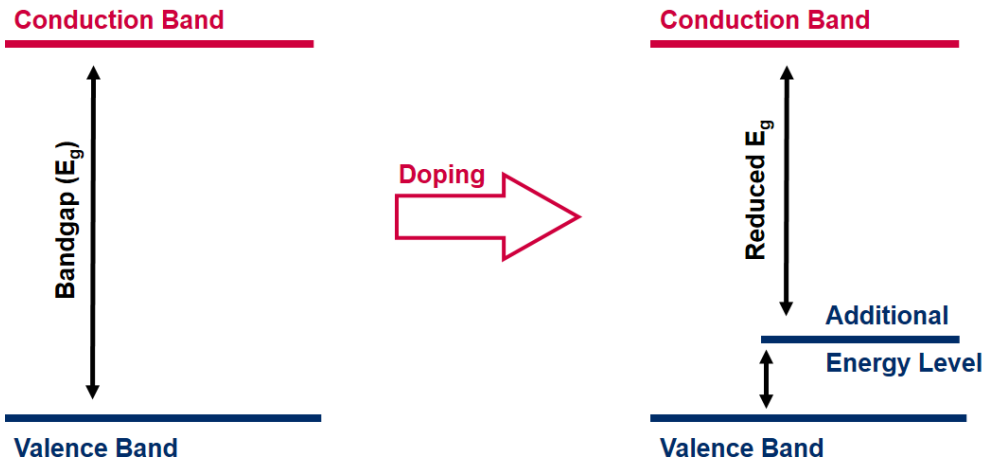

Figure 3. Scheme of the new energy level formation in the band electronic structure of the semiconductor due to doping.

The possible strategies for doping of TiO_2 and ZnO with nitrogen are chemical modification of the sol-gel method [41] and hydrothermal synthesis [40], nitridation reaction [42], plasma enhanced ALD in N_2/H_2 rich atmosphere [43], and the use of ammonium hydroxide as an additional precursor in the ALD process [44]. More sophisticated methods like Chemical Vapor Deposition [45], ion implantation [46,47] or magnetron sputtering [48,49] were also reported. However, their use on the industrial scale is currently impossible due to high costs and demanding technical facilities requirements.

Doping can be problematic because it is difficult to control the concentration of dopants in the material precisely. While their concentration on the TMOx surface is the most beneficial (because light absorption takes place there), too high a concentration of dopants in the bulk of the material is detrimental because the additional energy levels introduced may constitute a recombination center for charge carriers. Therefore, solutions such as gradient-like doping exhibit great promise but require highly advanced surface engineering [50].

1.4. Heterojunction formation

It is a phenomenon when an interface is formed between two dissimilar semiconductors or between a semiconductor and metal (e.g. plasmonic metal nanoparticle). Consequently, it significantly improves visible light absorption, increases the number of active sites and enhances photogenerated charge carrier separation [41]. Regarding semiconductor-semiconductor heterojunctions, several types can be indicated based on the band positions and charge transfer mechanism (**Figure 4**).

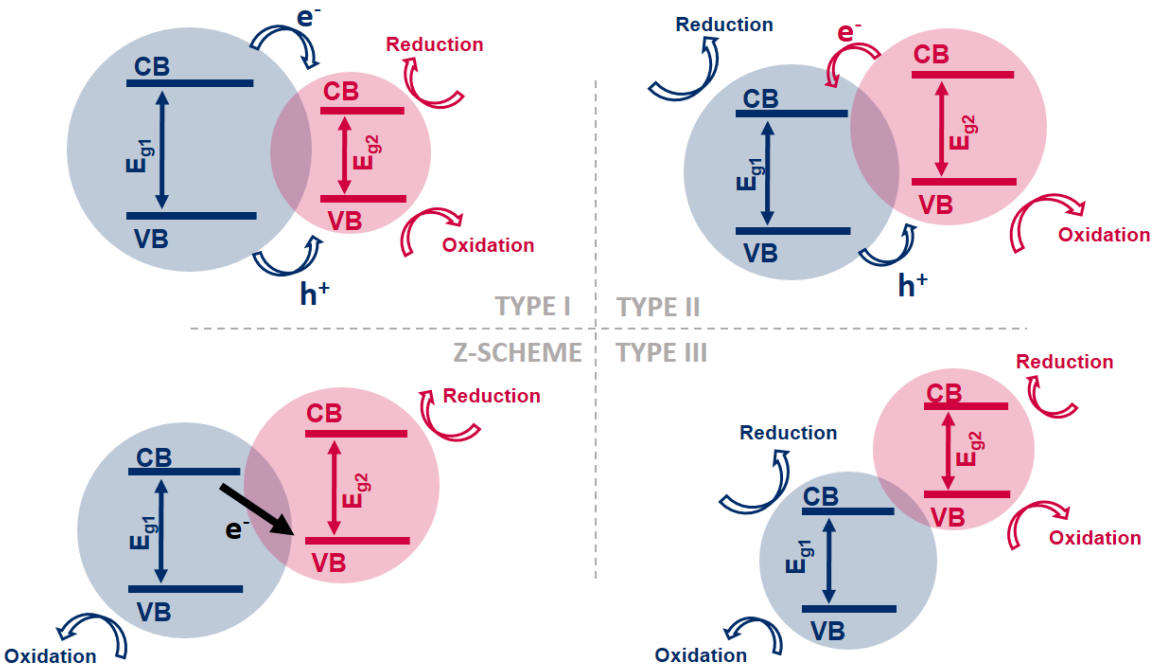

Figure 4. Classification scheme of different types of heterojunctions based on the charge transfer mechanism.

In type I, a semiconductor (S1) is interfaced with a greater bandgap's second semiconductor (S2). Thus, the Conduction Band and Valence Band levels of the S1 lie between those of the S2, resulting in a straddling band alignment. This causes charge carrier accumulation in the component with the lower E_g value. In heterojunction type I, the charge separation efficiency is relatively low [51–53]. Type II is similar to Type I; however, the charge carriers flow in opposite directions due to the alternating CB and VB bands of components S1 and S2. This leads to more effective charge carrier's separation [51–53]. In the Z-scheme (the sub-type of Type II), there is electron–hole interaction between the CB of the S1 and VB of the S2 levels. This makes the respective charge carriers occupying higher CB and lower VB levels available for ROS generation, resulting in higher oxidation and reduction potentials. There is also an S-scheme, a specific type of Z-scheme, wherein an internal band alignment-generated electric field causes higher charge separation efficiency [51–53]. Finally, the Type III heterojunction resembles the type II, but the CB and VB levels are positioned so that the band gaps of the semiconductor components do not intersect. Consequently, a stronger driving force is required for the charge transfer, e.g. the presence of a 3rd component [52,53].

However, the novel approaches in nanocomposite design often utilize sophisticated multicomponent architectures, leading to the more complex charge transfer mechanism, which could not be directly classified into one of these groups [53]. Moreover, the possibility of obtaining efficient heterojunctions has been limited to tightly adjacent in-situ generated nanocomposites (e.g., core-shell nanoparticles). Heterotypic materials in heterojunction, if only connected through electrostatic interaction, Van der Waals force or hydrogen-bond interactions, show limited improvement of photocatalytic performance due to large ohmic resistance at the interface and low stability [54,55]. So far, heterojunctions have not been successfully created on a macro scale and by *ex-situ* transfer of one material to the surface of another.

In turn, as opposed to TMOx-based multicomponent systems, polymers-based semiconductors can be obtained easily at a large scale and possess other advantages, such as optical stability, low costs and structural tunability [56]. This created a promising photocatalysis trend, namely, the construction of the Organic/Inorganic Hybrid structures.

1.5. Organic/Inorganic Hybrid Materials

There are two classes of organic components in hybrid organic-inorganic materials. First, small molecules such as dyes and molecular catalysts are mainly applied to sensitize the inorganic component [57]. This is a slightly different approach than heterojunction formation. Namely, the photosensitizers get excited from the ground to an excited state due to light absorption and then initiate the photochemical process by injecting excited electrons into the semiconductor's conduction band [58]. The second class is organic macromolecules or polymers. The latter is used for various modifications of the photocatalytic-related properties of the inorganic components, among others- heterojunction formation [57,59]. They are further promising for application because, apart from enhancement of photoelectronic properties, they offer benefits such as surface hydrophilic/hydrophobic modification and photo corrosion protection [57,59]. This class can be further divided into 4 subclasses depending on the base element of the composition: 1) g-C_3N_4. 2) Conjugated Polymers. 3) Graphene (GN), Graphene Oxide (GO), reduced Graphene Oxide (rGO). 4) Covalent Organic Frameworks (COFs), Metal Organic Frameworks (MOFs) and their composites. Some selected and relevant examples are presented in **Table 2**. Although other particularly interesting groups of carbon-based materials, MOFs and COFs were not taken into account, as their development in the field of photocatalysts is in the early stages. Compared to other systems, the photocatalytic efficiency of COFs-based composites is still significantly lower [57,60].

Table 2. Selected hybrid photocatalyst solutions

Base material	Hybrid Photocatalyst Scheme[1]
Poly(pyrrole) (PP)	PP/TiO_2 [61,62] PP/ZnO [63]
Poly(3,4-ethylene dioxythiophene) (PEDOT)	PEDOT/TiO_2 [64,65] TiO_2/PEDOT:PSS[1] [66] PEDOT@ZnO@GQDs[2] [67]
Polyaniline (PANI)	PANI/TiO_2 [68,69] PANI/ZnO [70,71] $ZnFe_2O_4$/TiO_2/PANI [72] rGO/$ZnFe_2O_4$/PANI [73] Cu_2O/ZnO-PANI [74] PANI@TiO_2/GN [75] PANI-rGO-MnO_2 [76] g-C_3N_4/TiO_2@PANI [77]
Chitosan (CS)	CS-TiO_2 [78] CS/ZnO [79,80] CS/ CdS [81] CS–ZnSe [82] CuO@CS-H [4] [83]
g-C_3N_4	g-C_3N_4/TiO_2 [84] g-C_3N_4/TiO_2@PANI [77] CoO/g-C_3N_4 [85] g-C_3N_4/SnS_2 [86] g-C_3N_4/ZrS_2 [86] Ni-Sn_3O_4/g-C_3N_4 [87] Cu_2O/g-C_3N_4 [88]
Graphene, Graphene Oxide, reduced Graphene Oxide	TiO_2–rGO [89] PANI@TiO_2/GN [75] PANI-rGO-MnO_2 [76] rGO-ZnO [90] PEDOT@ZnO@GQDs[2] [67] rGO/$ZnFe_2O_4$/PANI [73] CdS–rGO [91] MoS_2/GN [92]

1. The methodology for naming the composite structure schematically (e.g. @, /, - symbols, direction) was taken from source articles and was not agreed upon
2. PSS – Polystyrene sulfonate
3. GQDs – Graphene Quantum Dots
4. CS-H is Chitosan Hydrogel

As can be seen in **Table 2**, various configurations were developed and tested. However, some aspects of the fabrication and interaction of organic-inorganic heterojunction are still unclear. Therefore, despite their numerous advantages, the inorganic-organic hybrids are far from practical applications. Most importantly, developing green, low-cost and large-scale preparation methods is essential. Next, the focus on the stability of hybrid materials and photocatalytic performance should be set [93].

None of the organic-inorganic hybrid systems mentioned above (**Table 2**) are of a layered nanocomposite type. In comparison with zero-dimensional (0D) and one-dimensional (1D) nanocomposites, layered nanocomposites exhibit several extraordinary advantages, among which the most important is efficient interfacial charge transfer due to the large contact area at the materials' interfaces [94] (**Figure 5**). Moreover, the conventional powdered photocatalytic materials (0D, 1D) need attention to be handled at all levels of the photocatalytic process [95]. Therefore, they are usually deposited on supports, which minimizes their main advantage (i.e. large surface-to-volume ratio). Finally, nanoparticles and 1D materials are hazardous to the environment if they get away from the reaction vessel and enter groundwater, soil or air, so instead of contributing to the green transformation, they may cause further environmental pollution.

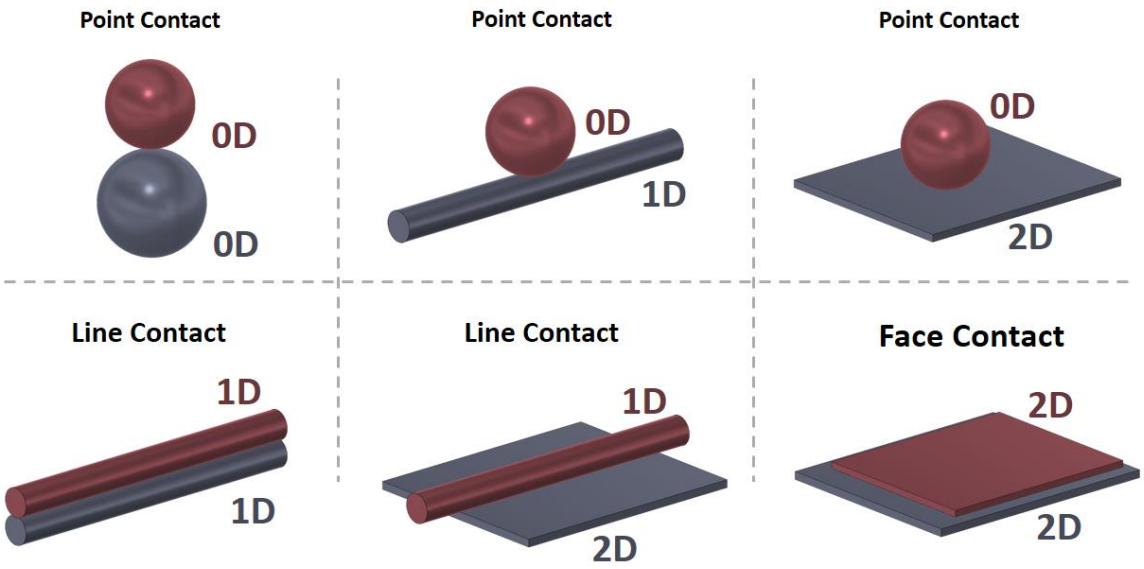

Figure 5. Scheme of the different types of the hybrid nanocomposites.

Therefore, taking into account that layered nanocomposites are the most promising for hybrid organic-inorganic photocatalysts and that large-scale (industrial scale) solutions are sought, attention has been directed to organic nanometrically thin films obtained on a large scale.

1.6. Thin organic films at the large scale

A thin film is a layer extending virtually infinitely along two directions but is restricted along the third. By definition, its thickness ranges from several nanometers to a few micrometres [96]. However, films with a thickness ranging from a few nanometers to several hundred nanometers are anticipated for applications in photocatalysis. In turn, when it comes to the dimensions in the remaining two directions, they should be macrometric, even above 1 cm [95]. Later in this work, each time the term "large-scale" is mentioned, it refers to the dimensions in these two remaining directions (not thickness), i.e., the surface-size scale.

Currently, many thin film deposition methods are in use (**Figure 6**). The possibility of obtaining large-scale layers on relatively large surfaces, at the moment, is only offered by chemical methods, especially sol-gel [96]. Moreover, the morphology control of the organic thin film is significantly more complicated than the control of inorganic materials.

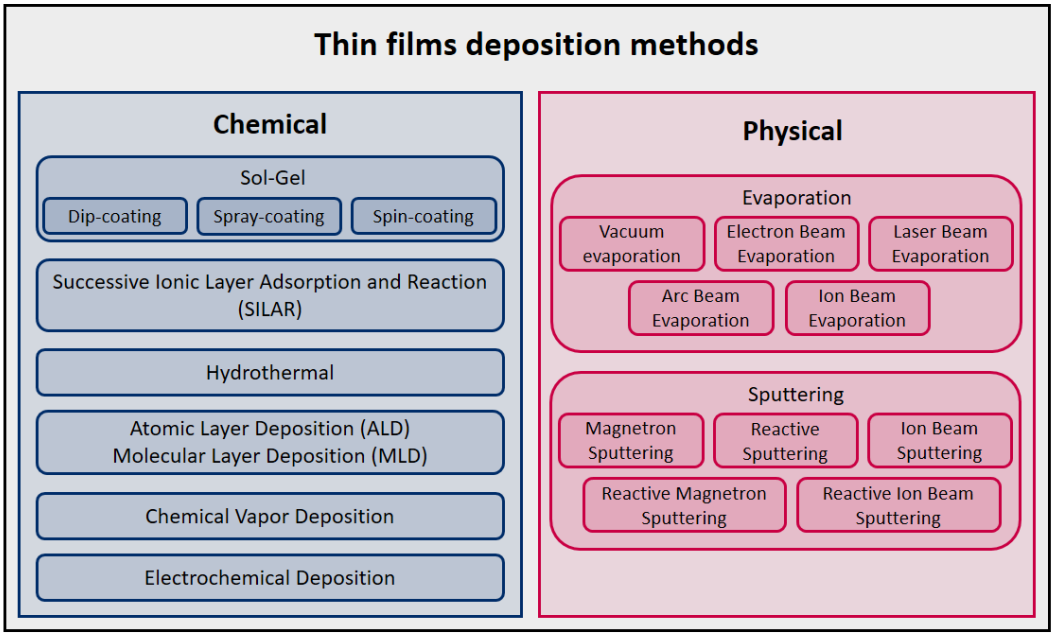

Figure 6. Classification of the thin film deposition methods

Of course, films could also be produced by processing 0D, 1D or 2D nanomaterials, e.g., by filtering a nanoparticle suspension solution and pressing the precipitate [97]. However, it has been repeatedly reported that the difficulty of processing powders into films is a significant obstacle in developing thin organic large-scale films [98]. Nevertheless, several systems based on hybrid organic-inorganic materials have been developed so far, the scale and performance of which can be described as large-scale or industrial-scale (Table 3).

Table 3. Reported Large-scale Hybrid Organic-Inorganic Photocatalytic systems

Photocatalyst	Reactor volume (L)	Application	Light source	Efficiency	Stability/ Reusability
TiO_2-rGO (nanoparticles suspension) [99]	35	Pesticides Photodegradation	Sunlight, 30 W m^{-2}	7 mg / 25 min	No data
CNTs/MOF-808 (Thin Film) [100]	0.2	Carbamazepine Photodegradation	400 W metal-halide lamps, 511 nm	0.9 mg / 90 min	8.5% efficiency drop during 5 cycles
CNTs/MOF-808 (Thin Film) [100]	0.2	Diazinon Photodegradation	400 W metal-halide lamps, 511 nm	1 mg / 90 min	7.6% efficiency drop during 5 cycles
C-TiO_2-polymer [1] (supported nanoparticles) [101]	4	Diclofenac Photodegradation	(8000 lux) 27 vis-LEDs > 400 nm	0.2 mg / 120 min	~0% efficiency drop during 6 cycles
TiO_2-GN (nanopillars suspension) [102]	0.1	Bisphenol A Photodegradation	350 W Xe lamp	0.006 mg / 30 min	5% efficiency drop during 5 cycles
N-TiO_2/PS [2] (nanoparticles supported on PS spheres) [103]	0.5	Methylene blue Photodegradation	vis-LEDs, 780 Wm^{-2}, 400–700 nm	0.5 mg / 120 min	~0% efficiency drop during 5 cycles
Pt/g-C_3N_4 (nanoparticles supported on the flat metal plate) [3] [104]	10	H_2 production	UV-Vis (sunlight spectrum) 800 Wm^{-2}	121 mL / 60 min	No data

1. C-TiO_2 refers to Carbon doped TiO_2 nanoparticles, polymer was not specified (it was used only for support)
2. N-TiO_2 refers to Nitrogen-doped TiO_2 nanoparticles, PS –polystyrene.
3. g-C_3N_4 nanoparticles were decorated with Pt nanoparticles. Additionally, Triethanolamine (10 vol%) was used as a sacrificial agent.

Based on the table above, it should be noted that none of the proposed applications are comprehensive. First, most of the solutions utilize artificial and powerful light sources, while there is a scientific consensus that efforts need to be directed toward the efficient use of free and abundant sunlight energy [35]. Moreover, efficient mass transfer of photocatalytic reaction products relies on separating the photocatalyst and reactants, which is hardly viable when the photocatalyst is in the form of nanoparticles or nanopillars slurry. Finally, as mentioned above, some of the organic materials applied in the systems are reduced to the role of supports and do not functionalize inorganic photocatalysts in any way.

Furthermore, in the case of repeated use of industrial-scale photocatalysts, the key property is mechanical stability, as they are prone to deformations and damage in reactor-operating environments (e.g. large water/air flux) [35]. Polymeric ultra-thin films may exhibit colossal differences in their mechanical properties (e.g., elasticity) compared to the bulk state [105–107]. For polymer to act as a versatile functionalization platform, it should be

easily transferable on macro-scale surfaces. Moreover, it should protect surfaces of sensitive and easily degradable photoactive materials.

Therefore, it is crucial to identify areas where progress is possible and find a material suited for the construction of large-scale hybrid organic-inorganic photocatalysts. A desirable candidate for polymer material element in the system should be characterized by good adhesion to virtually any other material from the groups listed in **Table 1**, high chemical resistance, non-toxicity, relatively low cost of preparation, sensitivity to UV-vis radiation, possibility of large-scale preparation and Hydrophilicity [57].

1.7. Polydopamine

One prominent candidate is Polydopamine (PDA), a biomimetic polymer discovered in 2007 [108]. The properties of PDA nanostructures vary between synthesis strategies, which were described later in this work. Notably, one of the most attractive general aspects of polydopamine is its organic semi-conductive character and behavior as an organic catalyst [109]. Therefore, it was studied in terms of creating hybrid heterojunctions with inorganic materials such as TiO_2[110], ZnO[111], ZnS[112], and CdS[113] for photocatalytic applications (all systems were based on nanoparticle suspensions). However, so far, no large-scale system has been developed. There has been no effective method for obtaining high-quality nanometrically thin PDA layers on large surfaces, although PDA can be deposited on virtually any type of substrate, even on a large scale, due to its very simple synthesis path [114]. In short, the material to be coated is placed in a dopamine solution, and after some time (the longer the time, the thicker the layer), it is pulled out. This creates an amorphous, hydrophilic black polymer with a rather irregular surface and poor mechanical properties. Alternatively, the electrochemical formation of polydopamine may be applied, it is oxidation of the dopamine in the presence of electric current. All the mentioned PDA-based hybrid systems relied on these approaches. However, the breakthrough discovery was a novel synthesis path based on the spontaneous oxidation of PDA at the air/water interface (a/w-PDA), where, through the use of specific synthesis conditions, the molecules are organized into a 2D-like layered film with exceptional mechanical properties [115]. It was previously known that a thin amorphous PDA film with quite poor mechanical properties could be formed at the air/water interface in the autooxidation process [116], but this was considered an attractive polydopamine property with no real application potential. The mentioned groundbreaking study, which revealed layered a/w-PDA, opened up the search for real applications, i.e. obtaining a new class of hybrid organic/inorganic large-scale laminar nanocomposites.

1.8. Broader Perspective

The previously mentioned information appears as a logical sequence that can be presented in the diagram (**Figure 7**)

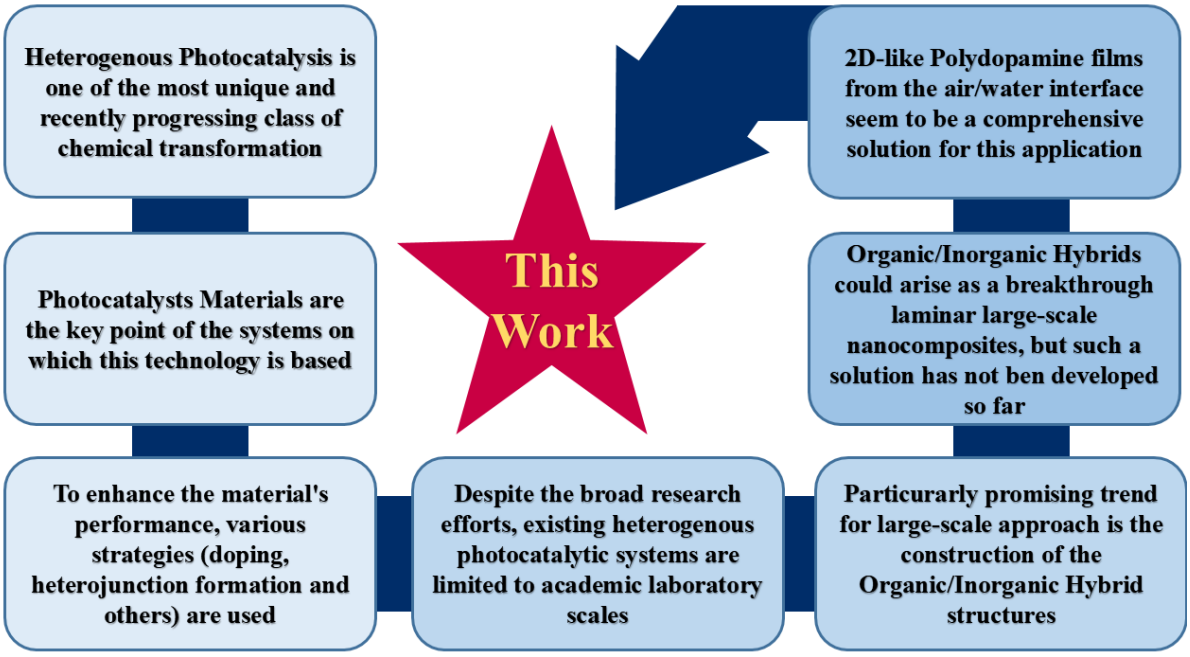

Figure 7. Scheme of the thought process that is the starting point for this work

As can be seen from the Figure above, taking up the topic of producing and transferring ultrathin free-standing a/w-PDA films onto functional semiconductor surfaces is highly justified and may contribute to significant progress in the field of modern materials for photocatalysis.

2

Main Goal and Research theses

The main goal of my work was to develop a novel, efficient, large-scale, laminar nanocomposite for photocatalysis based on polydopamine and selected transition metal oxides – TiO_2 and ZnO. At the same time, I set myself the goal of addressing the current limitations in the field of materials for photocatalysis by proposing a new system rather than improving the currently existing ones.

Thesis I: Photocatalytic-relevant properties of the polydopamine make it an attractive candidate for a new hybrid organic/inorganic photocatalyst type. The recent developments in the field of construction of PDA/semiconductor hybrids indicate an early stage of advancement but a great applicational potential. However, current film-production approaches based on electrochemistry are insufficient for large-scale applications in photocatalysis.

Thesis II: Polydopamine free-standing films from the air/water interface with layered-like structure possess promise for this work because, provided the synthesis process is highly controllable, they can be obtained on a macro scale and exhibit superior mechanical stability.

Thesis III: Effective ex-situ transfer of the large-scale PDA films from the air/water interface to the TiO_2 or ZnO surfaces will lead to the formation of a heterojunction at the organic/inorganic interface, as would be in the case of in-situ deposition of polydopamine films, directly from the solution.

Thesis IV: The novel approach of ex-situ transferring of the a/w-PDA films onto the semiconductor surfaces enables the formation of advanced architectures, e.g. large-scale multilayer laminar nanostructures.

3

Research Methodology

As specified in the Individual Research Plan, to verify the Theses 1-4, I planned the experiment which was based on 3 fundamental packages (WP 1-3). Each of them was carried out separately, but to be able to complete the experiment within 3 years, I decided to conduct parallel research in each of these directions. It was possible because the studies that were conducted were complementary, which led to the synergy effect. The last and fourth work packages were for writing this thesis (WP4). The workflow is presented in the diagram (**Figure 8**)

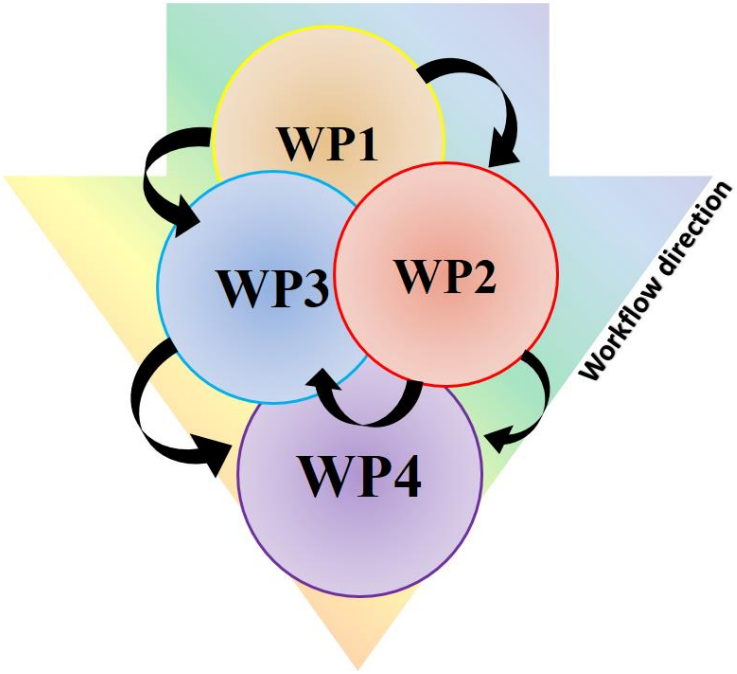

Figure 8. Scheme of the workflow

3.1. Comprehensive literature review on polydopamine photocatalytic-related properties and applications – WP1

This package aimed to summarize the current state of the art by collecting the latest developments and studies on photocatalytic nanocomposites with different semiconductors based on PDA. Implementing this package in the first year of the doctoral project duration was necessary because it allowed the selection of the best inorganic candidates for subsequent functionalization with PDA films at a large scale, thus creating a novel type of Hybrid Organic-Inorganic Photocatalyst. Moreover, it also helped to collect information about photocatalytic-related properties of the polydopamine *in-situ* deposited coatings and thus to select the most important features that large-scale polydopamine films from the air/water interface should exhibit.

Therefore, the literature review was divided into two main categories: 3.1.1. Photocatalytic-related properties of the polydopamine coatings and 3.1.2. Recent advances in the production of PDA-based nanocomposites for photocatalysis

3.1.1. Photocatalytic-related properties of the polydopamine coatings

The intrinsic properties of polydopamine from the point of view of heterogenous photocatalysis were derived into the following subcategories: chemical structure, color, optical absorption, fluorescence, Raman scattering, mechanical properties, wettability, electrical conductivity and other electrochemical properties. Next, the synthesis mechanisms concerning the synthesis strategies for nanocomposite creation were summarized. Finally, the air/water interface aspect was introduced, together with morphology control of the a/w-PDA strategies. However, until that time, no report about photocatalytic-related application of the a/w-PDA was reported.

3.1.2. Recent advances in the production of PDA-based nanocomposites for photocatalysis

Although polydopamine generates hydroxyl free radicals under UV irradiation [117], considering photocatalytic activity, PDA itself does not exhibit significantly interesting properties. However, it can synergize with other photocatalysts and create a charge transfer surface at the material's interface to enhance the photocatalytic performance of many semiconductors. The review was focused on the transition metal oxides (TiO_2, ZnO) and sulfides (ZnS, CdS). To expand the scope of this review, other emergent yet promising materials like MXenes, VdW materials (MoS and MoSe2) and Fe_xO_x were also included.

Overall, Publication (1) provides an in-depth description of the literature research and conclusions and perspectives for the future. Apart from its value, it was the basis for starting the tasks envisaged in WP 2-3, as it helped establish the input knowledge.

3.2. Polydopamine electrochemical films production and electronic related properties, literature review – WP1

The following review publication P2 was prepared to summarize information on the formation and application of polydopamine films and thin coatings. As described in P1, the application of PDA in the field of photocatalysis was mainly limited to nanoparticles. Therefore, a similar application area was chosen, where there was possible to find a numerous information on PDA films application. To date, electrochemical methods were employed for this purpose and the main application area was electrochemical sensing. Again, as in the case of P1, the aim was to take advantage of the current state of the art and to find the most desired features for the large-scale polydopamine films.

This literature review was divided into three main categories: 3.2.1. Fundamentals of the electrochemical dopamine oxidation 3.2.2. Electrochemical-related properties and deposition methods of the polydopamine thin films, 3.2.3. Recent advances in the production of PDA-based nanocomposites for electrochemical sensing

3.2.1. Fundamentals of the electrochemical dopamine oxidation

This section provides the general mechanism of dopamine oxidation under the influence of electric current, followed by the summary of the electrochemical oxidation methods. Next, the information about the influence of pH was provided, together with different conditions which are influencing the process. Finally, the kinetics of electrochemical dopamine oxidation is explained.

3.2.2. Electrochemical-related properties and deposition methods of the polydopamine thin films

The number of publications on the electrochemical production of large-scale PDA films is very limited, concerning real free-standing films, to date, there was only one experiment described. Therefore, in this section, the information on the methods used, along with their advantages and disadvantages are summarized. This section was primarily intended to answer the question whether the use of electrochemical methods would be an alternative approach than a/w-PDA for applications in photocatalysis.

3.2.3. Recent advances in the production of PDA-based nanocomposites for electrochemical sensing

Polydopamine is often an important element of composites used in analytical chemistry. However, due to the specific electrochemical properties leading to the undesired effects, PDA does not stand as the standalone solution for electrochemical sensing. The purpose of this section was to indicate how many combinations and advanced architectures can be obtained using PDA, and what role it can play in these solutions.

Overall, P2 provides an in-depth description of the literature research and conclusions and perspectives for the future. Although this literature review is not concerning photocatalysis directly (as in the case of P1), it was necessary to understand the limitations resulting from the previously used methods of depositing PDA films.

3.3. Large-scale *in-situ* control and synthesis of the a/w-PDA layered free-standing films – WP2

This work started with the recently reported 2D-like PDA films from the air/water interface (Section 1.3.2). These films were particularly interesting, as their mechanical resilience and layered-like structure held promise for successful application in large-scale surface functionalization. At the end of WP2, we needed to be able to synthesize them on a large scale (> 1cm^2) with high quality and precise thickness control. To achieve this, we conducted an extensive study to answer fundamental questions regarding the most beneficial synthesis conditions, their formation dynamics and control of the morphology, all to increase their application potential.

3.3.1. Synthesis in various conditions

As mentioned above, the formation of the amorphous free-standing PDA thin films at the air/water interface has already been well described in the literature. Moreover, it was shown, that the thickness of the dopamine-melanin coating and free-standing films relied on two main factors: concentration of dopamine in the reaction solution and reaction time. However, a recently shown 2D-like arrangement of PDA in a way, that put the state of the art of the synthesis conditions back at the beginning.

As in previous experiments, the a/w-PDA free-standing films were obtained at the air/water interface by a direct polymerization from solution in a Petri dish, allowing a large water surface area. As a novelty in relation to previous experiments, soft stirring was also applied. Control of the oxidation process, was performed multiple times and the following differential aspects were taken into account - concentration of dopamine, pH of the Tris buffer and stirring conditions i.e. speed (RPM value) and size of the stirrer. The polymerization time was up to 72h, but *in-situ* reflectance was held during all synthesis time.

3.3.2. *In-situ* reflectance measurements

The development of spectroscopic and microscopic methods, has made it possible to observe ongoing chemical and physical processes in real-time. Therefore, simply showing the final result of a chemical synthesis is often insufficient, and it is more desirable to track the *in-situ* mechanism accurately. Specifically, it is applicable to the processes that occur at surfaces and interfaces. Moreover, in chemistry, materials engineering, and physics, we observe an increasing importance of the integration of individual processes, which helps analyze data faster and more accurately. Therefore, in our study, an *in-situ* experimental setup was designed to investigate synthesis conditions' influence on a/w-PDA film growth and allow further control of the obtained film thickness and morphology. Specifically, the *in-situ* method was applied to control of the thickness growth at the air/water interface without damaging the film. For this purpose, a specially designed spectroscopic reflectometry (SR) apparatus was used. It was a much more handy, reliable and advanced approach than taking a sample of the film and performing profilometry measurements. This setup version's lower PDA film thickness detection limit was ~50 nm. This was possible due to cooperation with Prof. Jacek Gapiński and dr hab. Mikołaj Pochylski, prof. UAM, from the Faculty of Physics of AMU.

3.3.3. Physico-chemical characterization

A set of research methods based on spectroscopy (Raman Spectroscopy, X-ray photoelectron spectroscopy), diffractometry (X-Ray diffractometry), topography and microscopy (Atomic Force Microscopy) was applied to examine differences in the physical and chemical properties of the obtained a/w-PDA films. The analysis of the results focused on finding differences between films obtained using different synthesis conditions. Of the available, tested combinations, the most promising one was selected. This was intended to select the synthesis conditions that would be used in the production of films needed to make WP3, but also constituted a starting point for further research within WP2.

3.3.4. Molecular dynamics simulations

As mentioned in section 3.2.2, I wanted to understand the polydopamine 2D-like films self-assembly at the air/water interface process, rather than simply showing a final product. Therefore, molecular dynamics studies were performed by using Yasara software version 21.6.17, which was possible thanks to cooperation with dr hab. Kosma Szutkowski, prof. AMU. The precise analysis of the process of formation and aggregation of the macromolecules at the air/water interface exceeds the capabilities of SR equipment, which is why it was necessary to perform molecular dynamics simulations. The goals were set as follows: first, to identify the interaction sites for the growing aggregates with planar stacking. Next, the interaction of the macromolecules with the air/water surface will be investigated, and finally, the immobilization of the initially pre-arranged set of 80 macromolecules will be studied.

The methodology, results, and conclusions of the research mentioned above are comprehensively described in Publication 3.

3.4. Tuning of the mechanical properties of the large-scale a/w-PDA free-standing films – WP2

In the final conclusions of Publication 3, I specified that improving the transferring strategy of the a/w-PDA free-standing films to various functional substrates and improving their mechanical properties in the future was important. While transfer strategies are covered in Publication 4 (section 3.4), this section concerns tuning the mechanical properties.

Since, in our method, polydopamine is produced in the autoxidation process at the air/water interface, I decided to check the effect of the use of oxidation agents that would slow down or accelerate the oxidation process. Therefore, I applied a strong oxidant (Cu^{2+} ions) and a strong anti-oxidant (Boric Acid). However, for this experiment, it was also necessary to improve the SR apparatus because I assumed that the effect of oxidants and antioxidants would be most important in the initial hours of the synthesis, when the film on the interface is still too thin to observe its growth using the previous set-up.

3.4.1. Upgrade of the SR setup

By avoiding glass parts and using commercially available units: deuter-halogen light source AvaLight-DHc (Avantes) and AvaSpec-Mini2048CL spectrometer (Avantes) we developed a new version of the SR apparatus. It was crucial to reach the UV range of the reflectance spectrum to reduce the film thickness limit of detection. Another important modification was the application of the optical fiber in the all-closed setup, which is capable of operating in the broad UV–vis spectrum (220–800 nm). This all allowed us to obtain a reliable reflectance function for 30 nm thick PDA film.

3.4.2. Oxidation agents

The film synthesis was generally held in conditions determined in Publication 3. A standard dopamine oxidation medium (Tris buffer) was used for unmodified PDA films and Boric Acid-modified PDA films. In turn, for Cu^{2+} modification, a sodium acetate buffer was applied, because it is not possible to use Cu^{2+} as an oxidant at basic pH ~ 8. In such pH conditions, a spontaneous formation of $Cu(OH)_2$ occurs. Oxidant and antioxidant were used in three different concentrations to achieve various molar ratios of the dopamine/agent and thus, select the most appropriate formulation. The selection of oxidation agents was based on previous literature experiences regarding the preparation of standard amorphous PDA coatings and PDA nanoparticles. Specifically, there was indirect evidence that Cu^{2+} might reduce the degree of PDA macromolecule self-organization, while BA could increase the share of non-covalent cross-linking of the resulting thin films structure.

3.4.3. UV-Vis spectroscopy of the reaction liquid

UV–vis spectra were measured from 200 to 600 nm, as numerous absorption bands are in the given range for the dopamine oxidation products. The spectrum was measured at time

intervals from the start of the reaction of 1, 2, 4, 8, 24, 48 and 72 h, which allowed tracking the dynamics of dopamine oxidation with and without oxidation agents.

3.4.4. Dynamic Light Scattering and Transmission Electron Microscopy

As mentioned above, spherical PDA nanoparticles form in the reaction solution during the autoxidation of dopamine. Concerning a/w-PDA free-standing films, these nanoparticles are considered as a by-product of oxidation and they cause numerous problems: 1) they are sticking to the lower surface of the a/w-PDA films, decreasing its morphological homogeneity, 2) they damage the film during transferring from the air/water interface. To investigate the influence of the oxidation agents on spontaneous PDA nanoparticle formation, we performed DLS of the reaction liquids and TEM images of the nanoparticles formed in the solutions during oxidation transferred on the TEM grids.

3.4.5. Physico-chemical characterization of the modified films

The same set of research methods as in the case of Publication 3 was used (Section 3.2.3), but the aim was to determine the impact of oxidation agents on the obtained chemical structure of the a/w-PDA films. XPS spectroscopy was particularly important because it was intended to provide information on the final effects of the modified dopamine oxidation pathways.

3.4.6. Young's modulus of the a/w-PDA free-standing films

To extract the Young's Modulus, we performed 1) Nanoindentation tests- mainly by analyzing the unloading curves and 2) BLS spectroscopy- by probing thermally excited acoustic waves/phonons- in cooperation with dr hab. Bartłomiej Graczykowski, prof. UAM and dr Adam Krysztofik, from the Faculty of Physics of AMU. This was important from the point of view of the reliability of the obtained data, because we expected that the results obtained for a/w-PDA films would be extraordinarily good, compared to other free-standing thin polymeric films. Moreover, from the point of view of methodology, the measurements differed in that for nanoindentation, the measurement concerned films after transferring them to a Si(100) substrate, while in the case of BLS measurements, free-standing a/w-PDA films were actually measured because they were deposited on special Si_3N_4 membranes with cavities. The cavities were large enough that the a/w-PDA film filling them could certainly be described as free-standing.

The research mentioned above methodology, together with a description of the results and a comparison to other polymeric free-standing films and conclusions, is comprehensively described in the Publication 4.

3.5. Transferring of the a/w-PDA films onto semiconductor large surfaces – WP3

As mentioned earlier, only *in-situ* deposited PDA coatings have been proven to enhance the photocatalytic performance of the semiconductor materials. After achieving successful large-scale a/w-PDA free-standing film synthesis (as described in publication 3) I planned to move on to the key stage of this doctoral project, i.e. *ex-situ* transferring of the large-scale PDA films onto functional substrates. Due to the fundamental nature of this research, I wanted to choose semiconductors that could be considered a benchmark. My choice was transition metal oxides, specifically amorphous TiO_2 and ZnO, which are still one of the most promising candidates for real applications in photocatalysis. Moreover, they are also very well-researched and have a huge database of comparative literature, incl. successful *in-situ* heterojunction formation with PDA nanocoatings, which was crucial from the point of view of this experiment.

3.5.1. Transferring procedure

Two different transferring approaches were examined- scooping and stamping, and the names refer to the mechanical activities they resemble. It was to investigate both sides (surfaces) of the obtained films and check which method would generate higher-quality nanolaminates and better photocatalytic properties. Importantly, there was one important difference: the scooping method causes the side of the a/w-PDA film that was resting on the water to adhere to the semiconductor surface, while the stamping method makes the side of the a/w-PDA film that was exposed to the air to adhere to the semiconductor surface.

As the method of deposition of amorphous TiO_2 and ZnO thin films, I chose Atomic Layer Deposition (ALD), because the European Institute for the Membranes has highly modular, custom-made equipment, which allowed me not only to deposit the layers but also to gain operator and even service skills. The studies described in the following sections aimed to indicate which transferring procedure was more beneficial for applying the obtained nanolaminates in photocatalysis.

3.5.2. Physico-chemical characterization of the large-scale heterostructures

Water contact angle measurements were utilized to investigate wetting of the upper and lower surfaces of the a/w-PDA films. X-ray Diffractometry in standard and Grazing Incidence configurations was applied to examine the presence of a layered-like structure of the films after transferring. Profilometry data of the obtained nanolaminates were investigated via Atomic Force Microscopy. This was to provide information on the thickness of the a/w-PDA films and the roughness of the upper and lower surfaces. Finally, XPS and Raman Spectroscopy were scheduled to examine the presence of a key chemical moiety after transferring.

3.5.3. Photocatalytic-related properties of the large-scale laminates

The effective formation of the PDA/TiO_2 and PDA/ZnO heterojunction was examined in terms of 1) changing the photon absorption energy- bandgap change, 2) improving the ability to

photogenerated charge carriers and 3) increasing their stability. Moreover, 4) reducing the electron transfer resistance at the electrolyte/photocatalyst interface. To achieve this the following methods were applied 1) UV-Vis transmission spectroscopy 2) Ultrafast-Laser Transient Absorption Spectroscopy- which was possible due to cooperation with dr hab. Marcin Ziółek, prof. UAM, from the Faculty of Physics AMU- and Linear Sweep Voltammetry under chopped UV-vis light illumination, 3) The room temperature stationary Photoluminescence (PL) and 4) Electrochemical Impedance Spectroscopy with and without UV-vis illumination. The literature review provided within Publication 1 showed that it is possible to create an effective PDA/semiconductor heterojunction, but in this doctoral project, I had to demonstrate it anew, because the prospect of *ex-situ* functionalization with polydopamine, by transferring a large-scale a/w-PDA film to a large-scale surface semiconductor was an unknown. Therefore, the applied research was aimed at complementary characterization of the so-obtained heterojunction.

3.5.4. Photocatalytic performance of the large-scale heterostructures

The prime importance of publication 4 was the test of the photocatalytic performance of the obtained large-scale laminar heterostructures. Again, my idea was to choose a reliable benchmark application. Therefore, the photocatalytic degradation of the methylene blue test was conducted under moderate power UV-Vis light illumination. Methylene blue poses a real threat to the natural environment because it is widely used, for example, by the textile industry. However, what was even more important was that the photodegradation mechanism of the methylene blue uses both oxidation and reduction reactions on the photocatalyst surface. Therefore, the increase in efficiency would be due to photogenerated electrons and electron holes. The exact mechanism was investigated by executing a test with scavengers, and the stability of the obtained nanocomposite was tested during 4 subsequent cycles of photodegradation.

Publication 5 contains the mentioned research methodology together with a description of the obtained results and conclusions.

3.6. Preparation of the large-scale nanolaminates with advanced architecture – WP3

In publications 3-5, I showed that a/w-PDA large-scale free-standing films from the air/water interface can be ex-situ transferred to virtually any desired substrate due to their extraordinary mechanical and adhesive properties. Moreover, the efficient heterojunction is formed after transferring onto semiconductor surfaces (ZnO and TiO2). Because TiO_2 turned out to be a more promising substrate for this type of modification, I decided to use this TMOx to produce multilayer nanostructures. The idea was that since the beneficial photocatalytic effects occur at the material's interface, increasing the number of interfaces by creating multilayer nanostructures will allow for even more outstanding performance.

3.6.1. Production of the nanolaminates

Taking advantage of the previously utilized a/w-PDA *ex-situ* film transferring and the TiO_2 Atomic Layer Deposition, a first layer of the nanocomposite i.t. TiO_2/PDA was obtained. Next, for the formation of 2nd and 3rd layers, the method involved alternate layering of high-quality a/w-PDA nanometrically thin free-standing films with atomic layer deposition of the TiO_2 layers onto the polymer surface to obtain TiO_2/PDA/TiO_2/PDA (2 layers) and TiO_2/PDA/TiO_2/PDA/TiO_2/PDA (3 layers). It is worth emphasizing that all nanolaminates were produced on a large scale (about 1 cm^2 of surface).

3.6.2. Raman Spectroscopy and X-ray Diffractometry

As described earlier, I conducted these structural tests for a/w-PDA films numerous times before (as described in publications 3-5), but it was also crucial in the case of Publication 6. The aim was to investigate whether the increased temperature in the ALD process (200°C) would affect the structural properties of the layered-like PDA films (for samples 2 and 3 layers).

3.6.3. Multilayer Structure Imaging

High-resolution transmission Electron Microscopy was combined with in-depth Secondary Ion Mass Spectroscopy- (SIMS was possible thanks to cooperation with dr hab. Paweł Piotr Michałowski from Łukasiewicz Institute of Microelectronics and Photonics) to investigate whether the preparation of the large-scale multilayers with sharp interfaces was successful. Initially, the Ti, C, N, and O content profile spectra were supposed to confirm sharp interfaces of the perfect and uniform layered nanostructure of the PDA/semiconductor multilayers, as indicated via HRTEM images. However, the nitrogen content in the TiO_2 layers grown by ALD on the PDA surface was significant and exhibited a gradient-like nature. As described in section 1.3, nitrogen-doping of the TiO_2 is one useful modification to increase its photocatalytic efficiency by reducing bandgap, broadening the light absorption, and raising the number of photogenerated charge carriers. At this stage, I knew that this type of doping mechanism (nitrogen sourcing from the polymer substrate in the ALD deposition process) had never been described before, so a thorough study would need to be conducted to confirm the SIMS observations.

3.6.4. X-ray Photoelectron Spectroscopy deep-profiles

We employed the XPS in-depth profile mode, by etching the sample with Ar^+ ions and measuring spectra after 5 different times (0, 3, 21, 36, 53 min). By analyzing simple atomic elements content (Ti, C, N, O) it was possible to determine the speed of the Ar^+ ion etching process and the location where each measurement was made. In this manner, an etching profile was prepared, revealing successful sampling of the 5 different regions, enabling characterization of a/w-PDA films, PDA/TiO_2 interface, bulk TiO_2 with low nitrogen content and bulk TiO_2 with significant nitrogen content. Then, Ti 2p, N 1s, O 1s and C 1s high-resolution spectra were analyzed in these regions to provide information about interface formation, doping mechanism and chemical changes.

3.6.5. Optical properties of the nanolaminates

Apart from the key importance of optical-properties tests for the application potential of the obtained nanocomposites (bandgap reduction), it was crucial to confirm the results of SIMS and XPS tests using optical methods. Namely, it is known that the formation of the PDA/TiO_2 interface and nitrogen doping of the TiO_2 significantly affect the optical properties, therefore, UV-vis spectroscopy and ellipsometry were performed. Ellipsometric examination of such complex multilayer nanolaminates was difficult, but the developed model allowed the analysis of TiO_2 and PDA layers separately, which provided excellent insight into the opto-electrical changes.

3.6.6. Photo-electrochemical properties of the nanolaminates

Photo-electrochemical tests consisted of linear sweep voltammetry, Chronoamperometry, Open circuit photopotential (OCP) and Open circuit photocurrent (OCC) measurements. This rather modest but comprehensive set of tests made it possible to investigate the differences between 1, 2 and 3-layer nanocomposites in terms of their photogeneration of charge carriers efficiency, response time, stability and other similar photocatalyst-like behaviour.

Publication 6 contains the mentioned research methodology together with a description of the obtained results and conclusions.

To sum up, six thematically related works, two of which (P1, P2) are review articles and four (P3-P6) are research articles, were prepared within this doctoral thesis.

4

Results

The following section provides the results published in the scientific articles and organized by the research Theses.

The indicators for all mentioned publications are also provided (as of March 15, 2024), they were taken from the Web of Science database.

Thesis I - Photocatalytic-relevant properties of the polydopamine make it an attractive candidate for a new hybrid organic/inorganic photocatalyst type. The recent developments in the field of construction of PDA/semiconductor hybrids indicate an early stage of advancement but a great applicational potential. However, current film-production approaches based on electrochemistry are insufficient for large-scale applications in photocatalysis.

The Thesis I is addressed in the Publications 1-2

Publication 1

The Author's contribution to this publication includes Literature Review, Writing – original draft, Writing – review & editing, and Visualization. Moreover, selecting figures from cited publications and preparing collective figures (Figure 1-6 of the Publication 1).

Journal: CATALYSIS TODAY
ISSN: 0920-5861
Publisher: Elsevier
Journal Impact Factor: 5.3
Publication Date: 12.05.2022
Number of Citations: 27

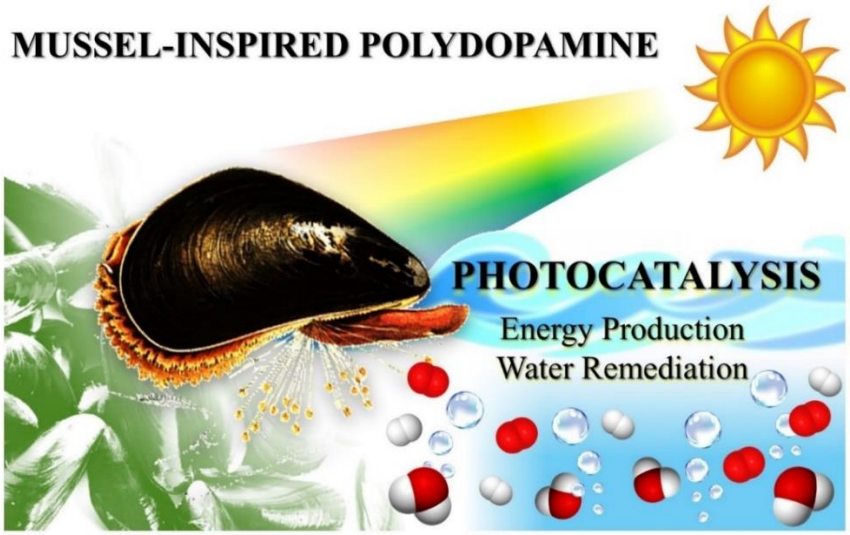

Figure 9. Graphical abstract of the P1

Catalysis Today 397-399 (2022) 316–349

Contents lists available at ScienceDirect

Catalysis Today

journal homepage: www.elsevier.com/locate/cattod

Recent developments in polydopamine-based photocatalytic nanocomposites for energy production: Physico-chemical properties and perspectives

Daniel Aguilar-Ferrer [1], Jakub Szewczyk [1], Emerson Coy [*]

NanoBioMedical Centre, Adam Mickiewicz University, Wszechnicy Piastowskiej 3, 61-614 Poznań, Poland

ARTICLE INFO

Keywords:
Photocatalysis
Composites
Semiconductors
Polydopamine
Functional materials
Hydrogen production

ABSTRACT

Light-driven photocatalysis might address many global energy concerns due to its implications for hydrogen production and the imperative need to reduce fossil fuel dependency. Polydopamine (PDA) is a popular mussel-inspired material with extensive applicability in biomedical and drug delivery fields, which has recently been gathering attention in the fields of catalysis and photocatalysis. PDA is highly attractive for catalysis due to its large number of functional groups and its easy polymerization on virtually any surface. In photocatalysis, however, its properties have not been well described and strongly depend on the generation of heterojunctions (PDA/Semiconductor). In this review, we summarize the latest developments and studies on photocatalytic nanocomposites based on PDA. We will introduce general aspects such as structure and polymerization control. Then, we will focus on aspects of relevance for photoactive materials, such as chromatic control and electrical properties. We will present and discuss the recent literature on metal oxides and metal sulfides and some emergent materials focusing on photoactive and photocatalytic applications. Finally, we will outline some of the opportunities in the field. We hope this review serves as a reference for researchers and allows the growing community to focus on future developments for PDA-based photocatalytic nanocomposites.

1. Introduction

Polydopamine (PDA) is a biomimetic polymer that has made a sizable impact in nanotechnology, biomedicine, and other fields, although relatively new in material chemistry. In recent years, biomimetics has become one of the most exploited trends in science, and this phenomenon does not only apply to materials science [1–3]. In response to this trend, polydopamine was developed and described for the first time in 2007 [4,5]. The inspiration came from the interest in replicating and understanding the mussel adhesive properties, where one of the proteins - responsible for this phenomenon -was rich in dopamine and lysine units. Further works were carried out with a strong focus on dopamine polymerization, which resulted in the preparation of polydopamine – a new, biocompatible polymer with strong adhesive properties and a relatively simple polymerization process [6].

Soon after the discovery of PDA, and in significant part due to its exceptional adhesive properties, which allow it to attach to virtually any surface, many composites were developed. These materials have been tested in several applications, as previously mentioned; however, they all share an essential aspect, the constants search for new green solutions in chemistry in order to diminish our environmental impact [6]. Among these, water remediation and photocatalysis have gained significant attention, especially in recent years [7–9]. The enormous consumption of dyes and other chemical reagents contributed to the increment of environmental pollution, and in an attempt to deal with this problem, solar-driven photocatalytic decomposition has shown promising results as a sustainable solution [7]. On the other hand, in the energy sector, the demand for new functional materials is still growing, as new perspectives and challenges appear, especially in those fields where the need for environmental protection meets fast development [10–13].

Polydopamine, with its versatile properties and biomimetic nature, may address many engineering and scientific issues. Up to date, polydopamine has been used in many fields, e.g. preparation of the Li-ions batteries, synthesis of antibacterial materials, biosensors engineering, molecular imprinting, tissue engineering and bioimaging [14]. However, one emerging aspect that still has not been thoroughly reviewed in

* Corresponding author.
E-mail address: coyeme@amu.edu.pl (E. Coy).
[1] The authors contributed equally and are listed alphabetically.

https://doi.org/10.1016/j.cattod.2021.08.016
Received 31 March 2021; Received in revised form 28 July 2021; Accepted 7 August 2021
Available online 11 August 2021

the literature is the photocatalytic applications of PDA. Polydopamine shares many essential features with an amorphous organic semiconducting polymer such as Melanin [15–18], making it a powerful ally in band structure engineering and electron transfer processes. However, most of the physical-chemical properties of PDA are still elusive, and its role in efficient photocatalysis has been mainly phenomenologically described. Therefore, much research is expected in the following years in the field, aiming to understand the properties of PDA and its role at the interface of PDA/Semiconductor nanomaterials for photocatalytic water splitting.

In this review article, the most critical applications and finding on the photocatalytic performance of PDA will be described. First, we will focus on the most relevant properties for the photocatalytic process, such as color, morphology, synthesis control, and catalytic pathways. We will discuss the inherent properties of PDA from the point of view of photocatalytic applications and describe the most critical developments in this field to date. Finally, some of the possible developments in the field and current challenges are addressed to provide a clear and comprehensive view of the importance of PDA-based nanocomposites in photocatalysis in the following decades.

1.1. Structure and physico-chemical properties

1.1.1. Structure

It is essential to take a step back and explain what the melanin group is to discuss the structure of polydopamine. Melanin is a systematic name for a family of heterogeneous, polymeric pigments widely found in biology. This name originates from the Greek word “melanos”, which means black or very dark, which is the most characteristic property of melanin [19]. A division into further subgroups is as follows, eumelanin, pheomelanin, and neuromelanin, mainly found in animal tissues, whereas allomelanin and pyomelanin are primarily found in microorganisms and plants (Fig. 1a) [20]. Describing the structure of individual compounds belonging to this group turns out to be difficult due to its high chemical complexity, poor solubility in most common solvents and high molecular weight [19,21,22]. However, over the past two decades,

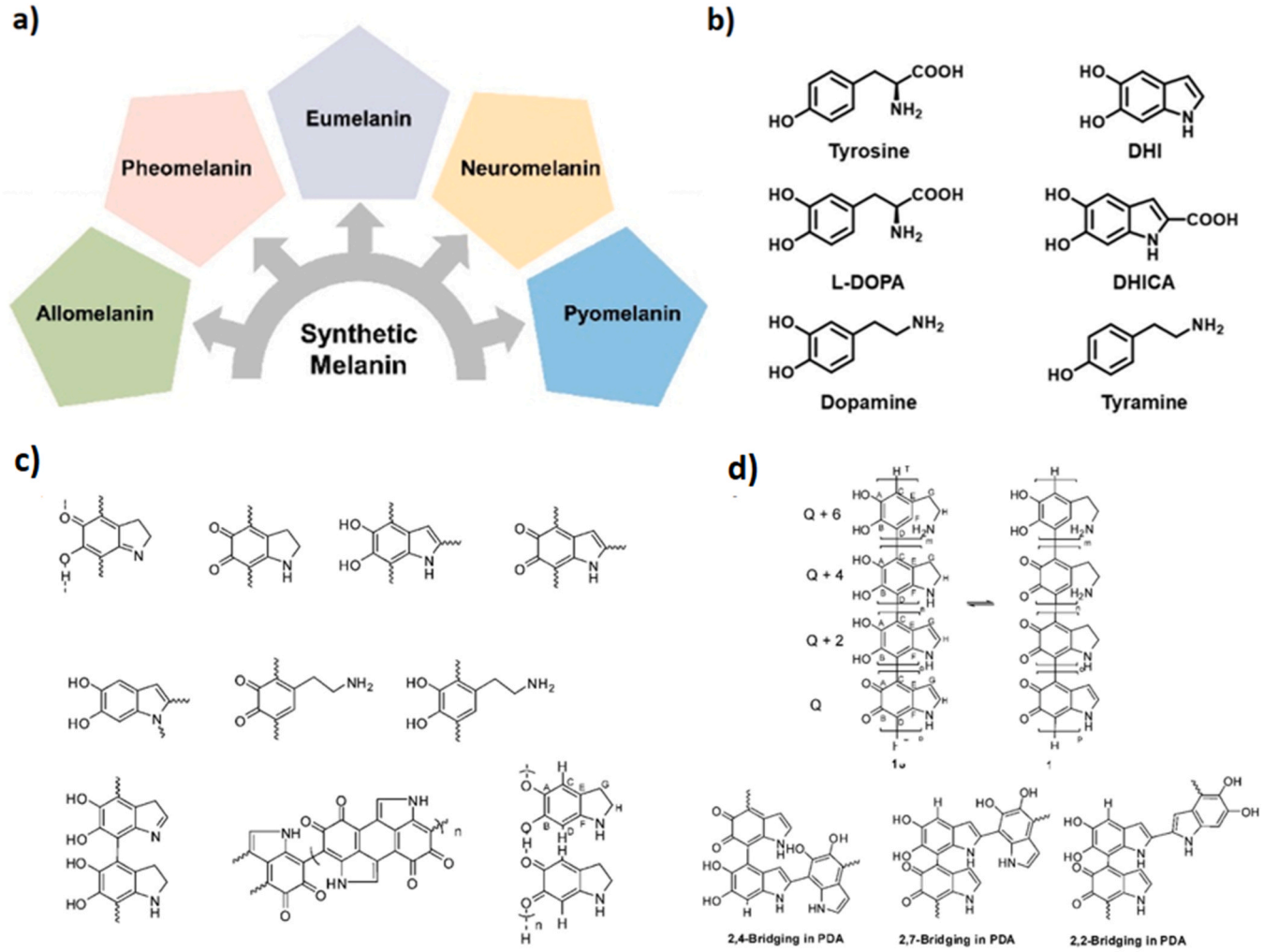

Fig. 1. (a) Five categories of melanin: eumelanin, neuromelanin, pheomelanin, pyomelanin and allomelanin (color: purple, yellow, pink, blue and green, respectively), (b) chemical structures of eumelanin monomers: tyrosine, l-3,4-dihydroxyphenylalanine (L-DOPA), dopamine, 5,6-dihydroxyindole (DHI), 5,6-dihydroxyindole- 2-carboxylic acid (DHICA), and tyramine. Adapted with permission from W. Cao, X. Zhou, N.C. McCallum, Z. Hu, Q.Z. Ni, U. Kapoor, C.M. Heil, K.S. Cay, T. Zand, A.J. Mantanona, A. Jayaraman, A. Dhinojwala, D.D. Deheyn, M.D. Shawkey, M.D. Burkart, J.D. Rinehart, N.C. Gianneschi, Unraveling the Structure and Function of Melanin through Synthesis, J. Am. Chem. Soc. (2021). https://doi.org/10.1021/jacs.0c12322. Copyright 2021 American Chemical Society [19] (c) Some structures of PDA proposed in the literature, (d) general structural proposal for PDA (only two possibilities out of other tautomers are shown) at the top of the picture and less likely alternative possibilities of bridging in PDA in the bottom of the picture. Adapted with permission from J. Liebscher, R. Mrówczyński, H.A. Scheidt, C. Filip, N.D. Haìdade, R. Turcu, A. Bende, S. Beck, Structure of polydopamine: A never-ending story?, Langmuir. 29 (2013) 10539–10548. https://doi.org/10.1021/la4020288. Copyright 2021 American Chemical Society [23]. (For interpretation of the references to color in this figure legend, the reader is referred to the web version of this article.)

significant progress was made in the synthesis and investigation of eumelanin based materials, especially in the case of PDA [6,20,23–28]. It is important to remark that PDA itself has been considered as the conventional stand-in for synthetic eumelanin.

Meanwhile, recent investigations suggest that PDA is distinct from natural eumelanins. Firstly, an essential characteristic of the structure of natural eumelanin is the 5,6-dihydroxyindole- 2-carboxylic acid (DHICA) unit. Certain eumelanins have more than 50% of these subunits [17,29]. In turn, PDA-based eumelanin contains mainly 5,6-dihydroxyindole (DHI) subunits, but this content is even further increased with the use of a Tris buffer, a commonly used base in synthetic routes (described in Sections 1.2.1 and 1.2.1.1) [19]. The chemical structures of eumelanin monomers, including those of which polydopamine is made, are shown in Fig. 1b. Secondly, PDA has more planar oligomeric structures due to the lack of the pendant –COOH responsible for a larger energy barrier of rotation and the inter-unit bond between adjacent moieties in DHICA [30]. Finally, ultrafast fluorescence spectroscopy and theoretical studies suggest that intramolecular excited-state proton transfer (ESPT) can only proceed in a DHICA (not in a DHI) dimer [31]. Therefore, the superior photoprotection based on ESPT is mainly absent in PDA-based materials [19,31].

Various studies have been performed on PDA, including chemical spectroscopy and mass spectrometry [19]. As a result, several hypotheses for the structure of PDA were described. However, two general categories can be distinguished. The first one is that PDA is a supramolecular aggregate of monomeric and/or oligomeric species– e.g. consisting of dopamine-quinone, dopamine, DHI, or eumelanin-like derivatives– that are held together through the weak interactions such as hydrogen bonding, p–p stacking, p–cation assembly and charge transfer [21,32–34]. The second category of hypotheses states that PDA is polymeric in nature and is formed by covalent coupling of the oxidized and cyclized dopamine monomers via aryl–aryl linkages [23,24]. Some PDA structures proposed in the literature are shown below (Fig. 1c and d).

Two great works are worth mentioning here. It was demonstrated that PDA could not consist of single indoline units just held together by hydrogen bonding [23]. Instead of this, the occurrence of the C−C connections between the monomer units was postulated. The presence of PDA oligomers in a different state of saturation (or unsaturation) was proved by high-resolution mass spectrometry (HR-MS). Moreover, this method evidenced that aminoethyl chains were found more likely than five-membered N-heterocycles in the oligomer PDA chain. Finally, a structural model of polydopamine was drawn, as composed of mixtures of different oligomers, with the occurrence of indole units and open-chain dopamine units [23].

In another recent paper, atomic force microscopy (AFM)-assisted single-molecule force spectroscopy (SMFS) was applied to investigate the structure of PDA [24]. SMFS is a technique that has been recognized as a powerful approach to study noncovalent and covalent interactions at a single-molecule level or intramolecular interactions. In the cited work, SMFS was used to study the cohesive and adhesive interactions of polydopamine, and it was shown that PDA films contain polymer chains of high molecular weight, with covalently connected subunits [24]. In turn, the intramolecular interactions included in PDA chains are non-covalent, which makes them weak and reversible. In addition, time-dependent force spectroscopy was applied during the early stages of the PDA coating formation. This study revealed that the film formation starts with the adsorption of a small oligomeric species, which then undergoes further polymerization to form higher-molecular-weight PDA chains finally. Researchers considered this as evidence of the polymeric nature of polydopamine [24]. Despite the ongoing controversy on the final structure of PDA, it is easily tailored, resulting in many optical properties, which are of great interest for photocatalytic and surface engineering applications.

1.1.2. Optical properties

Among some of the most striking and recently explored aspects of PDA, nanocomposites are their optical properties strongly dependent on their nano and microstructure. This section will describe some of the essential aspects and recent findings regarding the interaction of PDA membranes and coated materials with visible light.

1.1.2.1. Color. The majority of the PDAs materials are dark-black solids in color. There have been attempts to explain this feature based on the supramolecular arrangement of PDA chains, as described in the literature [23]. However, some studies indicated that the absorption spectrum of eumelanin material was derived from the subunits of its primary structure. Therefore, a characteristic black color was not a consequence of any higher-order organization [25]. In another study, the first demonstration of the deposition of PDA nanoparticles onto human hair was presented [35]. The influence of oxidation conditions on the resulting color was also investigated. Increasing concentration of base (ammonium hydroxide) resulted in a darker color, whereas the addition of H_2O_2 yielded warmer colors and orange/gold shades [35]. Melanin is a black component of human hair. Different content of melanin and its compositions are known to result in different individual colors [36]. It is puzzling that the same group of substances is responsible for the entire palette of countless colors in the natural world because melanin is essential for the structural color of organisms. Structural colors can be found in the vivid coloring of organisms such as birds and insects [37–39]. A famous example is the peacock feathers– inside them, rod-shaped melanin granules form a periodic microstructure that absorbs scattered light and provides its bright color.

In recent years, a significant contribution to the subject of structural colors was carried out, the obtained variations have been well described and documented in the literature [40–42]. In 2015 a method for obtaining non-iridescent bright structural color materials from black PDA particles that mimic black melanin granules was reported [43]. In this case, amorphous structures for non-iridescent structural colors and nanostructural elements for bright ones were combined. The normalized reflection spectra peaks of the materials obtained using PDA from 130 to 256 nm particles increased with the particle size from deep blue, blue, green, yellowish-green, orange to red. The experiment proved that the structural colors could be created by matching the size of the PDA black particles [43]. In another study, the formation of dopamine-melanin films of thickness range 50−200 nm, at an air/dopamine solution interface under static conditions was described [44]. Underneath these films, spherical melanin granules were formed in a bulk liquid phase. Firstly, the described structure colors were obtained as follows: the film edge and dish wall connections were cut off. Then, the solutions (under the films) were slowly pumped off using a small syringe to settle down the dopamine melanin film onto the dish bottom. Finally, the full dopamine-melanin thin-film reflectors were obtained after a drying procedure (Fig. 2a). The dependence of the dopamine concentration and reaction time on the film thickness was investigated, described in detail in Section 1.2.2. Thin film and granules with a double-layered structure were transferred onto a solid substrate in order to mimic the structures present in birds plumage (keratin layer)/(melanin granules) (Fig. 2b). The reflectance of the resulting surfaces was measured in the range of the visible light spectrum, and they exhibited a maximal reflectance value of 8−11%, which is comparable to that of bird plumage, around 11% (Fig. 2c) A different color spectrum of reflectors was obtained, depending on the film thickness. (Fig. 2d) [44].

Furthermore, the preparation of magnetically- responsive PDA particles using holmium-bearing surfactants (DDAH) was demonstrated in 2016. The PDA/DDAH particles were successfully collected by a magnetic field, causing a change in the structural colors of the resulting sediments [45]. In another study, the change in the structural color of hairy PDA particles caused by the increase in the distance between the PDA particles by modifying them with PHEMA-bearing “hairs” was

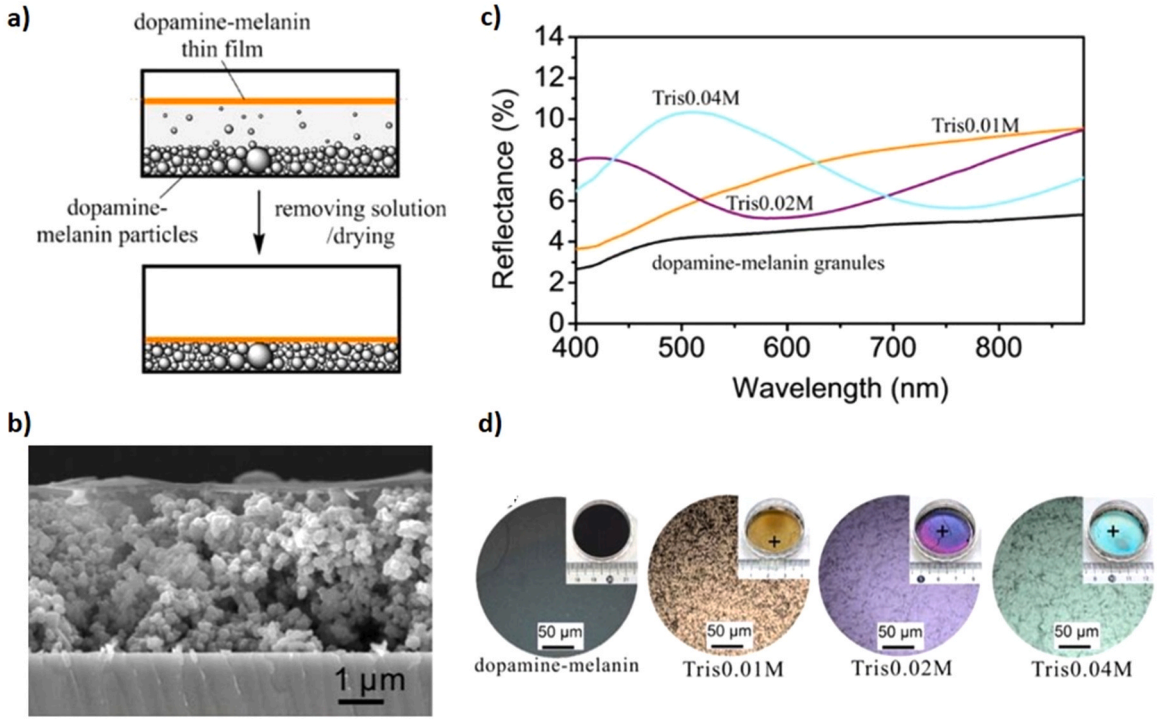

Fig. 2. (a) Scheme of the film-production procedure, (b) SEM photography of film and granules with a double-layered structure, (c) charts of the reflectance of the resulting surfaces in the range of the visible light spectrum, (d) Comparison of different colors of reflectors, depending on the Tris-buffer concentration - resulting in different thickness. Adapted with permission from T.F. Wu, J.D. Hong, Dopamine-melanin nanofilms for biomimetic structural colouration, Biomacromolecules. 16 (2015) 660–666. https://doi.org/10.1021/bm501773c. Copyright 2021, American Chemical Society [44].

described. The reflection peaks for the samples of the hairy PDA were red-shifted to 487 nm from the 473 nm reflection peak of the reference [46].

Significant progress has also been made in structural colouration based on thin films engineering by assembling PDA nanoparticles. Structural color change dependence on the film's thickness by utilizing the hygroscopicity of PDA particles [47,48] or controlling the thickness of multilayer films by the layer-by-layer (LBL) method [49] were investigated, and a variety of iridescent colors were obtained. PDA thin films can also be created via the self-polymerization of dopamine at the water/air interface (which will be explained in Section 1.2.2). With an appropriate synthesis procedure, a composite of nanoparticles with a thin film on their top can be created. This thin film act as a light-absorbing layer [44], or the structural colouration effect is obtained due to the hierarchical structure of the PDA membrane [41]. Later, uniform PDA thin film deposition on a silicon wafer resulted in large-scale and angle-independent structural colors with a high refractive index and uniformity [50]. Structural color engineering by coating a uniform polydopamine film of a precise thickness (from 30 to 250 nm) on a silicon nitride substrate was also investigated [51]. With the described procedure, one could tailor the reflectance of the surface along with the visible wavelength range. The color, a consequence of the interferential phenomenon, is uniform and easily tunable from blue to red by increasing the polydopamine thickness [51]. In another study, the method to tune color visibility and mechanical properties of angle-independent colloidal amorphous arrays (CAA) coating on a textile substrate with PDA was proposed. Both factors were improved, especially the visibility of the light colors [52].

1.1.2.2. Optical absorption. The optical absorption of PDA has been extensively studied and is well described in the literature, especially in a recent review that combines color, emission and absorption mechanism [53]. As already mentioned, PDA shares many characteristics with Melanin, which is a ubiquitous dark pigment widespread in many living organisms, is well known for protection against ultraviolet (UV) radiation due to its unique optical properties, primarily refractive and absorption specificity [53]. It is worth mentioning the role of the imaginary part of the refractive index (κ), which defines the bulk absorption property of a material. The imaginary index is linearly related to the absorption coefficient (α) according to the equation $\kappa = \frac{\alpha\lambda}{4\pi}$ where λ is a wavelength in meters. The imaginary refractive index of synthetic melanin nanoparticles monotonically decreases with a wavelength, from 0.33 (λ = 400 nm) to 0.09 (λ = 800 nm), while the light absorption of solid films depends on the parameters of the fabrication process [53]. Despite this, the PDA coatings/films have been much better tested for their optical properties. Different values of κ were reported, depending on the experimental preparation and aims of a given study. Firstly, from 0.286 (λ = 400 nm) to 0.083 (λ = 800 nm) [54]. Secondly, 0.064 for λ = 500 nm [55]. Finally, $\kappa \approx 0.2$ at λ = 260 nm and $\kappa \approx 0$ for λ > 460 nm [51].

The refractive index (n) is a significant parameter that affects the light scattered by a material. The Light scattering ability is increasing with the increment in the n parameter. Melanin's refractive index is higher than most polymers and biomaterials [53,56]. Reported values were 1.7 < n < 1.8 in the 400–800 nm region [47,57,58], ~1.7–1.85 in the 400–1000 nm region [59] and ~1.55 in the 400–800 nm region for PDA and melanin particles [60]. In turn, for thick PDA films, the value ~1.5 in the 300–900 nm region was reported [51]. Also, the real part of the refractive index was found to be 1.74 at a wavelength of 589 nm [48]. In general, the refractive index of PDA depends on the materials' microstructure and particle shape or size and thus the preparation method [61].

In recent years, the influence of various factors on the optical properties of PDA has been noted. According to the cited study, one can control these parameters by using UV radiation [59]. PDA exhibits a peak (~500 nm) in the real part (n) of RI with the highest values reaching 1.81 ± 0.01 for before UV treatment and 1.88 ± 0.01 for after UV treatment. Moreover, this treatment increases n, up to 4.5%, from

360 to 1700 nm and around 25% increment in the imaginary (κ) component for both regions below 600 nm (~36% especially < 400 nm). The increase in the κ component is exciting as melanin becomes a more efficient UV blocker after UV exposure. Surprisingly, the melanin absorbs more light (< 600 nm) after intense UV exposure, which could be a mechanism to explain melanin's photoprotective behavior [59].

1.1.2.3. Fluorescence. Synthetic eumelanins have meager radiative quantum yields and, simultaneously, efficient UV and visible energy dissipation characteristics [62]. It has been postulated that the high degree of polymerization and the complex molecular structure, leading to intramolecular or intermolecular stacking of backbones, was unfavorable for their fluorescent properties [63,64]. In turn, in a chemical disorder model with non-covalent self-assembly, the oligomers of DA were the primary source of a strong fluorescence. Therefore, the reduction in π–π bondings between the structural units in PDA seems to be a significant improvement for fluorescent properties [65,66]. Different groups have proposed four (iv) fabrication strategies during the most recent years: oxidation and degradation (*i* and *ii*), which aim at regulating π–π stacking interaction; conjugation (*iii*), in order to decrease intermolecular or intramolecular coupling, and carbonization (*iv*) by introducing sp^2 carbon inside the nanoparticles [67].

For PDA coatings, the same principle also applies. Investigation of the quenching efficiency (QE) of PDA of protein-PDA films have been done and described [68]. The thicker was the film, the more prominent was quenching effect, most possibly due to an increase of density of the conjugated chain in the PDA film. The fluorescence of a labeled protein was significantly quenched (up to 80% QE) when attached to thick PDA film. The influence of pH value and deposition time factors turned out to be as follows: a higher pH value or longer deposition time resulted in thicker PDA film (see Section 1.2.1.1) and simultaneously lowered fluorescent efficiency [68].

In the case of nanoparticles, their size significantly influences their fluorescence properties. Varying the DA concentration and NaOH:DA ratio in synthetic melanin nanoparticle synthesis could be used to achieve satisfactory control of batch mean diameter in the sub-100 nm range (from 28 to 117 nm) [69]. A method for synthesizing fluorescent PDA NPs with a diameter of less than 10 nm was developed [70]. Above mentioned structures were formed by oxidative polymerization in NaOH solution (pH 11) with magnetic stirring for 30 min at room temperature and then introducing the hydrochloric acid to reduce the polymerization speed. The prepared solution was filtered using a 0.22 μm aperture to remove large nonfluorescent PDA NPs and achieve even higher purity [70].

A different experiment showed that fluorescent PDA nanoparticles have an exciting potential to work under extreme conditions [71]. It was the first reported strategy for the large-scale synthesis of fluorescent PDANPs at room temperature via self-exothermic redox reaction in a rapid, facile, and green process. The following synthesis conditions were proposed as the optimum conditions to prepare fluorescent PDANPs.: the buffer pH value at 6.0 and DA concentration with 7.0 mg ml^{-1}. The as-prepared nanoparticles could be used in a wide pH range and shown good performance to resist high ionic strength. Moreover, their corresponding fluorescence intensity almost remained constant for 120 min [71]. Further and in-depth explanations of PDA properties can be found in an extensive and recently published review article [67].

1.1.2.4. Raman scattering and infrared spectroscopy. Despite the amorphous nature of PDA, several studies have been able to probe some of the structural arrangements of PDA by optical methods allowing for the identification of the organic constituents of PDA, most of which show strong similarities with Eumelanin. Some of them will be mentioned in this chapter. It is essential to mention that most of the Raman studies have been performed on coatings and thin films, while the infrared spectra have been observed in both coated nanoparticles and films/coatings. In the case of Eumelanin, it shows two characteristic broad Raman peaks, similar to the G and D bands in graphene and graphite. They were originating at around 1380 cm^{-1} from the linear stretching of C–C bonds within their aromatic rings and at around 1580 cm^{-1} from in-plane stretching of the aromatic rings [72]. For a further, more in-depth analysis, deconvolution of these broad peaks can be performed. The deconvolution of a wide peak at 1596 cm^{-1} by two components via Lorentzian fitting shows the following values: 1525 and 1596 cm^{-1}. Furthermore, the analysis showed a clear relationship correspondence of the present peaks 1206 to C–OH or/and C–O, 1386 cm^{-1} to N–H and C═O, 1528 to C═C, and 1595 to C–N [73]. Table 1 below summarizes the respective frequencies for the characteristic signals from PDA in the most cited and/or recent publications.

The following experiment can be cited as an exciting example of studying the interaction of polydopamine with infrared. Characterization of the growth of polydopamine thin films (on Si substrate) was carried out by means of in situ IR spectroscopic ellipsometry [76]. The amplitude of vibrational bands increased with the ongoing oxidation process from time $t = 1$ h to $t = 22$ h. It was additionally shown that the PDA films are stable in air conditions as the infrared spectra (bands assigned to polydopamine) did not change significantly over 30 days. Moreover, the influence of the different oxidation processes with the KIO4 as an oxidant was investigated in this study. This was achieved by recording the spectrum of the DPA films, which showed a strong absorption around 1724 cm^{-1} assigned to the formation of C═O groups in the PDA film, probably in place of numerous ─OH groups occurring in PDA film achieved in Tris buffer [76]. Table 2 below summarizes the respective frequencies for the characteristic signals from PDA in the most cited and/or recent publications.

When considering the signals originated from polydopamine-based photocatalytic nanocomposites, in the majority of cases, the resulting Raman or infrared spectra are a combination of the stacked materials [80]. For example, it was shown that when comparing the Raman spectra of MoS_2 and PDA, the spectrum of MoS_2@PDA nanoparticles was essentially the "sum" of the two. In this case, the two more substantial peaks at 385 cm^{-1} and 409 cm^{-1} originate from MoS_2 and the two weaker ones at 1353 cm^{-1} and 1583 cm^{-1} correspond to PDA [80]. Nevertheless, some interesting effects were recently reported, which we will discuss briefly. As it was described in the other study, before modification of ZnO nanorods with the PDA, composites had specific FTIR peaks at 400 cm^{-1} and 560 cm^{-1}, which correspond to ZnO vibrational modes. The formation of ZnO/PDA composites resulted in a shift of the FTIR peaks position by 12–20 cm^{-1} to lower values of wavenumbers [81]. In another study, CdTe@PDA-MPA QDs were synthesized following a standard method reported in the literature by using mercaptopropionic acid (MPA) as a capping agent. Raman spectroscopy measurements revealed the differences in the structure of the CdTe@MPA-PDA particles with respect to PDA, namely, the signal corresponding to C-N is noticeably enhanced by using the laser of 532 nm. Thus, according to these results, the authors concluded that it is possible to suggest that CdTe@MPA-PDA particles possess a higher number of indole moieties than pure PDA particles. Moreover, the

Table 1
Exemplary, frequently cited polydopamine-derived peaks recorded by Raman spectroscopy with references to the literature.

Peak origin	Peak position [cm^{-1}]
C═C Vibration in the aromatic ring	1607, 1581 and 1543 [74] 1528 [73]
Deformation of catechol groups	1581 [75]
N–H bending vibrations	1516 [74]
C═C or N–H	1386 [73]
Stretching of catechol groups	1370 [75]
Aromatic C–N stretching mode of the indole structure	1337 [74]
C–O or C–OH	1206 [73]

Table 2
Exemplary, frequently cited polydopamine-derived bands recorded by mid-infrared spectroscopy with references to the literature.

Band origin	Band position [cm^{-1}]
Methylene groups in PDA(—CH_3)	2870, 2940 [77] 2930 [78]
—C═O in the quinone-like structure	1728 [76]
C═C stretching in the ring or —NH_2	1596, 1608 [76]
C—C stretching in the benzene ring or —NH in the heterocycle	1510, 1518 [76]
C═C in rings	1450 [76]
O-H vibrational bending in catechol groups	1350 [79]
C-O stretching vibrations	1275 [79]

relative intensity of the FTIR band corresponding to -OH stretching mode for CdTe@MPA-PDA particles was higher than that for PDA. Furthermore, the shifts of the FTIR bands corresponding to the aromatic ring, C-N vibrational modes, and a new intense band assigned to $\Upsilon_{C\text{-}H}$ (at 648 cm^{-1}) suggested the modification of the polymeric structure for CdTe@MPA-PDA particles [82].

1.1.3. Mechanical properties

Although typically disregarded as merely an engineering aspect of materials, the mechanical properties of PDA are of crucial importance towards application. The adhesive nature of PDA and its mussel-inspired origin suggest a robust mechanical performance. However, it was shown that the PDA functional coatings exhibit rather poor mechanical performance [83]. The first data was reported for melanin in dry conditions, incited study Young's Modulus was equal 3,2 ± 0,53 GPa [84]. For Polydopamine coatings, this value was measured both experimentally (from 4,3 to 10,5 GPa) and in silico (5,0 ± 1,7 GPa) [85,86]. Other experimental works have investigated the mechanical response experimentally by nanoindentation, showing a soft response of 2.3 ± 0.8 GPAs [87]. Thin films of PDA have been recently investigated in both free-standing [88] and supported manner [89], with values of 6–12 GPa and 13 ± 4 GPAs, respectively. Despite the differences, many attempts to enhance the mechanical properties of PDA have been reported (i.e. by incorporation of oxidizing agents, cross-linkers, or carbonization of the films at ultrahigh temperatures) [83].

A computational model of the heterogeneous PDA system by mimicking the polymerization process of 5,6-Dihydroxyindole via controlled in silico covalent cross-linking between DHI monomers was proposed [86]. It was found that simulated Young's Modulus was a function of the degree of crosslinking, and the value was in a range of 4.1–4.4 GPa. At the highest degree of cross-linking (equal to 70%) the model mimicked and supported the previously proposed averaged tetrameric (linear and cyclic) structures for poly(dopamine) and melanin and resulted in mechanical properties in agreement with experimental and simulation studies on natural melanin. The possibility of tuning the chemical structure and the mechanical properties of PDA coatings by controlling the extent of polymerization was also demonstrated (via in silico). Based on these experiences, conclusions can be drawn that in order to achieve enhanced mechanical properties of the PDA coatings, longer reaction time or more oxidative agents should be applied to introduce more cross-links in the system [86].

In turn, a straightforward way to improve the mechanical properties of PDA coatings turned out to be a thermal treatment process at 130 °C [83]. Changes in properties such as resistance to dissolution (under solvent conditions that usually dissolve PDA coatings) and scratch resistance were observed. Molecular mechanical analysis performed by single-molecule force spectroscopy (SMFS) revealed significant changes that suggest enhanced intermolecular interactions in the structure. Thus, these results suggest that thermal treatment causes chemical and structural changes in the bulk PDA coating and simultaneously improving its mechanical performance [83].

Another physical method of improving the mechanical properties of the PDA coatings relied on the Blue diode Laser Annealing (BLA) [90]. A partial graphitization process plays a significant role in the mechanical strengthening of polydopamine films and can be easily controlled by modulating the laser power (Fig. 3a). In this experiment, the laser annealed PDA coatings (LAPDA) were obtained. It was shown, that the roughness of LAPDA film can be reduced from ~230 to ~15 nm by means of selective nanoparticles ablation during the BLA process (Fig. 3b). It is visible in the diagram that the roughness decreases (Fig. 3c). However, the authors stated that the main contributor for roughness is the randomly agglomerated PDA NPs, not the initial film thickness. During the scratch test with a diamond tip, the average scratch depth for the pristine PDA was 18.5 ± 1.1 nm under 50 μN average load, whereas the LAPDA films were still undamaged at this load (Fig. 3d). Scratches in LAPDA films were only observed at a much higher load, 500 μN (Fig. 3e). Herein, the scratch depth of a 37 nm thick LAPDA film was only 2.1 ± 0.8 nm, whereas the scratch depth of a new PDA film was equal to the whole film thickness (248 nm). This result is more than a 100 times increase in scratch resistance [90]. For better reference, the authors performed scratching experiments on bare substrates (TiO_2 and quartz) at a load of 500 μN, resulting in average scratch depths of 16.8 ± 1.2 nm for TiO_2 and 10.5 ± 1.0 nm for quartz (Fig. 3e). This indicated that the scratch resistance of the organic LAPDA film is even better than hard inorganic solids. Moreover, the described procedure did not adversely affect the secondary advantages of the PDA coatings, such as antifouling properties [90].

The stability and adhesion strength of polydopamine free-standing films may depend on many factors [91]. Such nanomembranes are stable under gentle mechanical manipulation and can be laminated underwater, in an orientation-dependent manner, to polydimethylsiloxane (PDMS) elastomer substrate. Two morphologically different surfaces of the PDA membrane can be distinguished, the basal side, which readily adheres to PDMS in underwater environments, and the apical side, which does not adhere. In the cited study, characteristic delamination rates were independent of the PDA thickness. Moreover, the delamination process is slower for films synthesized from more highly concentrated precursor solutions (e.g., 10 mM dopamine). This may be explained by the cooperative adhesive action of primary amines in the PDA films, i.e. these prepared from low aqueous concentrations of dopamine (e.g., 0.5 mM) contain lower concentrations of primary amines. Also, delamination of the PDA films is significantly accelerated by solutions containing group I cations. The time for complete delamination is 12 h in the absence of NaCl and 1 min in the 200 mM NaCl solution (pH 10) [91].

During their synthesis, the adhesion of polydopamine thin films to the metals oxides substrates is multimodal. It was experimentally shown that hydrogen bonding between PDA and SiO_2 is disrupted in monovalent salt solutions [91]. Metal cations (e.g. sodium) may competitively adsorb to the silica surface and thus, disrupt interfacial hydrogen bonds. Raising the pH of the NaCl solution from pH 9–10 has deprotonated catechols. However, adhesion may be stabilized by increasing the precursor's concentration during film synthesis or by adding multivalent cations in the delamination buffer (i.e. Ca^{2+}, Fe^{3+}). Thus, it was stated that catechol groups within a PDA network are necessary but not sufficient for underwater adhesion [91].

In the case of nanoparticles, a suspicion may appear that the mechanical properties are not that important as in the case of coatings. However, it has been proven that they depend on the size of the NPs [92]. In a recent study, the impact of NH_4OH / dopamine ratio on the NPs diameter and further on the Young's Modulus was investigated. Indeed, NPs hydrodynamic diameter was strongly dependent on the ratio mentioned above, with the NPs size decreasing from around 300 nm (for the ratio 10) to approximately 60 nm (for the ratio 50). It is worth underlining that the Young's Modulus of NPs decreased with their size. PDA nanoparticles with a mean diameter of 290 ± 2 nm, 161 ± 2 nm, 131 ± 2 nm and 106 ± 2 nm, exhibited a Young's modulus of 480 ± 108 MPa, 365 ± 59 MPa, 313 ± 76 MPa and 188 ± 42 MPa respectively. A given explanation suggested that PDANPs with different

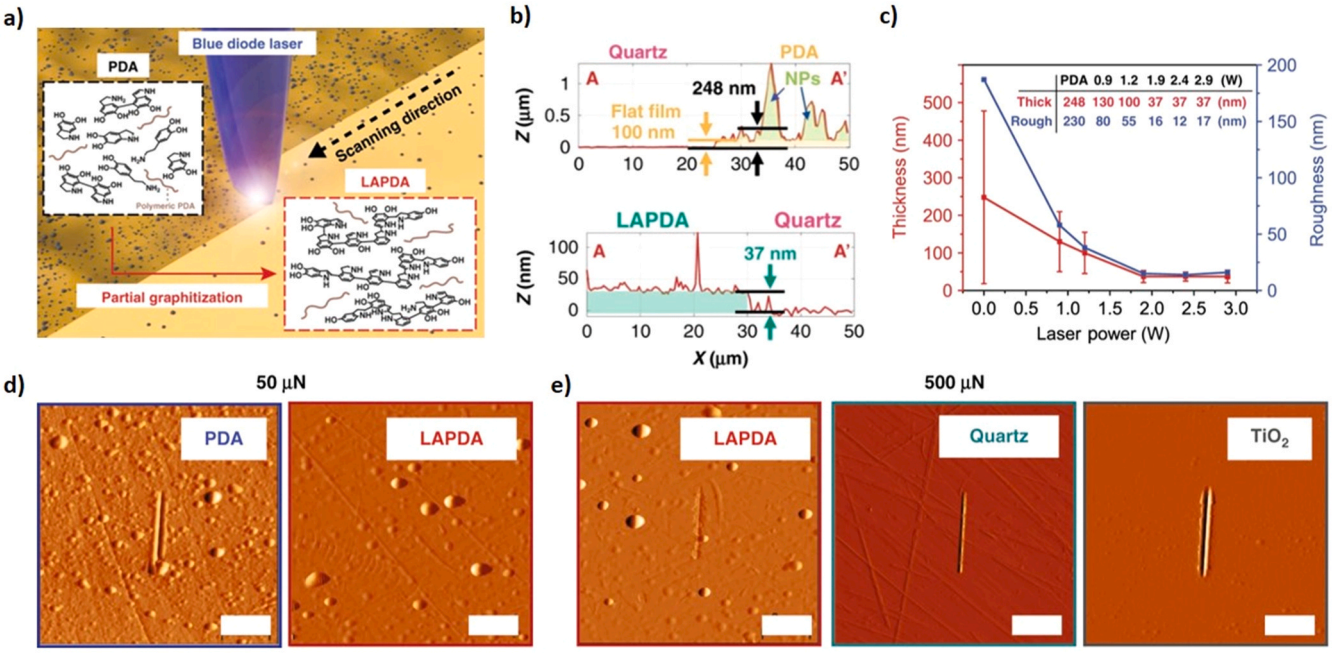

Fig. 3. (a) Mechanical strengthening via partial graphitization induced by the Blue diode laser scheme, (b) charts of the roughness of the sample with a clear improvement after BLA process, (c) thickness and roughness dependence on the laser power, (d) results of the scratch resistance tests with a diamond tip under the; (d) 50 and (e) 500 μN loads (the scale bar is 2 μm) [90].

sizes shows different geometric pecking orders of the oligomers/polymers in the core of NPs. Compared to other polymeric nanomaterials, the Young's modulus values for PDANPs are relatively low [92]. This could be related to the nature of the polymer but also their self-assembly process. As mentioned before, PDA exhibits a complex and heterogeneous structure, being the main reason behind the continued studies and debate in its polymerization mechanism [23].

Despite the mechanical differences and still open debate on the elastic modulus of PDA, the literature suggests that PDA shows a rather significant wear resistance, which combined with their inherent tolerance to water, provides essential protection for sensitive or easily degradable photoactive materials, as it will be shown in Section 2.3.

1.1.4. *Wettability*

Despite a variety of available materials for energy production and water remediation described in the literature, a large number of them suffer from poor water wettability, which is a critical aspect of their application. As expected, the high hydrophilic behavior of the surfaces is highly desirable [93,94]. The modification with PDA coatings may give rise to new perspectives by tuning their hydrophilic properties. In a pioneering study in 2011, Haeshin Lee and coworkers used the adhesive properties of PDA to increase the hydrophobicity of different surfaces by using PDA as an interfacial process [95]. However, detailed studies were reported recently, exploring the wettability of PDA-modified melanine foam (PDA-MF) by analyzing their water contact angle. Water droplets could be quickly absorbed into the PDA-MF, and it was spread over the surface within 0.5 s, indicating the super hydrophilic properties of the PDA-MF surface. Authors suggest that this can be ascribed to the abundant catechol and amine groups originating from the PDA coating [96]. In another work, MoS_2 was facilely modified by hydrophilic polydopamine (PDA) coating in a self-polymerization process. In that study, the samples were denoted as MoS_2/PDA-t, wherein t stands for the soak time. The wettability was characterized by the water contact angle measurement, revealing a typical hydrophobicity of the MoS_2 surface with an angle equal 71.0°. Importantly, with the coating of PDA, MoS_2/PDA-4, MoS_2/PDA-12 and MoS_2/PDA-24 showed decreased values of 60.50°, 52.00° and 42.50°, respectively [97] Moreover, PDA was also used to modify the surface of steel [98], polymers [99] and carbon [100,101] materials into more hydrophilic. In one study, graphite carbon/PDA (GC/PDA) electrodes- to be used as electrochemical biosensor interfaces- were prepared in another study, and again, the PDA coating turned out to be highly beneficial in terms of tuning the hydrophilic properties. The measured water contact value for the bare GC was 80 ± 2°, while for all samples from GC/PDA group, it was below 50° [101].

1.1.5. *Electrical conductivity*

In the 1970s, reversible electrical switching properties of eumelanin were discovered [15]. Since then, melanin, and in particular eumelanin, has been widely regarded as an amorphous organic semiconductor. In this model, the Highest Occupied Molecular Orbital (HOMO) level corresponds to the valence band in semiconductor whereby the Lowest Unoccupied Molecular Orbital (LUMO) level correspond to the conduction band in semiconductors [14]. As it was mentioned in Section 1.1.1, the eumelanin structure is composed of aromatics and conjugated molecules stacked by the π-bondings [23]. As a result, both HOMO and LUMO levels in eumelanin are characterized by the π-system. The movement of charge carriers through this system would lead to conductivity and semiconducting properties in eumelanin [14]. Without moisture, eumelanin and polydopamine show typically low values across 10^{-13} S m^{-1} in a vacuum, while under a humid atmosphere (relative humidity = 100%), it was reported to increase up to 10^{-5} S m^{-1}. These variations in humidity would change the local dielectric constant, as water is being absorbed by eumelanins [102]. In turn, another model describes eumelanin as an electronic-ionic hybrid conductor rather than an amorphous organic semiconductor. It was demonstrated that upon the absorption of water, free carriers would be generated according to the comproportionation reaction. Simultaneous production of extrinsic free radicals (electrons) and hydronium ions (protons) gives rise to hybrid ionic-electronic behaviors [18].

The method of preparation may be necessary for the electrical conductivity of polydopamine [103]. By using oxidative chemical vapor deposition (o-CVD) it was possible to generate conjugated and conductive PDA from dopamine [103]. The experimental setup of the o-CVD in

the tube furnace was shown (Fig. 4a). During the described procedure, PDA was deposited on glass substrates in the presence of the DA monomer, oxidation agents and under N_2 atmosphere at a reaction temperature of 300 °C. O-CVD method induces rapid growth of PDA, with a deposition rate of 5–6 nm per minute (Fig. 4b). In order to investigate the surface properties, i.e. topography and roughness, the authors applied atomic force microscopy. The images revealed homogenously formed, pinhole-free surfaces (Fig. 4c). To examine the structural variety of o-CVD PDA, thus the influence of discrete structural designs on the electronic properties, Fourier transform infrared spectroscopy, and Raman spectroscopy studies were applied (Fig. 4d and e, respectively). For a better comparison, o-CVD PDA was placed on the charts together with the actual monomer dopamine hydrochloride and solution-polymerized PDA. The obtained polydopamine layer not only turned out to be chemically consistent with the reference but also showed interesting electrical properties with a conductivity of 40 S m^{-1} at 300 K, which was measured by using 4-probe specimen, over a representative time scale and in inert conditions (Fig. 4f) [103].

Moreover, PDA can be carbonized by pyrolysis (heat treatment in the atmosphere of protective gas) as a result, carbonized PDA (cPDA) is created and exhibits high electrical conductivity [104–106]. Reported values of electrical conductivity of cPDA, were as high as 1.2×10^5 S m^{-1} [107] and 2.6×10^5 S m^{-1} [105]. Further research was carried out to investigate the influence of pyrolysis temperature on Seebeck coefficient, electrical conductivity, and power factor respective to annealing temperature (600, 700, 800 and 900 °C) [104]. For all temperatures, Seebeck coefficients showed negative values, indicating that cPDA is an n-type semiconductor. The highest electrical conductivity (1×10^4 S m^{-1}) was reported for a sample pyrolyzed at 800 °C [104]. In another study, graphene films (GFs) were fabricated by vacuum filtration of graphene oxide-polydopamine (GO-PDA) solutions and graphitization of the obtained GO-PDA films. The thermal annealing temperature had a significant effect on the electrical properties of the materials. The high-temperature thermal annealing fully repaired the defects of GO sheets and increased the grain size, leading to the increase of the electrical conductivity, up to 9×10^5 S m^{-1} (Fig. 5: a) [108]. Simultaneously, according to other research, PDA and cPDA films heat-treated below 600 °C were electrically insulating; thus- no Seebeck voltage could be measured. In turn, for samples heat-treated between 600 and 900 °C, a significant increase in electrical conductivity was observed with increasing temperature of treatment, reaching 1×10^4 S m^{-1} (Fig. 5: b) [104].

There are available reports about composites modification with the PDA towards better electrical properties, and some of the latest will be described briefly. In one of them, composite fibers were prepared through PDA modification and electroless plating with the Ag nanoparticles. The deposition rate of PDA onto the fiber surface was significantly improved by using $CuSO_4/H_2O_2$ as an oxidative mixture. The electrical resistance of PET/PDA/Ag fibers was measured by a two-point multimeter, exhibiting a value of 0.76 Ω over a length of 1 cm, indicating good conductivity after deposition of silver nanoparticles. After five cycles of standard washing, the electrical resistance of the fibers increased to 1.78 Ω over a length of 1 cm, indicating good stability of obtained composites [109]. Carbonized delignified wood/ polydopamine composite (CDW/PDA) embedded in epoxy was designed, where the most beneficial pyrolysis temperature was 1200 °C. This exhibits higher EC (0.46 S m^{-1}) than its counterpart filled with plain CDW (0.32 S m^{-1}). Authors state that the nitrogen atoms introduced to the graphite-like lattice served as electron donors, simultaneously promoting the n-type conductivity and improving the overall electrical conductivity [110]. In turn, PDA/rGO/Cu/STA (stearic acid) cotton was prepared by immersing the cotton fabric in PDA/rGO and copper ion-containing solutions. According to the authors, PDA/rGO cotton is nonconductive. However, after in situ growth of the copper nanoparticles, the resistance of PDA/rGO/Cu decreased to 0.85 Ω. After modification with stearic acid, the resistance increased slightly to 0.95 Ω. In order to investigate the stability of the electrical properties of the fabric, the bending test was carried out for 1000 cycles, with a slight increase in the resistance noted. However, the resistance was still lower than 4 Ω after 1000 bends [111].

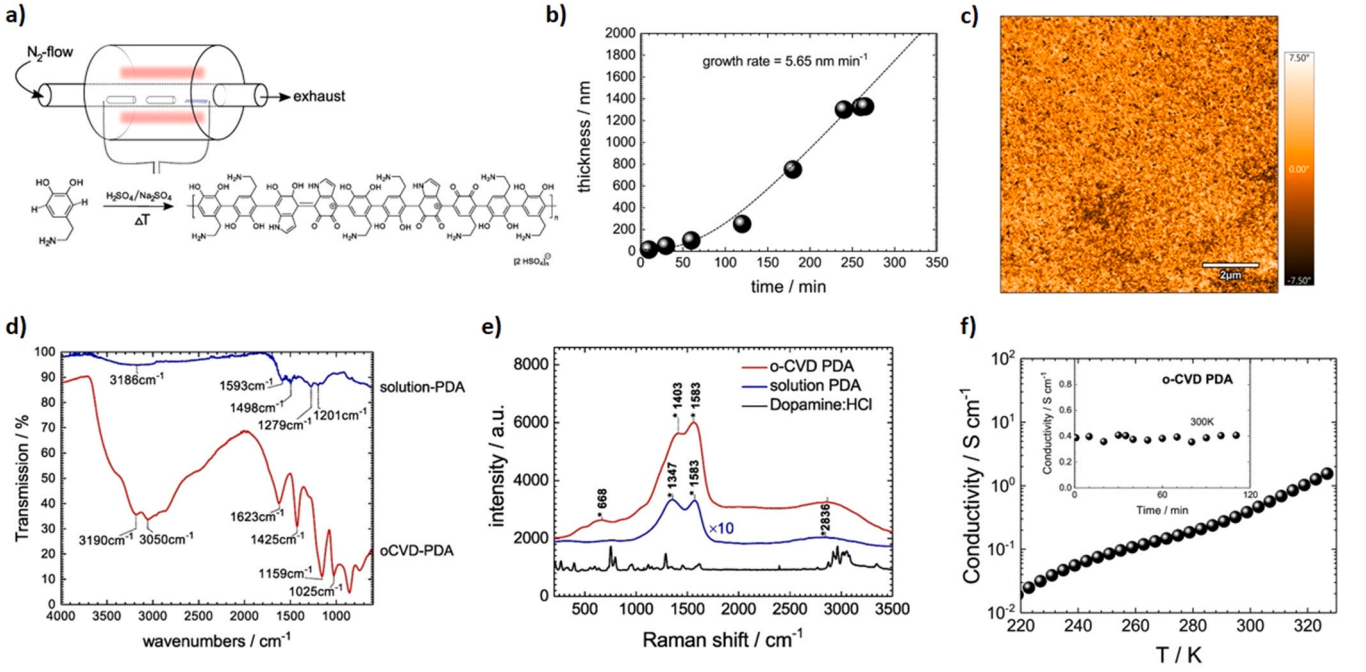

Fig. 4. (a) Experimental setup of the o-CVD in the tube furnace for preparation of conjugated and conductive PDA, (b) deposited polydopamine layer growth rate presented on the chart, (c) AFM image of the obtained surface, (d) Fourier Transform Infrared (FTIR), (e) Raman spectra of the obtained samples with clear bands originating from PDA, (f) electrical conductivity vs temperature chart for obtained coating. Reprinted from Thin Solid Films. 645, H. Coskun, A. Aljabour, L. Uiberlacker, M. Strobel, S. Hild, C. Cobet, D. Farka, P. Stadler, N.S. Sariciftci, Chemical vapor deposition - based synthesis of conductive polydopamine thin-films, 320–325, Copyright (2021), with permission from Elsevier [103].

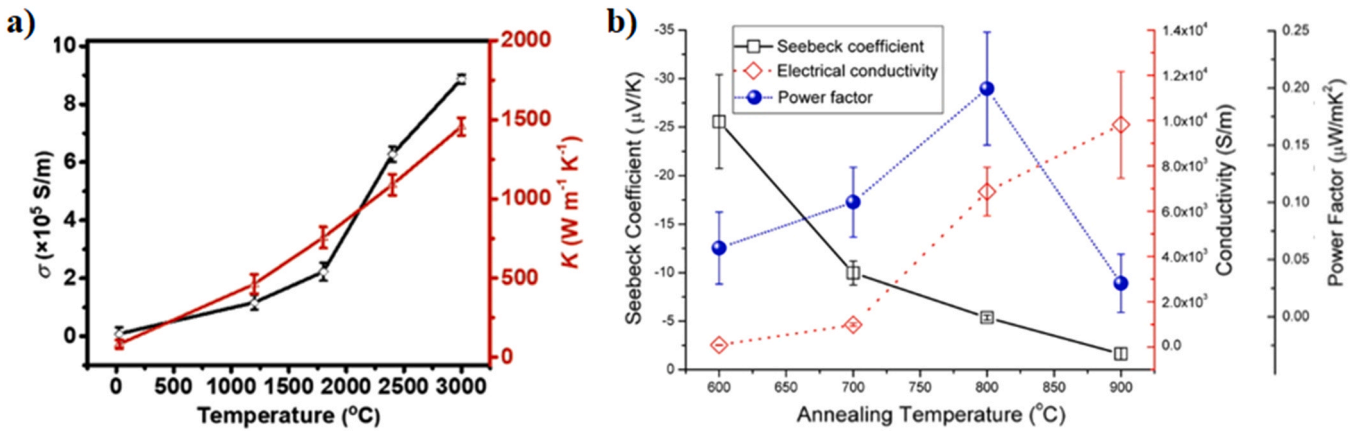

Fig. 5. (a) Electrical (black) and thermal (red) curves representing conductivities of GF-2 thermally annealed at different temperatures. Reprinted from Carbon N. Y, 149, R. Zou, F. Liu, N. Hu, H. Ning, X. Jiang, C. Xu, S. Fu, Y. Li, X. Zhou, C. Yan, Carbonized polydopamine nanoparticle reinforced graphene films with superior thermal conductivity, Copyright (2019), with permission from Elsevier [108]. (b) Seebeck coefficient, electrical conductivity, and power factor respective to annealing temperature. Adapted with permission from H. Li, Y. V. Aulin, L. Frazer, E. Borguet, R. Kakodkar, J. Feser, Y. Chen, K. An, D.A. Dikin, F. Ren, Structure Evolution and Thermoelectric Properties of Carbonized Polydopamine Thin Films, ACS Appl. Mater. Interfaces. 9 (2017) 6655–6660. https://doi.org/10.1021/acsami.6b15601, Copyright 2017 American Chemical Society [104]. (For interpretation of the references to color in this figure legend, the reader is referred to the web version of this article.)

Another work revealed the effect of three metal ions, i.e., Cu^{2+}, Mg^{2+} and Na^{+}, on PDA synthesis and its further conversion to cPDA. Both Cu^{2+} and Mg^{2+} interacted with PDA, which therefore influenced the electrical properties of heat-treated thin films. However, the effect was neither clear nor stable. Depending on the pyrolysis temperature, the presence of cations increased or decreased the effect. In contrast, the presence of Na^{+} ions during the synthesis of PDA did not show any significant effect [106].

It is important to remark that the previous results pose a critical case towards polydopamine as a carrier extractor and conductive junction. Moreover, the variations of electrical conductivity, which are increasing with hydration levels, provide an essential benchmark for their use in environmental remediation and photocatalysis.

1.1.6. Other electrochemical properties

Although, as described earlier in this article, there is no scientific consensus yet on the structure of polydopamine, important properties resulting directly from its structure have been identified, e.g. bandgap energy value. In the cited study, the electronic properties of polydopamine and the influence of electron beam irradiation (EBI) were studied [112]. In order to achieve this, PDA powders and films were exposed to an electron beam with various doses to investigate the effect of radiation on morphology, structure, and bandgap – which is the most important from the point of view of this review. The bandgap energy was designated with the UV Vis absorption spectra, and by Using the Kubelka--Munk function, the obtained value was 1.56 eV. The energy of the HOMO and LUMO levels were calculated as − 4.85 eV and − 3.29, respectively. The most significant influence of the EBI modification was assigned to the irradiation dose equal to 50 kGy [112].

The changes in bandgap (and other properties) were attributed to the influence of EBI on the conjugation system. In addition, the distortion of phenyl rings, irradiation-induced ring-opening reaction, the formation of the intramolecular hydrogen bond, and the enhanced interaction between PDA and substrate could be another reason for these changes [112]. Furthermore, PDA exhibits interesting electrical properties when combined with systems with various types of materials. According to the current state of the art, it behaves differently in combination with organic and inorganic materials [112–114].

1.2. Synthesis mechanism for nanocomposite

1.2.1. Direct polymerization

Since the discovery of polydopamine [4], its exact polymerization has not been unveiled, and its actual structure is still unknown. Thus, different theories about the structure and the polymerization process have been proposed in the past 10 years [23]. As a reminder, it should be emphasized that in this review, we shortly summarize some of them, and we aim to explain their main contributions to the PDA field and its current state of the art, especially towards the application of PDA in photocatalysis. It is indubitably that having a clear picture of the molecular structure of PDA would make any attempt to understand its electronic, catalytic and physicochemical properties a more manageable task; nevertheless, by carefully compiling experimental results, a few of the structural properties of PDA can be inferred and analyzed.

PDA can be synthesized in the laboratory by an oxidative polymerization of dopamine hydrochloride induced by alkaline pH, typically 8 or 8.5. In the overwhelming majority of the experiments carried out so far, Tris buffer (tris(hydroxymethyl)aminomethane) is used to obtain the previously mentioned appropriate pH. The molecular mechanism of formation of the polymer mentioned above is supposed to share several characteristics with that of melanin biosynthesis [115–117]. Dopamine is transformed through an oxidative pathway into 5,6 dihydroxyindole to continue through further polymerization steps in such a process. Due to those similarities, this shows a possible initial PDA structure based on melanine possible structure, which units are DHI dimers, trimers or tetramers [118–120] that are covalently bonded [4]. Despite that, it has been reported that aside from this covalent polymerization way, some studies show possible physical self-assembly between dopamine and DHI forming a physical trimer made by one molecule of DHI and two of PDA that interacts by π stacking and hydrogen bonds, which could play an important role in the PDA creation [21]. Those two pathways are not mutually exclusive, and in fact, both of them could contribute to PDA formation. C-C connections that hold the PDA units were demonstrated by using several analytical methods [23]. Also, it was shown that those units are not made only by DHI and dopamine dimers or trimers. Instead, they could be made by DHI and indoledione units with different degrees of saturation. Additionally, by HR-MS it was proved that also an open chain of dopamine units appears in the structure. These results are in agreement with previous theories regarding the existence of covalent polymerization with real C-C bonds holding the units, this does not ensure that units can not interact by hydrogen bonding and π-π stacking

but according to the opinion of these authors, it is unlikely to happen [23].

Polydopamine presents a high degree of disorder and amorphous character and is insoluble in polar and nonpolar solvents. As standard analytical techniques typically need to solubilize the sample in a solvent, insolubility is an essential issue as it presents enormous limitations when analytical techniques are used; thus, the experimental results are not conclusive. As a possible solution, non-invasive techniques like (FTIR) [121], electron paramagnetic resonance (EPR) [121], X-ray photoelectron spectroscopy (XPS) [34] or ultraviolet spectroscopy (UV) [23] can be carried out, and some characteristics of the structure can be confirmed. However, they do not offer an entirely accurate result. Regarding more invasive mass spectroscopy techniques, the results are ambiguous, and it is not easy to provide a clear view of the PDA structure. For instance, *m/z* peaks values up to 1226 were obtained by using electrospray ionization mass spectrometry (ESI MS) [119]. Meanwhile, matrix-assisted laser desorption/ionization mass spectrometry (MALDI-MS) showed *m/z* peaks until 402, which shows that the results are not compatible [122].

A combined 13C/1H/2H solid-state NMR on deuterated samples was carried out for more accurate results and looking to overcome those analytical limitations. Its results show that more than half of the phenyl ring positions are protonated in the final material, and most phenyl/indole rings are rigid due to the already said π-π interaction, which could be the reason why aggregation in PDA oligomers occur [123]. Also, it was found that water molecules experiment a slow diffusion inside PDA so, when the polymerization process is prepared in deuterated solvents, appears an exchange between deuteron (D) from D_2O and –OH labile protons of the PDA structure. This exchange competes with the polymerization process, and it is supposed that –OH groups from catechol are involved at the beginning in hydrogen bonds during PDA oxidation addressing poor deuteron incorporation to the final structure. Thereby, this phenomenon could be used to study the polymerization mechanism and the role of different molecules caged in the final PDA sample [123].

1.2.1.1. Thickness control. Nowadays, PDA has established itself as an essential surface modification polymer [6], the presence of 3,4-dihydroxy-L-phenylalanine leads to a high 3,4-dihydroxybenzene (catechol) content. Furthermore, PDA includes a high primary and secondary amine amount because of lysine (Lys) and histidine residues [115]. Combining these two compounds (catechol and amine) seems to be why PDA exhibits such excellent adhesion properties [4]. On the one hand, with a straightforward polymerization method and incredible adhesion capabilities, this substance can cover almost every inorganic or organic substrate regardless of size and shape by a simple dip-coating process or an ultrafast sprayable easy method [124]. On the other hand, high velocity and difficulties in conducting the polymerization process raise thickness and aggregation control complexity.

Based on the classical coating processes [4] (which provides the following conditions, 2 mg of dopamine hydrochloride per Tris buffer milliliter (10 mM), pH 8.5), some synthesis parameters have been studied for the last years to know their influence on the final coating. Results show that PDA surface energy is not dependent on dopamine concentration, but PDA film cover thickness increases when concentration flows from 0.1 to 5 mg ml^{-1}. Also, in general, roughness increases with thickness when dopamine concentration increases between 3 and 5 mg ml^{-1} [6]. By applying a lower concentration of dopamine to different substrates like particles [6,34,125–127], fibers [128] or nanotubes [129], it is possible to reduce PDA particle formation and, therefore, to reduce aggregation and surface roughness [130]. However, the thickness is going to be compromised due to its dependence on dopamine concentration. Aiming to solve this issue, another proper method to reduce roughness is to decrease the immersion time of the substrate [131]. If more thickness is required, it is possible to repeat the process as many times as necessary to achieve the final needful thickness with the appropriate roughness [132]. Despite that, another parameter that affects film thickness is pH. Thickness is higher when pH increases from pH 5–8.5. Thus, achieving a final PDA coated structure with the roughness and thickness required by controlling these parameters is possible. A reported concentration influences the kinetics of PDA deposition, surface energy, thickness, and roughness [120].

Beyond roughness and thickness control, the solvent choice can also affect the final polymer composition. While in most of the previous reports about PDA, aqueous solvents were used, there are other solvent possibilities with lower surface tension that can modify or alter the properties of the substrate. Besides, during the PDA polymerization process, the possibility of having unreacted dopamine [21] and surplus tris buffer [33] unavoidably and unfortunately will be added to the coating. This can be an issue because depending on the final compound added to the resulting PDA structure, and its physicochemical properties can be altered. In the case of having unreacted dopamine in the final structure, the resulting PDA compound starts to show cytotoxic effects [21]. However, in other circumstances, incorporation of -CH_2-OH groups from Tris buffer could provide to PDA significant antibacterial properties [133]. To avoid Tris buffer incorporation [134,135] another buffer can be used, such as amine-free organic ones or inorganic solvents, but on the other hand, this can aggravate and boost the creation of PDA aggregates [6].

1.2.2. Air/water interface

The use of conventional solution processing methods to prepare large-scale homogeneous melanin thin films is an arduous task, mainly due to the insolubility of natural and synthetic melanin [16]. Nevertheless, several attempts have been made to prepare DOPA melanin thin films by room temperature solvent evaporation (casting) or spin coating [16,26,136].

Meanwhile, during the autopolymerization of dopamine, three types of polydopamine can be distinguished, the membrane at the surface of the solution, the nanoparticles embedded in the solution, and the thin layer deposited on a substrate immersed in the solution [137]. However, no membrane formation can be observed on the surface of the vigorously stirred dopamine solution. The increased supply of oxygen and the higher concentration of reagents do not affect this observation. This effect originates from intense shear stress (due to magnetic stirring of the solution), removing PDA aggregates at that interface by applying stresses sufficient to disrupt the forming films [138]. However, by use of the appropriate static or soft-stirring conditions, It is possible to obtain nanofilms formed at an air/solution interface during the development of dopamine-melanin aggregates in a dopamine solution [138]. As was explained before in Section 1.1, the oligomers assemble in an ordered manner through π−π stacking to form small fundamental aggregates (size approximately 2−20 nm) in a supramolecular architecture. It has been reported that the oxygen-rich region at the air-water interface significantly enhances the crosslinking of PDA [139]. The aggregates become trapped at the air/water interface due to their hydrophobicity [140] and form the dopamine-melanin nanofilms. Additionally, a crucial aspect of controlling is the rapid water evaporation, which must be avoided during the preparation of dopamine-melanin films. This is because convective flows disturb the stationary state at the interface and hinder the formation of a homogeneous film. A widely used and cost-effective method to reduce evaporation or avoid the appearance of inhomogeneities is the use of a partial covering lid on the reaction vessel [44].

Due to solid adhesive forces between dopamine-melanin structures and solid surfaces, such a membrane is continuous and smooth, with a uniform thickness and can be easily transferred to other substrates or supports. Studies performed by AFM on the dopamine-melanin films reveal that the top surface is relatively smooth with a roughness of 36.0 ± 1.2 nm [44].

PDA thin films (50−200 nm thick) are formed at an air/solution interface under static conditions as described in the literature [44]. The

thickness of dopamine-melanin films relied on the concentration of dopamine solution and the reaction time, which increased linearly with both of these factors [44]. The film thickness increased linearly with the reaction time within 24 h with the determined growth rate of 3.2 nm h^{-1} using an aqueous dopamine HCl solution with concentrations of 10 mM. The average thickness of obtained PDA films from 10 mM, 20 mM, 40 mM solutions within 24 h were determined to be 105, 132, and 179 nm, respectively. Moreover, UV-Vis absorption spectra for thin films and nanoparticles formed in a liquid were investigated. The absorbance at 280 nm in both spectra was attributed to phenolic groups on the dopamine. The PDA film exhibited a monotonic broad absorption band, compatible with natural and synthetic melanins [44].

Later studies describe the fabrication of a humidity sensor with rapid response and high sensitivity by self-assembling PDA thin films at the air/solution interface. Unlike in the previously described procedure, this time, aniline was used as the deprotonating agent. Two milliliters of aqueous dopamine·HCl solution (10 mM) containing 5 mM aniline was poured into a plastic Petri dish (35 mm × 10 mm) at room temperature and lidded. The polymerization time was maintained for 6, 12, 18, and 24 h [141]. Once again, the film thickness was controlled at the nanoscale range by adjusting the reaction time. However, although the conditions were similar to those reported above [44], the growth rate was 7.9 nm h^{-1}.

Fully formed films from the air/water interface with a continuous, smooth surface and uniform thickness at the nanoscale level were reported and studied employing Field Emission Scanning Electron microscopy (FE-SEM) [141]. Further examination of the film surface morphology was carried out using AFM revealed that the surface was compact and smooth (Rms = 0.46 ± 0.09 nm) at the nanoscale level, on the 250 × 250 nm area [141]. In the same study, the electrical resistance of melanin self-assembled films was measured as the absolute humidity increased from 0% to 100%. The measured value decreased by more than two orders of magnitude, indicating that PDA films are susceptible to environmental humidity with an excellent response (5–7 s) and recovery (6–9 s) times [141]. This effect can be attributed to charge carriers (protons) production in melanin by water-involved comproportionation reaction, as previously mentioned in Section 1.1.4. Thus, increasing the water content in melanin will change the above-mentioned process, leading to a high charge carrier concentration and increased conductivity [141].

The surface properties of a polydopamine layer at the air-water interface were examined by dilatational surface rheology, ellipsometry, and Brewster angle microscopy (BAM) [142]. The studies evaluated the dynamic surface elasticity, film thickness, refractive index, and lateral film heterogeneity. When the concentration increased (from 0.75 mg ml^{-1} to 2 mg ml^{-1}), a significant increase in the dynamic surface elasticity was observed, with approximately a maximum value of approx. 60 mN m^{-1} (at a concentration of 1 mg ml^{-1}). When further increasing the concentration of the initial solution was carried out, decreased dynamic surface elasticity (in the concentration range from 2 mg ml^{-1} to 5 mg ml^{-1}) was noted. The refractive index at a concentration of 5 g l^{-1} was increasing for 16 h after the surface formation, approaching 1.706. Meanwhile, the corresponding maximum value at the concentration of 2 g l^{-1} solutions was only 1.662 [142]. That was probably due to the inaccuracy of the BAM, caused by polydopamine layer incomplete coverage, which could not be detected below the spatial resolution of the apparatus. For all samples – except the highest initial concentrations of dopamine – the surface film has not reached complete homogeneity. A state of separate close-packed domains is present for lower concentrations after a long surface lifetime, while the high concentration samples show a transition from this state to a homogeneous uniform film. Lower concentration films have low surface elasticity due to the loss of their integrity during deformation [142].

Finally, a very recent study has shown the apparition of a supramolecular ordering that resembles 2D-like ordering, which opens a whole new field to investigate PDA selforganizing thin films [89].

1.2.2.1. Control of morphological properties. A critical observation was the fact that the properties of PDA films have been changed after post-incubation in solutions containing redox-inactive metal cations (NaCl, $MgCl_2$ and $CaCl_2$). However, in the mentioned study, PDA films oxidized in bulk solutions were investigated [143]. A comparison between free-standing polydopamine films generated at the air/solution interface in the presence of various metallic cations (Na^+, Ca^{2+}, Mg^{2+} and Co^{2+}) was demonstrated [144]. These results were enriched with a comparison between obtained films and PDA nanoparticles generated in the solution phase. For preparing PDA (Na/Mg/Ca/Co) films and nanoparticles, the standard procedure described earlier in Section 1.3.1 was used, with an additional 100 mM of appropriate salts dissolved in water (NaCl, $MgCl_2{\cdot}6H_2O$, $CaCl_2$, $CoCl_2{\cdot}6H_2O$). What is interesting, the reactions were separatable from each other by different color changes [144].

The addition of ions induced different effects on the speed of oxidative polymerization of dopamine. Sodium ions showed no influence, calcium and magnesium ions slightly accelerated polymerization, while cobalt (II) ions significantly speeded it up [144]. Another interesting observation was the different colors of the PDA films. A blue-green color for Ca-PDA films, mirror-like shiny for an Mg-PDA film, and black for others. Scanning electron microscopy of the samples' cross-sections has proved previously mentioned dependence, that the color of PDA films is related to the films' morphology and thickness: which is equal to 145 nm, 195 and 270 for Na-PDA, Mg-PDA and Ca-PDA, respectively (Fig. 6) [144]. Moreover, a difference between the upper and lower surfaces of the membrane was noted.

The results show a smooth upper surface and a less smooth lower surface with different size nanoparticles on it. All upper surfaces presented a larger water contact angle than the lower surfaces, and this may result from a higher crosslinking degree of PDA in upper sections [144]. AFM characterizations of PDA films at different reaction times have been conducted. The growth of film thickness using AFM has been investigated, for all groups of samples approached its limit in several days. A study of 20 days on the thickness of membranes provided the following results: 800 nm for Co-PDA film, 500 nm for Ca- PDA film, and 400 nm for pristine PDA, Na-PDA or Mg-PDA films [144].

One of the possible ways to obtain films with improved stability is the enzyme oxidation by laccase, a multicopper-containing polyphenol oxidase [145,146]. The formation of such a modified film can be divided into numerous stages. Firstly laccase adsorbs at the interface, forming a dense layer. Secondly, the subsequent interaction of DA with laccase results in the rapid formation and growth of a PDA domain. Finally, the concentration of PDA in the film increases gradually, leading to an increase in the surface elasticity up to values that are about seven times higher than those for pure laccase or pure PDA films. In the following experiment, the mixed films demonstrated higher stability under deformation than a fragile film of pure PDA. A uniform continuous film with higher surface elasticity was formed even at low DA concentrations (0.1 g l-1 and 0.5 g l-1). The improved stability of PDA-laccase films results most probably as a consequence of the formation of additional links between the PDA building blocks during polymerization [146].

2. Applications in photocatalysis

2.1. Application in catalysis (catechol chemistry)

Because of its adhesive property [4], PDA can be firmly attached to many substrates like metal, metal oxide, or metal sulfide surfaces [147]. The attaching process consists of an "in-situ" oxidative polymerization of dopamine under alkaline conditions whereby tuning synthesis parameters such as dopamine concentration or dipping time, among others [148]. Using this process, it is possible to achieve a final structure made by a nanoparticle surrounded by a PDA shell. It is generally considered that this PDA layer will induce to the nanomaterial a biocompatible character and it is not going to serve only as a coating material but can also act as a template for future nano construction. For instance, a new

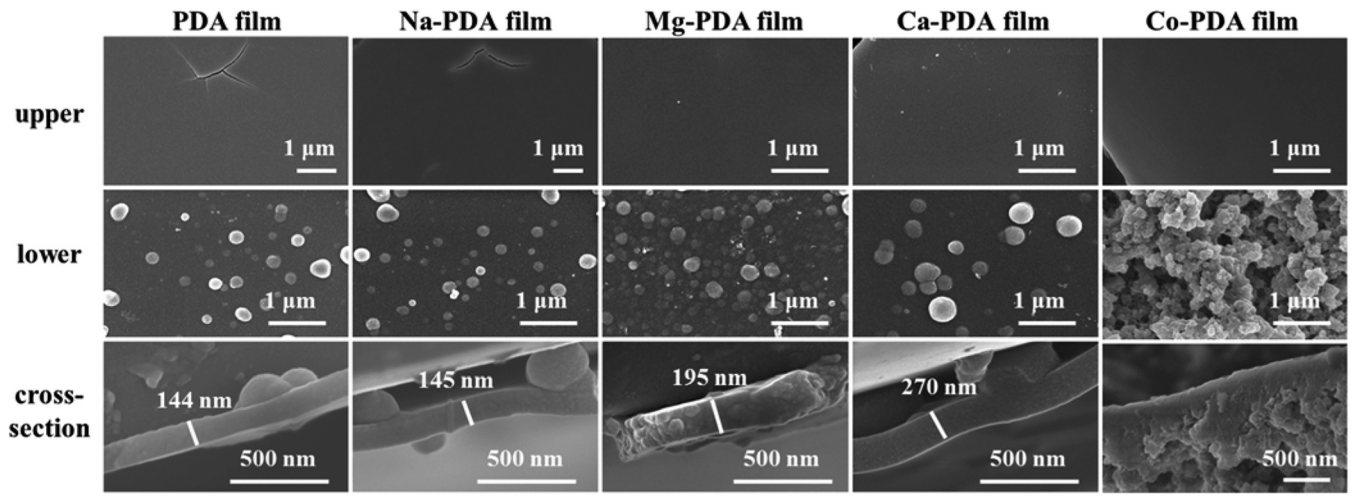

Fig. 6. Scanning electron microscopy images of the upper and lower surfaces and cross-sections of PDA coatings were obtained with the influence of various ions (sodium, magnesium, calcium and cobalt, respectively). The layer thickness was also marked for the first four cross-sections images [144] - Published by The Royal Society of Chemistry.

method where PDA acts as a template allows immobilizing TiO_2 nanoparticles on cotton fabrics by in situ reductions [149].

Dopamine monomers are supposed to interact first with the surface of the nanomaterial to be coated, catechol units exhibit a strong affinity towards several kinds of metal ions, and then take part in the self-polymerization to obtain the final PDA shell. This self-polymerization is pH sensible. Some studies based on ultraviolet-visible absorption spectra exhibit that catechol is reduced at pH 7, therefore the coordination complexes are not crosslinked [150], but at pH 8.5, this self-polymerization process is taking place, and covalent bonds between the rings are created [151]. Additionally, dopamine is known to present a redox nature as it can reduce metal nanomaterials and induce the creation of "seeds" without using any conventional seeding material or redactor [147]. This leads to an exciting way of creating nanoparticles that use PDA-NPs as templates to grow, for instance, AuNPs [152], and achieving a pomegranate-like structure where there are gold nanoparticles embedded into a PDA sphere. This strategy is also compatible with other metals like Cu or Ag [153] and has also been used to prepare spiky FeOOH structures [154–159]. Regarding the type of interaction between catechol and metals, a bonding study revealed that cross-linkage strength and stiffness are similar to a covalent bond that depend on the type of metal and the coordination state [160]. For instance, studies carried out with (AFM) and surface force apparatus (SFA) exhibit that a single L-Dopa residue can contact a wet TiO_2 surface with a reversible non-covalent interaction but with high strength (0.8 nN) [161].

Besides the biocompatibility mentioned above induced by PDA, it is possible to combine metal ions, metal oxides, metals, or plasmonic materials with PDA to improve their catalytic behavior [147]. Additionally, the functionalization of nanoparticles with PDA improves their colloidal stability [153], thus avoiding aggregations that can compromise the catalytic activity in the final suspension. Since the discovery of these hybrid materials, although several initial applications have been proposed, to this day, biomedicine and environmental remediation fields have gathered much attention. Those fields have attracted this recognition because of PDA's biocompatible and nonpoisonous characteristics, so in terms of biomedicine, it can be used in antibacterial coatings or drug transport and delivery [130,162–164]. In turn, regarding environmental issues, it is possible to apply PDA to separate and deplete poisonous and biological materials [165,166]. Within those fields, PDA-based composites have shown the capability of carrying out different reactions encompassing several reactants, such as thiols or amines as nucleophiles [167]. Moreover, PDA has the possibility of been used in other applications, PDA can act as an immobilization platform for some biomolecules or enzymes like polyethylene glycol or vascular endothelial growth factor [168–170], paramagnetic metal ion chelates as PDA-Mn^{2+}, Mn^{3+} or Fe^{3+} can be used as T1 contrast agents [171, 172]. At last, catechol/o-quinone moieties provide redox properties that allow reduction and deposition or collections of several metals such as Ag, Cu or Au [173–175]. Therefore transition metal oxides can be loaded on carbonized PDA working electrodes aiming for oxygen reduction reaction [176,177].

Nevertheless, although most of those reactions and applications are focused on being employed in biological and medical scenarios due to the non-poisonous character of PDA, the amino groups and the phenolic hydroxyl groups can be used in organocatalyst behavior in aldol reactions, which, although in some cases, can create undesirable side effects [178], advocate for the unique catalytic capabilities of PDA.

2.2. *Applications in light-driven environmental remediation*

As a typical carbon-based material, PDA itself does not have photocatalytic activity. However, numerous studies prove that PDA can synergize with semiconductor photocatalysts and create additional π-π* electron transfer channels to enhance photocatalytic performance [14]. Since polydopamine has been used and studied in many fields and environments [28], we focused only on the latest literature reports in this review.

Numerous functional groups in polydopamine, including catechols, amines, and imines, can serve as anchors for efficient organic contaminant removal. Moreover, due to excellent adhesive properties and hydrophilicity, it can modify various materials. PDA has demonstrated good light-harvesting ability and photothermal conversion performance, beneficial to solar-driven water desalination [179–181]. A bilayer structure composed of two environmentally sustainable materials, polydopamine (PDA) particles and bacterial nanocellulose (BNC), was proposed to obtain both superb optical/photothermal activity (~98% light absorption) and high porosity (~93%). A permeate flux of 1.0 kg m^{-2} h^{-1} under 1 sun irradiation (1 kW m^{-2}) and a high solar energy-to-collected water efficiency of 68% were achieved [181]. Besides, the interfacial photothermal disinfection activity of the membrane under solar light was reported, leading to the effective killing of adhered bacteria, thus reducing microbial accumulations and prolonging the membrane life by stopping the biofilm formation [181]. A renewable and bioinspired PDA functionalized cellulose aerogel (PDA-CA) for soluble contaminant adsorption, and oil-polluted for seawater and

wastewater purifications was proposed [182]. Due to the porous structure of CA, broad sunlight absorption spectrum in PDA, and excellent photothermal conventional effect, the proposed hybrid material exhibited an extraordinary water steam generation rate of ~1.36 kg m^{-2} h^{-1} of ~86% efficiency illuminated by 1 sun. Moreover, due to its enhanced hydrophilicity and underwater lipophobicity, the PDA-CA also showed promising anti-oil-fouling behavior [182].

Since the first report showing that the photocatalytic activity of TiO_2 can be significantly improved with the coating of PDA [183], similar hybrid materials have been studied in photocatalytic environmental remediation [14]. A core-shell nanostructure of TiO_2@PDA leads to much better catalytic activity for TiO_2 under visible light, while both pure PDA and TiO_2 nanospheres show no significant photocatalytic activity under visible light irradiation. During the described experiment, it was identified that a 1 nm PDA surface coating over TiO_2 nanospheres exhibits relatively high conversion efficiency of solar energy for the photodegradation of organic dyes, i.e. Rhodamine B (RhB). This study was described in details in Section 2.4.1.

Composite nanomaterials based on polydopamine was reported to be an excellent reducing agent, which can convert Fe^{3+} to Fe^{2+}. For this purpose, magnetically recyclable multi-functional Fe_3O_4@PDA nanocomposites were prepared. In such a procedure, Fe_3O_4 nano-cores were introduced to promote magnetic recycling. Reductive polydopamine (PDA) shells were introduced to improve the recycling efficiency of Fe^{3+}/Fe^{2+} and avoid sludge formation. According to this study, what is essential is that the Fe_3O_4@PDA system can operate in a wide pH range, from 3 to 9. Even after the 10th recycling run, it still achieved over 99% degradation efficiency with a total organic carbon degradation rate of 80% [184].

Another variation of a similar composite turned out to be a novel Fe^{3+} -stabilized magnetic polydopamine composite (Fe_3O_4/PDA-Fe^{3+}). The described system was constructed, systematically characterized, and subsequently applied, which was reported for the first time. The proposed solution turned out to be a versatile adsorbent for the treatment of Methylene blue (MB) in complex wastewater over a wide pH range (3−10). The maximum adsorption capacity of the adsorbent (q_{max}) was as high as 608.8 mg g^{-1}. The enhanced catalytic performance compared with Fe3O4/PDA composite results from the introduced Fe^{3+} ions, which act as MB sorption sites through the process of complexing Fe^{3+} with electronegative atoms (such as N and S) in Methylene blue. The authors also stated that MB could be selectively adsorbed and separated by Fe_3O_4/PDA-Fe^{3+} from complex wastewater (e.g. mixed dye solutions of MB/Methylene orange (MO), MB/RhB, or aqueous solution with high salinity). Finally, this composite could be repeatedly used without significant loss of adsorption performance, thus indicating its satisfactory stability and renewability [185].

Other materials have also been studied, and this is the case of CdS@PDA composite nanoparticles (described in detail in Section 2.5.2) with tunable inorganic patchy densities via different Cd^{2+} amounts (1.5 wt% for CdS@PDA-1 and 8.4 wt% for CdS@PDA-2) was reported. The purpose was to overcome numerous drawbacks of a CdS photocatalyst, described in detail in the above-mentioned (Section 2.5.2). After 3 h of photocatalytic MB degradation reaction progress, at the weight of catalyst equal 0.03 mg ml^{-1}, 33% and 67% of total organic carbon (TOC) were removed with CdS@PDA-1 and CdS@PDA-2, respectively. Meanwhile, the removal of TOC with a pure CdS reached only 15% within the same time. This result confirmed that the modification with PDA enhanced the catalytic ability of CdS for MB photodegradation. The photostability and reusability of both CdS@PDA-1 and CdS@PDA-2 catalysts were further evaluated by collecting and reusing them, and it was noted that they maintained their photocatalytic activities even after three rounds of testing [186].

Indirectly, PDA has been used as a multifunctional platform, as in the case of polydopamine/graphitic carbon nitride (PDA/g-C_3N_4) photosynthetic systems. Herein PDA played multiple roles: a light absorption substance, an electron transfer acceptor, and an adhesive interface. The photocatalysts' light-harvesting ability was gradually improved with increasing PDA/substrate ratio. In particular, the 10% PDA/g-C_3N_4 composite has shown high efficiency in degrading organic dyes methylene blue (MB), Rhodamine B (RhB), and phenol under visible light irradiation. The degradation efficiency of MB was around 98% after 3 h, and even after four cycles, the catalysts could remain degradation efficiency higher than 90% [187].

A novel strategy to construct a visible-light-driven ^2D–^2D heterojunction catalyst comprising graphitic-carbon nitride (g-C_3N_4) and calcined ZnAl-Layered double hydroxide (ZnAl-LDH) had been established via the polydopamine cross-linking method. The goal was to achieve photocatalytic activity for p-nitrophenol under visible-light (> 420 nm). In order to explain the charge separation observed in the heterojunction, a z-scheme charge transfer mechanism via PDA bridges was proposed. This mechanism relies on the recombination of photo-induced electrons directly on the ZnAl-LDH valence band through the PDA channel, and the holes capture at the conduction band energy level of the g-C_3N_4. The PDA on the interface caused strong light harvesting and electron transport capabilities by improving visible-light absorption and regulating the photo-generated carriers for efficient separation through π-π* electron transfer [188]. Because the inorganic photocatalytic layer and polymeric membrane typically exhibit poor compatibility [189] and thanks to polydopamines' versatile adhesive properties, ultra-thin membranes modified with laminar PDA in recent years coating gained much attention in many fields, also in water remediation [28,190–192]. However, in this review, we mainly focus on studies where photocatalytic performance is evaluated.

Interestingly enough, a strategy to execute heterogeneous photocatalytic coupling reactions using PDA and a noble metal nanoparticles catalyst was described [193]. In this model, a PDA nanofilm acted as a light-harvesting and transformation interface. To achieve a multicomponent system, authors first decorated PDA nanofilm onto the surface of silica gel (SG) or polyurethane sponge (PS). Secondly, noble metal nanoparticles (catalysts) were applied onto the resulting PDA surface through an in situ nucleation and growth process. In principles, electron-hole pairs, photogenerated in the PDA under irradiation of visible light, are separated along with the PDA networks. Then, the electron transfers to the catalyst nanoparticle's conduction band, resulting in the enhanced catalytic activity [193]. Described systems were used for photocatalytic Suzuki coupling reactions involving a broad range of aryl bromides/iodides and arylboronic acid substrates [193].

Despite the leading role of nanoparticulate materials in photocatalytic applications, some studies have use membranes or pseudo-2D structures for filtration and water remediation. Nanofiltration membranes were used to provide self-cleaning properties. Thus, a new type of composite was developed using PDA as a multipurpose element [189]. In the first step, a polydopamine/polyethyleneimine intermediate layer was fabricated on a polyacrylonitrile substrate via a co-deposition method. In the second step, the mineralization of a photocatalytic layer consisting of β-FeOOH nanorods took place. Apart from a suitable filtration property, the β-FeOOH nanorods provided photocatalytic efficiency for dye degradation under visible light irradiation in the presence of hydrogen peroxide (H_2O_2). Moreover, the β-FeOOH layer exhibits good stability during cyclic photocatalytic filtration. Finally, the bio-glue effect of the PDA–PEI layer immobilizes the β-FeOOH nanorods via strong coordination complexes between Fe^{3+} and catechol groups, providing extra stability to the β-FeOOH nanomaterials [189].

In another study, the multi-scale, hierarchical PDA@M-PAN/TiO_2 membrane was developed [190]. The fabrication process was as follows: firstly, electrospinning of hydrophilic polyacrylonitrile (PAN) nanofibers. Then, modification with electrospray PAN/TiO_2 spheres, and finally, coating by the polydopamine membrane via in-situ growth. The flux and efficiency of the PAN-based membrane increased after polydopamine deposition, which was due to the enhanced wettability. This approach led to a membrane with superhydrophobic (with a water

contact angle ~ 0°), and underwater superoleophobic (with an oil contact angle of around 152°) properties. The tested and described photocatalytic efficiency is of great importance. An excellent value for the organic pollutant (~98%) was achieved. It is worth emphasizing that after 5 cycles, the water flux still maintained a high level, simultaneously showing good recyclability. Additionally, this membrane showed enhanced water permeation and hydrophilic properties in comparison with a pure PAN membrane. Finally, the membrane shows good mechanical stability and water transportability [190].

2.3. Applications on photocatalysis

It is generally accepted that PDA is not directly exploitable as a photoactive material and that its photocatalytic properties are relatively marginal (see optical properties, Section 1.1.2.). It is necessary to know and control the nanomaterial characteristics to achieve a suitable and efficient photocatalytic activity. Like adsorption rate or photo stability, some of them are strongly dependent on the material structure, so controlling it is possible to tune these characteristics into the desirable ones. However, the most crucial attribute could be the capacity of the catalysts to produce electron-hole pairs (charge separation rate) and their ability not to recombine the carriers. These two phenomena can be enhanced by surface modification with PDA, thus ameliorating photocatalytic behavior by PDA incorporation in a nanocomposite can provoke different types of concentrations defects that can affect optical and electronic properties of the catalyst, thus leading to changes in excitonic (e-h pair) (See Section 1.1.2.2. and Section 1.1.2.4.). In short, an exciton is an electrically neutral quanta of electronic excitation energy that travels in a periodic structure of a crystal transporting energy but not charge [194]. Under appropriate light irradiation, photoactive material absorbs a photon that excites an electron of the valence band, moving it to the conduction band. As a direct consequence, it will leave a positively charged hole placed in the valence band, whereby this hole will interact via coulombic forces with the moving electron. The necessary excitation energy to produce an electron-hole pair forming a bound stationary state is not related to any particular parent atom (ion), and it can be transferred from one ion to the next one. When this takes place along the crystal, it creates “excitation waves” called excitons [195]. PDA can contribute to this exchange by enhancing the e-h charge separation and simultaneously decreasing the recombination rate by offering additional bands where electrons or holes can be placed. As a result, it improves the composites’ catalytic behavior [196,197]. In order to achieve these objectives, among others, like e.g. tuning bandgap value, creating a heterojunction, improving redox, and colloidal stability, a strategy that has recently gathered attention is to combine PDA with a photoactive semiconductor material such as TiO_2, ZnO, ZnS, Fe_3O_4. As a result, the photocatalytic response of the as-obtained composites is enhanced, and in some cases, it is possible to shift the absorption spectra from ultraviolet towards the visible region [188].

The photocatalytic behavior of PDA/Semiconductor hybrids can be enhanced by creating core-shell nanocomposites. This effect is present because, like in the case of melanin, PDA posses semiconducting properties. These nanocomposites can be understood or investigated as semiconductor junctions. It is well known that direct contact between two semiconductors with different bandgaps is resulting in the creation of a heterojunction in which the final behavior strongly depends on the energy band alignment at the interface (straddling gap, staggered gap and broken gap) [114,188]; hence the final bandgap is modified or tuned. Consequently, the final nanostructure may exhibit improved light absorption capabilities and electron/carrier flux, influencing its biocompatibility, electrical conductivity, electron transfer rate.

Moreover, in photocatalytic applications, it can decrease the recombination rate of photogenerated electrons and holes. Furthermore, an additional aspect of PDA, is that by creating a PDA-shell, PDA can also act as an “environmental isolator” that protects photocatalysts from stoichiometry losses and environmental damages [198–200], improving their lifetime and efficiency (Section 1.1.3.). The most widespread applications architecture mentioned above is found on metal-oxides/PDA nanocomposites, which are typically used in the reduction of organic pollutants, direct aldol reaction, catalytic transfer hydrogenation (CTH), oxygen reduction reaction (ORR), MRI contrast agents, Li-ion Batteries, therapy and theranostics or Suzuki couplings [147].

An application that can fully exploit PDA composites’ capabilities is their use in proton exchange membrane fuel cells (PEMFCs). PEMFCs are promising energy converting devices due to their high power density, efficiency, low or zero emissions, robust performance, and their possibility of using different kinds of fuels [201,202]. PEMFCs have just opened a promising field in the clean energy industry by their active role in generating renewable hydrogen gas, one of the most essential and promising energy vectors for the future. In order to understand a bit more this mechanism, here we shortly introduce the reactions that occur in the cell are; hydrogen oxidation at the anode, showed in Eq. (1), and oxygen reduction at the cathode, showed in Eq. (2) [203].

$$\textbf{\textit{Anode}} \quad H_2 \rightarrow 2H^+ + 2e^- \tag{1}$$

$$\textbf{\textit{Cathode}} \quad \frac{1}{2} O_2 + 2H^+ + 2e^- \rightarrow H_2O \tag{2}$$

$$H^+ + e^- \rightarrow H* \tag{3}$$

$$H^+ + e^- + H* \rightarrow H_2 \tag{4}$$

$$H* + H* \rightarrow H_2 \tag{5}$$

$$H_2O\ (l) + * \rightarrow OH^+ + e^- + H^+ \tag{6}$$

$$OH^+ \rightarrow O* + e^- + H^+ \tag{7}$$

$$H_2O\ (l) + O* \rightarrow *OOH + H^+ + e^- \tag{8}$$

$$*OOH \rightarrow O_2(g) + e^- + H^+ \tag{9}$$

The advantage over direct combustion of O_2 and H_2 is that it produces thermal energy. Meanwhile, PEM fuel cells transform the chemical energy, which is liberated from the reaction of hydrogen and oxygen, into electrical energy. In general, two different mechanisms for hydrogen evolution reaction (HER) in acid media are postulated; Volmer-Heyrovsky and Volmer-Tafel. The initial solution protons adsorption to create H* ($H^+ + e^- \rightarrow$H*) is the Volmer reaction shown in Eq. (3), which is considered to be quick (* is referred to as the active site of the catalyst). From this point, two possibilities appear, Herovsky and Tafel (see Eqs. (4 and 5), respectively). For the first one, one solvated proton from the solution reacts with the adsorbed intermediate H* to create H_2 ($H^+ + e^- + H^* \rightarrow H_2$), on the other hand, the second option proposes that H_2 is being created from two adsorbed intermediates placed next to each other which are going to react ($H^* + H^* \rightarrow H_2$) [204–207]. Regarding oxygen evolution reaction (OER) involves four elementary electron steps represented in Eqs. (6–9) [205,206,208]. Firstly, the H_2O molecule is dissociated on the surface of the catalysts giving. As a result, H^+ and *OH. Secondly, *OH is dissociated into H^+ and *O. Thereby, in third place, another H_2O is reacting with *O producing H^+ and *OOH. Finally, in the fourth step, *OOH is dissociated into H^+ and O_2, releasing oxygen molecules from the catalyst’s surface [209]. It should be noticed that hydrogen oxidation reaction (HOR) and oxygen reduction reaction (ORR) can be treated as the reverse of HER and OER [207]. Those reactions can be carried out efficiently on Pt electrocatalysts [210,211], but they suffer from the general drawbacks of Pt catalyst and architectures. Moreover, they are expensive, not abundant in nature and own insufficient durability. Recently, considering these disadvantages, non-noble metal-based electrocatalysts have attracted attention [212,213] as a promising new way to obtain better results with low cost-effective nanocatalysts.

Despite the limitations, it is possible to improve the efficiency of these catalysts by tuning their composition and morphology [214]. However, the slow kinetics of the cathodic oxygen reduction reaction (ORR) is a drawback in terms to obtain a low cost-effective non-noble metal catalyst that gives an adequate performance. Despite the advances, a standard method to enhance the activity of PEMFCs and decrease the Pt load amount, many works have focused on dispersing Pt nanoparticles on carbon support [215,216]. There exists an optimum size of Pt nanoparticles for the maximum hydrogen oxidation reaction (HOR), and oxygen reduction reaction (ORR) activity showed by electrochemical studies [217]. Another strategy is to substitute carbon materials with nitrogen-doped carbon because due to electronegativity, nitrogen atoms can create charged sites that will improve the charge and mass transfer during the ORR process [218].

Meanwhile, the main drawback should be noted, that the precursor synthesis such as polypyrrole and polyaniline need to be catalyzed in harsh conditions [147]. By trying to avoid that, recent studies have successfully tried to use polydopamine as the nitrogen-doped carbon precursor because of the facility to create coordination bonds with metallic ions and covalent bonds with thiol or/and amine groups via Schiff base reactions and/or Michael addition [4,14,219]. In this way, successful nitrogen-doped carbon sheets designed as an anode material for sodium-ion batteries were efficiently synthesized by using polydopamine as a carbon precursor [220].

A widely used and quite simple approach is based on the carbonization of PDA to achieve active nitrogen sites, which show a high level of electroactive graphitic and pyridinic enhanced electroconductivity, thereby efficient ORR activity [221]. In this case, metal catalysts can be quickly loaded into PDA and then metal oxides supported by nitrogen-doped carbon materials with catalytic efficiency to ORR. Furthermore, high stability can be achieved by a further carbonization process [147]. For instance, carbonized PDA-Fe_3O_4 spheres were synthesized using a one-pot fabrication method and were tested as ORR catalysts in a Zn-air battery. High ORR activity of carbonized PDA-Fe_3O_4 was demonstrated by cyclic voltammetry (CV) measurements, which exhibited a cathodic peak at − 0.27 V. The number of electrons transferred per oxygen molecule was close to 4, and the stable discharge voltage was over 200 h [222]. Those results carbonized metal-PDA is a rather stable, low-cost and efficient material for ORR in fuel cell and battery performance. Finally, due to the similar electronic structure, larger atomic radius and smaller electronegativity, it is possible to add sulfur into the N-doped carbons and thus improve the catalytic activity [223]. Studies have shown that CdS NPs can be used as a sulfur source and template; meanwhile, PDA can be a nitrogen and carbon source [224]. However, templating and carbonizing studies are not inherent in photocatalytic applications. Therefore, in the following sections, we compile the most important developments on PDA/Semiconductors and compile some of the key studies (Table 3).

Table 3
Examples of several catalysts and the PDA coating process or the PDA role in synthesizing the final material and its reported applications.

Catalyst	PDA coating process/PDA role at the synthesis	Applications
TiO_2/PDA	• Self-polymerization on the TiO_2 substrate [183] • Electrochemical polymerization on the TiO_2 substrate [343] • Photoelectric polymerization on the TiO_2 substrate [240]	• Organic dyes depletion (MB [240], MO, MV and RhB [199]) • Pentachlorophenol photodegradation [252] • Selective oxidation of sulfides with aerial O_2 [247]
ZnO/PDA	• Self-polymerization on the ZnO substrate [81]	• Photocatalytical CO_2 reduction [275] • Solar cells [273,276]
ZnS/PDA	• Self–polymerization on the ZnS substrate [114]	• Photocatalytic H_2 production [114]
CdS/PDA	• Self–polymerization on the CdS substrate [342]	• Photoelectrochemical water splitting [342]
PDA/MXene	• Direct reaction between MXene and PDA microspheres [344]	• Wastewater remediation and seawater desalination [344]
PEG@MPMF	• Self–polymerization on melamine foam and further addition of MXene dispersion [345]	• Solar to thermal energy conversion [345]
MoS_2@sponge	• Self-polymerization on the sponge [346]	• Solar desalination [346]
MoS_2/PDA	• Self-polymerization on MoS_2 [97]	• Capacitive deionization [97]
MoS_2/PDA/TiO_2	• Self-polymerization on TiO_2 nanotubes [347]	• Hydrogen evolution reaction [347]
$MoSe_2$	• Self-polymerization on polystyrene fibers used as a hard template for synthesizing $MoSe_2$ [348]	• Hydrogen evolution reaction [348]
MC@$MoSe_2$	• MC obtained from PDA calcination [349]	• Hydrogen evolution reaction [349]
TiO_2/MoS_2/PDA/RGD	• Self-polymerization on TiO_2/MoS_2 NAs [350]	• Antibacterial activities [350]
WS_2/black-TiO_2	• Self-polymerization on B-TiO2/CoA/AuNPs/WS2/ITO electrode [351]	• Photoelectrochemical biosensor for detecting histone acetyltransferase [351]
$MoSe_2$@PDA-Dox	• Self-polymerization on $MoSe_2$@PDA-Dox [352]	• Chemo-photothermal synergistic therapy [352]
Fe_3O_4/PDA	• Self-polymerization on Fe_3O_4 [163,184]	• Enrichment of polycyclic aromatic hydrocarbons from environmental water samples [163] • Co-catalyst for Fe^{3+} reduction in advanced oxidation processes [184]
Fe_3O_4/PDA-Fe^{3+}	• Self-polymerization of dopamine on Fe_3O_4 surfaces under an aerobic atmosphere in the presence of Fe^{3+} [185]	• Selective adsorption and separation of Methylene blue from complex wastewater [185]
Fe_3O_4/C-PDA	• $FeCl_3$ and dopamine reaction to achieve Fe(III)/DOPA which was further calcinated to achieve Fe_3O_4/Carbonized-PDA [222]	• Oxygen evolution reaction and cathode at Zn-Air battery [222]

2.4. Metal oxides

2.4.1. TiO_2/PDA composites

Titanium oxide (TiO_2) is a direct bandgap n-type semiconductor with an energy gap larger than 3 eV [225] (i.e. 3.0 eV for rutile and 3.2 eV for anatase) which presents an absorption edge around 410 nm [226], photoactive response under 400 nm [227]. These values have limited to a certain extent the development of TiO_2 photocatalysts. However, other properties such as large availability and rather well-understood electronic structure and environmentally friendliness have sustained its interest in the literature [227–232]. Despite its limitations, TiO_2 has been used as an efficient photocatalyst and more importantly, it is a material that is considered a model photocatalyst in the field.

Several TiO_2 nanoparticles of different shapes and sizes can be synthesized through a solvothermal method using titanium (IV) tetrafluoride as a titanium precursor. By modifying the reaction environment, capping agents and parameters, it is possible to obtain octahedral, decahedral, 2D anatase and rectangular prisms structures with different crystalline and exposed planes, which strongly influence their photocatalytic activity under UV light irradiation [233]. However, its bandgap properties and its necessity for UV light have limited many of the large-scale applications of TiO_2 [234]. In order to address these drawbacks, several methods have been proposed and tested to shift its performance towards visible light. Among the most common approaches are phase control [235], atomic doping [236], and surface modification [232], being this latter the most popular one. However, it still presents

some complications since commonly employed surface modifiers, like Ag, Au or $[Ru(bpy)_3]^{3+}$, can improve TiO_2 catalytic behavior, but they present low stability and are expensive [237–239].

An additional possibility is using PDA as a surface modifier in TiO_2/PDA nanocomposites, which has shown the capability of shifting the bandgap and achieving visible light absorption, thus maximizing its solar light spectrum absorption and providing a more efficient nanocatalyst [183]. It is worth mentioning the first studies of TiO_2 as a photocatalyst. In 1972 it was discovered that TiO_2, could work as an electrode, and in fact, could drive the water-splitting reaction under UV light [225]. The TiO_2/PDA nanostructures, due to the combination of optical properties from their constituents, can enlarge the absorption range, improving the photocatalysis of splitting water reaction, making it accessible under solar light conditions. TiO_2/PDA nanocomposites, for example, nanorods, can be synthesized via "in situ" self-polymerization, electropolymerization or photoelectric polymerization, of which the last one is providing the most uniform and percolated layers [240]. The preparation of PDA layers was also found to be thickness dependent, with the most suitable PDA shell thickness at around 1 nm (in photodegradation of organic dyes) [183]. Interestingly enough, thicker layers do not hinder performance but tend to show a similar response to bare TiO_2.

Regarding these studies, it has been proved that PDA modifies the surface of TiO_2, thus appearing as a new hybrid system, combining the photo-electronic properties of bare TiO_2 and those of, yet to be correctly described, PDA materials. Despite the uncertainty of the true origin of these improvements, PDA shells show an enhancement in light absorption, accelerating the photogenerated electrons and their transfer, thus improving photocatalytic behavior and decreasing the recombination rate [197]. In order to understand the first phenomenon, it is necessary to know the characteristics of the interactions between PDA and TiO_2. However, unfortunately, an accurate representation of the TiO2 and PDA heterojunction mechanism is not known, although some theoretical approaches have been proposed [241]. The main idea of this theory is that in TiO_2/PDA nanocomposites, the polydopamine units are bonded to Ti atoms through catechol linkers. Also, the reaction between different metal oxides and enediols have been studied. It was suggested that a dipole moment between Ti-ligand could be induced by the interaction between TiO_2 and dopamine [242]. Therefore, the optical properties and electronic structure of TiO_2 could be changed in this manner. These assumptions mean that TiO_2/PDA nanocomposites, with a homogeneous layer of PDA, show a new *p* orbital, which allows electrons generated under visible light excitation to be transferred directly from the edge of this new *p*-orbital to the conduction band of TiO_2. In this case, PDA is used as a "photosensitizer" that allows the excitation of TiO_2 under visible light and enhanced the carrier separation. This can also be understood as a Type II heterojunction (staggered gap), which is created when a direct pathway for electron transport through a photoinjector is made [183,243] (Fig. 7a). Considering the second phenomenon, PDA induces spatial separation of photogenerated charges (holes placed on dopamine) and electrons within the TiO_2 lattice, effectively enhancing the photocatalytic behavior by denying charge recombination [244].

Overall, the experimental research has shown that the bandgap of

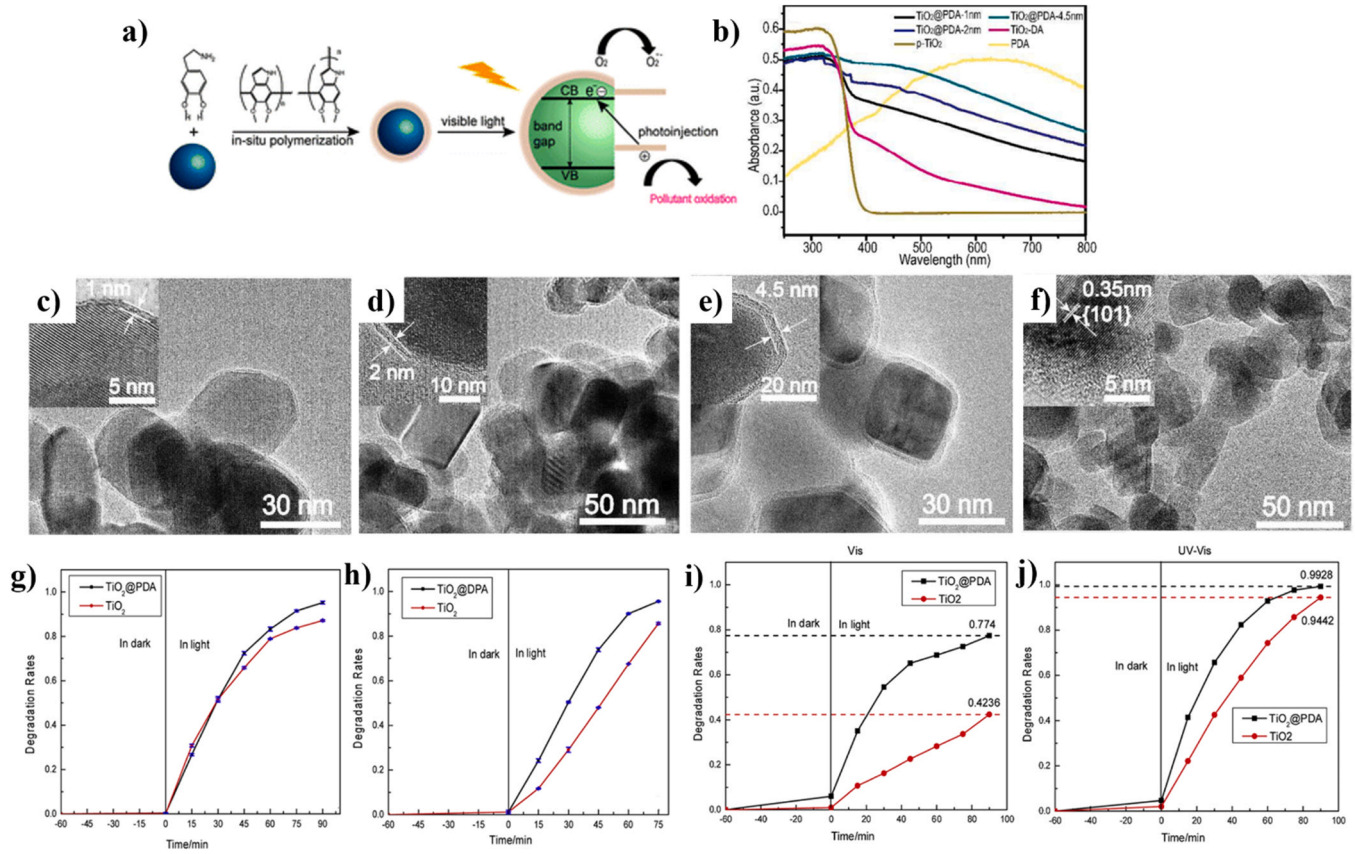

Fig. 7. (a) Creation, through an in-situ polymerization process, of TiO_2/PDA structure from TiO_2 and polydopamine precursor. A heterojunction between TiO_2 and PDA is created and stimulated by visible light, (b) UV–vis absorption spectra of PDA, pristine TiO_2, TiO_2/DA and TiO_2/PDA varying PDA coating thickness. TEM images: (c) TiO_2/PDA nanocomposite with a 1 nm uniform layer of PDA, (d) TiO_2/PDA with 2 nm PDA uniform layer, (e) TiO_2/PDA with 4.5 nm PDA uniform layer, (f) pristine Anatase TiO_2. Reproduced from Ref. [183] with permission from the Royal Society of Chemistry. Photocatalytic degradation study of (g) Methyl orange (MO) under UV-Vis light irradiation, (h) methyl violet (MV) under UV-Vis light irradiation, (i) Rhodamine B (RhB) under Vis light irradiation, (j) Rhodamine B (RhB) under UV-Vis light irradiation. Reprinted from Colloids and Surfaces A: Physicochemical and Engineering Aspects, 570, X. Sun, L. Yan, R. Xu, M. Xu, Y. Zhu, Surface modification of TiO_2 with polydopamine and its effect on photocatalytic degradation mechanism, (2019) 199–209. Copyright (2021) with permission from Elsevier.

TiO_2 Anatase of 3.2 eV was shifted to 2.35 eV by covering it with PDA ([PDA] = 4 mg ml^{-1} during 2 h), thus showing a significant shift towards visible light and allowing for the exploitation of both UV and Vis spectra (Fig. 7b). Additionally, as mentioned before, it was shown that this enhancement was thickness dependent. Different PDA thickness TiO_2/PDA nanocomposites are shown in Fig. 7c (1 nm), Fig. 7d (2 nm), Fig. 7e (4.5 nm) and basic pristine anatase TEM image shown in Fig. 7f, having significant photocatalytic performance when PDA thickness was ~1 nm [244]. The photoelectrochemical studies comparing bare TiO_2 with TiO_2/PDA nanocomposites reported the photocurrent for the different shells. This behavior is increased at low overpotential values. Otherwise, below 0.3 V at the coated photoanode, it is possible to notice spike-like peaks that suggest a higher recombination rate at this electrode. The PDA coated material showed a ≈ 35% increased photocurrent compared with bare TiO_2, a stable photocurrent density of 3.1 x 10^{-3} mA cm^{-2} [245]. This thickness dependency suggests tunneling and confinement effects presence, although the possibility of ordinated early stages ordinated growth and critical thickness is not discarded.

In other studies, TiO_2@PDA photocatalysts examined under UV-Vis light irradiation showed faster methyl orange (MO) and methyl violet (MV) depletion rates, when compared with bare TiO_2. The improvements are from 87.1% (bare TiO_2) to 95.2% for methyl orange, improving the catalytic efficiency by 8.1% (Fig. 7g). Regarding methyl violet, the catalytic behavior improved 9.9% from 85.7% (bare TiO_2) to 95.6%, (Fig. 7h). Additionally, by modifying the TiO_2 surface with PDA, the photocatalytic efficiency of degrading Rhodamine B (RhB) showed an improvement of 35.0% under Vis light irradiation (Fig. 7i). However, it is improved only by 4,86% under UV-Vis light (Fig. 7j), showing that the functionalization of TiO_2 with PDA exhibits an immediate improvement in the visible spectra [244].

Additional strategies have been investigated in order to improve the photocatalytic performance of TiO_2 composites further, for example, improving the surface area and available active sites. All of them aiming to achieve better photo-degradation performance of the already enhances TiO_2/PDA nanocomposite. Among these examples, we find a study in which a soft catalytic adsorbent is combined with PDA-modified bacterial cellulose (BC) in the shape of a nanofiber BC/PDA/TiO_2. The results were successful in fulfilling all these essential requirements allowing 6,4. 5.7 and 4.8 times faster photo-degradation of MO, RhB and methylene blue (MB) (respectively) than commercial P25 and other TiO_2- based photocatalysts. Also, BC/PDA/TiO_2 showed excellent stability and reusability with only a 5.5% of decrement in the degradation efficiency after 5 cycles [246]. Another interesting result was achieved by the combination of TiO_2 and PDA with another catalyst such as TEMPO. It has been shown that a strong synergistic effect between TEMPO and PDA exists and helps to achieve better conversion for selective oxidation of sulfides with aerial O_2 [247].

Overall, core-shell nanocomposites have large possible applications in different fields like biology, catalysis, energy conversion or storage device [248]. TiO_2 is a promising material with several applications in different fields related to photocatalysis, photovoltaics, sensors or photo/electrochromic [231,249–251]. Many applications can be enhanced or improved by modifying them with different inorganic and organic dyes [228]. PDA can also unveil new utilities, for instance, the regulation of toxic intermediates in hazardous waste depletion reactions. In the pentachlorophenol (PCP) photodegradation process, 2 toxic intermediates are created, 1,4 benzoquinone (TCBQ) and trichlorohydroxy-1,4- benzoquinone (OH-TrCBQ), unveiling a new issue by inducing a second pollution source. As the PDA layer can promote electrons transfer from H_2O_2 and $O_2^{\cdot-}$ to the P25 (TiO_2) conduction band, ROS can be synthesized at the surface of the photocatalyst P25@PDA provoking TCBA and OH-TrCBQ synthesis. As ROS are the reactive compounds that lead to the synthesis of the toxic intermediates, their dynamic control can be regulated by P25/PDA control [252].

2.4.2. ZnO/PDA composites

Zinc Oxide (ZnO) is an n-type semiconductor with a broad bandgap of 3.4 eV, which presents an absorption edge around 380 nm [253] and remarkable room-temperature luminescence [196]. ZnO is composed of oxygen and zinc atoms which are tetrahedrally bonded (wurtzite type unit cell). The positive charge and negative charge center can be displaced by external forces triggering lattice distortion, unleashing piezoelectric properties [254]. Regarding the radiative routes, both UV and Vis maxima have a strong dependence on the particle size [255, 256], and by studying this parameter, it was shown that visible emission is due to the transition of photo-generated electrons from the conduction band to a lower band [255]. Another possible explanation is that oxygen vacancies are responsible for the recombination centers that allow visible luminescence of ZnO [257–259].

Several ZnO nanoparticles can be synthesized, allowing for many morphologies and superior levels of control. Among them, ZnO nanospheres or nanobundles can be obtained by thermal decomposition or thermolysis using N.N'-bis(salicylaldehyde)ethylenediamine)zinc(II) as a precursor [260]. Also, several nanostructures like nanotubes [261], nanowires/nanorods [262,263] or nanotretapods [264] can be grown by multiple methods, including thermal evaporation, electrodeposition or vapor deposition. This large availability and versatility of morphologies have positioned ZnO among the most widely studied photoactive materials. Furthermore, as a part of its electronic and optical properties, ZnO nanoparticles have been used as antibacterial material and have shown the ability of light-driven processing wastewater. Although its optical activity can be compared with TiO_2, its absorption edge is broader, extending to part of the visible region, thus resulting in better performance under sunlight [265,266]. Nevertheless, ZnO is sensible to photo-corrosion, presenting low stability and experimenting with a fast recombination rate. These drawbacks have been addressed by coupling ZnO with other semiconductors, doping it with metals or functionalizing its surface with different organic polymers, effectively increasing its applicability [267]. Therefore, functionalizing the ZnO surface with PDA can result in overcoming those issues. PDA incorporation in a nanocomposite can provoke different types of concentration defects that can affect optical and electronic properties of ZnO, thus leading to changes in excitonic (e-h pair) and photoluminescence [81].

Studies on ZnO/PDA materials have shown similar trends observed in TiO_2/PDA materials. For example, bandgap values of ZnO/PDA nanorods (Fig. 8a) were influenced by dopamine concentration showing saturation at concentrations of 0.5–0.7 mg ml^{-1}, HRTEM images of different dopamine concentration ZnO/PDA interfaces are shown in: Fig. 8b (0.3 mg ml^{-1}), Fig. 8c (0.5 mg ml^{-1}), Fig. 8d (0.7 mg ml^{-1}) [81]. Studying several concentrations of PDA, it was found that all the values were lower than the one for ZnO single crystal, for instance, an average value of 3.22 eV for [PDA] = 0.3 mg ml^{-1} or 3.18 eV for [PDA] = 0.5 mg ml^{-1} (Fig. 8e). Therefore a clear trend appeared, in which lower bandgap values were observed at higher PDA concentration (thickness), as shown in Fig. 8f. Additionally, the reduction of vacancies and charge transfer from ZnO towards PDA could lead to this behavior. Similar effects are exhibited by acceptor-doped ZnO nanostructures or Schottky-type junction [268]. Typically, photoluminescence emission spectra is a simple method that can be used to detect surface defects [269,270]. In such cases, the emission vs excitation power plot enables us to know the quantum efficiency and the defect concentration [271, 272]. The authors reported on the PL spectra ZnO/PDA nanorods at room temperature, which showed 2 peaks located in the UV and Vis region corresponding with exciton and defect emission (Fig. 8g) [73, 269]. After variations in thickness (Fig. 8h) of the PDA, the PL spectra exhibited a small peak shift. The UV peak at 378 nm was downshifted to a shorter wavelength while, the Vis peak was shifted to a longer wavelength.

As a result, PDA deposition over ZnO was demonstrated to decrease oxygen vacancies from 1.5 x 10^{15} cm^{-3} to 1.2 x 10^{14} cm^{-2} resulting in a photoluminescence quantum efficiency decrease, from 0.28 to 0.12,

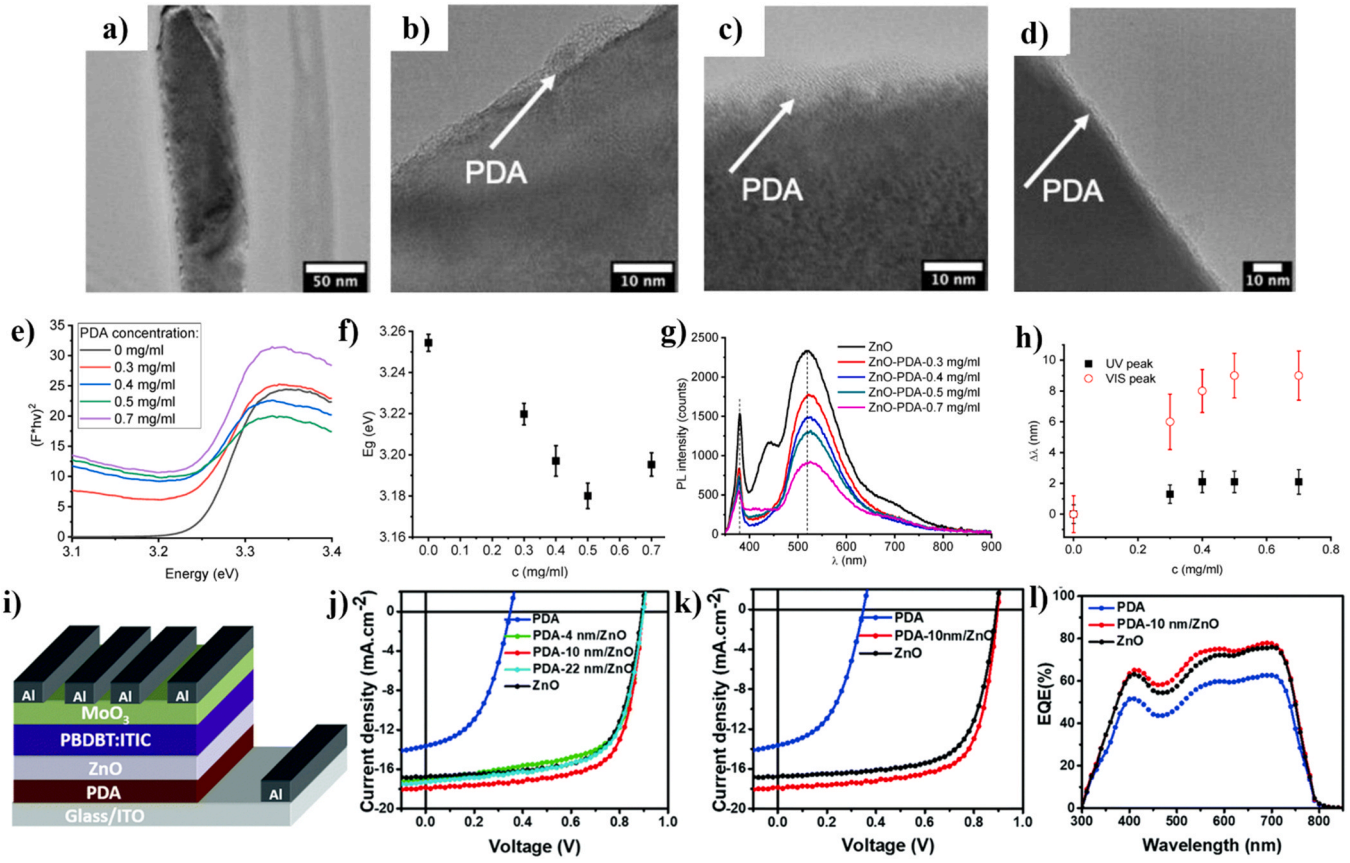

Fig. 8. (a) TEM image of ZnO/PDA nanorod (0.5 mg ml^{-1}). HRTEM images of: (b) ZnO/PDA interface (0.3 mg ml^{-1}), (c) ZnO/PDA interface (0.5 mg ml^{-1}), (d) ZnO/PDA interface (0.7 mg ml^{-1}) [81] Optical characterization of ZnO/PDA nanorods varying PDA concentration, (e) bandgap estimation graphical representation, (f) Bandgap variation with dopamine concentration, (g) PL spectra, (h) Change of the PL peak position for UV and Vis range [81], (i) Organic solar cell device structure, (j) Current density vs voltage (JV) characteristics PBDT-ITIC with different PDA/ZnO ETLs under AM 1.5 G solar irradiation (100 mW/cm^{-2}), (k) various ETLs in optimal conditions J-V curves of PBDT-ITIC solar cells, (l) External quantum efficiency spectra. Reproduced from Ref. [273] with permission from the Royal Society of Chemistry.

respectively. The PDA coating also modified the activation energies in ZnO/PDA decreasing exciton binding energy from 0.053 to 0.044 eV. Moreover, the PDA layer influenced photoluminescence quenching. The increment of PDA thickness enhanced PDA light absorption, thus increased the quenching effect [81]. Furthermore, the changes in the thickness of the PDA layer and the decreasing defect concentration can explain the reduction of PL intensity; meanwhile, the decreasing of activation energies and the peak shifting could be due to forming an additional local electrical field between PDA and ZnO [73]. Additionally, photo-induced electron-hole pair recombination kinetics has a strong influence on the catalytic efficiency of photocatalysts. PL emission arises by recombining free carriers and having lower emission intensity sign that the recombination rate is low with higher separation efficiency [274]. Moreover, regarding ZnO/PDA composites, catechol, besides being the PDA group that attaches to the surface of ZnO (binding hydroxyl groups from PDA with ZnO surface oxygen vacancies), can act as an electron trap due to their electron-withdrawing nature, avoiding the recombination of electron and holes (e-h pairs) decreasing the fast recombination rate and improving the photocatalytic behavior [196]. The available results agree with the direct Z-scheme ZnO/PDA photocatalyst, which favors charge separation and enlarges light-harvesting for photocatalytic performance, such as in the case of the CO_2 reduction reaction [275]. As a newfangled application, PDA can be used in solar cells and enhance photovoltaic performance. The strong adhesive properties of PDA combined with the strong chelating behavior towards metal ions leads to the construction of low-defect and uniform PDA thin films on ZnO, with enhanced electron transfer performance. Because of those characteristics, ZnO/PDA nanocomposites can be used as an electron transfer layer (ETL). Studies that implement ZnO/PDA as ETL in inverted non-fullerene organic (PBDBT:ITIC) solar cells [273] and polythieno[3,4-*b*]-thiophene/benzodithiophene:[6,6]-phenyl-C70-butyric acid methyl ester (PTB7:$PC_{70}BM$) bulk heterojunction solar cell [276], have shown an increased photovoltaic behavior when PDA is implemented along ZnO for electron transport. Regarding PBDBT:ITIC solar cells, several devices (Fig. 8i) were designed varying PDA thickness, 4, 10 and 22 nm, showing ZnO/PDA (10 nm PDA thickness) the best results in current vs voltage measurement (Fig. 8j and k) and external quantum efficiency (Fig. 8l). It produced the highest efficiency; J_{sc} = 17.86 mA cm^{-2}, V_{oc} = 0.88 V and FF = 70.91% allowing PCE = 11.14% obtaining an enhanced electrical conductivity, which evidences that the PDA layer improves carrier lifetime, charge extraction and decreases charge recombination [273]. About PTB7:$PC_{70}BM$ solar cells, samples with PDA thickness about 30–40 nm and 80–100 nm showed an increment of 9.8% for V_{oc}, 23.2% in case of FF and 13.8% for PCE. However, the trend was not the same for J_{sc}, which decreases with DPA. Even so, devices with ZnO/PDA showed a higher photoelectric conversion efficiency over the full absorption spectra than the one with only bare ZnO as ETL [276].

2.5. *Metal sulfides*

Metal sulfides are excellent candidates for photocatalysis due to their large availability and optical properties. However, they suffer from many drawbacks as photocatalytic aqueous environments strain their

chemical stability [277]. Here we present some of the recent advancements in the field of metal sulfides and PDA nanocomposites,

2.5.1. ZnS/PDA composites

ZnS is an n-type semiconductor that presents a direct bandgap energy value between 3.6 and 3.9 eV [278]. Its high reduction potential and the fast production of photocarriers allows ZnS based nanocatalysts to be employed in photochemical applications like the reduction of CO_2, H_2 production or purification of wastewater [279–283]. Different shapes and sizes have been synthesized, like rods, tubes, spheres or wires, and as in the case of other semiconductor materials, they can be prepared with several methods. In general, the shape and final structure of the nanomaterials strongly depend on the characteristics of the organic stabilizers, like concentration or molecular weight. The most employed methods in the literature are; a one-pot process that uses $ZnCl_2$ and $ZnSO_4$ as zinc precursors and Na_2S as sulfur precursor, sol-gel method [278] and hydrothermal synthesis with zinc nitrate, zinc acetate and zinc chloride as zinc precursors [284,285].

Though ZnS photocatalysts have appropriate characteristics to act as a straightforward catalyst, it has shown instability induced by the oxidation of sulfide ions, which is mainly caused by photogenerated holes. This photo corrosion is a drawback to the applicability of many sulfides, including zinc sulfides, since they do not meet photocatalytic and environmental stability requirements [286–289]. Several strategies have been developed to minimize those problems and increase the photochemical activity of sulfides, like doping with metal or metal/ions, use of sacrificial agent/layers or surface modification, and coating with conductive polymers [278,290–294]. The surface modification with PDA has been posed as a solution to this instability issue. Additionally, ZnS/PDA nanocomposites present a doubly staggered heterojunction, which is beneficial for the efficiency of the composites. This type II band alignment generates a considerable reduction of the bandgap (Fig. 9a). Studies have shown that coating ZnS by PDA, adds a layer of ZnSO to the nanocomposite, as a direct consequence of this band alignment, photoexcited electrons will be trapped in ZnSO conduction band; meanwhile, counter holes will be placed in the valence states of PDA. Recombination of charge carriers is going to be prevented by the charge separation between ZnSO (also ZnS) and PDA.

Additionally, the interface between ZnS/ZnSO presents a type I isotype heterojunction (n-n), which enhances the accumulation of photogenerated carriers in the ZnSO end of the interface (Fig. 9b). By all of these features, photocatalytic activity is enhanced [114]. Researched studied the influence of PDA shell in the final bandgap value, several samples with different thicknesses were synthesized i.e. ZnS/PDA1 (1.2 nm), ZnS/PDA2 (2.1 nm), ZnS/PDA3 (3.5 nm). The calculated bandgaps values using Kubelka-Munk function [292] provided values of 3.64, 3.57 and 3.54 eV, respectively, respectively, with a pristine ZnS bandgap value of 3,73 eV [114].

A recent H_2 production experiment by exploiting ZnS and PDA interface showed results in agreement with that theory. 1.2 nm PDA shell in ZnS/PDA1 nanocomposites exhibited a maximum hydrogen production rate of 2162.5 μmol h^{-1} $g^{-1,}$ maintaining 78.7% of its photoactivity after 24 h of continuous irradiation, see Fig. 9c and d, [114] what it makes ZnS/PDA competitive with other high-performing photoactive composites [295,296]. The transient photocurrent was also studied and compared with bare pristine ZnS (Fig. 9e). In this scenario, ZnS/PDA nanocomposites showed higher photocurrent density than pristine ZnS due to the higher charge efficiency given by the well-organized heterojunction interface. Fast charge-carrier recombination through direct bandgap for bare ZnS provoked a fast decay in photocurrent, not the same situation for ZnS/PDA nanocomposites that showed stable photocurrent during visible light irradiation. Finally,

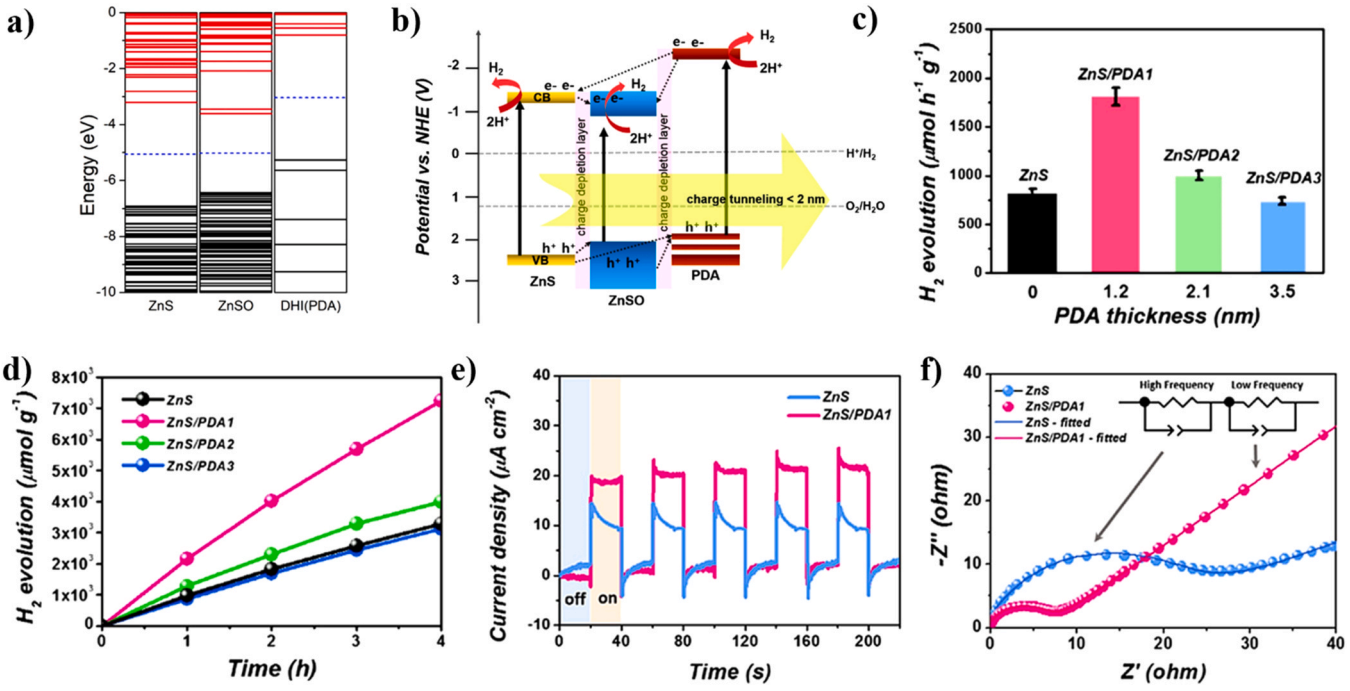

Fig. 9. (a) ZnS, $ZnS_{1-x}O_x$ (ZnSO) and 5,6- dihydroxyindole (DHI) electronic band structures. Black and red lines represent filled and unfilled states, respectively, (b) Representation of ZnSO, ZnS and PDA heterojunction and photocatalytic process considering charge carrier transfer. Oxygen incorporation in ZnSO decreases the conduction band edge, enlarging the light absorption region. Meanwhile, the LUMO of the DHI has an energy of 2.38 eV and is located above the conduction band edge of pristine ZnS, and its HOMO energy is around 1.5 eV above the fermi level of pristine ZnS [114]. Photocatalytic study for different PDA shell thickness values: ZnS/PDA1 (1.2 nm), ZnS/PDA2 (2.1 nm), ZnS/PDA3 (3.5 nm), (c) Photocatalytic H_2 production, (d) Time-dependent photocatalytic activity, (e) transient photocurrent response with and without light illumination, (f) electrochemical impedance spectra. Reprinted from Applied Catalysis B: Environmental, 280, Y. Kim, E. Coy, H. Kim, R. Mrówczyński, P. Torruella, D.W. Jeong, K.S. Choi, J.H. Jang, M.Y. Song, D.J. Jang, F. Peiro, S. Jurga, H.J. Kim, Efficient photocatalytic production of hydrogen by exploiting the polydopamine-semiconductor interface, 119423. Copyright (2021) with permission from Elsevier. (For interpretation of the references to color in this figure legend, the reader is referred to the web version of this article.)

electrochemical impedance spectroscopy (EIS) measurements were done to investigate charge transfer. As a result, more considerable charge transfer resistance for pristine ZnS (17.48 Ω) than for ZnS/PDA (6.62 Ω) showing a superior efficiency and reaction rate for the PDA nanocomposite (Fig. 9f) [114].

Overall, researchers have demonstrated that PDA attaches covalently on ZnS surfaces, adding a thin oxide layer, which enhances the photoactivity of the composite. Moreover, the efficiency of the ZnS/PDA was boosted as well as its chemical stability. The results are essential since they are one of the first studies showing direct bandgap reduction on a none metal oxide semiconductor, and at the same time, show similar trends on thickness dependence and bandgap tuning, which advocates for intrinsic PDA electronic effects [114].

2.5.2. CdS/PDA nanocomposites

Another excellent sulfide material, which, although extremely promising, has suffered from its somewhat hazardous degradation in aquatic media, is Cadmium Sulfide (CdS). CdS is an n-type semiconductor that presents a narrow gap of 2.4 eV [297], making it one of the most prominent photocatalysts for photocatalytic H_2 production [298–300]. CdS photocatalysts can absorb light in the visible region at shorter wavelengths than 516 nm, where it shows excellent photochemical properties and quantum efficiency [301]. Moreover, it also presents a good carrier transportation capacity, producing photogenerated electrons and holes within a considerable period. This effect extends the photogenerated carriers life, thus improving photocatalytic activity [302]. Due to these properties, CdS is employed in photocatalytic hydrogen production, degradation of pollutants and reduction of CO_2 [303,304].

Different structures have been studied in the case of CdS, and their influence on photocatalytic performance was evaluated. First, zero-dimensional structures (0D) can be obtained through several methods, i.e. combustion method, biogenic synthesis, complex thermolysis, sonochemical method or chemical precipitation, among others [305–311]. Even though it presents a large surface area, it tends to agglomerate in an aqueous solution, thus decreasing photocatalytic efficiency. One-dimensional nanostructures (1D) such as nanowires, nanorods and tetrapods can be synthesized by using ligand assisted growth [312–315], metal particle seed growth [316–318], ion exchange [298] and ligand-assisted growth [315,319]. Those structures exhibit a large specific surface area/volume ratio, fast separation of photogenerated carriers, and quantum confinement effects in radial and bulk-like carrier transport in the axial direction [318,320–322]. Recently, 2-dimensional CdS nanosheets have shown excellent photocatalytic properties [322–324]. It is possible to obtain two-dimensional structures (2D) from the one-step chemical solvothermal method [325], which show higher photocatalytic efficiency than 0D and 1D CdS nanoparticles [326]. 3-dimensional structures present a high surface/-volume ratio and low density [324,327,328]. Different kinds of such structures exist, e.g. hierarchical dendritic CdS, hollow spheres or porous nanosheet-assembled flowers [326]. Most of these structures can be created by a self-assembly process and the accumulation of CdS in different structures, granular or nanosheets [329]. Moreover, these structures have shown to be more conducive and exhibit improved photocatalytic activity [326].

Although the aforementioned CdS properties make it a promising catalyst, it is also common for the CdS nanocatalyst to suffer from photo corrosion during the photocatalytic process, directly affecting the application of CdS and CdS-based photocatalysts in the industrial field. Three different aspects cause this photo corrosion. The first one is because sulfur ions are going to be combined with the photogenerated electron-hole pairs created during the process and are going to be oxidized into sulfur. The second one implies that photogenerated holes on the surface of CdS provoke anode corrosion during the catalytic process. The last one is that the photocatalytic process leads to the emergence of defects on the surface of the CdS photocatalysts which contribute to photogenerated e-h pairs being trapped and causing redox reactions on the CdS surface under aerobic conditions. As a consequence of photocorrosion, photocatalysts become unstable and catalytic performance is decreased [330]. This situation is worsened by Cd's rather hazardous effect on aquatic life and human health [331,332].

Aiming to decrease photocorrosion several strategies have been studied in recent years. Strategies such as combining CdS with micro [333] and mesoporous materials [333,334], create composites with other layered oxides [335], coupling with metallic or non-metallic catalysts [334], creating core/shell structures [336], or building heterojunctions [337]. As expected, one of the most efficient ones is the preparation of passivating layer, which, although it tends to hinder some of the performance, retains most of the material's properties.

A photoelectrochemical (PEC) water splitting study using CdS/PDA nanoarrays synthesized on FTO substrate as catalysts compared the bare CdS and CdS/PDA/Co-Pi photocatalytic behavior. Linear sweep voltammetry (LSV) under AM 1.5 G simulated sunlight illumination (100 mW $cm^{-2)}$ was performed to study CdS, CdS/PDA and CdS/PDA/Co-Pi (Fig. 10a). Photocurrent intensities showed firstly an increment which, while PDA deposition was higher, turned into a decrement. This provoked the largest photocurrent density at 1 h for CdS/1PDA, exhibiting that the heterojunction built between CdS and PDA (Interface is shown in Fig. 10b and c) can promote charge separation of photogenerated carriers and the remain of PDA in this particular case could stand against this phenomenon [338]. EIS was used to check this, giving, as a result, smaller charge transfer resistance for CdS/1PDA than for bare CdS. 3063 Ω vs 3359 Ω respectively (Fig. 10d) agreement that the charge transfer is improved when exists an interface between CdS and DPA [339,340]. Two different effects explained this. Firstly, when the thickness is relatively large, as the effective transfer length of charge carriers is limited, they might not be transferred to the surface [114,341], and secondly, the light that reaches the surface of CdS/1PDA is reduced because of the absorption of the dark PDA layer which becomes darker with time [342]. Regarding photocurrent density, for CdS/1PDA, nanocomposite obtained a value of 1.08 mA cm^{-2} (0.28 V vs RHE), which is 2.4 times more than the one for bare CdS. Also, photocurrent stability studies showed that it decreased for bare CdS more than for CdS/1PDA, indicating that the interface between CdS and PDA could promote the hole concentration in CdS by creating a built-in field, thus ameliorating the photoelectric performance.

Aiming to promote the PEC performance of the nanocomposite, Co-Pi co-catalyst was added on the surface of the CdS/1PDA photoanode (Fig. 10e) before, several Co-Pi thicknesses, controlled by different times of photoelectric deposition (2.5 min, 5 min, 7.5 min, and 10 min), CdS/1PDA/Co-Pi nanocomposites were synthesized. CdS/1PDA/5Co-Pi showed the smallest radius leading to the best transfer and charge separation, decreasing the e-h recombination due to the Co-Pi catalyst. Moreover, photocurrent stability was enhanced, and it exhibited photocurrent density value up to 2.68 mA cm^{-2} at 0.28 V vs RHE, which is 5.7 times higher than bare CdS and 5.87 times higher than CdS/1PDA [342], see Fig. 10f.

The resulting heterojunction with PDA showed an increment in photocatalytic behavior due to the appropriate match of bandgap edges between CdS and PDA, making charge separation more efficient [200] and decreasing the recombination rate [245]. Furthermore, by adding another co-catalyst, those improvements can be enhanced and used in water splitting reactions [342] (see Fig. 10g).

2.6. Emergent materials

Despite being used as a surface modifier that can create heterojunctions with well-known semiconductor metal oxides, polydopamine can be incorporated into another material, creating a photosensitizer shell and acting on another purpose such as, for instance, templates. Here we summarized the most recent and promising emergent materials, which contain PDA in their structure for such diverse applications as

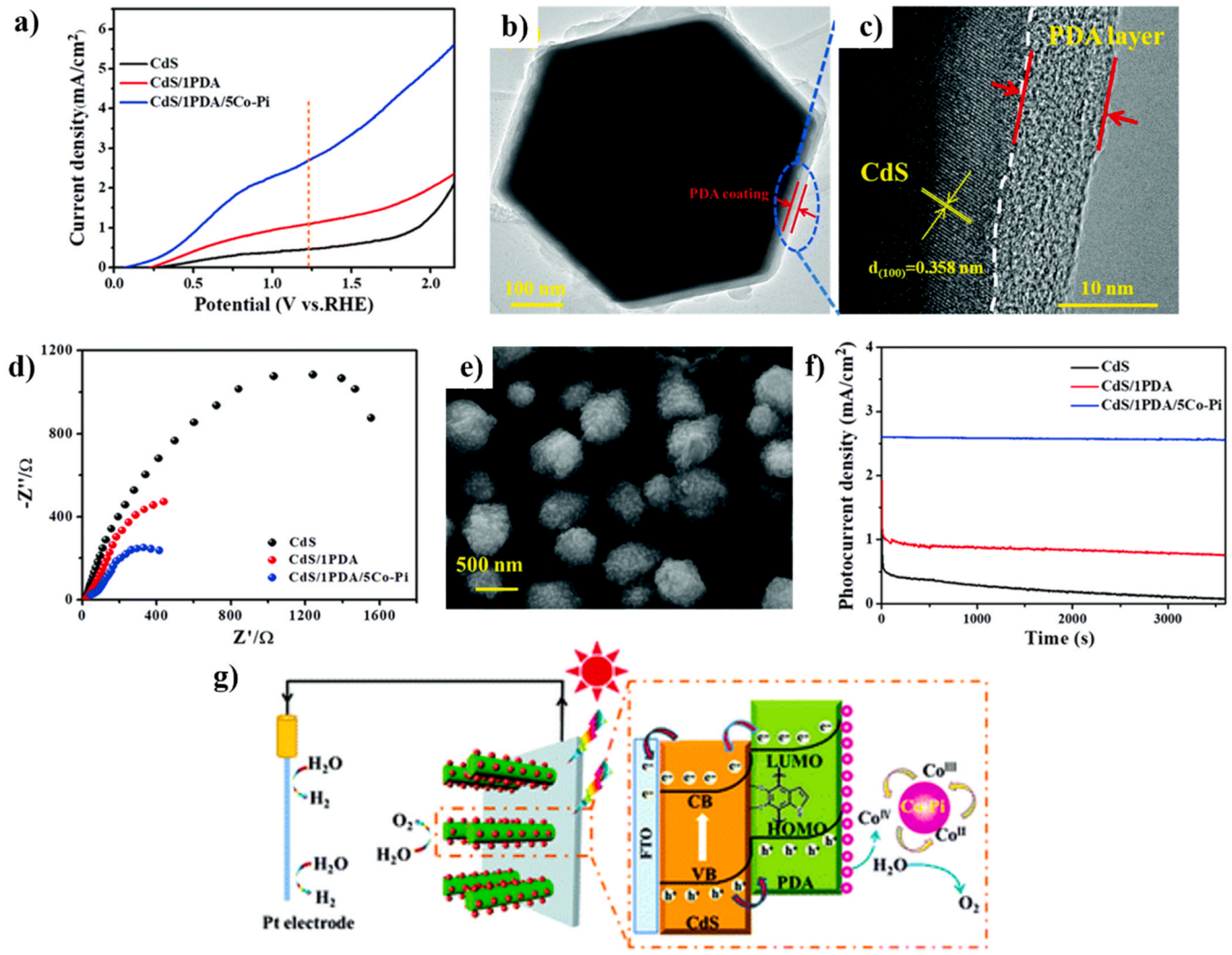

Fig. 10. (a) LSV plot for CdS, CdS/1PDA and CdS/1PDA/5Co-Pi photoanodes under AM 1.5 G illumination, (b) TEM image of CdS/1PDA, c) HRTEM image of CdS/PDA where the thickness of the PDA layer is shown, (d) EIS plot for CdS, CdS/1PDA and CdS/1PDA/5Co-Pi photoanodes, (e) Top-view SEM image of CdS/PDA/Co-Pi, (f) Photocurrent-time (I-T) graphical representation of CdS, CdS/1PDA and CdS/1PDA/5Co-Pi photoanodes at 0.28 V vs RHE under simulated sunlight illumination for a consistent 3600 s, (g) Proposed mechanism for CdS/PDA/Co-Pi acting as photoanodes for photoelectrochemical (PEC) water splitting, The interface between CdS and PDA as mentioned promotes charge separation which decreases the charge concentration and corrosion of CdS achieving an improvement of PEC activity besides the photoanode stability. Once Co-Pi OER is co-catalyst, it can act as a hole transfer channel where Co^{2+} can be oxidized by the photogenerated holes towards Co^{3+} or Co^{4+}, species that can improve the photostability of the composite by banning charge recombination and promoting water oxidation kinetics. Reproduced from Ref. [342] with permission from the Royal Society of Chemistry.

environmental remediation, fight against cancer or antibacterial performance in artificial implants.

Solar light can be used as an environmental-friendly and renewable energy source for wastewater purification and seawater desalination. Nevertheless, its use to achieve water steam is restricted by several factors like low energy conversion efficiency, low solar spectrum absorption or complex synthesis.

2.6.1. *MXenes*

A new material made by PDA and MXene has been developed, achieving overcoming these issues. It is an exciting example of a relatively new family of materials bases on transition metal carbide, nitride or carbonitrides (MXene). Since their discovery in 2011, they have become widely studied photocatalytic materials [353]. MXene has the following formula: $M_{n+1}X_nT_x$ where M represents the early transition metal (e.g. V, Ti, Zr and Nb), X symbolizes carbon and/or nitrogen, and T stands for the surface functional groups (such as –O, −OH and –F) [354]. The *n* range from 1 to 3, resulting in M_2XT_x, $M_3X_2T_x$ and $M_4X_3T_x$ structures, respectively [354]. To improve the photocatalytic properties of MXenes they might be combined with polydopamine for two main reasons. Firstly, it was demonstrated that the bandgap alignment of MXene could be modulated by means of surface chemistry. Secondly, the surface of the MXenes is terminated by functional groups (-OH, -O, and -F), which are beneficial for creating the contact interfaces between MXene and other semiconductors. Moreover, a layered structure with the conductive metal cores in MXene ensures an excellent metallic conductivity and electron acceptance ability [355]. To date, there were a few reports in the literature that a PDA/MXene heterojunction has been manufactured [191,344,356]. Interestingly, the PDA@MXene photothermal layered heterojunction in combination with a PVDF filter membrane exhibited outstanding water solar to-vapor generation performance with an efficiency of 85.2% under 1 sun illumination. Undoubtedly, significant light absorption (~ 96%) and great photothermal conversion were the essential features. This can be accomplished by the characteristics of the composite where; MXene amplifies the light absorption range of PDA, and the wrapping structure creates water transportation channels whiting the holes of the microspheres. On the other hand, the PVDF membrane allows water transportation towards

the heating surface meanwhile, the hydrophilicity of MXenes and PDA contributes to the properly wettability of the photothermal membrane [344]. Moreover, considering the high solar absorption of PDA and MXene composites, they can be combined with phased change materials (PCMs) to enhance solar to thermal energy conversion as another possible application. New composite PCM (CPCM) has been developed recently by caging polyethylene glycol (PEG) with combining melamine foam (MFO) and Mxene under the action of PDA. As a result, PEG/MPMF CPCM (PEG@MPMF) showed a melting enthalpy value up to 186.2 J/g, representing 99.5% of pure PEG, good heat storage properties improved light absorption and outstanding shape stability and reusability after 100 thermal cycles [345]. These results show an improvement in solving classical PEC thermal material issues like liquid phase leakage, poor photothermal conversion efficiency and low thermal conductivity [357], presenting possible applications of these materials in energy-saving buildings or solar energy storage systems.

Besides PDA/MXene, another recent material developed for solar desalination applications is the MoS_2-based evaporator (MPU-PPU). It is formed by a double layer structure (DLS) where there are two layers. The bottom layer originated from a polyurethane (PU) sponge that has been coating with PDA that will act as an insulation layer and water pump due to its hydrophobicity. The top layer is made of MoS_2 nanoparticles embedded onto 3D porous PU sponge frameworks. In this case, it is going to be responsible for solar light absorption and photothermal conversion. The final result was achieved with a straightforward construction process and exhibited good mechanical flexibility, high evaporation efficiency of 85% under low illumination of 1.0 kW m^{-2} and high evaporation efficiencies over 90% when the illumination was solar (1.5–2.5 kW m^{-2}). These fantastic results were achieved because of the high photothermal efficiency, localized heating effect, hydrophilic bottom layer, which can promote fluid flow to the hot region above and finally, a porous structure that allows adequate water supply and vapor channel. Superior desalination performance, joined with excellent recyclability, provides great potential in possible commercial use [346].

2.6.2. VdW materials (MoS and $MoSe_2$)

Molybdenum disulfide (MoS_2) is a semiconductor that possesses an indirect bandgap of 1.3 eV in bulk. It is considered unsuitable for inducing photocatalytic reactions due to the impossibility of separating charge carriers properly [358]. Nevertheless, MoS_2 2-dimensional nanoparticles, like nanosheets, modify indirect bandgap to a direct bandgap of 1.9 eV, turning the MoS_2 2D bandgap into a suitable VIs light harvesting. This fact, added to the high disponibility of MoS_2 on earth, turns it into a promising VIS responsive photocatalyst [359]. Among the different applications reported in the literature are hydrogen production [360], photosynthesis [361] and environmental remediation [362,363].

2D-MoS_2 nanoparticles or sheets can be synthesized by several methods classified into mechanical exfoliation, chemical exfoliation and bottom-up approaches [364,365]. All of them have their advantages and drawbacks. Among them, to create MoS_2 nanosheets, chemical exfoliation is one of the better options because it can provide a large amount of mono or few-layered nanosheets with higher carrier mobility than other methods, like mechanical exfoliation, making it suitable to scale up [366,367].

However, photogenerated e-h pairs suffer from fast recombination, difficulties in separating the photocatalysts after the reaction and a limited amount of active edge sites, thus decreasing the practical application of MoS_2 based nanocatalysts. Some strategies have been developed in order to minimize those problems. It is well known that the size and shape of MoS_2 influence photocatalytic performance [368]. Therefore by using different precursors like $(NH_4)_2S$, Na_2S or CH_4N_2S, it is possible to obtain different morphologies, as the transition from bulk to nanostructures has a strong influence in the catalytic behavior, for instance, in MoS_2 nanosheets, bandgap shifts from indirect 1.2 eV to direct 1.9 eV by decreasing the number of layers from 8 to 1 [369]. Changes in bandgap values help minimize photogenerated charge carriers' recombination rate improving photocatalytic performance [370]. Besides the varying morphology, other techniques can be used to modify bandgap energy. Decorate MoS_2 catalysts with chemical dopants is one of them, wherein impurities introduced by dopants can trap photogenerated charge carriers [371], and as a direct consequence, Visible light absorption will be increased [372,373]. Typical used metallic dopants are Ni [374], Co [374], Ag [371] or Fe [375] and the most common non-metallic dopants include P [376] and N [377,378]. Apart from doping, another ingenious method to alter bandgap values is to create heterojunction between MoS_2 and other semiconductors [379–381]. Creating MoS_2@PDA nanocomposites can be a suitable nanostructure to enhance the photocatalysis performance of MoS_2. Hitherto MoS_2@PDA nanocomposites have not been deeply studied. There is a lack of literature about properties and applications. A study about how MoS2@PDA nanocomposites can be used in capacitive deionization (CDI) exhibits lower inner resistance because of their better wettability, and much higher specific capacitance bared MoS_2. As a result, the electrosorption rate and desalination capacity are ameliorated. These facts added to the electrochemical stability given by PDA place MoS_2@PDA nanocomposites in a promising material for the CDI process [97].

Continuing within the environmental remediation field, water-splitting devices incorporation is a promising method to obtain H_2 and O_2 usable in energy applications. However, their large-scale production and commercial applications need to develop low-energy and high-efficiency photoelectrocatalysts able to catalyze its reactions without the use of expensive noble metal catalysts, which present several economic drawbacks (see Section 2.3). Regarding hydrogen evolution reaction (HER), recent research has led to the development of a self-sustained photo-driven PMFC which can be fabricated with MoS_2 nanomaterial and, thus, the construction of an electrode made by MoS_2/PDA/TiO_2 towards HER is possible. This nanocomposite can increase charge separation of photogenerated carriers through bio-electrons assistance, and under neutral conditions, it provides special dual-electrons (ebio/epho) route for nanomaterials synthesis and HER. The amorphous MoS_2/PDA/TiO_2 electrode perform outstanding catalytic and photoelectrochemical behavior, low overpotential, 351 mV vs SHE and an astonishing H_2 evolution rate up to 0.003 m^3 m^{-3} min^{-1} in comparison with the sample without the biosynthesis. Boosting continuous hydrogen generation can be achieved due to the ameliorated electricity energy from the PEMFC reactor by serving as a built-in bias [347]. Another interesting material is molybdenum diselenide ($MoSe_2$), which has recently received lots of attention due to its mechanical changes in confiment [382].

Using polystyrene (PS) fibers covered with PDA as a rigid template is possible to obtain a photocatalyst towards HER made of molybdenum diselenide, which is decorated by porous carbon fiber ($MoSe_2$-PCF). PDA covered PS fibers by in-situ polymerization, and PDA carbon fiber holds a highly conductive framework and nanoscale channels with a highly textured surface responsible for facilitating nucleation and growth of $MoSe_2$ nanosheets uniformly. Because of the synergistic effects of $MoSe_2$ and porous carbon fiber substrate, $MoSe_2$-PCF was able to perform good HER activity with a small onset potential of about 70 mV, low Tafel slope (65 mV dec^{-1}) and better long-term stability in acidic media if compared with another non-precious metal catalyst. As a final result, $MoSe_2$-PCF nanocomposite appears as a promising catalyst to HER [348]. Apart from being incorporated as a final material, PDA can be used during the synthesis process and be modified to achieve the final structure. In the particular case of MC@$MoSe_2$ hierarchical hollow nanoboxes, PDA is calcinated during the synthesis achieving a final N-doped carbon (NC) layer that will act as a hollow template and highly conductive substrate. Enhanced catalytic performance towards HER is accomplished due to the combination of functional and structural advantages of NC and two-dimensional layered transition metal dichalcogenides (TMDs), endowing MC@$MoSe_2$ nanoboxes with abundant active edges and high conductivity. The optimal thickness of $MoSe_2$ shell

MC@$MoSe_2$ nanoboxes showed a low onset potential of 61 mV, extremely small overpotential of 164 mV vs RHE at 10 mA cm^{-2}, great reduced Tafel slope value of 55 mV dec^{-1} and a higher exchange current density of 0.102 mA cm^{-2}. Finally, by density functional theory (DFT) calculations and experimental results, strong electronic coupling between NC and MoS_2 has been proved, allowing to an increased carrier density placed around Fermi level and activating H* adsorption places with reduced ΔG_H making MC@$MoSe_2$ nanoboxes a promising material towards HER catalysis [383].

Besides environmental remediation, polydopamine-based materials are of great importance in another actual and global concern application that is aimed to solve and eradicate health problems. Recently, new hybrid materials with PDA have been developed to sort out problems with artificial implants, specifically to fight against cancer or achieve an early diagnosis of several diseases. After implantation, the major issues of artificial implants are possible infections provoked by bacteria and insufficient bone tissue integration, leading to a possible implant failure [384,385]. A common method to enhance antimicrobial properties of implants is to release antimicrobial agents like Zn, Ag or Cu [386–388], but a principal and severe drawback appear, associated with toxicity aggravated by high concentrations [389,390]. The suggested method to overcome this disadvantage is a new bio-functionalized titanium dioxide (TiO_2)/molybdenum disulfide (MoS_2)/polydopamine (PDA)/arginine--glycine-aspartic acid (RGD) nanorod arrays (NAs) prepared on Ti. The composition of TiO_2/MoS_2/PDA/RGD NAs, both in vitro and in vivo, under 660 nm (vis light) and 808 (NIR light) irradiation possess astonishing antibacterial activity. By applying those light wavelength dual irradiation, MoS_2- doped NAs are generating a hyperthermia and reactive oxygen species (ROS) which synergistic effects enhance the bacterial membrane permeability, killing almost all the bacteria within 10 min and also destroying the biofilm. This material not only has antibacterial activity,moreover, it promotes the osteogenic activity. Cell experiments shows that TiO_2/MoS_2/PDA/RGD encourage proliferation and differentiation of osteoblasts, accomplishing a big potential in the noninvasive treatment of post-implantation infection [350].

PDA can be part of nanoplatforms designed for diagnosis. As a part of histone post-translational modification, histone acetylation works by genome stability regulation in repairing DNA damages, controlling nutrient metabolism and chromosome transcription [391,392]. Histone acetylation has been associated with several human diseases, like cancer, Alzheimer's, leukemia or cardiovascular [393]. This process is catalyzed by histone acetyltransferase (HAT) using coenzyme A as an acetyl group donor. Therefore the content of histone acetyltransferase has a strong influence on the expression level of histone acetylation. By developing a fast, sensitive and selective method for histone acetyltransferase detection, it is possible to obtain an early diagnosis about histone HAT-based diseases and the discovery of HAT-based drugs. Novel heterojunction made by black TiO_2 and WS_2 with photoelectrochemical activity was enhanced with a solid-state electron donor PDA, acting as a photoelectrochemical biosensor. The final result showed a wide linear range from 0.01 to 500 nM for HAT detection with a detection limit of 0.0033 nM (S/N = 3), good selectivity, reproducibility and stability being a great potential platform for the detection of the abovementioned diseases [351].

Regarding cancer, standard procedures to treat it such as radiation therapy, chemotherapy or surgery are accompanied by rather severe damage to the patient health. Therefore, a significant number of recent advances in nanotechnology have been focused on cancer diagnosis and therapy [394–396]. Within these applications, photothermal therapy has attracted much attention due to being a low-invasive technique. It consists of creating a high located and controlled hyperthermia by using optical energy and photothermal agent, thus leading to reactions inside the tumor and achieving cancer cell depletion as a result. Carbon-based materials [397–399] and gold nanoparticles-based materials [400–402] have been the most investigated for these applications, but other possibilities based on materials combined with PDA have appeared. The photothermal nanocarrier is made of selenide molybdenum coated by a PDA shell, and anticancer drug doxorubicin (Dox) loaded in it ($MoSe_2$@PDA-Dox) has been studied. By adding PDA onto the surface of MoS_2 nanosheets, the anchor places for loading Dox are being provided, and it is possible to enhance MoS_2 photothermal effects, simultaneously decreasing cytotoxicity. The final $MoSe_2$@PDA nanocomposite showed good biocompatibility, stability and high photothermal conversion efficiency, while it was possible to load doxorubicin in it, thus creating an efficient therapeutic agent capable of releasing Dox induced by pH and heat control. In vivo experiments, $MoSe_2$@PDA-Dox exhibited severe damage to tumor tissue by NIR-induced high located hyperthermia and fast drug release appearing as a great platform to combine chemical and PTT for anti-cancer treatment [403].

2.6.3. Fe_xO_x/PDA composites in photocatalysis?

Several iron oxides are existing, with different crystalline structures and properties. These magnetic materials have found extensive applicability in several fields, e.g., a drug carrier, hyperthermia and cancer therapy, magnetic resonance imaging (MRI), magnetic separation, proton exchange membranes, or sensors. Among others, the most common structures are magnetite (Fe_3O_4), hematite (α-Fe_2O_3) and maghemite (γ-Fe_2O_3) [404]. However, despite the typical application of Iron oxides in catalysis [405–407] and photocatalysis [408], not many studies explore PDA's enhancement or interactions with Iron Oxides. Instead, most of the studies focus on the fabrication advantages of PDA in order to anchor or template metal oxides in functional architectures [154,159, 189,198,409]. Nevertheless, here we summarize some of the most exciting properties of different iron oxides, which we believe can be studied in a combination of PDA heterojunctions.

Magnetite is a semiconductor material with a narrow optical gap that presents high carrier mobility durability and a cheap-straightforward fabrication method [410]. Previous studies about finding a value for optical gap reported its range between 0.1 and 1 eV [411], but more recent studies show that magnetite nanoparticles present a direct and indirect bandgap of 2.40 eV and 2.45 eV, respectively [412,413]. Meanwhile, thin films prepared by chemical vapor deposition (CVD) present values of 2.78 eV for direct and 2.17 eV for indirect bandgaps [414]. It is possible to assert that the crystallite size influences optical properties of magnetite due to the confinement effect [415–417]. Among those changes are optical properties, which affect nanomaterials' photocatalysis behavior [414].

Magnetite nanoparticles can be synthesized by several methods, whereby controlling the synthesis parameters it is possible to tune their shape and size. For instance, it is possible to obtain spherical particles up to 25 nm [418]. In turn, with the hydrolysis method, it is possible to obtain larger particles up to 50 nm with cubo-octahedral structures [419], among other morphologies and sizes obtained with other methods like sol-gel technique [420] or thermal decomposition [421]. Although the literature in this aspect is too vast to be summarized very briefly, it is essential to remark that these nanoparticles' general applicability and tunability are well established.

Another material is α-Fe_3O_4, which is an n-type semiconductor, that presents a narrow bandgap (2.2 eV) [422], lower than TiO_2 and ZnO. This property, combined with its chemical stability, high surface area, and capacity to absorb light up to 600 nm (collects 40% of the solar spectrum energy), makes it a promising material for photocatalytic applications. Due to the bandgap value and VB edge located lower than the water oxidation potential, its most promising application is photoelectrochemical water splitting (PEC). It presents a theoretical photocurrent of J_{sc} = 12.6 mA cm^{-2} under AM 1.5G solar irradiation allowing a PCE = 15.5% [423,424]. Nevertheless, a high concentration of iron ions is produced in the used bulk, requiring secondary treatment [425]. Moreover, it possesses a high e-h recombination effect, short excited-state lifetime (~1 ps) [426–428], and low diffusion length (~2–4 nm) [429,430], so its efficiency in collection and charge separation as PEC anode is limited. Also, the conduction band of hematite is

below H_2 evolution potential, so an external bias is required [431].

Despite these aspects, no studies have explored the PDA/ α-Fe_3O_4 for photocatalytic applications. Nevertheless, this research has much room since several methods and techniques to synthesize α-Fe_3O_4 nanoparticles are available. All of which can provide a large variety of morphologies and nanoparticle sizes. Nanoparticles, nanotubes, nanowires, nanoflowers and hollow spheres have been synthesized through solution-based methods like hydrothermal [432–434], sol-gel [435,436] and solvothermal [437,438], also is possible to create nanorod arrays, nano-dendritic structures, nanowires and thin films with gas-phase deposition technique [439–444].

Finally, regarding maghemite, a sharp absorption below 600 nm is observed. The experimentally reported bandgap is 2.0 eV [445]. However, it is possible to find other different values for other kinds of structures such as nanofibers which reported bandgap is ~4.2 eV [446]. To obtain different shapes and sizes of maghemite nanoparticles several methods can be performed. For example, maghemite particles of average diameter 8 nm can be grown by a coprecipitation method by using Fe^{2+} and Fe^{3+} salts as an iron precursor in an alkaline medium. Moreover, it is possible to obtain smaller particles using this method, even down to 2 nm, by adding citrate during γ-Fe_2O_3 crystal growth [447]. Another possible method to obtain maghemite nanoparticles is to synthesize maghemite nanoparticles before, by coprecipitation method (average diameter of 7 nm) or modified Massart method (13 nm of average diameter) and in a further step transform them into maghemite by aeration oxidizing [448].

Until now, there is a shortage of information about Fe_xO_y/PDA and its applications in photocatalysis, because most of the applications exploit them as co-catalyst or in the biomedical field [159,163,184,185,222]. Although the field has not been fully explored yet, many nanomaterials are available. Nanometer to micrometer magnetic particles have recently attracted attention because of their possible applications on magnetic recording and in a large of different biological and medical applications (vide supra). Here, hematite and magnetite present suitable characteristics for acting as proper photocatalysts. By surface modification via PDA, it would be possible to enhance their photocatalysis activity by solving problems like low diffusion length and high recombination rate aggregation or low chemical stability.

3. Conclusions and further perspectives

Many new findings related to polydopamine can be expected in the future. As it was shown here, there are several unexplored possibilities and architectures, which are waiting for their exploitation and investigation. In general terms, we would like to mention, e.g. variations of the original oxidation methodology, chemical post modifications of PDA, and the use of DA-derivatives or analogs [27]. However, in this review, we emphasize the photocatalytic performance and energy applications of PDA-based nanocomposites. Most of the referenced works addressed these issues directly or indirectly, showing the growing interest in these materials. Based on the presented literature, we can foresee the increment of studies and projects in this field PDA-based photocatalysis, emphasizing the control of its Physico-chemical properties. Among these studies, the following areas could be of high interest.

- Metal Sulfides like ZnS, MoS_2, CdS and others, are n-type semiconductors with appropriate bandgap structures what makes them a great candidate for photocatalytic applications [278–281,298–300,358]. However, they suffer from photocorrosion and fast charge carriers recombination [297,300,358]. But the latest studies have revealed the following relationship when preparing a composite from them and PDA, such heterojunctions are advantageous for photocatalytic reactions with respect to the charge transport, charge separation, and cycle stability [114,342]. That is why one should expect a significant increase in publications describing such solutions.
- Further research and development on the abovementioned MoS_2 and $MoSe_2$ and other materials with a 2D structure known as the van der Waals system raise the possibility of new types of quantum heterostructures with atomically sharp interfaces between 2D layers of dissimilar materials [449]. Especially, the family of transition-metal dichalcogenides (TMDs) is worth mentioning here because it includes several semiconductors with bandgaps ranging from 0.5 eV to 3 eV. Various heterostructured electrocatalysts have been obtained and tested, namely: MoS_2/$MoSe_2$ [450], MoS_2/rGO [451], MoS_2/VS_2 [452], MoS_2/WS_2 [453]. But in order to fully exploit the potential of van der Waals heterostructures for photocatalytic applications, huge progress in material science is needed. This can be achieved by further modification with polydopamine coatings or interfacial membranes. Moreover, laminar heterojunction between polydopamine and semiconductors may prove to be an interesting direction, especially those including 2D materials and stacked composites. However, the procedure for obtaining PDA thin layers at the air/-water interface should be improved [138,142,454], especially focusing on the control of truly 2D-like PDA structures [89]. One of the possible ways to obtain films with improved stability is enzyme oxidation, but only the laccase enzyme has been investigated so far [146], opening further opportunities and studies.
- Moreover, different properties of the upper and lower surfaces of the membrane were noted (e.g. roughness and probably water contact angle), which is a challenge for surface engineering [144]. Also, in the experiments described in Section 1.2.2, films have not reached complete homogeneity, which might be an essential aspect to explore in the future, as large scale transferable systems are more and more needed. Furthermore, no conclusive method for transferring membranes to a pre-prepared substrate has been systematically described, except for the rather rudimentary straightforward scooping from the solution surfaces. Nevertheless, more complex and sophisticated methods such as Langmuir Blodgett/Schaefer might be more featured in the following years.
- Considering metal oxides, some of which have already been well described, for instance, for TiO_2 and ZnO [114,225,229,254], but for other materials, it is not so well studied (i.e. Fe_xO_y). Heterojunction between metal oxides and PDA has already been described, but at this point, most of the studies report on experimental enhancements without providing much understanding of the fundamental mechanism and their complex interplay [73]. For example, ZnO nanoparticles have already shown applicability in wastewater treatment, thanks to their photocatalytic activity. Though the ZnO optical absorption edge is wider, reaching even a part of the visible region, thus resulting in better performance under sunlight, this advantage has not been well explored, especially in view of the PDA enhancements reviewed here [265,266]. Furthermore, the coupling of the pizoelectric response and PDA/ZnO composites is also still missing in the literature. It is known that the PDA layer decreases e-h pairs recombination, influences photoluminescence quenching, decreases activation energies, and shifts the absorption peak of ZnO semiconductors, thus improving photocatalytic performance [73,275]. This could also prove to be one of the more exciting research areas over the PDA in the coming years.
- An exciting group of metal oxides are magnetic particles because such nano or microparticles with photocatalytic properties could be used in many different fields, e.g. remediation, biological or medical applications [422]. So far, in the literature, there is little information about Fe_xO_y@PDA heterojunctions and their applications in photocatalysis. Whereas, modification of hematite or magnetite surface with PDA influences and eliminates some disadvantages, such as low diffusion length, high recombination rate, the tendency to aggregation or low chemical stability. Nevertheless, most of the studies are focused on the applications of Fe_xO_y@PDA nanomaterials on biomedicine [154,189,198,409], especially in photothermal therapy [455]. However, the inherent overlapping between electron transfer,

catalysis, physical properties and biocompatibility of these composites has yet to be fully explored, which could provide novel functionalities or a deeper understanding of the applicability of these composites.

Finally, several studies are needed in order to shed some light on the PDA/Semiconductor interface, for example, studies controlling the chromatic and crosslinking level of PDA layers from different reducing agents and their influence on the photocatalytic performance of such nanocomposites. Also, studies in which the PDA shells' hydration and conductivity are studied, perhaps in combination with diffusion experiments in deuterated media. Moreover, the investigation of hot electrons or piezoelectrically generated carriers on PDA-based composites might bring novel functionalities in piezo-catalysis and PDA applications. Overall, several studies can be sketched and outlined for the following years, especially those focusing on polydopamine's electronic and optical properties.

CRediT authorship contribution statement

Daniel Aguilar-Ferrer: Writing – original draft, Writing – review & editing, Visualization. **Jakub Szewczyk**: Writing – original draft, Writing – review & editing, Visualization. **Emerson Coy**: Writing – original draft, Writing – review & editing, Visualization, Supervision, Conceptualization, Funding acquisition.

Author Contribution

All authors reviewed and gave their approval for the submission of the manuscript.

Declaration of Competing Interest

The authors declare that they have no known competing financial interests or personal relationships that could have appeared to influence the work reported in this paper.

Acknowledgements

Authors acknowledge the financial support from the National Science Centre (NCN) of Poland by the OPUS grant 2019/35/B/ST5/00248.

References

[1] J. Hwang, Y. Jeong, J.M. Park, K.H. Lee, J.W. Hong, J. Choi, Biomimetics: forecasting the future of science, engineering, and medicine, Int. J. Nanomed. 10 (2015) 5701–5713, https://doi.org/10.2147/IJN.S83642.
[2] C. Chen, S. Bang, Y. Cho, S. Lee, I. Lee, S. Zhang, I. Noh, Research trends in biomimetic medical materials for tissue engineering: 3D bioprinting, surface modification, nano/micro-technology and clinical aspects in tissue engineering of cartilage and bone, Biomater. Res. 20 (2016) 10, https://doi.org/10.1186/s40824-016-0057-3.
[3] K. Wanieck, P.E. Fayemi, N. Maranzana, C. Zollfrank, S. Jacobs, Biomimetics and its tools, Bioinspired Biomim. Nanobiomater. 6 (2017) 53–66, https://doi.org/10.1680/jbibn.16.00010.
[4] H. Lee, S.M. Dellatore, W.M. Miller, P.B. Messersmith, Mussel-inspired surface chemistry for multifunctional coatings, Science 318 (2007) 426–430, https://doi.org/10.1126/science.1147241.
[5] H. Lee, J. Rho, P.B. Messersmith, Facile conjugation of biomolecules onto surfaces via mussel adhesive protein inspired coatings, Adv. Mater. 21 (2009) 431–434, https://doi.org/10.1002/adma.200801222.
[6] J.H. Ryu, P.B. Messersmith, H. Lee, Polydopamine surface chemistry: a decade of discovery, ACS Appl. Mater. Interfaces 10 (2018) 7523–7540, https://doi.org/10.1021/acsami.7b19865.
[7] S.N. Ahmed, W. Haider, Heterogeneous photocatalysis and its potential applications in water and wastewater treatment: a review, Nanotechnology 29 (2018), 342001, https://doi.org/10.1088/1361-6528/aac6ea.
[8] A. Kudo, Y. Miseki, Heterogeneous photocatalyst materials for water splitting, Chem. Soc. Rev. 38 (2009) 253–278, https://doi.org/10.1039/b800489g.
[9] D. Spasiano, R. Marotta, S. Malato, P. Fernandez-Ibañez, I. Di Somma, Solar photocatalysis: materials, reactors, some commercial, and pre-industrialized applications. A comprehensive approach, Appl. Catal. B Environ. 170–171 (2015) 90–123, https://doi.org/10.1016/j.apcatb.2014.12.050.
[10] E. Serrano, G. Rus, J. García-Martínez, Nanotechnology for sustainable energy, Renew. Sustain. Energy Rev. 13 (2009) 2373–2384, https://doi.org/10.1016/j.rser.2009.06.003.
[11] D.P. Tabor, L.M. Roch, S.K. Saikin, C. Kreisbeck, D. Sheberla, J.H. Montoya, S. Dwaraknath, M. Aykol, C. Ortiz, H. Tribukait, C. Amador-Bedolla, C.J. Brabec, B. Maruyama, K.A. Persson, A. Aspuru-Guzik, Accelerating the discovery of materials for clean energy in the era of smart automation, Nat. Rev. Mater. 3 (2018) 5–20, https://doi.org/10.1038/s41578-018-0005-z.
[12] G.V. Kaliyannan, S.V. Palanisamy, E.B. Priyanka, S. Thangavel, S. Sivaraj, R. Rathanasamy, Investigation on sol-gel based coatings application in energy sector – a review, Mater. Today Proc. 45 (2021) 1138–1143, https://doi.org/10.1016/j.matpr.2020.03.484.
[13] D. Ponnamma, H. Parangusan, K. Deshmukh, P. Kar, A. Muzaffar, S.K.K. Pasha, M.B. Ahamed, M. Al-Maadeed, Green synthesized materials for sensor, actuator, energy storage and energy generation: a review, Polym. Plast. Technol. Mater. 59 (2020) 1–62, https://doi.org/10.1080/25740881.2019.1614327.
[14] Y. Liu, K. Ai, L. Lu, Polydopamine and its derivative materials: synthesis and promising applications in energy, environmental, and biomedical fields, Chem. Rev. 114 (2014) 5057–5115, https://doi.org/10.1021/cr400407a.
[15] J. McGinness, P. Corry, P. Proctor, Amorphous semiconductor switching in melanins, Science 183 (1974) 853–855, https://doi.org/10.1126/science.183.4127.853.
[16] P. Meredith, T. Sarna, The physical and chemical properties of eumelanin, Pigment Cell Res. 19 (2006) 572–594, https://doi.org/10.1111/j.1600-0749.2006.00345.x.
[17] S. Ito, Reexamination of the structure of eumelanin, Biochim. Biophys. Acta (BBA) Gen. Subj. 883 (1986) 155–161, https://doi.org/10.1016/0304-4165(86)90146-7.
[18] A.B. Mostert, B.J. Powell, F.L. Pratt, G.R. Hanson, T. Sarna, I.R. Gentle, Role of semiconductivity and ion transport in the electrical conduction of melanin, Proc. Natl. Acad. Sci. USA (2012), https://doi.org/10.1073/pnas.1119948109.
[19] W. Cao, X. Zhou, N.C. McCallum, Z. Hu, Q.Z. Ni, U. Kappor, C.M. Heil, K.S. Cay, T. Zand, A.J. Mantanona, A. Jayaraman, A. Dhinojwala, D.D. Deheyn, M. D. Shawkey, M.D. Burkart, J.D. Rinehart, N.C. Gianneschi, Unraveling the structure and function of melanin through synthesis, J. Am. Chem. Soc. 143 (2021) 2622–2637, https://doi.org/10.1021/jacs.0c12322.
[20] W. Xie, E. Pakdel, Y. Liang, Y.J. Kim, D. Liu, L. Sun, X. Wang, Natural eumelanin and its derivatives as multifunctional materials for bioinspired applications: a review, Biomacromolecules 20 (2019) 4312–4331, https://doi.org/10.1021/acs.biomac.9b01413.
[21] S. Hong, Y.S. Na, S. Choi, I.T. Song, W.Y. Kim, H. Lee, Non-covalent self-assembly and covalent polymerization co-contribute to polydopamine formation, Adv. Funct. Mater. 22 (2012) 4711–4717, https://doi.org/10.1002/adfm.201201156.
[22] S. Hong, Y. Wang, S.Y. Park, H. Lee, Progressive fuzzy cation-π assembly of biological catecholamines, Sci. Adv. 4 (2018) 7457, https://doi.org/10.1126/sciadv.aat7457.
[23] J. Liebscher, R. Mrówczyński, H.A. Scheidt, C. Filip, N.D. Hădade, R. Turcu, A. Bende, S. Beck, Structure of polydopamine: a never-ending story? Langmuir 29 (2013) 10539–10548, https://doi.org/10.1021/la4020288.
[24] P. Delparastan, K.G. Malollari, H. Lee, P.B. Messersmith, Direct evidence for the polymeric nature of polydopamine, Angew. Chem. Int. Ed. 58 (2019) 1077–1082, https://doi.org/10.1002/anie.201811763.
[25] A.A.R. Watt, J.P. Bothma, P. Meredith, The supramolecular structure of melanin, Soft Matter 5 (2009) 3754, https://doi.org/10.1039/b902507c.
[26] J. Wünsche, F. Cicoira, C.F.O. Graeff, C. Santato, Eumelanin thin films: solution-processing, growth, and charge transport properties, J. Mater. Chem. B 1 (2013) 3836–3842, https://doi.org/10.1039/c3tb20630k.
[27] J. Liebscher, Erratum: Borderud SP, Li Y, Burkhalter JE, Sheffer CE and Ostroff JS. Electronic cigarette use among patients with cancer: Characteristics of electronic cigarette users and their smoking cessation outcomes. Cancer. doi: 10.1002/cncr.28811, Cancer 121 (2015) 800, https://doi.org/10.1002/ejoc.201900445.
[28] Q. Huang, J. Chen, M. Liu, H. Huang, X. Zhang, Y. Wei, Polydopamine-based functional materials and their applications in energy, environmental, and catalytic fields: state-of-the-art review, Chem. Eng. J. 387 (2020), 124019, https://doi.org/10.1016/j.cej.2020.124019.
[29] F. Solano, Erratum: Borderud SP, Li Y, Burkhalter JE, Sheffer CE and Ostroff JS. Electronic cigarette use among patients with cancer: Characteristics of electronic cigarette users and their smoking cessation outcomes. Cancer. doi: 10.1002/cncr.28811, Cancer 121 (2015) 800, https://doi.org/10.1002/pi.5117.
[30] M. D'Ischia, A. Napolitano, V. Ball, C.T. Chen, M.J. Buehler, Polydopamine and eumelanin: from structure-property relationships to a unified tailoring strategy, Acc. Chem. Res. 47 (2014) 3541–3550, https://doi.org/10.1021/ar500273y.
[31] A. Corani, A. Huijser, T. Gustavsson, D. Markovitsi, P.Å. Malmqvist, A. Pezzella, M. d'Ischia, V. Sundström, Superior photoprotective motifs and mechanisms in eumelanins uncovered, J. Am. Chem. Soc. 136 (2014) 11626–11635, https://doi.org/10.1021/ja501499q.
[32] D.R. Dreyer, D.J. Miller, B.D. Freeman, D.R. Paul, C.W. Bielawski, Elucidating the structure of poly(dopamine), Langmuir 28 (2012) 6428–6435, https://doi.org/10.1021/la204831b.
[33] N.F. Della Vecchia, R. Avolio, M. Alfè, M.E. Errico, A. Napolitano, M. d'Ischia, Building-block diversity in polydopamine underpins a multifunctional eumelanin-type platform tunable through a quinone control point, Adv. Funct. Mater. 23 (2013) 1331–1340, https://doi.org/10.1002/adfm.201202127.

[34] Y. Ding, L.-T. Weng, M. Yang, Z. Yang, X. Lu, N. Huang, Y. Leng, Insights into the aggregation/deposition and structure of a polydopamine film, Langmuir 30 (2014) 12258–12269, https://doi.org/10.1021/la5026608.
[35] C. Battistella, N.C. Mccallum, K. Gnanasekaran, X. Zhou, V. Caponetti, M. Montalti, N.C. Gianneschi, Mimicking natural human hair pigmentation with synthetic melanin, ACS Cent. Sci. 6 (2020) 1179–1188, https://doi.org/10.1021/acscentsci.0c00068.
[36] M. Kohri, Artificial melanin particles: new building blocks for biomimetic structural colouration, Polym. J. 51 (2019) 1127–1135, https://doi.org/10.1038/s41428-019-0231-2.
[37] S. Kinoshita, S. Yoshioka, Y. Fujii, N. Okamoto, Photophysics of Structural Colour in the Morpho Butterflies, FORMA, 2002.
[38] S. Yoshioka, S. Kinoshita, Structural or pigmentary? Origin of the distinctive white stripe on the blue wing of a Morpho butterfly, Proc. R. Soc. B Biol. Sci. 273 (2006). doi:10.1098/rspb.2005.3314.
[39] S. Yoshioka, S. Kinoshita, H. Iida, T. Hariyama, Phase-adjusting layers in the multilayer reflector of a jewel beetle, J. Phys. Soc. Jpn. 81 (2012), 054801, https://doi.org/10.1143/JPSJ.81.054801.
[40] M. Kohri, Progress in polydopamine-based melanin mimetic materials for structural colour generation, Sci. Technol. Adv. Mater. 21 (2020) 833–848, https://doi.org/10.1080/14686996.2020.1852057.
[41] A. Kawamura, M. Kohri, H. Oku, K. Hamada, K. Nakagawa, T. Taniguchi, K. Kishikawa, Structural color materials from polydopamine-inorganic hybrid thin films inspired by rock pigeon feathers, Kobunshi Ronbunshu 74 (2017) 54–58, https://doi.org/10.1295/koron.2016-0044.
[42] A. Kawamura, M. Kohri, S. Yoshioka, T. Taniguchi, K. Kishikawa, Structural colour tuning: mixing melanin-like particles with different diameters to create neutral colours, Langmuir 33 (2017) 3824–3830, https://doi.org/10.1021/acs.langmuir.7b00707.
[43] M. Kohri, Y. Nannichi, T. Taniguchi, K. Kishikawa, Biomimetic non-iridescent structural colour materials from polydopamine black particles that mimic melanin granules, J. Mater. Chem. C 3 (2015) 720–724, https://doi.org/10.1039/C4TC02383H.
[44] T.F. Wu, J.D. Hong, Dopamine-melanin nanofilms for biomimetic structural colouration, Biomacromolecules 16 (2015) 660–666, https://doi.org/10.1021/bm501773c.
[45] A. Kawamura, M. Kohri, T. Taniguchi, K. Kishikawa, Surface modification of polydopamine particles via magnetically-responsive surfactants, Trans. Mater. Res. Soc. Jpn. 41 (2016) 301–304, https://doi.org/10.14723/tmrsj.41.301.
[46] M. Kohri, K. Uradokoro, Y. Nannichi, A. Kawamura, T. Taniguchi, K. Kishikawa, Hairy polydopamine particles as platforms for photonic and magnetic materials, Photonics 5 (2018) 36, https://doi.org/10.3390/photonics5040036.
[47] M. Xiao, Y. Li, M.C. Allen, D.D. Deheyn, X. Yue, J. Zhao, N.C. Gianneschi, M. D. Shawkey, A. Dhinojwala, Bio-inspired structural colours produced via self-assembly of synthetic melanin nanoparticles, ACS Nano 9 (2015) 5454–5460, https://doi.org/10.1021/acsnano.5b01298.
[48] M. Xiao, Y. Li, J. Zhao, Z. Wang, M. Gao, N.C. Gianneschi, A. Dhinojwala, M. D. Shawkey, Stimuli-responsive structurally colored films from bioinspired synthetic melanin nanoparticles, Chem. Mater. 28 (2016) 5516–5521, https://doi.org/10.1021/acs.chemmater.6b02127.
[49] T. Eom, K. Woo, W. Cho, J.E. Heo, D. Jang, J.I. Shin, D.C. Martin, J.J. Wie, B. S. Shim, Nanoarchitecturing of natural melanin nanospheres by layer-by-layer assembly: macroscale anti-inflammatory conductive coatings with optoelectronic tunability, Biomacromolecules 18 (2017) 1908–1917, https://doi.org/10.1021/acs.biomac.7b00336.
[50] C. Zhang, B.H. Wu, Y. Du, M.Q. Ma, Z.K. Xu, Mussel-inspired polydopamine coatings for large-scale and angle-independent structural colors, J. Mater. Chem. C 5 (2017) 3898–3902, https://doi.org/10.1039/c7tc00530j.
[51] M. Vega, E.M. Martín del Valle, M. Pérez, C. Pecharromán, G. Marcelo, Colour engineering of silicon nitride surfaces to characterize the polydopamine refractive index, ChemPhysChem 19 (2018) 3418–3424, https://doi.org/10.1002/cphc.201800747.
[52] X. Shi, J. He, L. Wu, S. Chen, X. Lu, Rapid fabrication of robust and bright colloidal amorphous arrays on textiles, J. Coat. Technol. Res. 17 (2020) 1033–1042, https://doi.org/10.1007/s11998-019-00311-5.
[53] M. Xiao, M.D. Shawkey, A. Dhinojwala, Bioinspired melanin-based optically active materials, Adv. Opt. Mater. 8 (2020) 1–15, https://doi.org/10.1002/adom.202000932.
[54] J.P. Bothma, J. De Boor, U. Divakar, P.E. Schwenn, P. Meredith, Erratum: Borderud SP, Li Y, Burkhalter JE, Sheffer CE and Ostroff JS. Electronic cigarette use among patients with cancer: Characteristics of electronic cigarette users and their smoking cessation outcomes. Cancer. doi: 10.1002/ cncr.28811, Cancer 121 (2015) 800, https://doi.org/10.1002/adma.200703141.
[55] V. Ball, Determination of the extinction coefficient of “polydopamine” films obtained by using NaIO4 as the oxidant, Mater. Chem. Phys. 186 (2017) 546–551, https://doi.org/10.1016/j.matchemphys.2016.11.035.
[56] D. Geschke, Physical Properties of Polymers Handbook, Zeitschrift für Physikalische Chemie, 1997, https://doi.org/10.1524/zpch.1997.199.part_1.128.
[57] A. Kawamura, M. Kohri, G. Morimoto, Y. Nannichi, T. Taniguchi, K. Kishikawa, Full-color biomimetic photonic materials with iridescent and non-iridescent structural colors, Sci. Rep. 6 (2016) 33984, https://doi.org/10.1038/srep33984.
[58] D.G. Stavenga, H.L. Leertouwer, D.C. Osorio, B.D. Wilts, High refractive index of melanin in shiny occipital feathers of a bird of paradise, Light Sci. Appl. 4 (2015), e243, https://doi.org/10.1038/lsa.2015.16.
[59] A. Miller, R. Carchman, R. Long, S.A. Denslow, La Crosse viral infection in hospitalized pediatric patients in Western North Carolina, Hosp. Pediatr. 2 (2012) 235–242, https://doi.org/10.1063/5.0024229.
[60] Ü. Akın, İ. Çelik, Ç. Avcı, N. Tuğluoğlu, Ö.F. Yüksel, Some optical properties of melanin thick film, Mater. Today Proc. 18 (2019) 1972–1977, https://doi.org/10.1016/j.matpr.2019.06.688.
[61] R. Qie, S. Zajforoushan Moghaddam, E. Thormann, Parameterization of the optical constants of polydopamine films for spectroscopic ellipsometry studies, Phys. Chem. Chem. Phys. 23 (2021) 5516–5526, https://doi.org/10.1039/d0cp04796a.
[62] P. Meredith, J. Riesz, Radiative relaxation quantum yields for synthetic eumelanin, Photochem. Photobiol. 79 (2004) 211–216, https://doi.org/10.1562/0031-8655(2004)079<0211:rcrqyf>2.0.co;2.
[63] Z. Xu, N.J. Singh, J. Lim, J. Pan, H.N. Kim, S. Park, K.S. Kim, J. Yoon, Unique sandwich stacking of pyrene-adenine-pyrene for selective and ratiometric fluorescent sensing of ATP at physiological pH, J. Am. Chem. Soc. 131 (2009) 15528–15533, https://doi.org/10.1021/ja906855a.
[64] C. Pan, K. Sugiyasu, Y. Wakayama, A. Sato, M. Takeuchi, Thermoplastic fluorescent conjugated polymers: benefits of preventing π-π stacking, Angew. Chem. Int. Ed. 52 (2013) 10775–10779, https://doi.org/10.1002/anie.201305728.
[65] B. Xiong, Y. Chen, Y. Shu, B. Shen, H.N. Chan, Y. Chen, J. Zhou, H. Wu, Highly emissive and biocompatible dopamine-derived oligomers as fluorescent probes for chemical detection and targeted bioimaging, Chem. Commun. 50 (2014) 13578–13580, https://doi.org/10.1039/c4cc06139j.
[66] J.H. Lin, C.J. Yu, Y.C. Yang, W.L. Tseng, Formation of fluorescent polydopamine dots from hydroxyl radical-induced degradation of polydopamine nanoparticles, Phys. Chem. Chem. Phys. 17 (2015) 15124–15130, https://doi.org/10.1039/c5cp00932d.
[67] P. Yang, S. Zhang, X. Chen, X. Liu, Z. Wang, Y. Li, Recent developments in polydopamine fluorescent nanomaterials, Mater. Horiz. 7 (2020) 746–761, https://doi.org/10.1039/c9mh01197h.
[68] D. Chen, L. Zhao, W. Hu, Protein immobilization and fluorescence quenching on polydopamine thin films, J. Colloid Interface Sci. 477 (2016) 123–130, https://doi.org/10.1016/j.jcis.2016.05.042.
[69] D.R. Amin, C. Sugnaux, K.H.A. Lau, P.B. Messersmith, Size control and fluorescence labeling of polydopamine melanin-mimetic nanoparticles for intracellular imaging, Biomimetics 2 (2017) 1–19, https://doi.org/10.3390/biomimetics2030017.
[70] J.-X. Tian, Y.-Z. Fang, R. Yu, Z.-Y. Zhang, Y.-T. Zhuo, J.-Y. He, S. Wu, Q. Xiao, X. J. Kong, A redox modulated fluorescence nanoplatform for the detection of alkaline phosphatase activity with fluorescent polydopamine nanoparticles, Anal. Methods 13 (2021) 322–326, https://doi.org/10.1039/d0ay02129f.
[71] Y. Zhang, Y. Qiu, K. Zhou, K. Zhang, L. Wang, J. Zeng, B. Ji, D. Gao, Z. Xia, Q. Fu, Self-exothermic redox reaction-driven green synthesis of fluorescent poly (dopamine) nanoparticles for rapid and visual detection of Fe3+, Dyes Pigment. 183 (2020), 108692 https://doi.org/10.1016/j.dyepig.2020.108692.
[72] V. Capozzi, G. Perna, A. Gallone, P.F. Biagi, P. Carmone, A. Fratello, G. Guida, P. Zanna, R. Cicero, Raman and optical spectroscopy of eumelanin films, J. Mol. Struct. 744–747 (2005) 717–721, https://doi.org/10.1016/j.molstruc.2004.11.074.
[73] V. Fedorenko, R. Viter, R. Mrówczyński, D. Damberga, E. Coy, I. Iatsunskyi, Synthesis and photoluminescence properties of hybrid 1D core–shell structured nanocomposites based on ZnO/polydopamine, RSC Adv. 10 (2020) 29751–29758, https://doi.org/10.1039/D0RA04829A.
[74] D. Chen, Y. Mei, W. Hu, C.M. Li, Electrochemically enhanced antibody immobilization on polydopamine thin film for sensitive surface plasmon resonance immunoassay, Talanta 182 (2018) 470–475, https://doi.org/10.1016/j.talanta.2018.02.038.
[75] S. Kianersi, A.A.A. Varjani, Atefeh Solouk, J. Ai, B.P. Lee, Mussel-inspired polydopamine-coated silk fibroin as a promising biomaterial, Bioinspired Biomim. Nanobiomater. 9 (2020) 147–154, https://doi.org/10.1680/jbibn.19.00045.
[76] G. Sun, F. Zu, N. Koch, J. Rappich, K. Hinrichs, In situ infrared spectroscopic monitoring and characterization of the growth of polydopamine (PDA) films, Phys. Status Solidi Basic Res. 256 (2019) 1–8, https://doi.org/10.1002/pssb.201800308.
[77] X. Geng, J. Wang, J. Ye, S. Yang, Q. Han, H. Lin, F. Liu, Electrosprayed polydopamine membrane: surface morphology, chemical stability and separation performance study, Sep. Purif. Technol. 244 (2020), 116857, https://doi.org/10.1016/j.seppur.2020.116857.
[78] N.K. Khanzada, S. Rehman, S.Y. Leu, A.K. An, Evaluation of anti-bacterial adhesion performance of polydopamine cross-linked graphene oxide RO membrane via in situ optical coherence tomography, Desalination 479 (2020), 114339, https://doi.org/10.1016/j.desal.2020.114339.
[79] U. Farooq, J. Zhuang, X. Wang, S. Lyu, A recyclable polydopamine-functionalized reduced graphene oxide/Fe nanocomposite (PDA@Fe/rGO) for the enhanced degradation of 1,1,1-trichloroethane, Chem. Eng. J. 403 (2021), 126405, https://doi.org/10.1016/j.cej.2020.126405.
[80] Z. Xia, G. Liu, Y. Dong, Y. Zhang, Anticorrosive epoxy coatings based on polydopamine modified molybdenum disulfide, Prog. Org. Coat. 133 (2019) 154–160, https://doi.org/10.1016/j.porgcoat.2019.04.056.
[81] D. Damberga, V. Fedorenko, K. Grundšteins, Ş. Altundal, A. Šutka, A. Ramanavičius, E. Coy, R. Mrówczyński, I. Iatsunskyi, R. Viter, Influence of PDA coating on the structural, optical and surface properties of ZnO nanostructures, Nanomaterials 10 (2020) 2438, https://doi.org/10.3390/nano10122438.

[82] G.A. Ortega, J.C. Zuaznabar-Gardona, H.F. Mendoza-León, N. Cayetano-Castro, P. Acevedo-Peña, E. Reguera, Erratum: Borderud SP, Li Y, Burkhalter JE, Sheffer CE and Ostroff JS. Electronic cigarette use among patients with cancer: Characteristics of electronic cigarette users and their smoking cessation outcomes. Cancer. doi: 10.1002/ cncr.28811, Cancer 121 (2015) 800, https://doi.org/10.1002/macp.201900109.
[83] K.G. Malollari, P. Delparastan, C. Sobek, S.J. Vachhani, T.D. Fink, R.H. Zha, P. B. Messersmith, Mechanical enhancement of bioinspired polydopamine nanocoatings, ACS Appl. Mater. Interfaces 11 (2019) 43599–43607, https://doi.org/10.1021/acsami.9b15740.
[84] D.N. Moses, M.A. Mattoni, N.L. Slack, J.H. Waite, F.W. Zok, Role of melanin in mechanical properties of Glycera jaws, Acta Biomater. 2 (2006) 521–530, https://doi.org/10.1016/j.actbio.2006.05.002.
[85] J.D.A. Gracio, A.M.K. Singh, D. Ruch, M.J. Buehler, C.E.T. Al, Self-assembly of tetramers of 5,6-dihydroxyindole explains the primary physical properties of eumelanin: experiment, simulation, and design, ACS Nano 7 (2013) 1524–1532.
[86] S. Lin, C.T. Chen, I. Bdikin, V. Ball, J. Grácio, M.J. Buehler, Tuning heterogeneous poly(dopamine) structures and mechanics: in silico covalent cross-linking and thin film nanoindentation, Soft Matter 10 (2014) 457–464, https://doi.org/10.1039/c3sm51810h.
[87] F.R. Haoqi Li, Jiaxin Xi, Yao Zhao, Mechanical properties of polydopamine (PDA) thinfilms, MRS Adv. (2019), https://doi.org/10.1557/adv.201.
[88] T. Marchesi D'Alvise, S. Harvey, L. Hueske, J. Szelwicka, L. Veith, T.P.J. Knowles, et al., Erratum: Borderud SP, Li Y, Burkhalter JE, Sheffer CE and Ostroff JS. Electronic cigarette use among patients with cancer: Characteristics of electronic cigarette users and their smoking cessation outcomes. Cancer. doi: 10.1002/ cncr.28811, Cancer 121 (2015), 800, https://doi.org/10.1002/adfm.202000378.
[89] E. Coy, I. Iatsunskyi, J.C. Colmenares, Y. Kim, R. Mrówczyński, Polydopamine films with 2D-like layered structure and high mechanical resilience, acsami.1c02483, ACS Appl. Mater. Interfaces 13 (2021) 23113–23120, https://doi.org/10.1021/acsami.1c02483.
[90] K. Lee, M. Park, K.G. Malollari, J. Shin, S.M. Winkler, Y. Zheng, J.H. Park, C. P. Grigoropoulos, P.B. Messersmith, Laser-induced graphitization of polydopamine leads to enhanced mechanical performance while preserving multifunctionality, Nat. Commun. 11 (2020) 5–12, https://doi.org/10.1038/s41467-020-18654-8.
[91] L. Klosterman, Z. Ahmad, V. Viswanathan, C.J. Bettinger, Erratum: Borderud SP, Li Y, Burkhalter JE, Sheffer CE and Ostroff JS. Electronic cigarette use among patients with cancer: Characteristics of electronic cigarette users and their smoking cessation outcomes. Cancer. doi: 10.1002/ cncr.28811, Cancer 121 (2015), 800, https://doi.org/10.1002/admi.201700041.
[92] I. Zmerli, J.P. Michel, A. Makky, Bioinspired polydopamine nanoparticles: synthesis, nanomechanical properties, and efficient PEGylation strategy, J. Mater. Chem. B 8 (2020) 4489–4504, https://doi.org/10.1039/c9tb02769f.
[93] Y. Bai, Z. Hu, J.X. Jiang, F. Huang, Hydrophilic conjugated materials for photocatalytic hydrogen evolution, Chem. Asian J. 15 (2020) 1780–1790, https://doi.org/10.1002/asia.202000247.
[94] Y. Jiang, I. Lawan, W. Zhou, M. Zhang, G.F. Fernando, L. Wang, Z. Yuan, Synthesis, properties and photocatalytic activity of a semiconductor/cellulose composite for dye degradation-a review, Cellulose 27 (2020) 595–609, https://doi.org/10.1007/s10570-019-02851-w.
[95] B.H. Kim, D.H. Lee, J.Y. Kim, D.O. Shin, H.Y. Jeong, S. Hong, J.M. Yun, C.M. Koo, H. Lee, S.O. Kim, Mussel-inspired block copolymer lithography for low surface energy materials of teflon, graphene, and gold, Adv. Mater. 23 (2011) 5618–5622, https://doi.org/10.1002/adma.201103650.
[96] C. Ong, Y. Shi, J. Chang, F. Alduraiei, Z. Ahmed, P. Wang, Polydopamine as a versatile adhesive layer for robust fabrication of smart surface with switchable wettability for effective oil/water separation, Ind. Eng. Chem. Res. 58 (2019) 4838–4843, https://doi.org/10.1021/acs.iecr.8b06408.
[97] Q. Wang, F. Jia, S. Song, Y. Li, Hydrophilic MoS2/polydopamine (PDA) nanocomposites as the electrode for enhanced capacitive deionization, Sep. Purif. Technol. 236 (2020), 116298, https://doi.org/10.1016/j.seppur.2019.116298.
[98] L. Li, Z. Xu, W. Sun, J. Chen, C. Dai, B. Yan, H. Zeng, Bio-inspired membrane with adaptable wettability for smart oil/water separation, J. Membr. Sci. 598 (2020), 117661, https://doi.org/10.1016/j.memsci.2019.117661.
[99] H. Wei, J. Ren, B. Han, L. Xu, L. Han, L. Jia, Stability of polydopamine and poly (DOPA) melanin-like films on the surface of polymer membranes under strongly acidic and alkaline conditions, Colloids Surf. B Biointerfaces 110 (2013) 22–28, https://doi.org/10.1016/j.colsurfb.2013.04.008.
[100] S. Chen, Y. Cao, J. Feng, Polydopamine as an efficient and robust platform to functionalize carbon fiber for high-performance polymer composites, ACS Appl. Mater. Interfaces 6 (2014) 349–356, https://doi.org/10.1021/am404394g.
[101] L.C. Almeida, J.P. Correia, A.S. Viana, Electrochemical and optical characterization of thin polydopamine films on carbon surfaces for enzymatic sensors, Electrochim. Acta 263 (2018) 480–489, https://doi.org/10.1016/j.electacta.2018.01.077.
[102] M.M. Jastrzebska, H. Isotalo, J. Paloheimo, H. Stubb, Electrical conductivity of synthetic DOPA-melanin polymer for different hydration states and temperatures, J. Biomater. Sci. Polym. Ed. 7 (1995) 577–586, https://doi.org/10.1163/156856295X00490.
[103] H. Coskun, A. Aljabour, L. Uiberlacker, M. Strobel, S. Hild, C. Cobet, D. Farka, P. Stadler, N.S. Sariciftci, Chemical vapor deposition - based synthesis of conductive polydopamine thin-films, Thin Solid Films 645 (2018) 320–325, https://doi.org/10.1016/j.tsf.2017.10.063.
[104] H. Li, Y.V. Aulin, L. Frazer, E. Borguet, R. Kakodkar, J. Feser, Y. Chen, K. An, D. A. Dikin, F. Ren, Structure evolution and thermoelectric properties of carbonized polydopamine thin films, ACS Appl. Mater. Interfaces 9 (2017) 6655–6660, https://doi.org/10.1021/acsami.6b15601.
[105] J. Kong, W.A. Yee, L. Yang, Y. Wei, S.L. Phua, H.G. Ong, J.M. Ang, X. Li, X. Lu, Highly electrically conductive layered carbon derived from polydopamine and its functions in SnO2-based lithium ion battery anodes, Chem. Commun. 48 (2012) 10316–10318, https://doi.org/10.1039/c2cc35284b.
[106] H. Li, T. Marshall, Y.V. Aulin, A.C. Thenuwara, Y. Zhao, E. Borguet, D.R. Strongin, F. Ren, Structural evolution and electrical properties of metal ion-containing polydopamine, J. Mater. Sci. 54 (2019) 6393–6400, https://doi.org/10.1007/s10853-019-03337-7.
[107] R. Li, K. Parvez, F. Hinkel, X. Feng, K. Müllen, Bioinspired wafer-scale production of highly stretchable carbon films for transparent conductive electrodes, Angew. Chem. Int. Ed. Engl. 52 (2013) 5535–5538, https://doi.org/10.1002/anie.201300312.
[108] R. Zou, F. Liu, N. Hu, H. Ning, X. Jiang, C. Xu, S. Fu, Y. Li, X. Zhou, C. Yan, Carbonized polydopamine nanoparticle reinforced graphene films with superior thermal conductivity, Carbon 149 (2019) 173–180, https://doi.org/10.1016/j.carbon.2019.04.038.
[109] Y. Zhou, L. Jiang, Y. Guo, Z. Sun, Z. Jiang, S. Chen, et al., Erratum for PMID 21180585, Ther. Adv. Gastroenterol. 5 (2012) 371, https://doi.org/10.1177/0040517519826893.
[110] T. Zheng, S.M. Sabet, S. Pilla, Polydopamine coating improves electromagnetic interference shielding of delignified wood-derived carbon scaffold, J. Mater. Sci. 56 (2021) 10915–10925, https://doi.org/10.1007/s10853-021-06007-9.
[111] Y. Ni, J. Huang, S. Li, X. Wang, L. Liu, M. Wang, Z. Chen, X. Li, Y. Lai, Underwater, multifunctional superhydrophobic sensor for human motion detection, ACS Appl. Mater. Interfaces 13 (2021) 4740–4749, https://doi.org/10.1021/acsami.0c19704.
[112] L. Wang, L. Yan, X. Gao, Effect of electron beam irradiation on polydopamine and its application in polymer solar cells, Int. J. Energy Res. 42 (2018) 3496–3505, https://doi.org/10.1002/er.4087.
[113] J. Huang, S. Wang, Y. Xing, W. Zhou, J. Zhang, K. Cai, Interface-hybridization-enhanced photothermal performance of polypyrrole/polydopamine heterojunctions on porous nanoparticles, Macromol. Rapid Commun. 40 (2019) 1–6, https://doi.org/10.1002/marc.201900263.
[114] B.H. Park, M. Kim, N.K. Park, H.J. Ryu, J.I. Baek, M. Kang, Single layered hollow NiO-NiS catalyst with large specific surface area and highly efficient visible-light-driven carbon dioxide conversion, Chemosphere 280 (2021), 130759, https://doi.org/10.1016/j.apcatb.2020.119423.
[115] J.H. Waite, Surface chemistry: mussel power, Nat. Mater. 7 (2008) 8–9, https://doi.org/10.1038/nmat2087.
[116] M.G. Peter, H. Förster, On the structure of eumelanins: identification of constitutional patterns by solid-state NMR spectroscopy, Angew. Chem. Int. Ed. Engl. 28 (1989) 741–743, https://doi.org/10.1002/anie.198907411.
[117] S. Ito, IFPCS presidential lecture: a chemist's view of melanogenesis, Pigment Cell Res. (2003) 230–236, https://doi.org/10.1034/j.1600-0749.2003.00037.x.
[118] T.J. Park, J. Kim, T.K. Kim, H.M. Park, S.S. Choi, Y. Kim, Characterization of melanin-TiO2 complexes using FT-IR and 13C solid-state NMR spectroscopy, Bull. Korean Chem. Soc. 29 (2008) 2459–2464, https://doi.org/10.5012/bkcs.2008.29.12.2459.
[119] M. Arzillo, A. Pezzella, O. Crescenzi, A. Napolitano, E.J. Land, V. Barone, M. d'Ischia, Cyclic structural motifs in 5,6-dihydroxyindole polymerization uncovered: biomimetic modular buildup of a unique five-membered macrocycle, Org. Lett. 12 (2010) 3250–3253, https://doi.org/10.1021/ol101188c.
[120] V. Ball, D. Del Frari, M. Michel, M.J. Buehler, V. Toniazzo, M.K. Singh, J. Gracio, D. Ruch, Deposition mechanism and properties of thin polydopamine films for high added value applications in surface science at the nanoscale, Bionanoscience 2 (2012) 16–34, https://doi.org/10.1007/s12668-011-0032-3.
[121] R. Mrówczyński, L.E. Coy, B. Scheibe, T. Czechowski, M. Augustyniak-Jabłokow, S. Jurga, K. Tadyszak, Electron paramagnetic resonance imaging and spectroscopy of polydopamine radicals, J. Phys. Chem. B 119 (2015) 10341–10347, https://doi.org/10.1021/acs.jpcb.5b01524.
[122] Q. Lyu, N. Hsueh, C.L.L. Chai, Unravelling the polydopamine mystery: is the end in sight? Polym. Chem. 10 (2019) 5771–5777, https://doi.org/10.1039/C9PY01372E.
[123] M. Cîrcu, C. Filip, Closer to the polydopamine structure: new insights from a combined 13C/ 1H/ 2H solid-state NMR study on deuterated samples, Polym. Chem. 9 (2018) 3379–3387, https://doi.org/10.1039/C8PY00633D.
[124] S.H. Hong, S. Hong, M.-H. Ryou, J.W. Choi, S.M. Kang, H. Lee, Erratum: Borderud SP, Li Y, Burkhalter JE, Sheffer CE and Ostroff JS. Electronic cigarette use among patients with cancer: Characteristics of electronic cigarette users and their smoking cessation outcomes. Cancer. doi: 10.1002/ cncr.28811, Cancer 121 (2015), 800, https://doi.org/10.1002/admi.201500857.
[125] Y. Liu, K. Ai, J. Liu, M. Deng, Y. He, L. Lu, Dopamine-melanin colloidal nanospheres: an efficient near-infrared photothermal therapeutic agent for in vivo cancer therapy, Adv. Mater. 25 (2013) 1353–1359, https://doi.org/10.1002/adma.201204683.
[126] B.T. Luk, L. Zhang, Cell membrane-camouflaged nanoparticles for drug delivery, J. Control. Release 220 (2015) 600–607, https://doi.org/10.1016/j.jconrel.2015.07.019.
[127] H. Wang, J. Wu, C. Cai, J. Guo, H. Fan, C. Zhu, H. Dong, N. Zhao, J. Xu, Mussel inspired modification of polypropylene separators by catechol/polyamine for Li-ion batteries, ACS Appl. Mater. Interfaces 6 (2014) 5602–5608, https://doi.org/10.1021/am406052u.
[128] J. Xie, S. Zhong, B. Ma, F.D. Shuler, C.T. Lim, Controlled biomineralization of electrospun poly(ε-caprolactone) fibers to enhance their mechanical properties,

Acta Biomater. 9 (2013) 5698–5707, https://doi.org/10.1016/j.actbio.2012.10.042.
[129] B. Fei, B. Qian, Z. Yang, R. Wang, W.C. Liu, C.L. Mak, J.H. Xin, Coating carbon nanotubes by spontaneous oxidative polymerization of dopamine, Carbon 46 (2008) 1795–1797, https://doi.org/10.1016/j.carbon.2008.06.049.
[130] X. Liu, J. Cao, H. Li, J. Li, Q. Jin, K. Ren, J. Ji, Mussel-inspired polydopamine: a biocompatible and ultrastable coating for nanoparticles in vivo, ACS Nano 7 (2013) 9384–9395, https://doi.org/10.1021/nn404117j.
[131] G. Han, S. Zhang, X. Li, N. Widjojo, T.S. Chung, Thin film composite forward osmosis membranes based on polydopamine modified polysulfone substrates with enhancements in both water flux and salt rejection, Chem. Eng. Sci. 80 (2012) 219–231, https://doi.org/10.1016/j.ces.2012.05.033.
[132] S.H. Yang, D. Hong, J. Lee, E.H. Ko, I.S. Choi, Artificial spores: cytocompatible encapsulation of individual living cells within thin, tough artificial shells, Small 9 (2013) 178–186, https://doi.org/10.1002/smll.201202174.
[133] K. Patel, N. Singh, J. Yadav, J.M. Nayak, S.K. Sahoo, J. Lata, D. Chand, S. Kumar, R. Kumar, Polydopamine films change their physicochemical and antimicrobial properties with a change in reaction conditions, Phys. Chem. Chem. Phys. 20 (2018) 5744–5755, https://doi.org/10.1039/c7cp08406d.
[134] F. Bernsmann, V. Ball, F. Addiego, A. Ponche, M. Michel, J.J. Gracio, V. Toniazzo, D. Ruch, Dopamine-melanin film deposition depends on the used oxidant and buffer solution, Langmuir 27 (2011) 2819–2825, https://doi.org/10.1021/la104981s.
[135] N.F. Della Vecchia, A. Luchini, A. Napolitano, G. D'errico, G. Vitiello, N. Szekely, M. d'Ischia, L. Paduano, Tris buffer modulates polydopamine growth, aggregation, and paramagnetic properties, Langmuir 30 (2014) 9811–9818, https://doi.org/10.1021/la501560z.
[136] S.N. Dezidério, C.A. Brunello, M.I.N. Da Silva, M.A. Cotta, C.F.O. Graeff, Thin films of synthetic melanin, J. Non Cryst. Solids 338–340 (2004) 634–638, https://doi.org/10.1016/j.jnoncrysol.2004.03.058.
[137] V. Ball, Polydopamine films and particles with catalytic activity, Catal. Today 301 (2018) 196–203, https://doi.org/10.1016/j.cattod.2017.01.031.
[138] F. Ponzio, V. Ball, Polydopamine deposition at fluid interfaces, Polym. Int. 65 (2016) 1251–1257, https://doi.org/10.1002/pi.5124.
[139] S. Hong, C.F. Schaber, K. Dening, E. Appel, S.N. Gorb, H. Lee, Air/water interfacial formation of freestanding, stimuli-responsive, self-healing catecholamine janus-faced microfilms, Adv. Mater. 26 (2014) 7581–7587, https://doi.org/10.1002/adma.201403259.
[140] J. Jiang, L.L. Zhu, L.L. Zhu, B. Zhu, Y. Xu, Surface characteristics of a self-polymerized dopamine coating deposited on hydrophobic polymer films, Langmuir 27 (2011) 14180–14187, https://doi.org/10.1021/la202877k.
[141] T.F. Wu, B.H. Wee, J.D. Hong, An ultrasensitive and fast moisture sensor based on self-assembled dopamine-melanin thin films, Adv. Mater. Interfaces 2 (2015) 1–5, https://doi.org/10.1002/admi.201500203.
[142] O.Y. Milyaeva, A.G. Bykov, R.A. Campbell, G. Loglio, R. Miller, B.A. Noskov, Polydopamine layer formation at the liquid – gas interface, Colloids Surf. A Physicochem. Eng. Asp. 579 (2019), 123637, https://doi.org/10.1016/j.colsurfa.2019.123637.
[143] L. Klosterman, C.J. Bettinger, Calcium-mediated control of polydopamine film oxidation and iron chelation, Int. J. Mol. Sci. 18 (2016), https://doi.org/10.3390/ijms18010014.
[144] X. Han, F. Tang, Z. Jin, Free-standing polydopamine films generated in the presence of different metallic ions: the comparison of reaction process and film properties, RSC Adv. 8 (2018) 18347–18354, https://doi.org/10.1039/c8ra02930j.
[145] F. Li, Y. Yu, Q. Wang, J. Yuan, P. Wang, X. Fan, Polymerization of dopamine catalyzed by laccase: comparison of enzymatic and conventional methods, Enzyme Microb. Technol. 119 (2018) 58–64, https://doi.org/10.1016/j.enzmictec.2018.09.003.
[146] O.Y. Milyaeva, A.G. Bykov, R.A. Campbell, G. Loglio, R. Miller, B.A. Noskov, The dynamic properties of PDA-laccase films at the air-water interface, Colloids Surf. A Physicochem. Eng. Asp. 599 (2020), 124930, https://doi.org/10.1016/j.colsurfa.2020.124930.
[147] Z. Wang, Y. Zou, Y. Li, Y. Cheng, Metal-containing polydopamine nanomaterials: catalysis, energy, and theranostics, Small 1907042 (2020) 1–21, https://doi.org/10.1002/smll.201907042.
[148] X. Wang, Z. Chen, P. Yang, J. Hu, Z. Wang, Y. Li, Size control synthesis of melanin-like polydopamine nanoparticles by tuning radicals, Polym. Chem. 10 (2019) 4194–4200, https://doi.org/10.1039/C9PY00517J.
[149] D. Cheng, M. He, J. Ran, G. Cai, J. Wu, X. Wang, In situ reduction of TiO2 nanoparticles on cotton fabrics through polydopamine templates for photocatalysis and UV protection, Cellulose 25 (2018) 1413–1424, https://doi.org/10.1007/s10570-017-1606-1.
[150] M.J. Sever, J.J. Wilker, Visible absorption spectra of metal–catecholate and metal–tironate complexes, J. Chem. Soc. Dalton Trans. 4 (2004) 1061–1072, https://doi.org/10.1039/b315811j.
[151] H. Xu, J. Nishida, W. Ma, H. Wu, M. Kobayashi, H. Otsuka, A. Takahara, Competition between oxidation and coordination in cross-linking of polystyrene copolymer containing catechol groups, ACS Macro Lett. 1 (2012) 457–460, https://doi.org/10.1021/mz200217d.
[152] H. Xu, X. Liu, G. Su, B. Zhang, D. Wang, Electrostatic repulsion-controlled formation of polydopamine-gold Janus particles, Langmuir 28 (2012) 13060–13065, https://doi.org/10.1021/la302394e.
[153] Y. Ni, G. Tong, J. Wang, H. Li, F. Chen, C. Yu, Y. Zhou, One-pot preparation of pomegranate-like polydopamine stabilized small gold nanoparticles with superior stability for recyclable nanocatalysts, RSC Adv. 6 (2016) 40698–40705, https://doi.org/10.1039/c6ra05902c.
[154] Q. Zhou, W. Wu, S. Zhou, T. Xing, G. Sun, G. Chen, Polydopamine-induced growth of mineralized γ-FeOOH nanorods for construction of silk fabric with excellent superhydrophobicity, flame retardancy and UV resistance, Chem. Eng. J. 382 (2020), 122988, https://doi.org/10.1016/j.cej.2019.122988.
[155] J. Rose, M.M. Cortalezzi-Fidalgo, S. Moustier, C. Magnetto, C.D. Jones, A. R. Barron, M.R. Wiesner, J.Y. Bottero, Synthesis and characterization of carboxylate−FeOOH nanoparticles (ferroxanes) and ferroxane-derived ceramics, Chem. Mater. 14 (2002) 621–628, https://doi.org/10.1021/cm010583r.
[156] H. Song, X. Zhang, T. Chen, X. Jia, One-pot synthesis of bundle-like β-FeOOH nanorods and their transformation to porous α-Fe2O3 microspheres, Ceram. Int. 40 (2014) 15595–15602, https://doi.org/10.1016/j.ceramint.2014.07.037.
[157] T.M. Suzuki, T. Nonaka, A. Suda, N. Suzuki, Y. Matsuoka, T. Arai, S. Sato, T. Morikawa, Highly crystalline β-FeOOH(Cl) nanorod catalysts doped with transition metals for efficient water oxidation, Sustain. Energy Fuels 1 (2017) 636–643, https://doi.org/10.1039/c7se00043j.
[158] F. Geng, Z. Zhao, J. Geng, H. Cong, H.M. Cheng, A simple and low-temperature hydrothermal route for the synthesis of tubular α-FeOOH, Mater. Lett. 61 (2007) 4794–4796, https://doi.org/10.1016/j.matlet.2007.03.036.
[159] K. Żebrowska, E. Coy, K. Synoradzki, S. Jurga, P. Torruella, R. Mrówczyński, Facile and controllable growth of β-FeOOH nanostructures on polydopamine spheres, J. Phys. Chem. B 124 (2020) 9456–9463, https://doi.org/10.1021/acs.jpcb.0c06627.
[160] Z. Xu, Mechanics of metal-catecholate complexes: the roles of coordination state and metal types, Sci. Rep. 3 (2013) 7–9, https://doi.org/10.1038/srep02914.
[161] H. Lee, N.F. Scherer, P.B. Messersmith, Single-molecule mechanics of mussel adhesion, Proc. Natl. Acad. Sci. USA 103 (2006) 12999–13003. doi:10.1073/pnas.0605552103.
[162] K.C.L. Black, J. Yi, J.G. Rivera, D.C. Zelasko-Leon, P.B. Messersmith, Polydopamine-enabled surface functionalization of gold nanorods for cancer cell-targeted imaging and photothermal therapy, Nanomedicine 8 (2013) 17–28, https://doi.org/10.2217/nnm.12.82.
[163] Y. Wang, S. Wang, H. Niu, Y. Ma, T. Zeng, Y. Cai, Z. Meng, Preparation of polydopamine coated Fe3O4 nanoparticles and their application for enrichment of polycyclic aromatic hydrocarbons from environmental water samples, J. Chromatogr. A 1283 (2013) 20–26, https://doi.org/10.1016/j.chroma.2013.01.110.
[164] T. Shalev, A. Gopin, M. Bauer, R.W. Stark, S. Rahimipour, Non-leaching antimicrobial surfaces through polydopamine bio-inspired coating of quaternary ammonium salts or an ultrashort antimicrobial lipopeptide, J. Mater. Chem. 22 (2012) 2026–2032, https://doi.org/10.1039/c1jm13994k.
[165] H. Gao, Y. Sun, J. Zhou, R. Xu, H. Duan, Mussel-inspired synthesis of polydopamine-functionalized graphene hydrogel as reusable adsorbents for water purification, ACS Appl. Mater. Interfaces 5 (2013) 425–432, https://doi.org/10.1021/am302500v.
[166] M. Zhang, X. Zhang, X. He, L. Chen, Y. Zhang, A self-assembled polydopamine film on the surface of magnetic nanoparticles for specific capture of protein, Nanoscale 4 (2012) 3141–3147, https://doi.org/10.1039/c2nr30316g.
[167] H.W. Chien, W.H. Kuo, M.J. Wang, S.W. Tsai, W.B. Tsai, Tunable micropatterned substrates based on poly(dopamine) deposition via microcontact printing, Langmuir 28 (2012) 5775–5782, https://doi.org/10.1021/la300147p.
[168] R. Luo, L. Tang, J. Wang, Y. Zhao, Q. Tu, Y. Weng, R. Shen, N. Huang, Improved immobilization of biomolecules to quinone-rich polydopamine for efficient surface functionalization, Colloids Surf. B Biointerfaces 106 (2013) 66–73, https://doi.org/10.1016/j.colsurfb.2013.01.033.
[169] Q. Wei, B. Li, N. Yi, B. Su, Z. Yin, F. Zhang, J. Li, C. Zhao, Improving the blood compatibility of material surfaces via biomolecule-immobilized mussel-inspired coatings, J. Biomed. Mater. Res. Part A 96A (2011) 38–45, https://doi.org/10.1002/jbm.a.32956.
[170] Y. Ren, J.G. Rivera, L. He, H. Kulkarni, D.K. Lee, P.B. Messersmith, Facile, high efficiency immobilization of lipase enzyme on magnetic iron oxide nanoparticles via a biomimetic coating, BMC Biotechnol. 11 (2011) 63, https://doi.org/10.1186/1472-6750-11-63.
[171] D.E. Fullenkamp, L. He, D.G. Barrett, W.R. Burghardt, P.B. Messersmith, Mussel-inspired histidine-based transient network metal coordination hydrogels, Macromolecules 46 (2013) 1167–1174, https://doi.org/10.1021/ma301791n.
[172] Y. Liu, B. Xie, Z. Xu, Mechanics of coordinative crosslinks in graphene nanocomposites: a first-principles study, J. Mater. Chem. 21 (2011) 6707–6712, https://doi.org/10.1039/c1jm10300h.
[173] H.Y. Son, J.H. Ryu, H. Lee, Y.S. Nam, Silver-polydopamine hybrid coatings of electrospun poly(vinyl alcohol) nanofibers, Macromol. Mater. Eng. 298 (2013) 547–554, https://doi.org/10.1002/mame.201200231.
[174] H.-W. Hu, J.H. Xin, H. Hu, Highly efficient graphene-based ternary composite catalyst with polydopamine layer and copper nanoparticles, Chempluschem 78 (2013) 1483–1490, https://doi.org/10.1002/cplu.201300124.
[175] T. Zeng, X. Le Zhang, H.Y. Niu, Y.R. Ma, W.H. Li, Y.Q. Cai, In situ growth of gold nanoparticles onto polydopamine-encapsulated magnetic microspheres for catalytic reduction of nitrobenzene, Appl. Catal. B Environ. 134–135 (2013) 26–33, https://doi.org/10.1016/j.apcatb.2012.12.037.
[176] D. Zhou, L. Yang, L. Yu, J. Kong, X. Yao, W. Liu, Z. Xu, X. Lu, Fe/N/C hollow nanospheres by Fe(iii)-dopamine complexation-assisted one-pot doping as nonprecious-metal electrocatalysts for oxygen reduction, Nanoscale 7 (2015) 1501–1509, https://doi.org/10.1039/c4nr06366j.
[177] J. Yan, H. Lu, Y. Huang, J. Fu, S. Mo, C. Wei, Y.E. Miao, T. Liu, Polydopamine-derived porous carbon fiber/cobalt composites for efficient oxygen reduction

reactions, J. Mater. Chem. A 3 (2015) 23299–23306, https://doi.org/10.1039/c5ta06217a.
[178] R. Mrówczyński, A. Bunge, J. Liebscher, Polydopamine-an organocatalyst rather than an innocent polymer, Chem. Eur. J. 20 (2014) 8647–8653, https://doi.org/10.1002/chem.201402532.
[179] X. Wu, L. Wu, J. Tan, G.Y. Chen, G. Owens, H. Xu, Evaporation above a bulk water surface using an oil lamp inspired highly efficient solar-steam generation strategy, J. Mater. Chem. A 6 (2018) 12267–12274, https://doi.org/10.1039/c8ta03280g.
[180] Q. Jiang, H. Gholami Derami, D. Ghim, S. Cao, Y.S. Jun, S. Singamaneni, Polydopamine-filled bacterial nanocellulose as a biodegradable interfacial photothermal evaporator for highly efficient solar steam generation, J. Mater. Chem. A 5 (2017) 18397–18402, https://doi.org/10.1039/c7ta04834c.
[181] X. Wu, S. Cao, D. Ghim, Q. Jiang, S. Singamaneni, Y.S. Jun, A thermally engineered polydopamine and bacterial nanocellulose bilayer membrane for photothermal membrane distillation with bactericidal capability, Nano Energy 79 (2021), 105353, https://doi.org/10.1016/j.nanoen.2020.105353.
[182] Y. Zou, J. Zhao, J. Zhu, X. Guo, P. Chen, G. Duan, X. Liu, Y. Li, A mussel-inspired polydopamine-filled cellulose aerogel for solar-enabled water remediation, ACS Appl. Mater. Interfaces 13 (2021) 7617–7624, https://doi.org/10.1021/acsami.0c22584.
[183] W.X. Mao, X.J. Lin, W. Zhang, Z.X. Chi, R.W. Lyu, A.M. Cao, L.J. Wan, Core-shell structured TiO2@polydopamine for highly active visible-light photocatalysis, Chem. Commun. 52 (2016) 7122–7125, https://doi.org/10.1039/c6cc02041k.
[184] L. Fan, J. Xie, Z. Zhang, Y. Zheng, D. Yao, T. Li, Magnetically recoverable Fe3O4@ polydopamine nanocomposite as an excellent co-catalyst for Fe3+ reduction in advanced oxidation processes, J. Environ. Sci. 92 (2020) 69–78, https://doi.org/10.1016/j.jes.2020.02.006.
[185] B. Chen, Y. Cao, H. Zhao, F. Long, X. Feng, J. Li, X. Pan, A novel Fe3+-stabilized magnetic polydopamine composite for enhanced selective adsorption and separation of Methylene blue from complex wastewater, J. Hazard. Mater. 392 (2020), 122263, https://doi.org/10.1016/j.jhazmat.2020.122263.
[186] Y. Zou, Z. Wang, Z. Chen, Q.P. Zhang, Q. Zhang, Y. Tian, S. Ren, Y. Li, Synthetic melanin hybrid patchy nanoparticle photocatalysts, J. Phys. Chem. C 123 (2019) 5345–5352, https://doi.org/10.1021/acs.jpcc.8b10469.
[187] Z. Yu, F. Li, Q. Yang, H. Shi, Q. Chen, M. Xu, Nature-mimic method to fabricate polydopamine/graphitic carbon nitride for enhancing photocatalytic degradation performance, ACS Sustain. Chem. Eng. 5 (2017) 7840–7850, https://doi.org/10.1021/acssuschemeng.7b01313.
[188] X. Li, Z. Yu, L. Shao, H. Zeng, Y. Liu, X. Feng, A novel strategy to construct a visible-light-driven Z-scheme (ZnAl-LDH with active phase/g-C3N4) heterojunction catalyst via polydopamine bridge (a similar "bridge" structure), J. Hazard. Mater. 386 (2020), 121650, https://doi.org/10.1016/j.jhazmat.2019.121650.
[189] Y. Lv, C. Zhang, A. He, S.J. Yang, G.P. Wu, S.B. Darling, et al., Erratum: Borderud SP, Li Y, Burkhalter JE, Sheffer CE and Ostroff JS. Electronic cigarette use among patients with cancer: Characteristics of electronic cigarette users and their smoking cessation outcomes. Cancer. doi: 10.1002/ cncr.28811, Cancer 121 (2015) 800, https://doi.org/10.1002/adfm.201700251.
[190] F. Sun, T.T. Li, H.T. Ren, B.C. Shiu, H.K. Peng, J.H. Lin, C.W. Lou, Multi-scaled, hierarchical nanofibrous membrane for oil/water separation and photocatalysis: preparation, characterization and properties evaluation, Prog. Org. Coat. 152 (2021), 106125, https://doi.org/10.1016/j.porgcoat.2020.106125.
[191] X. Feng, Z. Yu, R. Long, Y. Sun, M. Wang, X. Li, G. Zeng, Polydopamine intimate contacted two-dimensional/two-dimensional ultrathin nylon basement membrane supported RGO/PDA/MXene composite material for oil-water separation and dye removal, Sep. Purif. Technol. 247 (2020), 116945, https://doi.org/10.1016/j.seppur.2020.116945.
[192] Z. Zhao, Y. Li, D. Jin, B. Van der Bruggen, Modification of an anion exchange membrane based on rapid mussel-inspired deposition for improved antifouling performance, Colloids Surf. A Physicochem. Eng. Asp. 615 (2021), 126267, https://doi.org/10.1016/j.colsurfa.2021.126267.
[193] A. Xie, K. Zhang, F. Wu, N. Wang, Y. Wang, M. Wang, Polydopamine nanofilms as visible light-harvesting interfaces for palladium nanocrystal catalyzed coupling reactions, Catal. Sci. Technol. 6 (2016) 1764–1771, https://doi.org/10.1039/c5cy01330e.
[194] W.Y. Liang, Excitons, Phys. Educ. 5 (1970) 226–228, https://doi.org/10.1088/0031-9120/5/4/003.
[195] J. Frenkel, On the transformation of light into heat in solids. i, Phys. Rev. 37 (1931) 17–44, https://doi.org/10.1103/PhysRev.37.17.
[196] J.H. Kim, M.K. Joshi, J. Lee, C.H. Park, C.S. Kim, Polydopamine-assisted immobilization of hierarchical zinc oxide nanostructures on electrospun nanofibrous membrane for photocatalysis and antimicrobial activity, J. Colloid Interface Sci. 513 (2018) 566–574, https://doi.org/10.1016/j.jcis.2017.11.061.
[197] J. Yan, Y. Huang, Y.E. Miao, W.W. Tjiu, T. Liu, Polydopamine-coated electrospun poly(vinyl alcohol)/poly(acrylic acid) membranes as efficient dye adsorbent with good recyclability, J. Hazard. Mater. 283 (2015) 730–739, https://doi.org/10.1016/j.jhazmat.2014.10.040.
[198] C. Zhang, H.-C.C. Yang, L.-S.S. Wan, H.-Q.Q. Liang, H. Li, Z.-K.K. Xu, Polydopamine-coated porous substrates as a platform for mineralized β-FeOOH nanorods with photocatalysis under sunlight, ACS Appl. Mater. Interfaces 7 (2015) 11567–11574, https://doi.org/10.1021/acsami.5b02530.
[199] S. Liu, Q. Hu, J. Qiu, F. Wang, W. Lin, F. Zhu, C. Wei, N. Zhou, G. Ouyang, Enhanced photocatalytic degradation of environmental pollutants under visible irradiation by a composite coating, Environ. Sci. Technol. 51 (2017) 5137–5145, https://doi.org/10.1021/acs.est.7b00350.
[200] M. Arvand, S. Sayyar, S. Hemmati, Visible-light-driven polydopamine/CdS QDs hybrid materials with synergistic photocatalytic activity, J. Electroanal. Chem. 848 (2019), 113288, https://doi.org/10.1016/j.jelechem.2019.113288.
[201] K. Lee, L. Zhang, H. Lui, R. Hui, Z. Shi, J. Zhang, Oxygen reduction reaction (ORR) catalyzed by carbon-supported cobalt polypyrrole (Co-PPy/C) electrocatalysts, Electrochim. Acta 54 (2009) 4704–4711, https://doi.org/10.1016/j.electacta.2009.03.081.
[202] T. Wilberforce, A.G. Olabi, Proton exchange membrane fuel cell performance prediction using artificial neural network, Int. J. Hydrog. Energy 46 (2021) 6037–6050, https://doi.org/10.1016/j.ijhydene.2020.07.263.
[203] A. Rowe, X. Li, Mathematical modeling of proton exchange membrane fuel cells, J. Power Sources 102 (2001) 82–96, https://doi.org/10.1016/S0378-7753(01)00798-4.
[204] G. Kluger, T. Glauser, G. Krauss, R. Seeruthun, C. Perdomo, S. Arroyo, Adjunctive rufinamide in Lennox-Gastaut syndrome: a long-term, open-label extension study, Acta Neurol. Scand. 122 (2010) 202–208, https://doi.org/10.1149/1.1856988.
[205] I.C. Man, H. Su, F. Calle-Vallejo, H.A. Hansen, J.I. Martínez, N.G. Inoglu, et al., Universality in oxygen evolution electrocatalysis on oxide surfaces, ChemCatChem 3 (2011) 1159–1165, https://doi.org/10.1002/cctc.201000397.
[206] J. Rossmeisl, Z.W. Qu, H. Zhu, G.J. Kroes, J.K. Nørskov, Electrolysis of water on oxide surfaces, J. Electroanal. Chem. 607 (2007) 83–89, https://doi.org/10.1016/j.jelechem.2006.11.008.
[207] J.K. Nørskov, J. Rossmeisl, A. Logadottir, L. Lindqvist, J.R. Kitchin, T. Bligaard, H. Jónsson, Origin of the overpotential for oxygen reduction at a fuel-cell cathode, J. Phys. Chem. B 108 (2004) 17886–17892, https://doi.org/10.1021/jp047349j.
[208] C. Ling, L. Shi, Y. Ouyang, X.C. Zeng, J. Wang, Nanosheet supported single-metal atom bifunctional catalyst for overall water splitting, Nano Lett. 17 (2017) 5133–5139, https://doi.org/10.1021/acs.nanolett.7b02518.
[209] Y. Yu, J. Zhou, Z. Sun, Erratum: Borderud SP, Li Y, Burkhalter JE, Sheffer CE and Ostroff JS. Electronic cigarette use among patients with cancer: Characteristics of electronic cigarette users and their smoking cessation outcomes. Cancer. doi: 10.1002/ cncr.28811, Cancer 121 (2015), 800, https://doi.org/10.1002/adfm.202000570.
[210] N. Cheng, S. Stambula, D. Wang, M.N. Banis, J. Liu, A. Riese, B. Xiao, R. Li, T. K. Sham, L.M. Liu, G.A. Botton, X. Sun, Platinum single-atom and cluster catalysis of the hydrogen evolution reaction, Nat. Commun. 7 (2016) 1–9, https://doi.org/10.1038/ncomms13638.
[211] T. Reier, M. Oezaslan, P. Strasser, Electrocatalytic oxygen evolution reaction (OER) on Ru, Ir, and pt catalysts: a comparative study of nanoparticles and bulk materials, ACS Catal. 2 (2012) 1765–1772, https://doi.org/10.1021/cs3003098.
[212] C.W.B. Bezerra, L. Zhang, K. Lee, H. Liu, A.L.B. Marques, E.P. Marques, H. Wang, J. Zhang, A review of Fe-N/C and Co-N/C catalysts for the oxygen reduction reaction, Electrochim. Acta 53 (2008) 4937–4951, https://doi.org/10.1016/j.electacta.2008.02.012.
[213] J.M. Ziegelbauer, T.S. Olson, S. Pylypenko, F. Alamgir, C. Jaye, P. Atanassov, S. Mukerjee, Direct spectroscopic observation of the structural origin of peroxide generation from Co-based pyrolyzed porphyrins for ORR applications, J. Phys. Chem. C 112 (2008) 8839–8849, https://doi.org/10.1021/jp8001564.
[214] Q. Wu, L. Yang, X. Wang, Z. Hu, From carbon-based nanotubes to nanocages for advanced energy conversion and storage, Acc. Chem. Res. 50 (2017) 435–444, https://doi.org/10.1021/acs.accounts.6b00541.
[215] H.A. Gasteiger, S.S. Kocha, B. Sompalli, F.T. Wagner, Activity benchmarks and requirements for Pt, Pt-alloy, and non-Pt oxygen reduction catalysts for PEMFCs, Appl. Catal. B Environ. 56 (2005) 9–35, https://doi.org/10.1016/j.apcatb.2004.06.021.
[216] T.R. Ralph, M.P. Hogarth, Catalysis for Low Temperature Fuel Cells PART II: THE ANODE CHALLENGES, n.d.
[217] S. Mukerjee, Particle size and structural effects in platinum electrocatalysis, J. Appl. Electrochem. 20 (1990) 537–548, https://doi.org/10.1007/BF01008861.
[218] C. Han, X. Bo, Y. Zhang, M. Li, L. Guo, One-pot synthesis of nitrogen and sulfur co-doped onion-like mesoporous carbon vesicle as an efficient metal-free catalyst for oxygen reduction reaction in alkaline solution, J. Power Sources 272 (2014) 267–276, https://doi.org/10.1016/j.jpowsour.2014.08.104.
[219] M. Krogsgaard, V. Nue, H. Birkedal, Mussel-inspired materials: self-healing through coordination chemistry, Chem. Eur. J. 22 (2016) 844–857, https://doi.org/10.1002/chem.201503380.
[220] F. Yang, Z. Zhang, K. Du, X. Zhao, W. Chen, Y. Lai, J. Li, Dopamine derived nitrogen-doped carbon sheets as anode materials for high-performance sodium ion batteries, Carbon 91 (2015) 88–95, https://doi.org/10.1016/j.carbon.2015.04.049.
[221] K. Ai, Y. Liu, C. Ruan, L. Lu, G. Lu, Sp2 C-dominant N-doped carbon sub-micrometer spheres with a tunable size: a versatile platform for highly efficient oxygen-reduction catalysts, Adv. Mater. 25 (2013) 998–1003, https://doi.org/10.1002/adma.201203923.
[222] J.M. Ang, Y. Du, B.Y. Tay, C. Zhao, J. Kong, L.P. Stubbs, X. Lu, One-pot synthesis of Fe(III)-polydopamine complex nanospheres: morphological evolution, mechanism, and application of the carbonized hybrid nanospheres in catalysis and Zn-air battery, Langmuir 32 (2016) 9265–9275, https://doi.org/10.1021/acs.langmuir.6b02331.
[223] W. Yang, L. Chen, X. Liu, X. Yue, C. Liu, J. Jia, N,S-Codoped microporous carbon nanobelts with blooming nanoflowers for oxygen reduction, J. Mater. Chem. A 4 (2016) 5834–5838, https://doi.org/10.1039/c6ta01263a.
[224] H. Zhao, C.C. Weng, Z.P. Hu, L. Ge, Z.Y. Yuan, CdS-polydopamine-derived N,S-codoped hierarchically porous carbons as highly active electrocatalyst for oxygen

reduction, ACS Sustain. Chem. Eng. 5 (2017) 9914–9922, https://doi.org/10.1021/acssuschemeng.7b01875.
[225] A. Fujishima, K. Honda, Electrochemical photolysis of water at a semiconductor electrode, Nature 238 (1972) 37–38, https://doi.org/10.1038/238037a0.
[226] C. Wang, Y. Wu, J. Lu, J. Zhao, J. Cui, X. Wu, Y. Yan, P. Huo, Bioinspired synthesis of photocatalytic nanocomposite membranes based on synergy of Au-TiO 2 and polydopamine for degradation of tetracycline under visible light, ACS Appl. Mater. Interfaces 9 (2017) 23687–23697, https://doi.org/10.1021/acsami.7b04902.
[227] T. Ochiai, A. Fujishima, Photoelectrochemical properties of TiO2 photocatalyst and its applications for environmental purification, J. Photochem. Photobiol. C Photochem. Rev. 13 (2012) 247–262, https://doi.org/10.1016/j.jphotochemrev.2012.07.001.
[228] X. Chen, S.S. Mao, Titanium dioxide nanomaterials: synthesis, properties, modifications and applications, Chem. Rev. 107 (2007) 2891–2959, https://doi.org/10.1021/cr0500535.
[229] V. Etacheri, C. Di Valentin, J. Schneider, D. Bahnemann, S.C. Pillai, Visible-light activation of TiO2 photocatalysts: advances in theory and experiments, J. Photochem. Photobiol. C Photochem. Rev. 25 (2015) 1–29, https://doi.org/10.1016/j.jphotochemrev.2015.08.003.
[230] A. Menard, D. Drobne, A. Jemec, Ecotoxicity of nanosized TiO2. Review of in vivo data, Environ. Pollut. 159 (2011) 677–684, https://doi.org/10.1016/j.envpol.2010.11.027.
[231] A.L. Linsebigler, G. Lu, J.T. Yates, Photocatalysis on TiO2 surfaces: principles, mechanisms, and selected results, Chem. Rev. 95 (1995) 735–758, https://doi.org/10.1021/cr00035a013.
[232] H. Park, Y. Park, W. Kim, W. Choi, Surface modification of TiO2 photocatalyst for environmental applications, J. Photochem. Photobiol. C Photochem. Rev. 15 (2013) 1–20, https://doi.org/10.1016/j.jphotochemrev.2012.10.001.
[233] M. Kowalkińska, S. Dudziak, J. Karczewski, J. Ryl, G. Trykowski, A. Zielińska-Jurek, Facet effect of TiO2 nanostructures from TiOF2 and their photocatalytic activity, Chem. Eng. J. 404 (2021), 126493, https://doi.org/10.1016/j.cej.2020.126493.
[234] J. Zou, Q. Zhang, K. Huang, N. Marzari, Ultraviolet photodetectors based on anodic TiO2 nanotube arrays, J. Phys. Chem. C 114 (2010) 10725–10729, https://doi.org/10.1021/jp1011236.
[235] Y. Cong, J. Zhang, F. Chen, M. Anpo, Synthesis and characterization of nitrogen-doped TiO2 nanophotocatalyst with high visible light activity, J. Phys. Chem. C 111 (2007) 6976–6982, https://doi.org/10.1021/jp0685030.
[236] S. Xie, H. Su, W. Wei, M. Li, Y. Tong, Z. Mao, Remarkable photoelectrochemical performance of carbon dots sensitized TiO2 under visible light irradiation, J. Mater. Chem. A 2 (2014) 16365–16368, https://doi.org/10.1039/c4ta03203a.
[237] J.B. Joo, Q. Zhang, M. Dahl, I. Lee, J. Goebl, F. Zaera, Y. Yin, Control of the nanoscale crystallinity in mesoporous TiO2 shells for enhanced photocatalytic activity, Energy Environ. Sci. 5 (2012) 6321–6327, https://doi.org/10.1039/c1ee02533c.
[238] H. Li, Z. Bian, J. Zhu, Y. Huo, H. Li, Y. Lu, Mesoporous Au/TiO2 nanocomposites with enhanced photocatalytic activity, J. Am. Chem. Soc. 129 (2007) 4538–4539, https://doi.org/10.1021/ja069113u.
[239] R. Asahi, Visible-light photocatalysis in nitrogen-doped titanium oxides, Science 293 (2001) 269–271, https://doi.org/10.1126/science.1061051.
[240] Z. Guo, G. Wang, H. Fu, P. Wang, J. Liao, A. Wang, Photocatalytic degradation of methylene blue by a cocatalytic PDA/TiO2electrode produced by photoelectric polymerization, RSC Adv. 10 (2020) 26133–26141, https://doi.org/10.1039/d0ra02076a.
[241] P. Persson, R. Bergstrom, S. Lunell, Quantum chemical study of photoinjection processes in dye-sensitized TiO2 nanoparticles, J. Phys. Chem. B 104 (2000) 10348–10351, https://doi.org/10.1021/jp002550p.
[242] T. Rajh, L.X. Chen, K. Lukas, T. Liu, M.C. Thurnauer, D.M. Tiede, Surface restructuring of nanoparticles: an efficient route for ligand-metal oxide crosstalk, J. Phys. Chem. B 106 (2002) 10543–10552, https://doi.org/10.1021/jp021235v.
[243] N.M. Dimitrijevic, E. Rozhkova, T. Rajh, Dynamics of localized charges in dopamine-modified TiO and their effect on the formation of reactive oxygen species, J. Am. Chem. Soc. 131 (2009) 2893–2899, https://doi.org/10.1021/ja807654k.
[244] X. Sun, L. Yan, R. Xu, M. Xu, Y. Zhu, Surface modification of TiO 2 with polydopamine and its effect on photocatalytic degradation mechanism, Colloids Surf. A Physicochem. Eng. Asp. 570 (2019) 199–209, https://doi.org/10.1016/j.colsurfa.2019.03.018.
[245] G. Loget, J.E. Yoo, A. Mazare, L. Wang, P. Schmuki, Highly controlled coating of biomimetic polydopamine in TiO2 nanotubes, Electrochem. Commun. 52 (2015) 41–44, https://doi.org/10.1016/j.elecom.2015.01.011.
[246] L. Yang, C. Chen, Y. Hu, F. Wei, J. Cui, Y. Zhao, X. Xu, X. Chen, D. Sun, Three-dimensional bacterial cellulose/polydopamine/TiO2 nanocomposite membrane with enhanced adsorption and photocatalytic degradation for dyes under ultraviolet-visible irradiation, J. Colloid Interface Sci. 562 (2020) 21–28, https://doi.org/10.1016/j.jcis.2019.12.013.
[247] J.L. Shi, X. Lang, Assembling polydopamine on TiO2 for visible light photocatalytic selective oxidation of sulfides with aerial O2, Chem. Eng. J. 392 (2020), 123632, https://doi.org/10.1016/j.cej.2019.123632.
[248] Q. Zhang, I. Lee, J.B. Joo, F. Zaera, Y. Yin, Core-shell nanostructured catalysts, Acc. Chem. Res. 46 (2013) 1816–1824, https://doi.org/10.1021/ar300230s.
[249] M. Grätzel, Photoelectrochemical cells, Nature 414 (2001) 338–344, https://doi.org/10.1038/35104607.
[250] A. Hagfeldt, M. Grätzel, Light-induced redox reactions in nanocrystalline systems, Chem. Rev. 95 (1995) 49–68, https://doi.org/10.1021/cr00033a003.
[251] A. Mills, S. Le Hunte, An overview of semiconductor photocatalysis, J. Photochem. Photobiol. A Chem. 108 (1997) 1–35, https://doi.org/10.1016/S1010-6030(97)00118-4.
[252] F. Chen, L. Zhao, W. Yu, Y. Wang, H. Zhang, L.H. Guo, Dynamic monitoring and regulation of pentachlorophenol photodegradation process by chemiluminescence and TiO2/PDA, J. Hazard. Mater. 399 (2020), 123073, https://doi.org/10.1016/j.jhazmat.2020.123073.
[253] G. Grinblat, L.J. Borrero-González, L.A.O. Nunes, M. Tirado, D. Comedi, Enhanced optical properties and (Zn, Mg) interdiffusion in vapour transport grown ZnO/MgO core/shell nanowires, Nanotechnology 25 (2014), 035705, https://doi.org/10.1088/0957-4484/25/3/035705.
[254] N.W. Emanetoglu, C. Gorla, Y. Liu, S. Liang, Y. Lu, Epitaxial ZnO piezoelectric thin films for saw filters, Mater. Sci. Semicond. Process. 2 (1999) 247–252, https://doi.org/10.1016/S1369-8001(99)00022-0.
[255] A. Van Dijken, E.A. Meulenkamp, D. Vanmaekelbergh, A. Meijerink, The kinetics of the radiative and nonradiative processes in nanocrystalline ZnO particles upon photoexcitation, J. Phys. Chem. B 104 (2000) 1715–1723, https://doi.org/10.1021/jp993327z.
[256] A. Van Dijken, E.A. Meulenkamp, D. Vanmaekelbergh, A. Meijerink, Identification of the transition responsible for the visible emission in ZnO using quantum size effects, J. Lumin. 90 (2000) 123–128, https://doi.org/10.1016/S0022-2313(99)00599-2.
[257] M. Anpo, Y. Kubokawa, Photoluminescence of Zinc Oxide Powder as a Probe of Electron-Hole Surface Processes, 1984.
[258] G. Ramakrishna, H.N. Ghosh, Effect of particle size on the reactivity of quantum size ZnO nanoparticles and charge-transfer dynamics with adsorbed catechols, Langmuir 19 (2003) 3006–3012, https://doi.org/10.1021/la020828u.
[259] F. van Craeynest, W. Maenhout-Van Der Vorst, W. Dekeyser, Interpretation of the yellow colour of heat treated ZnO powder, Phys. Status Solidi 8 (1965) 841–846, https://doi.org/10.1002/pssb.19650080322.
[260] M. Salavati-Niasari, F. Davar, A. Khansari, Nanospherical and nanobundles of ZnO: synthesis and characterization, J. Alloy. Compd. 509 (2011) 61–65, https://doi.org/10.1016/j.jallcom.2010.08.060.
[261] J. Zhang, L.D. Sun, X.C. Jiang, C.S. Liao, C.H. Yan, Shape evolution of one-dimensional single-crystalline ZnO nanostructures in a microemulsion system, Cryst. Growth Des. 4 (2004) 309–313, https://doi.org/10.1021/cg034142r.
[262] H. Zhou, Z. Li, Synthesis of nanowires, nanorods and nanoparticles of ZnO through modulating the ratio of water to methanol by using a mild and simple solution method, Mater. Chem. Phys. 89 (2005) 326–331, https://doi.org/10.1016/j.matchemphys.2004.09.006.
[263] P.X. Gao, Z.L. Wang, Substrate atomic-termination-induced anisotropie growth of ZnO nanowires/nanorods by the VLS process, J. Phys. Chem. B 108 (2004) 7534–7537, https://doi.org/10.1021/jp049657n.
[264] F. Liu, P.J. Cao, H.R. Zhang, J.Q. Li, H.J. Gao, Controlled self-assembled nanoaeroplanes, nanocombs, and tetrapod-like networks of zinc oxide, Nanotechnology 15 (2004) 949–952, https://doi.org/10.1088/0957-4484/15/8/013.
[265] M.J. Sampaio, R.R. Bacsa, A. Benyounes, R. Axet, P. Serp, C.G. Silva, A. Silva, J. L. Faria, Synergistic effect between carbon nanomaterials and ZnO for photocatalytic water decontamination, J. Catal. 331 (2015) 172–180, https://doi.org/10.1016/j.jcat.2015.08.011.
[266] Y. Wang, J. Ning, E. Hu, C. Zheng, Y. Zhong, Y. Hu, Direct coating ZnO nanocrystals onto 1D Fe3O4/C composite microrods as highly efficient and reusable photocatalysts for water treatment, J. Alloy. Compd. 637 (2015) 301–307, https://doi.org/10.1016/j.jallcom.2015.03.033.
[267] K. Qi, B. Cheng, J. Yu, W. Ho, Review on the improvement of the photocatalytic and antibacterial activities of ZnO, J. Alloy. Compd. 727 (2017) 792–820, https://doi.org/10.1016/j.jallcom.2017.08.142.
[268] R. Viter, Z. Balevicius, A. Abou Chaaya, I. Baleviciute, S. Tumenas, L. Mikoliunaite, A. Ramanavicius, Z. Gertnere, A. Zalesska, V. Vataman, V. Smyntyna, D. Erts, P. Miele, M. Bechelany, The influence of localized plasmons on the optical properties of Au/ZnO nanostructures, J. Mater. Chem. C 3 (2015) 6815–6821, https://doi.org/10.1039/c5tc00964b.
[269] D. Damberga, R. Viter, V. Fedorenko, I. Iatsunskyi, E. Coy, O. Graniel, S. Balme, P. Miele, M. Bechelany, Photoluminescence study of defects in ZnO-coated polyacrylonitrile nanofibers, J. Phys. Chem. C 124 (2020) 9434–9441, https://doi.org/10.1021/acs.jpcc.0c00326.
[270] R. Viter, M. Savchuk, N. Starodub, Z. Balevicius, S. Tumenas, A. Ramanaviciene, D. Jevdokimovs, D. Erts, I. Iatsunskyi, A. Ramanavicius, Photoluminescence immunosensor based on bovine leukemia virus proteins immobilized on the ZnO nanorods, Sens. Actuators B Chem. 285 (2019) 601–606, https://doi.org/10.1016/j.snb.2019.01.054.
[271] R. Viter, M. Savchuk, I. Iatsunskyi, Z. Pietralik, N. Starodub, N. Shpyrka, A. Ramanaviciene, A. Ramanavicius, Analytical, thermodynamical and kinetic characteristics of photoluminescence immunosensor for the determination of Ochratoxin A, Biosens. Bioelectron. 99 (2018) 237–243, https://doi.org/10.1016/j.bios.2017.07.056.
[272] R. Viter, A. Tereshchenko, V. Smyntyna, J. Ogorodniichuk, N. Starodub, R. Yakimova, V. Khranovskyy, A. Ramanavicius, Toward development of optical biosensors based on photoluminescence of TiO2 nanoparticles for the detection of Salmonella, Sens. Actuators B Chem. 252 (2017) 95–102, https://doi.org/10.1016/j.snb.2017.05.139.
[273] N. Ahmad, X. Zhang, S. Yang, D. Zhang, J. Wang, S. Zafar, Y. Li, Y. Zhang, S. Hussain, Z. Cheng, A. Kumaresan, H. Zhou, Polydopamine/ZnO electron transport layers enhance charge extraction in inverted non-fullerene organic solar

cells, J. Mater. Chem. C 7 (2019) 10795–10801, https://doi.org/10.1039/c9tc02781e.
[274] T. Bharathidasan, A. Mandalam, M. Balasubramanian, P. Dhandapani, S. Sathiyanarayanan, S. Mayavan, Zinc oxide-containing porous boron-carbon-nitrogen sheets from glycine-nitrate combustion: synthesis, self-cleaning, and sunlight-driven photocatalytic activity, ACS Appl. Mater. Interfaces 7 (2015) 18450–18459, https://doi.org/10.1021/acsami.5b04609.
[275] N. Nie, F. He, L. Zhang, B. Cheng, Direct Z-scheme PDA-modified ZnO hierarchical microspheres with enhanced photocatalytic CO 2 reduction performance, Appl. Surf. Sci. 457 (2018) 1096–1102, https://doi.org/10.1016/j.apsusc.2018.07.002.
[276] H. Wang, L. Yan, Polydopamine/ZnO nanocomposites as a new electron transport layer for PTB7: PC70BM solar cells, Colloids Surf. A Physicochem. Eng. Asp. 531 (2017) 198–202, https://doi.org/10.1016/j.colsurfa.2017.08.007.
[277] K. Zhang, L. Guo, Metal sulphide semiconductors for photocatalytic hydrogen production, Catal. Sci. Technol. 3 (2013) 1672–1690, https://doi.org/10.1039/c3cy00018d.
[278] S. Ummartyotin, Y. Infahsaeng, A comprehensive review on ZnS: from synthesis to an approach on solar cell, Renew. Sustain. Energy Rev. 55 (2016) 17–24, https://doi.org/10.1016/j.rser.2015.10.120.
[279] A. Kudo, M. Sekizawa, Photocatalytic H2 evolution under visible light irradiation on Ni-doped ZnS photocatalyst, Chem. Commun. (2000) 1371–1372, https://doi.org/10.1039/b003297m.
[280] J.-S. Hu, L.-L. Ren, Y.-G. Guo, H.-P. Liang, A.-M. Cao, L.-J. Wan, C.L. Bai, Mass production and high photocatalytic activity of ZnS nanoporous nanoparticles, Angew. Chem. Int. Ed. 44 (2005) 1269–1273, https://doi.org/10.1002/anie.200462057.
[281] X. Gao, J. Wang, J. Yu, H. Xu, Novel ZnO-ZnS nanowire arrays with heterostructures and enhanced photocatalytic properties, CrystEngComm 17 (2015) 6328–6337, https://doi.org/10.1039/c5ce01078k.
[282] G.J. Lee, S. Anandan, S.J. Masten, J.J. Wu, Photocatalytic hydrogen evolution from water splitting using Cu doped ZnS microspheres under visible light irradiation, Renew. Energy 89 (2016) 18–26, https://doi.org/10.1016/j.renene.2015.11.083.
[283] G. Wang, B. Huang, Z. Li, Z. Lou, Z. Wang, Y. Dai, M.H. Whangbo, Synthesis and characterization of ZnS with controlled amount of S vacancies for photocatalytic H2 production under visible light, Sci. Rep. 5 (2015) 1–7, https://doi.org/10.1038/srep08544.
[284] Z. Li, J. Wang, X. Xu, X. Ye, The evolution of optical properties during hydrothermal coarsening of ZnS nanoparticles, Mater. Lett. 62 (2008) 3862–3864, https://doi.org/10.1016/j.matlet.2008.05.004.
[285] M. Salavati-Niasari, F. Davar, M. Mazaheri, Synthesis and characterization of ZnS nanoclusters via hydrothermal processing from [bis(salicylidene)zinc(II)], J. Alloy. Compd. 470 (2009) 502–506, https://doi.org/10.1016/j.jallcom.2008.03.048.
[286] Z. Ul Abideen, F. Teng, Enhanced photochemical activity and stability of ZnS by a simple alkaline treatment approach, CrystEngComm 20 (2018) 7866–7879, https://doi.org/10.1039/c8ce01417e.
[287] P. Weide, K. Schulz, S. Kaluza, M. Rohe, R. Beranek, M. Muhler, Controlling the photocorrosion of zinc sulfide nanoparticles in water by doping with chloride and cobalt ions, Langmuir 32 (2016) 12641–12649, https://doi.org/10.1021/acs.langmuir.6b03385.
[288] M. Wang, L. Cai, Y. Wang, F. Zhou, K. Xu, X. Tao, Y. Chai, Graphene-draped semiconductors for enhanced photocorrosion resistance and photocatalytic properties, J. Am. Chem. Soc. 139 (2017) 4144–4151, https://doi.org/10.1021/jacs.7b00341.
[289] J. Zhang, J. Yu, Y. Zhang, Q. Li, J.R. Gong, Visible light photocatalytic H2-production activity of CuS/ZnS porous nanosheets based on photoinduced interfacial charge transfer, Nano Lett. 11 (2011) 4774–4779, https://doi.org/10.1021/nl202587b.
[290] Y. Tang, X. Hu, C. Liu, Perfect inhibition of CdS photocorrosion by graphene sheltering engineering on TiO2 nanotube array for highly stable photocatalytic activity, Phys. Chem. Chem. Phys. 16 (2014) 25321–25329, https://doi.org/10.1039/c4cp04057k.
[291] L. Yu, W. Chen, D. Li, J. Wang, Y. Shao, M. He, P. Wang, X. Zheng, Inhibition of photocorrosion and photoactivity enhancement for ZnO via specific hollow ZnO core/ZnS shell structure, Appl. Catal. B Environ. 164 (2015) 453–461, https://doi.org/10.1016/j.apcatb.2014.09.055.
[292] S. Ham, Y. Kim, M.J. Park, B.H. Hong, D.J. Jang, Graphene quantum dots-decorated ZnS nanobelts with highly efficient photocatalytic performances, RSC Adv. 6 (2016) 24115–24120, https://doi.org/10.1039/c5ra28026e.
[293] X. Deng, C. Wang, H. Yang, M. Shao, S. Zhang, X. Wang, M. Ding, J. Huang, X. Xu, One-pot hydrothermal synthesis of CdS decorated CuS microflower-like structures for enhanced photocatalytic properties, Sci. Rep. 7 (2017) 1–12, https://doi.org/10.1038/s41598-017-04270-y.
[294] S. Yu, X.B. Fan, X. Wang, J. Li, Q. Zhang, A. Xia, S. Wei, L.Z. Wu, Y. Zhou, G. R. Patzke, Efficient photocatalytic hydrogen evolution with ligand engineered all-inorganic InP and InP/ZnS colloidal quantum dots, Nat. Commun. 9 (2018) 1–10, https://doi.org/10.1038/s41467-018-06294-y.
[295] C. Gao, T. Wei, Y. Zhang, X. Song, Y. Huan, H. Liu, M. Zhao, J. Yu, X. Chen, A photoresponsive rutile TiO $_2$ heterojunction with enhanced electron-hole separation for high-performance hydrogen evolution, Adv. Mater. 31 (2019), 1806596, https://doi.org/10.1002/adma.201806596.
[296] Y. Chao, J. Zheng, J. Chen, Z. Wang, S. Jia, H. Zhang, Z. Zhu, Highly efficient visible light-driven hydrogen production of precious metal-free hybrid photocatalyst: CdS@NiMoS core-shell nanorods, Catal. Sci. Technol. 7 (2017) 2798–2804, https://doi.org/10.1039/c7cy00964j.
[297] A. Wu, C. Tian, Y. Jiao, Q. Yan, G. Yang, H. Fu, Sequential two-step hydrothermal growth of MoS2/CdS core-shell heterojunctions for efficient visible light-driven photocatalytic H2 evolution, Appl. Catal. B Environ. 203 (2017) 955–963, https://doi.org/10.1016/j.apcatb.2016.11.009.
[298] C. Yang, M. Li, W.H. Zhang, C. Li, Controlled growth, properties, and application of CdS branched nanorod arrays on transparent conducting oxide substrate, Sol. Energy Mater. Sol. Cells 115 (2013) 100–107, https://doi.org/10.1016/j.solmat.2013.03.023.
[299] H. Rong, W. Li, Z. Chen, X. Wu, One-step fabrication of CdS nanorod arrays via solution chemistry, J. Phys. Chem. C 112 (2008) 13457–13462, https://doi.org/10.1021/jp802745b.
[300] Y. Huang, F. Sun, T. Wu, Q. Wu, Z. Huang, H. Su, Z. Zhang, Photochemical preparation of CdS hollow microspheres at room temperature and their use in visible-light photocatalysis, J. Solid State Chem. 184 (2011) 644–648, https://doi.org/10.1016/j.jssc.2011.01.012.
[301] X. Li, T. Xia, C. Xu, J. Murowchick, X. Chen, Synthesis and photoactivity of nanostructured CdS-TiO2composite catalysts, Catal. Today 225 (2014) 64–73, https://doi.org/10.1016/j.cattod.2013.10.086.
[302] J. Mort, W.E. Spear, Hole drift mobility and lifetime in CdS crystals, Phys. Rev. Lett. 8 (1962) 314–315, https://doi.org/10.1103/PhysRevLett.8.314.
[303] A. Ye, W. Fan, Q. Zhang, W. Deng, Y. Wang, CdS-graphene and CdS-CNT nanocomposites as visible-light photocatalysts for hydrogen evolution and organic dye degradation, Catal. Sci. Technol. 2 (2012) 969–978, https://doi.org/10.1039/c2cy20027a.
[304] J. Yang, H. Yan, X. Wang, F. Wen, Z. Wang, D. Fan, J. Shi, C. Li, Roles of cocatalysts in Pt-PdS/CdS with exceptionally high quantum efficiency for photocatalytic hydrogen production, J. Catal. 290 (2012) 151–157, https://doi.org/10.1016/j.jcat.2012.03.008.
[305] A.D. Mani, N. Xanthopoulos, D. Laub, C.H. Subrahmanyam, Combustion synthesis of cadmium sulphide nanomaterials for efficient visible light driven hydrogen production from water, 2014.
[306] N. Bao, L. Shen, T. Takata, K. Domen, A. Gupta, K. Yanagisawa, C.A. Grimes, Facile Cd - thiourea complex thermolysis synthesis of phase-controlled CdS nanocrystals for photocatalytic hydrogen production under visible light, J. Phys. Chem. C 111 (2007) 17527–17534, https://doi.org/10.1021/jp076566s.
[307] D. Ayodhya, M. Venkatesham, A.S. Kumari, G.B. Reddy, D. Ramakrishna, G. Veerabhadram, Synthesis, characterization, fluorescence, photocatalytic and antibacterial activity of CdS nanoparticles using Schiff base, J. Fluoresc. 25 (2015) 1481–1492, https://doi.org/10.1007/s10895-015-1639-5.
[308] R. Chauhan, A. Kumar, R.P. Chaudhary, Synthesis, structural and photocatalytic studies of Mn-doped CdS nanoparticles, Res. Chem. Intermed. 39 (2013) 645–657, https://doi.org/10.1007/s11164-012-0586-x.
[309] M. Darwish, A. Mohammadi, N.A.-M.R. Bulletin, Microwave-assisted Polyol Synthesis and Characterization of pvp-capped cds Nanoparticles for the Photocatalytic Degradation of Tartrazine, Elsevier, 2016.
[310] M.A. Osman, W.A. El-Said, A.A. Othman, A.G. Abd-Elrahim, Influence of thermally induced structural and morphological changes, and UV irradiation on photoluminescence and optical absorption behavior of CdS nanoparticles, J. Phys. D Appl. Phys. 49 (2016), 165302, https://doi.org/10.1088/0022-3727/49/16/165302.
[311] A. Samadi-maybodi, F. Abbasi, R. Akhoondi, Aqueous synthesis and characterization of CdS quantum dots capped with some amino acids and investigations of their photocatalytic activities, Colloids Surf. A Physicochem. Eng. Asp. 447 (2014) 111–119, https://doi.org/10.1016/j.colsurfa.2014.01.036.
[312] F. Shieh, A.E. Saunders, B.A. Korgel, General shape control of colloidal CdS, CdSe, CdTe quantum rods and quantum rod heterostructures, J. Phys. Chem. B 109 (2005) 8538–8542, https://doi.org/10.1021/jp0509008.
[313] A. Sitt, A. Salant, G. Menagen, U. Banin, Highly emissive nano rod-in-rod heterostructures with strong linear polarization, Nano Lett. 11 (2011) 2054–2060, https://doi.org/10.1021/nl200519b.
[314] X. Peng, L. Manna, W. Yang, J. Wickham, E. Scher, A. Kadavanich, A.P. Alivisatos, Shape control of CdSe nanocrystals, Nature 404 (2000) 59–61, https://doi.org/10.1038/35003535.
[315] Y.W. Jun, S.M. Lee, N.J. Kang, J. Cheon, Controlled synthesis of multi-armed CdS nanorod architectures using monosurfactant system, J. Am. Chem. Soc. 123 (2001) 5150–5151, https://doi.org/10.1021/ja0157595.
[316] L. Amirav, A.P. Alivisatos, Photocatalytic hydrogen production with tunable nanorod heterostructures, J. Phys. Chem. Lett. 1 (2010) 1051–1054, https://doi.org/10.1021/jz100075c.
[317] K. Wu, W. Rodríguez-Córdoba, T. Lian, Exciton localization and dissociation dynamics in cds and cds-pt quantum confined nanorods: effect of nonuniform rod diameters, J. Phys. Chem. B 118 (2014) 14062–14069, https://doi.org/10.1021/jp504703t.
[318] K. Wu, H. Zhu, T. Lian, Ultrafast exciton dynamics and light-driven H2 evolution in colloidal semiconductor nanorods and Pt-tipped nanorods, Acc. Chem. Res. 48 (2015) 851–859, https://doi.org/10.1021/ar500398g.
[319] J. Joo, J.S. Son, S.G. Kwon, J.H. Yu, T. Hyeon, Low-temperature solution-phase synthesis of quantum well structured CdSe nanoribbons, J. Am. Chem. Soc. 128 (2006) 5632–5633, https://doi.org/10.1021/ja0601686.
[320] J. Yu, Y. Yu, P. Zhou, W. Xiao, B.C.-A.C.B. Environmental, undefined 2014, Morphology-dependent photocatalytic H2-production activity of CdS, Elsevier, n. d.

[321] T. Zhai, X. Fang, L. Li, Y. Bando, D. Golberg, One-dimensional CdS nanostructures: synthesis, properties, and applications, Nanoscale 2 (2010) 168–187, https://doi.org/10.1039/b9nr00415g.
[322] B. Weng, S. Liu, N. Zhang, Z.R. Tang, Y.J. Xu, A simple yet efficient visible-light-driven CdS nanowires-carbon nanotube ^{1}D–^{1}D nanocomposite photocatalyst, J. Catal. 309 (2014) 146–155, https://doi.org/10.1016/j.jcat.2013.09.013.
[323] K.Y. Lee, J.R. Lim, H. Rho, Y.J. Choi, K.J. Choi, J.G. Park, La Crosse viral infection in hospitalized pediatric patients in Western North Carolina, Hosp. Pediatr. 2 (2012) 235–242, https://doi.org/10.1063/1.2806937.
[324] T. Gao, T. Wang, Two-dimensional single crystal CdS nanosheets: synthesis and properties, Cryst. Growth Des. (2010) 4995–5000, https://doi.org/10.1021/cg1010852.
[325] B. Ahmed, S. Kumar, S. Kumar, A.K. Ojha, Shape induced (spherical, sheets and rods) optical and magnetic properties of CdS nanostructures with enhanced photocatalytic activity for photodegradation of methylene blue dye under ultra-violet irradiation, J. Alloy. Compd. 679 (2016) 324–334, https://doi.org/10.1016/j.jallcom.2016.03.295.
[326] L. Cheng, Q. Xiang, Y. Liao, H. Zhang, CdS-based photocatalysts, Energy Environ. Sci. 11 (2018) 1362–1391, https://doi.org/10.1039/c7ee03640j.
[327] J. Jin, J. Yu, G. Liu, P.K. Wong, Single crystal CdS nanowires with high visible-light photocatalytic H 2-production performance, J. Mater. Chem. A 1 (2013) 10927–10934, https://doi.org/10.1039/c3ta12301d.
[328] X. Han, Q. Kuang, M. Jin, Z. Xie, L. Zheng, Synthesis of titania nanosheets with a high percentage of exposed (001) facets and related photocatalytic properties, J. Am. Chem. Soc. 131 (2009) 3152–3153, https://doi.org/10.1021/ja8092373.
[329] T. Feng, W. Jia, W.H. Wang, C.C. Lin, H. Fan, J.S. Zhang, H.Y. Bao, The synthesis of elegant hierarchical CdS: Via a facile hydrothermal method assisted by inorganic salt, with photocorrosion inhibition, CrystEngComm 18 (2016) 7523–7529, https://doi.org/10.1039/c6ce01047d.
[330] D. Meissner, C. Benndorf, R.M.-A. surface science, undefined 1987, Photocorrosion of cadmium sulfide: analysis by photoelectron spectroscopy, Elsevier, n.d.
[331] E. Park, S. Kim, S.-H. Song, C.-W. Lee, J.-T. Kwon, M.K. Lim, E.Y. Park, Y.J. Won, K.W. Jung, B. Kim, Environmental exposure to cadmium and risk of thyroid cancer from national industrial complex areas: a population-based cohort study, Chemosphere 268 (2021), 128819, https://doi.org/10.1016/j.chemosphere.2020.128819.
[332] F.U. Haider, C. Liqun, J.A. Coulter, S.A. Cheema, J. Wu, R. Zhang, M. Wenjun, M. Farooq, Cadmium toxicity in plants: impacts and remediation strategies, Ecotoxicol. Environ. Saf. 211 (2021), 111887, https://doi.org/10.1016/j.ecoenv.2020.111887.
[333] S.Y. Ryu, W. Balcerski, T.K. Lee, M.R. Hoffmann, Photocatalytic production of hydrogen from water with visible light using hybrid catalysts of CdS attached to microporous and mesoporous silicas, J. Phys. Chem. C 111 (2007) 18195–18203, https://doi.org/10.1021/jp074860e.
[334] T. Hirai, Y. Bando, Immobilization of CdS nanoparticles formed in reverse micelles onto aluminosilicate supports and their photocatalytic properties, J. Colloid Interface Sci. 288 (2005) 513–516, https://doi.org/10.1016/j.jcis.2005.03.038.
[335] W. Shangguan, A. Yoshida, Photocatalytic hydrogen evolution from water on nanocomposites incorporating cadmium sulfide into the interlayer, J. Phys. Chem. B 106 (2002) 12227–12230, https://doi.org/10.1021/jp0212500.
[336] C. Wang, L. Wang, J. Jin, J. Liu, Y. Li, M. Wu, L. Chen, B. Wang, X. Yang, B.L. Su, Probing effective photocorrosion inhibition and highly improved photocatalytic hydrogen production on monodisperse PANI@CdS core-shell nanospheres, Appl. Catal. B Environ. 188 (2016) 351–359, https://doi.org/10.1016/j.apcatb.2016.02.017.
[337] J. Hou, C. Yang, Z. Wang, S. Jiao, H. Zhu, Hydrothermal synthesis of CdS/CdLa 2S 4 heterostructures for efficient visible-light-driven photocatalytic hydrogen production, RSC Adv. 2 (2012) 10330–10336, https://doi.org/10.1039/c2ra21641h.
[338] P. Guan, H. Bai, C. Li, Y. Ge, D. Xu, B. Chen, et al., Erratum: Borderud SP, Li Y, Burkhalter JE, Sheffer CE and Ostroff JS. Electronic cigarette use among patients with cancer: Characteristics of electronic cigarette users and their smoking cessation outcomes. Cancer. doi: 10.1002/ cncr.28811, Cancer 121 (2015), 800, https://doi.org/10.1002/admi.201701574.
[339] D. Chen, Z. Liu, S. Zhang, Enhanced PEC performance of hematite photoanode coupled with bimetallic oxyhydroxide NiFeOOH through a simple electroless method, Appl. Catal. B Environ. 265 (2020), 118580, https://doi.org/10.1016/j.apcatb.2019.118580.
[340] S. Zhang, Z. Liu, D. Chen, W. Yan, Effective immobilization of hexavalent chromium from drinking water by nano-FeOOH coating activated carbon: adsorption and reduction, J. Environ. Manag. 277 (2021), 111386, https://doi.org/10.1016/j.apcatb.2020.119197.
[341] A. Cai, X. Wang, A. Guo, Y. Chang, Mussel-inspired green synthesis of polydopamine-Ag-AgCl composites with efficient visible-light-driven photocatalytic activity, J. Photochem. Photobiol. B Biol. 162 (2016) 486–492, https://doi.org/10.1016/j.jphotobiol.2016.07.020.
[342] M. Ruan, D. Guo, Q. Jia, A uniformly decorated and photostable polydopamine–organic semiconductor to boost the photoelectrochemical water splitting performance of CdS photoanodes, Dalton Trans. 50 (2021) 1913–1922, https://doi.org/10.1039/d0dt04056h.
[343] S.Y. Lee, S.Y. Lim, D. Seo, J.Y. Lee, T.D. Chung, Erratum: Borderud SP, Li Y, Burkhalter JE, Sheffer CE and Ostroff JS. Electronic cigarette use among patients with cancer: Characteristics of electronic cigarette users and their smoking cessation outcomes. Cancer. doi: 10.1002/ cncr.28811, Cancer 121 (2015), 800, https://doi.org/10.1002/aenm.201502207.
[344] X. Zhao, X.J. Zha, L.S. Tang, J.H. Pu, K. Ke, R.Y. Bao, Zy Liu, M.B. Yang, W. Yang, Self-assembled core-shell polydopamine@MXene with synergistic solar absorption capability for highly efficient solar-to-vapor generation, Nano Res. 13 (2020) 255–264, https://doi.org/10.1007/s12274-019-2608-0.
[345] Y. Du, H. Huang, X. Hu, S. Liu, X. Sheng, X. Li, X. Lu, J. Qu, Melamine foam/polyethylene glycol composite phase change material synergistically modified by polydopamine/MXene with enhanced solar-to-thermal conversion, Renew. Energy 171 (2021) 1–10, https://doi.org/10.1016/j.renene.2021.02.077.
[346] Q. Wang, F. Jia, A. Huang, Y. Qin, S. Song, Y. Li, M. Arroyo, MoS2@sponge with double layer structure for high-efficiency solar desalination, Desalination 481 (2020), 114359, https://doi.org/10.1016/j.desal.2020.114359.
[347] L. Zeng, X. Li, S. Fan, M. Zhang, Z. Yin, M. Tadé, S. Liu, Photo-driven bioelectrochemical photocathode with polydopamine-coated TiO2 nanotubes for self-sustaining MoS2 synthesis to facilitate hydrogen evolution, J. Power Sources 413 (2019) 310–317, https://doi.org/10.1016/j.jpowsour.2018.12.054.
[348] J. Yan, Y. Zhang, Y. Huang, Y.-E. Miao, T. Liu, Erratum: Borderud SP, Li Y, Burkhalter JE, Sheffer CE and Ostroff JS. Electronic cigarette use among patients with cancer: Characteristics of electronic cigarette users and their smoking cessation outcomes. Cancer. doi: 10.1002/ cncr.28811, Cancer 121 (2015), 800, https://doi.org/10.1002/admi.201600825.
[349] W. Chen, R. Qiao, C. Song, L. Zhao, Z.J. Jiang, T. Maiyalagan, Z. Jiang, Tailoring the thickness of MoSe2 layer of the hierarchical double-shelled N-doped carbon@MoSe2 hollow nanoboxes for efficient and stable hydrogen evolution reaction, J. Catal. 381 (2020) 363–373, https://doi.org/10.1016/j.jcat.2019.11.013.
[350] G. Zhang, X. Zhang, Y. Yang, R. Chi, J. Shi, R. Hang, X. Huang, X. Yao, P.K. Chu, X. Zhang, Dual light-induced in situ antibacterial activities of biocompatibleTiO2/MoS2/PDA/RGD nanorod arrays on titanium, Biomater. Sci. 8 (2020) 391–404, https://doi.org/10.1039/c9bm01507h.
[351] Y. Chen, H. Yin, F. Li, J. Zhou, L. Wang, J. Wang, S. Ai, Polydopamine-sensitized WS2/black-TiO2 heterojunction for histone acetyltransferase detection with enhanced visible-light-driven photoelectrochemical activity, Chem. Eng. J. 393 (2020), 124707, https://doi.org/10.1016/j.cej.2020.124707.
[352] C. Wang, J. Bai, Y. Liu, X. Jia, X. Jiang, Polydopamine coated selenide molybdenum: a new photothermal nanocarrier for highly effective chemo-photothermal synergistic therapy, ACS Biomater. Sci. Eng. 2 (2016) 2011–2017, https://doi.org/10.1021/acsbiomaterials.6b00416.
[353] L. Cheng, X. Li, H. Zhang, Q. Xiang, Two-dimensional transition metal MXene-based photocatalysts for solar fuel generation, J. Phys. Chem. Lett. 10 (2019) 3488–3494, https://doi.org/10.1021/acs.jpclett.9b00736.
[354] J. Peng, X. Chen, W.J. Ong, X. Zhao, N. Li, Surface and heterointerface engineering of 2D MXenes and their nanocomposites: insights into electro- and photocatalysis, Chem 5 (2019) 18–50, https://doi.org/10.1016/j.chempr.2018.08.037.
[355] Z. Li, Y. Wu, 2D early transition metal carbides (MXenes) for catalysis, Small 15 (2019), 1804736, https://doi.org/10.1002/smll.201804736.
[356] T. Li, B. Ding, J. Wang, Z. Qin, J.F.S. Fernando, Y. Bando, A.K. Nanjundan, Y. V. Kaneti, D. Golberg, Y. Yamauchi, Sandwich-structured ordered mesoporous polydopamine/MXene hybrids as high-performance anodes for lithium-ion batteries, ACS Appl. Mater. Interfaces 12 (2020) 14993–15001, https://doi.org/10.1021/acsami.9b18883.
[357] C. Beust, E. Franquet, J.P. Bédécarrats, P. Garcia, Predictive approach of heat transfer for the modelling of large-scale latent heat storages, Renew. Energy 157 (2020) 502–514, https://doi.org/10.1016/j.renene.2020.04.135.
[358] Z. Li, X. Meng, Z. Zhang, Recent development on MoS2-based photocatalysis: a review, J. Photochem. Photobiol. C Photochem. Rev. 35 (2018) 39–55, https://doi.org/10.1016/j.jphotochemrev.2017.12.002.
[359] Y.-J. Yuan, H.-W. Lu, Z.-T. Yu, Z.-G. Zou, Noble-metal-free molybdenum disulfide cocatalyst for photocatalytic hydrogen production, ChemSusChem 8 (2015) 4113–4127, https://doi.org/10.1002/cssc.201501203.
[360] H.I. Karunadasa, E. Montalvo, Y. Sun, M. Majda, J.R. Long, C.J. Chang, A molecular MoS2 edge site mimic for catalytic hydrogen generation, Science 335 (2012) 698–702, https://doi.org/10.1126/science.1215868.
[361] L. Wang, C. Wang, W. Liu, Q. Chen, M. He, Visible-light-induced aerobic thiocyanation of indoles using reusable TiO2/MoS2 nanocomposite photocatalyst, Tetrahedron Lett. 57 (2016) 1771–1774, https://doi.org/10.1016/j.tetlet.2016.03.028.
[362] Y. Rong, L. Tang, Y. Song, S. Wei, Z. Zhang, J. Wang, A new visible-light driving nanocomposite photocatalyst Er3+:Y3Al5O12/MoS2-NaTaO3-PdS for photocatalytic degradation of a refractory pollutant with potentially simultaneous hydrogen evolution, RSC Adv. 6 (2016) 80595–80603, https://doi.org/10.1039/c6ra15320h.
[363] T. Xiong, M. Wen, F. Dong, J. Yu, L. Han, B. Lei, Y. Zhang, X. Tang, Z. Zang, Three dimensional Z-scheme (BiO)2CO3/MoS2 with enhanced visible light photocatalytic NO removal, Appl. Catal. B Environ. 199 (2016) 87–95, https://doi.org/10.1016/j.apcatb.2016.06.032.
[364] Z. He, W. Que, Molybdenum disulfide nanomaterials: structures, properties, synthesis and recent progress on hydrogen evolution reaction, Appl. Mater. Today 3 (2016) 23–56, https://doi.org/10.1016/j.apmt.2016.02.001.
[365] I. Song, C. Park, H.C. Choi, Synthesis and properties of molybdenum disulphide: from bulk to atomic layers, RSC Adv. 5 (2015) 7495–7514, https://doi.org/10.1039/c4ra11852a.
[366] V. Nicolosi, M. Chhowalla, M.G. Kanatzidis, M.S. Strano, J.N. Coleman, Liquid exfoliation of layered materials, Science 340 (2013), 1226419, https://doi.org/10.1126/science.1226419.

[367] J.N. Coleman, M. Lotya, A. O'neill, S.D. Bergin, P.J. King, U. Khan, K. Young, A. Gaucher, S. De, R.J. Smith, I.V. Shvets, S.K. Arora, G. Stanton, H.Y. Kim, K. Lee, G.T. Kim, G.S. Duesberg, T. Hallam, J.J. Boland, J.J. Wang, J.F. Donegan, J. C. Grunlan, G. Moriarty, A. Shmeliov, R.J. Nicholls, J.M. Perkins, E.M. Grieveson, K. Theuwissen, D.W. McComb, P.D. Nellist, V. Nicolosi, Two-dimensional nanosheets produced by liquid exfoliation of layered materials, Science 331 (2011) 568–571, https://doi.org/10.1126/science.1194975.
[368] K.H. Hu, X.G. Hu, Y.F. Xu, X.Z. Pan, The effect of morphology and size on the photocatalytic properties of MoS2, React. Kinet. Mech. Catal. 100 (2010) 153–163, https://doi.org/10.1007/s11144-010-0173-3.
[369] A. Kuc, N. Zibouche, T. Heine, Influence of quantum confinement on the electronic structure of the transition metal sulfide TS2, Phys. Rev. B 83 (2011), 245213, https://doi.org/10.1103/PhysRevB.83.245213.
[370] W. Zhou, Z. Yin, Y. Du, X. Huang, Z. Zeng, Z. Fan, H. Liu, J. Wang, H. Zhang, Synthesis of few-layer MoS $_2$ nanosheet-coated TiO $_2$ nanobelt heterostructures for enhanced photocatalytic activities, Small 9 (2013) 140–147, https://doi.org/10.1002/smll.201201161.
[371] S.W. Hu, L.W. Yang, Y. Tian, X.L. Wei, J.W. Ding, J.X. Zhong, P.K. Chu, Simultaneous nanostructure and heterojunction engineering of graphitic carbon nitride via in situ Ag doping for enhanced photoelectrochemical activity, Appl. Catal. B Environ. 163 (2015) 611–622, https://doi.org/10.1016/j.apcatb.2014.08.023.
[372] X. Liu, Z. Xing, Y. Zhang, Z. Li, X. Wu, S. Tan, X. Yu, Q. Zhu, W. Zhou, Fabrication of 3D flower-like black N-TiO2-x@MoS2 for unprecedented-high visible-light-driven photocatalytic performance, Appl. Catal. B Environ. 201 (2017) 119–127, https://doi.org/10.1016/j.apcatb.2016.08.031.
[373] X. Li, J. Yu, S. Wageh, A.A. Al-Ghamdi, J. Xie, Graphene in photocatalysis: a review, Small 12 (2016) 6640–6696, https://doi.org/10.1002/smll.201600382.
[374] X. Ma, J. Li, C. An, J. Feng, Y. Chi, J. Liu, J. Zhang, Y. Sun, Ultrathin Co(Ni)-doped MoS2 nanosheets as catalytic promoters enabling efficient solar hydrogen production, Nano Res. 9 (2016) 2284–2293, https://doi.org/10.1007/s12274-016-1115-9.
[375] X. Wang, M. Hong, F. Zhang, Z. Zhuang, Y. Yu, Recyclable nanoscale zero valent iron doped g-C3N4/MoS2 for efficient photocatalysis of RhB and Cr(VI) driven by visible light, ACS Sustain. Chem. Eng. 4 (2016) 4055–4063, https://doi.org/10.1021/acssuschemeng.6b01024.
[376] Y. Liu, S. Xie, H. Li, X. Wang, A highly efficient sunlight driven ZnO nanosheet photocatalyst: synergetic effect of P-doping and MoS_2 atomic layer loading, ChemCatChem 6 (2014) 2522–2526, https://doi.org/10.1002/cctc.201402191.
[377] F. Carraro, L. Calvillo, M. Cattelan, M. Favaro, M. Righetto, S. Nappini, I. Píš, V. Celorrio, D.J. Fermín, A. Martucci, S. Agnoli, G. Granozzi, Fast one-pot synthesis of MoS2/crumpled graphene p-n nanonjunctions for enhanced photoelectrochemical hydrogen production, ACS Appl. Mater. Interfaces 7 (2015) 25685–25692, https://doi.org/10.1021/acsami.5b06668.
[378] F. Meng, J. Li, S.K. Cushing, M. Zhi, N. Wu, Solar hydrogen generation by nanoscale p-n junction of p-type molybdenum disulfide/n-type nitrogen-doped reduced graphene oxide, J. Am. Chem. Soc. 135 (2013) 10286–10289, https://doi.org/10.1021/ja404851s.
[379] S. Ma, J. Xie, J. Wen, K. He, X. Li, W. Liu, X. Zhang, Constructing 2D layered hybrid CdS nanosheets/MoS 2 heterojunctions for enhanced visible-light photocatalytic H 2 generation, Appl. Surf. Sci. 391 (2017) 580–591, https://doi.org/10.1016/j.apsusc.2016.07.067.
[380] Y.J. Yuan, D. Chen, J. Zhong, L.X. Yang, J. Wang, M.J. Liu, W.G. Tu, Z.T. Yu, Z. G. Zou, Interface engineering of a noble-metal-free ^{2}D–^{2}D MoS2/Cu-ZnIn2S4 photocatalyst for enhanced photocatalytic H2 production, J. Mater. Chem. A 5 (2017) 15771–15779, https://doi.org/10.1039/c7ta04410k.
[381] Y.J. Yuan, Z.T. Yu, Y.H. Li, H.W. Lu, X. Chen, W.G. Tu, Z.G. Ji, Z.G. Zou, A MoS2/6,13-pentacenequinone composite catalyst for visible-light-induced hydrogen evolution in water, Appl. Catal. B Environ. 181 (2016) 16–23, https://doi.org/10.1016/j.apcatb.2015.07.030.
[382] V. Babacic, D. Saleta Reig, S. Varghese, T. Vasileiadis, E. Coy, K.J. Tielrooij, B. Graczykowski, Thickness-dependent elastic softening of few-layer free-standing MoSe 2, Adv. Mater. 33 (2021), 2008614, https://doi.org/10.1002/adma.202008614.
[383] W. Chen, R. Qiao, C. Song, L. Zhao, Z.-J. Jiang, T. Maiyalagan, Z. Jiang, Tailoring the thickness of MoSe2 layer of the hierarchical double-shelled N-doped carbon@MoSe2 hollow nanoboxes for efficient and stable hydrogen evolution reaction, J. Catal. 381 (2020) 363–373, https://doi.org/10.1016/j.jcat.2019.11.013.
[384] K.G. Neoh, X. Hu, D. Zheng, E.T. Kang, Balancing osteoblast functions and bacterial adhesion on functionalized titanium surfaces, Biomaterials 33 (2012) 2813–2822, https://doi.org/10.1016/j.biomaterials.2012.01.018.
[385] Z. Zhao, R. Yan, X. Yi, J. Li, J. Rao, Z. Guo, Y. Yang, W. Li, Y.Q. Li, C. Chen, Bacteria-activated theranostic nanoprobes against methicillin-resistant Staphylococcus aureus infection, ACS Nano 11 (2017) 4428–4438, https://doi.org/10.1021/acsnano.7b00041.
[386] Z. Xu, M. Li, X. Li, X. Liu, F. Ma, S. Wu, K.W. Yeung, Y. Han, P.K. Chu, Antibacterial activity of silver doped titanate nanowires on Ti implants, ACS Appl. Mater. Interfaces 8 (2016) 16584–16594, https://doi.org/10.1021/acsami.6b04161.
[387] C. Kaweeteerawat, C.H. Chang, K.R. Roy, R. Liu, R. Li, D. Toso, H. Fischer, A. Ivask, Z. Ji, J.I. Zink, Z.H. Zhou, G.F. Chanfreau, D. Telesca, Y. Cohen, P. A. Holden, A.E. Nel, H.A. Godwin, Cu nanoparticles have different impacts in Escherichia coli and Lactobacillus brevis than their microsized and ionic analogues, ACS Nano 9 (2015) 7215–7225, https://doi.org/10.1021/acsnano.5b02021.
[388] J. Li, L. Tan, X. Liu, Z. Cui, X. Yang, K.W.K. Yeung, P.K. Chu, S. Wu, Balancing bacteria-osteoblast competition through selective physical puncture and biofunctionalization of ZnO/polydopamine/arginine-glycine-aspartic acid-cysteine nanorods, ACS Nano 11 (2017) 11250–11263, https://doi.org/10.1021/acsnano.7b05620.
[389] P.V. AshaRani, G.L.K. Mun, M.P. Hande, S. Valiyaveettil, Cytotoxicity and genotoxicity of silver nanoparticles in human cells, ACS Nano 3 (2009) 279–290, https://doi.org/10.1021/nn800596w.
[390] L. Guo, D.D. Yan, D. Yang, Y. Li, X. Wang, O. Zalewski, B. Yan, W. Lu, Combinatorial photothermal and immuno cancer therapy using chitosan-coated hollow copper sulfide nanoparticles, ACS Nano 8 (2014) 5670–5681, https://doi.org/10.1021/nn5002112.
[391] M.A. Holbert, R. Marmorstein, Structure and activity of enzymes that remove histone modifications, Curr. Opin. Struct. Biol. 15 (2005) 673–680, https://doi.org/10.1016/j.sbi.2005.10.006.
[392] Q. Chen, X. Xu, D. Xu, H. Zhang, C. Zhang, G. Li, WRKY18 and WRKY53 coordinate with histone acetyltransferase1 to regulate rapid responses to sugar, Plant Physiol. 180 (2019) 2212–2226, https://doi.org/10.1104/pp.19.00511.
[393] Y. Han, H. Li, Y. Hu, P. Li, H. Wang, Z. Nie, S. Yao, Time-resolved luminescence biosensor for continuous activity detection of protein acetylation-related enzymes based on DNA-sensitized terbium(III) probes, Anal. Chem. 87 (2015) 9179–9185, https://doi.org/10.1021/acs.analchem.5b01338.
[394] G. Chen, I. Roy, C. Yang, P.N. Prasad, Nanochemistry and nanomedicine for nanoparticle-based diagnostics and therapy, Chem. Rev. 116 (2016) 2826–2885, https://doi.org/10.1021/acs.chemrev.5b00148.
[395] Y. Lu, A.A. Aimetti, R. Langer, Z. Gu, Bioresponsive materials, Nat. Rev. Mater. 2 (2016) 1–17, https://doi.org/10.1038/natrevmats.2016.75.
[396] G. De Crozals, R. Bonnet, C. Farre, C. Chaix, Nanoparticles with multiple properties for biomedical applications: a strategic guide, Nano Today 11 (2016) 435–463, https://doi.org/10.1016/j.nantod.2016.07.002.
[397] O. Akhavan, E. Ghaderi, Graphene nanomesh promises extremely efficient in vivo photothermal therapy, Small 9 (2013) 3593–3601, https://doi.org/10.1002/smll.201203106.
[398] J. Ryu, H.S. Kim, H.T. Hahn, D. Lashmore, Carbon nanotubes with platinum nano-islands as glucose biofuel cell electrodes, Biosens. Bioelectron. 25 (2010) 1603–1608, https://doi.org/10.1016/j.bios.2009.11.019.
[399] Z. Hu, F. Zhao, Y. Wang, Y. Huang, L. Chen, N. Li, J. Li, Z. Li, G. Yi, Facile fabrication of a C60-polydopamine-graphene nanohybrid for single light induced photothermal and photodynamic therapy, Chem. Commun. 50 (2014) 10815–10818, https://doi.org/10.1039/c4cc04416a.
[400] D.B. Pacardo, B. Neupane, S.M. Rikard, Y. Lu, R. Mo, S.R. Mishra, J.B. Tracy, G. Wang, F.S. Ligler, Z. Gu, A dual wavelength-activatable gold nanorod complex for synergistic cancer treatment, Nanoscale 7 (2015) 12096–12103, https://doi.org/10.1039/c5nr01568e.
[401] F. Hu, Y. Zhang, G. Chen, C. Li, Q. Wang, Double-walled Au nanocage/SiO2 nanorattles: integrating SERS imaging, drug delivery and photothermal therapy, Small 11 (2015) 985–993, https://doi.org/10.1002/smll.201401360.
[402] M.S. Noh, S. Lee, H. Kang, J.-K. Yang, H. Lee, D. Hwang, J.W. Lee, S. Jeong, Y. Jang, B.H. Jun, D.H. Jeong, S.K. Kim, Y.S. Lee, M.H. Cho, Target-specific near-IR induced drug release and photothermal therapy with accumulated Au/Ag hollow nanoshells on pulmonary cancer cell membranes, Biomaterials 45 (2015) 81–92, https://doi.org/10.1016/j.biomaterials.2014.12.036.
[403] C. Wang, J. Bai, Y. Liu, X. Jia, X. Jiang, Polydopamine coated selenide molybdenum: a new photothermal nanocarrier for highly effective chemo-photothermal synergistic therapy, ACS Biomater. Sci. Eng. 2 (2016) 2011–2017, https://doi.org/10.1021/acsbiomaterials.6b00416.
[404] K. Petcharoen, A. Sirivat, Synthesis and characterization of magnetite nanoparticles via the chemical co-precipitation method, Mater. Sci. Eng. B Solid State Mater. Adv. Technol. 177 (2012) 421–427, https://doi.org/10.1016/j.mseb.2012.01.003.
[405] S. Rahim Pouran, A.A. Abdul Raman, W.M.A. Wan Daud, Review on the application of modified iron oxides as heterogeneous catalysts in Fenton reactions, J. Clean. Prod. 64 (2014) 24–35, https://doi.org/10.1016/j.jclepro.2013.09.013.
[406] M. Ashraf, I. Khan, M. Usman, A. Khan, S.S. Shah, A.Z. Khan, K. Saeed, M. Yaseen, M.F. Ehsan, M.N. Tahir, N. Ullah, Hematite and magnetite nanostructures for green and sustainable energy harnessing and environmental pollution control: a review, Chem. Res. Toxicol. 33 (2020) 1292–1311, https://doi.org/10.1021/acs.chemrestox.9b00308.
[407] A. Masudi, G.E. Harimisa, N.A. Ghafar, N.W.C. Jusoh, Magnetite-based catalysts for wastewater treatment, Environ. Sci. Pollut. Res. 27 (2020) 4664–4682, https://doi.org/10.1007/s11356-019-07415-w.
[408] Y.L. Pang, S. Lim, H.C. Ong, W.T. Chong, Research progress on iron oxide-based magnetic materials: synthesis techniques and photocatalytic applications, Ceram. Int. 42 (2016) 9–34, https://doi.org/10.1016/j.ceramint.2015.08.144.
[409] D. Cheng, Y. Zhang, X. Bai, Y. Liu, Z. Deng, J. Wu, S. Bi, J. Ran, G. Cai, X. Wang, Mussel-inspired fabrication of superhydrophobic cotton fabric for oil/water separation and visible light photocatalytic, Cellulose 27 (2020) 5421–5433, https://doi.org/10.1007/s10570-020-03149-y.
[410] F. Ansari, M. Salavati-Niasari, O. Amiri, N. Mir, B. Abdollahi Nejand, V. Ahmadi, Magnetite as inorganic hole transport material for lead halide perovskite-based solar cells with enhanced stability, Ind. Eng. Chem. Res. 59 (2020) 743–750, https://doi.org/10.1021/acs.iecr.9b05173.
[411] V. Antonov, B. Harmon, A. Yaresko, Electronic structure and magneto-optical properties of solids, 2004.

[412] D. Tahir, B. Abdullah, B. Armynah, H.J. Kang, Electronic properties of composite iron (II, III) oxide (Fe3O4) carbonaceous absorber materials by electron spectroscopy, J. Electron Spectrosc. Relat. Phenom. 229 (2018) 47–51, https://doi.org/10.1016/j.elspec.2018.09.008.
[413] B. Lesiak, N. Rangam, P. Jiricek, I. Gordeev, J. Tóth, L. Kövér, M. Mohai, P. Borowicz, Surface study of Fe3O4 nanoparticles functionalized with biocompatible adsorbed molecules, Front. Chem. 7 (2019) 642, https://doi.org/10.3389/fchem.2019.00642.
[414] P.M. Kouotou, A. El Kasmi, L.N. Wu, M. Waqas, Z.Y. Tian, Particle size-band gap energy-catalytic properties relationship of PSE-CVD-derived Fe3O4 thin films, J. Taiwan Inst. Chem. Eng. 93 (2018) 427–435, https://doi.org/10.1016/j.jtice.2018.08.014.
[415] J.R. Rajabathar, J.J. Vijaya, A. Prabakaran, Z.A. Issa, A.M. Atta, A.O. Ezzat, A. M. Al-Mayouf, H.A. Al-Lohedan, Synthesis, characterization and catalytic sorption activity of various method prepared magnetite (Fe3O4) nanoparticle deposition on porous BiMnOx nanotubes, J. Alloy. Compd. 698 (2017) 1077–1085, https://doi.org/10.1016/j.jallcom.2016.12.192.
[416] M. Amir, S. Güner, A. Yıldız, A. Baykal, Magneto-optical and catalytic properties of Fe3O4@HA@Ag magnetic nanocomposite, J. Magn. Magn. Mater. 421 (2017) 462–471, https://doi.org/10.1016/j.jmmm.2016.08.037.
[417] S. Sheik Fareed, N. Mythili, H. Mohamed Mohaideen, K. Saravanakumar, R. Chandramohan, G. Ravi, Studies on the simplified SILAR deposited magnetite (Fe3O4) thin films annealed at different temperatures, J. Mater. Sci. Mater. Electron. 27 (2016) 3420–3426, https://doi.org/10.1007/s10854-015-4174-x.
[418] X. Liu, M.D. Kaminski, Y. Guan, H. Chen, H. Liu, A.J. Rosengart, Preparation and characterization of hydrophobic superparamagnetic magnetite gel, J. Magn. Magn. Mater. 306 (2006) 248–253, https://doi.org/10.1016/j.jmmm.2006.03.049.
[419] J. Mürbe, A. Rechtenbach, J. Töpfer, Synthesis and physical characterization of magnetite nanoparticles for biomedical applications, Mater. Chem. Phys. 110 (2008) 426–433, https://doi.org/10.1016/j.matchemphys.2008.02.037.
[420] B. Unal, Z. Durmus, H. Kavas, A. Baykal, M.S. Toprak, Synthesis, conductivity and dielectric characterization of salicylic acid-Fe3O4 nanocomposite, Mater. Chem. Phys. 123 (2010) 184–190, https://doi.org/10.1016/j.matchemphys.2010.03.080.
[421] S. Asuha, B. Suyala, X. Siqintana, S. Zhao, Direct synthesis of Fe3O4 nanopowder by thermal decomposition of Fe-urea complex and its properties, J. Alloy. Compd. 509 (2011) 2870–2873, https://doi.org/10.1016/j.jallcom.2010.11.145.
[422] S. Bakardjieva, V. Stengl, J. Subrt, V. Houskova, P. Kalenda, Photocatalytic efficiency of iron oxides: degradation of 4-chlorophenol, J. Phys. Chem. Solids 68 (2007) 721–724, https://doi.org/10.1016/j.jpcs.2006.12.004.
[423] K.X. Wang, Z. Yu, V. Liu, M.L. Brongersma, T.F. Jaramillo, S. Fan, Photon management for near-total solar absorption in hematite photoanodes, in: Materials Research Society Symposium Proceedings, Materials Research Society, 2014, pp. 8–13. doi:10.1557/opl.2014.417.
[424] J. Brillet, M. Comuz, F. Le Formal, J.H. Yum, M. Grätzel, K. Sivula, Examining architectures of photoanode-photovoltaic tandem cells for solar water splitting, J. Mater. Res. 25 (2010) 17–24, https://doi.org/10.1557/jmr.2010.0009.
[425] H. Kušić, A. Lončarić Božić, N. Koprivanac, S. Papić, Fenton type processes for minimization of organic content in coloured wastewaters. Part II: combination with zeolites, Dye Pigment. 74 (2007) 388–395, https://doi.org/10.1016/j.dyepig.2006.01.050.
[426] U. Björkstén, J. Moser, M. Grätzel, Photoelectrochemical studies on nanocrystalline hematite films, Chem. Mater. 6 (1994) 858–863, https://doi.org/10.1021/cm00042a026.
[427] N.J. Cherepy, D.B. Liston, J.A. Lovejoy, H. Deng, J.Z. Zhang, Ultrafast studies of photoexcited electron dynamics in γ- and α-Fe2O3 semiconductor nanoparticles, J. Phys. Chem. B 102 (1998) 770–776, https://doi.org/10.1021/jp973149e.
[428] A.G. Joly, J.R. Williams, S.A. Chambers, G. Xiong, W.P. Hess, D.M. Laman, La Crosse viral infection in hospitalized pediatric patients in Western North Carolina, Hosp. Pediatr. 2 (2012) 235–242, https://doi.org/10.1063/1.2177426.
[429] S. Shen, J. Zhou, C.L. Dong, Y. Hu, E.N. Tseng, P. Guo, L. Guo, S.S. Mao, Surface engineered doping of hematite nanorod arrays for improved photoelectrochemical water splitting, Sci. Rep. 4 (2014) 1–9, https://doi.org/10.1038/srep06627.
[430] M. Mishra, D.M. Chun, α-Fe2O3 as a photocatalytic material: a review, Appl. Catal. A Gen. 498 (2015) 126–141, https://doi.org/10.1016/j.apcata.2015.03.023.
[431] D.A. Wheeler, G. Wang, Y. Ling, Y. Li, J.Z. Zhang, Nanostructured hematite: synthesis, characterization, charge carrier dynamics, and photoelectrochemical properties, Energy Environ. Sci. 5 (2012) 6682–6702, https://doi.org/10.1039/c2ee00001f.
[432] Y. Ling, G. Wang, D.A. Wheeler, J.Z. Zhang, Y. Li, Sn-doped hematite nanostructures for photoelectrochemical water splitting, Nano Lett. 11 (2011) 2119–2125, https://doi.org/10.1021/nl200708y.
[433] Z. Li, X. Lai, H. Wang, D. Mao, C. Xing, D. Wang, Direct hydrothermal synthesis of single-crystalline hematite nanorods assisted by 1,2-propanediamine, Nanotechnology 20 (2009), 245603, https://doi.org/10.1088/0957-4484/20/24/245603.
[434] D.C. Golden, D.W. Ming, R.V. Morris, T.G. Graff, Hydrothermal synthesis of hematite spherules and jarosite: implications for diagenesis and hematite spherule formation in sulfate outcrops at Meridiani Planum, Mars, Am. Mineral. 93 (2008) 1201–1214, https://doi.org/10.2138/am.2008.2737.
[435] L. Armelao, G. Granozzi, E. Tondello, P. Colombo, G. Principi, P.P. Lottici, G. Antonioli, Nanocrystalline α-Fe2O3 sol-gel thin films: a microstructural study, J. Non Cryst. Solids 192–193 (1995) 435–438, https://doi.org/10.1016/0022-3093(95)00387-8.
[436] K. Woo, H.J. Lee, J.-P. Ahn, Y.S. Park, Sol–gel mediated synthesis of Fe2O3 nanorods, Adv. Mater. 15 (2003) 1761–1764, https://doi.org/10.1002/adma.200305561.
[437] H.J. Kim, K.I. Choi, A. Pan, I.D. Kim, H.R. Kim, K.M. Kim, C.W. Na, G. Cao, J. H. Lee, Template-free solvothermal synthesis of hollow hematite spheres and their applications in gas sensors and Li-ion batteries, J. Mater. Chem. 21 (2011) 6549–6555, https://doi.org/10.1039/c0jm03516e.
[438] J. Li, X. Lai, C. Xing, D. Wang, One-pot synthesis of porous hematite hollow microspheres and their application in water treatment, J. Nanosci. Nanotechnol. 10 (2010) 7707–7710, https://doi.org/10.1166/jnn.2010.2795.
[439] J.A. Glasscock, P.R.F. Barnes, I.C. Plumb, N. Savvides, Enhancement of photoelectrochemical hydrogen production from hematite thin films by the introduction of Ti and Si, J. Phys. Chem. C 111 (2007) 16477–16488, https://doi.org/10.1021/jp074556l.
[440] Y. Lin, S. Zhou, S.W. Sheehan, D. Wang, Nanonet-based hematite heteronanostructures for efficient solar water splitting, J. Am. Chem. Soc. 133 (2011) 2398–2401, https://doi.org/10.1021/ja110741z.
[441] J.J. Wu, Y.L. Lee, H.H. Chiang, D.K.P. Wong, Growth and magnetic properties of oriented α-Fe2O 3 nanorods, J. Phys. Chem. B 110 (2006) 18108–18111, https://doi.org/10.1021/jp0644661.
[442] A. Kay, I. Cesar, M. Grätzel, New benchmark for water photooxidation by nanostructured α-Fe 2O3 films, J. Am. Chem. Soc. 128 (2006) 15714–15721, https://doi.org/10.1021/ja064380l.
[443] S.D. Tilley, M. Cornuz, K. Sivula, M. Grätzel, Light-inducedwater splitting with hematite: improved nanostructure and iridium oxide catalysis, Angew. Chem. Int. Ed. 49 (2010) 6405–6408, https://doi.org/10.1002/anie.201003110.
[444] K. Sivula, F. Le Formal, M. Grätzel, WO3-Fe2O3 photoanodes for water splitting: a host scaffold, guest absorber approach, Chem. Mater. 21 (2009) 2862–2867, https://doi.org/10.1021/cm900565a.
[445] M.I. Litter, M.A. Blesa, Photodissolution of iron oxides. IV. A comparative study on the photodissolution of hematite, magnetite, and maghemite in EDTA media, Can. J. Chem. 70 (1992) 2502–2510, https://doi.org/10.1139/v92-316.
[446] N.A.M. Barakat, Synthesis and characterization of maghemite iron oxide (γ-Fe 2O 3) nanofibers: novel semiconductor with magnetic feature, J. Mater. Sci. 47 (2012) 6237–6245, https://doi.org/10.1007/s10853-012-6543-7.
[447] A. Bee, R. Massart, S. Neveu, Synthesis of very fine maghemite particles, J. Magn. Magn. Mater. 149 (1995) 6–9, https://doi.org/10.1016/0304-8853(95)00317-7.
[448] Y.K. Sun, M. Ma, Y. Zhang, N. Gu, Synthesis of nanometer-size maghemite particles from magnetite, Colloids Surf. A Physicochem. Eng. Asp. 245 (2004) 15–19, https://doi.org/10.1016/j.colsurfa.2004.05.009.
[449] P. Ajayan, P. Kim, K. Banerjee, Two-dimensional van der Waals materials, Phys. Today 69 (2016) 38–44, https://doi.org/10.1063/PT.3.3297.
[450] J. Yang, J. Zhu, J. Xu, C. Zhang, T. Liu, MoSe2 nanosheet array with layered MoS2 heterostructures for superior hydrogen evolution and lithium storage performance, ACS Appl. Mater. Interfaces 9 (2017) 44550–44559, https://doi.org/10.1021/acsami.7b15854.
[451] S. Zheng, L. Zheng, Z. Zhu, J. Chen, J. Kang, Z. Huang, D. Yang, MoS2 nanosheet arrays rooted on hollow rGO spheres as bifunctional hydrogen evolution catalyst and supercapacitor electrode, Nano Micro Lett. 10 (2018) 62, https://doi.org/10.1007/s40820-018-0215-3.
[452] C. Du, D. Liang, M. Shang, J. Zhang, J. Mao, P. Liu, W. Song, In situ engineering MoS2 NDs/VS2 lamellar heterostructure for enhanced electrocatalytic hydrogen evolution, ACS Sustain. Chem. Eng. 6 (2018) 15471–15479, https://doi.org/10.1021/acssuschemeng.8b03929.
[453] D. Vikraman, S. Hussain, K. Akbar, L. Truong, A. Kathalingam, S.-H. Chun, J. Jung, H.J. Park, H.S. Kim, Improved hydrogen evolution reaction performance using MoS 2 –WS 2 heterostructures by physicochemical process, ACS Sustain. Chem. Eng. 6 (2018) 8400–8409, https://doi.org/10.1021/acssuschemeng.8b00524.
[454] F. Ponzio, P. Payamyar, A. Schneider, M. Winterhalter, J. Bour, F. Addiego, M. P. Krafft, J. Hemmerle, V. Ball, Polydopamine films from the forgotten air/water interface, J. Phys. Chem. Lett. 5 (2014) 3436–3440, https://doi.org/10.1021/jz501842r.
[455] D. Maziukiewicz, B. Grześkowiak, E. Coy, S. Jurga, R. Mrówczyński, NDs@PDA@ICG conjugates for photothermal therapy of glioblastoma multiforme, Biomimetics 4 (2019) 3, https://doi.org/10.3390/biomimetics4010003.

Publication 2

The Author's contribution to this publication includes Literature Review, Writing – original draft, Writing – review & editing, and Visualization. Moreover, selecting figures from cited publications and preparing collective figures (Figure 1-4 and 9-11 of the Publication 2).

Journal: European Polymer Journal
ISSN: 0014-3057
Publisher: Elsevier
Journal Impact Factor: 6.0
Publication Date: 05.07.2022
Number of Citations: 25

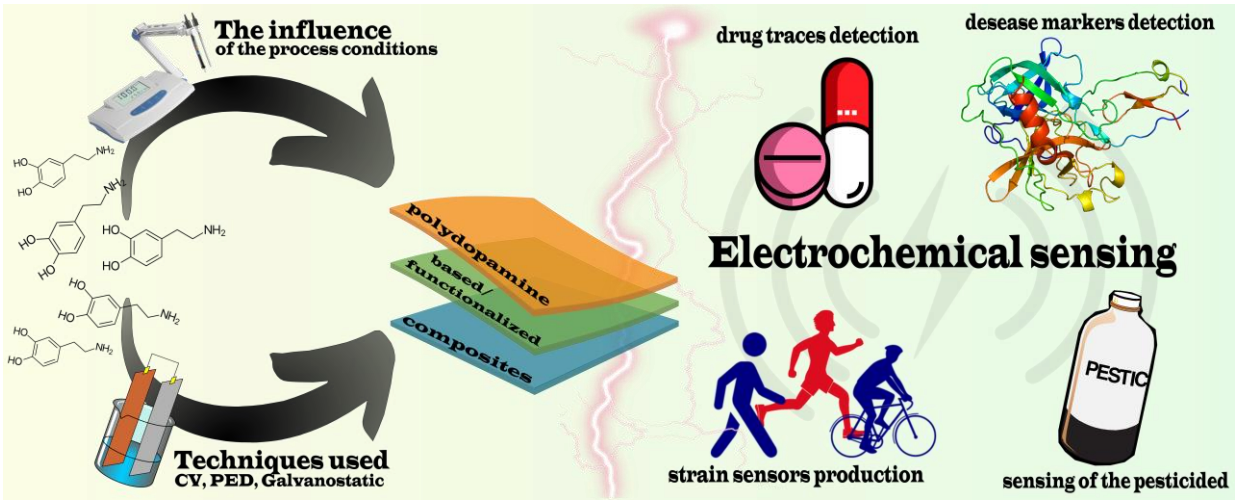

Figure 10. Graphical abstract of the P2

European Polymer Journal 174 (2022) 111346

Contents lists available at ScienceDirect

European Polymer Journal

journal homepage: www.elsevier.com/locate/europolj

Polydopamine films: Electrochemical growth and sensing applications

Jakub Szewczyk, Daniel Aguilar-Ferrer, Emerson Coy *

NanoBioMedical Centre, Adam Mickiewicz University, Wszechnicy Piastowskiej 3, 61-614 Poznań, Poland

ARTICLE INFO

Keywords:
Polydopamine
Functional materials
Sensors
Thin films
Electrochemistry

ABSTRACT

Polydopamine is one of the most promising biomimetic polymers for environmental, biomedical and energy applications. This review presents the current state of the art in the electrochemistry of polydopamine nanomaterials and its applications in the electrochemical analysis and sensing field. First, the mechanism of electrochemical oxidation of dopamine is given concerning the influence of the electrodeposition method and processing conditions, e.g. the pH value is presented, as well as the particularities of polydopamine in electro impedance spectroscopy studies. The electrochemical formation of the polydopamine free-standing thin films is also discussed. Moreover, literature examples of polydopamine for construction or functionalization of the electrochemical sensors for drug traces, disease markers and pesticide contaminants detecting, potentiometric sensing, and wearable strain sensors construction are presented. Finally, we outline the future developments and perspectives of the field.

1. Introduction

Polydopamine (PDA) is a biomimetic polymer, developed and described for the first time in 2007 [1]. The marine mussel adhesive properties inspired the investigation of the mechanism, where one of the proteins - responsible for this phenomenon -was found to be rich in dopamine (DA) and lysine units. Interest in replicating and understanding this mechanism resulted in the fabrication of polydopamine – a new, biocompatible polymer with strong adhesive properties [2]. PDA has made a sizable impact in nanotechnology [3–6], biomedicine [3,7,8], catalysis [9], photocatalysis [10], water remediation [9,11] and other fields, especially in recent years [4,6,9–13]. To date, PDA films and nanoparticles are predominantly formed via autoxidation in slightly alkaline aqueous dopamine solution (>pH 7.4). In this process, the formation of the PDA is triggered by the oxidation and self-polymerization in the presence of oxidizing species, where the film thickness or the nanoparticles' size and other properties rest on the condition used [1,2]. As a versatile and relatively simple method, autoxidation has gained much attention; however, this method suffers from low-efficiency selectivity and is hard to control in situ [4].

Moreover, the real-time detection of dopamine is a critical issue in analytical chemistry and medicine [14–18]. Fortunately, electrochemical techniques stand as an affordable and accurate solution for dopamine's real-time in-vivo detection [15,18]. However, a significant problem with these techniques is the fouling of the working electrode (where the interaction between analyte and sensing probe takes place), which is considered to be the main reason for biosensors' ineffectiveness in vivo [19,20]. The electrochemical fouling process forms an insulating layer on the electrode due to the reaction used for the detection. This is a typical aspect of DA, as its oxidation products are very reactive and moreover - it is well known that under a proper environment (pH > 7.5), polydopamine formation occurs spontaneously [10,21]. Fortunately, this property of dopamine does not have to be viewed solely as a disadvantage. Therefore, researchers decided to use the mechanism of electrochemical oxidation of dopamine to obtain thin polydopamine layers on the electrodes' surface. Electrochemically induced polymerization is a relatively novel strategy of the PDA thin-film deposition at conductive or semiconductive substrates [22]. This procedure allows faster deposition times than autoxidation, being capable of reducing the duration of the process to a few seconds [22]. Fortunately, PDA is recognized as an organic semiconductor, thus allowing the layer to grow even after the substrate is completely covered [10]. Moreover, high spatial control and selectivity are achieved during the electropolymerization occurring at the interface between the solution and electrode. In other words, the possible electro-oxidation of dopamine on different electrode materials and/or under divergent conditions leads to relatively good control over the process compared with autoxidation, as explained in Section 3 [23]. Finally, a more homogenous morphology with less particulate material of the deposited films is obtained, precisely controlling the film thickness [23].

* Corresponding author.
E-mail address: coyeme@amu.edu.pl (E. Coy).

https://doi.org/10.1016/j.eurpolymj.2022.111346
Received 11 March 2022; Received in revised form 19 May 2022; Accepted 7 June 2022
Available online 10 June 2022

As described until now, there are strong prospects for exploiting the electrochemical methods in detecting dopamine and obtaining the PDA thin films and coatings. Nevertheless, polydopamine can also be utilized to produce electrochemically active composite electrodes. Significant many applications remain without dedicated or appropriate sensors, e.g., measuring hazardous chemicals like pesticides in water [20]. Simultaneously, some of the properties of conducting polymers (CP) based composites make them promising competitors in electrochemical sensor device manufacturing. Furthermore, the functionalization of CP with biochemical molecules has been utilized to monitor drug transport and bioimaging approaches [24]. Also, the development of novel electrochemical sensors exploiting nanomaterials' superior properties has recently gained significant attention [25]. The careful selection of the active material in a given sensor is critical for sensor performance [26]. Polydopamine combines both the properties of CP and nanomaterials, acting as a versatile and promising candidate for a multifunctional component of the electrochemical sensor for numerous applications. Moreover, PDA addresses crucial concerns in constructing and applying smart wearable sensors for humans, considering its excellent adhesion to virtually any type of substrate [1], biocompatibility [27,28], and semiconducting electrical nature [21,29].

This review aims to explain and summarize the current state of the art on the electrochemical deposition of the PDA thin films and shed light on some selected, novel applications of the PDA for the construction of electrochemical and intelligent wearable sensors. As expected, we build upon relevant reviews on electrodeposition of catecholamines and PDA based coatings [30], Sensors [31] and surface chemistry [32], to provide a general view of the current panorama of PDA sensing films/coatings. We start with a detailed description of the mechanism underlying the electrochemical oxidation of dopamine. Next, the PDA deposition by cyclic voltammetry (CV), pulsed electrochemical and galvanostatic methods are described, focusing on the examples described in the literature. Moreover, the influence of the pH value, deposition method, and deposited coating thickness on the dopamine oxidation process is shown, focusing on the electron transfer process insights revealed by electro impedance spectroscopy. Then, a few available reports about free-standing PDA ultrathin films fabricated using electrochemical deposition methods are described, showing promising achievements in this recent and unexplored field. Finally, a chapter about the novel and highly applicable sensors based on polydopamine or modified with this material for electrochemical analysis methods, enriched with the latest wearable strain sensors for motion monitoring. This review shows a comprehensive picture of electrochemical-related studies and applications for PDA materials, schematically shown in Fig. 1.

2. Electrochemical deposition of the PDA films

This section discusses the general mechanism of polydopamine deposition under the influence of electric current, which is similar to the self-assembly of melanin in solution [33]. It also shows how this process occurs depending on the electrochemical deposition technique used, pH value and dopamine concentration. Moreover, a detailed look into dopamine oxidation process insights is provided.

2.1. Mechanism

In 1967, electrochemical techniques were applied to study catecholamines' oxidation pathways in vitro for the first time [34]. In turn, the first report on dopamine electro oxidation was made in 2006 [35]. Two mechanisms of electrochemical catecholamine oxidation could be distinguished: the so-called ECC (electron transfer- chemical reaction-chemical reaction) and ECE (electron transfer- chemical reaction- electron transfer) [13,34]. The slow cyclization rate for dopamine suggests DA has a greater tendency for "primary recombination" and thus follows the ECE mechanism [34,36]. Therefore, the polymerization goes through the following steps: the generation of o-dopaminoquinone after an interchange of two electrons and protons (1), o-dopaminoquinone intramolecular cyclization via 1,4-Michael addition, which leads to leucodopaminochrome (2) and oxidation to dopaminochrome (3), which is likely to transform into the material of interest, namely-melanin polymer [13,37]. Moreover, the full pathway for DA oxidation and further polymer growth carries out three (3) more steps: isomerization (a second "C" step), redox reaction (a third "E" step) and final oxidation, followed by polymer deposition (the last "E" step) thus ECECEE mechanism [35], as shown in Fig. 2**a**. Therefore, the DA oxidation may be regarded as a series of processes where the total number of exchanged electrons and protons is equal $6 + x$ and depends on the final "E" step (x is the number of protons/electrons involved in the last step).

A further in-depth explanation of the electrochemically enhanced PDA formation process depends on the technique used. Predominantly, cyclic voltammetry in alkaline and oxygen-free dopamine solution is applied. Moreover, the literature has also described galvanostatic and pulsed deposition methods. In the following sections, we describe these approaches.

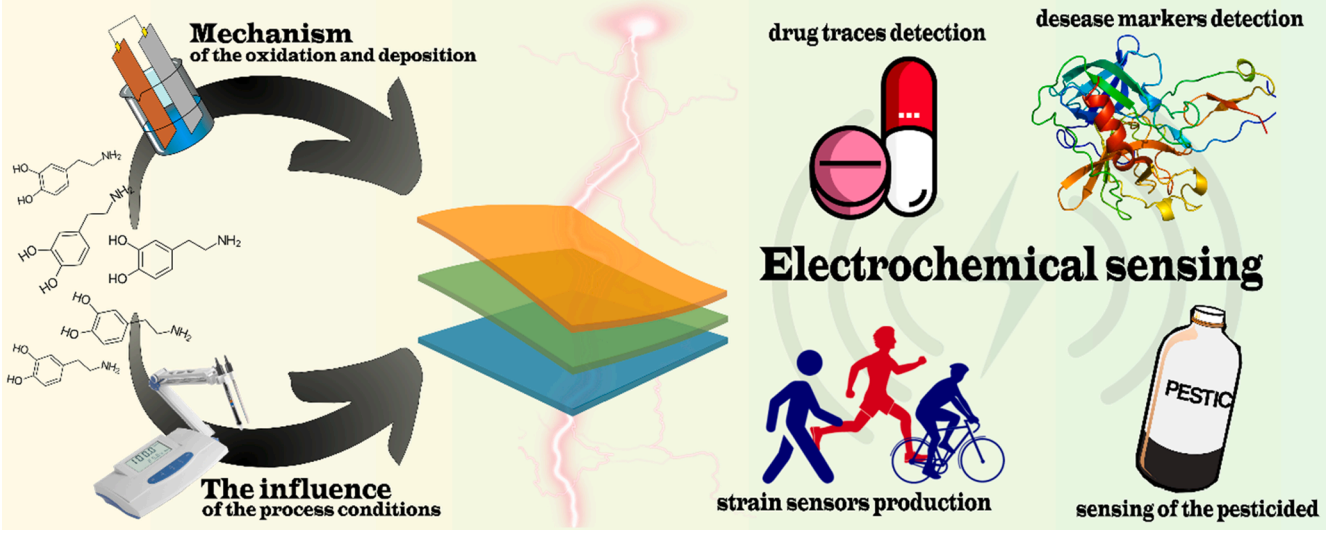

Fig. 1. Graphical overview displaying the most important subjects of the review i.e. mechanism of the dopamine electrochemical oxidation and importance of the polydopamine in prime electrochemical sensing applications.

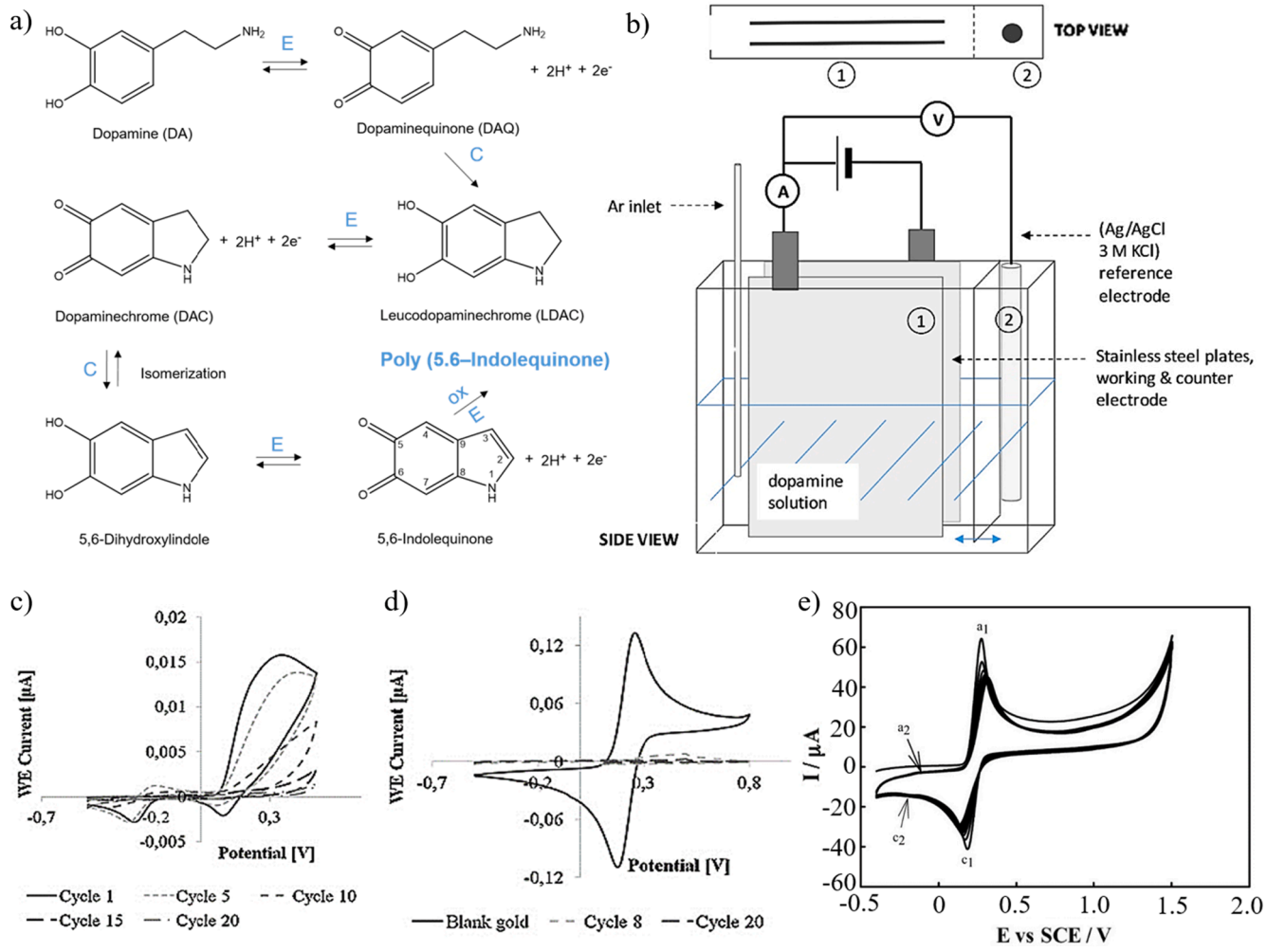

Fig. 2. **a)** Scheme of the ECECEE mechanism. Reprinted with permission from [35]. **b)** Scheme of the pouch cell used for anodic coating of stainless steel plates. Left: top and side view. Two stainless steel plates form the anode, and counter electrode (1), (Ag/AgCl, 3 M KCl) reference electrode (2) Adapted with permission from S. Schindler, N. Aguiló-Aguayo, U. Dornbierer, T. Bechtold, Anodic Coating of 1.4622 Stainless Steel with Polydopamine by Repetitive Cyclic Voltammetry and Galvanostatic Deposition, Ind. Eng. Chem. Res. 59 (2020). https://doi.org/10.1021/acs.iecr.9b05603. Copyright 2021 American Chemical Society [38]. **c)** CV measurements during the electro-polymerization of dopamine **d)** CV measurements for characterization after polymerization [23]. **e)** Cyclic voltammograms of electro-polymerization of PDA nanofilm at the surface of GCE. Concentration of dopamine solution was 5 mM in 0.1 M acetate buffer solution pH = 5. The scan rate was 0.05 V s^{-1}. Reprinted from Sensors Actuators, B Chem, 228, M. Amiri, E. Amali, A. Nematollahzadeh, H. Salehniya, Poly-dopamine films: Voltammetric sensor for pH monitoring (2016) 53–58. Copyright (2021) with permission from Elsevier.

2.1.1. *Cyclic voltammetry towards dopamine oxidation*

Cyclic voltammetry is a powerful and widely-used electrochemical technique to investigate molecular species' reduction and oxidation processes [39]. A detailed description of this method can be found in the literature [39–41]. Nevertheless, here we discuss the critical elements for the deposition of polydopamine thin films using this approach. The CV setup presented in Fig. 2**b** is a typical example of the set-up used; in this system, the probed process occurs on the working electrode. In the case of deposition of PDA layers, it is the electrochemical oxidation of dopamine.

Coating with PDA was applied for the working electrodes made out of stainless steel [38], Gold [35,38,42,43], Titanium alloys [44], polycrystalline platinum [45], tetrahedral amorphous carbon [45], TiO_2 [46] and ITO coated glass [47]. In turn, Ag/AgCl (KCl saturated) or standard Calomel reference electrodes and steel plate [38], platinum wire [23], or gold wire [45] counter electrodes were used in all the above-described experiments. The electrolyte solutions used in the reported experiments were acetate buffer [48], phosphate buffer saline [35,49,50], buffered NaCl solution [38] and Tris-buffered saline [47]. Moreover, an inert gas (argon or nitrogen) atmosphere is crucial, as the oxygen is forming a radical anion (superoxide, $O_2^{\bullet-}$) within a reversible one-electron reduction process.

What is of great importance is that the dopamine-containing electrolyte is not disposable. Instead, it serves for multiple electro-polymerization processes [46]. The number of CV cycles can be employed to control the thickness of the polymer film. As the polymerization proceeds, each cycle deposits more PDA on the electrode; consequently, the current decreases (Fig. 2**c**). After numerous cycles (depending on the literature source cited numbers are: 5, 10 [23], 15 [46], 20 [51], 25 [23]), the increasing amount of deposited polydopamine leads to the insulation of the working electrode, until almost complete insulation (Fig. 2**d**) [23]. An average deposition of 82 ng cm^{-2} was observed in the first cycles, decreasing to 36 ng cm^{-2} in the 25th cycle with an average increase of 60.2 ng cm^{-2} and 4.1 nm per CV cycle. In this way, precision thin films of required thickness can be created on-demand rapidly, offering potential applications in templating, molecular imprinting, ultra-thin protective coating, electro-polymerization of synthetic dopamine derivatives, and functional membranes [23].

Cyclic voltammetry experiments support the aforementioned electro-polymerization mechanism of PDA. Fig. 2**e** shows the repetitive

cyclic voltammograms obtained after the electrodeposition of a 5.0 mM DA solution onto a glassy carbon electrode (GCE). Starting from 0 and moving to the oxidation direction, the first anodic peak (a1) located at 0.28 V is assigned to the anodic oxidation of dopamine. Once the direct scan has finished, the reverse scan shows two cathodic peaks (c1 and c2) at 0.23 V and −0.16 V, which corresponds to the reduction of dopaminechrome (DAC), dopaminequinone (DAQ), and the product of its intramolecular cyclization leucodopaminechrome (LDAC). Finished the complete oxidation–reduction scan and starting the second one, the already formed LDAC is going to be oxidized, showing a new anodic peak (a2) at 0.12 V. Further oxidation–reduction cycles will decrease a1 and c1 peaks and increase a2 and c2 due to the growth of the PDA film on the GCE [52]. DA can be successfully electropolymerized onto the surface of the GCE by cyclic potential scanning in a repetitive manner ten (10) times in a range from −0.4 to + 1.5 V at 50 mV s^{-1} in 0.1 M acetate buffer (pH = 5.0) containing 5.0 mM DA [52,53].

2.1.2. Pulsed electrochemical PDA deposition

Compared with the direct current electrochemical deposition, pulsed electrochemical deposition (PED) offers enhanced process control by employing additional variables: pulse on-time (t_{on}) and pulse off-time (t_{off}).. In the pulsed reverse electrochemical deposition, short anodic pulses are present alongside the cathodic ones (Fig. 3**a**). Fig. 3**b** shows an exemplary setup, where a scanning electrochemical microscopy (SECM) apparatus was applied for the PED deposition of a PDA coating. SECM is considered an appropriate tool for in-situ localized surface modifications. It is helpful in creating microscopic or nanoscopic structures f metals, conductive polymers and insulative materials [54]. In order to achieve this, feedback mode [55], or direct mode [56] is usually applied. In direct mode, the Pt SECM tip was used as the counter electrode, gold-coated Si substrate as the working electrode and the standard Ag/AgCl (3 M KCl) electrode as the reference. In this study, polydopamine was deposited from a solution of dopamine hydrochloride concentration 1 mg mL^{-1} in 0.01 M PBS (pH 7.4), which was purged with argon for 20 min before the deposition [57]. Elsewhere, PDA thin films were deposited onto the conductive colloidal AFM-SECM golden coated probe [49], and the other parameters (reference, counter electrode and dopamine solution used) were similar as previously described [57].

The other type of PED setup for obtaining PDA coatings, which was not based on SECM apparatus, was applied and reported only once, to the best of our knowledge. However, the obtained film was a multilayer nanocomposite of hydroxyapatite (HA) and polydopamine [58]. Nevertheless, a fascinating approach was presented, where the working electrode was a Ti foil as the counter electrode was a Pt plate, and the reference was a saturated calomel electrode. The electrolyte was an aqueous solution containing $Ca(NO_3)_2$, $NH_4H_2PO_4$ and dopamine [58]. The electrochemical process included two pulses. During t_c pulse, the potential was set at 1 V with reference to the SCE with a pulse width of 50 s and the growth of the PDA layer was achieved employing oxidative reaction (Fig. 3**c**). In turn, during t_a pulse, the potential was changed to −1.5 V with a pulse width of 600 s. Thus, the growth of the HA layer was ongoing through a reductive reaction.

2.1.3. The galvanostatic PDA deposition

Unlike the previously described methods, galvanostatic deposition refers to a technique where a constant direct current is applied. Anodic formation of polydopamine involves the transfer of at least two electrons per dopamine molecule. Therefore, the obtained film thickness is related proportionally to the charge transmitted through the electrode [38,47].

Two detailed descriptions of the PDA galvanostatic deposition can be found in the literature. At first, anodic coating of the 1.4622 stainless steel with the polydopamine was reported. A potential for galvanostatic deposition in this experiment was set as +1100 mV, the current was −15 mA, while the active area of the anode was 45 × 60 mm, thus corresponding to a current density of 5.5 μA cm^{-2}. Steel plates were coated in 5 mM dopamine solution at pH 5.0 (acetate buffer) and pH 6.5 (phosphate buffer). As a result of the coating of the anode surface, an increase in anode potential is observed. In this study, a threshold value for the anode was set as the electrode potential of +1100 mV. Then, the deposition was stopped. When a current of −15 mA was applied for a

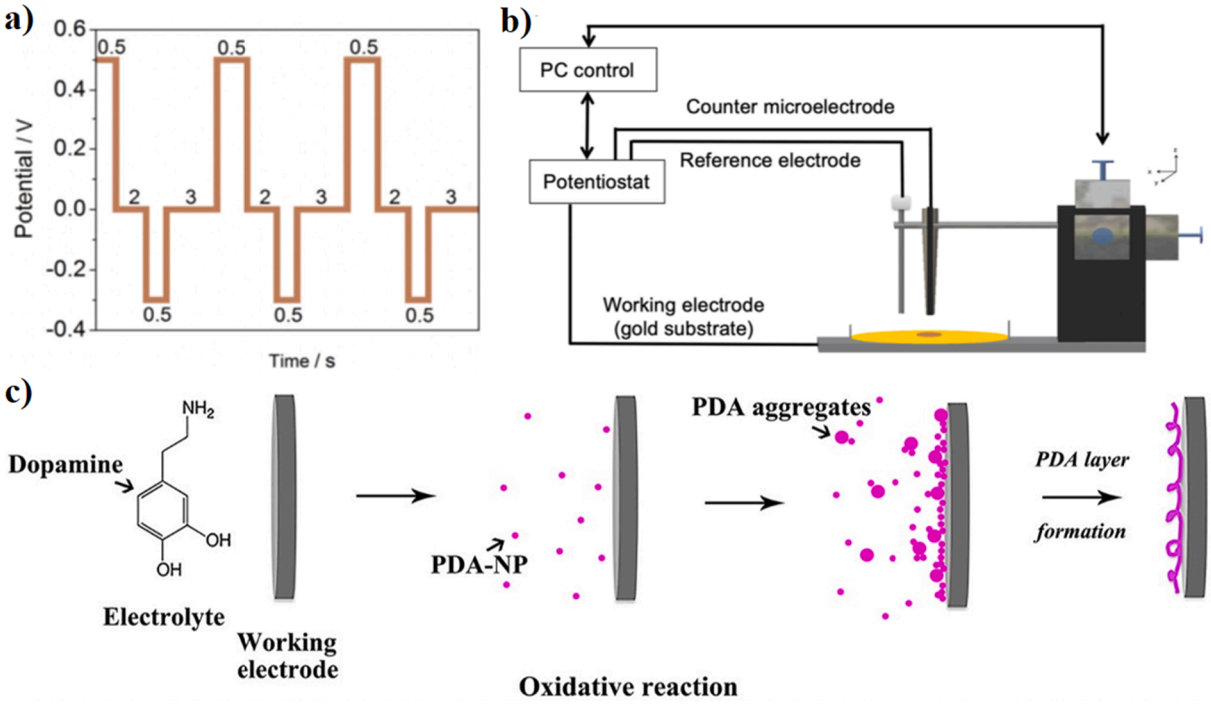

Fig. 3. a) Pulse profile for the PED ongoing process. Reprinted with permission from [57]. **b)** Scheme of the SECM direct mode approach for micro-structured PDA. **c)** Oxidation reaction of the PDA coating growth via PED-LbL. Reprinted with permission from C. Xie, X. Lu, K. Wang, H. Yuan, L. Fang, X. Zheng, C. Chan, F. Ren, C. Zhao, Pulse Electrochemical Driven Rapid Layer-by-Layer Assembly of Polydopamine and Hydroxyapatite Nanofilms via Alternative Redox in Situ Synthesis for Bone Regeneration, ACS Biomater. Sci. Eng. 2 (2016). https://doi.org/10.1021/acsbiomaterials.6b00015. Copyright 2021 American Chemical Society [58].

time of 280 s, a charge flow of 4.2 °C was obtained, which corresponds to oxidation of 2.2 × 10^{-5} mol or 3.3 mg of dopamine. Assuming an average density for polydopamine of 1.5 g cm^{-3}, the thickness of a uniform polydopamine coating on a stainless steel electrode was 820 nm [38]. However, the thickness would be reduced accordingly if higher oxidation states were formed during the anodic polymerization of dopamine. Thus a value of 820 nm must be considered as an upper limit for the thickness of the polydopamine layer [38].

Elsewhere, a constant current density of 20 μA cm^{-2} was applied to ITO electrodes (~1 cm^2) until high potential values (~2 V) were reached to deposit different catechol-based polymer films: 3-(3,4-dihydroxyphenyl)-L-alanine, (L-DOPA), 5-hydroxytryptophan (L-5-HTP), and (±)-epinephrine hydrochloride (Adrenalin). Moreover, the behaviour of these four compounds was investigated, and differences in the electrochemical process were revealed. The potential of the ITO electrode rose quickly (>600 s) to a high value in the L-5-HTP solution, while this process took approximately 3000 and 6000 s in the DA and L-DOPA solutions, respectively (Fig. 4**a**). The resultant polymeric films had a thickness in the order L-DOPA > PDA > L-5-HTP, confirmed by the AFM measurements (Fig. 4**b**). No film formation for Adrenalin was noted. The AFM images of the polymeric coatings indicate that all obtained films were relatively uniform, and the surface roughness increased with increasing film thickness (Fig. 4**c**) [47].

2.1.4. *Influence of pH on anodic oxidation and polymerization*

The distribution of dopamine species is directly influenced by the pH value of the surrounding environment. Different distributions of species can influence the electro-polymerization process. The molecular structure of dopamine presents two phenolic groups that can be deprotonated and one primary amino group that can be protonated, making possible the appearance of three dissociation constants(pK_a) [59]. Regarding these pK_a values, a species distribution scheme at different pHs in an aqueous solution is shown in Fig. 5**a and b**. Typically, pH values employed to induce self-polymerization of dopamine are under 8.5 [10]. In conditions as shown in Fig. 5**a**, until pH ≈ 7.5, all the dopamine has its primary amine protonated. Meanwhile, hydroxyl groups are not dissociated ($DPAH_3^+$). As the pH value approaches 9, the most acidic hydroxyl group will dissociate, and an equilibrium appears, as shown in Fig. 5**b** ($DAPH_2$). The proposed mechanism for anodic oxidation, under pH = 9, of polydopamine (Fig. 5**c**), is explained through an electron transfer reaction that creates a semiquinone radical at the anode. This will be further transformed into 5,6 dihydroxyindole and 5,6 indolequinone, which will polymerize, creating polydopamine [60]. At pH values higher than 9, the non-protonated amino groups start to have a strong presence. Thus, another possible mechanism appears where the amine group acts as a nucleophile [35,48,61–63].

Cyclic voltammograms (Fig. 6**a**) at pH = 5.8 and pH = 7.0 using gold as an electrode and a dopamine concentration of 5 mM were used to test the proposed mechanism for anodic oxidation of dopamine. The voltammograms show a shift towards lower potentials for both peak potentials (anodic and cathodic), due to the action of protons in redox reactions when pH is increased from 5.8 to 7.0 [60]. This trend is in agreement with another study where the oxidation peak potential shifted from 449 mV to 341 mV when the pH was modified from 2.10 to 3.94. Similar shifts are observed after a pH increase from 6.12 to 7.93, with a change in potential from 234 mV to 128 mV. Finally, the study showed that when the pH is modified from 10.10 to 11.70, oxidation peak potential shifts from 0 mV to −101 mV [52].

On the one hand, at 50 mV s^{-1} the anodic peak decreases from −48 μA to −41 μA when pH decreases. On the other hand, the cathodic peak presents a higher pH dependence decreasing from 23 μA to 3μA when pH increases from 5.8 to 7.0 [60]. Variation of pH means that different species have to be considered. At the suitable pH, the protonated I-$DPAH_3^+$ is the most likely to be present, as shown in Fig. 5**c**, the anodic oxidation towards the corresponding semiquinone (II-$DPAH_2^{+\cdot}$) is the proposed first part. This process is divided into two steps. The first one consists of a fast single-electron oxidation (E), leading to the formation of the semiquinone radical intermediate, followed by the second and final step, which consists of fast deprotonation (C) that will stabilize the proton placed in between the two phenolic oxygen atoms, in agreement

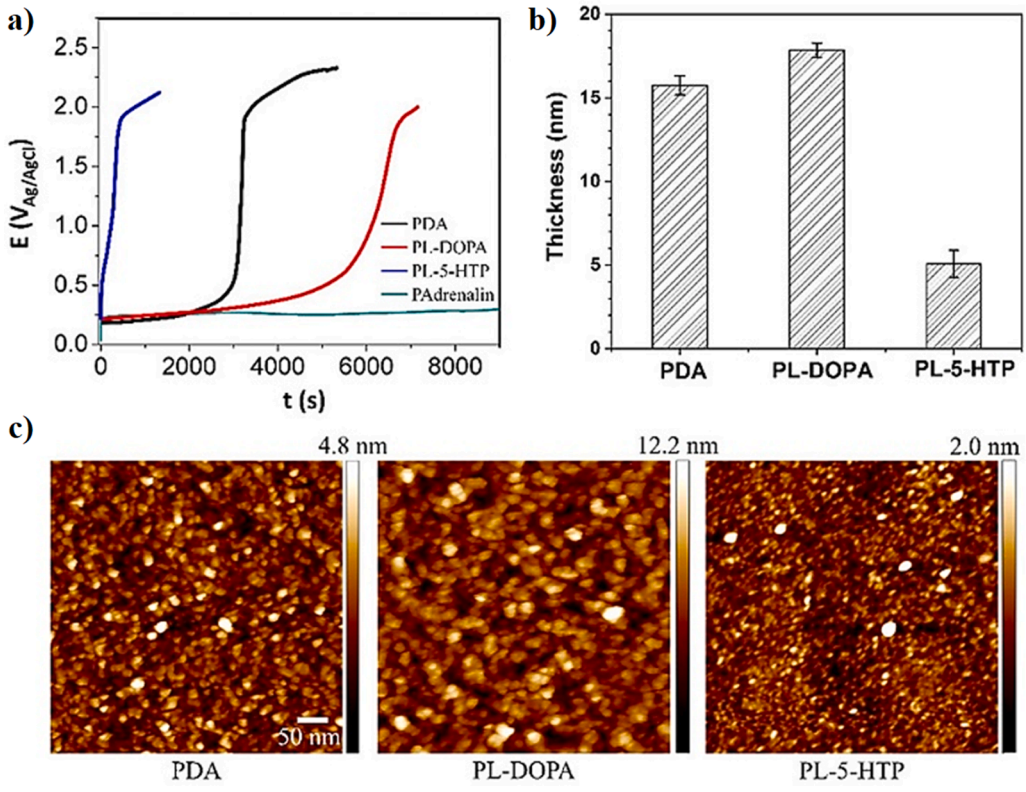

Fig. 4. a) Comparison of the potential profiles of the ITO electrodes during the electrodeposition of PDA, PL-DOPA, PL-5-HTP, and PAdrenalin polymer films using the galvanostatic method. b) thickness of the PDA, PL-DOPA, and PL-5-HTP films by AFM measurements. c) surface morphology of the PDA, PL-DOPA, and PL-5-HTP films by AFM measurements (scale bar is 50 nm for each image). Reprinted with permission from S. Li, H. Wang, M. Young, F. Xu, G. Cheng, H. Cong, Properties of Electropolymerized Dopamine and Its Analogues, Langmuir. 35 (2019). https://doi.org/10.1021/acs.langmuir.8b01444. Copyright 2021 American Chemical Society [47].

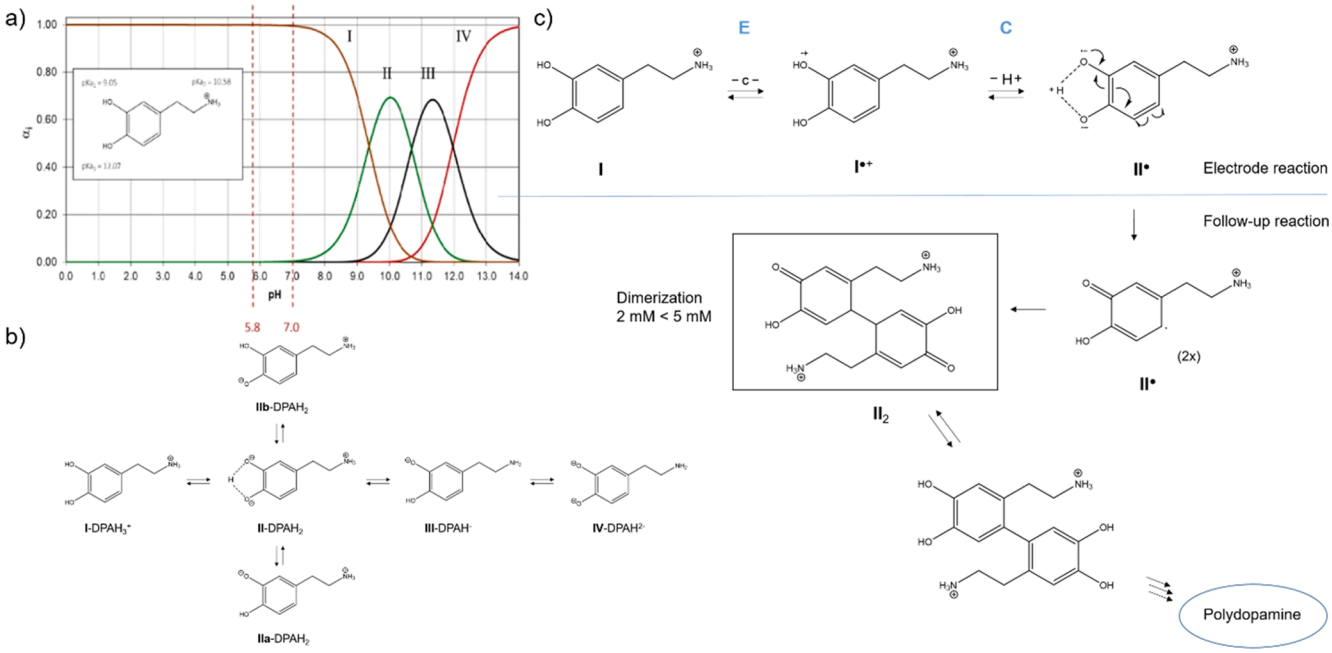

Fig. 5. a) Different dopamine species distribution (α_i) at an aqueous solution as a function of pH with pK_a values given by literature [59]. **b)** pH-dependent equilibrium at aqueous solution between the different DA species. **c)** Possible anodic oxidation mechanism at the electrode and further polymerizationReprinted from J. Electroanal. Chem. 836, S. Schindler, T. Bechtold, Mechanistic insights into the electrochemical oxidation of dopamine by cyclic voltammetry (2019) 94–101. Copyright (2021) with permission from Elsevier.

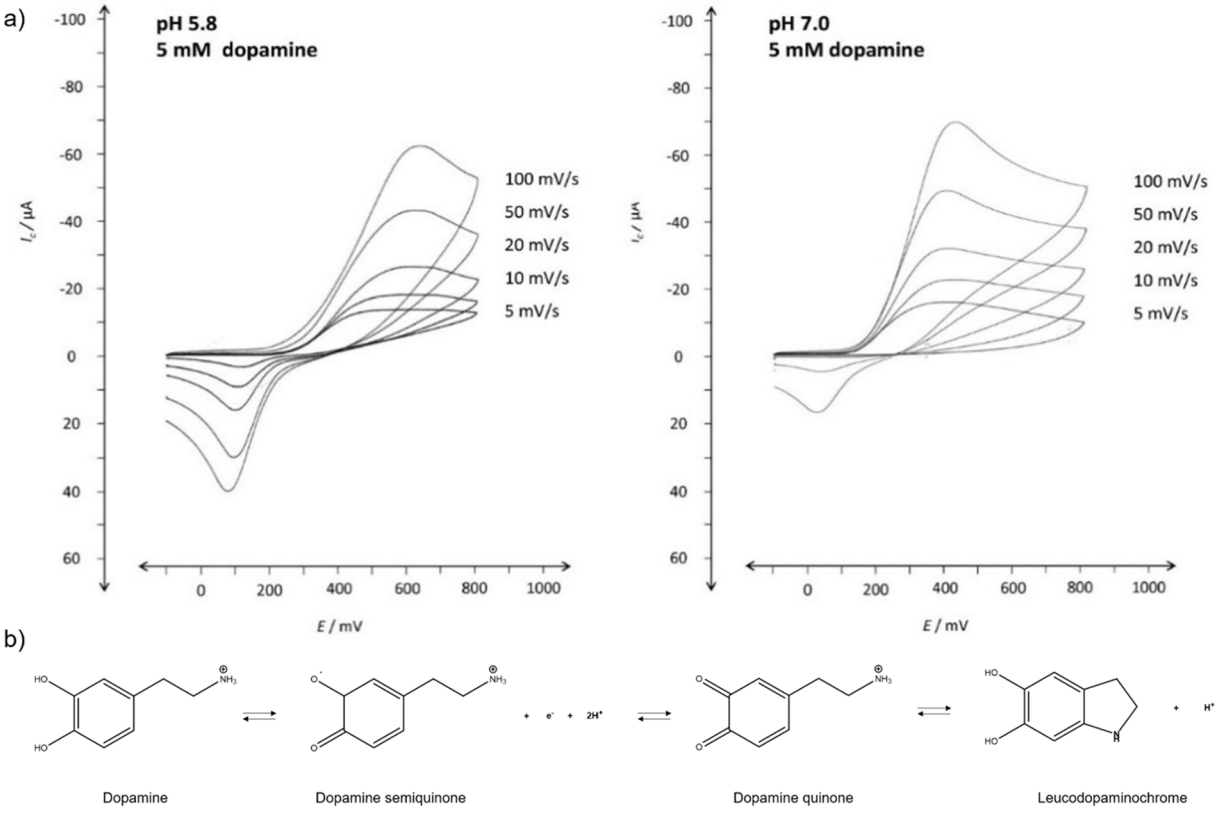

Fig. 6. a) CV at different scan rates, pH = 5.8 and pH = 7.0, [DA] = 5 mM. Reprinted from J. Electroanal. Chem. 836, S. Schindler, T. Bechtold, Mechanistic insights into the electrochemical oxidation of dopamine by cyclic voltammetry (2019) 94–101. Copyright (2021) with permission from Elsevier. **b)** Leucodopaminochrome formation from dopamine through semiquinone and quinone intermediates.

with ^{13}C NMR data published [64]. This pathway will result in II-$DPAH_2^{+\cdot}$. The small influence of the pH on the anodic peak values obtained and the electrochemical reversibility of the electrode process suggest a fast and pH-independent EC mechanism. Once the II-$DPAH_2^{+\cdot}$ is formed, the second part starts; it consists of the dissociation of II-$DPAH_2^{+\cdot}$, leading to the irreversible polydopamine formation (in agreement with the literature [65]). This part is a fast pH-dependent equilibrium reaction because it depends on the semiquinone (II-$DPAH_2^{+\cdot}$) radical concentration, which depends on pH, and it is higher (in this case) at pH = 7.0. Semiquinone radical acting as an intermediate in the process justifies the creation of oligomers based on catecholamine as precursors in the formation of polydopamine. Once semiquinone is formed following the mechanism mentioned above, it can go to a quinone form that can suffer a cyclization reaction and polymerization [66–69] (Fig. 6**b**). This process is not favoured at low pH values because the deprotonation is strongly disadvantaged, and Michael type reaction between or within oxidized dopamine molecules is hard to carry out [60,70].

2.2. Electron transfer and electrochemical impedance spectroscopy

Electrochemical impedance spectroscopy (EIS) is a well-recognized technique for understanding the electrochemical properties of materials, led by applying an AC potential through the electrochemical cell and measuring the excitation signal from current floating through the cell [71]. EIS measurements at different pH values and electrodeposition methods can unveil their influence on the electron transfer (ET) behaviour [22]. For example, the pulsed deposition is less likely employed to obtain electrodeposited polydopamine than CV, despite some undoubted advantages of the PED process over CV, which can be

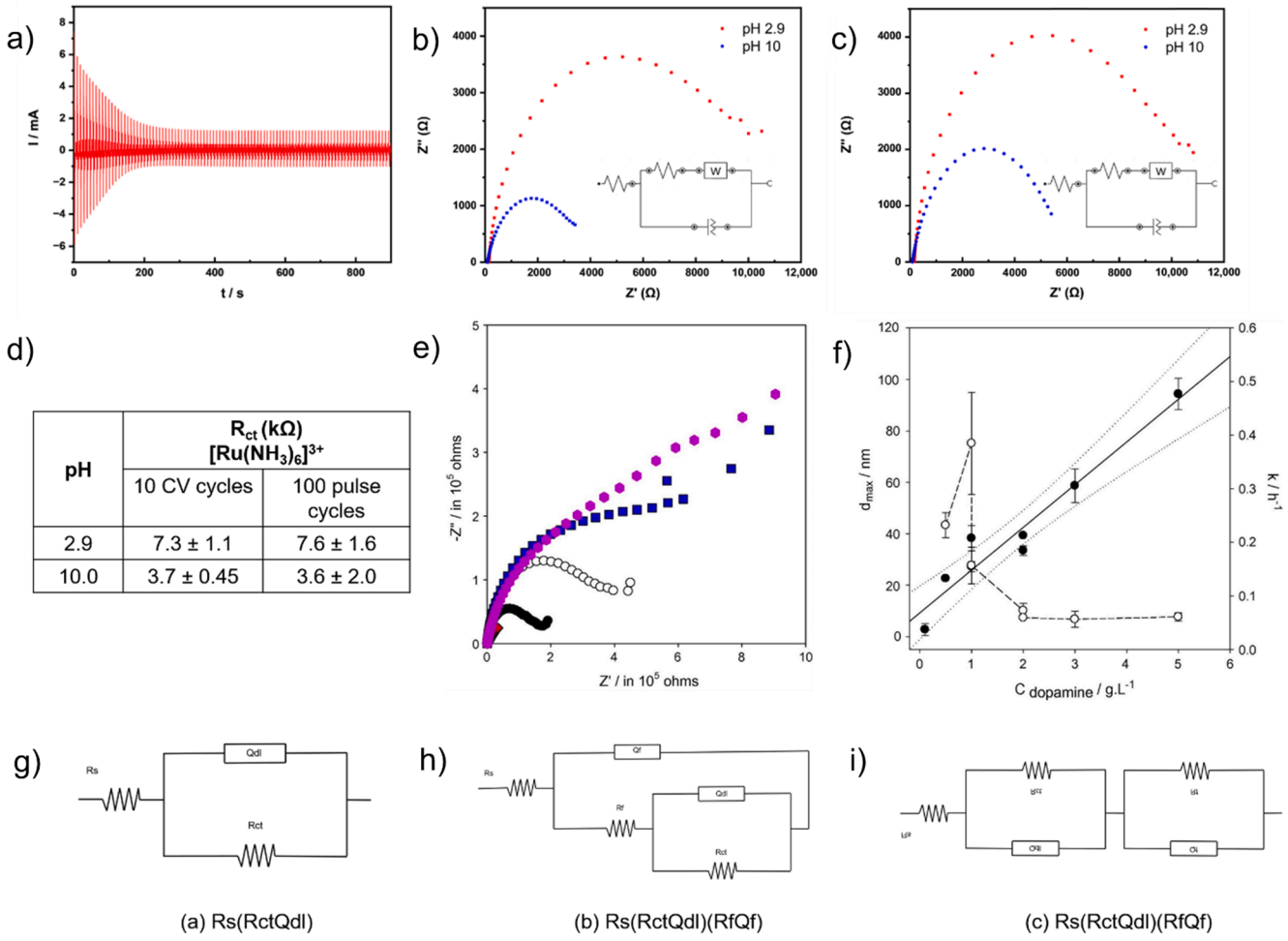

pH	R_{ct} (kΩ) $[Ru(NH_3)_6]^{3+}$	
	10 CV cycles	100 pulse cycles
2.9	7.3 ± 1.1	7.6 ± 1.6
10.0	3.7 ± 0.45	3.6 ± 2.0

Fig. 7. a) Pulse deposition (100 cycles) I-t curve. 1 mg cm^{-3} DA, pH = 7 at Au macro electrode. Nyquist plots at pH = 2.9 and pH = 10. Impedance spectra were recorded with a bias potential of −200 mV, an amplitude of 10 mV using hexaammineruthenium (III) chloride as a redox probe. **b)** PDA deposited by CV (10 cycles). **c)** PDA deposited by pulsed deposition (100 cycles). Figures reproduced from ref. [22]. **d)** Rct obtained from the fitting Randles circuit model of the impedance data. **e)** PDA coating on amorphous carbon electrodes Nyquist plots. 1 h electropolymerization time for several dopamine concentrations; 0 mg cm^{-3} (red colour), 0.5 mg cm^{-3} (black), 2 mg cm^{-3} (white) and 5 mg cm^{-3} (blue). Additional data for 12 h reaction (2) mg cm^{-3} (pink). **f)** maximal PDA film deposited on silicon substrates in the presence, at pH = 8.5, of several dopamine concentration thickness variations. (●, left-hand scale) and of the rate constant (k) (—○—, right-hand scale). Fitting parameter values are calculated by using **Eq.** (1). The straight full line is due to the linear fit to the maximal thickness compared with the initial dopamine concentration. Dotted lines are the confidence interval (95%), and error bars are because of the standard deviation on the value of the fitted parameters. Reprinted from, J. Colloid Interface Sci. 386, V. Ball, D. Del Frari, V. Toniazzo, D. Ruch, Kinetics of polydopamine film deposition as a function of pH and dopamine concentration: Insights in the polydopamine deposition mechanism, (2012) 366–372. Copyright (2021) with permission from Elsevier. **g),h),i)** Equivalent electrical circuits (EECs), where: testing solution resistance is represented by R_s; the resistance and capacitance which are associated with the charge transfer process occurring at the surface of the substrate are given by Rct and Qdl; Rf and Qf are the parameters related with the resistance and the capacitance of the forming films. Capacitive elements are reported as modelled by Constant Phase elements. Reprinted from J. Mol. Struct. 982, F. Yu, S. Chen, Y. Chen, H. Li, L. Yang, Y. Chen, Y. Yin, Experimental and theoretical analysis of polymerization reaction process on the polydopamine membranes and its corrosion protection properties for 304 Stainless Steel, (2010) 152–161. Copyright (2021) with permission from Elsevier.

explained based on the EIS data. Fig. 7**a** shows a pulsed electrodeposited PDA film. After 30 cycles, the faradaic current decreases by 86%, hinting that the redox reaction that leads to DA's electrodeposition is reaching its end. Is it possible to notice that the capacitive current contributes to the current response due to the darkening effect it induces at the faradaic contribution for the higher numbers of the cycle pulses. The advantage that it brings compared with CV is the concentration of the monomer at the electrode surface that is restored after each pulse, as the resting interval allows the diffusion of dopamine which, at pH around 8.5, should be fully protonated (Fig. 5**a, b**) and will experience different reactions towards film formation as evidenced by the linearly decreasing current [22].

2.2.1. The influence of the pH, electrodeposition methods and the PDA thickness.

The charge transfer resistance (R_{ct}) can be calculated by studying the diameter of the semicircle at Nyquist plots [72]. Nyquist plots for the deposition on Glassy Carbon Electrodes (GCE) of PDA using CV and pulsed deposition techniques at different pHs are shown in Fig. 7**b and 7c**. The Randles circuit with a constant phase element (CPE) was used for modelling, and it revealed, in the chosen frequency range, that heterogenous ET is mainly driven by the resistance, unveiling the kinetically controlled process nature of the electrode reaction at the film interface. R_{ct} values (Fig. 7**d**) differ more between different pH values than with different electrodeposition techniques. At pH = 2.9, the dominant species is I-DPAH$_3^+$ (Fig. 5**b**), where the amino group is protonated; thus, dopamine has a positive charge. However, at pH = 10 it appears to be an equilibrium between IIa-DPAH$_2$ and IIb-DPAH$_2$ where

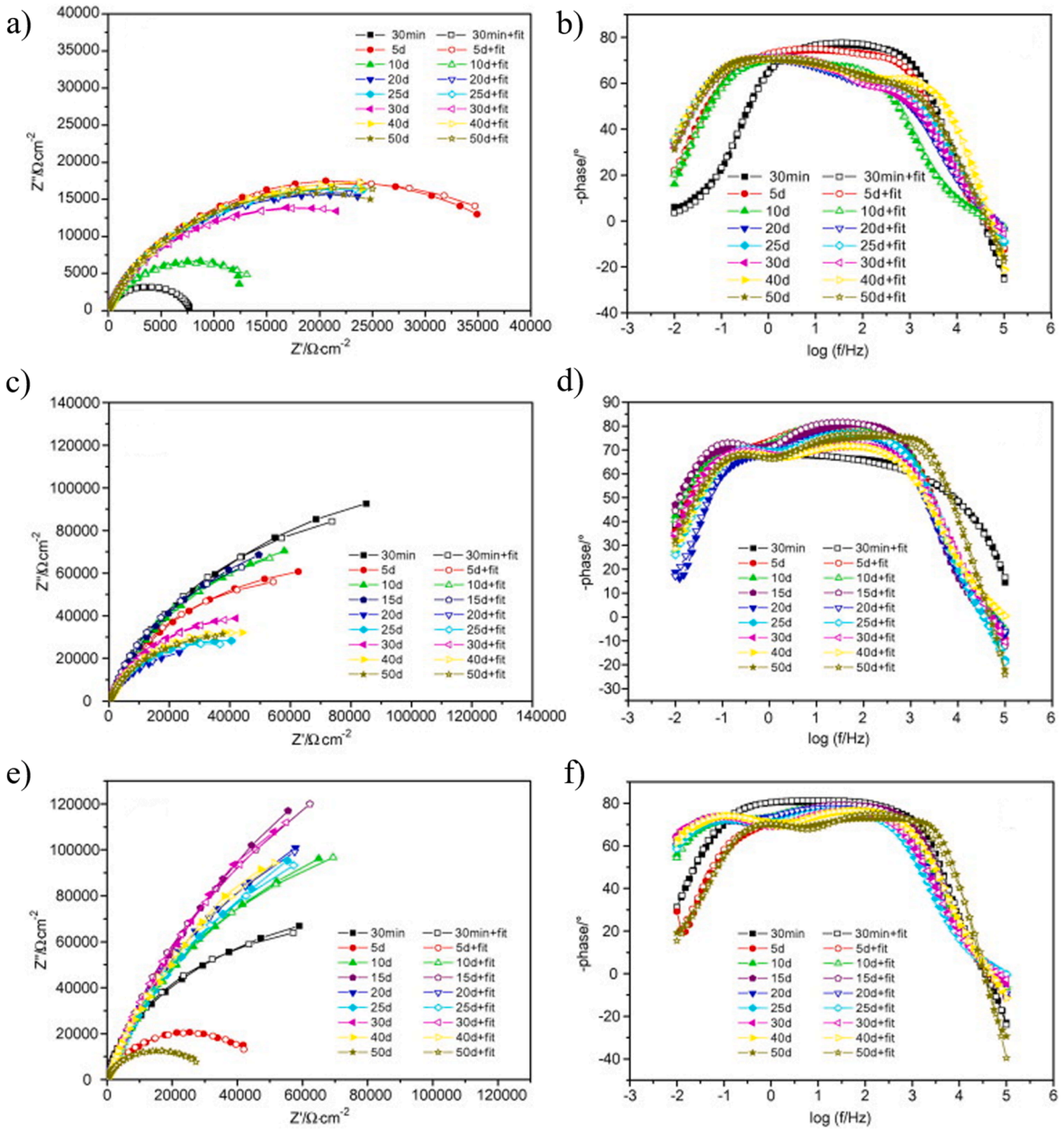

Fig. 8. Nyquist and phase angle-log (frequency) plots at different exposure times. **a,b)** 3.5% NaCl solution for 304 SS electrodes. **c,d)**24 °C PDA/304 SS electrodes. **e, f)** 34 °C PDA/304 SS. Electrodes Reprinted from J. Mol. Struct. 982, F. Yu, S. Chen, Y. Chen, H. Li, L. Yang, Y. Chen, Y. Yin, Experimental and theoretical analysis of polymerization reaction process on the polydopamine membranes and its corrosion protection properties for 304 Stainless Steel, (2010) 152–161. Copyright (2021) with permission from Elsevier.

dopamine, apart from having a positive charge in the protonated amino group, has also a negative charge at the deprotonated hydroxyl group ameliorating charge transfer in a 50% [22]. Fig. 7**b and 7c** show this trend and compare different deposition methods (CV and pulsed deposition) exhibiting a similar behaviour for the same film thickness but different deposition methods. Rct values obtained for different pH and deposition techniques are shown in Fig. 7**d.** A more concentrated dopamine solution shows higher impedance data and bigger semicircles, revealing that more impermeable and compact films are deposited onto amorphous carbon electrodes [73]. When the electropolymerization time is the same (1 h), semicircles of the Nyquist plot are longer for higher DA concentration in the solution (Fig. 7**e**), revealing that the electron transfer resistance is higher for thicker and more compact films (which have been achieved with higher DA concentrations as shown in Fig. 7**f**). These more compact films can also be obtained with lower concentrations of PDA but with more significant deposition times. As shown in Fig. 7**e**, Nyquist plot radius are pretty similar when dopamine concentration is 5 mg cm^{-3} and the time of electrodeposition is 1 h compared with the experiment where 2 mg cm^{-3} of dopamine and 12 h of reaction have been carried out. These impedance spectra follow a clear trend. When the thickness of the film increases, Nyquist plots cannot be adequately fitted in a single model like in Randles equivalent circuit [73,74]. Electron transfer resistance behaviour regarding the thickness of the PDA films deposited onto GCE and amorphous carbon electrodes is similar to other substrates like indium tin oxide glass, for example [75].

Finally, the long-term impedance characteristics of PDA can also be studied by EIS. In this case, PDA films were made by self-polymerising dopamine precursor at the surface of 304 stainless steel (304SS) coupons which acted as working electrodes. The corrosion behaviour studied by EIS was carried out by submerging the electrodes in 3.5% NaCl solution at different temperatures and for different days. The three other Equivalent Electrical Circuits (EECs) proposed to model the impedance spectra data are shown in Fig. 7**g, h and i.** All the results agree between the experimental data and the fitting, although the exponent alpha of the constant phase elements might have been reported incorrectly as per their value > 1. [76] Fig. 8 shows experimental and fitting data of Nyquist, and corresponding phase angle-log (frequency) plots for blank SS and SS covered with PDA electrodes on various days. For the bare 304 SS, charge transfer resistance experienced an increment during the first 5 days of exposure **(**Fig. 8**a).** This behaviour can appear because of the passivation films that are formed on the electrode. The maximum is reached on day 5, and from here, the charge transfer resistance decays. In the Bode plot (Fig. 8**b),** it appears two-time constants, one is for the charge transfer resistance, and the other is for the passivation of films. The semicircle observed in the Nyquist plot decreases when time passes. This behaviour hints that the passivation films are broken due to the aggressiveness of the Cl^-; however, Rct and the resistance of the film (Rf) remain steady due to the reparation of the broken passivation films during the following exposure times. The electrode covered by PDA at 24 °C exhibits higher Rct values than the bare sample. Also, the PDA layer protects the samples decreasing the corrosion rate and showing a better resistance than the non-surface-functionalized. Finally, because of water penetration, Rct value decreases in the next 5 days [77]. In Fig. 8**c,** the impedance semicircle is gradually larger in the Nyquist plot, and Rf also increases during the next 10 days. This can be attributed to the redox capacity of PDA [69]; after 20 days, the changes shown in the Nyquist plot and Bode plot (Fig. 8**d**) are attributed to the penetration of Cl- and water within the PDA film. Hence, Rct and Rf values show a decrease, meaning that the protection given by PDA is being hidden.

Finally, the PDA membrane created at 34 °C shows the most protective capacity (Fig. 8**e**).

The Bode plot in Fig. 8**f,** shows one time constant due to the strong binding between the 304 SS electrode and PDA. As in the previous electrode, Rct value decreases in 5 days because of the interactions of the liquid. Nevertheless, from 10 to 40 days, the electrode still exhibits high Rct and Rf values [77]**.** It is considered that the corrosion mechanism during the experiment is stainless steel pitting corrosion [78–80]. It is interesting to note that the PDA modified electrode presents an open-circuit voltage. Under the voltage, dopamine and polydopamine, by losing electrons, can protect the metallic electrode from corrosion damage. PDA modified electrodes present a high anti-corrosion behaviour; considering the experimental data, the sample prepared at 34 °C the one with the highest performance. Taking into account the EIS studies, there are two possible explanations. On the one hand, PDA at 34 °C is thicker than at 24 °C, ameliorating the anti-corrosion properties. Or on the other hand, much more binding strength and binding sites exist between PDA and/or DA and 304 SS [77].

2.2.2. *Kinetics of the dopamine deposition*

As explained before, EIS experiments show that the initial concentration of dopamine in bulk is directly related to the thickness of PDA film. Higher concentration means that thicker, compact and impermeable films are obtained. It is possible to propose a model for PDA deposition based on a rate equation that takes into account different interactions between PDA aggregates placed on the surface and on the solution [73]. **Eq. (1)** shows the deposition kinetics fitted with an exponential decay function where d_{max} is the maximum thickness and k is the kinetic constant. The deposition rate formula is its derivative as a function of time (**Eq. (2)**).

$$d(t) = d_0 + d_{max}\left(1 - e^{(-kt)}\right) \tag{1}$$

$$d\frac{d(t)}{dt} = d_{max}ke^{(-kt)} \tag{2}$$

$$d_{max} = \alpha c \tag{3}$$

$$d\frac{d(t)}{dt} = \alpha kce^{(-kt)} \tag{4}$$

Having in consideration experimental data relating to film thickness and dopamine concentration (Fig. 7**f**) it is defined that the maximum thickness is equal to the dopamine concentration (c) multiplied by a constant (α) (**Eq. (2)**). **Eq. (4)** is obtained by combining Eqs. (2) and (3), showing that the deposition rate is proportional to the concentration and decreases exponentially when time passes. k is dependent on the dopamine concentration at the bulk (Fig. 7**f**). It slightly decreases when the concentration increases. The exponential term shows a fast decrement with time in the probability for a small oligomer or oxidized dopamine to attach to the surface. This can be because of steric hindrance effects and repulsive forces that suffer the aggregates already deposited on the surface or are at the solution. As PDA at pH = 8.5 is negatively charged, electrostatic repulsions could contribute to these repulsive forces. In **Eq. (4)**, the deposition rate increases with dopamine molecules that are present in the solution, this behaviour is expected for first-order kinetics with respect to the precursor molecule. However, the concentration of free dopamine decreases with time (as the reaction is taking place), and the effect is not very meaningful because the concentration of species is almost constant because there is much more dopamine in the solution than in the electrode surface where the reaction occurs. Considering all of these hypotheses, the deposition rate of polydopamine appears from the competition between two antagonistic effects; one because of the attractive forces and the other one because of repulsive forces. Higher initial dopamine concentration means higher attractive forces between the aggregates in solution and on the surface, leading to higher film thickness for a given deposition time.

Nevertheless, at a dopamine concentration of 2 mg cm^{-3}, aggregates are significant and play a minor role in the deposition process, unveiling that only small aggregates grow the film. The assumed attractive forces that appear between these small aggregates (of unknown nature) are enough to balance the influence of electrostatic repulsive forces that

appear between the aggregates either in solution or at the surface. This scenario agrees with data shown in Fig. 7**e** where the impedance of the film increases with the increment of the initial dopamine (and film thickness) concentration due to the insulating behaviour of polydopamine [73].

3. Ultrathin PDA free-standing films

Due to their unique properties, ultrathin PDA free-standing films gained much attention in recent years. However, several developments, especially in their preparation and transfer onto the desired substrate, fully exploit their potential, e.g. for constructing the new van der Waals heterostructures or a laminar heterojunction between polydopamine and semiconductors is needed [10]. Unfortunately, due to the insolubility of natural and synthetic melanin, the use of conventional solution processing methods to prepare large-scale homogeneous melanin thin films is challenging [81]. Notably, it was reported that the PDA free-standing thin films (50–200 nm thick) are being formed at an air/solution interface under static or soft-stirring conditions during a simple autoxidation of dopamine [82–86]. A very recent study has shown the apparition of what appears to be a supramolecular ordering that resembles 2D-like ordering. Although not fully understood till now, this might allow investigating several aspects of PDA self-organizing thin films [87,88]. However, to the best of our knowledge, there were no reported experiments on obtaining the polydopamine thin film from the air/water interface, where the growth rate or control over the process was enhanced with electrochemical methods. Moreover, the information about the electrochemical formation of the PDA free-standing membranes, in general, is minimal. This low number of publications might be attributed to the language freedom among authors regarding membrane/films. While strictly speaking, membranes provide permeability and filtration capabilities, many authors address them as free-standing structures. Therefore, this section will explain the mechanisms behind these studies and summarize the recent developments in related fields.

3.1. Electrochemically generated free-standing PDA ultrathin films

To this day, the direct formation of a free-standing PDA membrane via electrochemically enhanced oxidation has been reported only once [89]. The procedure, schematically presented in Fig. 9**a**, started from the deposition of the PDA thin coating layer by dipping the gold substrate into the dopamine solution and sweeping the potential for several cycles from −0.5 to +0.5 V. Then, to remove the film from the surface of the substrate, the sample was immersed for 30 min into a carbonate buffer of pH equal 10, to promote cross-linking of the dopamine species- that is, oligomers and monomers- absorbed into the film, making it more stable. Subsequently, the sample was immersed in phosphate buffer, and another three CV cycles were carried out over a wider range of potential (from −800 to 1200 mV). The goal was to over oxidize the system, thus forming an oxide layer on gold to reduce the adhesion between the coating film and substrate to allow the PDA's detachment by reducing the Au–N coordination. In the corresponding Cyclic Voltammogram (Fig. 9**b**), the PDA film's effective removal and the PVA layer are visible. Next, the polydopamine film was coated with a PVA layer to ensure adhesive and mechanical support. Finally, the coating was carried out by drop-casting of a PVA solution in water, followed by drying the layer at 40 °C for 25 min. Then, the PDA thin film was stripped off the substrate and the PVA film. Lastly, PVA was removed by immersing the PVA–PDA film in water. The ultrathin PDA film floating at the air/water interface was then transferred to various substrates (e.g. nylon mesh) and characterized by scanning electron microscopy (Fig. 9**c**). Therefore obtained film could stand freely without needing other supporting material, owing to their relatively high mechanical resilience, Young's modulus of about 12 GPa [89].

Remarkably enough, the films prepared by this method have recently

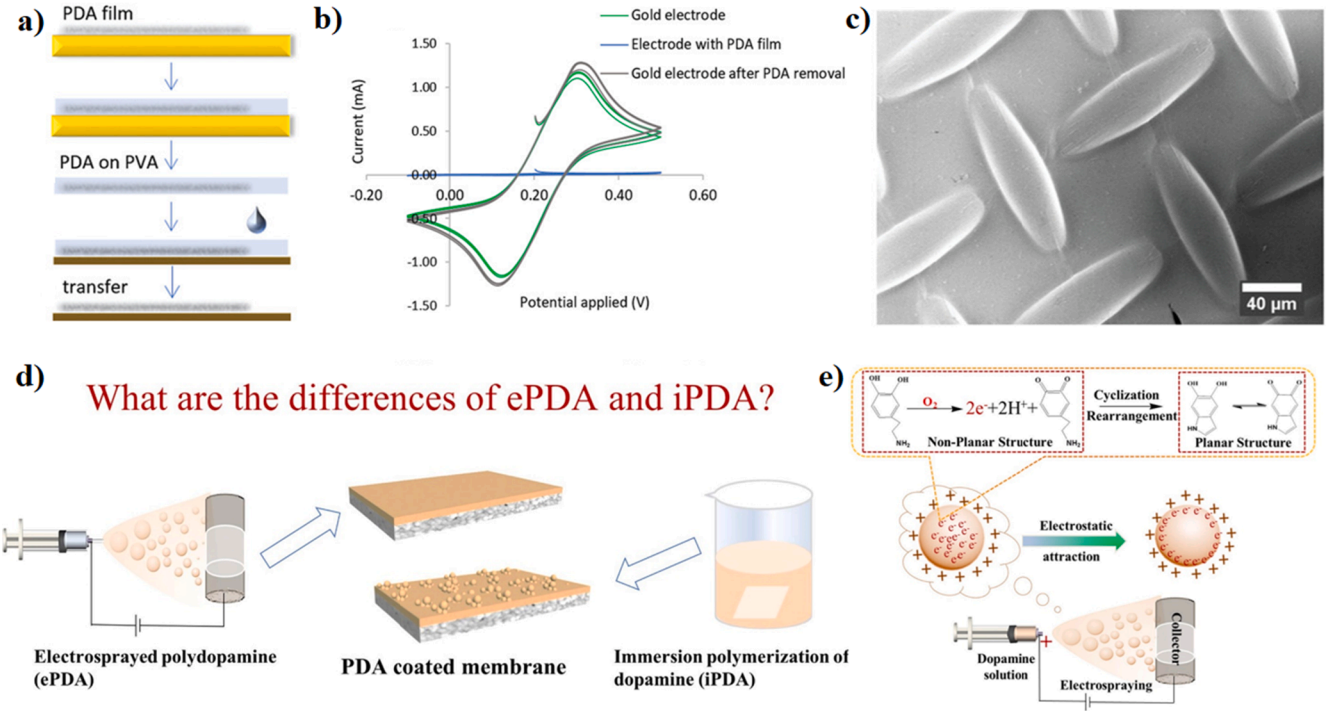

Fig. 9. a) Schematic procedure of the removal and transfer procedure of free-standing PDA films (grey) on gold substrate (yellow), scheme of the three main steps (top) and Photos recorded of each sample during the corresponding procedure (bottom). **b)** CV voltammogram of the golden electrode before PDA deposition (green), PDA-coated golden electrode (blue) and the golden electrode after the PDA detachment (brown). **c)** SEM image of PDA film on a nylon mesh. Reprinted with permission from [89]. **d)** Scheme of the difference between fabrication process and morphology of the electrospray and immerse coated polydopamine. **e)** Chemical and electrostatic character of ePDA for a PDA formation. Reprinted with permission from [90].

shown outstanding light-driven motion [91]. The results show exceptionally applicability for sensing, as they are sensitive to moisture and heat, while many other applications can be developed in the future. The question of whether the electropolymerization method is somehow involved in this feature or an inherent property of PDA will need to be addressed. Significantly, the formation of thin PDA coatings on a high-surface-area boron-doped carbon nanowall electrodes has been studied very recently [92], providing important insights into the polymerization dynamics and control of PDA layers. These results may be helpful in further experimental works toward free-standing films. On the other hand, other methods utilize the potential differences to produce thin free-standing films (albeit with a different morphology), such as electrospinning and electrospraying. We will briefly discuss this topic in the context of a polydopamine in the next sections.

3.2. Electrospraying polydopamine films

In the electrospray process, the charged liquid is forced out of the tip of a needle and then is sprayed into fine droplets with diameters ranging from micrometre to nanometer. Due to the mutual repulsion, the emitted droplets are well self-dispersed in the space without aggregation during the flight to the collector. The flying droplets are gradually solidified due to the evaporation of the solvent. Predominantly, this method is being used for surface functionalization and interface construction [93,94]. Recently, an electrospray method for PDA coating with zero wastewater discharge and the feasibility of dopamine polymerization during electrospray was demonstrated [94].

Elsewhere, double-layered membranes were obtained via electrospraying of the PDA as a coating onto Polyethersulfone (PES) membrane as a substrate [90]. This modification was named as ePDA. For comparison, Immersion PDA (iPDA) membrane was prepared through the substrate coating by simple immersion in dopamine/tris solution and simultaneously the autoxidation process. This differentiation was schematically shown in Fig. 9**d.** The ePDA provided a fast and controlled coating growth way, which produced a relatively smooth and uniform structure, enhanced chemical stability, higher water flux and dye/salt selectivity compared with iPDA. This approach is the closest to the free-standing PDA ultrathin membrane obtained via electrospraying, above all others found in the literature. Therefore, a conducted method will be briefly explained. Firstly, a standard 10 mM Tris aqueous buffer was prepared, and the pH value was adjusted to 8.5. Then, the solution was bubbled with nitrogen for 30 min to remove dissolved oxygen. After that, dopamine hydrochloride was added to achieve a concentration 1.0 g dm^{-3} or 2.0 g dm^{-3}. Such freshly prepared mixture solution was sealed in the syringe with a metal needle. Next, the syringe was mounted to the equipment for electrospraying, and a high voltage of about 10 kV was applied. The collector was a metal roller mounted with a PES membrane. The distance between the needle and corrector was 10 cm. The rolling rate of the collector was set at 80 rpm, and the feed rate of the electrospraying solution was about 0.75 ml h^{-1}. The obtained composite membrane via ePDA strategy was detached from the collector and kept in the air for further use. The thickness of ePDA coating at 8 h was determined to be 37 nm by using a spectroscopic ellipsometer [90].

Notably, significant structural differences between iPDA and ePDA were reported. XPS results suggested that more dopamine molecules were prone to cyclization in ePDA process. In other words, more 5,6-dihydroxyindole (DHI) and 5,6-indolequinone (IDQ) components existed in ePDA. This might be the main reason that ePDA exhibited enhanced stability compared to iPDA due to the critical role of DHI in cross-linking of PDA. The explanation relies on the characteristics of the electrospraying method. Namely, electrospray dopamine droplets carried a certain amount of positive charges due to applied positive high voltage during electrospraying. Simultaneously, the positively charged character of the electrosprayed dopamine droplet benefits the removal of electrons released from the dopamine oxidation process. Therefore, more dopamine molecules were prone to be oxidized due to enhanced oxygen availability and electron removal based on chemical equilibrium theory [90,95]. Schematically, the difference between iPDA and ePDA is shown in Fig. 9**e.**

3.3. Electrospinning polydopamine films

Electrospinning is a widely used technique for the fabrication of micro-and nano-fibrous membranes for several applications in different fields like electrocatalytic degradation [96] or biomedical field (e.g. tissue engineering and drug delivery [97]). Generally, the basis is the application of a high voltage at the tip of a needle containing a polymer in the form of a solution, suspension, melt or blend. The solvent evaporates from the charged solution during the time of flight, and the obtained fibres are collected on the grounded target [97]. Unfortunately, no experiment was described in the literature concerning electrospinning of the pure PDA to the best of our knowledge. Instead, numerous reports about direct PDA coating from the solution of the substrates made of electrospinning membranes are available [98–103].

However, there is one study about PDA-based composite obtained via electrospinning described hitherto. Namely, the konjac glucomannan (KGM)/PDA nanofibers have been prepared via the electrospinning technique [104]. PDA changed the macrostructures of the KGM nanofiber membrane due to the strong hydrogen-bond interaction between KGM and PDA. Moreover, the as-prepared nanofiber membrane showed high moisture adsorption and good drug release ability, making it an attractive candidate for drug delivery.

Nevertheless, this approach did not explore the potential of electro-oxidation of the PDA. Instead, the polymerization had already taken place in the starting solution before the start of the electrospinning procedure. Therefore, there is still a need for research on possible PDA or PDA-based fibres production via this technique. However, until now, only droplets and aggregates have been formed [90]. In the future, the development of high-performance and multifunctional bio-based electrospun nanofiber membranes will become a significant research direction [105].

4. Electrochemical sensing using PDA

Recently, numerous approaches have been proposed to improve selectivity or the other characteristics of the electrochemical analysis methods. Most of these techniques are based on the modification of electrodes, e.g., creating selective electroactive sites on their surfaces [106]. Moreover, the modifiers have an electrocatalytic or redox effect on the investigated substance, as well as they could show a different kind of electrochemical interaction. Simultaneously, nanomaterials have gained much attention because of their increasing sensitivity by enlarging the active surface area of the electrodes [107]. Another emergent topic is the biocompatibility of the sensors for analysis of the clinical samples [108]. A very recent and popular research direction is also the construction of strain sensors for motion monitoring [109,110]. Due to its unique properties- like biocompatibility [27,28,111], environmental friendliness [112,113], catalytic performance [10], electrical (semi)conductivity [114], hydrophilicity [114,115]- polydopamine addresses many of these issues. However, the PDA coating is not a panacea for any complications related to analytic applications. For example, PDA has a high affinity to protein adhesion which might lead to the risk of thrombus formation when analyzing blood samples. Therefore, further surface functionalization may be needed on the PDA-modified composites. Thus, PDA often does not stand as the standalone solution [116]. Taking it all into account, in this section, we will present recent developments in the application of PDA or PDA-based composites for the construction of novel electrochemical sensors, starting from the table (Table 1) summarizing chosen articles in the field. Later on, some examples will be explained, focusing on PDA's role in constructing such sensor elements. In this work, we will not explain the latest applications for polydopamine in other fields, although many interesting examples

Table 1
The summary of the chosen, recent examples of the development in electrochemical sensors construction using PDA-based or PDA-modified functional composites.

Field	Specific application	Detection method	Nanostructure	Ref.
Drug traces detection	Chlorpromazine detection	amperometric	GCE[1]/**PDA**@RGO	[120]
	Metronidazole detection	CV, DPV	GCE/MWCNTs - COOH[2]/**PDA**	[121]
	chloramphenicol	CV, DPV	GCE/**PDA**-VGCF[3]	[122]
	sodium diclofenac	DPV	CCE[4]-**PDA**@Fe_3O_4-Aptamer[5]	[123]
	atenolol	CV, DPV	GCE/**PDA**	[53]
Detection of biocompounds in biological fluids	dopamine, acetaminophen, xanthine	CV, DPV	GCE/**PDA**-MWCNTs[6]	[124]
	ascorbic acid	CV	CFE[7]/SBMA[8]-**PDA**	[125]
	dopamine and uric acid in the presence of ascorbic acid	DPV	GCE/MWCNTs/ **PDA**@Graphene	[126]
Disease markers detection	carcinoembryonic antigen	DPV	Cu-MOFs[9]-TB[10]/**PDA**	[127]
		DPV	GCE/**PDA**-PSBMA[11]	[128]
	Human epidermal growth factor receptor 2	DPV	rGO-**PDA**-Fc[12]/ Au@Ag NSs[13] and Ni@PtNi HNCs-Thi[14]	[129]
	pancreatic cancer-associated microRNA, miR-196b	CV	**PDA**-Au@SPCE[15]	[130]
Ion sensing	Pb^{2+} and Cd^{2+} ions	SWV[16], SWASV[17]	GCE/**PDA**@Fe_3O_4	[131]
	Ca^{2+}	Potentiometric	GCE/PEDOT[18]-PSS[19]/**PDA**	[132]
Skin-attached wearable sensors	motion monitoring	Function of the RCR ($\Delta R/R_0$) vs Strain (%)	PU[20]-nanofiber /graphene/**PDA**/ PFDT[21]	[133]
			CB[22]/NBR[23]/**PDA**	[134]
		Function of the RCR ($\Delta R/R_0$) vs time	PS[24]-PAM[25]/**PDA** hydrogel	[135]
Sensing of pesticides in food and environment	dichlorodiphenyltrichloroethane	EIS	**PDA**@Fe_3O_4 MIP-MNPs[26]	[136]
	Organophosphorus compounds	CV, DPV	AuPt-**PDA** hydrogel	[137]
	Malathion	DPV	GCE/**PDA**-AuNPs/CP[27]/MCH[28]/ Aptamer	[50]

1- glassy carbon electrode
carboxylic multi-walled carbon nanotubes
vapor-grown carbon fiber
carbon ceramic electrode
A diclofenac single-strand DNA amino functionalized aptamer
multiwalled carbon nanotubes
carbon fiber electrode
zwitterionic sulfobetaine methacrylate
Metal-organic frameworks
toluidine bluepoly
(sulfobetaine methacrylate)
polydopamine-grafted-ferrocene
Au@Ag nanoshuttles
Ni@PtNi yolk-shell nanocages-thionine

2- screen-printed carbon electrodes
Squarewave voltammetry
Square-Wave Anodic Stripping Voltammetrypoly
(3,4-ethylenedioxythiophene)Poly
(sodium 4-styrenesulfonate)
polyurethane
1H,1H,2H,2H-perfluorodecanethiol
Carbon black
Nitrile butadiene rubber
polystyrene particles
polyacrylamide
Molecularly imprinted polymer magnetic nanoparticles
Ferrocene modified capture probe
6-mercapto-1-hexanol

could be found e.g. nanoscale actuators [91], adsorption promotion [117,118] and metacomposites preparation [119]. We focus on electrochemical sensing applications.

4.1. Drug traces detection

Chlorpromazine (CPZ) is a first-generation antipsychotic drug in the family of phenothiazine derivatives and has been widely applied to treat different psychic diseases. However, the over usage and excess concentration of CPZ can create severe health issues. Therefore, monitoring its concentration in biological fluids or environments [138,139]. Highly selective, amperometric detection of CPZ was achieved employing the RGO@PDA composite electrode, prepared via a simple electrochemical method. This process was schematically shown in Fig. 10**a** [120]. The resulting electrode showed significantly higher electrochemical and electrocatalytic activity towards CPZ than other modified electrodes (GO, GO@PDA, and RGO) that were investigated by cyclic voltammetry. The analytical sensitivity defined as the slope/electrode active surface area ratio of the CPZ sensor was higher than the graphene paste electrode, carbon nanotube-polyethyleneimine electrode, poly-3-methyl thiophene combined with the γ-cyclodextrin composite electrode, and Alizarin Red modified electrode. In turn, to assess the selectivity of the RGO@PDA composite electrode, the amperometric i-t method was used. A clear amperometric response was reported repeatability with the addition of 1 μM CPZ, while additions of potentially interfering drugs in relatively high amounts (100 μM) did not result in any amperometric response on the electrode of interest.

4.2. Sensing of pesticides in food and environmental samples

An important field where PDA-based electrochemical sensors found numerous applications is sensing of pesticides in food and environmental samples. A detailed and recent review work concerning this topic is available [140]. Therefore, only the most recent and important studies will be mentioned here. Acetylcholinesterase (AChE) biosensors are among the PDA-based sensors that researchers most commonly used to detect some pesticides in food and environmental matrices. However, the AChE enzyme should be immobilized on the sensor's electrode to function correctly. Thus, many researchers are now resorting to the use of PDA-based immobilization techniques [50,136,137]. These approaches show promising real-applicational perspectives, e.g., detecting malathion in cauliflower and cabbage samples in a concentration range from 0.5 to 600 ng/L with a relative standard deviation of less than 6.14% [50]. The use of dopamine as a functional monomer resulting in the formation of PDA-based Molecularly imprinted polymers (MIP) sensors is, gaining popularity among researchers. PDA-based magnetic

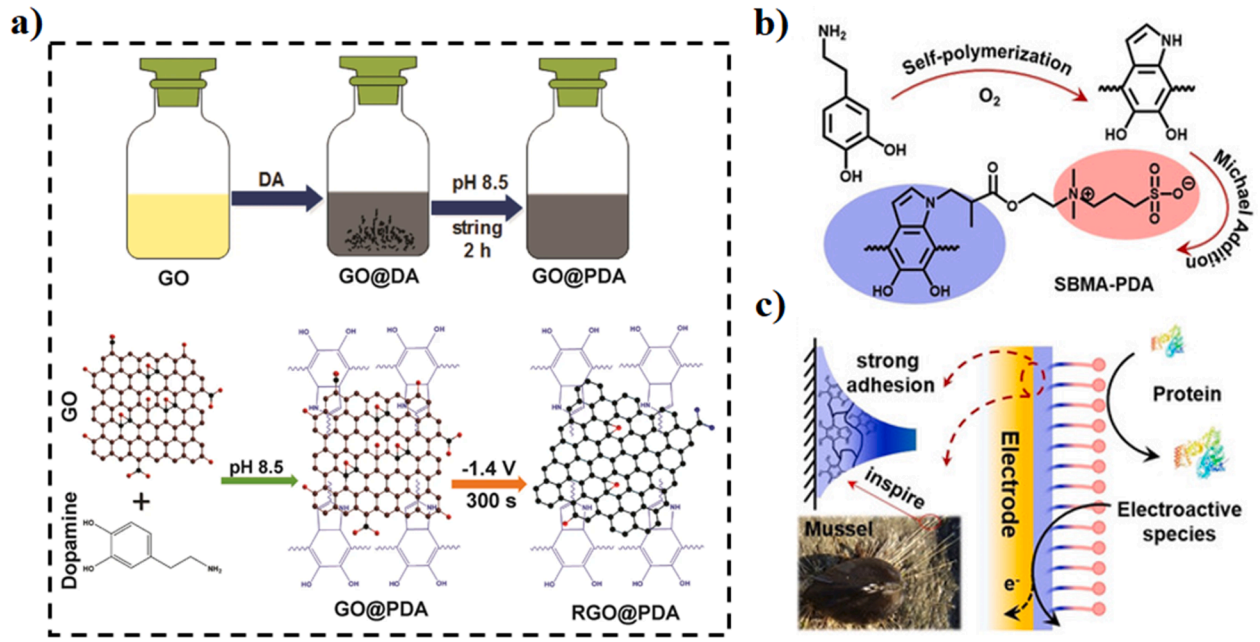

Fig. 10. a) Schematic representation for the electrochemical fabrication of RGO@PDA composite. Reprinted with permission from [120]. **b)**Illustration of tailing SBMA on PDA-engineered bio-interfacing by Michael Addition. **c)**Illustration of SBMA-PDA on electrode surface for antifouling and the strong adhesion of PDA primer on almost all types of the electrode surface. Reprinted with permission from [125].

MIP sensor formation for dichlorodiphenyltrichloroethane (DDT) detection in food samples was achieved by using Fe_3O_4 magnetic nanoparticles, bisphenol molecules as dummy templates, and dopamine as the functional molecules. The detection of DDT by the sensor was based on the fact that the electrochemical impedance of PDA@Fe_2O_4 MIP magnetic nanoparticles increased with the adsorption of DDT. Thus, the PDA-based MIP sensor they developed showed a relationship between the electrochemical impedance response and the concentration of DDT in the samples [136]. PDA can also play a role in the preparation of electrochemical aptasensors. The PDA-based electrochemical aptasensors involve using an aptamer, an oligonucleotide or peptide that binds to a specific molecule [141].

4.3. Detection of Bio-Compounds and disease markers in biological fluids

Electrochemical detection of disease markers in complex biological fluids is frequently used to diagnose, prevent, and treat many diseases. However, a remarkable drop in current response due to nonspecific binding of coexisting species to the electrode surface is reported frequently [142,143]. Moreover, nonspecific binding of proteins onto the tissue-implantable sensing interface could cause a numeric undesirable immune response [125]. To overcome these drawbacks, a novel bio-interface was recently developed using PDA, which enables interfacial tailing of zwitterionic sulfobetaine methacrylate (SBMA) molecules by Michael Addition. The fabrication process is schematically shown in Fig. 10**b**.

Furthermore, PDA can act as an intelligent scavenger of free radicals and a strong adhesive primer. To evaluate the electron transfer and mass transport property of SBMA-PDA the cyclic voltammetry (CV) performance of ferrocenylmethanol (FcMeOH) at the SBMA-PDA-coated carbon fibre electrode (CFE) was investigated. Results suggested that the SBMA-PDA does not impede either electron transfer or mass transfer in the electrochemical process, which might be ascribed to the ultrathin feature of the SBMA-PDA membrane. Moreover, the SBMA-PDA-coated CFE demonstrates exceptional electrochemical stability attributed to the strong adhesion of the PDA primer on the electrode surface. The main features of the obtained electrode are shown in Fig. 10**c**. Described composite has an excellent ability to prevent nonspecific protein binding while retaining the electrochemical performance of the electrode in complex biological fluids [125].

Elsewhere, a novel strategy for constructing sensitive and antifouling biosensors capable of detecting typical tumour markers, carcinoembryonic antigen (CEA), was developed [128]. The fabrication method was a simple one-step copolymerization of polydopamine (PDA) and poly(sulfobetaine methacrylate) (PSBMA) process. Importantly, this biosensor was able to work in complex biological media [128].

4.4. Potentiometric ion sensing

In numerous clinical applications, potentiometry with polymeric membrane ion-selective electrodes (ISEs) has become the standard technique in the analysis of electrolyte ions such as Na^+, K^+, Ca^{2+}, and Cl^- [132,144]. However, when these sensors are continuously in contact with samples (e.g. in vivo analysis), they suffer from biofouling, which leads to a decrease in electrochemical performance and biocompatibility, affecting both the functionality of the material and the patient's life quality [145]. It was reported that biocompatibility might be increased by simply coating with hydrophilic materials, but improved adhesion of these coatings to membranes was desired. In response, a facile approach via polydopamine coating was proposed (see Fig. 11**a**). The hydrophilic surface modification of poly(vinyl chloride) (PVC)-based polymeric membrane Ca^{2+}-was simply achieved by immersion of the sensor in a dopamine solution at pH 8.5. Significantly, the improvement in sensor biocompatibility should not influence the analytical performance. Therefore, the potentiometric response of modified and unmodified membranes was tested in the concentration range of $10^{-8} - 10^{-2}$ M. The results are shown in Fig. 11**b**. No significant difference could be observed between both electrodes, which indicates that the polydopamine modification has little effect on the electrode performance of the polymeric membrane. Indeed, the response slope and the detection limit remain almost the same. However, the response time of the modified electrode appears to be significantly longer than that of the classical unmodified one. In turn, nearly all potentiometric selectivity coefficients of the modified membrane are comparable to those of the unmodified classical membrane. As illustrated in Fig. 11**c**, the hydrophobic membrane surface becomes

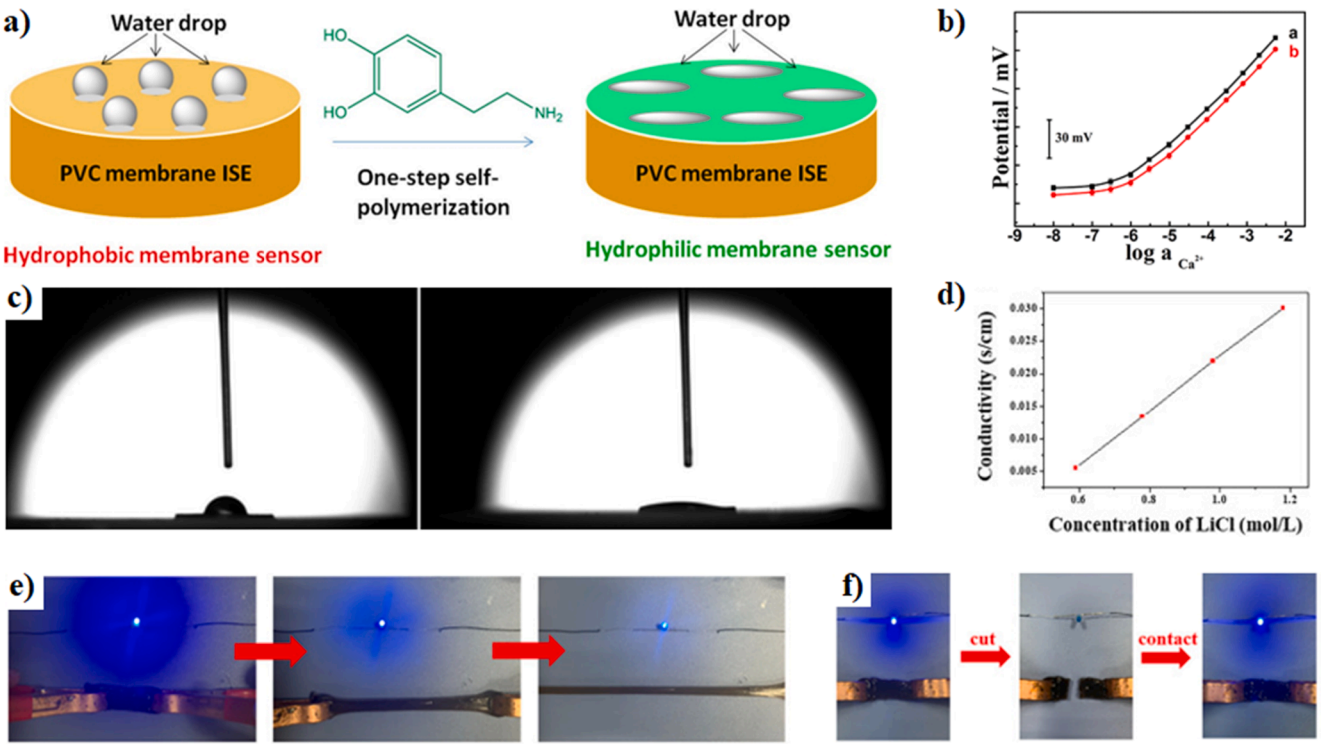

Fig. 11. a) Schematic Illustration of One-Step Hydrophilic Conversion of the PVC Membrane ISE. **b)** Potentiometric responses of (black) unmodified and (red) polydopamine-modified polymeric membrane Ca^{2+}-ISEs. **c)** Contact angles of the water drops for (left) the classical unmodified and (right) polydopamine-modified PVC Ca^{2+}-selective membranes. Reprinted with permission from [146]. **d)** Electrical conductivity changed with the concentration of LiCl increased. **e)** Luminance change of LED when the double-layer hydrogel was stretching. **f)** LED could light again when the gel self-healed. Reprinted with permission from [135].

hydrophilic with a significant decrease in the contact angle after polydopamine deposition from 77.9° ± 3.5° to 33.5° ± 1.5°. Thus, it can be demonstrated that the hydrophilic modification does not influence the selectivity coefficients. Moreover, a significant decrease in platelet adhesion is observed for the polydopamine-modified hydrophilic membrane, which stands as proof of biocompatibility improvement. Also, the proposed electrode has good reproducibility and long-term stability for Ca^{2+} ions detection. In summary, the proposed PDA-modified hydrophilic sensor can be successfully used to detect trace-level Ca^{2+} ions in the presence of a high protein background, while the data obtained by the unmodified PVC-based sensor seriously deviate from the real values, indicating that the hydrophilic sensor shows an excellent anti-biofouling ability [132].

4.5. *Strain-sensors for motion monitoring*

High-performance, wearable, and flexible strain sensors for motion detection have been widely investigated recently for body motion detection, health monitoring, and smart clothing. Conductive polymer composites (CPCs) are in the spotlight, as they combine excellent mechanical and electrical properties with low fabrication costs. In principles, a mechanical strain applied to the CPC either forces the embedded conductive particles to come closer to each other, resulting in higher conductivity or vice versa. The most crucial parameters of strain sensor materials are sensitivity, applied strain range, repeatability, and stability [134]. PDA does not act as a conductor in these composites but rather ensures appropriate mechanical or biocompatibility properties. Nevertheless, this topic is highly important and can significantly influence the revolution in electronics. Therefore it is worth mentioning here a few examples of PDA-based composites for a strain sensors construction.

A flexible and super-hydrophobic PFDT/PDA/graphene/PU nanofiber composite was synthesized by using graphene decoration onto polyurethane (PU) nanofibers, followed by PDA modification and then 1H,1H,2H,2H-perfluorodecanethiol (PFDT) fluorination [133]. With the introduction of PDA, a similar “brick and mortar” structure was constructed, with graphene as the brick and PDA as the mortar. The elongation at break was improved from around 352% for TPU nanofibrous membranes to 449% for the nanofiber composite. The $\Delta R/R_0$ curve for each cycle was almost identical, and the response intensity (defined as the maximum value $\Delta R/R_0$ for each cycle) maintained stable with the value of 0.8 during all 1000 cycles test. In summary, the nanofiber composite could serve as a strain sensor with excellent stretchability, controllable sensitivity, high durability and good cyclic stability [133].

In a different work, a simple direct coating with polydopamine from the solution was introduced again to develop a sandwich-shaped strain sensor with nitrile butadiene rubber (NBR) as the polymer matrix and carbon black (CB) as the conductive filler [134]. The purpose of the modification was to reduce the loss of CB particles during stretching, preserve the mechanical and electrical properties of the films, and endow biocompatibility to the film. Uniaxial strain-sensing tests showed that the NBR/CB and PDA/NBR/CB composites are characterized by high sensitivity and a wide sensitivity range, whereas cyclic electromechanical tests revealed good stability and reproducibility. Moreover, compared to the NBR/CB composite, the PDA/NBR/CB strain sensors are more biocompatible and thus, they can be used to detect detailed bending motions (e.g. for human fingers, elbows, and knee joints) with higher sensitivity [134].

Due to the advantages of stretchability and biocompatibility, hydrogel-based strain sensors have been greatly expanded in recent years [147]. However, to adhere to the skin, traditional hydrogels require additional adhesives, increasing the size of the device and thus reducing comfort. Simultaneously, hydrogels that lack self-healing properties are challenging to repair and reuse after damage, which reduces their service lifetime. However, PDA-based hydrogel sensors with biocompatible, self-healing and highly stretchable properties were

described in the literature [148,149]. Elsewhere, a double layer hydrogel containing a tough (duct) layer and the adhesive layer was prepared [135]. Because of the addition of Li^+ and Cl^- ions in the PS-PAM layer, the hydrogel was conductive to light up a blue LED when connected to the circuit (Fig. 11**d**). After stretching the hydrogel, the LED light was significantly dimmed due to the increase in electrical resistance. Subsequently, the LED lights were extinguished when the hydrogel was cut into two parts. However, after the two parts of the broken gels were re-contacted, the LED light immediately relit, proving that the developed material can rapidly self-healing (Fig. 11**e**). The electrical conductivity of double-layered hydrogel was related to the concentration of LiCl. As shown in Fig. 11**f**, when the concentration of lithium chloride was 1.2 mol dm^{-3}, the conductivity of the hydrogel could reach 0.03 s cm^{-1} [135].

5. Conclusions and future perspectives

This review aimed to introduce the reader to the topic and summarize the current state of the art on the electrochemical formation of polydopamine. We have described selected novel applications of the PDA for the construction of the electrochemical sensors and provided a general view of their mechanism. Firstly, a detailed ECECEE mechanism has been explained, representing the current state of the art (see Section 2.1). To better understand the process, the electrochemical deposition technique and conditions must be taken into account. Therefore, available reports from the literature concerning cyclic voltammetry (Section 2.1.1), pulsed electrochemical deposition (Section 2.1.2.) and galvanostatic deposition (Section 2.1.3.) towards the production of the polydopamine were summarized. Their development in itself is an important aspect that can bring significant advances in the preparation of PDA and other related materials. Thus a deeper understanding of PDA's deposition mechanism and structure is still needed.

To summarize the current state of the art and to build possibly the most comprehensive picture of the dopamine electrochemical oxidation, the pH-dependency (Sections 2.1.4. and 2.2.1.), electron transfer insights (Section 2.2.1.) and the kinetics (Section 2.2.2.) of the process were described. Significantly, based on the cyclic voltammetry experiments, the aspect of the pH dependence of the electrochemical PDA deposition process was explained. Namely, the first stage (anodic oxidation) can be described as pH-independent, while the second stage (polydopamine irreversible formation) is fast and pH-dependent. In turn, electrochemical impedance spectroscopy reveals that the electron transfer resistance is higher for thicker and more compact films (obtained with higher dopamine concentration or longer deposition times). This observation is similar for different types of substrates (e.g. ITO or GCE), and, although this behaviour is expectable, it correlates well with other catecholamines [30]. Moreover, it was reported that EIS was used for corrosion resistance studies by submerging the electrodes in 3.5% NaCl solution at different temperatures and at different times. PDA modified electrodes presented a high anti-corrosion behaviour, and the influence of the temperature at which the PDA was obtained was significant. Also, the EIS studies about the kinetics of the dopamine oxidation were shown to indicate higher attractive forces between the aggregates in solution and on the surface, leading to higher film thickness for a higher initial dopamine concentration. All the facts mentioned above helped build a complete picture of the impact of individual factors on the polydopamine EC deposition process and allow for better future planning of experiments.

Next, the topic of thin PDA membranes was introduced (Section 3), which surprisingly shows a relatively small number of publications on this matter. Nevertheless, we show the first report about the successful production of free-standing PDA films (Section 3.1) and a few works concerning PDA-based composite membranes obtained with the use of electrospraying (Section 3.2) and electrospinning (Section 3.3.), which sheds some light on these promising aspects. Considering the presently increasing interest in ultrathin free-standing film applications and relatively simple EC polydopamine deposition methods, significant progress in the fabrication of the PDA and PDA-based ultrathin membranes should be expected.

Furthermore, the application of polydopamine for the construction or tuning of the electrochemical sensors is another prominent topic. Thus, we summarized recent examples of developing electrochemical sensor construction using PDA (Table 1). Based on the table, it can be noted that most experiments rely on the CV and DPV methods. Therefore, it can be concluded that the prospectives of e.g. potentiometric or EIS measurements, using PDA-based composites as the working electrode, have not been fully discovered. Later, we mention five very promising directions in different fields, exploiting the potential of the PDA modified and based electrochemical sensors, namely: drug traces detection (Section 4.1), sensing of pesticides in food and environmental samples (Section 4.2), disease markers detection (Section 4.3), potentiometric ion sensing (Section 4.4) and strain sensors construction (Section 4.5). Advances in these areas require the use of new functional materials, e.g. polydopamine. Among all the positive effects of PDA, the increase of electrocatalytic activity, selectivity enhancement (binding to specific molecules), adhesion promotion, intelligent scavenging of free radicals, biocompatibility, hydrophilicity and mechanical strength enhancement should be emphasized.

Based on the literature review, it is clear that there is still a vast space for undertaking polydopamine based solutions in various analytic and analytics-related fields. Here we mention a few of the main aspects in which we expect the PDA research field to develop in the following years.

- One of the key advantages of PDA is its easy attachability or "stickiness", which might also become one of its drawbacks for specific applications. Many of the devices or methodologies here presented are of a single application. This might not be a problem, given the relatively straightforward polymerization of PDA and its affordable manufacturing process. However, we can expect that this aspect will limit some of the applications of PDA films, signalling a certain maturity of the topic.
- Electrochemical methods for producing polydopamine films produce high quality and reproducible PDA coatings, which, as shown here, are exploitable in free-standing structures. However, the self polymerizing mechanism at the air/water interface might still have much to offer in this field. The main advantage of this method is its relatively large scalability and, perhaps, transferability, which can be even more cost-effective in the fabrication and integration of large-area sensing or bioactive surfaces. We consider this aspect a significant player in the years to come, especially if PDA based solutions can effectively be transferred to industrial applications.
- The recent discovery of PDA fast photoactuation [91] provides a fascinating opportunity for its implementation in transducers and other light-activated architectures. The strong dependence on the humidity of PDA and the rapid reaction observed in the study opens the door for many applications in which PDA is the active sensing platform and the transductor. This new effect, combined with PDA composites' inherent chromatic and photoactive response, might dominate the organic and hybrid electronics fields.
- The study of PDA analogues compounds and catecholic derivatives in similar applications, such as thin-film synthesis, sensing and other functional strategies, is expected. Not only because of the similarity of chemical compounds but the possible insights into the polymerization pathways of PDA [150].

To conclude, further research and nanostructures based on polydopamine and other functional materials should be expected, as well as chemical modifications and enhanced control of the PDA deposition process. Although we are slowly reaching the maturity of the PDA field, there are plenty of fundamental questions on this "miracle" polymer that wait for answers, and, as is often the case, much research is still needed

and very welcomed.

Author Contribution

All authors reviewed and gave their approval for the submission of the manuscript.

Declaration of Competing Interest

The authors declare that they have no known competing financial interests or personal relationships that could have appeared to influence the work reported in this paper.

Acknowledgements

The authors acknowledge the financial support from Poland's National Science Centre (NCN) by the OPUS grant 2019/35/B/ST5/00248. This research was supported by a French Government Scholarship.

References

[1] H. Lee, S.M. Dellatore, W.M. Miller, P.B. Messersmith, Mussel-inspired surface chemistry for multifunctional coatings, Science 318 (2007) 426–430, https://doi.org/10.1126/science.1147241.
[2] H. Lee, J. Rho, P.B. Messersmith, Facile conjugation of biomolecu les onto surfaces via mussel adhesive protein inspired coatings, Adv. Mater. 21 (2009) 431–434, https://doi.org/10.1002/adma.200801222.
[3] X. Xie, J. Tang, Y. Xing, Z. Wang, T. Ding, J. Zhang, K. Cai, Intervention of Polydopamine Assembly and Adhesion on Nanoscale Interfaces: State-of-the-Art Designs and Biomedical Applications, Adv. Healthc. Mater. 10 (2021) 2002138, https://doi.org/10.1002/adhm.202002138.
[4] J.H. Ryu, P.B. Messersmith, H. Lee, Polydopamine Surface Chemistry: A Decade of Discovery, ACS Appl. Mater. Interfaces. 10 (2018) 7523–7540, https://doi.org/10.1021/acsami.7b19865.
[5] V. Ball, Polydopamine films and particles with catalytic activity, Catal. Today. 301 (2018) 196–203, https://doi.org/10.1016/j.cattod.2017.01.031.
[6] M. Liu, G. Zeng, K. Wang, Q. Wan, L. Tao, X. Zhang, Y. Wei, Recent developments in polydopamine: An emerging soft matter for surface modification and biomedical applications, Nanoscale. 8 (2016) 16819–16840, https://doi.org/10.1039/c5nr09078d.
[7] P. Samyn, Polydopamine and Cellulose: Two Biomaterials with Excellent Compatibility and Applicability, Polym. Rev. 61 (2021) 814–865, https://doi.org/10.1080/15583724.2021.1896545.
[8] L.N. Nguyen, N. Kaushik, P. Lamichhane, S. Mumtaz, R. Paneru, P. Bhartiya, J. S. Kwon, Y.K. Mishra, L.Q. Nguyen, N.K. Kaushik, E.H. Choi, In situ plasma-assisted synthesis of polydopamine-functionalized gold nanoparticles for biomedical applications, Green Chem. 22 (2020) 6588–6599, https://doi.org/10.1039/d0gc01348j.
[9] Q. Huang, J. Chen, M. Liu, H. Huang, X. Zhang, Y. Wei, Polydopamine-based functional materials and their applications in energy, environmental, and catalytic fields: State-of-the-art review, Chem. Eng. J. 387 (2020) 124019, https://doi.org/10.1016/j.cej.2020.124019.
[10] D. Aguilar-Ferrer, J. Szewczyk, E. Coy, Recent developments in polydopamine-based photocatalytic nanocomposites for energy production: Physico-chemical properties and perspectives, Catal. Today. (2021), https://doi.org/10.1016/j.cattod.2021.08.016.
[11] Z. Yan, Y. Zhang, H. Yang, G. Fan, A. Ding, H. Liang, G. Li, N. Ren, B. Van der Bruggen, Mussel-inspired polydopamine modification of polymeric membranes for the application of water and wastewater treatment: A review, Chem. Eng. Res. Des. 157 (2020) 195–214, https://doi.org/10.1016/j.cherd.2020.03.011.
[12] P. Yang, S. Zhang, X. Chen, X. Liu, Z. Wang, Y. Li, Recent developments in polydopamine fluorescent nanomaterials, Mater. Horizons. 7 (2020) 746–761, https://doi.org/10.1039/c9mh01197h.
[13] P. Palladino, F. Bettazzi, S. Scarano, Polydopamine: surface coating, molecular imprinting, and electrochemistry—successful applications and future perspectives in (bio)analysis, Anal. Bioanal. Chem. 411 (2019) 4327–4338, https://doi.org/10.1007/s00216-019-01665-w.
[14] J.-M. Beaulieu, R.R. Gainetdinov, D.R. Sibley, The physiology, signaling, and pharmacology of dopamine receptors, Pharmacol. Rev. 63 (1) (2011) 182–217.
[15] E. Peltola, S. Sainio, K.B. Holt, T. Palomäki, J. Koskinen, T. Laurila, Electrochemical Fouling of Dopamine and Recovery of Carbon Electrodes, Anal. Chem. 90 (2018) 1408–1416, https://doi.org/10.1021/acs.analchem.7b04793.
[16] G. Mathew, P. Dey, R. Das, S.D. Chowdhury, M. Paul Das, P. Veluswamy, B. Neppolian, J. Das, Direct electrochemical reduction of hematite decorated graphene oxide (α-Fe2O3@erGO) nanocomposite for selective detection of Parkinson's disease biomarker, Biosens. Bioelectron. 115 (2018) 53–60, https://doi.org/10.1016/j.bios.2018.05.024.
[17] J. Wu, W. Dong, Z. Zhang, J. Liu, M. Akioma, J. Liu, Y. Liu, A. Pliss, X. Zhang, P. Luan, Emerging two-dimensional materials-based diagnosis of neurodegenerative diseases: Status and challenges, Nano Today. 40 (2021) 101284, https://doi.org/10.1016/j.nantod.2021.101284.
[18] M. Kujawska, S.K. Bhardwaj, Y.K. Mishra, A. Kaushik, Using graphene-based biosensors to detect dopamine for efficient parkinson's disease diagnostics, Biosensors. 11 (2021) 433, https://doi.org/10.3390/bios11110433.
[19] N. Wisniewski, M. Reichert, Methods for reducing biosensor membrane biofouling, Colloids Surfaces B Biointerfaces. 18 (2000) 197–219, https://doi.org/10.1016/S0927-7765(99)00148-4.
[20] J.S. Noori, J. Mortensen, A. Geto, Recent development on the electrochemical detection of selected pesticides: A focused review, Sensors (Switzerland). 20 (2020) 2221, https://doi.org/10.3390/s20082221.
[21] Y. Liu, K. Ai, L. Lu, Polydopamine and its derivative materials: Synthesis and promising applications in energy, environmental, and biomedical fields, Chem. Rev. 114 (2014) 5057–5115, https://doi.org/10.1021/cr400407a.
[22] J. Kund, S. Daboss, T.M. D'alvise, S. Harvey, C.V. Synatschke, T. Weil, C. Kranz, Physicochemical and electrochemical characterization of electropolymerized polydopamine films: Influence of the deposition process, Nanomaterials. 11 (2021) 1964, https://doi.org/10.3390/nano11081964.
[23] B. Stöckle, D.Y.W. Ng, C. Meier, T. Paust, F. Bischoff, T. Diemant, R.J. Behm, K.-E. Gottschalk, U. Ziener, T. Weil, Precise Control of Polydopamine Film Formation by Electropolymerization, Macromol. Symp. 346 (2014) 73–81, https://doi.org/10.1002/MASY.201400130.
[24] S.A. Alqarni, M.A. Hussein, A.A. Ganash, A. Khan, Composite Material-Based Conducting Polymers for Electrochemical Sensor Applications: a Mini Review, Bionanoscience. 10 (2020) 351–364, https://doi.org/10.1007/s12668-019-00708-x.
[25] A.S. Agnihotri, A. Varghese, M. Nidhin, Transition metal oxides in electrochemical and bio sensing: A state-of-art review, Appl. Surf. Sci. Adv. 4 (2021) 100072, https://doi.org/10.1016/j.apsadv.2021.100072.
[26] L. Qian, S. Durairaj, S. Prins, A. Chen, Nanomaterial-based electrochemical sensors and biosensors for the detection of pharmaceutical compounds, Biosens. Bioelectron. 175 (2021) 112836, https://doi.org/10.1016/j.bios.2020.112836.
[27] D. Hauser, D. Septiadi, J. Turner, A. Petri-Fink, B. Rothen-Rutishauser, From bioinspired glue to medicine: Polydopamine as a biomedical material, Materials (Basel). 13 (2020) 1730, https://doi.org/10.3390/ma13071730.
[28] P. Zhang, Q. Xu, J. Du, Y. Wang, Polydopamine-based nanoparticles with excellent biocompatibility for photothermally enhanced gene delivery, RSC Adv. 8 (2018) 34596–34602, https://doi.org/10.1039/C8RA06916F.
[29] A.B. Mostert, B.J. Powell, F.L. Pratt, G.R. Hanson, T. Sarna, I.R. Gentle, P. Meredith, Role of semiconductivity and ion transport in the electrical conduction of melanin, Proc. Natl. Acad. Sci. USA 109 (2012) 8943–8947, https://doi.org/10.1073/pnas.1119948109.
[30] V. Ball, Electrodeposition of coatings made from catecholamines, polyphenols and aminimalonitrile: Common features, perspectives and challenges, Prog. Org. Coatings. 131 (2019) 441–447, https://doi.org/10.1016/j.porgcoat.2019.02.027.
[31] A. Prabhu, R.D. Crapnell, K. Eersels, B. van Grinsven, A.K. Kunhiraman, P. Singla, J. McClements, C.E. Banks, K. Novakovic, M. Peeters, Reviewing the use of chitosan and polydopamine for electrochemical sensing, Curr. Opin. Electrochem. 32 (2022) 100885, https://doi.org/10.1016/j.coelec.2021.100885.
[32] H.A. Lee, E. Park, H. Lee, Polydopamine and Its Derivative Surface Chemistry in Material Science: A Focused Review for Studies at KAIST, Adv. Mater. 32 (2020) 1907505, https://doi.org/10.1002/adma.201907505.
[33] V. Ball, D. Del Frari, M. Michel, M.J. Buehler, V. Toniazzo, M.K. Singh, J. Gracio, D. Ruch, Deposition Mechanism and Properties of Thin Polydopamine Films for High Added Value Applications in Surface Science at the Nanoscale, Bionanoscience. 2 (2012) 16–34, https://doi.org/10.1007/s12668-011-0032-3.
[34] M.D. Hawley, S.V. Tatawawadi, S. Piekarski, R.N. Adams, Electrochemical Studies of the Oxidation Pathways of Catecholamines, J. Am. Chem. Soc. 89 (1967) 447–450, https://doi.org/10.1021/ja00978a051.
[35] Y. Li, M. Liu, C. Xiang, Q. Xie, S. Yao, Electrochemical quartz crystal microbalance study on growth and property of the polymer deposit at gold electrodes during oxidation of dopamine in aqueous solutions, Thin Solid Films. 497 (2006) 270–278, https://doi.org/10.1016/j.tsf.2005.10.048.
[36] E. Walaas, The chemical transformation of the catecholamines induced by UV irradiation, Photochem. Photobiol. 2 (1963) 9–24, https://doi.org/10.1111/j.1751-1097.1963.tb08115.x.
[37] T. Łuczak, Preparation and characterization of the dopamine film electrochemically deposited on a gold template and its applications for dopamine sensing in aqueous solution, Electrochim. Acta. 53 (2008) 5725–5731, https://doi.org/10.1016/j.electacta.2008.03.052.
[38] S. Schindler, N. Aguiló-Aguayo, U. Dornbierer, T. Bechtold, Anodic Coating of 1.4622 Stainless Steel with Polydopamine by Repetitive Cyclic Voltammetry and Galvanostatic Deposition, Ind. Eng. Chem. Res. 59 (2020) 236–244, https://doi.org/10.1021/acs.iecr.9b05603.
[39] N. Elgrishi, K.J. Rountree, B.D. McCarthy, E.S. Rountree, T.T. Eisenhart, J. L. Dempsey, A Practical Beginner's Guide to Cyclic Voltammetry, J. Chem. Educ. 95 (2018) 197–206, https://doi.org/10.1021/acs.jchemed.7b00361.
[40] G.A. Mabbott, An introduction to cyclic voltammetry, J. Chem. Educ. 60 (1983) 697–702, https://doi.org/10.1021/ed060p697.
[41] N. Aristov, A. Habekost, Cyclic Voltammetry - A Versatile Electrochemical Method Investigating Electron Transfer Processes, World, J. Chem. Educ. 3 (2015) 115–119, https://doi.org/10.12691/wjce-3-5-2.
[42] K. Liu, W.Z. Wei, J.X. Zeng, X.Y. Liu, Y.P. Gao, Application of a novel electrosynthesized polydopamine-imprinted film to the capacitive sensing of nicotine, Anal. Bioanal. Chem. 385 (2006) 724–729, https://doi.org/10.1007/s00216-006-0489-z.

[43] G. Loget, J.B. Wood, K. Cho, A.R. Halpern, R.M. Corn, Electrodeposition of polydopamine thin films for DNA patterning and microarrays, Anal. Chem. 85 (2013) 9991–9995, https://doi.org/10.1021/ac4022743.

[44] A. GhavamiNejad, L.E. Aguilar, R.B. Ambade, S.H. Lee, C.H. Park, C.S. Kim, Immobilization of silver nanoparticles on electropolymerized polydopamine films for metal implant applications, Colloids Interface, Sci. Commun. 6 (2015) 5–8, https://doi.org/10.1016/j.colcom.2015.08.001.

[45] S. Chumillas, T. Palomäki, M. Zhang, T. Laurila, V. Climent, J.M. Feliu, Analysis of catechol, 4-methylcatechol and dopamine electrochemical reactions on different substrate materials and pH conditions, Electrochim. Acta. 292 (2018) 309–321, https://doi.org/10.1016/j.electacta.2018.08.113.

[46] J. Cai, J. Huang, M. Ge, J. Iocozzia, Z. Lin, K.Q. Zhang, Y. Lai, Immobilization of Pt Nanoparticles via Rapid and Reusable Electropolymerization of Dopamine on TiO2 Nanotube Arrays for Reversible SERS Substrates and Nonenzymatic Glucose Sensors, Small. 13 (2017) 1604240, https://doi.org/10.1002/smll.201604240.

[47] S. Li, H. Wang, M. Young, F. Xu, G. Cheng, H. Cong, Properties of Electropolymerized Dopamine and Its Analogues, Langmuir. 35 (2019) 1119–1125, https://doi.org/10.1021/acs.langmuir.8b01444.

[48] J. Li, B.M. Christensen, Effect of pH on the oxidation pathway of dopamine and dopa, J. Electroanal. Chem. 375 (1994) 219–231, https://doi.org/10.1016/0022-0728(94)03389-7.

[49] S. Daboss, J. Lin, M. Godejohann, C. Kranz, Redox Switchable Polydopamine-Modified AFM-SECM Probes: A Probe for Electrochemical Force Spectroscopy, Anal. Chem. 92 (2020) 8404–8413, https://doi.org/10.1021/acs.analchem.0c00995.

[50] G. Xu, J. Hou, Y. Zhao, J. Bao, M. Yang, H. Fa, Y. Yang, L. Li, D. Huo, C. Hou, Dual-signal aptamer sensor based on polydopamine-gold nanoparticles and exonuclease I for ultrasensitive malathion detection, Sensors Actuators, B Chem. 287 (2019) 428–436, https://doi.org/10.1016/j.snb.2019.01.113.

[51] L. Li, Z. Xu, W. Sun, J. Chen, C. Dai, B. Yan, H. Zeng, Bio-inspired membrane with adaptable wettability for smart oil/water separation, J. Memb. Sci. 598 (2020), 117661, https://doi.org/10.1016/j.memsci.2019.117661.

[52] M. Amiri, E. Amali, A. Nematollahzadeh, H. Salehniya, Poly-dopamine films: Voltammetric sensor for pH monitoring, Sensors Actuators, B Chem. 228 (2016) 53–58, https://doi.org/10.1016/j.snb.2016.01.012.

[53] M. Amiri, E. Amali, A. Nematollahzadeh, Poly-dopamine thin film for voltammetric sensing of atenolol, Sensors Actuators, B Chem. 216 (2015) 551–557, https://doi.org/10.1016/j.snb.2015.04.082.

[54] P.R. Unwin, J. V. Macpherson, Localized flux measurements and kinetic imaging at interfaces, in: Scanning Electrochem. Microsc. Second Ed., 2012: pp. 417–450. 10.1201/b11850.

[55] D. Mandler, A.J. Bard, A New Approach to the High Resolution Electrodeposition of Metals via the Feedback Mode of the Scanning Electrochemical Microscope, J. Electrochem. Soc. 137 (4) (1990) 1079–1086.

[56] C. Kranz, M. Ludwig, H.E. Gaub, W. Schuhmann, Lateral deposition of polypyrrole lines by means of the scanning electrochemical microscope, Adv. Mater. 7 (1995) 38–40, https://doi.org/10.1002/adma.19950070106.

[57] J. Lin, S. Daboss, D. Blaimer, C. Kranz, Micro-structured polydopamine films via pulsed electrochemical deposition, Nanomaterials. 9 (2019) 242, https://doi.org/10.3390/nano9020242.

[58] C. Xie, X. Lu, K. Wang, H. Yuan, L. Fang, X. Zheng, C. Chan, F. Ren, C. Zhao, Pulse Electrochemical Driven Rapid Layer-by-Layer Assembly of Polydopamine and Hydroxyapatite Nanofilms via Alternative Redox in Situ Synthesis for Bone Regeneration, ACS Biomater. Sci. Eng. 2 (2016) 920–928, https://doi.org/10.1021/acsbiomaterials.6b00015.

[59] A.E. Sánchez-Rivera, S. Corona-Avendaño, G. Alarcón-Angeles, A. Rojas-Hernández, M.T. Ramírez-Silva, M.A. Romero-Romo, Spectrophotometric study on the stability of dopamine and the determination of its acidity constants, Spectrochim, Acta Part A Mol. Biomol. Spectrosc. 59 (2003) 3193–3203, https://doi.org/10.1016/S1386-1425(03)00138-0.

[60] S. Schindler, T. Bechtold, Mechanistic insights into the electrochemical oxidation of dopamine by cyclic voltammetry, J. Electroanal. Chem. 836 (2019) 94–101, https://doi.org/10.1016/J.JELECHEM.2019.01.069.

[61] S. Corona-Avendaño, G. Alarcón-Angeles, M.T. Ramírez-Silva, G. Rosquete-Pina, M. Romero-Romo, M. Palomar-Pardavé, On the electrochemistry of dopamine in aqueous solution. Part I: The role of [SDS] on the voltammetric behavior of dopamine on a carbon paste electrode, J. Electroanal. Chem. 609 (2007) 17–26, https://doi.org/10.1016/J.JELECHEM.2007.05.021.

[62] F. Zhang, G. Dryhurst, Oxidation Chemistry of Dopamine: Possible Insights into the Age-Dependent Loss of Dopaminergic Nigrostriatal Neurons, Bioorg. Chem. 21 (1993) 392–410, https://doi.org/10.1006/BIOO.1993.1033.

[63] J. Yang, M.A.C. Stuart, M. Kamperman, Jack of all trades: versatile catechol crosslinking mechanisms, Chem. Soc. Rev. 43 (2014) 8271–8298, https://doi.org/10.1039/C4CS00185K.

[64] S. Corona-Avendaño, G. Alarcón-Angeles, G.A. Rosquete-Pina, A. Rojas-Hernández, A. Gutierrez, M.T. Ramírez-Silva, M. Romero-Romo, M. Palomar-Pardavé, New Insights on the Nature of the Chemical Species Involved during the Process of Dopamine Deprotonation in Aqueous Solution: Theoretical and Experimental Study, J. Phys. Chem. B 111 (7) (2007) 1640–1647.

[65] J. Liebscher, R. Mrówczyński, H.A. Scheidt, C. Filip, N.D. Haìdade, R. Turcu, A. Bende, S. Beck, Structure of polydopamine: A never-ending story? Langmuir. 29 (2013) 10539–10548, https://doi.org/10.1021/la4020288.

[66] E. Herlinger, R.F. Jameson, W. Linert, Spontaneous autoxidation of dopamine, J. Chem. Soc. Perkin Trans. 2 (1995) 259–263, https://doi.org/10.1039/P29950000259.

[67] Q. Wei, F. Zhang, J. Li, B. Li, C. Zhao, Oxidant -induced dopamine polymerization for multifunctional coatings, Polym. Chem. 1 (2010) 1430–1433, https://doi.org/10.1039/C0PY00215A.

[68] D.R. Dreyer, D.J. Miller, B.D. Freeman, D.R. Paul, C.W. Bielawski, Elucidating the structure of poly(dopamine), Langmuir. 28 (2012) 6428–6435, https://doi.org/10.1021/la204831b.

[69] N. Umek, B. Geršak, N. Vintar, M. Šoštarič, J. Mavri, Dopamine Autoxidation Is Controlled by Acidic pH, Front. Mol. Neurosci. (2018) 467, https://doi.org/10.3389/FNMOL.2018.00467.

[70] R.P. Bacil, L. Chen, S.H.P. Serrano, R.G. Compton, Dopamine oxidation at gold electrodes: mechanism and kinetics near neutral pH, Phys. Chem. Chem. Phys. 22 (2020) 607–614, https://doi.org/10.1039/C9CP05527D.

[71] M. Ates, Review study of electrochemical impedance spectroscopy and equivalent electrical circuits of conducting polymers on carbon surfaces, Prog. Org. Coatings. 71 (2011) 1–10, https://doi.org/10.1016/j.porgcoat.2010.12.011.

[72] S. Themsirimongkon, K. Ounnunkad, S. Saipanya, Electrocatalytic enhancement of platinum and palladium metal on polydopamine reduced graphene oxide support for alcohol oxidation, J. Colloid Interface Sci. 530 (2018) 98–112, https://doi.org/10.1016/J.JCIS.2018.06.072.

[73] V. Ball, D. Del Frari, V. Toniazzo, D. Ruch, Kinetics of polydopamine film deposition as a function of pH and dopamine concentration: Insights in the polydopamine deposition mechanism, J. Colloid Interface Sci. 386 (2012) 366–372, https://doi.org/10.1016/J.JCIS.2012.07.030.

[74] F. Bernsmann, J.C. Voegel, V. Ball, Different synthesis methods allow to tune the permeability and permselectivity of dopamine–melanin films to electrochemical probes, Electrochim. Acta. 56 (2011) 3914–3919, https://doi.org/10.1016/J.ELECTACTA.2011.02.028.

[75] J. Yang, L. Niu, Z. Zhang, J. Zhao, L. Chou, Electrochemical Behavior of a Polydopamine Nanofilm, Anal. Lett. 48 (2015) 2031–2039, https://doi.org/10.1080/00032719.2015.1010120.

[76] J. Bisquert, G. Garcia-Belmonte, P. Bueno, E. Longo, L.O.S. Bulhões, Impedance of constant phase element (CPE)-blocked diffusion in film electrodes, J. Electroanal. Chem. 452 (1998) 229–234, https://doi.org/10.1016/S0022-0728(98)00115-6.

[77] F. Yu, S. Chen, Y. Chen, H. Li, L. Yang, Y. Chen, Y. Yin, Experimental and theoretical analysis of polymerization reaction process on the polydopamine membranes and its corrosion protection properties for 304 Stainless Steel, J. Mol. Struct. 982 (2010) 152–161, https://doi.org/10.1016/J.MOLSTRUC.2010.08.021.

[78] W. Schwenk, Theory Of Stainless Steel Pitting, Corrosion. 20 (1964) 129–137, https://doi.org/10.5006/0010-9312-20.4.129t.

[79] W. Tian, N. Du, S. Li, S. Chen, Q. Wu, Metastable pitting corrosion of 304 stainless steel in 3.5% NaCl solution, Corros. Sci. 85 (2014) 372–379, https://doi.org/10.1016/J.CORSCI.2014.04.033.

[80] Y. Tsutsumi, A. Nishikata, T. Tsuru, Pitting corrosion mechanism of Type 304 stainless steel under a droplet of chloride solutions, Corros. Sci. 49 (2007) 1394–1407, https://doi.org/10.1016/J.CORSCI.2006.08.016.

[81] P. Meredith, T. Sarna, The physical and chemical properties of eumelanin, Pigment Cell Res. 19 (2006) 572–594, https://doi.org/10.1111/j.1600-0749.2006.00345.x.

[82] S. Hong, C.F. Schaber, K. Dening, E. Appel, S.N. Gorb, H. Lee, Air/water interfacial formation of freestanding, stimuli-responsive, self-healing catecholamine janus-faced microfilms, Adv. Mater. 26 (2014) 7581–7587, https://doi.org/10.1002/adma.201403259.

[83] F. Ponzio, V. Ball, Polydopamine deposition at fluid interfaces, Polym. Int. 65 (2016) 1251–1257, https://doi.org/10.1002/pi.5124.

[84] X. Han, F. Tang, Z. Jin, Free-standing polydopamine films generated in the presence of different metallic ions: The comparison of reaction process and film properties, RSC Adv. 8 (2018) 18347–18354, https://doi.org/10.1039/c8ra02930j.

[85] O.Y. Milyaeva, A.G. Bykov, R.A. Campbell, G. Loglio, R. Miller, B.A. Noskov, Polydopamine layer formation at the liquid – gas interface, Colloids Surfaces A Physicochem. Eng. Asp. 579 (2019), 123637, https://doi.org/10.1016/j.colsurfa.2019.123637.

[86] O.Y. Milyaeva, A.G. Bykov, R.A. Campbell, G. Loglio, R. Miller, B.A. Noskov, The dynamic properties of PDA-laccase films at the air-water interface, Colloids Surfaces A Physicochem. Eng. Asp. 599 (2020), 124930, https://doi.org/10.1016/j.colsurfa.2020.124930.

[87] E. Coy, I. Iatsunskyi, J.C. Colmenares, Y. Kim, R. Mrówczyński, Polydopamine Films with 2D-like Layered Structure and High Mechanical Resilience, ACS Appl. Mater. Interfaces. 13 (2021) 23113–23120, https://doi.org/10.1021/acsami.1c02483.

[88] J. Szewczyk, M. Pochylski, K. Szutkowski, M. Kempiński, R. Mrówczyński, I. Iatsunskyi, J. Gapiński, E. Coy, In-situ thickness control of centimetre-scale 2D-Like polydopamine films with large scalability, Mater. Today Chem. 24 (2022) 100935, https://doi.org/10.1016/j.mtchem.2022.100935.

[89] T. Marchesi D'Alvise, S. Harvey, L. Hueske, J. Szelwicka, L. Veith, T.P.J. Knowles, D. Kubiczek, C. Flaig, F. Port, K. Gottschalk, F. Rosenau, B. Graczykowski, G. Fytas, F.S. Ruggeri, K. Wunderlich, T. Weil, Ultrathin Polydopamine Films with Phospholipid Nanodiscs Containing a Glycophorin A Domain, Adv. Funct. Mater. 30 (2020) 2000378, https://doi.org/10.1002/adfm.202000378.

[90] X. Geng, J. Wang, J. Ye, S. Yang, Q. Han, H. Lin, F. Liu, Electrosprayed polydopamine membrane: Surface morphology, chemical stability and separation performance study, Sep. Purif. Technol. 244 (2020) 116857, https://doi.org/10.1016/j.seppur.2020.116857.

[91] T. Vasileiadis, T. Marchesi D'Alvise, C.-M. Saak, M. Pochylski, S. Harvey, C. V. Synatschke, J. Gapinski, G. Fytas, E.H.G. Backus, T. Weil, B. Graczykowski,

Fast Light-Driven Motion of Polydopamine Nanomembranes, Nano Lett. 22 (2021) 578–585, https://doi.org/10.1021/acs.nanolett.1c03165.
[92] A. Olejnik, M. Ficek, K. Siuzdak, R. Bogdanowicz, Multi-pathway mechanism of polydopamine film formation at vertically aligned diamondised boron-doped carbon nanowalls, Electrochim. Acta. 409 (2022) 140000, https://doi.org/10.1016/j.electacta.2022.140000.
[93] V.B. Shah, P. Biswas, Aerosolized droplet mediated self-assembly of photosynthetic pigment analogues and deposition onto substrates, ACS Nano. 8 (2014) 1429–1438, https://doi.org/10.1021/nn405251h.
[94] J. Wang, X. Pei, G. Liu, Q. Han, S. Yang, F. Liu, "Living" electrospray – A controllable polydopamine nano-coating strategy with zero liquid discharge for separation, J. Memb. Sci. 586 (2019) 170–176, https://doi.org/10.1016/j.memsci.2019.05.071.
[95] S. Dushman, A theory of chemical reactivity. Calculation of rates of reactions and equilibrium constants, J. Am. Chem. Soc. 43 (1921) 397–433, https://doi.org/10.1021/ja01436a003.
[96] W. Xie, Y. Shi, Y. Wang, Y. Zheng, H. Liu, Q. Hu, S. Wei, H. Gu, Z. Guo, Electrospun iron/cobalt alloy nanoparticles on carbon nanofibers towards exhaustive electrocatalytic degradation of tetracycline in wastewater, Chem. Eng. J. 405 (2021) 126585, https://doi.org/10.1016/j.cej.2020.126585.
[97] L. Liverani, A.R. Boccaccini, Versatile production of poly(Epsilon-caprolactone) fibers by electrospinning using benign solvents, Nanomaterials. 6 (2016) 75, https://doi.org/10.3390/nano6040075.
[98] Y. Jia, X. Yue, Y. Wang, C. Yan, G. Zheng, K. Dai, C. Liu, C. Shen, Multifunctional stretchable strain sensor based on polydopamine/ reduced graphene oxide/ electrospun thermoplastic polyurethane fibrous mats for human motion detection and environment monitoring, Compos. Part B Eng. 183 (2020) 107696, https://doi.org/10.1016/j.compositesb.2019.107696.
[99] J. Yan, Y. Huang, Y.E. Miao, W.W. Tjiu, T. Liu, Polydopamine-coated electrospun poly(vinyl alcohol)/poly(acrylic acid) membranes as efficient dye adsorbent with good recyclability, J. Hazard. Mater. 283 (2015) 730–739, https://doi.org/10.1016/j.jhazmat.2014.10.040.
[100] C. Wang, J. Yin, R. Wang, T. Jiao, H. Huang, J. Zhou, L. Zhang, Q. Peng, Facile preparation of self-assembled polydopamine-modified electrospun fibers for highly effective removal of organic dyes, Nanomaterials. 9 (2019) 116, https://doi.org/10.3390/nano9010116.
[101] N.G. Rim, S.J. Kim, Y.M. Shin, I. Jun, D.W. Lim, J.H. Park, H. Shin, Mussel-inspired surface modification of poly(l-lactide) electrospun fibers for modulation of osteogenic differentiation of human mesenchymal stem cells, Colloids Surfaces B Biointerfaces. 91 (2012) 189–197, https://doi.org/10.1016/j.colsurfb.2011.10.057.
[102] X. Yang, Y. Zhou, Z. Sun, C. Yang, D. Tang, Synthesis and Cr adsorption of a super-hydrophilic polydopamine-functionalized electrospun polyacrylonitrile, Environ. Chem. Lett. 19 (2021) 743–749, https://doi.org/10.1007/s10311-020-01086-7.
[103] Y. Fu, L. Liu, L. Zhang, W. Wang, Highly conductive one-dimensional nanofibers: Silvered electrospun silica nanofibers via poly(dopamine) functionalization, ACS Appl. Mater. Interfaces. 6 (2014) 5105–5112, https://doi.org/10.1021/am5002663.
[104] L. Wang, R.J. Mu, Y. Yuan, J. Gong, Y. Ni, W. Wang, J. Pang, Novel nanofiber membrane fabrication from konjac glucomannan and polydopamine via electrospinning method, J. Sol-Gel Sci. Technol. 85 (2018) 253–258, https://doi.org/10.1007/s10971-017-4559-9.
[105] Y. Deng, T. Lu, J. Cui, S. Keshari Samal, R. Xiong, C. Huang, Bio-based electrospun nanofiber as building blocks for a novel eco-friendly air filtration membrane: A Review, Sep. Purif. Technol. (2021) 119623, https://doi.org/10.1016/J.SEPPUR.2021.119623.
[106] M. Fouladgar, Application of ZnO Nanoparticle/Ion Liquid Modified Carbon Paste Electrode for Determination of Isoproterenol in Pharmaceutical and Biological Samples, J. Electrochem. Soc. 163 (2016) 38–42, https://doi.org/10.1149/2.0611603jes.
[107] S. Negahban, M. Fouladgar, G. Amiri, Improve the performance of carbon paste electrodes for determination of dobutamine using MnZnFe2O4 nanoparticles and ionic liquid, J. Taiwan Inst. Chem. Eng. 78 (2017) 51–55, https://doi.org/10.1016/j.jtice.2017.05.032.
[108] P. Naderi Asrami, P. Aberoomand Azar, M. Saber Tehrani, S.A. Mozaffari, Glucose Oxidase/Nano-ZnO/Thin Film Deposit FTO as an Innovative Clinical Transducer: A Sensitive Glucose Biosensor, Front. Chem. 8 (2020) 503, https://doi.org/10.3389/fchem.2020.00503.
[109] J. Chen, Q. Yu, X. Cui, M. Dong, J. Zhang, C. Wang, J. Fan, Y. Zhu, Z. Guo, An overview of stretchable strain sensors from conductive polymer nanocomposites, J. Mater. Chem. C. 7 (2019) 11710–11730, https://doi.org/10.1039/c9tc03655e.
[110] Q. Li, H. Liu, S. Zhang, D. Zhang, X. Liu, Y. He, L. Mi, J. Zhang, C. Liu, C. Shen, Z. Guo, Superhydrophobic Electrically Conductive Paper for Ultrasensitive Strain Sensor with Excellent Anticorrosion and Self-Cleaning Property, ACS Appl. Mater. Interfaces. 11 (2019) 21904–21914, https://doi.org/10.1021/acsami.9b03421.
[111] X. Liu, J. Cao, H. Li, J. Li, Q. Jin, K. Ren, J. Ji, Mussel-inspired polydopamine: A biocompatible and ultrastable coating for nanoparticles in vivo, ACS Nano. 7 (2013) 9384–9395, https://doi.org/10.1021/nn404117j.
[112] G. Wang, J. Zhang, S. Lin, H. Xiao, Q. Yang, S. Chen, B. Yan, Y. Gu, Environmentally friendly nanocomposites based on cellulose nanocrystals and polydopamine for rapid removal of organic dyes in aqueous solution, Cellulose. 27 (2020) 2085–2097, https://doi.org/10.1007/s10570-019-02944-6.
[113] G. Hong, H. Cheng, Y. Meng, J. Lin, Z. Chen, S. Zhang, W. Song, Mussel-inspired polydopamine as a green, efficient, and stable platform to functionalize bamboo fiber with amino-terminated alkyl for high performance poly(butylene succinate) composites, Polymers (Basel). 10 (2018) 461, https://doi.org/10.3390/polym10040461.
[114] Q. Du, J. An, J. Li, L. Zhou, N. Li, X. Wang, Polydopamine as a new modification material to accelerate startup and promote anode performance in microbial fuel cells, J. Power Sources. 343 (2017) 477–482, https://doi.org/10.1016/j.jpowsour.2017.01.093.
[115] H. Guo, Y. Deng, Z. Tao, Z. Yao, J. Wang, C. Lin, T. Zhang, B. Zhu, C.Y. Tang, Does Hydrophilic Polydopamine Coating Enhance Membrane Rejection of Hydrophobic Endocrine-Disrupting Compounds? Environ. Sci. Technol. Lett. 3 (2016) 332–338, https://doi.org/10.1021/acs.estlett.6b00263.
[116] L. Li, L. Yang, Y. Liao, H. Yu, Z. Liang, B. Zhang, X. Lan, R. Luo, Y. Wang, Superhydrophilic versus normal polydopamine coating: A superior and robust platform for synergistic antibacterial and antithrombotic properties, Chem. Eng. J. 402 (2020) 126196, https://doi.org/10.1016/j.cej.2020.126196.
[117] T. Wang, Wusigale, D. Kuttappan, M.A. Amalaradjou, Y. Luo, Y. Luo, Luo, Polydopamine-coated chitosan hydrogel beads for synthesis and immobilization of silver nanoparticles to simultaneously enhance antimicrobial activity and adsorption kinetics, Adv. Compos. Hybrid Mater. 4 (3) (2021) 696–706.
[118] Y. Qian, Y. Yuan, H. Wang, H. Liu, J. Zhang, S. Shi, Z. Guo, N. Wang, Highly efficient uranium adsorption by salicylaldoxime/polydopamine graphene oxide nanocomposites, J. Mater. Chem. A. 6 (2018) 24676–24685, https://doi.org/10.1039/C8TA09486A.
[119] H. Gu, X. Xu, M. Dong, P. Xie, Q. Shao, R. Fan, C. Liu, S. Wu, R. Wei, Z. Guo, Carbon nanospheres induced high negative permittivity in nanosilver-polydopamine metacomposites, Carbon N. Y. 147 (2019) 550–558, https://doi.org/10.1016/j.carbon.2019.03.028.
[120] S. Palanisamy, B. Thirumalraj, S.M. Chen, Y.T. Wang, V. Velusamy, S.K. Ramaraj, A Facile Electrochemical Preparation of Reduced Graphene Oxide@Polydopamine Composite: A Novel Electrochemical Sensing Platform for Amperometric Detection of Chlorpromazine, Sci. Rep. 6 (2016) 33599, https://doi.org/10.1038/srep33599.
[121] S. Tursynbolat, Y. Bakytkarim, J. Huang, L. Wang, Ultrasensitive electrochemical determination of metronidazole based on polydopamine/carboxylic multi-walled carbon nanotubes nanocomposites modified GCE, J. Pharm. Anal. 8 (2018) 124–130, https://doi.org/10.1016/J.JPHA.2017.11.001.
[122] C. Karuppiah, K. Venkatesh, L.F. Hsu, P. Arunachalam, C.C. Yang, S.K. Ramaraj, R.J. Ramalingam, S. Arokiyaraj, H.A. Al-Lohedan, An improving aqueous dispersion of polydopamine functionalized vapor grown carbon fiber for the effective sensing electrode fabrication to chloramphenicol drug detection in food samples, Microchem. J. 170 (2021) 106675, https://doi.org/10.1016/j.microc.2021.106675.
[123] T. Rohani, S.Z. Mohammadi, N. Gholamhosein Zadeh, M.B. Askari, A novel carbon ceramic electrode modified by Fe3O4 magnetic nanoparticles coated with aptamer-immobilized polydopamine: An effective label-free aptasensor for sensitive detection of diclofenac, Microchem. J. 166 (2021) 106274, https://doi.org/10.1016/j.microc.2021.106274.
[124] M. Shahbakhsh, S. Narouie, M. Noroozifar, Modified glassy carbon electrode with Polydopamine-multiwalled carbon nanotubes for simultaneous electrochemical determination of biocompounds in biological fluids, J. Pharm. Biomed. Anal. 161 (2018) 66–72, https://doi.org/10.1016/j.jpba.2018.08.034.
[125] T. Feng, W. Ji, Y. Zhang, F. Wu, Q. Tang, H. Wei, L. Mao, M. Zhang, Zwitterionic Polydopamine Engineered Interface for In Vivo Sensing with High Biocompatibility, Angew. Chemie - Int. Ed. 59 (2020) 23445–23449, https://doi.org/10.1002/anie.202010675.
[126] C. Wang, J. Li, K. Shi, Q. Wang, X. Zhao, Z. Xiong, X. Zou, Y. Wang, Graphene coated by polydopamine/multi-walled carbon nanotubes modified electrode for highly selective detection of dopamine and uric acid in the presence of ascorbic acid, J. Electroanal. Chem. 770 (2016) 56–61, https://doi.org/10.1016/j.jelechem.2016.03.038.
[127] J. Liu, Y. Shang, J. Xu, Y. Chen, Y. Jia, J. Zheng, A novel electrochemical immunosensor for carcinoembryonic antigen based on Cu-MOFs-TB/polydopamine nanocarrier, J. Electroanal. Chem. 877 (2020) 114563, https://doi.org/10.1016/j.jelechem.2020.114563.
[128] Z. Xu, R. Han, N. Liu, F. Gao, X. Luo, Electrochemical biosensors for the detection of carcinoembryonic antigen with low fouling and high sensitivity based on copolymerized polydopamine and zwitterionic polymer, Sensors Actuators, B Chem. 319 (2020) 128253, https://doi.org/10.1016/j.snb.2020.128253.
[129] X.Y. Wang, Y.G. Feng, A.J. Wang, L.P. Mei, P.X. Yuan, X. Luo, J.J. Feng, A facile ratiometric electrochemical strategy for ultrasensitive monitoring HER2 using polydopamine-grafted-ferrocene/reduced graphene oxide, Au@Ag nanoshuttles and hollow Ni@PtNi yolk-shell nanocages, Sensors Actuators, B Chem. 331 (2021) 129460, https://doi.org/10.1016/j.snb.2021.129460.
[130] C. Ss, K.T. Chen, A.F.J.J. Chen, Polydopamine-gold composite-based electrochemical biosensor using dual-amplification strategy for detecting pancreatic cancer-associated microRNA, Biosens. Bioelectron. 173 (2021) 112815, https://doi.org/10.1016/j.bios.2020.112815.
[131] Q. Song, M. Li, L. Huang, Q. Wu, Y. Zhou, Y. Wang, Bifunctional polydopamine@Fe3O4 core-shell nanoparticles for electrochemical determination of lead(II) and cadmium(II), Anal. Chim. Acta. 787 (2013) 64–70, https://doi.org/10.1016/j.aca.2013.06.010.
[132] X. Jiang, P. Wang, R. Liang, W. Qin, Improving the Biocompatibility of Polymeric Membrane Potentiometric Ion Sensors by Using a Mussel-Inspired Polydopamine Coating, Anal. Chem. 91 (2019) 6424–6429, https://doi.org/10.1021/acs.analchem.9b00039.
[133] B. Li, J. Luo, X. Huang, L. Lin, L. Wang, M. Hu, L. Tang, H. Xue, J. Gao, Y.W. Mai, A highly stretchable, super-hydrophobic strain sensor based on polydopamine

and graphene reinforced nanofiber composite for human motion monitoring, Compos. Part B Eng. 181 (2020) 107580, https://doi.org/10.1016/j.compositesb.2019.107580.
[134] M. Qu, Y. Qin, Y. Sun, H. Xu, D.W. Schubert, K. Zheng, W. Xu, F. Nilsson, Biocompatible, Flexible Strain Sensor Fabricated with Polydopamine-Coated Nanocomposites of Nitrile Rubber and Carbon Black, ACS Appl. Mater. Interfaces. 12 (2020) 42140–42152, https://doi.org/10.1021/acsami.0c11937.
[135] L. Han, M. Liu, B. Yan, Y.S. Li, J. Lan, L. Shi, R. Ran, Polydopamine/polystyrene nanocomposite double-layer strain sensor hydrogel with mechanical, self-healing, adhesive and conductive properties, Mater. Sci. Eng. C. 109 (2020) 110567, https://doi.org/10.1016/j.msec.2019.110567.
[136] J. Miao, A. Liu, L. Wu, M. Yu, W. Wei, S. Liu, Magnetic ferroferric oxide and polydopamine molecularly imprinted polymer nanocomposites based electrochemical impedance sensor for the selective separation and sensitive determination of dichlorodiphenyltrichloroethane (DDT), Anal. Chim. Acta. 1095 (2020) 82–92, https://doi.org/10.1016/j.aca.2019.10.027.
[137] Y. Wu, L. Jiao, W. Xu, W. Gu, C. Zhu, D. Du, Y. Lin, Polydopamine-Capped Bimetallic AuPt Hydrogels Enable Robust Biosensor for Organophosphorus Pesticide Detection, Small. 15 (2019) 632, https://doi.org/10.1002/smll.201900632.
[138] A.A. Ensafi, E. Heydari, Determination of some phenothiazines compounds in pharmaceuticals and human body fluid by electrocatalytic oxidation at a glassy carbon electrode using methylene blue as a mediator, Anal. Lett. 41 (2008) 2487–2502, https://doi.org/10.1080/00032710802352555.
[139] N. Sebastian, W.C. Yu, Y.C. Hu, D. Balram, Y.H. Yu, Sonochemical synthesis of iron-graphene oxide/honeycomb-like ZnO ternary nanohybrids for sensitive electrochemical detection of antipsychotic drug chlorpromazine, Ultrason. Sonochem. 59 (2019) 104696, https://doi.org/10.1016/j.ultsonch.2019.104696.
[140] H. Musarurwa, N. Tawanda Tavengwa, Extraction and electrochemical sensing of pesticides in food and environmental samples by use of polydopamine-based materials, Chemosphere. 266 (2021) 129222. 10.1016/j.chemosphere.2020.129222.
[141] C. Chen, J. Shi, Y. Guo, L. Zha, L. Lan, Y. Chang, Y. Ding, A novel aptasensor for malathion blood samples detection based on DNA-silver nanocluster, Anal. Methods. 10 (2018) 1928–1934, https://doi.org/10.1039/c8ay00428e.
[142] M. Zhang, P. Yu, L. Mao, Rational design of surface/interface chemistry for quantitative in vivo monitoring of brain chemistry, Acc. Chem. Res. 45 (2012) 533–543, https://doi.org/10.1021/ar200196h.
[143] C.L. Sawyers, The cancer biomarker problem, Nature. 452 (2008) 548–552, https://doi.org/10.1038/nature06913.
[144] E. Zdrachek, E. Bakker, Potentiometric Sensing, Anal. Chem. 91 (2019) 2–26, https://doi.org/10.1021/acs.analchem.8b04681.
[145] K.N. Ekdahl, J.D. Lambris, H. Elwing, D. Ricklin, P.H. Nilsson, Y. Teramura, I. A. Nicholls, B. Nilsson, Innate immunity activation on biomaterial surfaces: A mechanistic model and coping strategies, Adv. Drug Deliv. Rev. 63 (2011) 1042–1050, https://doi.org/10.1016/j.addr.2011.06.012.
[146] X. Huang, K. Qiao, L. Li, G. Liu, X. Xu, R. Lu, H. Gao, D. Xu, Preparation of a magnetic graphene/polydopamine nanocomposite for magnetic dispersive solid-phase extraction of benzoylurea insecticides in environmental water samples, Sci. Rep. 9 (2019) 8919, https://doi.org/10.1038/s41598-019-45186-z.
[147] C. Hu, Y. Zhang, X. Wang, L. Xing, L. Shi, R. Ran, Stable, Strain-Sensitive Conductive Hydrogel with Antifreezing Capability, Remoldability, and Reusability, ACS Appl. Mater. Interfaces. 10 (2018) 44000–44010, https://doi.org/10.1021/acsami.8b15287.
[148] X. Jing, H.Y. Mi, X.F. Peng, L.S. Turng, Biocompatible, self-healing, highly stretchable polyacrylic acid/reduced graphene oxide nanocomposite hydrogel sensors via mussel-inspired chemistry, Carbon N. Y. 136 (2018) 63–72, https://doi.org/10.1016/j.carbon.2018.04.065.
[149] X. Jing, H.Y. Mi, Y.J. Lin, E. Enriquez, X.F. Peng, L.S. Turng, Highly Stretchable and Biocompatible Strain Sensors Based on Mussel-Inspired Super-Adhesive Self-Healing Hydrogels for Human Motion Monitoring, ACS Appl. Mater. Interfaces. 10 (2018), https://doi.org/10.1021/acsami.8b06475.
[150] M. Szukowska, Ł. Popenda, E. Coy, C. Filip, J. Grajewski, M. Kempiński, Y. Kim, R. Mrówczyński, Replacing amine by azide: dopamine azide polymerization triggered by sodium periodate, Polym. Chem. 13 (22) (2022) 3325–3334.

Thesis II - Polydopamine free-standing films from the air/water interface with layered-like structure possess a promise for the purpose of this work because, provided the synthesis process is highly controllable, they can be obtained on a macro scale and exhibit superior mechanical stability.

Thesis II is addressed in the Publications 3-4

Publication 3

The Author's individual contribution to this publication includes: Investigation, Visualization, Methodology, Conceptualization, Validation, Data curation and Writing - Original Draft. Moreover, the author participated in the construction, validation and calibration of a new type of equipment for measurements using the SR method.

Journal: Materials Today Chemistry
ISSN: 2468-5194
Publisher: Elsevier
Journal Impact Factor: 7.3
Publication Date: 12.05.2022
Number of Citations: 9

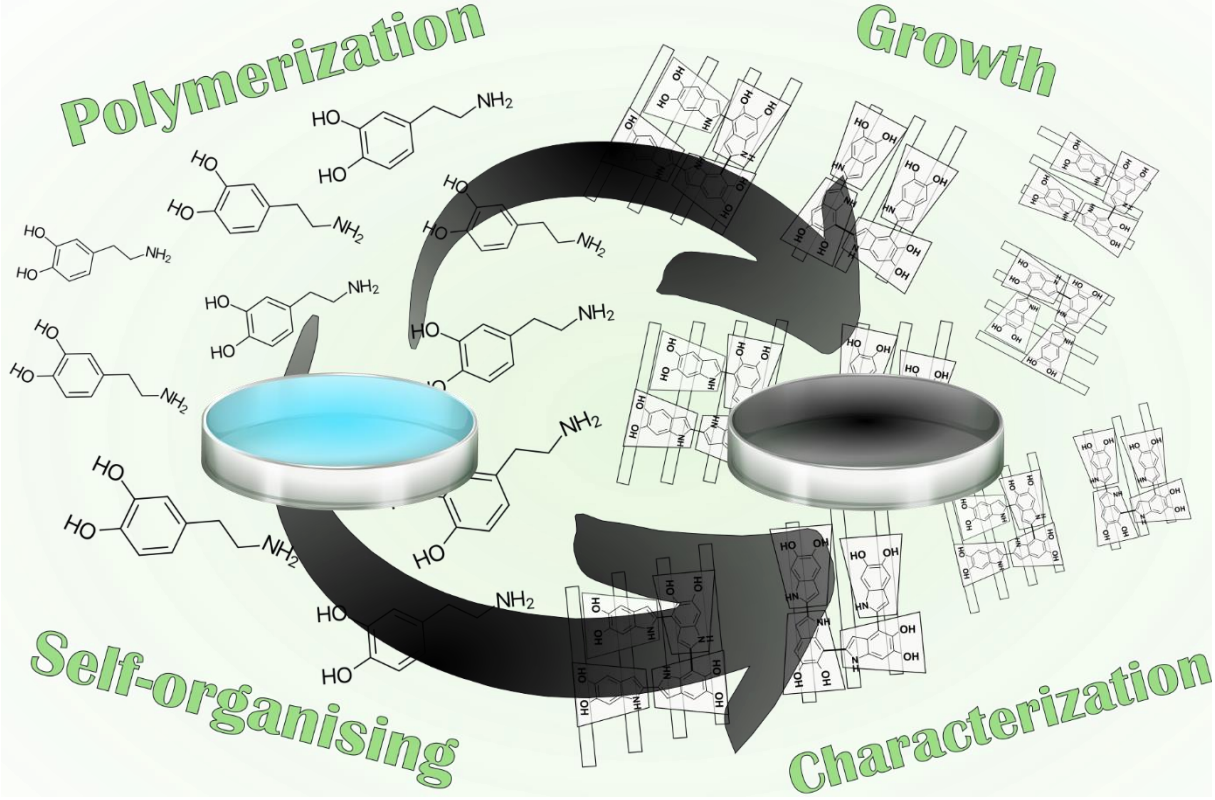

Figure 11. Graphical abstract of the P3

Materials Today Chemistry 24 (2022) 100935

Contents lists available at ScienceDirect

Materials Today Chemistry

journal homepage: www.journals.elsevier.com/materials-today-chemistry/

In-situ thickness control of centimetre-scale 2D-Like polydopamine films with large scalability

J. Szewczyk [a], M. Pochylski [b], K. Szutkowski [a], M. Kempiński [b], R. Mrówczyński [c, d], I. Iatsunskyi [a], J. Gapiński [b], E. Coy [a, *]

[a] NanoBioMedical Centre, Adam Mickiewicz University, Wszechnicy Piastowskiej 3, Poznan, 61-614, Poland
[b] Faculty of Physics, Adam Mickiewicz University, Uniwersytetu Poznańskiego 2, Poznań, 61-614, Poland
[c] Faculty of Chemistry, Adam Mickiewicz University, ul. Uniwersytet Poznańskiego 8, Poznań, 61-614, Poland
[d] Center for Advanced Technologies, Uniwersytetu Poznańskiego 10, Poznań, 61-614, Poland

ARTICLE INFO

Article history:
Received 4 February 2022
Received in revised form
21 March 2022
Accepted 3 April 2022
Available online 12 May 2022

Keywords:
Spectroscopy
Reflectometry
Molecular dynamics
Interface
Optimisation
Dopamine
Oxidation

ABSTRACT

The possible 2D-like arrangement of monomers in polydopamine films obtained by autoxidation of the dopamine at the air/water interface was recently reported. Therefore, the morphological and chemical properties should be controllable by tuning the synthesis conditions. In this work, to optimise the synthesis conditions, films were obtained at the air/water interface with different dopamine concentrations, various pH and stirring speeds. The growth of the films was monitored *in situ* by spectroscopic reflectometry. The obtained films were transferred onto Si(100) substrates, and their morphological parameters were examined by Atomic force microscopy. X-ray diffractometry, Raman spectroscopy, and X-ray photoelectron spectroscopy allowed studying the chemistry of the films. The control of the growth process was achieved at the centimetre-scale level in terms of thickness homogeneity, chemical and structural characteristics of the obtained films. Transfer of the films onto substrates did not affect the homogeneity, foreshadowing an opportunity for large scalability of the process. Structural and chemical studies revealed successful synthesis of a clear 2D-like ordered structure without unreacted dopamine moieties. Finally, molecular dynamics simulations showed a good agreement with the literature information and revealed new insights on the self-assembly process at the air/water interface.

1. Introduction

Since its initial development in 2007 [1], Polydopamine (PDA) has become one of the most famous and well-researched synthetic melanin (specific eumelanin). The interest in replicating and understanding the mussel adhesive properties can be regarded as the primary source of inspiration for the researchers who developed PDA [2]. Further studies focused on dopamine polymerisation processes resulted in preparing a new, biocompatible polymer with strong adhesive properties [3]. Up to date, polydopamine has been applied in many fields, e.g. synthesis of antibacterial materials, preparation of the Li-ions batteries, catalysis [4], corrosion protection [5,6], and biomedicine [7–14]. Moreover, eumelanin has been widely regarded as an amorphous organic semiconductor [15–17]. One of the most important features associated with PDA that have recently been gathering attention is its unexpected photocatalytic performance. This property is observed when combined with semiconductor nanomaterials [18–21]. Polydopamine was used both as an intermediate layer in composites [22,23] and as a direct functional surface coating in catalytic applications [24].

Undoubtedly, one of the most important reasons polydopamine has gained so much attention is its straightforward preparation. PDA can be synthesized by oxidative polymerisation of dopamine hydrochloride (DA) induced by alkaline pH, most often achieved through the use of Tris buffer (tris(hydroxymethyl) aminomethane) [1]. During the auto-oxidation process in solution, three types of polydopamine-based nanomaterials can be obtained, each one of them unique in terms of properties and potential applications. These are films on the air/water (a/w) interface, nanoparticles embedded in the solution, and a thin layer deposited on a substrate immersed in the solution [25,26]. In the oxygen-rich region at the a/w interface, oligomers assemble in an ordered manner through $\pi-\pi$ stacking to form small (2–20 nm) fundamental aggregates

* Corresponding author
E-mail address: coyeme@amu.edu.pl (E. Coy).

https://doi.org/10.1016/j.mtchem.2022.100935

[27]. Due to the removal of these aggregates from the surface by shear stresses, no film formation can be observed in a vigorously stirred dopamine solution, and this effect is even independent of the dopamine concentration and the oxygen supply. On the contrary, using the appropriate static or mild stirring conditions resulted in the formation of nanofilms at the a/w interface. Moreover, to avoid disturbance from convective flows, rapid water evaporation must be avoided during the preparation of homogeneous film [27]. The special properties of the a/w interface as a medium include two main features. First, the water's surface is exceptionally well defined due to its flatness and homogeneity. Secondly, molecules' mobility at the interface is limited to the horizontal plane and therefore, the effective dimensionality of the assembly process is reduced to two dimensions only [28]. In general, interfacial synthesis is promising approach for a thin free-standing films formation, allowing for precise control of the size and thickness of the synthesized thin film. Moreover, the films produced on a liquid surface show substantial motional freedom, due to the flexibility of liquid surfaces [29]. As was found in the literature [30], the formation of PDA thin films at an a/w interface under static conditions showed a linear dependence of the thickness (in the range 50–200 nm) on the concentration of dopamine solution and on the reaction time. Further studies concerned the relationship between the dopamine concentration and the films' mechanical properties (surface elasticity), showing a maximum value of approx. 60 mN/m at a concentration of 1 mg/mL [31]. It was also reported that the humidity level influences the electrical conductivity of these films, as the measured resistance value decreased by more than two orders of magnitude with the humidity increasing in the range from 0% to 100% [32]. One of the ways to improve the PDA film formation efficiency and stability is the use of enzymes. Such films were obtained using laccase, a multicopper containing polyphenol oxidase. The enzymatically tuned films demonstrated higher stability under deformation than the one reported for pure PDA [33,34].

The aforementioned studies focused on the growth process [30], control of physical parameters [33,34] and the general properties of free-standing PDA films [31,32]. Nevertheless, so far, no higher supramolecular ordering has been described in the present films, suggesting a somewhat amorphous nature, with little or no long-range ordering. However, a recently published study shows that PDA films from the a/w interface have a 2D-like structure [35], with clear similarities to graphite or graphene oxide materials. These findings have opened much interest in determining to which extent such 2D-like polymer films could be developed. Moreover, we also described their mechanical properties, indicating a satisfactory Young's modulus ($E = 13 \pm 4$ GPa) and hardness ($H = 0.21 \pm 0.03$ GPa) values, enabling the transfer of these films to substrates of relatively large areas [35]. The PDA films from a/w interface with a highly ordered structure and macroscopic dimensions could find many interesting applications, such as different 2D-like free-standing interfacial films [29]. For example, if the 2D-like supramolecular ordering is present, combining them with other Van der Waals materials (MoS_2, $MoSe_2$, MXenes, among others) is very attractive for many electronic and catalytic applications. Moreover, 2D-like PDA films seem to be promising candidates for the development of the new type of composites, such as the heterojunction between conductive polymers and semiconductors, which have been recently proposed [18]. They can also address an area gaining popularity, namely hybrid 2D–3D architecture materials with a high catalytic activity [36]. Very recently, it was reported that free-standing PDA membranes without any additional mechanical or photothermal components exhibit photoactuation, with the ultrafast response time [37]. Moreover, authors reported contraction and expansion of these membranes driven by heat and moisture. Taking it into account, these materials have potential to be used as multistimuli building blocks for soft micro- and nanodevices [37]. Importantly, in the mentioned study, the membranes were obtained by a more sophisticated-electropolymerization- method. We believe that it is worth exploring the less researched and equally promising path, i.e. autoxidation at the interface. Nevertheless, conclusive evidence of these films' tunability, growth dynamics, physico-chemical aspects and a proper outline of their self-assembly mechanism beyond their structural characterisation needs to be addressed.

In this work, we expand upon the recently reported 2D-like PDA films from the a/w interface and conduct an extensive study in order to answer fundamental questions regarding their formation dynamics and morphology and to increase their application potential. Here we use a combination of spectroscopic, x-ray diffraction and atomic force microscopy techniques, combined with molecular dynamics simulations to shed some light on the growth dynamics and the apparition of the 2D-like structure in the films.

2. Materials and methods

2.1. Chemical reagents

Materials of analytical purity level were used in all synthesis procedures without any further purifications. Dopamine hydrochloride (s, >98%), Trizma® base (s, >99%), Hydrochloric acid (l, 25%) from Sigma-Aldrich and ultrapure deionised water from a Hydrolab Ultra UV system.

2.2. PDA 2D-like films synthesis

The synthesis of films was carried out in a Petri dish (8 cm in diameter, 2 cm in height) containing Tris buffer solution (10 mmol, 65 mL) followed by the addition of dopamine hydrochloride. The size of a Petri dish was chosen to minimize the influence of the meniscus generated, thus change of the profile of the water surface [38]. Another limitation was the maximum travel of the translation stage in the Spectroscopic Reflectometry set-up (see section 2.3). Stirring took place on a magnetic plate throughout the whole synthesis time (72 h), and a glass lid covered the vessel with a small gap to allow air exchange. The goal of the experiment was to optimise synthesis conditions. Therefore, different configurations were examined. The effects of dopamine concentration (2 mg/mL, 1 mg/mL and 0.5 mg/mL), pH value (8.5, 8.0 and 7.5), size of magnetic stirrer (12×4.5 mm and 20×6 mm) and its revolutions per minute (RPM) ratio (300, 250, 200 and 150) were checked. The following conditions were taken as a reference – dopamine concentration 1 mg/mL, pH value 8.0, 150 RPM, and stirrer size equal 12×4.5 mm. Only one of the parameters was modified during each synthesis to investigate their impact on the morphology and structure.

2.3. In-situ *reflectance measurements*

In order to measure the thickness of the growing films without damaging them, a spectroscopic reflectometry (SR) set-up was designed (Fig. 1a).

The white light from a halogen bulb was introduced into multimode fibre through a lens C1. The other end of the fibre served as a quasi-point light source. The light emitted from a fibre was collimated using lens L1 ($f = 160$ mm), and after passing through a 50:50 beam-splitter (BS) was focused onto the sample with a lens L2 ($f = 200$ mm). The mirror M was used to direct the beam perpendicular to the sample surface. The use of lenses L1 and L2 allowed for the illumination of a circular area of the sample with a

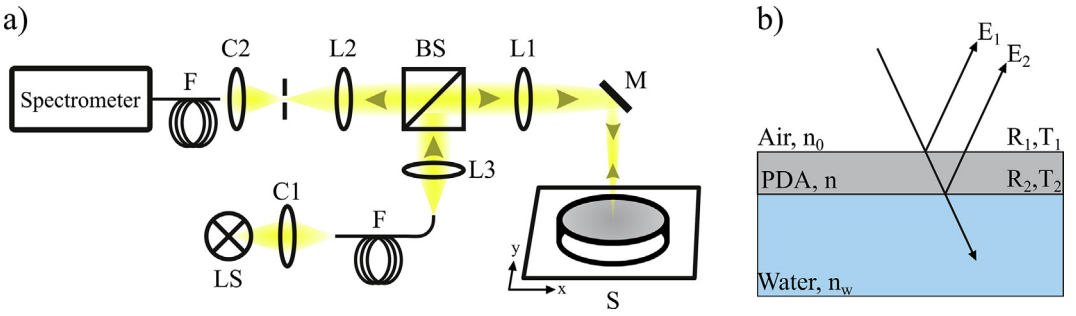

Fig. 1. a) Scheme of the SR set-up. LS is halogen lamp light source, F are fibres, L's are collimating and imaging lenses, C's are fibre coupling lenses, BS is beam-splitter, M is a mirror, A is an aperture, S is the sample on 2D translation stage. **b)** Schematic presentation of the striking and reflected beams for a PDA film on the surface of the water. R_i and T_i are the reflection and transmission coefficients at i-th interface, respectively. E_1 and E_2 denote the electric field values of the beams reflected from the upper and lower surface of the PDA film. Interference of E_1 and E_2 leads to the I_r value of the resultant reflected beam intensity ($I_R = |E_1+E_2|^2$).

diameter of about 1 mm. The light reflected from this area was directed back with mirror M and collected by lens L2. After passing through a beam-splitter, the reflection from the sample was imaged by lens L3 ($f = 120$ mm) on a circular aperture (300 μm), the purpose of which was to eliminate excess background light. The light which passed through the aperture was coupled into the fibre connected with Avantes AvaSpec spectrometer (HSC1024x58TEC-EVO). Recorded spectra can be used to estimate the thickness of the film from the illuminated area. For this purpose, a proper model describing the wavelength dependence of reflected light intensity is required.

We consider a beam of light striking perpendicular on a PDA film of thickness d resting on the surface of the water (Fig. 1b). In the scheme, the inclination of the rays is introduced only for clarity. For a beam perpendicular striking an interface between media 1 and 2 the reflection coefficient is given by Equation 1a, where n_1 and n_2 denote the refractive indices of media 1 and 2, respectively.

$$R = \left(\frac{n_1 - n_2}{n_1 + n_2}\right)^2 \tag{1a}$$

$$R_1 = \left(\frac{n - n_0}{n + n_0}\right)^2 \tag{1b}$$

$$R_2 = \left(\frac{n - n_w}{n + n_w}\right)^2 \tag{1c}$$

$$T_1 = 1 - R_1 \tag{1d}$$

In the case of a PDA film resting on water, reflection coefficients from its upper and lower surfaces are given by Equations 1b and 1c, respectively, where n_0, n_w and n are the refractive indices of air, water and PDA film, respectively. Taking $n_w = 1.33$ [39], $n_0 = 1.0$ and $n = 1.80$ [40], we obtain $R_1 = 0.0816$ and $R_2 = 0.0225$. As the higher-order reflections will be orders of magnitude weaker, it is enough to calculate the interference of the two reflected beams, which is indicated in Fig. 1b. The relative intensity of light reflected from the whole film is given by Equation (2), where d denotes film thickness and λ is the light wavelength.

$$\frac{I_{refl}}{I_0} = R_1 + R_2 T_1^2 \pm 2T_1\sqrt{R_1 R_2}\cos\left(2\pi\frac{2nd}{\lambda}\right) \tag{2}$$

where the sign before the last term depends on the difference $n_{water} - n$. As it is negative in our case, the "−" sign should be taken.

In fact, it is the dependence of I_{refl} on λ that makes the measurement of d possible. Quasi-white light from a halogen bulb, used as a light source, had a working spectral range of 350−1000 nm after passing through all optical components. To extract the actual form of $I_{refl}(\lambda)$, a series of three measurements had to be made: so-called "dark" intensity $I_{dark}(\lambda)$ resulting from readout noise of the detector and ambient light in the lab, the reference spectrum of the light source measured as a reflection from the clean water surface, $I_{water}(\lambda)$, and the actual measurement of the intensity of light reflected from the film $I_{membr}(\lambda)$.

The true reflected intensity $I_{refl}(\lambda) = \frac{I_{membr}(\lambda) - I_{dark}(\lambda)}{I_{water}(\lambda) - I_{dark}(\lambda)}$ and such obtained spectrum was fitted with Equation (2) by adjusting the thickness d and the scaling factor, which accounted for the effect of unknown light absorption. The major feature of the measured curve that allowed for extracting the film thickness was the occurrence of the first minimum of the cosine function. The corresponding maximum in the $I_{refl}(\lambda)$ curve could be found with an accuracy better than 5%. It is important to realise that within the available spectrum range and for the assumed value of $n = 1.80$, film thickness had to exceed 50 nm to produce this maximum at the position of $\lambda_{max} = 4nd$. For thicker films ($d > 100$ nm in our system) multiple extrema are produced in the measured spectrum and d could be estimated with much better accuracy (<1%). As the measurement of d is based on finding the position of λ_{max}, absorption of light by PDA should not disturb this measurement. Therefore, it was not included explicitly in the model and its influence on the amplitude of the cosine function was accounted for by an adjustable scaling factor.

The reference measurement was made each time the experiment was started. For this purpose, a small cut was made mechanically in the film, and the light beam reflected from pure water was recorded. Similarly, the background measurement was performed each time to limit the influence of external factors. Stirring was stopped during optical measurements.

All reflectometric measurements were executed after 72 h of polymerisation, excluding the final measurements of the optimised film, which were executed from time $t = 8$ h to $t = 24$ h in the 1 h intervals and then, after 48 h and 72 h. A Petri dish was placed on a 2-axis translation stage to allow scanning of the film and radial spacing, with an angle of 90°. In preliminary test measurements, full scans of the whole film were performed, and it was found that for the films produced in our set-up an excellent radial symmetry of their thickness was preserved in all cases, results shown comprehend statistics for more than 10 samples, with negligible dispersion. Therefore, for final samples, the scanning was conducted by starting from the centre (0,0) point and moving with a 1 mm step through the dish radius until reaching the curved region close to the border of the dish. The border regions presented a concave shape due to the adhesion forces to the dish wall and evaporation of liquid. The set-up prepared in this way allowed for *in-situ* control of

the thickness growth of the polydopamine film, described in detail in Sections 3.1 - 3.4.

2.4. Physico-chemical characterisation

All structural characterisation studies were performed on the films obtained after 72 h of polymerisation. X-ray diffraction (XRD) and grazing incident X-ray diffraction (GiXRD) characterisation were executed with the use of MRD-X'pert ^{3} diffractometer (PANalytical), working in 45 kV and 40 mA (Cu source). Films were scooped onto clean Silicon (100) wafers substrates, dried and placed in holders designated for XRD measurements. The scheme of the scooping procedure is shown in Fig. S1. Raman studies were performed using a 633 nm laser in backscattering geometry in an NT-MDT (Renishaw) set-up. For Raman spectroscopic measurements, films were scooped onto clean Si/Au substrates, dried and placed in dedicated holders. Park Systems XE7 atomic force microscope was used to evaluate the results obtained by spectroscopic reflectometry and determine the films' roughness. Complementary Gwyddion software was used for general height field and image processing, specifically for the analysis of profilometry data and thickness [41]. After completing the spectroscopic measurement, AFM samples were simply scooped from the film surface onto the silicon Si (100) substrates. The thickness of films was determined from the average of 10 measurements on randomly selected sections crossing the crack in the film on which the substrate was exposed. The roughness was determined from the average of ten measurements of the root mean square (RMS) value in the area of 10 $\times$ 10 μm of the films. X-ray photoelectron spectroscopy (XPS) was performed by a SPECS Surface Nano Analysis GmbH equipped with an Energy analyser PHOIBOS 150 MCD and an Al monochromatic source. The base vacuum was 4 $\times$ 10^{-10} mbars. The PDA samples were transferred to clean silicon wafers and measured without flood gun or sputtering cleaning. Peaks fitting and analysis were performed in CasaXPS while spectra were corrected by the spurious carbon method. High-Resolution Transmission Electron Microscopy (HR-TEM) experiments were performed by a JEOL-ARM200f (200eV) microscope. Samples were prepared by scooping the PDA films on the Holley carbon-Cu, and vacuum drying them overnight.

2.5. Molecular dynamics simulations

Molecular dynamics simulations were performed using Yasara version 21.6.17 [42,43]. The simulations were carried out in an HP GL380 Gen8 server with 32 Intel Xeon cores and the Nvidia Tesla K20 OpenCL/CUDA computing GPU. We divided our simulations into three major parts. First, we wanted to identify the interaction sites for the growing aggregates with planar stacking. The interaction energies and dissociation constants K_d between larger molecular stacks and single tetramer molecules were performed using the VINA docking algorithm [44]. The docking analysis searched for a maximum of 5 receptor sites, and each docking analysis was iterated 32 times. The ligand molecule (single tetramer) was not rigid and was allowed to adopt its conformation. The temperature was set to 298 K, and AMBER03 forcefield was used to calculate interaction energies. After docking, 16 structures were generated with the highest interaction energies (VdW only). The structure with the highest energy score was then used as an input for the subsequent docking of larger stacks (chain-like manner).

In the second, we focused on the interaction of tetramers with the water-air surface. The simulation box was 150 $\times$ 92 $\times$ 116 Å^3 (periodic boundary conditions), in which around 150 tetramer molecules were placed at the water-air interface. The water phase consists of around 28,000 molecule atoms, and the simulation box contained around 93,000 atoms. Naturally, the air interface is simply a vacuum since adding a few nitrogen and oxygen molecules will not change the nature of the interactions at this molecular scale. Simply speaking, at this scale, the simulation of air does not differ much from a vacuum. At this stage of the simulation, we used the AMBER15IPQ force field. The electrostatic interactions were limited to 12 Å (Cut-off), and long-range Coulomb forces were calculated using particle-mesh Ewald summation (PME method). The simulation temperature was set to 298 K, and the simulation step was 1 fs.

The third phase of the simulation included analysing the initially pre-arranged set of 80 tetramer molecules immobilised at the edge of the simulation box of size 103 $\times$ 60 $\times$ 108 Å ^{3}. The periodic boundary conditions were not applied. Therefore pre-ordered tetramer molecules were immobilised directly by the edge of the simulation box, e.g. only the parts within the box are allowed to move and interact, the parts outside of the box are immobilised. In this way, the molecular dynamics of interacting parts of the immobilised tetramer molecule was maintained. The electrostatic interactions cut-off distance was set to 10.5 Å and the water phase was treated as a continuous medium using NOVA2 force field. Given the circumstances, we have minimized the potential problems with the addition of the following tetramer molecules into the water phase in the case of regular simulations. The addition of molecules into the equilibrated water phase poses severe problems in equilibrating the system, and the simulation usually cannot be performed correctly. This way, any new molecule was easily placed within the simulation box without interference with other molecules.

This NOVA2 force field was very successful for protein studies. It uses knowledge-based potentials of interactions with implicit water that accelerates the calculations manifold [45,46]. Having said that tetramer molecule is very similar to the tryptophan molecule Trp (although the precursor for L-Dopa/Dopamine is phenylalanine Phe). In the course of the simulation, a single tetramer molecule was introduced into the simulation box one by one. This way, we wanted to prevent two effects: (1) immediate aggregation of monomers, (2) interaction of an ordered layer with oligomers. We simply introduced single tetramer molecules into the system and then observed how they interact with the pre-ordered layer of tetramers. At this point, it should be noted that the simulations do not take into account the buoyancy force. A lower density than water characterises the ordered layer of tetramers; therefore, it remains on the surface of the liquid, as we showed in the previous publication [35].

3. Results and discussion

As indicated in Fig. 2, the starting point is the film synthesis (see section 2.1 and **2.2**) and *in-situ* thickness growth process control, for which a specially designed apparatus is used (see section 2.3). There are reports about the use of spectroscopic reflectometry (SR) for a thin film thickness measurement [47,48]. However, no such experiment has been carried out so far to investigate the thickness of the polydopamine films, especially those formed at the a/w interface. We show the conditions under which the films obtained are the most homogeneous in terms of thickness, quality and roughness. Subsequently, utilising X-ray diffraction (XRD), X-ray photoelectron (XPS) and Raman Spectroscopy, we confirm the presence of the 2D-like ordering of the structures. Finally, a molecular dynamics (MD) study on the possible self-assembly scenarios leading to the apparition of the structure of the 2D-like PDA films is presented, supporting our experimental observations.

Films were grown and examined *in-situ* using the set-up and methodology presented in the experimental section (see section

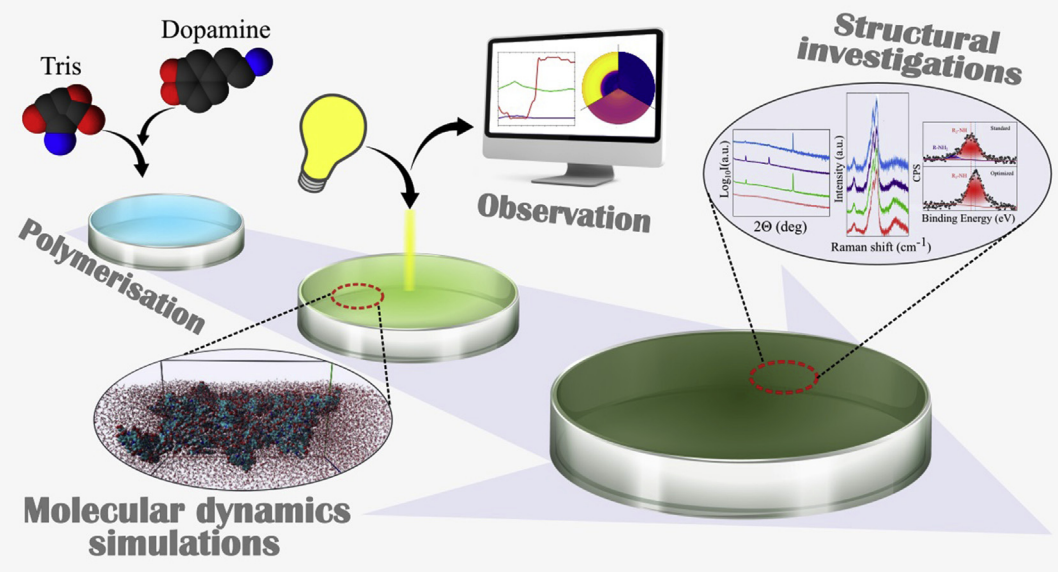

Fig. 2. Scheme of the workflow. We start with the synthesis of a/w films, their growth monitoring by SR method and their further control according to the relevant experimental parameters. Additionally, the growth mechanism and the influence of the a/w in the PDA films' structure is studied by MD simulations.

2.2). In the experiment, a slow increase of film thickness was recorded over the entire surface of the Petri dish over time. This procedure aimed at maintaining the film integrity during its whole growth process, thus avoiding the damage introduced by mechanical taking (scooping) samples if the AFM measurements were to be used. For this purpose, a spectroscopic method based on the interference of incident and reflected beams was applied as a direct and non-destructive technique. Such methods can be applied to determine film thickness on smooth surfaces, taking only the refractive indices of all components as input parameters. Although in general, both transmittance and reflectance measurements can be performed [49], due to our set-up specificity (the solution quickly becoming non-transparent due to the presence of polydopamine nanoparticles and the additional PDA film on the surface of the Petri dish), only the reflectance version was applicable. It is worth noting that the growing undisturbed films had mirror-like properties. Several aspects of the synthesis conditions influence the growth dynamics of the films. In order to control and understand these aspects, we have divided the important parameters into three (3) groups and investigated their influence implausible on the thickness and morphology of the films. A comparative figure of the produced films after 72 h of polymerisation was prepared (Fig. S2).

3.1. The influence of dopamine concentration

The first aspect we investigated was the concentration of dopamine in the Tris buffer solution. In the literature, values ranging between 10 mg/mL and 0.5 mg/mL can be found [27,30,34,35,50,51]. However, the most common value is 2 mg/mL and most of the sources indicate that lower concentrations result in lower thickness and roughness of the PDA. Therefore, in this study, concentrations of 0.5, 1.0 and 2.0 mg/mL were chosen for the experiments. In Fig. 3a, the graph shows the values of the thickness of the films obtained by AFM (box chart) and SR (point graph).

It was found that the films obtained from the lowest dopamine concentration were characterised by a thickness of about 70 ± 12 nm. For higher concentrations, the films were thicker, with a median value around 125 and 160 nm and a mean value around 120 ± 35 and 175 ± 50 nm for 1.0 and 2.0 mg/mL respectively. This observation is consistent with previous reports about the influence of dopamine concentration on film thickness [30,31]. Dopamine is a substrate in the oxidative film formation reaction, and therefore, an increase of film thickness is expected for higher dopamine concentrations. The remarkable similarity of the thicknesses measured with the SR with the AFM results should be emphasised. Fig. S3a summarises the roughness results measured with the AFM, where a surprisingly low value (mean and median around 12 nm) was obtained for the lowest concentration. Relatively low roughness was also obtained for the concentration of 1.0 mg/mL, with 24 and 26 nm for median and mean values, respectively. Simultaneously, the sample obtained using the highest concentration was characterised by high roughness with a median and mean value of 50 ± 15 nm. The plots in Fig. 3b and c were generated only on the basis of SR results. They illustrate the thickness uniformity and thus the quality of the films. Moreover, they show the potential of this method for the *in-situ* observation of films formed at the a/w interface. Fig. 3b shows the film thickness mapping made with a resolution of 1 mm in plane. A clear dependence on molar concentration is visible, suggesting that the increment in dopamine content influences the thickness uniformity of the film. Fig. 3c shows thickness profiles from the centre of the dish outwards across the entire radius. It is important to note that two (2) different regions are distinguishable for all concentrations: one region closer to the centre and one closer to the dish borders (starting around 20 mm from the centre). The latter one is more homogeneous than the central region. For the highest concentration, a step-like variation in thickness of around 100 nm was found on the border region, while for the concentration of 1 mg/mL, the thickness changes by a maximum of 20 nm and only by 5 nm for the lowest concentration. As a partial conclusion, we have shown that the lower the dopamine concentration, the more homogeneous films are grown within the studied concentration range. The reason behind this may be the higher ratio of oxygen to dopamine in the reaction mixture, whose oxygen supply is not hindered by the rapidly growing film observed for higher dopamine concentrations. Although further research is needed, this observation is supported by the strong influence of oxygen on the dopamine oxidation kinetics in aqueous media in solution [52]. The higher O_2 supply results in the increased concentration of the fully conjugated

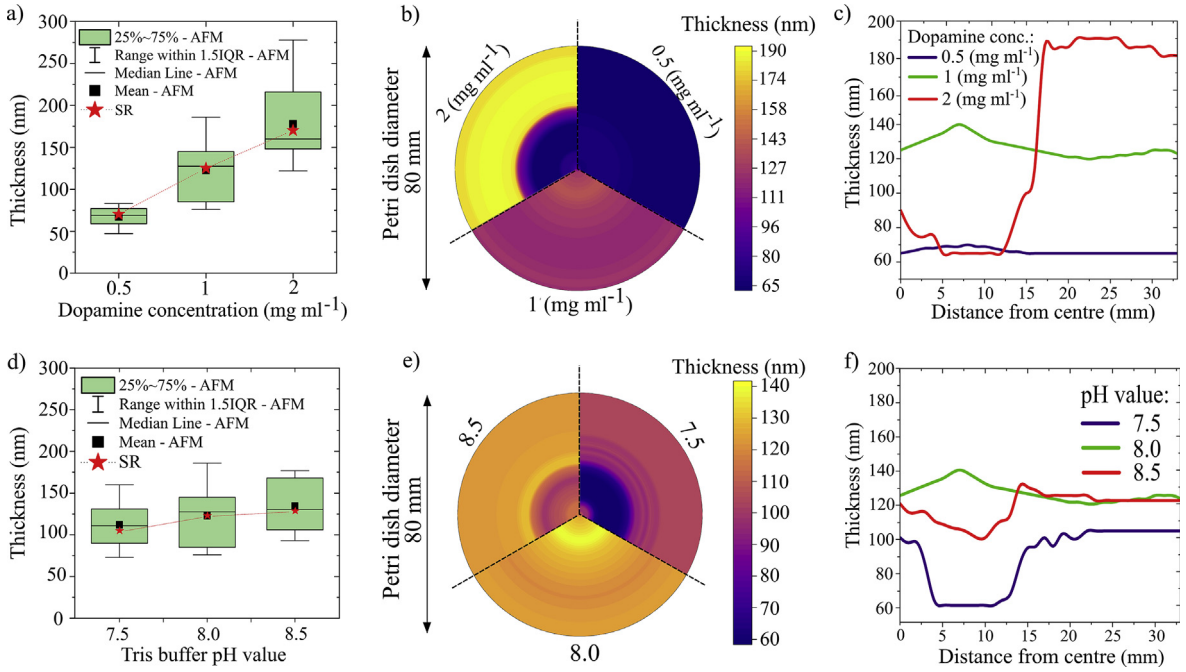

Fig. 3. a) Box (AFM) and point (SR) comparative charts of film thicknesses for different dopamine concentrations. **b)** Mapping of film thickness for different dopamine concentrations along film radius with a resolution of 1 mm by SR method. **c)** Line chart (SR) of film thickness for different dopamine concentrations along the radius of the film. **d)** Comparative charts of film thicknesses for different pH values of the Tris buffer. **e)** Mapping of film thickness for different pH values of the Tris buffer. **f)** Line chart of film thickness for different pH values of the Tris buffer.

polydopamine products that provide homogenous and smooth PDA coatings [52]. Photographs of the actual films produced at the air/water interface for different dopamine concentrations are shown in Figs. S2a-c.

3.2. The influence of pH of the tris buffer

The second synthesis parameter being studied was the pH of the Tris buffer solution. In the literature, values of 8.0 and 8.5 are found most often [27,31,35,50,53]. However, the most common value is 8.5 and the synthesis performed at lower pH shows larger integrability on other chemical processes. Therefore, we have chosen 7.5, 8.0 and 8.5 for the following experiment. In Fig. 3d the influence of pH on the thickness of the films is not as dramatic as the one observed for dopamine concentration. However, there is a slight trend towards increasing film thickness as the pH value increases. The film thicknesses measured by SR are as follows: 104, 120 and 125 nm for pH of 7.5, 8.0 and 8.5, respectively. These variations in thickness are expected, as the initial reactions (formation of dopaminequinone and leucodopaminechrom) that trigger the dopamine oxidation process are strongly pH-dependent [54,55]. Overall, the oxidation reaction rate is inversely proportional to the hydrogen-ion concentration [56], explaining the higher thickness of the films obtained with a higher pH of the solution. Fig. S3b shows a roughness comparison and indicates slightly lower values (24 and 26 nm for median and mean, respectively) for the pH of 8.0 with respect to others. The highest value was 35 ± 13 nm for a pH value of 8.5. Fig. 3e gives an overview of the film thickness mapping and seems to indicate that the film obtained using pH = 8.0 is the most homogeneous. The uniform colour distribution proves this on the thickness map without sharp transitions. Fig. 3f, shows the thickness profiles confirming the aforementioned dependence with the film prepared at pH 8.0, showing fewer variations. The differences in thickness between the central and external regions of the films were measured as 40, 30 and 20 nm for the samples 7.5, 8.5 and 8.0, respectively. Photographs of the actual films generated at the air/water interface in solutions of different pH are shown in Figs. S2d-e.

3.3. The influence of the size of the stirrer and stirring speed

The chosen type of stirrer was a round cylindrical bar suited for the flat-bottomed vessels. Petri dishes were selected for the synthesis of the films to obtain a large a/w interface area, however, their low height allows the use of small stirrers only. Accordingly, two sizes of stirrers were tested (12 × 4.5 mm and 20 × 6 mm). Of the two, the larger stirrer dragged the film too much, most probably by producing a large funnel (b), a change of local fluid level (Δh) (see Fig. S4a) and generating too strong flow. This phenomenon is illustrated by the photography of the actual funnel generated by the magnetic stirring in water in the same Petri dish like the one used in our experiment (see Fig. S4b). Consequently, PDA on the surface took the form of loosely moving “islands” of small dimensions without forming any continuous layer (Fig. S2f). A significant increase in length and diameter of the stirrer led to critical deformation of the solution surface on which a uniform continuous film could not be formed. Therefore, we focused on further investigations on the smaller size stirrer (12 × 4.5 mm).

After choosing the stirrer size, the influence of stirring speed was studied. Note, that no influence of the static (non-stirring) conditions was investigated, as it has been described in the literature [30,31,50]. Fig. 4a shows thickness variations of the films, both measured by the SR and AFM methods, as a function of the stirring speed. The exact results obtained by SR are as follows: 122, 117, 124, 131 nm for 150, 200, 250 and 300 RPM, respectively. AFM measurements confirmed these values. Slightly more significant variation occurs in the case of roughness measurements (Fig. S3c). The highest value of both median (38 nm)

and mean (37 ± 12 nm) was reported for the 250 RPM sample, while the results of the remaining samples were somewhat smaller. Very promising results were obtained by mapping the film thickness using the SR method, as shown in Fig. 4b. A perfectly uniform film thickness was obtained with 300 RPM. Stirring speeds of 150 RPM and 200 RPM turned out to be less beneficial towards thickness uniformity, and the speed of 250 RPM was very unfavourable due to the increase of funnel and drag in the fluid. This RPM resulted in a largely uneven surface when compared with the rest of the samples. This is well illustrated in Fig. 4c, where the difference in the film thickness was up to 70 nm between internal and external areas. It is worth remarking that for 250 RPM, the films show an almost twofold variation of thickness between the external and internal regions. In turn, from this chart, it can be concluded that the film obtained at a mixing speed of 300 RPM is perfectly uniform in thickness. Therefore, the stirring speed of 300 RPM was selected as the optimum value. There is no clear reason behind the larger thickness variation for 250 RPM sample as compared to the 300 RPM one. The mechanism of self-assembly of the PDA film air/water interface at these conditions is complex and most likely interdependent on several parameters, which are not even considered here. Further studies are in progress to understand the variations observed. Photographs of the actual films generated at the air/water interface with the use of different stirring speeds are shown in Figs. S2g-i.

3.4. Kinetics of film growth in the optimised conditions

Based on the results described above (Sections 3.1–3.3), the optimised conditions for the preparation of the films were determined as: pH 8.0, dopamine concentration 0.5 mg/mL, and stirring speed of 300 RPM. Using these parameters, the kinetics of film growth was followed using spectroscopic reflectometry during the period of 72 h. Due to the limitations of the method, the first valid measurement could be made when the film thickness reached ~55 nm, which took place after ~8 h from the start of the polymerisation reaction. The next three points were taken in 2 h intervals to follow the fast initial kinetics of growth. The last three points were taken after 24, 48 and 72 h from the start of the reaction to check if growth saturation occurs (Fig. 4d). Due to the low thickness of the film, a measurement error of ±2 nm ($\sigma+$ and σ-) was determined based on a comparison of 15 series of measurements. As can be seen in the chart, the fastest thickness increase was observed in the range of 8–14 h. However, after extrapolation in this range, the extrapolation line does not cross the point (0,0) within the experimental error, which suggests that at the beginning of the process (t < 8 h), the layer growth is much faster (Fig. S5). Further, in the range of 14–24 h, we see a slight decrease in the speed of thickness increase. Eventually, film growth was stopped after 24 h, reaching the thickness of 62 ± 2 nm. This observation is consistent with the AFM test, which showed the mean and median film thickness after 72 h as 60.5 and 61.5 nm, respectively. To evaluate the quality in terms of the roughness, thickness uniformity and homogeneity of the obtained film, a reference sample was obtained under the following conditions: pH 8.0, dopamine concentration 2 mg/mL, and stirring speed of 150 RPM. The AFM roughness test showed that the so-called "optimised" film had the mean and median RMS values 5 times lower than the reference sample (Fig. S3d).

The use of scanning spectroscopic reflectometry allowed to show the films' thickness uniformity in the centimetre-scale, over the entire radius equal 33 mm (Fig. 4e). A photograph of the actual optimised film generated at the air/water interface before transferring onto substrates is shown in Fig. S2j. The comparative AFM image of the surfaces of pairs of samples scooped from the reference (R1 and R2) and the optimised (O1 and O2) films are presented

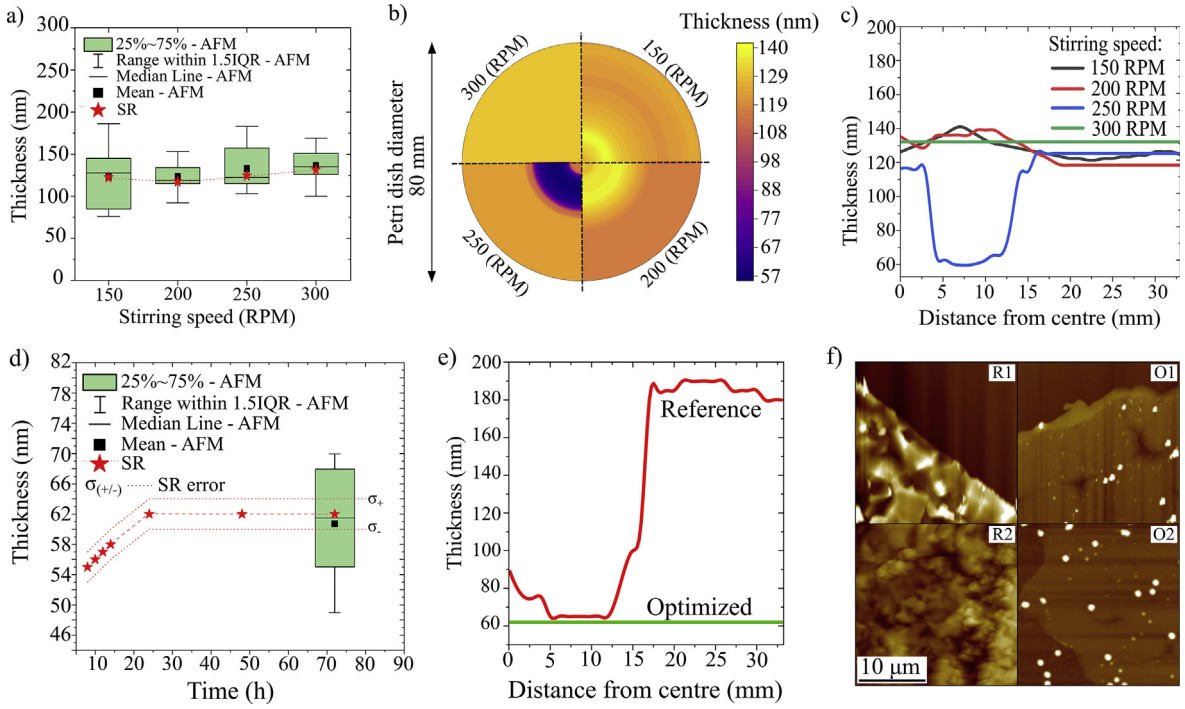

Fig. 4. a) Comparative charts of film thicknesses for different stirring speeds. b) Mapping of film thickness for different stirring speeds. c) Line chart of film thickness for different stirring speeds. d) Box chart (AFM) and point chart (SR) of the optimised film thicknesses for different times of polymerisation. e) Line chart (SR) of film thickness for reference and optimised samples. f) Comparative image (AFM) of the optimised and reference film surfaces.

in Fig. 4f. Despite the few holes and discontinuities, the optimised film is homogeneous and tightly covers the substrate, while the reference film surface is wavy and irregular. The visible bright spots in the AFM images are the polydopamine nanoparticles and their aggregates that have been "stuck" to the film during the process of applying it to the substrate, or "scooping". The larger aggregates of the nanoparticles were also indicated via optical microscopy, visible as black inclusions (Fig. S6a). From the AFM data can be concluded that they contribute to a significant increase in the roughness parameter, well explaining its values for films obtained with higher dopamine concentrations (section 3.1). The transferring process is being currently under optimisation and refinement. However, despite the presence of nanoparticles, it is clearly seen that the ultrathin films are continuous in the millimetre-scale (Fig. S6b, c). After transferring onto atomic-flat mica substrate, a photograph of the film is shown in Fig. S6d, showing centimetre-scale tight coverage.

3.5. Influence of the growth conditions on the structure of PDA

To elucidate the influence of the growth conditions on the physicochemical properties of the PDA films, we performed grazing incidence X-ray diffractometry, X-ray photoelectron spectroscopy and Raman spectroscopy measurements. As a result, we have shown that the 2D-like structure and other fundamentally unique features of the PDA films reported in the literature are preserved after optimisation procedures [35].

3.5.1. X-ray diffractometry

The first diffractogram (Fig. 5a) was obtained using the goniometric set-up. It reveals a set of peaks at the 2θ angle equal 10.9° (d = 8.11 Å), 21.8° (d = 4.07 Å) and 32.9° (d = 2.72 Å). These results are similar to those obtained in our previous study on PDA films from the air/water interface [35]. Moreover, it was concluded that the peak at ~32.9° can be assigned to both the substrate—silicon wafer [57] and part of the in-plane periodicity of PDA [58]. However, the intermittent apparition of the peak makes it inconclusive for interpretation. Therefore it has been omitted in the description of the results [57,59].

Interestingly, the number of peaks decreases with increasing film thickness, indicating most probably an amorphous structure without any peaks for the film obtained with the highest dopamine concentration. This observation is of great importance, especially while considering that there is evidence in the literature about the influence of the thickness of the PDA layer onto its structure. It has been shown that despite the observed differences during the initial stage of layer formation on various substrates, the structure of a thick layer of PDA was, in essence, identical in all cases and independent of the underlying surface [60]. In turn, the determination of grain (layer) size from the XRD pattern was inspired by the recently published study and the geometric adjustment was based on this publication [61]. Thus, these sizes calculated from the Scherrer equation for the optimised film were 69.9 (10.9°) and 49.3 nm (21.8°). These calculated grain sizes are similar or smaller than the thicknesses of the optimised film (62 ± 2 nm). The positions of XRD peaks and the calculated grain sizes suggest the presence of structural order, resembling the ones found in 2D carbon-based materials, graphene oxide (~10°) and reduced graphene oxide (~20°) [62–65].

Regarding previously described results for 2D-like PDA films, a peak located near 41° should be visible. However, therein a set of peaks was characterised by a reduction in their intensity at higher 2θ angles [35]. Therefore, due to the very low thickness of obtained films, a peak of very low intensity may be present. The second diffractogram (Fig. S7) was obtained with the grazing incidence angle of diffraction set-up, revealing only two positions of peaks at the 2θ angle equal 10.6° and 39.5°. For the film obtained with the highest DA concentration (2 mg/mL) only one peak (39.5°) is present, once again showing a more amorphous nature of this particular sample. The optimised film also shows only one peak (10.6°), which is probably attributed to the lower thickness of this sample.

3.5.2. Raman Spectroscopy and X-ray photoelectron spectroscopy

As shown in Fig. 5b, the normalised Raman spectra for the four films show identical features compared to those from our previous studies [35]. All four spectra show the clear presence of the D (~1430 cm^{-1}) and G (~1550 cm^{-1}) peaks, which are typical for sp^2 carbonaceous materials and commonly observed in PDA-based materials [66,67]. The D band is associated to the presence of structural defects in the hexagonal carbon lattice and to edge effects. The G band, in turn, corresponds to the in-plane vibration of the sp2 carbon atoms [68,69]. To investigate the level of disorder of the graphene-like structure, the intensity of these peaks was

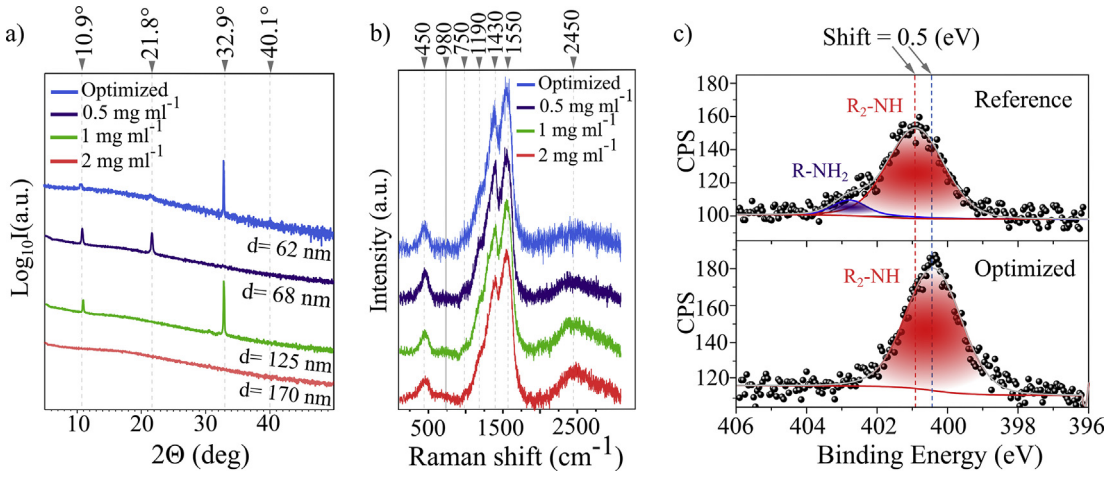

Fig. 5. a) Diffractogram (goniometric set-up) of the films on Si substrates, obtained with different concentrations of dopamine hydrochloride in starting solution (purple, green and red) and with the optimised conditions (blue). **b)** Raman spectra of the films on gold substrates, obtained with different concentrations of dopamine hydrochloride in starting solution and with the optimised conditions. **c)** N 1s high-resolution spectra of standard and optimised films. Dashed lines show the shift of binding energy in the R_2-NH.

compared by calculation of the I_D/I_G ratio which was equal to 0.9259, 0.8488, 0.8212 and 0,8608 for 0.5, 1 and 2 mg/ml and optimised sample, respectively. The important conclusion is that disorder increases as PDA film thickness decreases, but by using optimised synthesis conditions this effect can be minimized. Some vibrations reveal a resemblance to the experimental and theoretical results for eumelanin and can be attributed to the C–H, O–H, and O–H deformations (~980 cm^{-1}), and the stretching of C–C, C–OH, C–H, and N–H bonds present in amide, phenolic, and possibly pyrrole groups (~1190 cm^{-1}). Other vibrations at lower frequencies are in the spectral region that is typical for skeletal vibrations of nitrogen-containing aromatic rings [70]. Most probably, the typical peak of g-C_3N_4, is located at ~750 cm^{-1} [71]. The strong peak located near 400 cm^{-1} (~450 cm^{-1}) was previously described in the literature for the PDA, but simultaneously the peaks at these frequencies cannot be detected in 5,6-dihydroxyindole (DHI) melanin materials samples. All these features seem to prove that obtained films are composed of polydopamine exclusively [72]. A very crucial observation is the presence of G' (2D) peak near 2500 cm^{-1} and diversity in its intensity. It was reported that the G-peak intensity tends to increase with the number of layers, so it is sensible to assume that more layers are stacked due to the increasing thickness of the obtained films [73].

The permanence of the PDA functional groups was investigated by XPS (see also Fig. S8), as shown in Fig. 5c. The high-resolution spectra of the core level N 1s show the presence of the R_2-NH from secondary amine functionalities both in the optimised and in standard samples. In turn, the R–NH_2 (primary amine functionalities) component is present in the standard sample only. The presence of this component was reported in the previous study [35] and might come from the open etylamino chains reported already in the PDA structures [74,75]. We still cannot exclude that this moiety belongs to the (dopamine)$_2$/DHI 5,6-(dihydroxyindole) complex [76]. It is worth noting that in the samples containing free amino groups the peak of the R_2-NH component is shifted with regard to its position in pure PDA samples to higher binding energy (Δ0.5 eV) values. That strongly suggest influences on the electronic and chemical environment of the R_2-NH moiety. Thus, the presence of (dopamine)$_2$/DHI 5,6-(dihydroxyindole) complex is highly probable in the obtained material, and this complex may be responsible for more homogenous surfaces with better thickness control [76]. For a supplement, we have also obtained the spectrum of O1s and C1s and have included them in the supplementary information (Fig. S8). As expected, for these two components, the spectra of standard and optimised samples do not differ.

Until here, we have studied the thickness growth of PDA films and, most importantly, have shown that the attractive 2D-like structure remains undisturbed during this process. However, despite this section's broad chemical and structural characterisation, several aspects of PDA from the a/w interface remain elusive. Therefore, in the following section, we will provide a growth and self-organization scenario that closely resembles the experimental conditions for our films, which we believe should consider the a/w interface and the XRD insights described previously [35].

4. Growth and self-organising mechanism

In our recent study of PDA films, we discussed the possible origin of the XRD results in the context of PDA similarities to eumelanin [35]. In short, we proposed that the interplanar distances observed in the XRD experiments corresponded to the distance between indole-5,6-quinone stacks ~21.6° (d = 4.1 Å) [77–84]. Additionally, we associated the XRD diffraction peak at ~10.7° (d = 8.3 Å) to both the height of the molecule [78,81] and its partial destacking [77] and the peaks ~32.4° (d = 2.8 Å) and ~41° (d = 2.2 Å) to the in-plane periodicity observed at the mesoscale [58,85]. Despite the feasibility of the models and supramolecular ordering, the mechanism behind the co-assembly of quasi ordered structures and quasi textured arrangement of the PDA films is still unclear. Transmission Electron Microscopy (TEM) studies on our films (Fig. S9a), show a similar amorphous structure as the one reported in our previous study [35]. However, high-resolution TEM images suggest the presence of $\pi-\pi$ stacked sections (Fig. S9b), without clear crystalline planes (Fig. S9c). Molecular dynamics studies on eumelanin and PDA structures have shown the feasibility for self-organising layered aggregated via $\pi-\pi$ interactions [86]. Moreover, recent studies have shown that protomolecules of indole-5,6-quinone form covalent bonds of tetra- or pentamers [87]. These aggregates can generate graphite-like layered structures thanks to their stability and planar arrangement [72,86,88–90].

Because of the shear flow induced by the magnetic stirrer, it is plausible that flattened molecules of tetramers and other protomolecules are constantly exposed to shear and thus tend to align along the solution surface. The flow and shear forces create a continuous source of new DA molecules in a planar configuration, ready for stacking on the surface. Additionally, as dopamine oxidises, it has been shown that it starts the oligomerisation process, where the assembled species quickly migrate to the a/w interface, anchoring to the surface and, more importantly, serving as "semi crystallisation" seeds for the development of PDA films [50]. Further studies on the growth dynamics of PDA layers on different substrates showed that in the absence of negatively charged oxide/hydroxide anchoring points (covalent linkers), the PDA layer shows a higher presence of quinone groups C (sp^2)-H, which leads to more robust $\pi-\pi$ interactions [60]. Moreover, the growth of aggregates without templating was shown to generate a mixture of $\pi-\pi$ interactions leading to cluster forms, which tend to be spherical in gas and ill-defined in liquid [91]. Therefore, in our simulations, we used nearly planar tetramers in a liquid solution as they have shown to be the most stable ones [86]. The superior stability is also associated with their planarity and thus their easy $\pi-\pi$ stacking, which is an additional reason behind the selection of tetramers as main protomolecule [91]. Therefore, with the help of MD we aim to find similarities between the observed 2D-like structure of the films, using the insights here described from XRD, Raman and TEM, and the stablished PDA polymerisation pathways in the presence of a air/water interface.

4.1. Molecular docking

In the course of our computational research, we focused on simulations of one of the stable tetramers studied already by Chen et al. [86]. Molecular dynamics simulations of these systems are challenging since every collision described by Smoluchowski equation upon thermally driven self-diffusion leads to an immediate "sticking" and subsequent stacking. Using VINA docking analysis, we have determined the receptor-ligand interaction sites, where the receptor for the following docking is taken from the prior docking result. The docking structures are shown in Fig. 6a. On the course of analysis, we have determined three (3) specific interaction sites related to three types of possible aggregate growing schemes: normal stacking as depicted in Fig. 6b and c and two side types of interactions where tetramer interacts with one of the faces

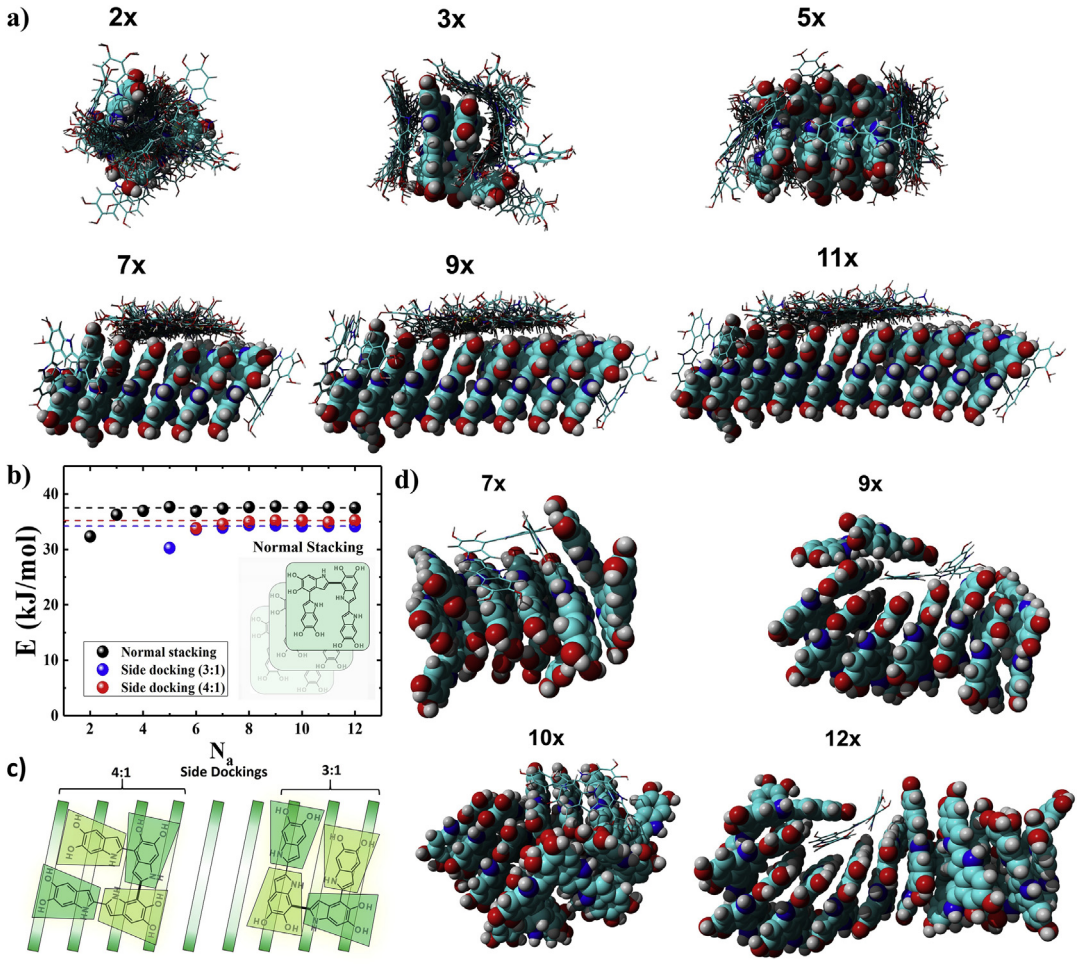

Fig. 6. a) Tetramer-tetramer VINA docking experiments. The interaction energies vary from around 26 to 34 kJ/mol. An average structure shows the preferable stacking order. **b)** Cluster size-dependent interaction energy between the cluster and additional tetramer molecule as the total number of clusters (N_a) (derived from VINA docking calculations. **c)** The normal stacking and 3:1/4:1 types of stacking as depicted. **d)** Selected MD equilibrated structures resulting from VINA docking showing that 3:1 type of stacking promotes the stabilisation of the typical stack structure.

of the already grown aggregate. Due to the specific arrangements in the latter cases, we named them 3:1 and 4:1 (also shown in Fig. 6b). The first type of stacking has already been identified previously [86].

Interestingly, the interaction energies for normal stacking vary with respect to the number of molecules in the aggregate. The smallest interaction energy is calculated for two interacting molecules and gives the interaction energy around 26–32 kJ/mol (dissociation constant $K_d \approx 2$ μM). The interaction energy for two tetramer molecules (2x) varies slightly due to many possible molecular rearrangements and ligand conformations. The corresponding values of dissociation constants K_d for dimers range from 0.26 up to 2.17 μM, which means that the majority of the tetramer molecules form aggregates, and this aggregation is weakly reversible.

Following the arguments mentioned above, the energy of aggregates was calculated as a function of the number of units (n). The energy turned out to be an increasing function of n and reached a plateau at ~38 kJ/mol for $n = 5$ molecules in the aggregate, which is in agreement with former studies [35,77,78,83,90]. Interestingly, once the cluster size reached 5 molecules (four molecules for receptor and one for ligand), a new assembly type was observed, namely one of those mentioned above as **3:1** or **4:1** type of assembly (Fig. 6c). The difference between those two types of stacking is the orientation of the tetramer molecule with respect to the side face of the growing stack (11x in Fig. 6a). In the **3:1** configuration, the tetramer molecule is oriented across the stack while in the **4:1** the longer axis of the tetramer molecule is kept along with the stack. The interaction energy observed for longer stacks and the **4:1** type of stacking was around 35 kJ/mol and 34 kJ/mol for the **3:1**. Although these are theoretical values for a perfectly ordered stack of tetramers, these are good starting points for further simulations and structure optimisations, and as we show in Fig. 6d, some of the 3:1 interactions stabilise the typical stacking structure. For this type of stacking (planar tetramer molecules), only one face of the growing stack interacts with the tetramer molecule: the one with the largest width. Small folding occurs at the end of the aggregates due to π-π interactions that are not limited only to the parallel alignment of the quinone rings but also to perpendicular orientation. Additionally, we observed a different stacking pathway for the tetramer molecules (results for docking not shown) where the molecule is not entirely planar in shape. These interactions would need further investigation and study.

4.2. Effects at the air-water interface

MD simulations at the air-water surface can be complex due to the quick aggregation and lack of buoyant force that holds the aggregates afloat and close to the air-water surface. Because of this, during the simulation time, the aggregate eventually drifts towards the water phase while maintaining its structure. In Fig. 7a, we show the MD simulation snapshots and the resulting aggregates orientation. We can observe that the size of aggregates with stacked units varies. Their size is not uniform, and the stacking alignment deviates slightly from ideal parallel ordering. What can be observed is that aggregates (normal stacking) create quasi-ordered structures resembling the house-of-cards model.

Simulations were carried out using implicit water NOVA2 forcefield without saving the MD trajectory. A tetramer was added to the simulation environment every time a molecule 'docked' to the oligomerised surface layer to simulate the growth of the PDA layers. Subsequent molecules were added one by one at a sufficient distance so that the initial setting did not determine its orientation. We believe that this process represents a more realistic view with respect to the diffusive collision probability, given by the Smoluchowski equation, at a given concentration. While simultaneous addition of all molecules at once will result in structures very similar to those obtained from MD with water as in Fig. 7a, the one by one addition results in a lack of pre-aggregates and only a single molecule approach to the air-water interface.

Interestingly, the interaction energy for any stacking configuration exceeds 30 kJ/mol. Therefore, it is unlike traditional MD that might resolve these structures at realistic concentrations. Moreover, the simulation results in chaotic aggregates, which might not evolve during the simulation time, as shown in Fig. 7a. Accordingly, we may propose an arrangement of the tetramer molecules as shown in Fig. 7b, where a semi-smectic-c arrangement characterises the air-water interface. Our experiments show that the tetramer structures form a sort of "semi-smectic c" phase at the surface, albeit with defects, and the order range is limited to very few molecules due to bending forces, e.g. the stacking distance without bending is less than 10 molecules. The structure can be observed already in Fig. 7a at 11 ns. The proposed stacking arrangement and Radial Distribution Function (RDF), shown in Fig. 7b and **c,** respectively, are compatible with those previously observed and studied in similar systems [35,77,78,83,90].

The results show that the supramolecular ordering observed in our experiments can be attributed, of course not exclusively, to the following aspects. On the one hand, the tetramers at the a/w interface quickly trap other planar molecules due to the strong $\pi-\pi$ interactions. On the other hand, molecules can stack in a 'house of cards' configuration, with similar propagation limitations, as the growth is still dominated by $\pi-\pi$ interactions. However, the layered aggregates are more energetically preferable, as also shown in the literature [77,86,91]. The initial orientation on the a/w interface is most likely a single layer of smectic-c alignment, perhaps similarly to the early growth stages of PDA on Au surfaces [60].

5. Final remarks and conclusions

Previously, the PDA film formation description at the air/water interface under static conditions was evaluated via ellipsometric and Brewster angle microscopy observation of the water surface [31]. Noteworthy, an important conclusion was the reduction of the oxygen access from the air to the dissolved dopamine hydrochloride due to polymerisation progress and the film growth [31]. This determines the consistency of mentioned experiment with our study because we previously confirmed a smaller amount of unreacted dopamine moieties in the optimised (i.e. thinner) film

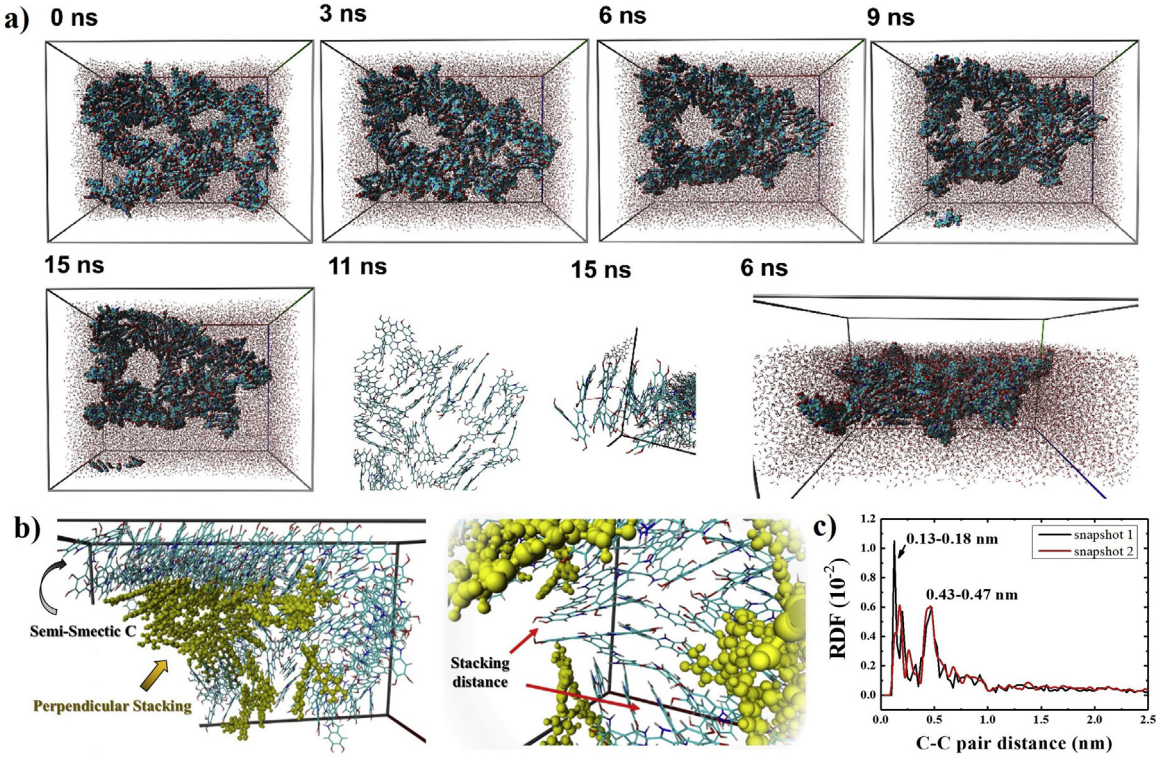

Fig. 7. a) Selected structures resulting from MD simulations at the air-water interface. **b)** Selected snapshot from MD simulation with implicit water showing semi-smectic C arrangement on the air-water surface. The right panel shows a zoom-in of the layers with the interplanar distance. **c)** the RDF function for two different simulation snapshots.

Table 1
Summary of the related previous approaches towards the production of the free-standing PDA thin films from the air/water interface and outcoming structures characteristics.

Dopamine conc. (mg/mL)	Thickness (nm) and growth control[1]		Functional agent	Described structure or nanostructure	Conditions[2]	Ref.
2	50 after 3 h	−/−	–	coalescence of small islands[3]	static	[50]
~1.53 ~3.06 ~6.13	105 after 24 h 132 after 24 h 179 after 24 h	+/−	–	Double-layered dopamine-melanin thin films and granules[4]	static	[30]
~1.53	151 after 24 h	+/−	Aniline[5]	Continous uniform films at the nanoscale level[6]	static	[32]
2	600 after 24 h	+/−	PEI[7]	Continous uniform Janus-faced films[4]	static	[92]
1 2 5	40 after 10 h 50 after 10 h 80 after 10 h	+/−	–	coalescence of aggregates[8]	Static/compressed water surface	[31]
0.1 0.5 1 2 3 5	~40 after 6 h ~60 after 6 h ~75 after 6 h ~65 after 6 h ~50 after 6 h ~55 after 6 h	+/−	Laccase[9]	continuous composite films[8]	Static/compressed water surface	[34]
~1.53	144 after 48 h 400 after 480 h 145 after 48 h 400 after 480 h 195 after 48 h 400 after 480 h 270 after 48 h 500 after 480 h – 800 after 480 h	−/−	– NaCl $MgCl_2 \cdot 6H_2O$ $CaCl_2$ $CoCl_2 \cdot 6H_2O$	Continuous smooth film of PDA aggregates[10]	static	[51]
2	55 for each monolayer after 24 h	−/−	–	Continuous films at the nanoscale level of 2D-like layered structure[11]	Soft-stirring	[35]
0.5	62 ± 2 after 72 h	+/+	-	Continuous films at the centimetre scale of 2D-like layered structure[12]	Soft-stirring	**This study**

1- Thickness vs time or dopamine concentration dependence/thickness homogeneity control (supra nanoscale)
2- Dynamic or static conditions applied to bulk liquid and/or water surface
3- Evaluated with Brewster angle microscopy, scanning electron microscopy
4- Evaluated with field-emission scanning electron microscopy
5- Aniline – deprotonating agent
6- Evaluated with field-emission scanning electron microscopy, atomic force microscopy
7- PEI- poly (ethlyenimine) – crosslinking agent
8- Evaluated with Brewster angle microscopy, ellipsometry
9- Laccase - enzyme laccase – as an accelerator of the polymerisation process
10- Evaluated with scanning electron microscopy
11- Evaluated with X-ray diffractometry, transmission electron microscopy, atomic force microscopy, scanning electron microscopy, Raman spectroscopy
12- Evaluated with X-ray diffractometry, atomic force microscopy, Raman spectroscopy

(see section 3.4). However, to date, without the use of additional agents (e.g. cross-linking agents) homogeneity and continuity of the obtained free-standing films at the nanoscale only were noted [27]. Moreover, it was believed that the loose domains of polydopamine are formed at the interface when initial dopamine concentration is very low (<1 mg/mL), and they do not form a continuous layer [31]. However, the real extend and origin of the observed supramolecular ordering is still unknown and detailed structural studies are on their way to understanding the origin of the XRD diffraction peaks and the associated PDA ordering [35]. For clarity and to underline the novelty of this work, Table 1 is provided below, which helps to see the similarities and differences of the experiments concerning PDA free-standing films from the air/water interface. From this comparison, we can conclude that the main innovation in this work was obtaining continuous, homogeneous and ordered structures of the 2D-like type PDA films of a large (centimetre) scale, using a considerable low concentration of dopamine and without functional agents.

In summary, we successfully controlled the synthesis of polydopamine from the air/water interface with a centimetre scale. Therefore, a new approach towards the production of ultrathin free-standing polydopamine films was proposed, opening up the possibility of entirely new applications for this multifunctional material [18]. Moreover, as another important innovation, we designed and applied a spectroscopic reflectometry set-up dedicated to the *in-situ* and live observation of the growth of the films over the entire surface during polymerisation, which allows for large scalability and integration. The research hypothesis was examined, namely-the morphological properties and chemical structure should be controllable by tuning the synthesis conditions. During the experiment, the following optimised conditions for the preparation of the films were attained: pH 8.0, dopamine concentration 0.5 mg mL-1, and stirring speed of 300 RPM. The resulting film had ~5 times lower roughness (root mean square factor), and ~3 times lower thickness compared to the reference sample, obtained using so-called “standard” conditions. Further optimisation, if needed, could be planned using appropriate procedures-the response surface methodology and the central composite design (CCD). In turn, structural characterisation suggests a 2D-like structure of the films, with multiple layers and more amorphous character in the thicker (standard) film. Moreover, apparent similarities to the graphene-based materials with our films can be postulated by the Raman and XRD studies [61–65]. X-ray photoelectron spectroscopy analysis showed that the R_2-NH moiety is shifted to lower binding energy values by Δ0.5 eV under controlled synthesis conditions, which can indicate the presence of

(dopamine)$_2$/5,6-Dihydroxyindole complex in the structure of the 2D polydopamine films [74–76].

Finally, molecular dynamics were performed to understand better the polydopamine 2D-like film self-assembly process, and a new concept was proposed. Using VINA docking analysis, the receptor-ligand interaction sites were determined, which are related to the three types of possible aggregate growing schemes, among which only one was previously identified in the literature, and the other two stand as a new concept [86]. The size of aggregates is not uniform, and the stacking alignment deviates slightly from ideal parallel ordering. Moreover, it was concluded that the initial orientation on the a/w interface is most likely a single layer of smectic-c alignment, $\pi - \pi$ interactions dominate further growth and the layered aggregates are energetically preferable [60,77,86,91].

Nevertheless, to increase the application potential of the obtained free-standing films, their roughness and the number of cracks and damages after transferring them to functional substrates should be reduced. Therefore, it is imperative to improve the transferring of films to functional substrates and improve their mechanical properties in the future.

CRediT author statement

Jakub Szewczyk: Investigation, Visualization, Methodology, Conceptualization, Validation, Data curation and Writing - Original Draft, **Mikołaj Pochylski**: Software, Formal analysis, Data curation, Investigation and Writing – review and editing. **Kosma Szutkowski**: Investigation, Software, Formal analysis, Writing – review and editing. Data curation and Visualization. **Mateusz Kempiński:** Investigation, **Radosław Mrówczyński:** Investigation, **Igor Iatsunskyi**: Investigation, **Jacek Gapiński:** Software, Formal analysis, Resources, Data curation, Investigation and Writing – review and editing. **Emerson Coy:** Investigation, Visualization, Methodology, Conceptualization, Data curation, Validation, Funding acquisition, Resources, Project administration, Supervision and Writing - Original Draft.

Data availability

The raw/processed data required to reproduce these findings cannot be shared at this time as the data also forms part of an ongoing study. Data might be shared upon reasonable request to the corresponding author.

Declaration of competing interest

The authors declare the following financial interests/personal relationships which may be considered as potential competing interests:

Emerson Coy reports financial support was provided by National Science Centre Poland.

Acknowledgements

The authors acknowledge the financial support from the National Science Centre of Poland (NCN) by the OPUS grant 2019/35/B/ST5/00248. **R.M:** acknowledges the partial financial support from the NCN OPUS 2018/31/B/ST8/02460 in the XPS experiments of this work. **K.S:** acknowledges the partial financial support from H2020-INFRAIA-2016-2017 under research grant "EUSMI - European infrastructure for spectroscopy, scattering and imaging of soft matter", contract number GA731019, funded under H2020-EU.1.4.1.2.–RI, for the Yasara Software.

Appendix A. Supplementary data

Supplementary information contains The scheme of the scooping procedure (S1), Pictures of the Films (S2), Stirring Conditions Calculations (S3), Extended growth kinetics of the optimised membrane (S4), Milimetre-scale and centimetre-scale homogeneity presentation (S5), XPS Data (S6), HR-TEM data (S7).

Supplementary data to this article can be found online at https://doi.org/10.1016/j.mtchem.2022.100935.

References

[1] H. Lee, S.M. Dellatore, W.M. Miller, P.B. Messersmith, Mussel-inspired surface chemistry for multifunctional coatings, Science 318 (2007) 426–430, https://doi.org/10.1126/science.1147241.
[2] H. Lee, J. Rho, P.B. Messersmith, Facile conjugation of biomolecules onto surfaces via mussel adhesive protein inspired coatings, Adv. Mater. 21 (2009) 431–434, https://doi.org/10.1002/adma.200801222.
[3] J.H. Ryu, P.B. Messersmith, H. Lee, Polydopamine surface chemistry: a decade of discovery, ACS Appl. Mater. Interfaces 10 (2018) 7523–7540, https://doi.org/10.1021/acsami.7b19865.
[4] R. Mrówczyński, A. Nan, R. Turcu, J. Leistner, J. Liebscher, Polydopamine - a versatile coating for surface-initiated ring-opening polymerization of lactide to polylactide, Macromol. Chem. Phys. 216 (2015) 211–217, https://doi.org/10.1002/macp.201400380.
[5] Z. Chen, W. Yang, Y. Chen, X. Yin, Y. Liu, Smart coatings embedded with polydopamine-decorated layer-by-layer assembled SnO2 nanocontainers for the corrosion protection of 304 stainless steels, J. Colloid Interface Sci. 579 (2020) 741–753, https://doi.org/10.1016/j.jcis.2020.06.118.
[6] Z. Zheng, L. Xiao, P. Huang, F. Wang, Polydopamine improved anticorrosion of graphene on copper: inhibiting galvanic corrosion and healing structure defects, Appl. Mater. Today 24 (2021) 101069, https://doi.org/10.1016/j.apmt.2021.101069.
[7] Z. Li, H. Xu, J. Shao, C. Jiang, F. Zhang, J. Lin, H. Zhang, J. Li, P. Huang, Polydopamine-functionalized black phosphorus quantum dots for cancer theranostics, Appl. Mater. Today 15 (2019) 297–304, https://doi.org/10.1016/j.apmt.2019.02.002.
[8] X.-F. Du, Y. Li, J. Long, W. Zhang, D. Wang, C.-R. Li, M.-X. Zhao, Y. Lai, Fabrication of cisplatin-loaded polydopamine nanoparticles via supramolecular self-assembly for photoacoustic imaging guided chemo-photothermal cancer therapy, Appl. Mater. Today 23 (2021) 101019, https://doi.org/10.1016/j.apmt.2021.101019.
[9] Y. Liu, K. Ai, L. Lu, Polydopamine and its derivative materials: synthesis and promising applications in energy, environmental, and biomedical fields, Chem. Rev. 114 (2014) 5057–5115, https://doi.org/10.1021/cr400407a.
[10] Z. Wang, C. Li, J. Xu, K. Wang, X. Lu, H. Zhang, S. Qu, G. Zhen, F. Ren, Bioadhesive microporous architectures by self-assembling polydopamine microcapsules for biomedical applications, Chem. Mater. 27 (2015) 848–856, https://doi.org/10.1021/cm5038765.
[11] D. Maziukiewicz, B. Grześkowiak, E. Coy, S. Jurga, R. Mrówczyński, NDs@PDA@ICG conjugates for photothermal therapy of glioblastoma multiforme, Biomimetics 4 (2019) 3, https://doi.org/10.3390/biomimetics4010003.
[12] A. Jędrzak, B.F. Grześkowiak, K. Golba, E. Coy, K. Synoradzki, S. Jurga, T. Jesionowski, R. Mrówczyński, Magnetite nanoparticles and spheres for chemo-and photothermal therapy of hepatocellular carcinoma in vitro, Int. J. Nanomed. 15 (2020) 7923–7936, https://doi.org/10.2147/IJN.S257142.
[13] B.F. Grześkowiak, D. Maziukiewicz, A. Kozłowska, A. Kertmen, E. Coy, R. Mrówczyński, Polyamidoamine dendrimers decorated multifunctional polydopamine nanoparticles for targeted chemo- and photothermal therapy of liver cancer model, Int. J. Mol. Sci. 22 (2021) 738, https://doi.org/10.3390/ijms22020738.
[14] J. Hu, Q. Wang, Y. Wang, G. You, P. Li, L. Zhao, H. Zhou, Polydopamine-based surface modification of hemoglobin particles for stability enhancement of oxygen carriers, J. Colloid Interface Sci. 571 (2020) 326–336, https://doi.org/10.1016/j.jcis.2020.03.046.
[15] A.B. Mostert, B.J. Powell, F.L. Pratt, G.R. Hanson, T. Sarna, I.R. Gentle, P. Meredith, Role of semiconductivity and ion transport in the electrical conduction of melanin, Proc. Natl. Acad. Sci. U.S.A. 109 (2012) 8943–8947, https://doi.org/10.1073/pnas.1119948109.
[16] M.M. Jastrzebska, H. Isotalo, J. Paloheimo, H. Stubb, Electrical conductivity of synthetic DOPA-melanin polymer for different hydration states and temperatures, J. Biomater. Sci. Polym. Ed. 7 (1995) 577–586, https://doi.org/10.1163/156856295X00490.
[17] J. McGinness, P. Corry, P. Proctor, Amorphous semiconductor switching in melanins, Science 183 (1974) 853–855, https://doi.org/10.1126/science.183.4127.853.
[18] D. Aguilar-Ferrer, J. Szewczyk, E. Coy, Recent developments in polydopamine-based photocatalytic nanocomposites for energy production: physicochemical properties and perspectives, Catal. Today (2021), https://doi.org/10.1016/j.cattod.2021.08.016.

[19] Y. Kim, E. Coy, H. Kim, R. Mrówczyński, P. Torruella, D.W. Jeong, K.S. Choi, J.H. Jang, M.Y. Song, D.J. Jang, F. Peiro, S. Jurga, H.J. Kim, Efficient photocatalytic production of hydrogen by exploiting the polydopamine-semiconductor interface, Appl. Catal. B Environ. 280 (2021) 119423, https://doi.org/10.1016/j.apcatb.2020.119423.
[20] V. Fedorenko, R. Viter, R. Mrówczyński, D. Damberga, E. Coy, I. Iatsunskyi, Synthesis and photoluminescence properties of hybrid 1D core–shell structured nanocomposites based on ZnO/polydopamine, RSC Adv. 10 (2020) 29751–29758, https://doi.org/10.1039/D0RA04829A.
[21] Q. Huang, J. Chen, M. Liu, H. Huang, X. Zhang, Y. Wei, Polydopamine-based functional materials and their applications in energy, environmental, and catalytic fields: state-of-the-art review, Chem. Eng. J. 387 (2020) 124019, https://doi.org/10.1016/j.cej.2020.124019.
[22] P.Y. Lin, G. He, J. Chen, A.K. Dwivedi, S. Hsieh, Monitoring the photoinduced surface catalytic coupling reaction and environmental exhaust fumes with an Ag/PDA/CuO modified 3D glass microfiber platform, J. Ind. Eng. Chem. 82 (2020) 424–432, https://doi.org/10.1016/j.jiec.2019.11.006.
[23] H.K. Chin, P.Y. Lin, J. Chen, R. Kirankumar, Z.H. Wen, S. Hsieh, Polydopamine-mediated ag and zno as an active and recyclable sers substrate for rhodamine b with significantly improved enhancement factor and efficient photocatalytic degradation, Appl. Sci. 11 (2021) 4914, https://doi.org/10.3390/app11114914.
[24] Z.H. Huang, S.W. Peng, S.L. Hsieh, R. Kirankumar, P.F. Huang, T.M. Chang, A.K. Dwivedi, N.F. Chen, H.M. Wu, S. Hsieh, Polydopamine ultrathin film growth on mica via *in-situ* polymerization of dopamine with applications for silver-based antimicrobial coatings, Materials 14 (2021) 1–16, https://doi.org/10.3390/ma14030671.
[25] V. Ball, Polydopamine films and particles with catalytic activity, Catal. Today 301 (2018) 196–203, https://doi.org/10.1016/j.cattod.2017.01.031.
[26] C. Bergtold, D. Hauser, A. Chaumont, S. El Yakhlifi, M. Mateescu, F. Meyer, M.H. Metz-Boutigue, B. Frisch, P. Schaaf, D. Ihiawakrim, O. Ersen, C.A. Monnier, A. Petri-Fink, B. Rothen-Rutishauser, V. Ball, Mimicking the chemistry of natural eumelanin synthesis: the KE sequence in polypeptides and in proteins allows for a specific control of nanosized functional polydopamine formation, Biomacromolecules 19 (2018) 3693–3704, https://doi.org/10.1021/acs.biomac.8b00818.
[27] F. Ponzio, V. Ball, Polydopamine deposition at fluid interfaces, Polym. Int. 65 (2016) 1251–1257, https://doi.org/10.1002/pi.5124.
[28] N. Reitzel, D.R. Greve, K. Kjaer, P.B. Howes, M. Jayaraman, S. Savoy, R.D. Mccullough, J.T. Mcdevitt, T. Bjørnholm, Self-assembly of conjugated polymers at the air/water interface . Structure and properties of Langmuir and Langmuir - blodgett films of amphiphilic regioregular polythiophenes, J. Am. Chem. Soc. 347 (2000) 5788–5800, https://doi.org/10.1021/ja9924501.
[29] D. Yadav, A. Kumar, J.Y. Kim, N.J. Park, J.O. Baeg, Interfacially synthesized 2D COF thin film photocatalyst: efficient photocatalyst for solar formic acid production from CO2and fine chemical synthesis, J. Mater. Chem. A. 9 (2021) 9573–9580, https://doi.org/10.1039/d1ta00802a.
[30] T.F. Wu, J.D. Hong, Dopamine-melanin nanofilms for biomimetic structural coloration, Biomacromolecules 16 (2015) 660–666, https://doi.org/10.1021/bm501773c.
[31] O.Y. Milyaeva, A.G. Bykov, R.A. Campbell, G. Loglio, R. Miller, B.A. Noskov, Polydopamine layer formation at the liquid – gas interface, Colloids Surfaces A Physicochem. Eng. Asp. 579 (2019) 123637, https://doi.org/10.1016/j.colsurfa.2019.123637.
[32] T.F. Wu, B.H. Wee, J.D. Hong, An ultrasensitive and fast moisture sensor based on self-assembled dopamine-melanin thin films, Adv. Mater. Interfac. 2 (2015) 1–5, https://doi.org/10.1002/admi.201500203.
[33] F. Li, Y. Yu, Q. Wang, J. Yuan, P. Wang, X. Fan, Polymerization of dopamine catalyzed by laccase: comparison of enzymatic and conventional methods, Enzym. Microb. Technol. 119 (2018) 58–64, https://doi.org/10.1016/j.enzmictec.2018.09.003.
[34] O.Y. Milyaeva, A.G. Bykov, R.A. Campbell, G. Loglio, R. Miller, B.A. Noskov, The dynamic properties of PDA-laccase films at the air-water interface, Colloids Surfaces A Physicochem. Eng. Asp. 599 (2020) 124930, https://doi.org/10.1016/j.colsurfa.2020.124930.
[35] E. Coy, I. Iatsunskyi, J.C. Colmenares, Y. Kim, R. Mrówczyński, Polydopamine films with 2D-like layered structure and high mechanical resilience, ACS Appl. Mater. Interfaces 13 (2021) 23113–23120, https://doi.org/10.1021/acsami.1c02483.
[36] S.S. Mofarah, L. Schreck, C. Cazorla, X. Zheng, E. Adabifiroozjaei, C. Tsounis, J. Scott, R. Shahmiri, Y. Yao, R. Abbasi, Y. Wang, H. Arandiyan, L. Sheppard, V. Wong, E. Doustkhah, P. Koshy, C.C. Sorrell, Highly catalytically active CeO2-: X-based heterojunction nanostructures with mixed micro/meso-porous architectures, Nanoscale 13 (2021) 6764–6771, https://doi.org/10.1039/d0nr08097g.
[37] T. Vasileiadis, T. Marchesi D'Alvise, C.-M. Saak, M. Pochylski, S. Harvey, C. V Synatschke, J. Gapinski, G. Fytas, E.H.G. Backus, T. Weil, B. Graczykowski, Fast light-driven motion of polydopamine nanomembranes, Nano Lett. 22 (2021) 578–585, https://doi.org/10.1021/acs.nanolett.1c03165.
[38] J. Schuderer, N. Kuster, Effect of the meniscus at the solid/liquid interface on the SAR distribution in Petri dishes and flasks, Bioelectromagnetics 24 (2003) 103–108, https://doi.org/10.1002/bem.10066.
[39] I. Thormählen, J. Straub, U. Grigull, Refractive index of water and its dependence on wavelength, temperature, and density, J. Phys. Chem. Ref. Data 14 (1985) 933–945, https://doi.org/10.1063/1.555743.
[40] R. Qie, S. Zajforoushan Moghaddam, E. Thormann, Parameterization of the optical constants of polydopamine films for spectroscopic ellipsometry studies, Phys. Chem. Chem. Phys. 23 (2021) 5516–5526, https://doi.org/10.1039/d0cp04796a.
[41] D. Nečas, P. Klapetek, Gwyddion: an open-source software for SPM data analysis, Cent. Eur. J. Phys. 10 (2012) 181–188, https://doi.org/10.2478/s11534-011-0096-2.
[42] E. Krieger, G. Vriend, YASARA View—molecular graphics for all devices—from smartphones to workstations, Bioinformatics 30 (2014) 2981–2982, https://doi.org/10.1093/bioinformatics/btu426.
[43] E. Krieger, G. Vriend, New ways to boost molecular dynamics simulations, J. Comput. Chem. 36 (2015) 996–1007, https://doi.org/10.1002/jcc.23899.
[44] O. Trott, A.J. Olson, AutoDock Vina, Improving the speed and accuracy of docking with a new scoring function, efficient optimization, and multithreading, J. Comput. Chem. 31 (2009) 455–461, https://doi.org/10.1002/jcc.21334.
[45] E. Krieger, G. Koraimann, G. Vriend, Increasing the precision of comparative models with YASARA NOVA-a self-parameterizing force field, Proteins Struct. Funct. Bioinforma. 47 (2002) 393–402, https://doi.org/10.1002/prot.10104.
[46] E. Krieger, K. Joo, J. Lee, J. Lee, S. Raman, J. Thompson, M. Tyka, D. Baker, K. Karplus, Improving physical realism, stereochemistry, and side-chain accuracy in homology modeling: four approaches that performed well in CASP8, Proteins Struct. Funct. Bioinforma. 77 (2009) 114–122, https://doi.org/10.1002/prot.22570.
[47] K. Kim, S. Kwon, H.J. Pahk, Fast analysis of film thickness in spectroscopic reflectometry using direct phase extraction, Curr. Opt. Photonics. 1 (2017) 29–33, https://doi.org/10.3807/COPP.2017.1.1.029.
[48] Y.Z. Hu, R. Sharangpani, S.-P. Tay, Kinetic investigation of copper film oxidation by spectroscopic ellipsometry and reflectometry, J. Vac. Sci. Technol. A Vacuum, Surfaces, Film. 18 (2000) 2527, https://doi.org/10.1116/1.1287156.
[49] A. Piegari, E. Masetti, Thin film thickness measurement: a comparison of various techniques, Thin Solid Films 124 (1985) 249–257, https://doi.org/10.1016/0040-6090(85)90273-1.
[50] F. Ponzio, P. Payamyar, A. Schneider, M. Winterhalter, J. Bour, F. Addiego, M.P. Krafft, J. Hemmerle, V. Ball, Polydopamine films from the forgotten Air/water interface, J. Phys. Chem. Lett. 5 (2014) 3436–3440, https://doi.org/10.1021/jz501842r.
[51] X. Han, F. Tang, Z. Jin, Free-standing polydopamine films generated in the presence of different metallic ions: the comparison of reaction process and film properties, RSC Adv. 8 (2018) 18347–18354, https://doi.org/10.1039/c8ra02930j.
[52] H.W. Kim, B.D. McCloskey, T.H. Choi, C. Lee, M.J. Kim, B.D. Freeman, H.B. Park, Oxygen concentration control of dopamine-induced high uniformity surface coating chemistry, ACS Appl. Mater. Interfaces 5 (2013) 233–238, https://doi.org/10.1021/am302439g.
[53] Z. Yan, Y. Zhang, H. Yang, G. Fan, A. Ding, H. Liang, G. Li, N. Ren, B. Van der Bruggen, Mussel-inspired polydopamine modification of polymeric membranes for the application of water and wastewater treatment: a review, Chem. Eng. Res. Des. 157 (2020) 195–214, https://doi.org/10.1016/j.cherd.2020.03.011.
[54] J. Yang, M.A.C. Stuart, M. Kamperman, Jack of all trades: versatile catechol crosslinking mechanisms, Chem. Soc. Rev. 43 (2014) 8271–8298, https://doi.org/10.1039/C4CS00185K.
[55] M. Salomäki, L. Marttila, H. Kivelä, T. Ouvinen, J. Lukkari, Effects of pH and oxidants on the first steps of polydopamine formation: a thermodynamic approach, J. Phys. Chem. B 122 (2018) 6314–6327, https://doi.org/10.1021/acs.jpcb.8b02304.
[56] T.E. Young, B.W. Babbitt, Electrochemical study of the oxidation of α-methyldopamine, α-methylnoradrenaline, and dopamine, J. Org. Chem. 48 (1983) 562–566, https://doi.org/10.1021/jo00152a029.
[57] T. Ami, M. Suzuki, MOCVD growth of (100)-oriented CeO2 thin films on hydrogen-terminated Si(100) substrates, Mater. Sci. Eng. B 54 (1998) 84–91, https://doi.org/10.1016/s0921-5107(98)00133-0.
[58] Z. Tian, W. Hwang, Y.J. Kim, Mechanistic understanding of monovalent cation transport in eumelanin pigments, J. Mater. Chem. B. 7 (2019) 6355–6361, https://doi.org/10.1039/C9TB01211G.
[59] W. Chebil, A. Fouzri, A. Fargi, B. Azeza, Z. Zaaboub, V. Sallet, Characterization of ZnO thin films grown on different p-Si substrate elaborated by solgel spin-coating method, Mater. Res. Bull. 70 (2015) 719–727, https://doi.org/10.1016/j.materresbull.2015.06.003.
[60] J. Svoboda, M. Král, M. Dendisová, P. Matějka, O. Pop-Georgievsk, Unraveling the influence of substrate on the growth rate, morphology and covalent structure of surface adherent polydopamine films, Colloids Surf. B Biointerfaces 205 (2021) 111897, https://doi.org/10.1016/j.colsurfb.2021.111897.
[61] D.J. Lim, N.A. Marks, M.R. Rowles, Universal Scherrer equation for graphene fragments, Carbon N. Y. 162 (2020) 475–480, https://doi.org/10.1016/j.carbon.2020.02.064.
[62] N. Rono, J.K. Kibet, B.S. Martincigh, V.O. Nyamori, A review of the current status of graphitic carbon nitride, Crit. Rev. Solid State Mater. Sci. 46 (2021) 189–217, https://doi.org/10.1080/10408436.2019.1709414.
[63] B. Gurzęda, A. Subrati, P. Florczak, Z. Kabacińska, T. Buchwald, L. Smardz, B. Peplińska, S. Jurga, P. Krawczyk, Two-step synthesis of well-ordered layered graphite oxide with high oxidation degree, Appl. Surf. Sci. 507 (2020) 145049, https://doi.org/10.1016/j.apsusc.2019.145049.

[64] A. Subrati, S. Mondal, M. Ali, A. Alhindi, R. Ghazi, A. Abdala, D. Reinalda, S. Alhassan, Developing hydrophobic graphene foam for oil spill cleanup, Ind. Eng. Chem. Res. 56 (2017) 6945–6951, https://doi.org/10.1021/acs.iecr.7b00716.
[65] F.T. Johra, J.W. Lee, W.G. Jung, Facile and safe graphene preparation on solution based platform, J. Ind. Eng. Chem. 20 (2014) 2883–2887, https://doi.org/10.1016/j.jiec.2013.11.022.
[66] R. Tejido-Rastrilla, G. Baldi, A.R. Boccaccini, Ag containing polydopamine coating on a melt-derived bioactive glass-ceramic: effect on surface reactivity, Ceram. Int. 44 (2018) 16083–16087, https://doi.org/10.1016/j.ceramint.2018.05.198.
[67] H. Li, J. Xi, A.G. Donaghue, J. Keum, Y. Zhao, K. An, E.R. McKenzie, F. Ren, Synthesis and catalytic performance of polydopamine supported metal nanoparticles, Sci. Rep. 10 (2020) 10416, https://doi.org/10.1038/s41598-020-67458-9.
[68] C. Silva, F. Simon, P. Friedel, P. Pötschke, C. Zimmerer, Elucidating the chemistry behind the reduction of graphene oxide using a green approach with polydopamine, Nanomaterials 9 (2019) 902, https://doi.org/10.3390/nano9060902.
[69] A.C. Ferrari, Raman spectroscopy of graphene and graphite: disorder, electron-phonon coupling, doping and nonadiabatic effects, Solid State Commun. 143 (2007) 47–57, https://doi.org/10.1016/j.ssc.2007.03.052.
[70] M.K. Marchewka, Infrared and Raman spectra of melaminium chloride hemihydrate, Mater. Sci. Eng. B Solid-State Mater. Adv. Technol. 95 (2002) 214–221, https://doi.org/10.1016/S0921-5107(02)00235-0.
[71] I. Papailias, T. Giannakopoulou, N. Todorova, D. Demotikali, T. Vaimakis, C. Trapalis, Effect of processing temperature on structure and photocatalytic properties of g-C3N4, Appl. Surf. Sci. 358 (2015) 278–286, https://doi.org/10.1016/j.apsusc.2015.08.097.
[72] M.L. Alfieri, R. Micillo, L. Panzella, O. Crescenzi, S.L. Oscurato, P. Maddalena, A. Napolitano, V. Ball, M. D'Ischia, Structural basis of polydopamine film formation: probing 5,6-dihydroxyindole-based eumelanin type units and the porphyrin issue, ACS Appl. Mater. Interfaces 10 (2018) 7670–7680, https://doi.org/10.1021/acsami.7b09662.
[73] Y.S. No, H.K. Choi, J.S. Kim, H. Kim, Y.J. Yu, C.G. Choi, J.S. Choi, Layer number identification of CVD-grown multilayer graphene using Si peak analysis, Sci. Rep. 8 (2018) 571, https://doi.org/10.1038/s41598-017-19084-1.
[74] J. Liebscher, R. Mrówczyński, H.A. Scheidt, C. Filip, N.D. Haïdade, R. Turcu, A. Bende, S. Beck, Structure of polydopamine: a never-ending story? Langmuir 29 (2013) 10539–10548, https://doi.org/10.1021/la4020288.
[75] S. Rella, E. Mazzotta, A. Caroli, M. De Luca, C. Bucci, C. Malitesta, Investigation of polydopamine coatings by X-ray Photoelectron Spectroscopy as an effective tool for improving biomolecule conjugation, Appl. Surf. Sci. 447 (2018) 31–39, https://doi.org/10.1016/j.apsusc.2018.03.057.
[76] S. Hong, Y.S. Na, S. Choi, I.T. Song, W.Y. Kim, H. Lee, Non-covalent self-assembly and covalent polymerization co-contribute to polydopamine formation, Adv. Funct. Mater. 22 (2012) 4711–4717, https://doi.org/10.1002/adfm.201201156.
[77] A.A.R. Watt, J.P. Bothma, P. Meredith, The supramolecular structure of melanin, Soft Matter 5 (2009) 3754–3760, https://doi.org/10.1039/b902507c.
[78] Y.T. Thathachari, M.S. Blois, Physical studies on melanins, Biophys. J. 9 (1969) 77–89, https://doi.org/10.1016/S0006-3495(69)86370-8.
[79] J. Cheng, S.C. Moss, M. Eisner, X-ray characterization of melanins—II, Pigm. Cell Res. 7 (1994) 263–273, https://doi.org/10.1111/j.1600-0749.1994.tb00061.x.
[80] K.B. Stark, J.M. Gallas, G.W. Zajac, M. Eisner, J.T. Golab, Spectroscopic study and simulation from recent structural models for eumelanin: II. Oligomers, J. Phys. Chem. B 107 (2003) 11558–11562, https://doi.org/10.1021/jp034965r.
[81] G.W. Zajac, J.M. Gallas, J. Cheng, M. Eisner, S.C. Moss, A.E. Alvarado-Swaisgood, The fundamental unit of synthetic melanin: a verification by tunneling microscopy of X-ray scattering results, Biochim. Biophys. Acta Gen. Subj. 1199 (1994) 271–278, https://doi.org/10.1016/0304-4165(94)90006-X.
[82] X. Yu, H. Fan, Y. Liu, Z. Shi, Z. Jin, Characterization of carbonized polydopamine nanoparticles suggests ordered supramolecular structure of polydopamine, Langmuir 30 (2014) 5497–5505, https://doi.org/10.1021/la500225v.
[83] K.B. Stark, J.M. Gallas, G.W. Zajac, J.T. Golab, S. Gidanian, T. McIntire, P.J. Farmer, Effect of stacking and redox state on optical absorption spectra of Melanins–Comparison of theoretical and experimental results, J. Phys. Chem. B 109 (2005), https://doi.org/10.1021/jp046710z, 1970–1977.
[84] A. Casadevall, A. Nakouzi, P.R. Crippa, M. Eisner, Fungal melanins differ in planar stacking distances, PLoS One 7 (2012) e30299, https://doi.org/10.1371/journal.pone.0030299.
[85] F.R. Kohl, C. Grieco, B. Kohler, Ultrafast spectral hole burning reveals the distinct chromophores in eumelanin and their common photoresponse, Chem. Sci. 11 (2020) 1248–1259, https://doi.org/10.1039/C9SC04527A.
[86] C.T. Chen, F.J. Martin-Martinez, G.S. Jung, M.J. Buehler, Polydopamine and eumelanin molecular structures investigated with ab initio calculations, Chem. Sci. 8 (2017) 1631–1641, https://doi.org/10.1039/C6SC04692D.
[87] S. Meng, E. Kaxiras, Theoretical models of eumelanin protomolecules and their optical properties, Biophys. J. 94 (2008) 2095–2105, https://doi.org/10.1529/biophysj.107.121087.
[88] W. Cao, X. Zhou, N.C. McCallum, Z. Hu, Q.Z. Ni, U. Kapoor, C.M. Heil, K.S. Cay, T. Zand, A.J. Mantanona, A. Jayaraman, A. Dhinojwala, D.D. Deheyn, M.D. Shawkey, M.D. Burkart, J.D. Rinehart, N.C. Gianneschi, Unraveling the structure and function of melanin through synthesis, J. Am. Chem. Soc. 143 (2021) 2622–2637, https://doi.org/10.1021/jacs.0c12322.
[89] M. D'Ischia, A. Napolitano, V. Ball, C.T. Chen, M.J. Buehler, Polydopamine and eumelanin: from structure-property relationships to a unified tailoring strategy, Acc. Chem. Res. 47 (2014) 3541–3550, https://doi.org/10.1021/ar500273y.
[90] A. Büngeler, B. Hämisch, O. Strube, The supramolecular buildup of eumelanin: structures, mechanisms, controllability, Int. J. Mol. Sci. 18 (2017) 1901, https://doi.org/10.3390/ijms18091901.
[91] J. Yana, N. Chiangraeng, P. Nimmanpipug, V.S. Lee, A theoretical study of supramolecular aggregation of polydopamine tetramer subunits in aqueous solution, J. Mol. Graph. Model. 107 (2021) 107946, https://doi.org/10.1016/j.jmgm.2021.107946.
[92] H.C. Yang, W. Xu, Y. Du, J. Wu, Z.K. Xu, Composite free-standing films of polydopamine/polyethyleneimine grown at the air/water interface, RSC Adv. 4 (2014) 45415–45418, https://doi.org/10.1039/c4ra04549a.

Publication 4

The Author's individual contribution to this publication includes: Investigation, Visualization, Methodology, Conceptualization, Validation, Data curation and Writing - Original Draft, Funding Acquisition, Project Management and Manuscript Submission. Author is the Principal Investigator of the PRELUDIUM20 grant 2021/41/N/ST5/00211 which was the main funding source for this publication.

Journal: ACS Applied Materials & Interfaces
ISSN: 1944-8244
Publisher: American Chemical Society
Journal Impact Factor: 9.5
Publication Date: 25.07.2023
Number of Citations: 1

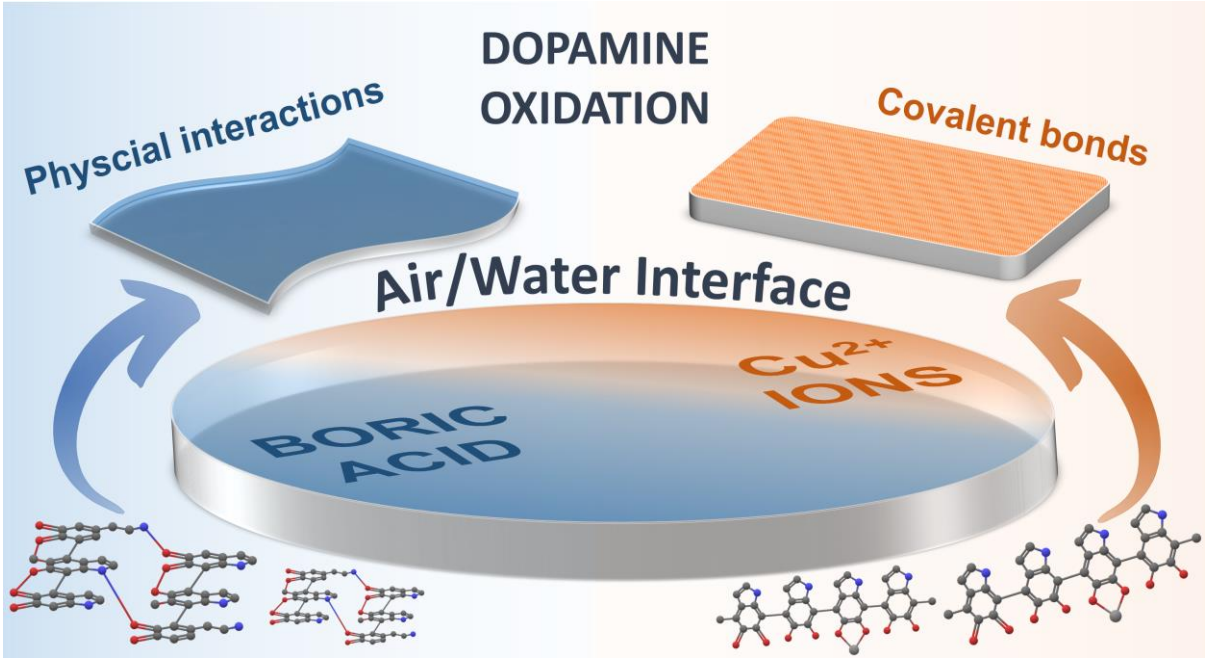

Figure 12. Graphical abstract of the P4

ACS APPLIED MATERIALS & INTERFACES

www.acsami.org

Research Article

Control of Intermolecular Interactions toward the Production of Free-Standing Interfacial Polydopamine Films

Jakub Szewczyk,* Visnja Babacic, Adam Krysztofik, Olena Ivashchenko, Mikołaj Pochylski, Robert Pietrzak, Jacek Gapiński, Bartłomiej Graczykowski, Mikhael Bechelany, and Emerson Coy*

Cite This: *ACS Appl. Mater. Interfaces* 2023, 15, 36922−36935

Read Online

ACCESS | Metrics & More | Article Recommendations | Supporting Information

ABSTRACT: Aggregation of the polydopamine (PDA) molecular building blocks at the air/water interface leads to obtaining large surface nanometric-thin films. This mechanism follows two possible pathways, namely, covalent or non-covalent self-assembly, which result in a different degree of structure order and, consequently, different structural properties. Control of this mechanism could be vital for applications that require true self-support PDA free-standing films, for example, electrochemical sensing or membrane technology. Here, we are considering the impact of boric acid (BA) and Cu^{2+} ions on the mentioned mechanism exclusively for the free-standing films from the air/water interface. We have employed and refined our own spectroscopic reflectometry method to achieve an exceptionally high real-time control over the thickness growth. It turned out that BA and Cu^{2+} ions significantly impact the film growth process. Reduction of the nanoparticles size and their number was examined via UV−vis spectroscopy and transmission electron microscopy, showing a colossal reduction in the mean diameter of nanoparticles in the case of BA and a moderate reduction in the case of Cu^{2+}. This modification is leading to significant enhancement of the process efficiency through moderation of the topological properties of the films, as revealed by atomic force microscopy. Next, applying infrared, Raman, and X-ray photoelectron spectroscopy, we presented small amounts of metal (B or Cu) in the final structure of PDA and simultaneously their vital role in the oxidation mechanism and cross-linking through covalent or non-covalent bonds. Therefore, we revealed the possibility of synthesizing films via the expected self-assembly mechanism which has hitherto been out of control. Moreover, modification of mechanical properties toward exceptionally elastic films through the BA-assisted synthesis pathway was shown by achieving Young's modulus value up to 24.1 ± 5.6 and 18.3 ± 6.4 GPa, using nanoindentation and Brillouin light scattering, respectively.

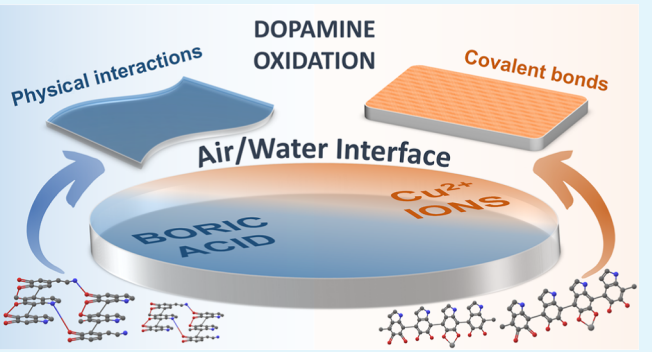

KEYWORDS: *dopamine, oxidation, self-assembly, air−water interface, Brillouin light scattering*

1. INTRODUCTION

Polydopamine (PDA) is a nature-inspired polymer that gained exceptional attention in chemistry due to its unique adhesive properties and multiple surface functionalization ability.[1] A relatively simple synthesis can produce various forms of this material or its analogues,[2−4] that is, directly deposited coatings,[5,6] functional nanoparticles,[7−9] or free-standing films from the air/water interface.[10−13] The latter is particularly interesting due to the self-assembly of PDA macromolecules at the interface, leading to high-quality nanometric-thin polymer films that can be transferred to various functional substrates.[14]

When applied to the modification of functional materials, PDA exhibits exceptional properties, such as hydrophilicity, anti-fouling,[15] the enhancement of photocatalytic performance,[16] and the increase of electrocatalytic activity,[17] among others. Moreover, PDA thin coating on the transition-metal oxide-based electrode surface was recently shown to decrease charge-transfer resistance at the electrode−phosphate-buffered saline solution interface.[18] However, so far, surface modifications with PDA leading to the improvement of the above-mentioned properties have been based on the in situ deposition of coatings by oxidizing dopamine (DA) directly on the surface of the targeted material, preventing the integration on sensitive substrates. Nevertheless, an attractive alternative methodology is the possibility of ex situ functionalization of surfaces by PDA transferring, especially those that can tackle large-area functionalization.

Electrochemically grown PDA films have significant applicability in many fields, including sensing and electronics.[17]

Received: April 12, 2023
Accepted: July 11, 2023
Published: July 25, 2023

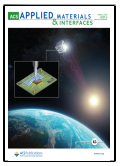

However, their main drawback resides in the relatively small lateral side of the film produced by this method. The size of these films is directly limited by the size of the electrode used to oxidize DA. Conversely, the self-assembly of DA by oxidation at the air/water interface does not suffer from this limitation since the main limiting aspect is the water surface exposed to the air, typically in the range of tens of centimeters. Our recent work determined the influence of synthesis conditions for these PDA films to be transferable to functional substrates,[19] showing similar thickness and roughness control as in the electrochemical deposition of PDA films but with the added value of retaining the so-called 2D-like ordering of the films.[14,19] Molecular dynamics simulations have provided some insights into the macromolecular self-assembly at the air/water interface. However, it has not yet been shown how to control this process.

There are two possible pathways of aggregation of PDA molecules: (i) non-covalent self-assembly of the subunits forming H-bond and $\pi-\pi$ interaction,[20] (ii) covalent oxidative polymerization of the monomer subunits,[21] and these pathways are simultaneously co-contributing to PDA formation.[22] For potential applications of free-standing PDA films, to have the possibility of tuning the degree of supramolecular order is crucial, for example, toward obtaining a polymer more conjugated with $\pi-\pi$ interactions, for the construction of even more efficient heterojunctions for photocatalytic applications.[23] In turn, the covalent organic frameworks (COFs)—highly ordered structures with covalently linked organic units that can be topologically grown into various architectures—stormed the world of chemistry and functional materials in recent years.[24−26] Moreover, it has already been proven that PDA can be obtained as COF, but only for nanoparticles, not for functional free-standing films.[27] Therefore, we resolved to find chemical agents that would allow us to direct the synthesis toward covalent or non-covalent intramolecular interactions.

Boric acid (BA) was very recently successfully used to tune the diameter of PDA nanoparticles.[28] Here, we are considering what impact BA can have on free-standing films from the air/water interface. Interestingly, at pH = 8.0, adding BA leads to reversible catechol-boron monocomplex formation, significantly increasing the share of non-covalent cross-linking of the structure.[29] In turn, metallic ions (Na^+, Ca^{2+}, Mg^{2+}, and Co^{2+}) were used to modify free-standing PDA films, which greatly impacted the growth dynamics, interaction with nanoparticles suspended in the solution, and particulate properties such as hydrophilicity.[30] However, in that study authors did not verify if metal ions (in particular Cu^{2+}) could direct the DA oxidation process toward the desired intramolecular ordering type. Indeed, it was previously shown that Cu^{2+} might influence the structure of the colloids obtained in DA oxidation, reducing the degree of their self-organization.[31]

In this article, we analyze the impact of these two promising agents—BA and Cu^{2+} ions—on the synthesis and the resulting structure of free-standing PDA films from the air/water interface. The influence on thickness growth dynamics and mechanical properties of PDA films obtained at the air/water interface using BA and Cu^{2+} was further investigated. More importantly, we discovered that two divergent oxidation pathways lead to more favorable covalent or physical self-assembly of the molecules in the resulting material. Especially, the later ones are leading to exceptionally elastic films, with tuneable mechanical response. As mentioned above, the ability to precisely influence the structure of this material is crucial from the point of view of its application in photocatalysis, photovoltaics,[32,33] and other emerging fields.

2. MATERIALS AND METHODS

2.1. Chemical Reagents. Materials in all synthesis procedures were used without any further purifications. DA hydrochloride (CAS: 62-31-7, s, >98%), trizma base (CAS: 77-86-1, s, >99%), hydrochloric acid (CAS: 7647-01-0, l, 25%), copper(II) sulfate pentahydrate (CAS: 7758-99-8, s, ≥98.0%), acetic acid (CAS: 64-19-7, l, ≥99%), sodium acetate (CAS: 127-09-3, s, ≥99%), BA (CAS: 10043-35-3, s, ≥99.5%), sodium hydroxide (CAS: 1310-73-2, s, ≥98%), and silicon wafer (Si 100, CAS: 7440-21-3, s) from Sigma-Aldrich and ultrapure deionized water from a Hydrolab Ultra UV system were used.

2.2. Synthesis of the PDA Free-Standing Films. The film synthesis was carried out based on the optimized conditions determined in our previous work.[19] DA (0.5 mg mL^{-1}) in the form of DA hydrochloride powder was added to a Petri dish (7.5 cm in diameter, 2 cm in height) containing Tris buffer (10 mmol, 45 mL, pH = 8.0) or sodium acetate buffer (10 mmol, 45 mL, pH = 4.5) and an oxidation agent (BA or $CuSO_4$, solid) in three different concentrations to achieve molar ratios of the DA/agent equal 1:1, 1:3, and 1:6. This is corresponding to 0.52, 1.56, and 3.12 mg mL^{-1} for copper(II) sulfate pentahydrate and 0.20, 0.60, and 1.20 mg mL^{-1} for BA, respectively. For clarity, all mixtures are summarized in Table 1. Stirring (300 rpm) occurred on a magnetic plate throughout the synthesis time (72 h), and a glass lid covered the vessel with a small gap to allow air exchange. The use of a buffer with an acidic pH of 4.5 in the case of Cu^{2+} as an oxidant is justified by the mechanism of DA oxidation in an acidic environment. Utilizing these ions in the presence of chloride ions and dissolved oxygen assumes an increase of the Cu(II)/Cu(I) redox potential.[34] Note that it is not possible to use Cu^{2+} as an oxidant at basic pH = 8 because according to Pourbaix's diagram of copper, the spontaneous formation of $Cu(OH)_2$ occurs in that case.[35,36] The optimized synthesis path (as mentioned above) allowed us to obtain homogeneous films with a size corresponding to the diameter of a Petri dish (7.5 cm). During the synthesis of all samples, an identical reaction was simultaneously carried out in the second vessel to collect the solution for UV−vis and dynamic light scattering (DLS) tests. After the desired oxidation time, the films were transferred in pieces to a silicon substrates (1 × 1 cm) using the simple scooping technique (Figure S1) that is a deposition of a fragment of the free-standing film on a substrate immersed in the solution using the gravity force. No additional washing was done, and purification of the samples of the so-transferred films was carried out. Although films obtained in the experiment are structurally PDA (not DA), for clarity, while describing all experimental results, we will be using the same nomenclature for mixtures and for films obtained from them.

Table 1. Composition of the Mixtures Used in the Experiment

name	buffer	pH	oxidation agent	DA/agent molar ratio
DA	tris	8.0	none	n.a.
DA/BA 1:1	tris	8.0, readjusted by NaOH	BA	1:1
DA/BA 1:3	tris	8.0, readjusted by NaOH	BA	1:3
DA/BA 1:6	tris	8.0, readjusted by NaOH	BA	1:6
DA/Cu 1:1	acetate	4.5	$CuSO_4$ (Cu^{2+})	1:1
DA/Cu 1:3	acetate	4.5	$CuSO_4$ (Cu^{2+})	1:3
DA/Cu 1:6	acetate	4.5	$CuSO_4$ (Cu^{2+})	1:6

https://doi.org/10.1021/acsami.3c05236
ACS Appl. Mater. Interfaces 2023, 15, 36922−36935

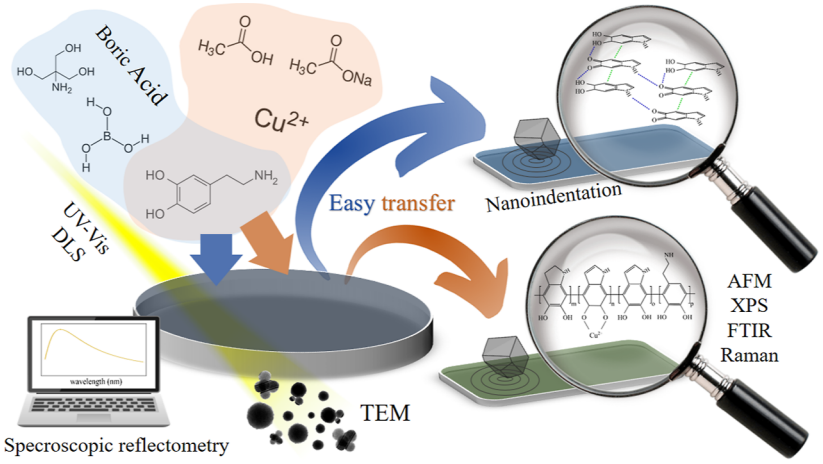

Figure 1. Scheme of the workflow—the synthesis proceeded under close observation of the oxidation, nanoparticles, and film growth dynamics, followed by a structural, chemical, and nanomechanical examination of the obtained films.

2.3. Physico-chemical Characterization. In our former publication,[19] we described a home-made instrument for spectroscopic reflectometry (SR) built to study the dynamics of the free-standing film thickness growth at the air/water interface. Based on that experience, we have designed an improved and more compact version of such an instrument using commercially available units and avoiding glass parts to reach the UV range necessary to reduce the lower membrane thickness limit of detection. It is composed of the deuter-halogen light source AvaLight-DHc (Avantes), AvaSpec-Mini2048CL spectrometer (Avantes), and an optical fiber capable of operating in the broad UV−vis spectrum (220−800 nm). Previously, it was possible to determine with high accuracy the thickness of films starting from 50 nm. Lowering the wavelength to 200 nm allowed us to reveal the first maximum of the reflectance function already for 30 nm thick PDA film, as shown in Figure S1. For atomic force microscopy (AFM) measurements, we used an ICON-Bruker microscope with complementary Gwyddion software to analyze profilometry data, thickness, and roughness.[37] To investigate the thickness of films after 72 h, we calculated the average of 10 measurements on randomly selected sections crossing the crack in the film with the exposed substrate. For roughness determination, we calculated the average of 10 measurements of the root-mean-square (rms) factor value in the area of 2 × 2 μm of the films. Transmission electron microscopy was performed with JEOL 1400 TEM. Samples were drop-cast on a copper grid (Lacey/Carbon film 200 mesh made by Ted Pella) directly from the reaction solution mixture and dried in a vacuum desiccator without any centrifugation. UV−vis measurements were performed using a LAMBDA 950 spectrophotometer (PerkinElmer). DLS and zeta-potential measurements were performed on the Zetasizer Nano ZS (Malvern Panalytical). The mean size of the nanoparticle hydrodynamic diameter was calculated basing on the number-based distribution. Due to the low DA concentration used in the experiment (0.5 mg mL^{-1}), the samples for UV−vis and DLS measurements were not further diluted. The photograph of the remaining nanoparticle aggregates at the bottom and walls of the Petri dish was taken with a digital Xiaomi 50MP AI Quad Camera without additional intervention, after all liquid was slowly removed from the vial with a syringe. Raman spectroscopy was carried out employing a Renishaw instrument equipped with microscope enclosure RE04, 532 nm laser source, and Leica N PLAN 50×/0.5 objective lens. Exposure time was set to 0.1 s with 0.1% of the power of the laser source (corresponding to 20 μW), and the number of accumulations was 3. X-ray photoelectron spectroscopy (XPS) was performed in an ultra-high vacuum chamber (Specs) using a monochromatic X-ray source (Al anode). The vacuum in the analysis chamber was in 10^{-9} mbar range. The pass energy for the survey was set to 60 eV, while the high-resolution regions were collected for the pass energy of 20 eV. Data analysis was performed using the CasaXPS program. X-ray diffraction (XRD) characterization was executed with the use of an MRD-X'pert^3 diffractometer (PANalytical), operating at 45 kV and 40 mA with a Cu Kα radiation source (wavelength of 1.54 Å). Nanoindentation of the film's experiment was performed using a TI-950 (Hysitron) triboindenter with a Berkovich tip. Load and displacement curves were analyzed according to the Oliver and Pharr method.[38,39] The methodology is described elsewhere.[40] Finally, Brillouin light scattering (BLS) measurements were performed in the p−p backscattering geometry using the high-contrast tandem type Fabry−Perot interferometer (table stable) and the solid-state laser (Excelsior, Spectra-Physics, λ = 532 nm). The incident and backscattered light were focused and collected, respectively, using the microscope objective with a 10× magnification and a numerical aperture NA = 0.25. The incident power of the laser light was 0.8 mW. The spectrometer mirror spacing was set to 33 mm, and the scanning amplitude was 200 nm, allowing measurements in the ±1.7 GHz frequency range. All the spectra were recorded at a room temperature of 296.5 K (23.3 °C) and relative humidity of 39%. Ultra-thin films (below 30 nm) were needed for this experiment; therefore, the oxidation time was 12 h. When presenting data in the graphical form, error bars were included, except for the SR and UV−vis methods, where the error bars are smaller than the data point symbols.

3. RESULTS AND DISCUSSION

As illustrated in Figure 1, the work was divided into the following steps. We started with the production of DA, DA/BA, and DA/Cu free-standing films at the air/water interface. To follow the oxidation process, we measured the change in UV−vis absorbance of the solution and the growth dynamics of nanoparticles using the DLS and TEM methods. It was of a great importance because nanoparticle inclusions negatively affect the efficiency of the process and the quality of the PDA films at the air/water interfaces. At the same time, we studied the growth kinetics of films in situ at the interface using the non-destructive SR method. In the next step, we transferred the PDA thin films on silicon substrates to perform their topological (AFM) and structural and chemical (Raman, FTIR, and XPS spectroscopies) characterization. Moreover, we performed nanoindentation tests to check the flexibility and hardness of the obtained films. Finally, the elastic properties of the free-standing films were examined by BLS. Additionally, we present photographs of the films at the air/water interface and after transferring on the Si substrates (Figure S3).

As mentioned above, we investigated the growth of the films in situ via SR (Figure 2a). In the first 24 h, the influence of BA

https://doi.org/10.1021/acsami.3c05236
ACS Appl. Mater. Interfaces 2023, 15, 36922−36935

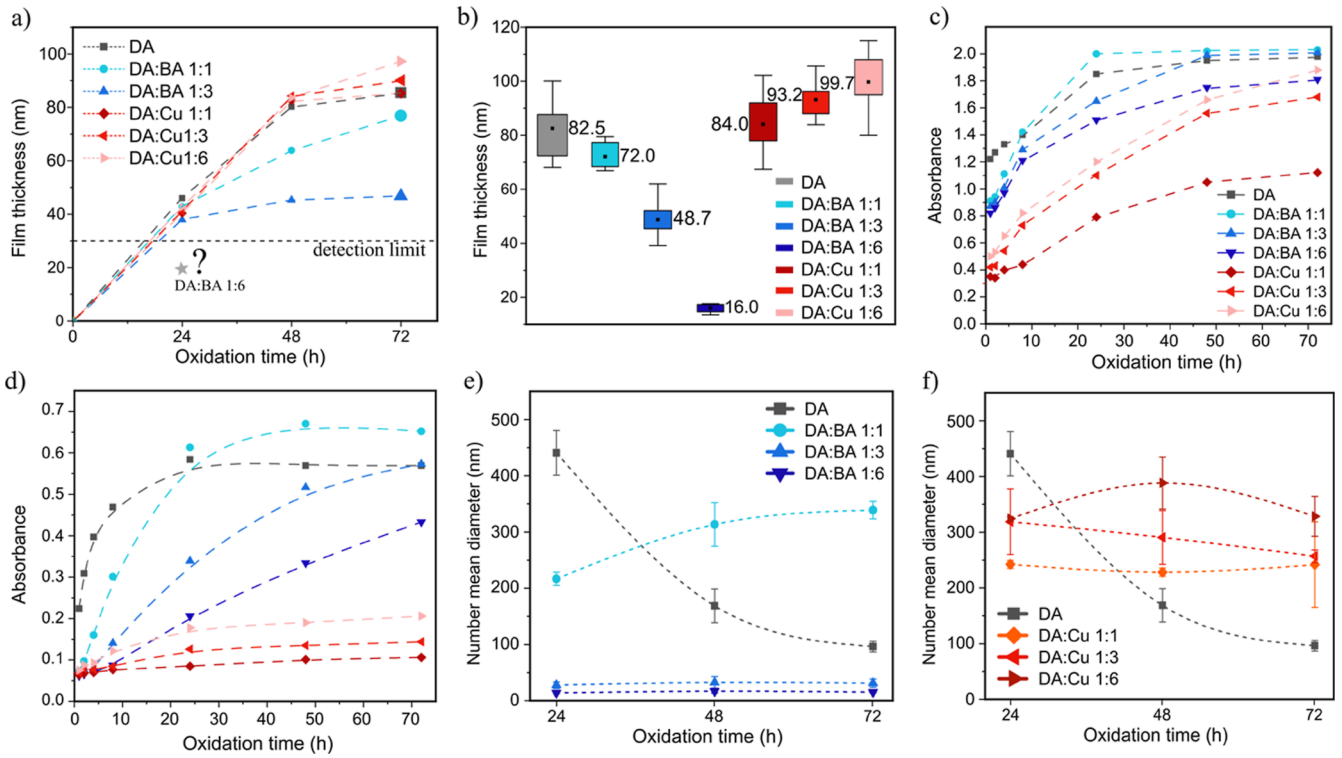

Figure 2. (a) In situ thickness growth of the films at the air/water interface measured by SR, (b) final thickness of the films transferred on Si substrates after 72 h measured by AFM, (c) UV−vis absorbance change during 72 h of the DA oxidation at the wavelength 305 and (d) 600 nm, and (e) DLS examination of the mean diameter of the PDA nanoparticles in the solution during 72 h of the DA oxidation modified with BA and (f) Cu^{2+}. All dashed lines connecting data points on graphs are guide to the eye of the viewer only.

and Cu^{2+} is not significant, except for DA/BA 1:6, where the growth of the film was almost completely inhibited. The last finding is in agreement with a recent observation that when the BA to DA ratio is higher than 3:1, the autoxidation of DA into PDA both in solution and at interfaces is terminated.[41] In the next 24 h (24−48 h), in a mixture of DA and DA/Cu 1:1, 1:3, and 1:6, an almost linear increase in film thickness continues, while the growth rate of films DA/BA 1:3 and 1:6 slows down. Finally, in the last 24 h (48−72 h), we note a slow film thickness increase for all samples except for DA/Cu 1:6, where the growth rate is still significant. From our previous work, it follows that in the first step at the air/water interface, the forming DA tetramers quickly trap other planar molecules by physical forces (preferably $\pi-\pi$ interactions), which induces quasi-ordered stacking of subsequently supplied molecules in the second step.[19] For now, it can be concluded that Cu^{2+}, as a good oxidant in these conditions, increases the efficiency of stacking the subsequent molecules to the already formed film at the air/water interface but does not significantly affect the efficiency of initial layer formation.

After 72 h, films from the air/water interface were transferred on a Si wafer and investigated via AFM for subsequent examination of the thickness (Figure 2b). The results are consistent with those obtained with SR. Using AFM, we managed to measure also the thickness of the DA/BA 1:6 film, which was not possible with SR due to the thickness detection limit (see Section 2.3). It turned out that an ultrathin, continuous, easy-to-transfer film with a thickness of less than 20 nm was obtained in these conditions. It was completely transparent and colorless, almost invisible when transferred to silicon.

To study the DA oxidation and growth of the nanoparticles in the reaction solution, first, UV−vis spectra were measured in the range from 200 to 600 nm (Figure S4). The full spectrum of the DA oxidation mixture after 72 h shows broad absorption in this range because of the formation of the DA oxidation products that is 5,6-dihydroxyindole (DHI).[42] The absorption at ∼350 nm corresponds to the quinone units in the PDA structure,[43,44] providing evidence that a mixture of DHI and 5,6-indolequinone (IDQ) was obtained as assumed by the DA oxidation model. The absorption corresponding to boron-catechol bonds typically shows up at 490 nm, but here it is not visible due to the reversible boron-catechol interactions at pH = 8.0.[29] Two wavelengths were chosen for plotting absorbance kinetics: 305 nm (Figure 2c) and 600 nm (Figure 2d). A strong peak at about 305 nm originates from the conversion of *o*-quinone to dopaminochrome,[45,46] indicating an important intermediate oxidation step. Note that this step is so fast for DA and DA/BA samples that absorbance at $t = 0$ (corresponding to about 1 min) is significantly elevated, but this effect is limited for DA/Cu samples as the cyclization rate of *o*-quinone at acidic pH is slower.[34] At 600 nm, only PDA nanoparticles are responsible for light absorption.[28,30] At both wavelengths, DA alone with no agents shows fast absorbance change during the first 24 h and then plateau-like behavior. This suggests the fast and spontaneous generation of the PDA nanoparticles, consistent with the observed rapid color change of the solution. At $\lambda = 305$ nm, both the addition of BA and Cu^{2+} (except DA/Cu 1:1) resulted in a smoother curve and a similar final absorbance after 72 h, enabling to control the process. However, the very rapid increase in absorbance at $t = 0$ did not occur for Cu samples. This first step of the DA oxidation reaction may be partially coursed by aminochrome

https://doi.org/10.1021/acsami.3c05236
ACS Appl. Mater. Interfaces 2023, 15, 36922−36935

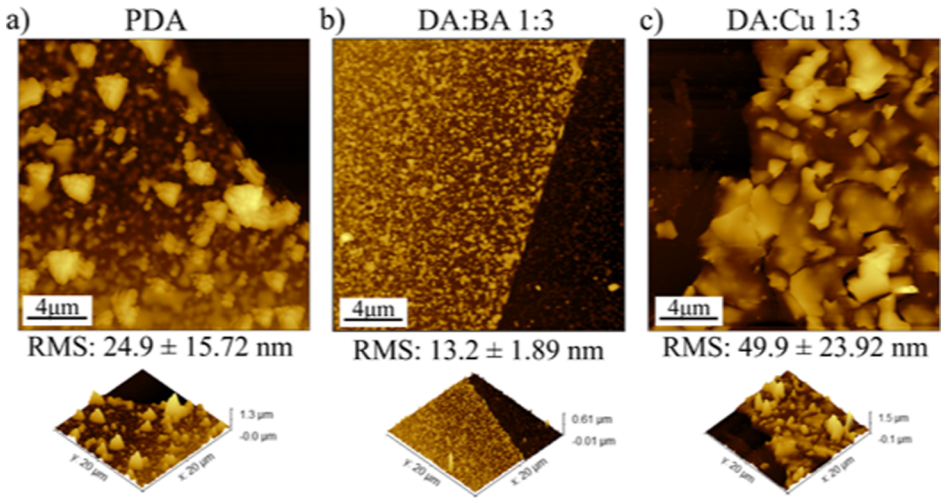

Figure 3. AFM topography images of the films after 72 h of oxidation at the air/water interface of the (a) PDA, (b) DA/BA 1:3, and (c) DA/Cu 1:3 solutions.

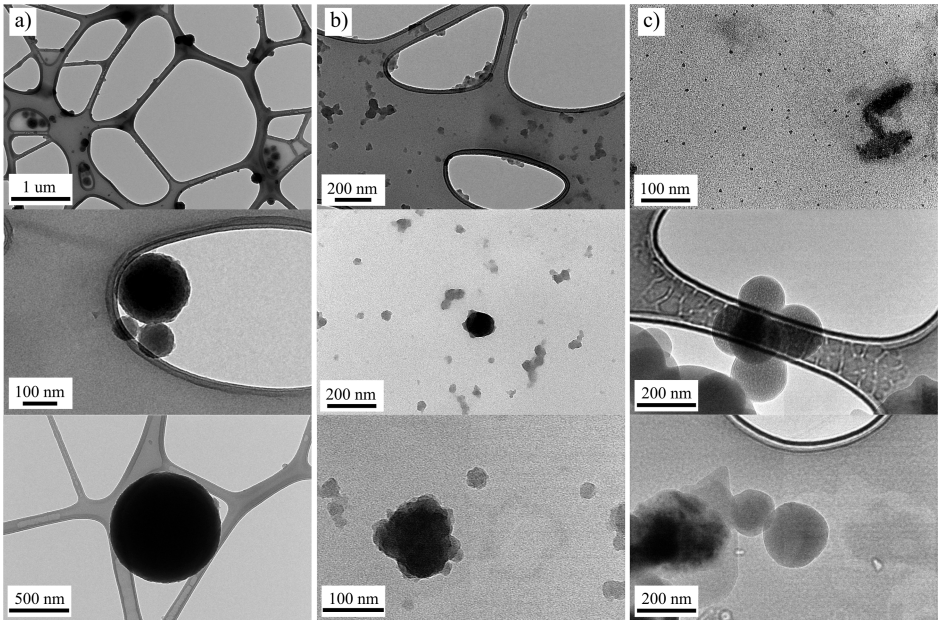

Figure 4. TEM images of the nanoparticles suspended in the (a) DA, (b) DA/BA 1:3, and (c) DA/Cu 1:3 solutions, after 72 h.

synthesis directly from active redox metal−DA adducts.[47] Different mechanisms were reported for polyaniline film formation in the presence of Cu^{2+} ions, where deprotonated imine and amine nitrogen atoms form complexes with coordinating Cu^{2+} ions.[48] This difference is due to the unique catechol-chemistry of DA, causing redox active metal ions to ligate to the adjacent hydroxyl groups of DA.[49] BA (1:3 and 1:6) caused the λ = 600 nm curve to change shape and indicates the inhibition of the formation of nanoparticles, especially in the first 24 h. BA in a molar ratio 1:1 does not alter this behavior drastically. This is consistent with literature reports which indicate that for a drastic inhibition of DA oxidation to PDA, the required BA/DA ratio is higher than 3:1.[41] Nevertheless, inhibition of the increase in absorbance at the wavelength 600 nm was achieved using Cu^{2+}, which seems contrary to the assumptions as it should accelerate the oxidative generation of the PDA nanoparticles. To explain this feature, DLS measurements were performed (Figure 2e,f). The unexpected drop in the mean size of the nanoparticles in the case of pure DA after 24 h is caused by sedimentation of the large nanoparticle aggregates to the bottom and walls of the Petri dish (Figure S5). Aggregation of the PDA nanoparticles and increase of the stability of the nanoparticles/solution colloid can be achieved by positive ζ (zeta potential).[50] Using Cu^{2+} as an oxidant in pH 4.5 leads to positively charged nanoparticles, as reported in the literature[31,51] and confirmed in our study (Figure S6). Moreover, in the following sections, we will provide AFM and TEM evidence of the presence of large (>500 nm) nanoparticles in the pure DA reaction solution after 72 h. Back to the DLS results, in case of BA (Figure 2e), an appearance of 200 nm PDA aggregates and their slight growth within 72 h was observed for low concentration (1:1), but no such big aggregates of the nanoparticles throughout the whole oxidation time were noted for DA/BA 1:3 and DA/BA 1:6 mixtures. Based on the UV−vis and DLS results, it can be concluded that the increase in the diameter of the nanoparticles is stopped below 50 nm at the beginning of the oxidation. The slow

https://doi.org/10.1021/acsami.3c05236
ACS Appl. Mater. Interfaces 2023, 15, 36922−36935

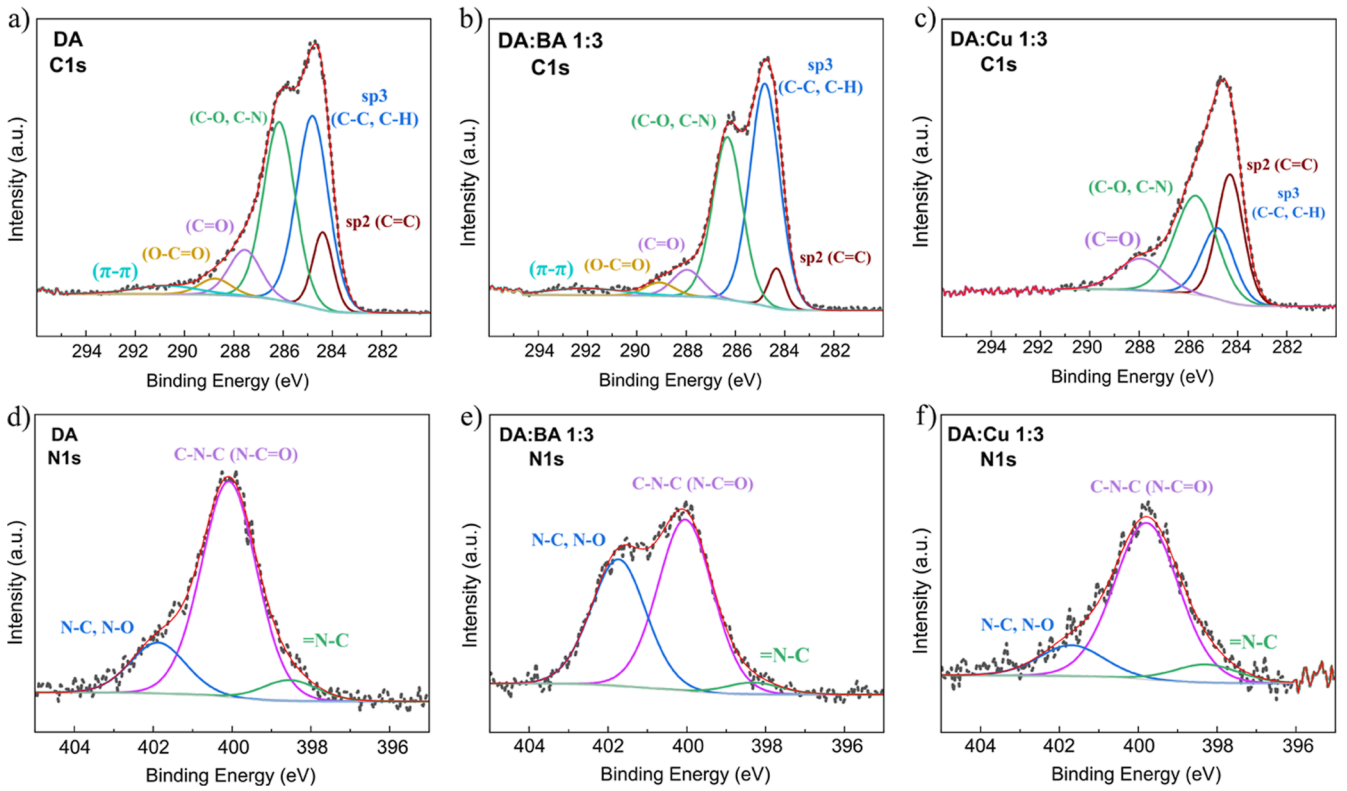

Figure 5. (a) X-ray photoelectron high-resolution spectra of the C 1s region for the DA, (b) DA/BA 1:3, and (c) DA/Cu 1:3 films, (d) high-resolution spectra of the N 1s region for the DA, (e) DA/BA 1:3, and (f) DA/Cu 1:3 films.

further change in the color of the solution is caused only by the increase in the number of suspended nanoparticles. By analyzing graphs for Cu^{2+} containing samples (Figure 2f), we can see that for all mixture compositions, the growth of nanoparticles stopped at a level of a diameter below 200 for 1:1 and 400 nm for 1:3 and 1:6. This further confirms the weaker λ = 600 nm absorbance compared to pure DA that was observed in UV−vis tests. To conclude, based on the SR, UV−vis, and DLS results, we found that BA is a moderate inhibitor of the PDA free-standing film growth rate at the air/water interface and an exceptional inhibitor of the PDA nanoparticle size growth. Cu^{2+} ions in acidic pH (4.5) are slightly inhibiting the growth of the PDA nanoparticles but simultaneously accelerating the PDA free-standing film growth rate at the air/water interface.

AFM was also applied to investigate the topography of the films (Figure 3). BA led to smooth and continuous film formation, showing an almost two times lower rms roughness coefficient than pure DA (Figure 3a,b). Although the nanoparticles in the DA/Cu 1:3 solution were smaller than that in pure DA, as demonstrated by UV−vis and DLS, these films' roughness is the highest (Figure 3c). The reason is the scaly structure of the films. All films AFM topography images after transferring on the Si substrate (Figure S7) and corresponding roughness rms parameters (Table S1) are shown in Supporting Information.

Transmission electron microscopy images of the nanoparticles formed in the solution and transferred dropwise on the TEM grids after 72 h of oxidation (Figure 4) confirm UV−vis and DLS findings. Note that no special protocol for obtaining and centrifuging nanoparticles was used. Therefore, all nanoparticles visible in the pictures were generated spontaneously. DA solution contains large single nanoparticles of a diameter >500 nm and numerous aggregates of the smaller nanoparticles (Figure 4a). In the DA/BA 1:3 mixture, there are very small nanoparticles (<50 nm), as shown before, but some nanoparticle aggregates can also be found, which, however, do not exceed 100 nm (Figure 4b). Electrostatically positively charged nanoparticles from the DA/Cu 1:3 mixture did not deposit so evenly on the TEM grids, but there were a lot of them on the grid rim. Therefore, the images are not perfectly sharp, but they still confirm previous observations, showing that the diameter of 200 nm dominates for the observed nanoparticles (Figure 4c).

To investigate the influence of oxidation agents on the chemical structure of the PDA, we performed an XPS study (Tables S2−S4). The most important (C 1s and N 1s) spectra are shown in Figure 5a−c,d−f, respectively. Others (O 1s, Si 2p, Cl 2p, B 1s, Cu 2p, and S2p) can be seen in the Supporting Information (Figures S8 and S10). The first and most important observation is the presence of $\pi-\pi$ bonds for DA and DA/BA 1:3 films, especially for the latter. This is an important indicator of the non-covalent self-assembly mechanisms of PDA aggregation through $\pi-\pi$ and hydrogen bonds.[52] Note that no $\pi-\pi$ bonds presence was noted for DA/Cu 1:3, but on the other hand, a much larger contribution of sp^2 carbon compared to sp^3 carbon was detected. The occurrence of oxygen and hydrogen atoms bonded to carbon inside the graphene-like domains increases the $C(sp^3)/C(sp^2)$ ratio.[53,54] We have strong evidence that using BA promotes PDA aggregation through physical (non-covalent) self-assembly. This observation is supported by Table S5 summarizing sp^2 and sp^3 carbon XPS subpeaks areas, showing that sp^2/sp^3 ratio for DA/Cu 1:3 is almost 15 times higher

https://doi.org/10.1021/acsami.3c05236
ACS Appl. Mater. Interfaces 2023, 15, 36922−36935

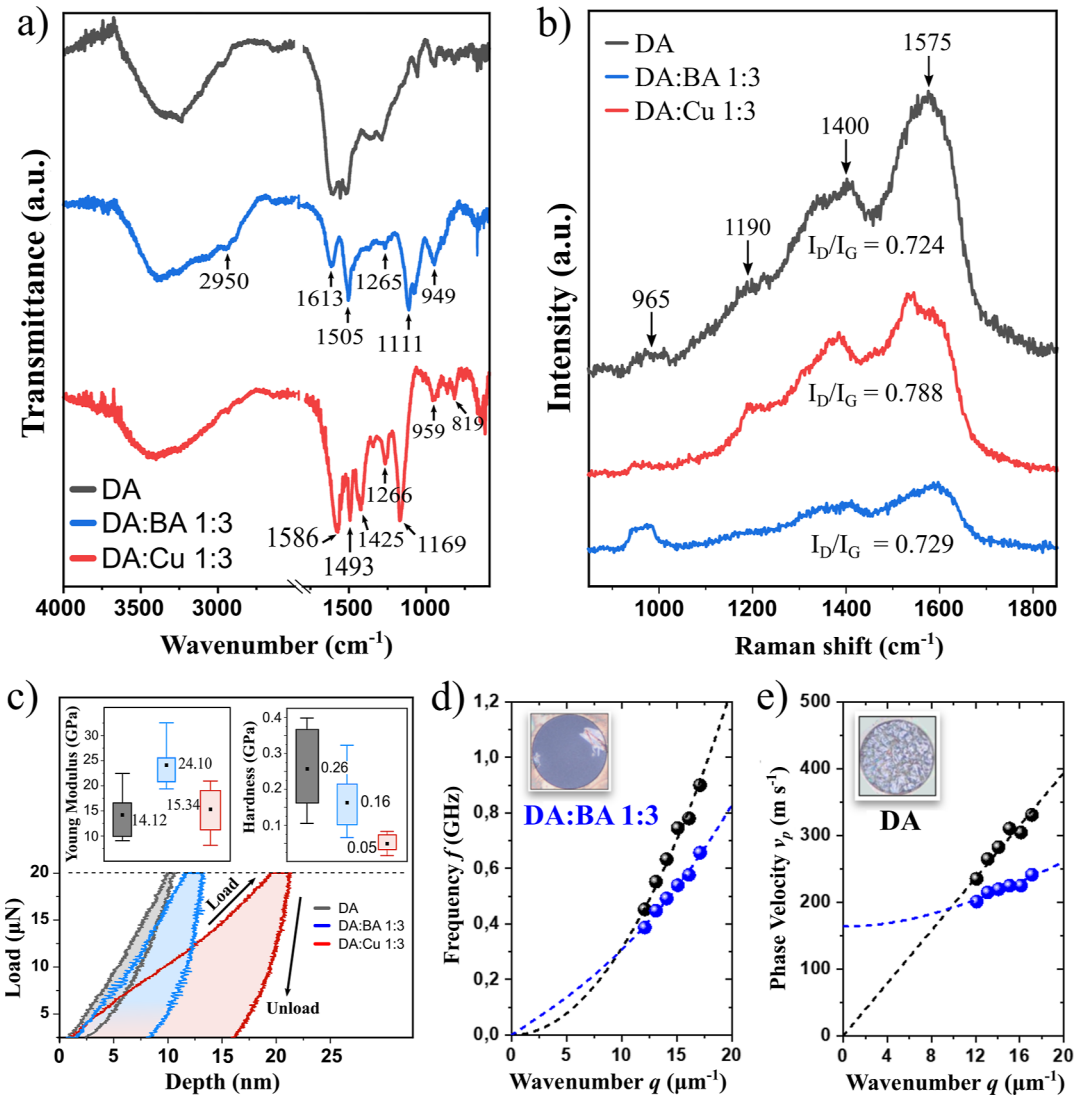

Figure 6. (a) Transmission Fourier-transform infrared spectra of the films, (b) Raman spectra of the films, (c) nanoindentation load−unload curves and box charts (inset) of the real Young modulus and hardness of the films, dispersion relations (d) $f(q)$ and (e) $v(q)$ of fundamental antisymmetric Lamb (flexural) waves measured with BLS spectroscopy for BA (blue points) and PDA (black points) membranes. The dashed lines represent the fit according to eqs 1 and 2. Inset images in (d,e) present optical microscopy images of the free-standing membranes DA/BA 1:3 and DA, respectively.

than that for DA/BA 1:3. The PDA subunits form the hydrogen bonds and $\pi-\pi$ interactions via the catechol groups and aromatic skeleton. In turn, strong oxidant Cu^{2+} promotes covalent oxidative polymerization of the monomer subunits, forming long chains with only rare connections through physical interactions. This is further confirmed by the analysis of N 1s high-resolution spectra of the films since the primary-amine part of the spectrum (N−C) is less significant for the DA/Cu 1:3 sample. A very recent study showed that primary amine contribution decreases with the oxidation time; thus, the decreased level indicates a higher oxidation level.[55] Simultaneously, secondary amine abundance in the DA oxidation products indicates the elevated intramolecular cyclization rate.[56,57] Therefore, the effect of the Cu^{2+} ions appears in both intermolecular and intramolecular interactions. Moreover, XPS showed that copper is present in the obtained films only in the form of the +2 ion (Figure S10). The structural units that make up the PDA can bind to Cu^{2+} via catechol groups.[49,58] Apparently, catechol−Cu^{2+} complexes are not the basis of the structure of the obtained material because the EDX analysis showed a very small signal from copper (Figure S11). However, we believe that such complexes are present, but in low numbers, because the N 1s spectrum for DA/Cu 1:3 has an increased (=N−C) to (C−N−C) signal ratio in comparison to the other films (Figure 5d−f), and it was previously postulated that such effect could be due to the complexation of the catecholate group with a metal cation.[59] Correspondingly, the presence of Cu^{2+} is confirmed also by the presence of a satellite (shake up) in the binding-energy range of 939−963 eV.[31] No well-developed hybrid nanostructures resulting from the complexation process were formed, as shown in Figure 4c. This is due to weak metallic ion incorporation into the polymer structure. To change this behavior, a PBS buffer with a pH above 5 would be required.[60] In turn, the boron-catechol mono-complexes trace amount in obtained DA/BA 1:3 film is credible on account of the mild XPS peak at around 192 eV, as previously reported.[28,61] At this point, it is worth emphasizing that utilizing XPS we did not

https://doi.org/10.1021/acsami.3c05236
ACS Appl. Mater. Interfaces 2023, 15, 36922−36935

detect any signs of metallic boron or copper in the resulting material. Finally, our observations point out that the contribution of C−O and C−N bonds is almost identical for all films, which confirms the catechol and eumelanin chemistry of the obtained films.

The FTIR spectra of our PDA films are shown in Figure 6a. The broad peak between 3200 and 3500 cm^{-1} indicates hydroxyl and N−H bonds in the catechol groups.[62] However, this broad peak consists of individual bands,[63] that is, "free" O−H stretch at ∼3525−3600 cm^{-1} and "bound" O−H stretch at 3360−3430 cm^{-1}. For DA/Cu 1:3, the proportion of "free" O−H seems to be much higher, which can be seen in the deconvoluted part of the spectrum in the range 2800−3700 cm^{-1} (Figure S12). "Bonded" O−H is associated with the occurrence of hydrogen bonds. In turn, the presence of the 2950 cm^{-1} band is associated with CH_2 stretching vibrations.[64] Its low intensity for the DA/Cu 1:3 sample suggests weak H-bonding of the CH_2 groups.[65] In the case of DA/BA 1:3, it is a significant band, suggesting a large number of hydrogen bonds, while for DA, its intensity is moderate. Next, we can see a whole set of bands typical for PDA: 1613 cm^{-1} (shifted to 1586 cm^{-1} in the Cu sample) and 1505 cm^{-1} (shifted to 1493 cm^{-1} in Cu) corresponding to C═C resonance vibrations in the benzene rings[66] and N−H vibration of the amine group,[64] respectively. Importantly, C═C resonance vibrations are much stronger for DA/Cu 1:3 than that for DA/BA 1:3, while N−H vibration is similarly intensive. This confirms previous XPS observations. Moreover, 1111 and 1169 cm^{-1} bands originate from C−O stretching vibration.[64] Finally, the peaks at 1425 and 1266 cm^{-1} are assigned to the phenolic C−O−H bending and stretching vibration, respectively.[67] Additional peaks for DA/Cu 1:3 at lower frequencies, especially 819 cm^{-1}, most probably originate from Cu−O stretching.[68,69]

Raman spectroscopy (Figure 6b) indicated the existence of two very important bands for all samples, namely, D band (1400 cm^{-1}) attributed to structural defects in the hexagonal carbon lattice and G band (1575 cm^{-1}) band linked with the in-plane vibration of the sp^2 carbon atoms.[70] The I_D/I_G ratio was also calculated, showing less similarity to nanocrystalline graphite of DA/Cu samples, which suggests probably less planar-oriented structure than DA and DA/BA films.[14,71,72] The peak at about 965 cm^{-1} indicates the C−H or O−H out-of-plane deformations. It is much less intense for DA/Cu, which confirms the lower impact of hydrogen bonds in the created structure. The band around 1190 cm^{-1} is assigned to the NH in-plane deformation mode originating from the pyrrole ring in the PDA structure and is the strongest for the DA/Cu 1:3 sample. Pyrrolic rings may participate in the formation of $\pi-\pi$ or O−H interactions, which would weaken or shift the band. In the covalent structure, these rings are the basic elements of the construction of structural units (DHI, indolequinone). Moreover, the shape of so-called 2D (G') peak was compared for DA and DA/Cu 1:3 films (Figure S13). DA/BA 1:3 was excluded from the analysis due to the low thickness of the films and thus significantly less intense bands in the whole spectrum. We can see that this peak is more intense for the DA sample, suggesting more planar interactions resulting from $\pi-\pi$ bonding. Moreover, the peak for DA/Cu 1:3 is shifted toward lower wavenumbers, suggesting a higher oxidation level.[73]

X-ray diffractometry was performed to confirm the above information (Figure S14). As reported before, diffractograms for DA and DA/BA 1:3 show characteristic diffraction peaks for PDA free-standing films produced at the air/water interface.[14,19] On the contrary, DA/Cu 1:3 diffractogram does not show any peaks which is in accordance with the lack of $\pi-\pi$ interactions,[74] as revealed by XPS.

To perform nanoindentation tests, we took advantage of the experience gained in our previous experiment.[14] As our goal was to compare the effects of chemical environment (BA vs Cu^{2+}) in the first place, we decided, as in previous chemical and structural studies, to compare samples prepared with identical molar ratios (1:3) and the same oxidation time (72 h). The film thicknesses were equal to 82.5, 48.7, and 93.2 nm for DA, DA/BA 1:3, and DA/Cu 1:3, respectively. The loading curves (Figure 6c) clearly indicate that the films deform in different ways. The DA film deforms the least, the DA/BA 1:3 film has a moderate deformation susceptibility, and the DA/Cu 1:3 film is almost plastic. The unloading curve can provide more information because we can extract sample Young's modulus from its shape and slope. The highest Young's modulus (24 GPa) was estimated for the film DA/BA 1:3. It is almost twice as high as the one obtained for DA (14 GPa); additionally, the load vs displacement curves show the high recovery of the DA film, with an almost ≈80% of elastic recovery, followed by DA/BA 1:3 with ≈40% and DA/Cu 1:3 with ≈25%. The shape of the curves also shows the higher plastic deformation on the DA/Cu 1:3 with respect of the other samples, despite the similar mechanical response. The average Young's modulus for the DA/Cu 1:3 film (15 GPa) is slightly higher than that for the DA film, however within the measurement error (see the left inset in Figure 6c). In turn, the highest average hardness value was achieved for the DA film (0.26 GPa). The mean values for DA/BA 1:3 and DA/Cu 1:3 films were 0.16 and 0.05 GPa, respectively.

The elastic properties in the GHz frequency (f) range of BA and PDA membranes grown for 12 h were measured in a contactless and non-destructive manner by means of BLS spectroscopy probing thermally excited acoustic waves/phonons. By changing the scattering angle θ from 30 to 46°, the magnitude of the acoustic wavevector q was varied in the range of ∼12−17 μm^{-1} according to the formula $q = 4\pi \sin\theta/\lambda$, where λ = 532 nm is the wavelength of the probing laser light. Such obtained dispersion relations $f(q)$ (Figure 6d) correspond to the antisymmetric, flexural Lamb waves (A0 mode). To determine the Young modulus E and the residual stress σ_0, the experimental data were fitted with the eq 1[75]

$$f = \frac{q}{2\pi}\sqrt{\frac{E}{(1-\nu^2)}\frac{d^2}{12\rho}q^2 + \frac{\sigma_0}{\rho}} \quad (1)$$

where $v_p = 2\pi f/q$, is the phase velocity, d is the membrane thickness, ρ = 1750 kg m^{-3} is the film mass density, and ν = 0.25 stands for the Poisson ratio.[76] For film thickness, we adopted the values estimated from AFM topography maps (Figures S15 and S16), d_{BA} = 10.5 ± 1.5 nm and d_{PDA} = 23 ± 3 nm for DA/BA and DA membranes, respectively. For the DA/BA 1:3 membrane, we obtained E = 18.3 ± 6.4 GPa and σ_0 = 47 ± 6 MPa, while for the PDA membrane, E = 14.4 ± 4.0 GPa and σ_0 = 0 as in this case, the data had not indicated any statistically significant residual stress. This last observation is better illustrated in the v_p vs q dependence since for $q \to 0$, the eq 2 is

$$v_p^{q\to 0} = \sqrt{\sigma_0/\rho} \quad (2)$$

https://doi.org/10.1021/acsami.3c05236
ACS Appl. Mater. Interfaces 2023, 15, 36922−36935

(Figure 6e), and it is compatible with optical microscopy images shown in the insets in Figure 6d,e. The determined values of the Young modulus are in a reasonable agreement with the nanoindentation results. Unfortunately, the DA/Cu samples could not be measured by means of BLS because of their poor stability in free suspension. Membranes transferred on the substrates broke even when suspended over the smallest holes (1 μm), which confirms their poor elasticity, as observed in nanoindentation.

From this study, it can be concluded that the DA/BA 1:3 sample has competitive elastic properties, with a moderate elastic recovery, the highest Young's modulus, and intermediate hardness. In turn, the DA/Cu 1:3 film does show low elastic recover, high plasticity, and low hardness. Noteworthy, it was shown that a more complex molecular structure promotes increasing hardness for the tested polymers,[77] in agreement with the results of our experiment. Weakly physical cross-linked polymer materials more likely undergo a deformation induced by a reduction in molecular order under external stimuli,[78] as observed for DA/Cu 1:3 films. More importantly, it was shown that the boron-catechol mono-complexes prevent oxidative covalent cross-linking and promote non-covalent cross-linking, resulting in a higher elasticity modulus of the obtained materials, which is confirmed in our experiment.

Polymeric thin films can display colossal differences in their mechanical properties when compared to the bulk state.[79−81] It was shown that the PDA in situ deposited coatings poses rather poor mechanical performance,[82] and the techniques used to improve these properties such as thermal treatment process[82] and blue diode laser annealing[83] are unlikely to be applicable to PDA films from the air/water interface. For a versatile-functionalization platform, PDA free-standing films should be easily transferable on macro-scale surfaces and protect sensitive and easily degradable photoactive materials.[16] Therefore, evaluating the mechanical property test results obtained for the PDA ultra-thin films to be transferred on the multifunctional substrates is important. To put these information in context, we have compared Young's modulus values for various ultra-thin polymer films reported in the literature and this experiment (Figure 7). It can be seen that PDA free-standing films have a particularly high modulus of elasticity, especially DA/BA 1:3, when compared to available data for other similar materials.

The lack of error-bars for some materials in Figure 7 means that the measurement error was not given in the publication or its value was so small that the error-bar is smaller than the data point symbol. The comparison indicates that except PDA free-standing films, no polymeric nanometric-thin film exceeds the value of 10 GPa of Young's modulus, including poly(methyl methacrylate) (PMMA) nanoscale thin films which are widely used in the emerging two-dimensional material nanotechnology applications.[84−86] In particular, the outstanding properties of DA/BA 1:3 films should be emphasized here, which, within the measurement error, showed more than 2x higher Young's modulus, with a similar thickness to PMMA.

For clarity, information presented in Figure 7 is summarized in Table 2 below. Importantly, the measurement techniques used were also specified.

Finally, in Figure 8, we present a scheme of DA oxidation pathways with respect to used agents—BA (Figure 8a) and Cu^{2+} ions (Figure 8b). Although the final structure of the obtained materials results from various intermolecular

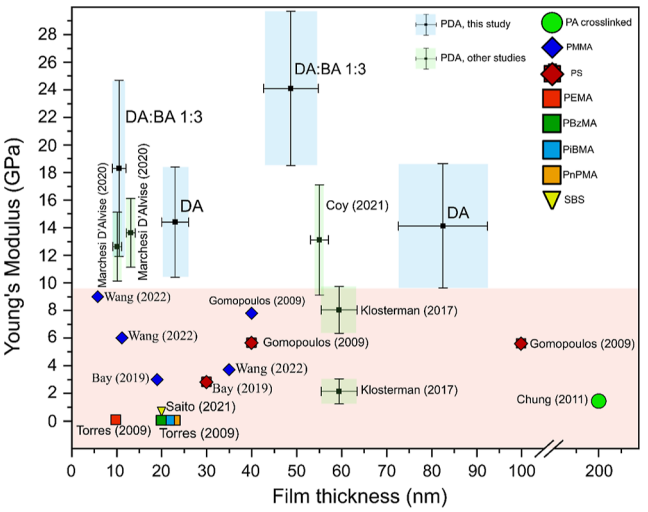

Figure 7. Comparison of Young's modulus of selected thin (thickness less than 200 nm) polymeric films reported in the literature and obtained in this study, evaluated via different techniques.

interactions, the diagram is intended to detail the moderation properties of BA and Cu^{2+}. The diagram shows the DA oxidation reaction, which proceeds according to a mechanism well-described in the literature,[6,52,95,96] but the first step, that is the conversion of DA to *o*-quinone and subsequently to dopaminochrome, can be partially coursed by direct aminochrome synthesis through Cu−DA adducts or can be partially coursed and reversed by boron-catechol mono-complexes formation. Then, from the final products of the oxidation reaction, that is DHI and IDQ (and intermediate products in case of DA/BA films), PDA is formed as a result of different intermolecular processes, namely, covalent self-assembly and non-covalent self-assembly ($\pi-\pi$ interactions and hydrogen bonds). Although very small amounts of metal ions (B and Cu) enter the final structure of PDA, their influence on the oxidation mechanism and cross-linking through covalent or coordination bonds is crucial.

4. CONCLUSIONS

In summary, we produced free-standing PDA films at the air/water interface with the use of two oxidation agents—BA and Cu^{2+} ions. We have effectively limited the arbitrary production of nanoparticles and aggregates of PDA nanoparticles suspended in a solution, especially for the films modified with BA. It is of great importance because these inclusions were previously reported to negatively affect the homogeneity and physico-chemical properties of the obtained films. Next, we showed, from the chemical point of view, the build from the nature-inspired polymer−PDA, but they show significant structural differences that is favored macromolecule aggregation type-through covalent (Cu^{2+}) or non-covalent (BA) interactions, namely, $\pi-\pi$ interactions and hydrogen bonds. Importantly for the oxidation mechanism, the conversion of DA to dopaminechrome through *o*-quinone can be partially coursed by direct aminochrome synthesis from Cu−DA adducts or can be partially coursed and reversed by boron-catechol mono-complex formation. Therefore, the agents used in the synthesis pose a vital role in the oxidation mechanism, with only small amounts of metals (B or Cu) detected in the final structure of PDA. XPS and FTIR revealed that catechol−Cu complex structural units are present in the Cu^{2+}-modified

https://doi.org/10.1021/acsami.3c05236
ACS Appl. Mater. Interfaces 2023, 15, 36922−36935

Table 2. Summary of Young's Modulus Measurements Data for Different Thin Polymer Films[a]

polymer thin film	thickness (nm)[b]	Young's modulus (GPa)[b]	measurement method	refs
PMMA	40	7.8 ± 0.3	BLS	87
	19	3 ± 0.3	tensile tester	88
	5.8	9	AFM deflection test	89
	11.2	6		
	35	3.70		
poly(ethyl methacrylate) (PEMA)	9.8 ± 1.3	0.08 ± 0.03	surface wrinkling measurements	90
poly(*n*-propyl methacrylate) (PnPMA)	22.2 ± 2.7	0.039 ± 0.020		
poly(benzyl methacrylate) (PBzMA)	21.6 ± 1.5	0.042 ± 0.020		
poly(isobutyl methacrylate) (PibMA)	20.7 ± 1.9	0.05 ± 0.020		
polystyrene (PS)	30	2.8 ± 0.3	tensile tester	91
	40	5.7 ± 0.3	BLS	87
	100	5.6 ± 0.3		
polystyrene-*b*-polybutadiene-*b*-polystyrene block copolymer (SBS)	20	0.7	tensile tester	92
polyamide (PA)/cross-linked	200	1.50 ± 0.53	surface wrinkling measurements	93
PDA/genipin cross-linked	59.4 ± 4.0	7.9 ± 1.7	tensile tester	94
PDA	10 ± 1	12.5 ± 2.5	BLS	76
	13 ± 1	13.5 ± 2.5		
	23.3 ± 3.0	**14.4 ± 4.0**		**t.s.**
	55 ± 2	13 ± 4	nanoindentation	14
	82.5 ± 9.9	**14.1 ± 4.5**		**t.s.**
PDA/BA modified	**10.5 ± 1.5**	**18.3 ± 6.4**	BLS	**t.s.**
	48.7 ± 6.1	**24.1 ± 5.6**	nanoindentation	

[a]t.s.—this study. [b]Error values are given as in the reference publications, without standardization.

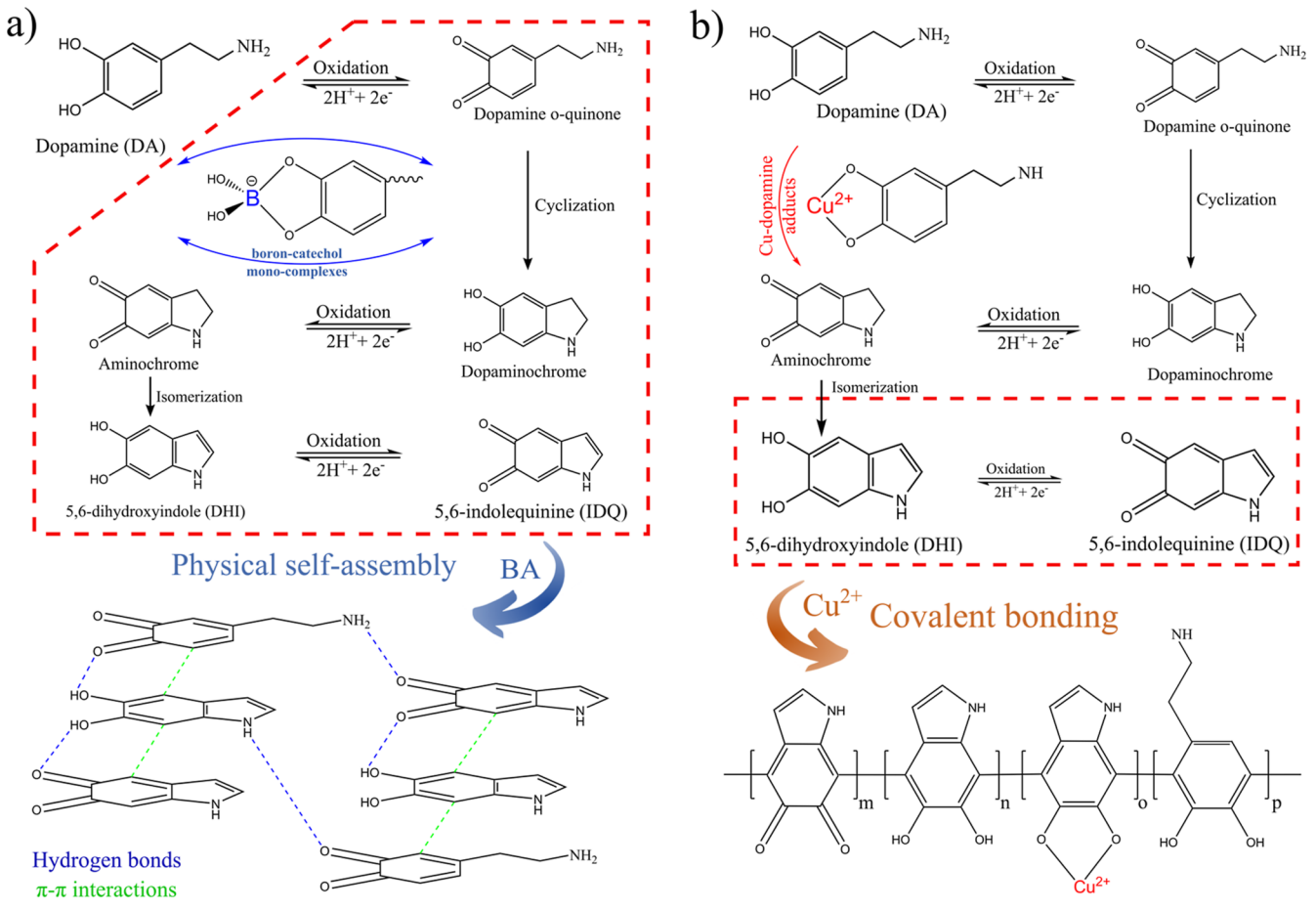

Figure 8. Scheme of the DA oxidation pathways with respect to used agents: (a) BA and (b) Cu^{2+} ions.

films, while catechol-boron monocomplexes are unstable and are not embedded in the PDA structure. A here-only trace amount of boron was present in the free form. This allows for a better understanding of the self-assembly mechanism of

https://doi.org/10.1021/acsami.3c05236
ACS Appl. Mater. Interfaces 2023, 15, 36922−36935

molecules at the air/water interface and the formation of the thin free-standing films.

Furthermore, nanoindentation and BLS experiments revealed advantageous mechanical properties of BA-modified films, specifically its relatively large Young's modulus and a finite residual stress. We postulate that they result from the favorably occurring non-covalent self-assembly mechanism. In combination with the results of our previous research, we have achieved exceptional control over the manufacturing process of these materials, that is, a precise measurement of their thickness growth in real-time, reduction of impurities, and selective self-assembly mechanism toward specific mechanical properties.

So far, the exploitation of PDA-thin films in applications such as photocatalytic enhancement and hierarchical architectures has been limited to in situ deposited PDA coatings, which are inherently mechanically poor and lack homogeneity and smoothness. Our study opens new perspectives for using mechanically resilient, free-standing films, with large-scale perspective, especially in applications in such as phononics, thermoelectrics, or nanometric-thin-layered composites for energy applications, which are applications where robust self-supporting functional PDA films might be needed. Additionally, due to the air/water nature of the films, large scalability can be achieved, reaching lateral sizes in the 10 s of centimeters, suitable for industrial photovoltaics or other energy applications.

Finally, our work provides unique insights into the mechanical (plastic and elastic) response of PDA films and the relationship between the structure, oxidation, and functionality of these films. It paves the way for future applications in layered nanocomposite engineering, where mechanically different but chemically compatible polymeric films can be integrated easily with other prospective materials, such as 2D van der Waals materials, resulting in the development of unique hybrid laminar architectures.

■ ASSOCIATED CONTENT

Supporting Information

The Supporting Information is available free of charge at https://pubs.acs.org/doi/10.1021/acsami.3c05236.

Scooping free-standing film-transferring technique; presentation of the detection limit in the new version of the SR setup; films from the air/water interface before and after transferring; UV−vis full spectra of the reaction solutions; Petri dishes after 24 h of oxidation and removal of the reaction mixture; ζ of the nanoparticles in the solution during the DA oxidation; AFM topography images of the films after 72 h of oxidation; roughness rms for a free-standing films after transferring on Si substrates; XPS data for the chemical analysis of the DA film; XPS full spectra and high-resolution spectra of the DA film; XPS data for the chemical analysis of the DA/BA 1:3 film; XPS full spectra and high-resolution spectra of the DA/BA 1:3 film; XPS data for the chemical analysis of the DA/Cu 1:3 film; XPS full spectra and high-resolution spectra of the DA/Cu 1:3 film; quantitative analysis of the XPS sp^2/sp^3 carbon subpeak areas; EDX chemical analysis of the DA/Cu 1:3 sample; results of the EDX chemical analysis of the DA/Cu 1:3 sample; deconvoluted part of the FTIR spectra in range 2800−3700 cm^{-1}; Raman spectra; 2D (G') peak intensity and maximum position comparison; X-ray diffractogram of the DA, DA/BA 1:3, and DA/Cu 1:3 films; peaks and structural parameters obtained from the XRD diffractogram; AFM topography of the DA sample after 12 h of oxidation; and AFM topography of the DA/BA 1:3 sample after 12 h of oxidation (PDF)

■ AUTHOR INFORMATION

Corresponding Authors

Jakub Szewczyk − *NanoBioMedical Centre, Adam Mickiewicz University, 61-614 Poznan, Poland; Institut Européen des Membranes, IEM, UMR 5635, Univ Montpellier, CNRS, 34095 Montpellier Cedex 5, France;* orcid.org/0000-0001-9149-6731; Email: jaksze3@amu.edu.pl

Emerson Coy − *NanoBioMedical Centre, Adam Mickiewicz University, 61-614 Poznan, Poland;* orcid.org/0000-0002-4149-9720; Email: coyeme@amu.edu.pl

Authors

Visnja Babacic − *Faculty of Chemistry, Adam Mickiewicz University, 61-614 Poznań, Poland*

Adam Krysztofik − *Faculty of Physics, Adam Mickiewicz University, 61-614 Poznań, Poland*

Olena Ivashchenko − *NanoBioMedical Centre, Adam Mickiewicz University, 61-614 Poznan, Poland*

Mikołaj Pochylski − *Faculty of Physics, Adam Mickiewicz University, 61-614 Poznań, Poland;* orcid.org/0000-0003-0160-0895

Robert Pietrzak − *Faculty of Chemistry, Adam Mickiewicz University, 61-614 Poznań, Poland*

Jacek Gapiński − *Faculty of Physics, Adam Mickiewicz University, 61-614 Poznań, Poland*

Bartłomiej Graczykowski − *Faculty of Physics, Adam Mickiewicz University, 61-614 Poznań, Poland*

Mikhael Bechelany − *Institut Européen des Membranes, IEM, UMR 5635, Univ Montpellier, CNRS, 34095 Montpellier Cedex 5, France; Gulf University for Science and Technology, GUST, 32093 Hawally, Kuwait;* orcid.org/0000-0002-2913-2846

Complete contact information is available at: https://pubs.acs.org/10.1021/acsami.3c05236

Notes

The authors declare no competing financial interest.

The raw/processed data required to reproduce these findings cannot be shared at this time as the data also forms part of an ongoing study. Data might be shared upon reasonable request to the corresponding author.

■ ACKNOWLEDGMENTS

The authors acknowledge the financial support from the National Science Centre of Poland (NCN) by the PRELUDIUM20 grant 2021/41/N/ST5/00211. This research was supported by a French Government Scholarship. J.S. is a scholarship holder of the Foundation of the University of Adam Mickiewicz in Poznań for the academic year 2022/2023. A.K. and B.G acknowledge the National Science Centre of Poland (NCN) by the OPUS grant 2021/41/B/ST5/03038 for the BLS measurements in this work.

REFERENCES

(1) Lee, H.; Dellatore, S. M.; Miller, W. M.; Messersmith, P. B. Mussel-Inspired Surface Chemistry for Multifunctional Coatings. *Science* **2007**, *318*, 426−430.

(2) Li, S.; Wang, H.; Young, M.; Xu, F.; Cheng, G.; Cong, H. Properties of Electropolymerized Dopamine and Its Analogues. *Langmuir* **2019**, *35*, 1119−1125.

(3) Mrówczyński, R.; Markiewicz, R.; Liebscher, J. Chemistry of Polydopamine Analogues. *Polym. Int.* **2016**, *65*, 1288−1299.

(4) Szukowska, M.; Popenda, Ł.; Coy, E.; Filip, C.; Grajewski, J.; Kempiński, M.; Kim, Y.; Mrówczyński, R. Replacing Amine by Azide: Dopamine Azide Polymerization Triggered by Sodium Periodate. *Polym. Chem.* **2022**, *13*, 3325−3334.

(5) Barclay, T. G.; Hegab, H. M.; Clarke, S. R.; Ginic-Markovic, M. Versatile Surface Modification Using Polydopamine and Related Polycatecholamines: Chemistry, Structure, and Applications. *Adv. Mater. Interfaces* **2017**, *4*, 1601192.

(6) Ryu, J. H.; Messersmith, P. B.; Lee, H. Polydopamine Surface Chemistry: A Decade of Discovery. *ACS Appl. Mater. Interfaces* **2018**, *10*, 7523−7540.

(7) Bigaj-Józefowska, M. J.; Grześkowiak, B. F. Polymeric Nanoparticles Wrapped in Biological Membranes for Targeted Anticancer Treatment. *Eur. Polym. J.* **2022**, *176*, 111427.

(8) Jin, A.; Wang, Y.; Lin, K.; Jiang, L. Nanoparticles Modified by Polydopamine: Working as "Drug" Carriers. *Bioact. Mater.* **2020**, *5*, 522−541.

(9) Żebrowska, K.; Coy, E.; Synoradzki, K.; Jurga, S.; Torruella, P.; Mrówczyński, R. Facile and Controllable Growth of β-FeOOH Nanostructures on Polydopamine Spheres. *J. Phys. Chem. B* **2020**, *124*, 9456−9463.

(10) Ponzio, F.; Payamyar, P.; Schneider, A.; Winterhalter, M.; Bour, J.; Addiego, F.; Krafft, M. P.; Hemmerle, J.; Ball, V. Polydopamine Films from the Forgotten Air/Water Interface. *J. Phys. Chem. Lett.* **2014**, *5*, 3436−3440.

(11) Wang, H.; Jiang, Q.; Yang, J.; Li, D.; Zhou, X.; Cai, L.; Yu, G. Polydopamine Film Self-Assembled at Air/Water Interface for Organic Electronic Memory Devices. *Adv. Mater. Interfaces* **2020**, *7*, 2000979.

(12) Ponzio, F.; Ball, V. Polydopamine Deposition at Fluid Interfaces. *Polym. Int.* **2016**, *65*, 1251−1257.

(13) Marchesi D'Alvise, T.; Harvey, S.; Hueske, L.; Szelwicka, J.; Veith, L.; Knowles, T. P. J.; Kubiczek, D.; Flaig, C.; Port, F.; Gottschalk, K. E.; Rosenau, F.; Graczykowski, B.; Fytas, G.; Ruggeri, F. S.; Wunderlich, K.; Weil, T. Ultrathin Polydopamine Films with Phospholipid Nanodiscs Containing a Glycophorin A Domain. *Adv. Funct. Mater.* **2020**, *30*, 2000378.

(14) Coy, E.; Iatsunskyi, I.; Colmenares, J. C.; Kim, Y.; Mrówczyński, R. Polydopamine Films with 2D-like Layered Structure and High Mechanical Resilience. *ACS Appl. Mater. Interfaces* **2021**, *13*, 23113−23120.

(15) Huang, Q.; Chen, J.; Liu, M.; Huang, H.; Zhang, X.; Wei, Y. Polydopamine-Based Functional Materials and Their Applications in Energy, Environmental, and Catalytic Fields: State-of-the-Art Review. *Chem. Eng. J.* **2020**, *387*, 124019.

(16) Aguilar-Ferrer, D.; Szewczyk, J.; Coy, E. Recent Developments in Polydopamine-Based Photocatalytic Nanocomposites for Energy Production: Physico-Chemical Properties and Perspectives. *Catal. Today* **2022**, *397*−*399*, 316−349.

(17) Szewczyk, J.; Aguilar-Ferrer, D.; Coy, E. Polydopamine Films: Electrochemical Growth and Sensing Applications. *Eur. Polym. J.* **2022**, *174*, 111346.

(18) Viter, R.; Fedorenko, V.; Gabriunaite, I.; Tepliakova, I.; Ramanavicius, S.; Holubnycha, V.; Ramanavicius, A.; Valiūnienė, A. Electrochemical and Optical Properties of Fluorine Doped Tin Oxide Modified by ZnO Nanorods and Polydopamine. *Chemosensors* **2023**, *11*, 106.

(19) Szewczyk, J.; Pochylski, M.; Szutkowski, K.; Kempiński, M.; Mrówczyński, R.; Iatsunskyi, I.; Gapiński, J.; Coy, E. In-Situ Thickness Control of Centimetre-Scale 2D-Like Polydopamine Films with Large Scalability. *Mater. Today Chem.* **2022**, *24*, 100935.

(20) Chen, C. T.; Martin-Martinez, F. J.; Jung, G. S.; Buehler, M. J. Polydopamine and Eumelanin Molecular Structures Investigated with Ab Initio Calculations. *Chem. Sci.* **2017**, *8*, 1631−1641.

(21) Ding, Y. H.; Floren, M.; Tan, W. Mussel-Inspired Polydopamine for Bio-Surface Functionalization. *Biosurf. Biotribol.* **2016**, *2*, 121−136.

(22) Hong, S.; Na, Y. S.; Choi, S.; Song, I. T.; Kim, W. Y.; Lee, H. Non-Covalent Self-Assembly and Covalent Polymerization Co-Contribute to Polydopamine Formation. *Adv. Funct. Mater.* **2012**, *22*, 4711−4717.

(23) Kim, S.; Moon, G. h.; Kim, G.; Kang, U.; Park, H.; Choi, W. TiO2 Complexed with Dopamine-Derived Polymers and the Visible Light Photocatalytic Activities for Water Pollutants. *J. Catal.* **2017**, *346*, 92−100.

(24) Jiang, D. Covalent Organic Frameworks: An Amazing Chemistry Platform for Designing Polymers. *Chem* **2020**, *6*, 2461−2483.

(25) Geng, K.; He, T.; Liu, R.; Dalapati, S.; Tan, K. T.; Li, Z.; Tao, S.; Gong, Y.; Jiang, Q.; Jiang, D. Covalent Organic Frameworks: Design, Synthesis, and Functions. *Chem. Rev.* **2020**, *120*, 8814−8933.

(26) Côté, A. P.; Benin, A. I.; Ockwig, N. W.; O'Keeffe, M.; Matzger, A. J.; Yaghi, O. M. Chemistry: Porous, Crystalline, Covalent Organic Frameworks. *Science* **2005**, *310*, 1166−1170.

(27) Gao, P.; Wei, R.; Liu, X.; Chen, Y.; Wu, T.; Shi, M.; Wang, M.; Li, N.; Tang, B. Covalent Organic Framework-Engineered Polydopamine Nanoplatform for Multimodal Imaging-Guided Tumor Photothermal-Chemotherapy. *Chem. Commun.* **2021**, *57*, 5646−5649.

(28) Huang, C.; Wang, X.; Yang, P.; Shi, S.; Duan, G.; Liu, X.; Li, Y. Size Regulation of Polydopamine Nanoparticles by Boronic Acid and Lewis Base. *Macromol. Rapid Commun.* **2023**, *44*, 2100916.

(29) Wang, B.; Jeon, Y. S.; Park, H. S.; Kim, Y. J.; Kim, J. H. Mussel-Mimetic Self-Healing Polyaspartamide Derivative Gel via Boron-Catechol Interactions. *Express Polym. Lett.* **2015**, *9*, 799−808.

(30) Han, X.; Tang, F.; Jin, Z. Free-Standing Polydopamine Films Generated in the Presence of Different Metallic Ions: The Comparison of Reaction Process and Film Properties. *RSC Adv.* **2018**, *8*, 18347−18354.

(31) Ball, V.; Gracio, J.; Vila, M.; Singh, M. K.; Metz-Boutigue, M. H.; Michel, M.; Bour, J.; Toniazzo, V.; Ruch, D.; Buehler, M. J. Comparison of Synthetic Dopamine-Eumelanin Formed in the Presence of Oxygen and Cu2+ Cations as Oxidants. *Langmuir* **2013**, *29*, 12754−12761.

(32) Malinkiewicz, O.; Yella, A.; Lee, Y. H.; Espallargas, G. M.; Graetzel, M.; Nazeeruddin, M. K.; Bolink, H. J. Perovskite Solar Cells Employing Organic Charge-Transport Layers. *Nat. Photonics* **2014**, *8*, 128−132.

(33) Raj, A.; Kumar, M.; Anshul, A. Recent Advancement in Inorganic-Organic Electron Transport Layers in Perovskite Solar Cell: Current Status and Future Outlook. *Mater. Today Chem.* **2021**, *22*, 100595.

(34) Salomäki, M.; Marttila, L.; Kivelä, H.; Ouvinen, T.; Lukkari, J. Effects of PH and Oxidants on the First Steps of Polydopamine Formation: A Thermodynamic Approach. *J. Phys. Chem. B* **2018**, *122*, 6314−6327.

(35) Bernsmann, F.; Ball, V.; Addiego, F.; Ponche, A.; Michel, M.; Gracio, J. J. D. A.; Toniazzo, V.; Ruch, D. Dopamine-Melanin Film Deposition Depends on the Used Oxidant and Buffer Solution. *Langmuir* **2011**, *27*, 2819−2825.

(36) Marín, O. A.; Ordóñez, J. I.; Gálvez, E. D.; Cisternas, L. A. Pourbaix Diagrams for Copper Ores Processing with Seawater. *Physicochem. Probl. Miner. Process.* **2020**, *56*, 624−640.

(37) Nečas, D.; Klapetek, P. Gwyddion: An Open-Source Software for SPM Data Analysis. *Cent. Eur. J. Phys.* **2012**, *10*, 181−188.

(38) Oliver, W. C.; Pharr, G. M. An Improved Technique for Determining Hardness and Elastic Modulus Using Load and Displacement Sensing Indentation Experiments. *J. Mater. Res.* **1992**, *7*, 1564−1583.

https://doi.org/10.1021/acsami.3c05236
ACS Appl. Mater. Interfaces 2023, 15, 36922−36935

(39) Oliver, W. C.; Pharr, G. M. Measurement of Hardness and Elastic Modulus by Instrumented Indentation: Advances in Understanding and Refinements to Methodology. *J. Mater. Res.* **2004**, *19*, 3−20.
(40) Coy, E.; Yate, L.; Kabacińska, Z.; Jancelewicz, M.; Jurga, S.; Iatsunskyi, I. Topographic Reconstruction and Mechanical Analysis of Atomic Layer Deposited Al2O3/TiO2 Nanolaminates by Nanoindentation. *Mater. Des.* **2016**, *111*, 584−591.
(41) Schneider, A.; Hemmerlé, J.; Allais, M.; Didierjean, J.; Michel, M.; D'Ischia, M.; Ball, V. Boric Acid as an Efficient Agent for the Control of Polydopamine Self-Assembly and Surface Properties. *ACS Appl. Mater. Interfaces* **2018**, *10*, 7574−7580.
(42) Lemaster, J. E.; Jeevarathinam, A. S.; Kumar, A.; Chandrasekar, B.; Chen, F.; Jokerst, J. V. Synthesis of Ultrasmall Synthetic Melanin Nanoparticles by UV Irradiation in Acidic and Neutral Conditions. *ACS Appl. Bio Mater.* **2019**, *2*, 4667−4674.
(43) Wu, M.; Wang, T.; Müller, L.; Müller, F. A. Adjustable Synthesis of Polydopamine Nanospheres and Their Nucleation and Growth. *Colloids Surf., A* **2020**, *603*, 125196.
(44) Yue, Q.; Wang, M.; Sun, Z.; Wang, C.; Wang, C.; Deng, Y.; Zhao, D. A Versatile Ethanol-Mediated Polymerization of Dopamine for Efficient Surface Modification and the Construction of Functional Core-Shell Nanostructures. *J. Mater. Chem. B* **2013**, *1*, 6085−6093.
(45) Herlinger, E.; Jameson, R. F.; Linert, W. Spontaneous Autoxidation of Dopamine. *J. Chem. Soc., Perkin Trans. 2* **1995**, 259−263.
(46) Ponzio, F.; Barthès, J.; Bour, J.; Michel, M.; Bertani, P.; Hemmerlé, J.; D'Ischia, M.; Ball, V. Oxidant Control of Polydopamine Surface Chemistry in Acids: A Mechanism-Based Entry to Superhydrophilic-Superoleophobic Coatings. *Chem. Mater.* **2016**, *28*, 4697−4705.
(47) Boag, M. K.; Roberts, A.; Uversky, V. N.; Ma, L.; Richardson, D. R.; Pountney, D. L. Ferritinophagy and α-Synuclein: Pharmacological Targeting of Autophagy to Restore Iron Regulation in Parkinson's Disease. *Int. J. Mol. Sci.* **2022**, *23*, 2378.
(48) Deshmukh, M. A.; Gicevicius, M.; Ramanaviciene, A.; Shirsat, M. D.; Viter, R.; Ramanavicius, A. Hybrid Electrochemical/Electrochromic Cu(II) Ion Sensor Prototype Based on PANI/ITO-Electrode. *Sens. Actuators, B* **2017**, *248*, 527−535.
(49) Szpoganicz, B.; Gidanian, S.; Kong, P.; Farmer, P. Metal Binding by Melanins: Studies of Colloidal Dihydroxyindole-Melanin, and Its Complexation by Cu(II) and Zn(II) Ions. *J. Inorg. Biochem.* **2002**, *89*, 45−53.
(50) Arzillo, M.; Mangiapia, G.; Pezzella, A.; Heenan, R. K.; Radulescu, A.; Paduano, L.; D'Ischia, M. Eumelanin Buildup on the Nanoscale: Aggregate Growth/Assembly and Visible Absorption Development in Biomimetic 5,6-Dihydroxyindole Polymerization. *Biomacromolecules* **2012**, *13*, 2379−2390.
(51) Ball, V. Physicochemical Perspective on "Polydopamine" and "Poly(Catecholamine)" Films for Their Applications in Biomaterial Coatings (Review). *Biointerphases* **2014**, *9*, 030801.
(52) Yana, J.; Chiangraeng, N.; Nimmanpipug, P.; Lee, V. S. A Theoretical Study of Supramolecular Aggregation of Polydopamine Tetramer Subunits in Aqueous Solution. *J. Mol. Graph. Model.* **2021**, *107*, 107946.
(53) Titantah, J. T.; Lamoen, D. Sp3/Sp2 Characterization of Carbon Materials from First-Principles Calculations: X-Ray Photoelectron versus High Energy Electron Energy-Loss Spectroscopy Techniques. *Carbon* **2005**, *43*, 1311−1316.
(54) Lesiak, B.; Kövér, L.; Tóth, J.; Zemek, J.; Jiricek, P.; Kromka, A.; Rangam, N. C. C sp2/sp3 hybridisations in carbon nanomaterials − XPS and (X)AES study. *Appl. Surf. Sci.* **2018**, *452*, 223−231.
(55) Hemmatpour, H.; De Luca, O.; Crestani, D.; Stuart, M. C. A.; Lasorsa, A.; van der Wel, P. C. A.; Loos, K.; Giousis, T.; Haddadi-Asl, V.; Rudolf, P. New Insights in Polydopamine Formation via Surface Adsorption. *Nat. Commun.* **2023**, *14*, 664.
(56) Kim, Y.; You, A.; Kim, D.; Bisht, H.; Heo, Y.; Hong, D.; Kim, M.; Kang, S. M. Effect of N-Methylation on Dopamine Surface Chemistry. *Langmuir* **2022**, *38*, 6404−6410.
(57) Zhang, C.; Xiang, L.; Zhang, J.; Liu, C.; Wang, Z.; Zeng, H.; Xu, Z. K. Revisiting the Adhesion Mechanism of Mussel-Inspired Chemistry. *Chem. Sci.* **2022**, *13*, 1698−1705.
(58) Fujisawa, K.; Ono, T.; Okamura, M. Synthesis and Characterization of Catecholato Copper(II) Complexes with Sterically Hindered Neutral and Anionic N3 Type Ligands: Tris(3,5-Diisopropyl-1-Pyrazolyl)Methane and Hydrotris(3,5-Diisopropyl-1-Pyrazolyl)Borate. *Inorganics* **2020**, *8*, 37.
(59) Salomäki, M.; Ouvinen, T.; Marttila, L.; Kivelä, H.; Leiro, J.; Mäkilä, E.; Lukkari, J. Polydopamine Nanoparticles Prepared Using Redox-Active Transition Metals. *J. Phys. Chem. B* **2019**, *123*, 2513−2524.
(60) Celik, C.; Ildiz, N.; Ocsoy, I. Building Block and Rapid Synthesis of Catecholamines-Inorganic Nanoflowers with Their Peroxidase-Mimicking and Antimicrobial Activities. *Sci. Rep.* **2020**, *10*, 2903.
(61) Narkar, A. R.; Kendrick, C.; Bellur, K.; Leftwich, T.; Zhang, Z.; Lee, B. P. Rapidly Responsive Smart Adhesive-Coated Micropillars Utilizing Catechol-Boronate Complexation Chemistry. *Soft Matter* **2019**, *15*, 5474−5482.
(62) Mun, M. K.; Jang, Y. J.; Kim, J. E.; Yeom, G. Y.; Kim, D. W. Plasma Functional Polymerization of Dopamine Using Atmospheric Pressure Plasma and a Dopamine Solution Mist. *RSC Adv.* **2019**, *9*, 12814−12822.
(63) Fedor, A. M.; Toda, M. J. Investigating Hydrogen Bonding in Phenol Using Infrared Spectroscopy and Computational Chemistry. *J. Chem. Educ.* **2014**, *91*, 2191−2194.
(64) Ghorbani, F.; Zamanian, A.; Sahranavard, M. Mussel-Inspired Polydopamine-Mediated Surface Modification of Freeze-Cast Poly (ϵ-Caprolactone) Scaffolds for Bone Tissue Engineering Applications. *Biomed. Tech.* **2020**, *65*, 273−287.
(65) Kataoka, Y.; Kitadai, N.; Hisatomi, O.; Nakashima, S. Nature of Hydrogen Bonding of Water Molecules in Aqueous Solutions of Glycerol by Attenuated Total Reflection (ATR) Infrared Spectroscopy. *Appl. Spectrosc.* **2011**, *65*, 436−441.
(66) Lin, C. C.; Fu, S. J. Osteogenesis of Human Adipose-Derived Stem Cells on Poly(Dopamine)-Coated Electrospun Poly(Lactic Acid) Fiber Mats. *Mater. Sci. Eng., C* **2016**, *58*, 254−263.
(67) Fu, J.; Chen, Z.; Wang, M.; Liu, S.; Zhang, J.; Zhang, J.; Han, R.; Xu, Q. Adsorption of Methylene Blue by a High-Efficiency Adsorbent (Polydopamine Microspheres): Kinetics, Isotherm, Thermodynamics and Mechanism Analysis. *Chem. Eng. J.* **2015**, *259*, 53−61.
(68) Raul, P. K.; Senapati, S.; Sahoo, A. K.; Umlong, I. M.; Devi, R. R.; Thakur, A. J.; Veer, V. CuO Nanorods: A Potential and Efficient Adsorbent in Water Purification. *RSC Adv.* **2014**, *4*, 40580−40587.
(69) Singh, P.; Nath, P.; Arun, R. K.; Mandal, S.; Chanda, N. Novel Synthesis of a Mixed Cu/CuO-Reduced Graphene Oxide Nanocomposite with Enhanced Peroxidase-like Catalytic Activity for Easy Detection of Glutathione in Solution and Using a Paper Strip. *RSC Adv.* **2016**, *6*, 92729−92738.
(70) Ferrari, A. C. Raman Spectroscopy of Graphene and Graphite: Disorder, Electron-Phonon Coupling, Doping and Nonadiabatic Effects. *Solid State Commun.* **2007**, *143*, 47−57.
(71) Yu, X.; Fan, H.; Liu, Y.; Shi, Z.; Jin, Z. Characterization of Carbonized Polydopamine Nanoparticles Suggests Ordered Supramolecular Structure of Polydopamine. *Langmuir* **2014**, *30*, 5497−5505.
(72) Li, H.; Aulin, Y. V.; Frazer, L.; Borguet, E.; Kakodkar, R.; Feser, J.; Chen, Y.; An, K.; Dikin, D. A.; Ren, F. Structure Evolution and Thermoelectric Properties of Carbonized Polydopamine Thin Films. *ACS Appl. Mater. Interfaces* **2017**, *9*, 6655−6660.
(73) Alkhouzaam, A.; Qiblawey, H.; Khraisheh, M. Polydopamine Functionalized Graphene Oxide as Membrane Nanofiller: Spectral and Structural Studies. *Membranes* **2021**, *11*, 86.
(74) He, J.; Liao, Y.; Hu, Q.; Zeng, Z.; Yi, L.; Wang, Y.; Lu, H.; Pan, M. Investigation of Polyimide as an Anode Material for Lithium-Ion Battery and Its Thermal Safety Behavior. *Ionics* **2020**, *26*, 3343−3350.

(75) Graczykowski, B.; Sledzinska, M.; Placidi, M.; Saleta Reig, D.; Kasprzak, M.; Alzina, F.; Sotomayor Torres, C. M. Elastic Properties of Few Nanometers Thick Polycrystalline MoS2 Membranes: A Nondestructive Study. *Nano Lett.* **2017**, *17*, 7647−7651.
(76) Marchesi D'Alvise, T.; Harvey, S.; Hueske, L.; Szelwicka, J.; Veith, L.; Knowles, T. P. J.; Kubiczek, D.; Flaig, C.; Port, F.; Gottschalk, K. E.; Rosenau, F.; Graczykowski, B.; Fytas, G.; Ruggeri, F. S.; Wunderlich, K.; Weil, T. Ultrathin Polydopamine Films with Phospholipid Nanodiscs Containing a Glycophorin A Domain. *Adv. Funct. Mater.* **2020**, *30*, 2000378.
(77) Han, C. S. Influence of the Molecular Structure on Indentation Size Effect in Polymers. *Mater. Sci. Eng., A* **2010**, *527*, 619−624.
(78) Lugger, S. J. D.; Houben, S. J. A.; Foelen, Y.; Debije, M. G.; Schenning, A. P. H. J.; Mulder, D. J. Hydrogen-Bonded Supramolecular Liquid Crystal Polymers: Smart Materials with Stimuli-Responsive, Self-Healing, and Recyclable Properties. *Chem. Rev.* **2022**, *122*, 4946−4975.
(79) Wang, X.; Xu, P.; Han, R.; Ren, J.; Li, L.; Han, N.; Xing, F.; Zhu, J. A Review on the Mechanical Properties for Thin Film and Block Structure Characterised by Using Nanoscratch Test. *Nanotechnol. Rev.* **2019**, *8*, 628−644.
(80) G, M.; Ghosh, P. Pile-up Response of Polymer Thin Films to Static and Dynamic Loading. *Thin Solid Films* **2019**, *677*, 1−12.
(81) Zhang, S.; Galuska, L. A.; Gu, X. Water-Assisted Mechanical Testing of Polymeric Thin-Films. *J. Polym. Sci.* **2022**, *60*, 1108−1129.
(82) Malollari, K. G.; Delparastan, P.; Sobek, C.; Vachhani, S. J.; Fink, T. D.; Zha, R. H.; Messersmith, P. B. Mechanical Enhancement of Bioinspired Polydopamine Nanocoatings. *ACS Appl. Mater. Interfaces* **2019**, *11*, 43599−43607.
(83) Lee, K.; Park, M.; Malollari, K. G.; Shin, J.; Winkler, S. M.; Zheng, Y.; Park, J. H.; Grigoropoulos, C. P.; Messersmith, P. B. Laser-Induced Graphitization of Polydopamine Leads to Enhanced Mechanical Performance While Preserving Multifunctionality. *Nat. Commun.* **2020**, *11*, 4848−4912.
(84) Kotsilkova, R.; Todorov, P.; Ivanov, E.; Kaplas, T.; Svirko, Y.; Paddubskaya, A.; Kuzhir, P. Mechanical Properties Investigation of Bilayer Graphene/Poly(Methyl Methacrylate) Thin Films at Macro, Micro and Nanoscale. *Carbon* **2016**, *100*, 355−366.
(85) Pantano, M. F.; Pavlou, C.; Pastore Carbone, M. G.; Galiotis, C.; Pugno, N. M.; Speranza, G. Highly Deformable, Ultrathin Large-Area Poly(Methyl Methacrylate) Films. *ACS Omega* **2021**, *6*, 8308−8312.
(86) Reina, A.; Son, H.; Jiao, L.; Fan, B.; Dresselhaus, M. S.; Liu, Z. F.; Kong, J. Transferring and Identification of Single- and Few-Layer Graphene on Arbitrary Substrates. *J. Phys. Chem. C* **2008**, *112*, 17741−17744.
(87) Gomopoulos, N.; Cheng, W.; Efremov, M.; Nealey, P. F.; Fytas, G. Out-of-Plane Longitudinal Elastic Modulus of Supported Polymer Thin Films. *Macromolecules* **2009**, *42*, 7164−7167.
(88) Bay, R. K.; Zarybnicka, K.; Jančář, J.; Crosby, A. Mechanical Properties of Ultrathin Polymer Nanocomposites. *ACS Appl. Polym. Mater.* **2020**, *2*, 2220−2227.
(89) Wang, G.; Najafi, F.; Ho, K.; Hamidinejad, M.; Cui, T.; Walker, G. C.; Singh, C. V.; Filleter, T. Mechanical Size Effect of Freestanding Nanoconfined Polymer Films. *Macromolecules* **2022**, *55*, 1248−1259.
(90) Torres, J. M.; Stafford, C. M.; Vogt, B. D. Elastic Modulus of Amorphous Polymer Thin Films: Relationship to the Glass Transition Temperature. *ACS Nano* **2009**, *3*, 2677−2685.
(91) Bay, R. K.; Crosby, A. J. Uniaxial Extension of Ultrathin Freestanding Polymer Films. *ACS Macro Lett.* **2019**, *8*, 1080−1085.
(92) Saito, M.; Ito, K.; Yokoyama, H. Mechanical Properties of Ultrathin Polystyrene-b-Polybutadiene-b-Polystyrene Block Copolymer Films: Film Thickness-Dependent Young's Modulus. *Macromolecules* **2021**, *54*, 8538−8547.
(93) Chung, J. Y.; Lee, J. H.; Beers, K. L.; Stafford, C. M. Stiffness, Strength, and Ductility of Nanoscale Thin Films and Membranes: A Combined Wrinkling-Cracking Methodology. *Nano Lett.* **2011**, *11*, 3361−3365.
(94) Klosterman, L.; Ahmad, Z.; Viswanathan, V.; Bettinger, C. J. Synthesis and Measurement of Cohesive Mechanics in Polydopamine Nanomembranes. *Adv. Mater. Interfaces* **2017**, *4*, 1700041.
(95) Liebscher, J.; Mrówczyński, R.; Scheidt, H. A.; Filip, C.; Hădade, N. D.; Turcu, R.; Bende, A.; Beck, S. Structure of Polydopamine: A Never-Ending Story? *Langmuir* **2013**, *29*, 10539−10548.
(96) Bisaglia, M.; Mammi, S.; Bubacco, L. Kinetic and Structural Analysis of the Early Oxidation Products of Dopamine: Analysis of the Interactions with α-Synuclein. *J. Biol. Chem.* **2007**, *282*, 15597−15605.

https://doi.org/10.1021/acsami.3c05236
ACS Appl. Mater. Interfaces 2023, 15, 36922−36935

Thesis III - Effective ex-situ transfer of the large-scale PDA films from the air/water interface to the TiO_2 or ZnO surfaces will lead to the formation of a heterojunction at the organic/inorganic interface, as would be in the case of in-situ deposition of polydopamine films, directly from the solution.

Thesis III is addressed in the Publication 5

Publication 5

The Author's individual contribution to this publication includes: Conceptualization, Data curation, Investigation, Methodology, Validation, Visualization, Writing – original draft, Writing – review & editing.

Journal: European Polymer Journal
ISSN: 0014-3057
Publisher: Elsevier
Journal Impact Factor: 6.0
Publication Date: 21.01.2024
Number of Citations: 1

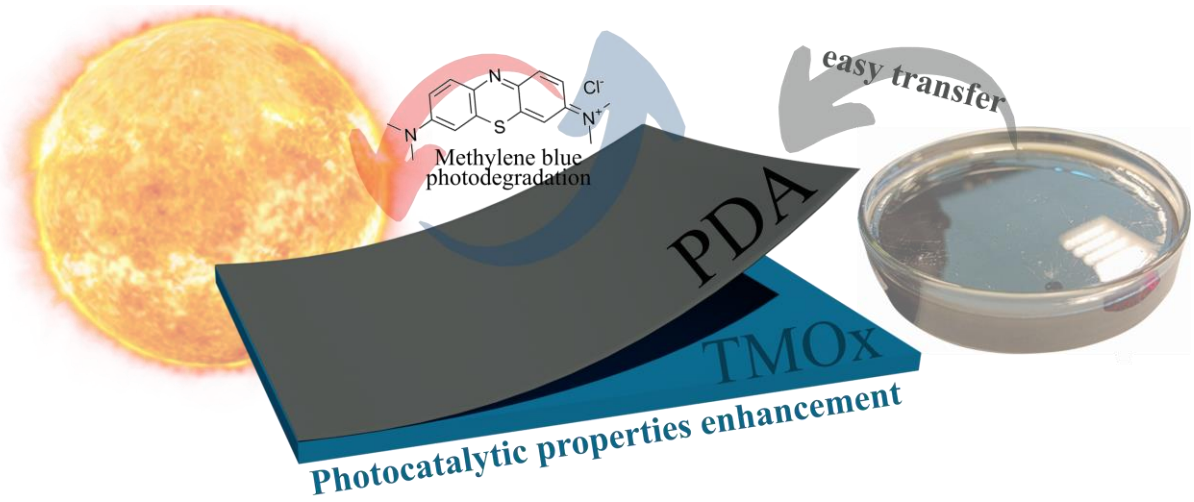

Figure 13. Graphical abstract of the P5

European Polymer Journal 206 (2024) 112781

Contents lists available at ScienceDirect

European Polymer Journal

journal homepage: www.elsevier.com/locate/europolj

Ex-situ transferring of polydopamine films on semiconductor interface: Evidence of functional hybrid heterojunction

Jakub Szewczyk [a,b], Marcin Ziółek [c], Katarzyna Siuzdak [d], Igor Iatsunskyi [a], Mikołaj Pochylski [c], Daniel Aguilar-Ferrer [a,b], Mateusz Kempiński [c], Fida Tanos [b], Jacek Gapiński [c], Mikhael Bechelany [b,e], Emerson Coy [a,*]

[a] NanoBioMedical Centre, Adam Mickiewicz University, Wszechnicy Piastowskiej 3, 61-614 Poznan, Poland
[b] Institut Europeen des Membranes, IEM, UMR 5635, Univ Montpellier, ENSCM, CNRS, 34730 Montpellier, France
[c] Faculty of Physics, Adam Mickiewicz University, ul. Uniwersytet Poznańskiego 2, 61-614 Poznań, Poland
[d] Centre of Laser and Plasma Engineering, The Szewalski Institute of Fluid-Flow Machinery, Fiszera 14 Str., 80-231 Gdańsk, Poland
[e] Gulf University for Science and Technology, GUST, 32093 Hawally, Kuwait

ARTICLE INFO

Keywords:
Polydopamine
Functional surfaces
Interfaces
Electron transfer
Metal oxides
Photo degradation

ABSTRACT

Polydopamine (PDA) films, when combined with model nanometric semiconductor substrates like titanium dioxide (TiO_2) and zinc oxide (ZnO), enhance photocatalytic performance, generating a unique *ex-situ* functional heterojunction. We investigate PDA air/water films transferred onto large surfaces, revealing Janus-like films with strong chemical attachment. Spectroscopic methods confirm a functional hybrid heterojunction, while electrochemical studies show significant improvements with transfer resistance enhancement of ~2250 %. This opens doors to various practical applications for hybrid heterojunctions.

1. Introduction

Polydopamine (PDA) is a biomimetic material of constantly increasing interest since its discovery in 2007 [1]. Its biomimetic character comes from imitating the eumelanin-based biopolymer responsible for marine mussel adhesive properties [1–4]. One of the main advantages of this material is its straightforward production pathway, namely the autooxidation of dopamine in a solution of slightly basic pH [1,5] or electrodeposition of the PDA from the dopamine solution [6]. These are typical procedures for generating PDA nanoparticles [7,8] or functional PDA coating on various materials, resulting in all types of composites: 0D (0 dimensional) [9–12], 1D [13–18], 2D [19] and 3D [20,21]. It is worth noting that in the case of *in-situ* growth, the structure of the polymer depends on the substrate [22]. However, a breakthrough discovery was the observation of a free-standing polydopamine film generated at the air/water (a/w) interface during the autooxidation process [23]. [24,25]. Moreover, structures with 2D or 2D-like laminar features in these PDA a/w films were observed in a recent study [26]. Apparent similarities to graphite or graphene oxide materials have been shown using X-ray diffractometry (XRD) and Raman spectroscopy. Since no known synthetic pathway leads to such materials from dopamine solution, the hypothesis of a 2D-like supramolecular ordering of PDA is the most plausible scenario. Further studies have attempted to control the synthesis of the a/w films, aiming to produce thin, homogeneous and chemically pure films. As a result, high-quality material on a centimetre scale was obtained [27], and the production process seems to be easily scalable. Importantly, we have shown their superior mechanical strength and stability, allowing them to act easily as transferable free-standing films [28]. An additional fascinating aspect of the a/w films is the possible difference between the water and air-exposed surfaces, resembling Janus films or Janus membranes, as observed by Hong *et al.* in catecholamine microfilms from the air/water interface [29], however, no such studies have been performed for a/w PDA films so far, despite growing interest in the field of Janus films [30].

Another interesting aspect to investigate is the application potential of the a/w films in energy and remediation-related fields. For example, a recent review article discussed the application and perspectives of polydopamine-based composites for photocatalytic processes [31]. One of the most exciting applications in this field is the solar-driven photocatalytic decomposition of dyes and other chemical reagents for water remediation [32]. It has been shown that several disadvantages characterizing pure TiO_2, ZnO and other wide bandgap semiconductors e.g.

* Corresponding author.
E-mail address: coyeme@amu.edu.pl (E. Coy).

https://doi.org/10.1016/j.eurpolymj.2024.112781
Received 28 November 2023; Received in revised form 9 January 2024; Accepted 15 January 2024
Available online 21 January 2024

ZnS composites, could often be minimized or eliminated by modifying their surface with polydopamine, e.g. reduction of photoluminescence [33] decrease of the bandgap [34], increased effectiveness of transport and tunneling of charge carriers [14]an enhancement of the light absorption in vis range (redshift), and efficient separation of photogenerated charge carriers [35]. Finally- it was previously shown that the charge–discharge property of polydopamine induces electron backflow following the S-scheme heterojunction mechanism between TiO_2 and PDA. Briefly, the interfacial electron transfer (electron charge) occurs when the light is on, while the backflow of accumulated electrons from PDA to TiO_2 (electron discharge) happens when the light is turned off [36]. Nevertheless, these nanocomposites were obtained by direct polymerization of PDA in solution, and the effect of enhanced photocatalytic properties was mainly observed in nanoparticles, porous meshes and nanorods. No similar effect has been described for laminar nanocomposites based on PDA transferable films deposited on the photocatalyst surface. In general, the electronic properties of PDA nanomaterials are quite different from those of PDA/semiconductor interfaces, and the observed enhancement is often attributed to the *in-situ* polymerization and, possibly, to the quasi-ordinated growth of PDA on crystalline materials. Thus, the *ex-situ* growth of PDA films and the transfer of ready products on functional substrates might allow the exploitation of the properties of PDA/semiconductor interfaces in many fields. In this sense, there are many questions to be answered. For example, thin films of PDA grown *in-situ* (<5 nm) typically exhibit higher performance than thicker ones. Whereas PDA films from a/w, are an order of magnitude thicker (>15 nm) than their *in-situ* counterparts. Therefore, it is important to answer whether *ex-situ* transferring of fully polymerized PDA films onto functional substrates also results in photocatalytic enhancement. If so, How does it scale with achievable film thickness (>15 nm)? This would ultimately allow the proposal of a model for the light interaction at the polydopamine-inorganic semiconductor interface.

Taking it all into account, here we provide a comprehensive study of the following aspects: *i)* the differences between the chemical and physical properties of the upper and bottom surfaces of the laminar 2D-like thin PDA films from the air/water interface and their different application potential, *ii)* thickness dependence to evaluate its influence onto physicochemical and electrochemical properties and determine the most promising candidate for *ex-situ* transferring towards electrochemical experiments, *iii)* whether *ex-situ* transferred PDA films carry with them the previously observed photocatalytic enhancement, boosting the efficiency of photocatalytic degradation of the methylene blue (MB) in comparison to the TiO_2 thin films on a centimetre-scale. The latter is also an important application aspect because MB is a widely used dye in the textile industry. It is toxic, carcinogenic, and non-biodegradable and thus poses a health threat to living organisms [37]. Our results bring us closer to the practical application of relatively cheap and easy-to-obtain large-size materials for photocatalytic applications, e.g. organic pollutants degradation, an emerging topic [38–41].

2. Materials and methods

2.1. Chemical reagents

Materials of analytical purity level were used in all synthesis procedures without any further purifications. Dopamine hydrochloride (CAS: 62-31-7, s, >98 %), Trizma® base (CAS: 77–86-1, s, >99 %), Hydrochloric acid (CAS: 7647-01-0, l, 25 %), Diethylzinc (CAS: 557-20-0), Titanium tetrachloride (CAS: 7550-45-0), Sodium sulfate (CAS: 7757-82-6, s), Methylene Blue hydrate (CAS: 122965-43-9), Silicon wafer (Si 100, CAS: 7440-21-3, s), Quartz (fused, thickness: 1.0 mm) from Sigma-Aldrich and ultrapure deionized water from a Hydrolab Ultra UV system were used.

2.2. Synthesis of the polydopamine films

The synthesis of films was carried out in the optimised conditions determined in our previous work [27]. Dopamine (0.5 mg ml^{-1}) in the form of dopamine hydrochloride was added to a Petri dish (7.5 cm in diameter, 2 cm in height) containing Tris buffer solution (10 mmol, 45 mL). Stirring (300 RPM) took place on a magnetic plate throughout the whole synthesis time (10 and 24 h), and a glass lid covered the vessel with a small gap to allow air exchange. The purpose of using two different synthesis times was to obtain PDA a/w films of various thicknesses.

2.3. Transfer of the films

Two different transferring methods were applied to investigate both sides (surfaces) of the obtained films. By the use of the first procedure (scooping), the bottom surface of the film was in contact with a substrate, and the upper surface was exposed. Scooping is a simple procedure of immersing the substrate under the previously cut fragment of the floating film at a low angle (~30°) and withdrawing the substrate, utilizing gravity force to attach the film to the substrate, shown schematically in Fig. 1a. Although much less known than the Langmuir-blodgett technique, this method has several advantages, such as simplicity and lack of influence on the structure of the material [42]. Films transferred by employing this method will be denoted with the "sc" abbreviation. The stamping procedure seems much more elusive, and to the best of our knowledge, we applied it for the first time to transfer films from the water surface. Again, a fragment of the floating film is being cut, but the substrate is reversed upside down and slowly touches the film's upper surface. The film is adhesively attached to the substrate and can be detached from the water surface by lifting the "stamp". As shown in Fig. 1b, it is the bottom surface of the film that is exposed by using the stamping procedure. Films transferred by employing the stamping procedure will be denoted with the "st" abbreviation.

2.4. Substrates and coatings

Depending on the characterization method, different substrates were prepared, such as: bare Silicon (1 0 0) wafers, Si wafers covered by a thin (<100 nm) coating of TiO_2 or ZnO (denoted as Si/TiO_2 and Si/ZnO, respectively) and quartz glass covered by a thin (<100 nm) coating of TiO_2 (denoted as Q/TiO_2). TiO_2 and ZnO layers were deposited by the atomic layer deposition (ALD) method, which is described in detail elsewhere [43–45]. Thin amorphous films were deposited to obtain a continuous layer with low roughness [45]. For clarity, the differentiation and naming of the samples are summarised in Table S1.

2.5. Physico-chemical characterization

Water contact angle (θ) measurements were performed using SEO – Phoenix 300 Touch Automatic Contact Angle Analyzer equipped with the industrial zoom lens Navitar TV zoom 7000 and SurfaceWare software. The test was performed two times for each sample (for each group, there were four samples, so x8 tests for each group) by using 50 uL of deionized water. The result of each measurement is the average of 10 automatically determined values of the θ angle after t = 5 and 300 s. All structural characterization studies were performed on the polydopamine films obtained after 10 h and 24 h of oxidation, deposited on silicon Si (1 0 0) substrate using both transferring techniques and coded Si/PDA/10sc, Si/PDA/10st, Si/PDA/24sc and Si/PDA/24st, respectively. Grazing Incidence X-ray diffraction (GIXRD) characterization was executed with the use of an MRD-X'pert^3 diffractometer (PANalytical), operating at 45 kV and 40 mA with a Cu Kα radiation source (wavelength of 1.54 Å). Films were transferred via scooping or stamping onto clean Si wafers, dried and placed in the appropriate holders. Atomic Force Microscopy

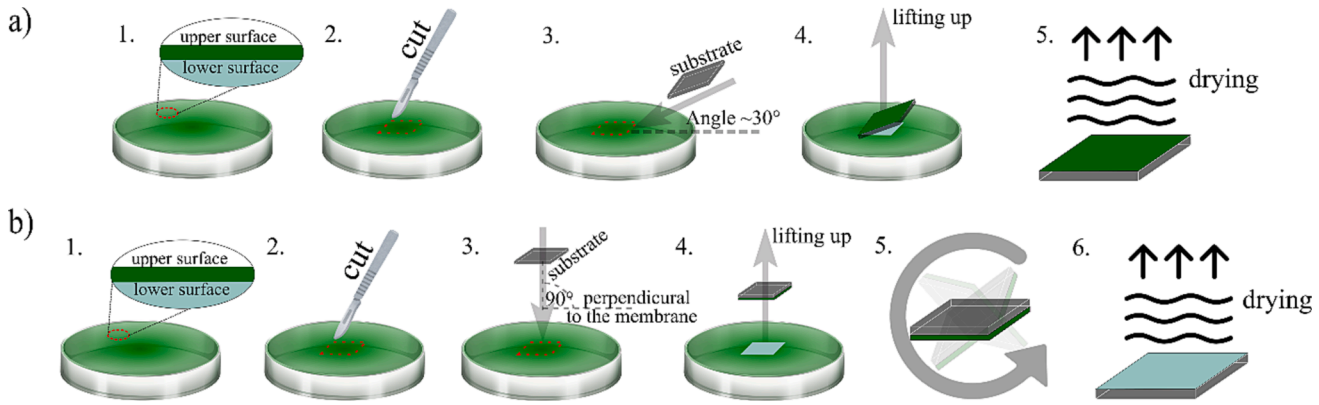

Fig. 1. Scheme of the (a) scooping (b) stamping transferring procedure.

measurements (AFM) were performed using an ICON–Bruker microscope. Complementary Gwyddion software was used for general height field and image processing, specifically for the analysis of profilometry data and thickness [46]. The thickness of films was determined from the average of 10 measurements on randomly selected sections crossing the crack in the film on which the substrate was exposed. The roughness was determined from the average of ten measurements of the root mean square (RMS) value in the area of 2 × 2 μm of the films. The roughness factor (*r*'), defined as the ratio between the actual and projected surface area, was appointed as the average of 10 measurements for each sample with the implemented functions of Gwyddion software. Raman Spectroscopy was performed using a Renishaw instrument equipped with microscope enclosure RE04, 633 nm laser source and Leica objective lens × 50. Exposure time was set to 1 s with 0.1 % of the power of the laser source (corresponding to 60 mW), and the number of accumulations was 10. Raman spectra of each sample are an average from 5 measurements in different areas. X-ray photoelectron spectroscopy (XPS) was performed using KRATOS:AXIS Ultra DLD, X-ray source: Al-Kalpha, 1486.6 eV - FWHM resolution 0.45 eV, acquisition time 0.1 s. High-resolution spectra of the regions corresponding to Si2p (112–92 eV), C1s (290–274 eV), O1s (540–520 eV) and N1s (408–390 eV) were investigated.

2.6. Spectroscopy and electrochemical studies

The room temperature stationary Photoluminescence (PL) properties of the bare and PDA-modified Si/ZnO were measured after excitation by IK Series Helium-Cadmium HeCd Laser Systems (325 nm) and collected by spectrometer Ocean Optics QE65 Pro. Stationary transmission UV–Vis spectroscopy was applied to investigate the bare and PDA-modified glass/TiO_2 bandgap using Ocean Optics DH-2000 Deuterium-Halogen lamp as a light source and Ocean Optics QE65 Pro Scientific-grade spectrometer. Obtained spectra of TiO_2 (an indirect band gap semiconductor) and ZnO (a direct band gap semiconductor) were transformed according to [47] and plotted against the photon energy. For transient absorption spectroscopic analysis of the bare and PDA-modified quartz/TiO_2 samples, a Helios spectrometer (Ultrafast Systems) and Spectra-Physics fs laser system were used. Measurements were performed in the spectral ranges of 300–900 nm and in the time range of up to 3 ns. Time evolution curves (kinetics) of differential absorption spectra were obtained. The excitation beam fell on the sample from the TiO_2 or PDA side. The pump pulses were set at 310 nm, and the pump pulse energy was 0.2, 1 and 5 μJ, corresponding to low, medium and high energy levels, respectively. Those energies correspond to energy densities between 100 and 2500 μJ cm^{-2}. To assign individual components of the decay signal, a mathematical fit was made, using the following function for the mixed first and second-order decay [48] $\Delta A(t) = \frac{An_0k_1}{k_1 exp(k_1(t-t_0))+n_0k_2(\exp(k_1(t-t_0))-1)}$ where n_0 is a dimensionless quantity proportional to the pump pulse energy, A is relative absorbance, t_0 is the time of maximum A, and k_1, k_2 are first and second order decay rate constants, respectively. The superior or satisfactory fit was obtained for all presented kinetic curves, which is summarized in Table S3. The global analysis was performed to obtain wavelength-dependent amplitudes of the indicated time constants using Surface Explorer software from Ultrafast Systems, described in detail elsewhere [49]. All electrochemical studies were carried out using Autolab PGStat 302 N potentiostat–galvanostat systems (Metrohm, Autolab) in a three-electrode system where the investigated sample served as a working electrode, Pt-mesh as a counter electrode and Ag/AgCl/0.1 M KCl as a reference electrode in 0.5 M Na_2SO_4 electrolyte solution. Light sweep voltammetry (LSV) experiments were developed in a potential range from −0.7 to +1 V where the linear increase of potential was equal 10 mV/s, and the light/dark cycle length was 5 s. Two types of irradiation were used UV–vis and Vis. Cyclic amperometry (CA) experiments were developed during 300 s when the light/dark cycle length was equal to 5 s. Cyclic voltammetry (CV) experiments were developed from −1 to +1 V, where the increased potential speed was 50 mV/s. Electrochemical impedance spectroscopy (EIS) measurements were carried out in the range from 20 kHz to 0.1 Hz, where the amplitude was 10 mA. Before each measurement, 2 min conditioning time was ensured. The experiment was carried out in conditions without irradiation (dark) and when the working electrode was exposed to UV–vis and Vis radiation. The LV curves and EIS spectra were recorded in different light conditions using the solar simulator (Oriel), which was equipped with the optical filter to eliminate the radiation < 420 nm.

2.7. Photocatalytic performance

To evaluate the beneficial effect of the PDA a/w films deposition on the photocatalytic performance of the TiO_2 nanofilms, the experiment on the photocatalytic degradation of the methylene blue (MB) was planned. The concentrations of the MB solution were 2, 3 and 5 ppm, and it was stored in a Quartz cuvette of the volume 3 $cm^{3;}$ it was placed on a stirrer to allow the solution to mix during the experiment. The surface size of the catalyst was 1 cm^2. The photodegradation light source used in the experiment was a 300 W Xe arc lamp of Sciencetech's Tunable Light Source with 0.01 W cm^{-2} intensity and a spectral range 300–1800 nm. A filter was set to cut out the infrared radiation - a quartz cuvette filled with distilled water. The experiments were run for 1 h, for the stability test experiment was run 4 times, including changing the solution with a new one every hour and using the same photocatalyst sample. A spectrum of the solution illuminated with Ocean Optics DH-2000 Halogen lamp was measured every 5 min and the decrease in the maximum absorbance of the UV–Vis spectra of the methylene blue (658 nm) was measured via Ocean Optics QE65 Pro Scientific-grade spectrometer. A photo of the cuvette with the photocatalyst placed in

it, the beam of light falling on its surface for driving photocatalytic degradation, and the perpendicularly mounted optical fiber directed to the spectrometer for recording the spectrum of the solution were shown in Fig. S1. Before and after the photodegradation experiment, the surface of the catalyst was examined via an optical microscope Keyence VHX 7100. The photograph of the MB solution before and after the photodegradation experiment was taken with a digital Xiaomi 50MP AI Quad Camera.

Additionally, methylene blue filtration efficiency was investigated on PVDF membrane filters (0.1 μm) and PDA/PVDF modified filters. The test was performed in a 10 mL omicon 8010 closed system under an applied pressure of 0.2 bar. Filtration efficiency was measured in the same manner as photodegradation efficiency.

3. Results and discussion

As indicated in Fig. 2, the work was divided into three steps. Firstly, polydopamine films were synthesized at the air/water interface using a previously optimized procedure (see section 2.2), and different procedures were applied to transfer films from the a/w interface on the surface of the Si(1 0 0) wafer, Si/TiO_2 and Si/ZnO (see section 2.3). The morphological, chemical and structural divergence resulting from varying dopamine oxidation time and transferring techniques were investigated with the use of the AFM, water contact angle measurements, XRD, Raman Spectroscopy, FTIR and XPS (see section 3.1). Next, within step II, thin TiO_2 and ZnO coatings were deposited on the Silicon substrate via ALD method, and the polymer was deposited on top using the most promising PDA transferring procedure. Finally, in the last step, we investigated the effect of the PDA/semiconductor interface on the optical and electrochemical properties and photocatalytic MB degradation efficiency (see section 3.2).

3.1. Morphological, chemical and structural properties

To investigate the influence of the transferring procedure and synthesis time on the thickness and roughness of the transferred PDA a/w films, Atomic force microscopy was applied. In Fig. 3a the box chart shows the results of film thickness obtained for the films transferred on three types of substrates- Si, Si/ZnO and Si/TiO_2. Regardless of the substrate type, the mean thickness of the films transferred after 10 and 24 h of the synthesis was ~17.5 and ~30 nm, respectively. Certainly, this is not a linear increment, which is consistent with the former studies suggesting a faster thickness increase in the first hours of synthesis [25,27]. Notably, the transferring procedure had a negligible influence on the film thickness obtained after 10 h growth (random variations), but after 24 h all the films transferred with the stamping procedure were significantly thicker than the scooping ones. We speculate that capillary forces and stretching of the films, which are more effective in the scooping procedure, might compress the films. Moreover, the chemical environment of both surfaces could play a role in their attachment and, therefore, their compression. In turn, the roughness (RMS) of the obtained composite surfaces clearly depends on the transferring procedure regardless of the growth time (Fig. 3b). For Si/ZnO and Si/TiO_2 samples, stamping resulted in higher roughness compared to scooping, in contrast to Si/PDA sample, where a reverse effect was found. We think the degree of hydrophobicity determines this c because the water contact angle on the bare Si is around 10° lower than on Si/ZnO and Si/TiO_2. That leads to the conclusion that the scooping technique is the best choice to maintain low film roughness after its transfer onto a more hydrophobic substrate. As previously reported, using the optimised synthesis conditions (stirring speed, pH, dopamine concentration) provides minimum achievable roughness of the PDA a/w film before transfer [27]. Interestingly, there is no significant influence of the thickness of the film on its roughness after transfer.

Water contact angle measurements estimated the wettability of the samples. Due to finite samples' surface roughness, the measured angles had to be corrected using the Wenzels equation with the r' roughness parameter values taken from AFM results (see Supplementary Information for details). The results of direct measurements and the correction effects are shown in Table S2 of Supplementary Information. The final (true) values of water contact angles for all samples are shown in Fig. 3c-e. They are only slightly higher than the directly measured values, resulting from relatively small surface roughness and the respective correction. Three main observations can be made from the results of contact angle measurements: *i)* the same PDA film transferred on different substrates may reveal different hydrophilicity, *ii)*

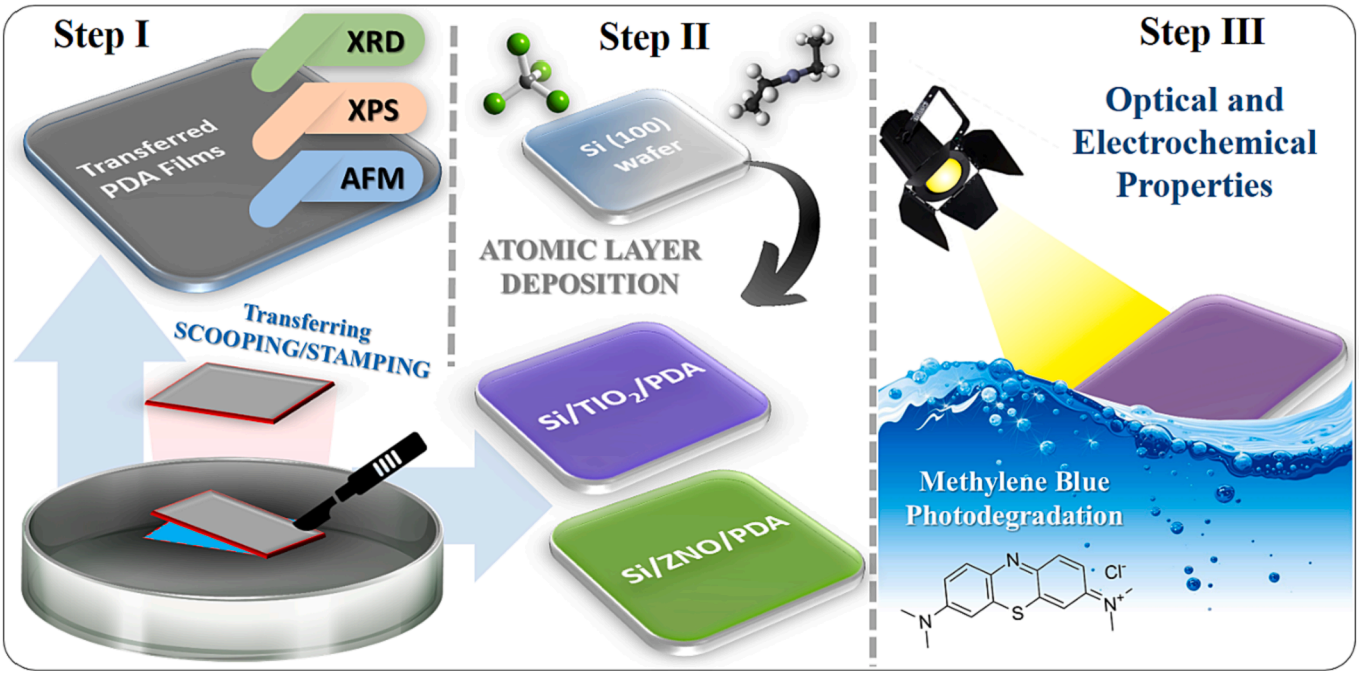

Fig. 2. Scheme of the workflow. We start with production and transfer of the PDA thin films, followed by their morphological, structural and chemical investigation before executing optical, electrochemical and photocatalytic experiments to investigate composites properties.

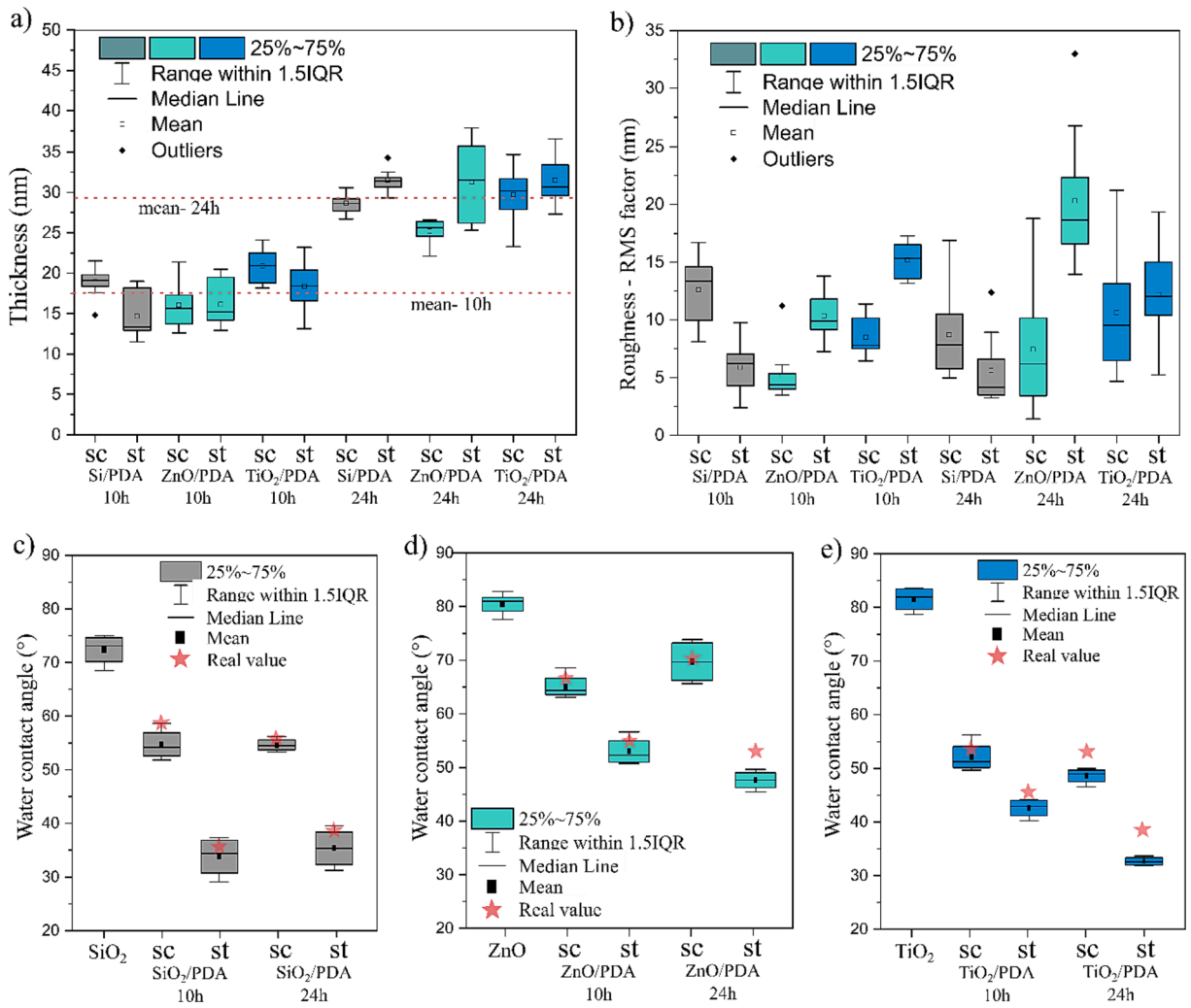

Fig. 3. (a) Thickness of the transferred PDA films on various substrates measured with AFM. (b) Roughness (RMS) of various samples surfaces measured with AFM. (c) Hydrophilic properties expressed by Water contact angle measurements before and after transfer of the PDA films on different substrates: Si, (d) Si/ZnO, (e) Si/TiO_2.

hydrophilicity of transferred films depends on film growth time, and *iii)* scooping and stamping identical films transferred onto identical supports have different water contact angles (scooping always higher). All these findings are very interesting. The first one confirms that the interaction of the substrate surface with the PDA film modifies the film properties. Si/PDA and TiO_2/PDA samples seem to be quite similar, especially for the film grown for 24 h, but the ZnO/PDA samples are much more hydrophobic. The hydrophilicity of polymers is complex, but one of the most important factors is surface energy [50]. The question arises: what is the reason for the lower surface energy of the PDA/ZnO interface? All substrates- acidic SiO_2, amphiphilic TiO_2 and ZnO- can accept electrons from electron-donating PDA catechol groups at the interface [51,52]. Probably due to the fewer adsorption sites on the ZnO surface, less electron-donor interaction occurs, affecting electron transfer through the interface [53]. This will be investigated later in the article. The second finding suggests that either the films change with the growth time or their interaction with the substrates depends on the film thickness or roughness. The third finding is very interesting because it provides a strong argument that the film is strongly asymmetric with regard to the chemical or structural composition of the bottom and top surfaces. During the self-assembly at the air/water interface, the hydrophilic parts of structural units building PDA films are directed toward the water to minimize the creation of a new interface and stabilize the structure [50,54,55]. Therefore, the stamping transferring method leads to more hydrophilic composites' surfaces (smaller water contact angle on the bottom surface). From Table S2 in the Supporting Information, we read that the difference between contact angles of the scooping and stamping samples equals 7.8° for Si/TiO_2/PDA/10, 14.3° for Si/TiO_2/PDA/24, 11.1° for Si/ZnO/PDA/10, 17.1° for Si/ZnO/PDA/24, 21.7° for Si/PDA/10, and 18.1° for Si/PDA/24. The AFM thickness and roughness data suggest that the bottom side of the PDA thin films is characterised by different chemical or structural arrangements, leading to a more hydrophilic character than the upper side, which was revealed by the water contact angle measurements. These chemical and structural divergences were investigated and described below. They show a clear picture, which, together with different hydrophilicity of the upper and lower side, suggest that we have obtained Janus PDA free-standing films.

Thanks to the discrete form of XRD spectra from crystalline substrates, the presence of a thin layer of the substrates can be detected and analyzed from XRD measurements. Especially if their characteristic peaks appear at angles different from those from the substrate and their crystalline phases are out-of-plane. We focus on the 2D-like structure of the films in different samples by evaluating their XRD data compared with the spectra from pure substrates (Fig. S2 of the Supplementary information).

Fig. 4a shows the results of such an experiment performed on the Si/PDA/24 samples (scooping and stamping). The peak at ~33.1° can be

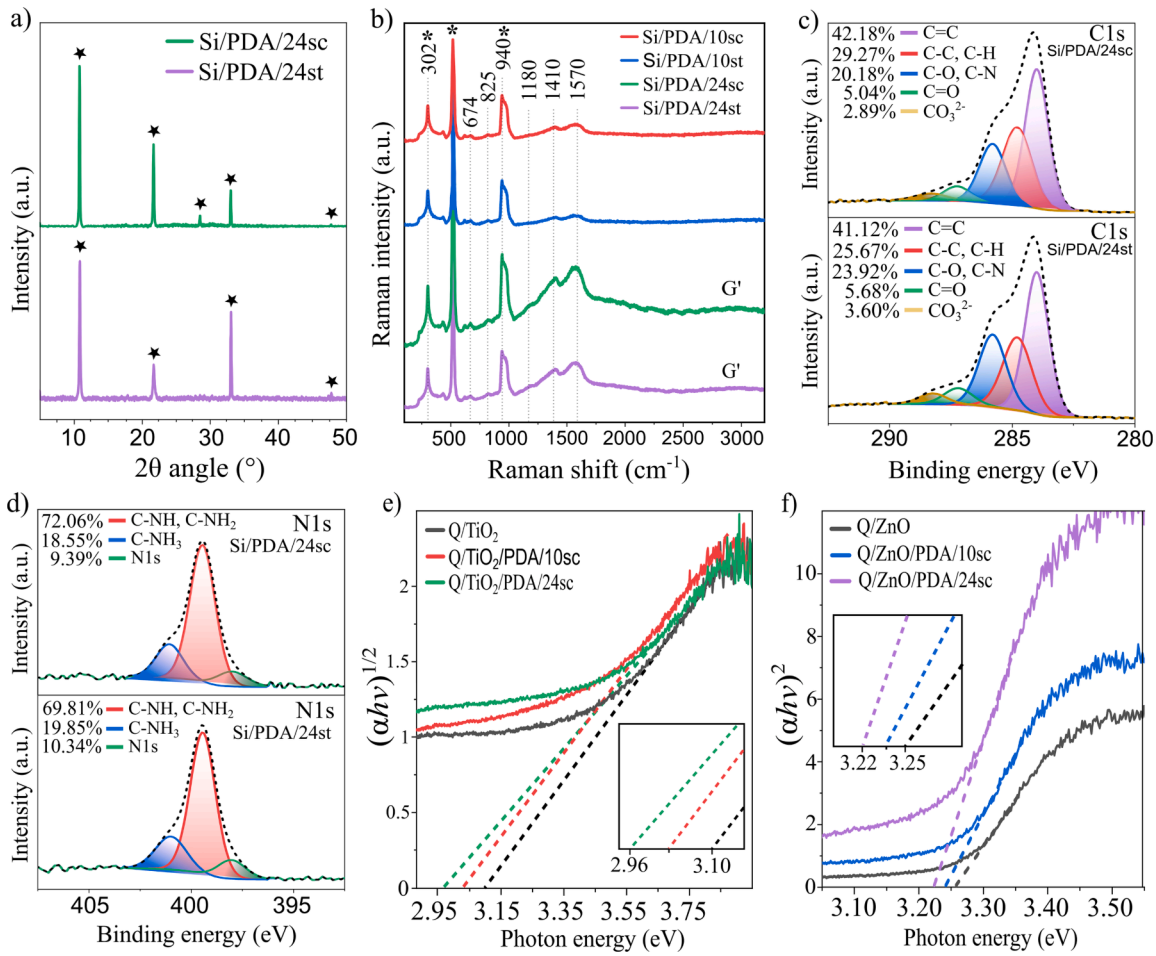

Fig. 4. (a) X-ray diffractogram of Si/PDA/24sc and Si/PDA/24st samples. (b) Raman spectra of Si/PDA/10sc, Si/PDA/10st, Si/PDA/24sc and Si/PDA/24st. The lines are shifted vertically for clarity. (c) X-ray photoelectron spectra for C1s region of the Si/PDA/24sc sample (upper) and Si/PDA/24st (lower), (d) N1s region of the Si/PDA/24sc sample (upper) and Si/PDA/24st (lower). (e) Transmission UV–Vis Tauc Plot of Quartz/TiO_2, Quartz/TiO_2/PDA/10sc, Quartz/TiO_2/PDA/24sc and samples, inset: zoom to photon energy 2.95–3.15 range. (f) Transmission UV–Vis Tauc Plot of Quartz/ZnO, Quartz/ZnO/PDA/10sc, Quartz/ZnO/PDA/24sc and samples, inset: zoom to photon energy 3.20–3.30 range.

assigned to both the substrate–silicon wafer [56] and part of the in-plane periodicity of PDA [57]. Therefore, it will be omitted from the analysis. In addition, the diffractograms for ZnO and TiO_2 coatings do not show any additional peaks, which confirms their assumed amorphous character (Fig. S2). The presence and positions of XRD peaks for Si/PDA/24 samples (Fig. 4a) suggest the presence of structural order resembling the ones found in 2D carbon-based materials, graphene oxide (~11°) and reduced graphene oxide (~22°) [58–61]. Moreover, the weak but noticeable diffraction peaks located near 47° may resemble peaks previously assigned to the (1 0 1) planes of graphite carbon [62–64], however, a similar peak is present in the spectrum of the pure Si substrate. Finally, there is a peak close to ~28° only in the scooping sample, originating most probably from the ordering similar to (0 0 2) face of graphitic crystals [65], indicating a more 2D-resembling structure.

The presence of certain chemical groups in Si/PDA samples was verified by means of Raman spectroscopy experiments (Fig. 4b). In all samples, the characteristic for carbonaceous materials peaks sp^2 can be observed: the D peak (~1410 cm^{-1}), which is attributed to structural defects in the hexagonal carbon lattice, and the G peak (~1570 cm^{-1}) linked with the in-plane vibration of the sp^2 carbon atoms [66–69]. There is a clear increase in these peaks intensity as the thickness of polydopamine films increases with the growth time, which is an expected observation and confirms the thickness differences as shown by the AFM method. Moreover, their intensity also slightly depends on the transferring method: it is lower for stamping. As the scattering signal comes from the whole membrane thickness present in the microscope confocal volume, this difference may originate either from membrane compression/expansion specific for its orientation-dependent interaction with the substrate or from the reduction of the number of freely oscillating carbon bonds due to the contact of the upper PDA surface with the silicon substrate. The I_D/I_G ratio was also calculated, which was used to assess the disorder level of the graphene-like structure. The slight differences 0.916 for Si/PDA/10sc, 0.922 for Si/PDA/10st, 0.914 for Si/PDA/24sc, and 0.913 for Si/PDA/24st do not indicate any trend. However, thanks to the appropriate laser wavelength (633 nm) and relatively high energy used, the lower part of the spectrum (below 1000 cm^{-1}) can provide more information about the structural disorder employing the double-resonance (DR) Raman scattering mechanism [70,71]. Weak yet significant characteristic bands assigned to layer breathing vibrations (~825 cm^{-1}) were revealed [72], resembling the ones characteristic of defective and twisted carbons [71–73]. The peak at the wavenumber ~940 cm^{-1} indicates that the C–H and/or O–H out-of-plane deformations [60] are significantly stronger compared to previous studies [27].

Similarly to the band around 302 cm^{-1}, it can be observed in the spectrum of pure Si subjected to the cleaning procedure in acetone and ethanol (Fig. S3), so they probably come from Si-H and Si-O bonds on the silicon surface. Another important observation is the presence of the ~1180 cm^{-1} band, which is assigned to the NH in-plane deformation mode originating from the pyrrole ring in PDA structure [74], but it is

only visible for samples from the 24-hour series. The peak located at 674 cm^{-1} originates from the stretching and deformation of aromatic rings [70] and remains visible in all samples, as these rings are the basic building blocks of PDA [75].

The position of 2D (G′) peak (for Si/PDA/24sc and Si/PDA/24st samples) is shifted towards higher wavenumbers in comparison to previous studies of thicker PDA a/w films [27]. As this type of shift is characteristic of PDA-based samples with lower oxygen content [76], it should be concluded that this is related to the oxidation time of dopamine. For much thinner Si/PDA/10 samples, 2D peak is very weak due to the much smaller scattering volume of these films and presumably, it is further shifting towards higher wavenumbers.

FTIR spectroscopy of the Si/PDA/24sc sample was performed to further confirm the chemical nature of the obtained polymer (Fig. S4). The broad band at 3190 cm^{-1} indicates the presence of the hydroxyl and N–H groups [77]. At 1640 cm^{-1} - The bending vibration peak of N–H [77] overlaps with C=O band [78]. Bands at 1300 cm^{-1} and 1500 cm^{-1} were assigned to C–O bonds and C=C ring stretching, respectively [77,78]. Finally, the strong absorption band at 1105 cm^{-1} originates from Si-O bonds (PDA-substrate through catechol groups or native SiO_2 on Si substrate surface) [79].

To fully understand the difference between the top/and bottom faces of the PDA films, we performed XPS measurements, as shown in Fig. 4c and d. To properly understand the XPS results, it is important to remark that native oxide was not removed from the Si substrates (Fig. S3). Furthermore, it is important to keep in mind that other peaks originating from Silicon are visible at the Si2p spectrum of all PDA-deposited samples (Si-O), indicating the presence of the silane moieties (Figs. S5, S6, S7 and S8) [80], which proves the fact of binding of functional groups present in polydopamine to the silicon substrate. Importantly, the Si-O component has the largest share of the spectrum for the Si/PDA/10sc sample, followed by the Si/PDA/24sc. The stamping samples have a lower share of this component, which may indicate a weaker bond to the Si substrate. Due to the low penetration depth of the coating in the XPS test, the Si-O component is higher for thinner PDA layers in Si/PDA/10sc than for thicker one in Si/PDA/24sc. Furthermore, considering the C1s spectrum (Fig. 4c), there is a minor yet significant advantage in the sp^2 bonded carbons (C=C) subpeak area for scooping samples compared to the stamping, suggesting a more significant proportion of sp^2 hybridization rings in the structure of the obtained material. Nevertheless, the C–C and C–H bonds are related to sp^3 carbon, implying the presence of branched chains not subjected to pure 2D symmetry [81]. The presence of C–O and C=O subpeaks suggests that both catechol and quinone functional groups are formed, thus confirming the obtained PDA structure [82].

The C-NH and C-NH_2 peaks in the N1s spectrum (Fig. 4d), representing the final and intermediate dopamine oxidation products, are slightly stronger for the scooping samples. In turn, C-NH_3 most probably represents the protonated amino group ($–NH_3^+$) which is expected in basic pH as side chains contain nitrogen and resemble ammonia [81]. This component level is higher for stamping samples, which may be a result of the impurities contribution. The C1s, N1s and O1s spectra for the pure Si substrate and the Si/PDA/10 samples are presented in supplementary info (Figs. S3-S7).

3.2. Optical, photocatalytic and electrochemical properties

To investigate the influence of PDA films (particularly the method of transferring) on the semiconductor's optical properties, especially the bandgap value, UV–vis transmission spectroscopic measurements were carried out. Fig. 4e and 4f show Tauc Plots for TiO_2 and ZnO, respectively. The plots are compared with bare metal oxides and PDA samples of different thicknesses. For both experiments, the introduction of PDA24sc film showed a greater impact on the bandgap value, shifting it by 0.14 eV (TiO_2) and 0.03 eV (ZnO) towards lower photon energy. This effect is of minor importance for ZnO, because such a small shift cannot significantly affect the optical and photocatalytic properties of the material, although it remains consistent with the effect observed in ZnO NWs (~0.1 eV) [34]. However, thanks to a significant shift after deposition of the PDA, TiO_2 can exploit a part of the Vis spectrum (blue region of irradiation) for photocatalytic reactions. The presence of PDA10sc film also induces a smaller value shift, around 0.08 eV. Nevertheless, the possible mechanism was investigated using the transient absorption spectroscopy method described later in this section. To confirm whether the observed change in the bandgap energy value is not a result of the stationary absorption effect, Fig. S9 shows the measured absorbance spectra for the samples with TiO_2 and PDA. As it can be seen, a thin PDA film does not dramatically increase the absorption of radiation in the investigated spectrum, which is advantageous because most of the radiation can reach the surface of the semiconductor/PDA interface.

Fig. 5a presents the photoluminescence spectrum for bare Si/ZnO substrate and samples of different thicknesses and transferring techniques of the PDA films onto Si/ZnO. This substrate was selected because ZnO-based nanostructures are known for their photoluminescent properties [83], which reduces their suitability as photocatalysts [34]. The ZnO bright UV emission (near-band emission, NBE) is close to its absorption edge and produced by excitonic or band-band recombination [84]. Focusing on the literature reports, the room-temperature PL spectrum of ZnO is dominated by the free-exciton longitudinal optical (LO) phonon replica emissions [83,85]. This effect – exciton-phonon coupling – affects the stability of excitons [86]. In Fig. 5a, the position and intensity of the single NBE peak differ for various samples. As PDA shows significant light absorption in the UV region, the bands' intensity was normalized to compare their maximum positions (inset in Fig. 5a) [87]. A significant shift of the maximum of the peak towards higher photon-energy should be noted. It is ~0.03 and ~0.06 eV for thinner (10 h) and thicker (24 h) PDA films, respectively. Although it was found that the crystalline size (d_{size}) of the ZnO nanostructures greatly influences the photon energy of the emission peak [86], this cannot explain the shift observed in our experiment since the deposition of the PDA film could not affect the crystalline size of the ZnO. Instead, we postulate that the PDA coating increases energy required for electron–phonon recombination, which positively affects the stability of excitons in ZnO nanostructures.

In turn, deep-level emissions (DLE) in the visible-NIR range (from 3.1 eV to 1.653 eV) originate from crystalline defects and different film stoichiometry (Fig. 5 b and c), indicating the low ZnO's surface thermodynamic stability [88]. Three major types of emission can be distinguished, namely: green (2.19–2.48 eV), yellow-orange (1.98–2.19 eV), and red (1.65–1.98 eV) [84,89]. The differences in emission energies originate from different defect-related transitions. Orange and red luminescence bands that were observed in our experiment are assigned to oxygen interstitials (O_i) [90–93]. Deconvolution of the spectra showed that the functionalization of the surface with PDA film, compared to ZnO itself, must have influenced the concentration of defects, as it significantly quenched the appearance of bands close to 1.70 and 1.91 eV. Note that in the Fig. 5 b-c, the area under the peaks (a.u.) was embedded at each peak. It can also be concluded that the thicker the PDA coating (and thus the longer oxidation time), the stronger the effect. In turn, the band at ~2.15 eV is ascribed to the transition of an electron from the conduction band to deeply trapped holes in the oxygen interstitials [93–95]. The surface functionalization with a thin film of PDA did not significantly affect this type of emission. In short, polydopamine, with a high degree of oxidation by bonding through functional groups, had a positive effect on stoichiometry and the reduction of ZnO surface defects, contributing to the increase of its stability.

To measure the excitation's photogenerated excited state absorption energies and associated lifetimes, the time evolutions of differential absorption changes (kinetics) were obtained (Fig. 6a–c). Transient absorption changes were measured upon excitation at 310 nm for the samples with TiO_2 on quartz (to avoid direct excitation of the substrate

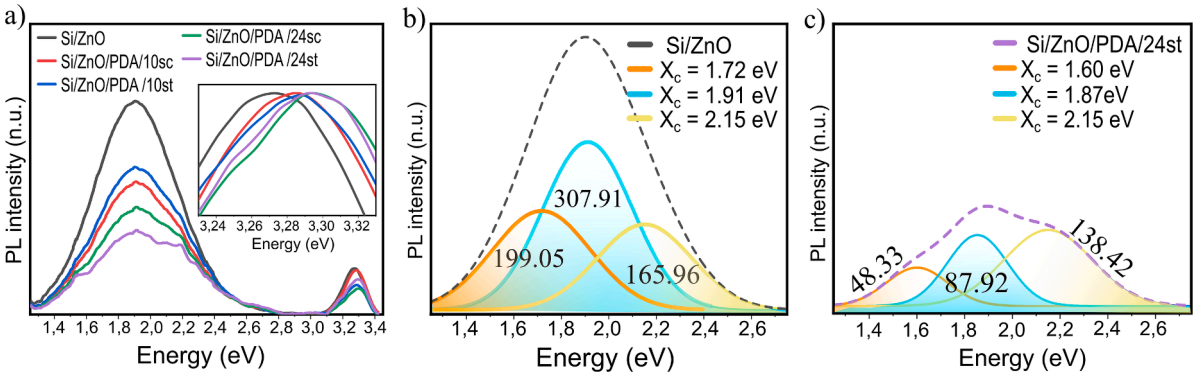

Fig. 5. (a) Photoluminescence spectra of the bare Si/ZnO and after deposition of PDA films. Inset: zoom to the NBE region, normalized. (b) PL spectra broadband in the visible- NIR range deconvoluted for bare Si/ZnO and (c) Si/ZnO/PDA/24st.

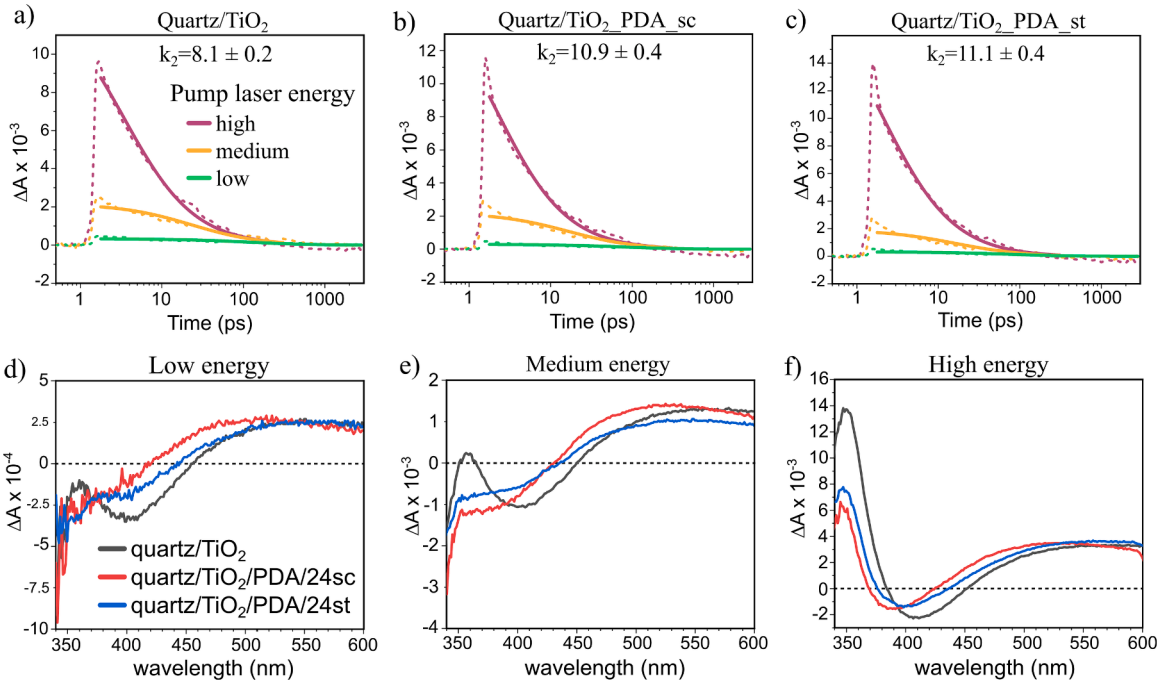

Fig. 6. (a) Representative emission decay traces for Q/TiO_2, (b) Q /TiO_2/PDA/24sc, (c) Q /TiO_2/PDA/24st. (d) Representative transient absorption spectra for a 10 ps time delay between pump and probe pulses for low energy, (e) medium energy, (f) high energy.

with UV irradiation). Kinetics at 590 nm (Fig. 6a-c) represent the decay of the population of holes in TiO_2 [48]. No signals from PDA alone or quartz alone were observed. The excitation from either the coating or the quartz side allows selective probing of different interfaces due to the small penetration depth of TiO_2 at the excitation wavelength of 310 nm. The kinetics were fitted with mixed first and second-order decay functions (Table S3). This model does not take into account the charge diffusion component, but high R^2 values and more or less constant values of A for different pump pulse energies are strong evidence of a good fit of the model (Table S3). For all samples and both excitation sides, a dominant share is of the second-order decay, even for the lowest pump pulse energies. The values of the first-order rate constant (k_1) are either very small compared to the temporal range of the experiment or fitted with high relative error (reaching 100 %) for all samples; therefore, no conclusions can be drawn. When excited from the quartz side, similar radiative, second-order recombination rate constant (k_2) values are observed for the samples with and without PDA. On the contrary, when excited from the coating side, the constant rate k_2 is higher for samples with PDA sc and PDA st of about 35 % and 37 %, respectively (Table S3 and Fig. 6a–c), than that for the control samples with only TiO_2. This proves that PDA indeed affects the properties of TiO_2 close to its interface. Possible reasons for these significant differences will be discussed later in this paragraph. Importantly, a shorter excitation lifetime does not necessarily mean inferior photocatalytic properties. It was previously shown that despite the almost 10 times slower recombination kinetics of rutile than anatase, the photoactivity and catalytic properties of rutile were lower due to the deficit of surface electron holes [96]. It can also be noted that strong second-order recombination conditions are usually not fulfilled at typical sunlight intensities for photocatalysis but rather observed only with laser pulses.

For easy comparison, the spectrum at 10 ps after excitation was plotted to investigate trapped species contribution, and for clarity, spectra were presented in the range 320–600 nm in Fig. 6 d-f. It was previously reported that due to relaxation through deep sites, absorption bands in the transient absorption spectra of TiO_2 shift towards blue as deeply trapped carriers absorb photons of shorter wavelengths [97–99]. Oxygen vacancies (V_{ox}) can induce shallow defects when the thermodynamic effects of the structural relaxation are taken into account

[100–102]. Perhaps PDA passivates oxygen deficiency, which may affect the surface charge properties of the TiO_2 [103].

For a deeper analysis of the previously described kinetic differences, global fitting was performed using the approximation of the two-exponential plus constant offset function. Pre-exponential factor spectra of the components τ_1 and τ_2, that is, the amplitude spectra associated with the individual fitted time constants, were plotted along with the constant offset (const. offset), which stands for constant component, i.e. the final spectrum after 3 ns (Fig. S10). On the one hand, it was found that each decay curve has a fast component of a time constant between 0.86 and 6.1 ps standing for quenching of the photogenerated electrons (e.g. transfer, recombination or trapping). Note that for samples illuminated from the coating side, regardless of the energy used, this component is always faster for PDA-coated samples, as the heterojunction boosts the transfer of electrons from TiO_2 conduction band to PDA through the π-conjugated structure and functional groups. A slow component with a time constant between 14 and 230 ps is standing for the relaxation of trapped electrons. Further analyzing the spectra, we notice that samples with PDA (measured from the PDA side) show a smaller and shorter-wave share of the negative signal, which in samples with TiO_2 alone stretches up to ~500 nm. This signal may come from the steady-state absorption of the trap states in TiO_2 [104–106]. The method of PDA deposition is of little importance for this effect. In turn, the strong signal with a maximum of 340–350 nm, originating most probably from the direct hot transition in TiO_2 [48], is decreased for PDA- coated samples, which may indicate that local heating at the interface is lowered due to heterojunction. This is most probably caused by the difference in trapped holes (O^-) concentration, as postulated above [104]. The above differences around 350 nm for the TiO_2 samples with and without PDA can also be noticed in the transient absorption spectra at 10 ps (Fig. 6 d–f).

Considering all the previously obtained results, PDA films from group 24sc were selected as the most promising and they were subjected to electrochemical tests after deposition onto Si/TiO_2 and Si/ZnO. Cyclic Voltammograms of Si/ZnO/PDA (Fig. 7a) and Si/TiO_2/PDA (Fig. S11) indicate an increase in reduction peak in the cathodic regime; this is a promising indicator of the positive performance impact of PDA-modified composites compared to pure inorganic semiconductors. Next, the linear sweep voltammograms were generated by measurements under chopped illumination of visible (Fig. 7b) and UV–vis (Fig. S12a) light, showing higher photocurrent density (PD) for the TiO_2 samples with deposited PDA films in negative and positive potentials range. For ZnO, a positive effect can be seen for the VIS light illumination (Fig. S12b) and, partially, for the UV–vis illumination experiment (Fig. S12c). This experiment provides information on the photoelectrochemical activity of samples and shows that PDA enhances efficient charge separation, generating functional heterojunction, thus reducing electron-hole recombination.

The results of the EIS measurements are presented in Fig. 7c and d, where the significant influence of PDA on the curves can be seen. To analyze this effect, a fitting procedure (Table S4) and equivalent electric circuits (Fig.s S13 and S14) have been proposed and described in detail in the supplementary information (see pages S16-S21). Firstly, the models show that the real part of the impedance is higher for both TiO_2 and ZnO without irradiation (dark) and under the influence of light in the visible range. On the other hand, it decreases under the influence of UV–vis radiation. This indicates the correctness of the models and is fully in line with the theoretical assumptions, as both TiO_2 and ZnO are active in the UV range and not active in the visible range. More importantly, PDA greatly impacts the decrease in the real impedance component, representing charge transfer resistance. The mentioned decrease is reaching an extremely high value, especially for TiO_2, i.e. ~1920 % (dark), ~1080 % (UV–vis) and ~2250 % (Vis) in comparison to bare TiO_2. This is a higher result than previously described in the literature ~613 % (dark) for *in-situ* deposited PDA on TiO_2 nanorods [107]. Simultaneously, the results obtained for ZnO/PDA are also very promising. It is a 310 % (dark), 215 % (UV–Vis) and 216 % (Vis) decrease in comparison to bare ZnO. The most important result obtained in the present experiment proves that thin PDA films have particularly favorable photoactive properties (in a wide range from UV to Vis), but are also electrochemical (dark- no irradiation), positively influencing the electrochemical performance of inorganic semiconductor materials.

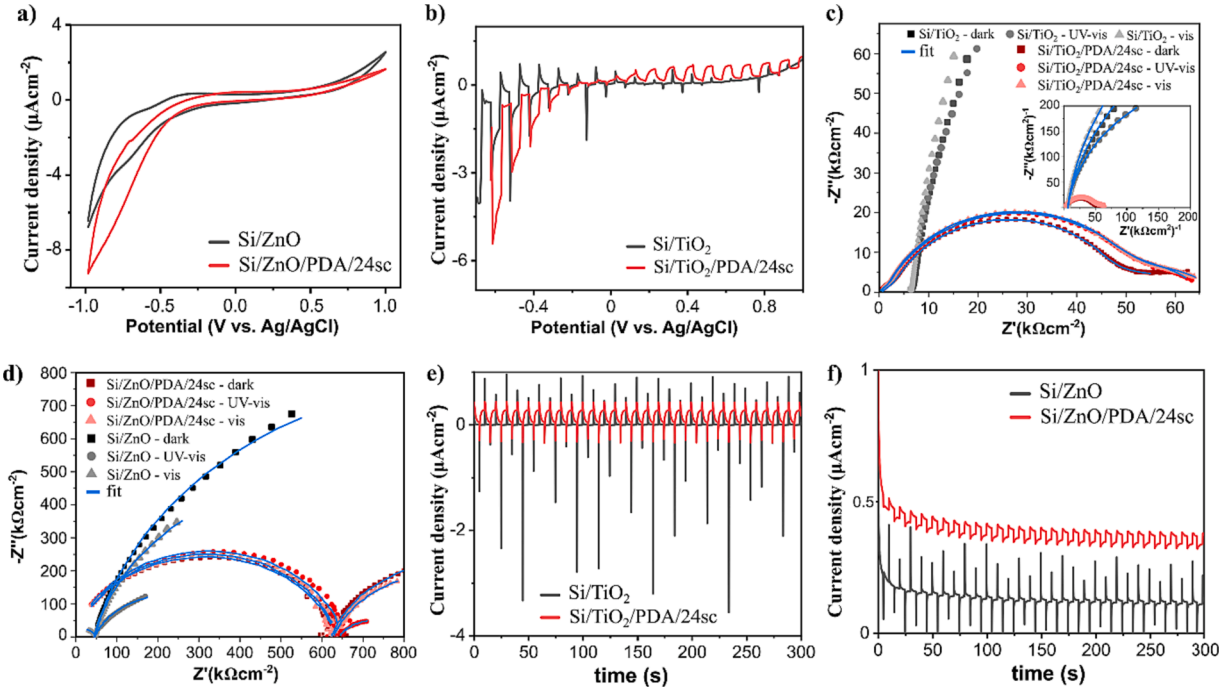

Fig. 7. (a) Cyclic voltammogram of Si/ZnO and Si/ZnO/PDA/24sc samples. (b) Light sweep voltammogram of Si/TiO_2 and Si/TiO_2/PDA/24sc samples under vis irradiation c) Electrochemical impedance spectra under different irradiation conditions of Si/TiO_2, Si/TiO_2/PDA/24sc, (d) Si/ZnO and Si/ZnO/PDA/24sc samples. (e) Cyclic light sweep amperometry under vis irradiation of Si/TiO_2, Si/TiO_2/PDA/24sc, (f) Si/ZnO and Si/ZnO/PDA/24sc samples.

However, the model of TiO_2/PDA taking into account charge transfer resistance at the PDA/electrolyte interphase (Fig. S12) indicates that the irradiation (vis and UV–Vis range) reduces impedance by ~60 % in comparison to dark conditions. In this case, a significant influence of irradiation is of great importance.

The *j–t* graphs for TiO_2 (Fig. 7e) and ZnO (Fig. 7f) show the amperometric response for the visible light on/off cycles. A significant contribution from the pyroelectric potential indicated by the sharp peaks (spikes) is visible. The pyro-phototronic effect was described in detail elsewhere [108–110]. It originates from the nanosecond-scale process of vis light-induced rapid temperature increase [109], as it was previously described that coupling of light and cooling of the device could enhance photocurrent stability [111]. Within this process, a charge carrier transport across the heterojunction is enhanced; hence, numerous recombinations occur, and a transient high output current is observed. After a short time, the photocurrent is stabilized due to the relatively slow photoexcitation process in comparison to trap states induced leakage current [109,112]. PDA caused a significant reduction in the intensity of these spikes, flattening the photocurrent density chart, which is further evidence of its positive effect on reducing the charge carrier's recombination rate [111]. Oxygen vacancy in amorphous TiO_2 could promote hole conduction by providing a "leaky" channel [113]. The oxygen vacancy defects in the amorphous ZnO films and their contribution to hole conduction were also reported [114]. Therefore, considering the amperometric responses of TiO_2/PDA and ZnO/PDA, we postulate that oxygen deficiency at the surface was modified by PDA film. The low photocurrent density was caused by the poor contact electrical contact with TiO_2 or ZnO, but in consistency with literature reports, polydopamine modification contributed to an increase in its value through efficient electron extraction [115].

Finally, the photocatalytic degradation of the methylene blue efficiency was investigated, and the mechanism was drawn as follows. Light-induced generation of the electron (e^-) *hole* (h^+) pairs (1). Generation of the hydroxyl radical through the hole (2). The reaction of the MB with the hydroxyl radical, degradation of the methylene blue (2b). Alternatively, the generation of the superoxide radical (3) and the reaction of the MB with the superoxide radical, thus, degradation of the methylene blue (3b).

$$TiO_2 + hv \rightarrow h^+ + e^-(1)$$

$$h^+ + OH^- \rightarrow OH^\bullet(2a)$$

$$OH^\bullet + MB \rightarrow CO_2 + H_2O(2b)$$

$$O_2 + e^- \rightarrow O_2^{\bullet -}(3a)$$

$$O_2^{\bullet -} + MB \rightarrow CO_2 + H_2O(3b)$$

The results of the photodegradation test are shown in Fig. 8a (photodegradation efficiency) and Fig. S16 (optical digital photographs). After the deposition of the PDA a/w films, the photocatalytic performance of the TiO_2 was significantly enhanced beyond 14 % after 1 h. Moreover, this trend was maintained during the four stability test cycles (Fig. 8b). In subsequent cycles, the increase in efficiency was lower yet significant. In addition, the stability of the composites was evaluated by providing optical microscopy photographs of the surface of the samples before and after the test (after drying under normal conditions) presented in Fig. S17. An important factor is the kinetics of photodegradation, here, we determined the rate constants by fitting the results to the first-order mechanism (Fig. S18). For MB solution with a concentration of 2 ppm, the constant k was equal $9.2 \times 10^{-3} \pm 5$ x 10^{-4} and $5.2 \times 10^{-3} \pm 4 \times 10^{-4}$ for Si/TiO_2/PDA and Si/TiO_2 respectively. This corresponds to degradation rates (DR) 3.31 and 1.87 (ug h^{-1} cm^{-2}), confirming significant TiO_2 photocatalytic performance improvement by *ex-situ* transfer of the polydopamine film. We developed additional tests to exclude the major influence of other effects like heat and MB adsorption on the PDA film. As can be seen in Fig. S19a, the photodegradation of the MB for the reference Si sample was 12.22 % after 1 h under UV–Vis. In turn, a filtration test was performed to investigate the possible adsorption of MB on PDA film (Fig. S19b). The filtration efficiency of the PVDF filter was slightly increased by modification with polydopamine by 12.45 %. Therefore, taking into account the large surface area of the filter (4.9 cm^2) and pressure-forced flux of molecules, the adsorption of MB at the PDA surface is a relatively minor effect. Next, we performed tests with scavengers to investigate the contribution of photogenerated electrons and electron holes in the photocatalytic decomposition of MB. The ethylenediaminetetraacetic acid (EDTA), p-benzoquinone (BQ) and isopropyl alcohol (IPA) were applied as h+, superoxide radicals and hydroxyl radicals scavengers, respectively. A significant decrease in process efficiency was noted for EDTA and BQ. Indicating a slight advantage of the share of electron holes over electrons (Fig. S20). A moderate decrease was noted for IPA since hydroxyl radicals are produced indirectly by TiO_2 and directly by PDA [116]. Small but noticeable degradation efficiency for the reference sample (Si substrate) is related to the absorption of the IR spectrum in the range of which Si(1 0 0) exhibits low photoactivity [117]. *Ex-situ* transfer of the polydopamine film onto TiO_2 surface enhances photocatalytic MB degradation efficiency. First, a bandgap energy value is lowered, leading to the broader light spectrum utilization in a photocatalytic reaction. Secondly, oxygen deficiency at the semiconductor materials surface is modified by PDA film, and shallow defects concentration is decreased, resulting in less probable electron-hole recombinations on the trap states. Generated heterojunction promotes charge transfer and separation. Finally, when presented to the water, the composite shows a more hydrophilic character in comparison to the bare TiO_2 surface, enabling more water molecules to reach the surface and undergo reactions of the hydroxyl radicals generation.

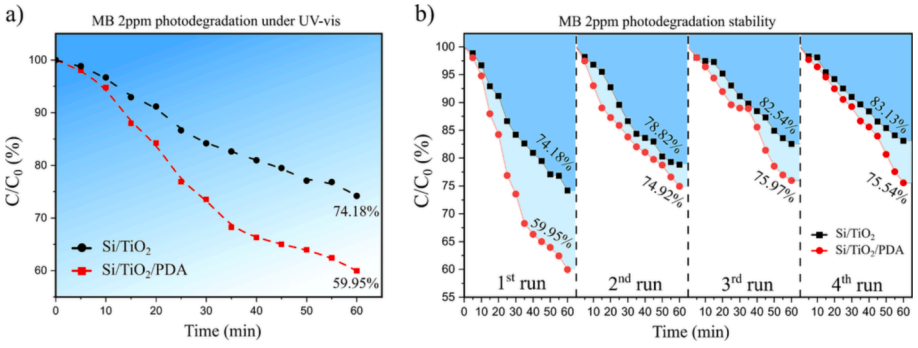

Fig. 8. (a) Graph of the photocatalytic degradation of the Methylene blue efficiency under UV–Vis light illumination. (b) Photocatalysts stability evaluation during 4 photocatalytic MB degradation cycles.

4. Conclusions

In summary, we successfully enhanced the ZnO and TiO_2 photocatalytic and photocatalytic-related properties using easy-transferable and centimetre-scale polydopamine films from the air/water interface. Starting from the previously developed optimised strategy, we prepared films of different thicknesses it is ~17.5 nm and ~30 nm. Next, have conclusively shown that PDA free-standing films can be successfully transferred on multiple functional substrates and resemble Janus structure with two distinct surfaces without losing the exceptional electronic properties observed in PDA/semiconductor interface in nanoparticles.

UV–Vis spectroscopy has shown a 0.14 eV bandgap value shift toward lower photon energies in TiO_2 thin coating using ~30 nm scooping PDA thin film. Photoluminescence spectroscopy has shown that PDA thin films are quenching the photoluminescence bands assigned to the oxygen defect-assisted recombinations in ZnO. Transient absorption spectroscopy in the femtosecond range provided insights into the mechanism of the enhancement of the electrical properties of the composites after PDA deposition by passivating the shallow defect states, boosting the electron transfer at the interface and lowering the local-heating effect in TiO_2 nanofilms. Finally, electrochemical studies were carried out. Most importantly, Electrochemical impedance spectroscopy revealed that PDA films have particularly favorable photoactive properties (in a wide range from UV to Vis), but are also purely electrochemical (dark- no irradiation). The postulated equivalent electrochemical circuit poses an exceptional drop in the charge transfer resistance component at the electrode/electrolyte interface after PDA deposition, reaching a ~2250 % drop for TiO_2 in Vis irradiation and ~310 % without irradiation for ZnO. Moreover, cyclic light sweep amperometry revealed a significant quenching of the pyro-phototronic effect, which in bare TiO_2 and ZnO originates from photogenerated electron-hole recombination. Further, the photocatalytic degradation of the methylene blue efficiency was investigated, and remarkable efficiency enhancement for the Si/TiO_2/PDA composite was noted, 14 % after 1 h in comparison to Si/TiO_2. Higher efficiency was also obtained in the subsequent four cycles. These benefits result from the creation of a functional organic/inorganic heterojunction.

Finally, although we have focused mainly on the photocatalytic aspects of such composites as a benchmarking of the transferring method, our findings can be easily applied to biomedicine, electronics and water remediation.

CRediT authorship contribution statement

Jakub Szewczyk: Conceptualization, Data curation, Investigation, Methodology, Validation, Visualization, Writing – original draft, Writing – review & editing. **Marcin Ziółek:** Data curation, Investigation, Methodology, Validation, Writing – review & editing. **Katarzyna Siuzdak:** Data curation, Funding acquisition, Investigation, Methodology, Validation, Writing – review & editing. **Igor Iatsunskyi:** Investigation, Methodology, Validation, Writing – review & editing. **Mikołaj Pochylski:** Investigation, Methodology. **Daniel Aguilar-Ferrer:** Investigation, Methodology. **Mateusz Kempiński:** Investigation, Methodology. **Fida Tanos:** Investigation, Methodology. **Jacek Gapiński:** Methodology, Validation, Writing – review & editing. **Mikhael Bechelany:** Funding acquisition, Methodology, Resources, Supervision, Validation, Writing – review & editing. **Emerson Coy:** Conceptualization, Funding acquisition, Investigation, Methodology, Resources, Supervision, Validation, Writing – review & editing.

Declaration of competing interest

The authors declare that they have no known competing financial interests or personal relationships that could have appeared to influence the work reported in this paper.

Data availability

The raw/processed data required to reproduce these findings cannot be shared at this time as the data also forms part of an ongoing study. Data might be shared upon reasonable request to the corresponding author.

Acknowledgments

The authors acknowledge the financial support from the National Science Centre of Poland (NCN) by the OPUS grant 2019/35/B/ST5/00248. This research was supported by a French Government Scholarship. J.S. is a scholarship holder of the Foundation of the Adam Mickiewicz University in Poznań for the academic year 2022/2023. K.S. acknowledges the partial financial support from the NCN Sonata-Bis 2017/26/E/ST5/00416 in the electrochemical section of this manuscript. Authors acknowledge as well the financial support of project H2020-MSCA-RISE-2017, 'Novel 1D photonic metal oxide nanostructures for early stage cancer detection' (Project number: 778157).

Appendix A. Supplementary material

Supplementary data to this article can be found online at https://doi.org/10.1016/j.eurpolymj.2024.112781.

References

[1] H. Lee, S.M. Dellatore, W.M. Miller, P.B. Messersmith, Mussel-inspired surface chemistry for multifunctional coatings, Science. 318 (2007) 426–430, https://doi.org/10.1126/science.1147241.
[2] L. Yang, S.L. Phua, J.K.H. Teo, C.L. Toh, S.K. Lau, J. Ma, X. Lu, A biomimetic approach to enhancing interfacial interactions: Polydopamine-coated clay as reinforcement for epoxy resin, ACS Appl. Mater. Interfaces. 3 (2011) 3026–3032, https://doi.org/10.1021/am200532j.
[3] T.G. Barclay, H.M. Hegab, S.R. Clarke, M. Ginic-Markovic, Versatile surface modification using polydopamine and related polycatecholamines: chemistry, structure, and applications, Adv. Mater. Interfaces. 4 (2017) 1601192, https://doi.org/10.1002/admi.201601192.
[4] G. Kafkopoulos, C.J. Padberg, J. Duvigneau, G.J. Vancso, Adhesion engineering in polymer-metal comolded joints with biomimetic polydopamine, ACS Appl. Mater. Interfaces. 13 (2021) 19244–19253, https://doi.org/10.1021/acsami.1c01070.
[5] J. Liebscher, Chemistry of polydopamine – scope, variation, and limitation, European J. Org. Chem. 2019 (2019) 4976–4994, https://doi.org/10.1002/ejoc.201900445.
[6] J. Szewczyk, D. Aguilar-Ferrer, E. Coy, Polydopamine films: Electrochemical growth and sensing applications, Eur. Polym. J. 174 (2022) 111346, https://doi.org/10.1016/j.eurpolymj.2022.111346.
[7] K. Żebrowska, E. Coy, K. Synoradzki, S. Jurga, P. Torruella, R. Mrówczyński, Facile and controllable growth of β-FeOOH nanostructures on polydopamine spheres, J. Phys. Chem. b. 124 (2020) 9456–9463, https://doi.org/10.1021/acs.jpcb.0c06627.
[8] C.C. Ho, S.J. Ding, The pH-controlled nanoparticles size of polydopamine for anticancer drug delivery, J. Mater. Sci. Mater. Med. 24 (2013) 2381–2390, https://doi.org/10.1007/s10856-013-4994-2.
[9] A. Jin, Y. Wang, K. Lin, L. Jiang, Nanoparticles modified by polydopamine: Working as "drug" carriers, Bioact. Mater. 5 (2020) 522–541, https://doi.org/10.1016/j.bioactmat.2020.04.003.
[10] R. Mrówczyński, A. Nan, R. Turcu, J. Leistner, J. Liebscher, Polydopamine - a versatile coating for surface-initiated ring-opening polymerization of lactide to polylactide, Macromol. Chem. Phys. 216 (2015) 211–217, https://doi.org/10.1002/macp.201400380.
[11] A. Petran, R. Mrówczyński, C. Filip, R. Turcu, J. Liebscher, Melanin-like polydopa amides-synthesis and application in functionalization of magnetic nanoparticles, Polym. Chem. 6 (2015) 2139–2149, https://doi.org/10.1039/c4py01467g.
[12] A. Jędrzak, B.F. Grześkowiak, K. Golba, E. Coy, K. Synoradzki, S. Jurga, T. Jesionowski, R. Mrówczyński, Magnetite nanoparticles and spheres for chemo- and photothermal therapy of hepatocellular carcinoma in vitro, Int. J. Nanomed. 15 (2020) 7923–7936, https://doi.org/10.2147/IJN.S257142.
[13] G. Loget, J.E. Yoo, A. Mazare, L. Wang, P. Schmuki, Highly controlled coating of biomimetic polydopamine in TiO2 nanotubes, Electrochem. Commun. 52 (2015) 41–44, https://doi.org/10.1016/j.elecom.2015.01.011.
[14] Y. Kim, E. Coy, H. Kim, R. Mrówczyński, P. Torruella, D.W. Jeong, K.S. Choi, J. H. Jang, M.Y. Song, D.J. Jang, F. Peiro, S. Jurga, H.J. Kim, Efficient photocatalytic production of hydrogen by exploiting the polydopamine-semiconductor interface, Appl. Catal. B Environ. 280 (2021) 119423, https://doi.org/10.1016/j.apcatb.2020.119423.

[15] M. Ruan, D. Guo, Q. Jia, A uniformly decorated and photostable polydopamine–organic semiconductor to boost the photoelectrochemical water splitting performance of CdS photoanodes, Dalt. Trans. 50 (2021) 1913–1922, https://doi.org/10.1039/d0dt04056h.

[16] D. Aguilar-Ferrer, T. Vasileiadis, I. Iatsunskyi, M. Ziółek, K. Żebrowska, O. Ivashchenko, P. Błaszkiewicz, B. Grześkowiak, R. Pazos, S. Moya, M. Bechelany, E. Coy, Understanding the photothermal and photocatalytic mechanism of polydopamine coated gold nanorods, Adv. Funct. Mater. 33 (2023) 2304208. https://doi.org/10.1002/adfm.202304208.

[17] A. Olejnik, K. Polaczek, M. Szkodo, A. Stanisławska, J. Ryl, K. Siuzdak, Laser-induced graphitization of polydopamine on titania nanotubes, ACS Appl. Mater. Interfaces. 15 (2023) 52921–52938, https://doi.org/10.1021/acsami.3c11580.

[18] M.J. Bigaj-Józefowska, E. Coy, K. Załęski, T. Zalewski, M. Grabowska, K. Jaskot, P. Perrigue, R. Mrówczyński, B.F. Grześkowiak, Biomimetic theranostic nanoparticles for effective anticancer therapy and MRI imaging, J. Photochem. Photobiol. B Biol. 249 (2023) 112813. https://doi.org/10.1016/j.jphotobiol.2023.112813.

[19] C. Cheng, S. Li, J. Zhao, X. Li, Z. Liu, L. Ma, X. Zhang, S. Sun, C. Zhao, Biomimetic assembly of polydopamine-layer on graphene: Mechanisms, versatile 2D and 3D architectures and pollutant disposal, Chem. Eng. J. 228 (2013) 468–481, https://doi.org/10.1016/j.cej.2013.05.019.

[20] Z. Xu, N. Wang, P. Liu, Y. Sun, Y. Wang, F. Fei, S. Zhang, J. Zheng, B. Han, Poly (dopamine) coating on 3D-printed poly-lactic-co-glycolic acid/β-tricalcium phosphate scaffolds for bone tissue engineering, Molecules. 24 (2019) 4397, https://doi.org/10.3390/molecules24234397.

[21] J.L. Chakka, T. Acri, N.Z. Laird, L. Zhong, K. Shin, S. Elangovan, A.K. Salem, Polydopamine functionalized VEGF gene-activated 3D printed scaffolds for bone regeneration, RSC Adv. 11 (2021) 13282–13291, https://doi.org/10.1039/d1ra01193f.

[22] J. Svoboda, M. Král, M. Dendisová, P. Matějka, O. Pop-Georgievsk, Unraveling the influence of substrate on the growth rate, morphology and covalent structure of surface adherent polydopamine films, Colloids Surf. B Biointerf. 205 (2021) 111897, https://doi.org/10.1016/j.colsurfb.2021.111897.

[23] F. Ponzio, P. Payamyar, A. Schneider, M. Winterhalter, J. Bour, F. Addiego, M. P. Krafft, J. Hemmerle, V. Ball, Polydopamine films from the forgotten air/water interface, J. Phys. Chem. Lett. 5 (2014) 3436–3440, https://doi.org/10.1021/jz501842r.

[24] F. Ponzio, V. Ball, Polydopamine deposition at fluid interfaces, Polym. Int. 65 (2016) 1251–1257, https://doi.org/10.1002/pi.5124.

[25] O.Y. Milyaeva, A.G. Bykov, R.A. Campbell, G. Loglio, R. Miller, B.A. Noskov, Polydopamine layer formation at the liquid – gas interface, Colloids Surfaces A Physicochem. Eng. Asp. 579 (2019) 123637, https://doi.org/10.1016/j.colsurfa.2019.123637.

[26] E. Coy, I. Iatsunskyi, J.C. Colmenares, Y. Kim, R. Mrówczyński, Polydopamine films with 2D-like layered structure and high mechanical resilience, ACS Appl. Mater. Interfaces. 13 (2021) 23113–23120, https://doi.org/10.1021/acsami.1c02483.

[27] J. Szewczyk, M. Pochylski, K. Szutkowski, M. Kempiński, R. Mrówczyński, I. Iatsunskyi, J. Gapiński, E. Coy, In-situ thickness control of centimetre-scale 2D-Like polydopamine films with large scalability, Mater. Today Chem. 24 (2022) 100935. https://doi.org/10.1016/j.mtchem.2022.100935.

[28] J. Szewczyk, V. Babacic, A. Krysztofik, O. Ivashchenko, M. Pochylski, R. Pietrzak, J. Gapiński, B. Graczykowski, M. Bechelany, E. Coy, Control of intermolecular interactions toward the production of free-standing interfacial polydopamine films, ACS Appl. Mater. Interfaces. 15 (2023) 36922–36935, https://doi.org/10.1021/acsami.3c05236.

[29] S. Hong, C.F. Schaber, K. Dening, E. Appel, S.N. Gorb, H. Lee, Air/water interfacial formation of freestanding, stimuli-responsive, self-healing catecholamine janus-faced microfilms, Adv. Mater. 26 (2014) 7581–7587, https://doi.org/10.1002/adma.201403259.

[30] B.N. Ren, H.H. Pi, Y.S. Gu, R. Wang, X.Q. Zhang, J. Wu, Research progress in preparation and application of Janus membranes, Cailiao Gongcheng/J. Mater. Eng. 48 (2020) 72–80. https://doi.org/10.11868/j.issn.1001-4381.2019.000530.

[31] D. Aguilar-Ferrer, J. Szewczyk, E. Coy, Recent developments in polydopamine-based photocatalytic nanocomposites for energy production: physico-chemical properties and perspectives, Catal. Today. 397–399 (2022) 316–349, https://doi.org/10.1016/j.cattod.2021.08.016.

[32] S.N. Ahmed, W. Haider, Heterogeneous photocatalysis and its potential applications in water and wastewater treatment: A review, Nanotechnology. 29 (2018) 342001, https://doi.org/10.1088/1361-6528/aac6ea.

[33] V. Fedorenko, R. Viter, R. Mrówczyński, D. Damberga, E. Coy, I. Iatsunskyi, Synthesis and photoluminescence properties of hybrid 1D core–shell structured nanocomposites based on ZnO/polydopamine, RSC Adv. 10 (2020) 29751–29758, https://doi.org/10.1039/D0RA04829A.

[34] D. Damberga, V. Fedorenko, K. Grundšteins, Ş. Altundal, A. Šutka, A. Ramanavičius, E. Coy, R. Mrówczyński, I. Iatsunskyi, R. Viter, Influence of pda coating on the structural, optical and surface properties of zno nanostructures, Nanomaterials. 10 (2020) 1–11, https://doi.org/10.3390/nano10122438.

[35] X. Sun, L. Yan, R. Xu, M. Xu, Y. Zhu, Surface modification of TiO 2 with polydopamine and its effect on photocatalytic degradation mechanism, Colloids Surfaces A Physicochem. Eng. Asp. 570 (2019) 199–209, https://doi.org/10.1016/j.colsurfa.2019.03.018.

[36] L. Wang, J. Zhang, H. Yu, I.H. Patir, Y. Li, S. Wageh, A.A. Al-Ghamdi, J. Yu, Dynamics of photogenerated charge carriers in inorganic/organic s-scheme heterojunctions, J. Phys. Chem. Lett. 13 (2022) 4695–4700, https://doi.org/10.1021/acs.jpclett.2c01332.

[37] I. Khan, K. Saeed, I. Zekker, B. Zhang, A.H. Hendi, A. Ahmad, S. Ahmad, N. Zada, H. Ahmad, L.A. Shah, T. Shah, I. Khan, Review on methylene blue: its properties, uses, toxicity and photodegradation, Water (switzerland). 14 (2022) 242, https://doi.org/10.3390/w14020242.

[38] D. Liu, C. Li, C. Zhao, Q. Zhao, T. Niu, L. Pan, P. Xu, F. Zhang, W. Wu, T. Ni, Facile synthesis of three-dimensional hollow porous carbon doped polymeric carbon nitride with highly efficient photocatalytic performance, Chem. Eng. J. 438 (2022) 135623, https://doi.org/10.1016/j.cej.2022.135623.

[39] D. Liu, H. Li, R. Gao, Q. Zhao, Z. Yang, X. Gao, Z. Wang, F. Zhang, W. Wu, Enhanced visible light photoelectrocatalytic degradation of tetracycline hydrochloride by I and P co-doped TiO2 photoelectrode, J. Hazard. Mater. 406 (2021) 124309, https://doi.org/10.1016/j.jhazmat.2020.124309.

[40] D. Liu, C. Li, J. Ge, C. Zhao, Q. Zhao, F. Zhang, T. Ni, W. Wu, 3D interconnected g-C3N4 hybridized with 2D Ti3C2 MXene nanosheets for enhancing visible light photocatalytic hydrogen evolution and dye contaminant elimination, Appl. Surf. Sci. 579 (2022) 152180, https://doi.org/10.1016/j.apsusc.2021.152180.

[41] U. Chakraborty, G. Kaur, H.-G. Rubahn, A. Kaushik, G.R. Chaudhary, Y.K. Mishra, Advanced metal oxides nanostructures to recognize and eradicate water pollutants, Prog. Mater. Sci. 139 (2023) 101169. https://doi.org/10.1016/j.pmatsci.2023.101169.

[42] N. Vogel, S. Goerres, K. Landfester, C.K. Weiss, A convenient method to produce close- and non-close-packed monolayers using direct assembly at the air-water interface and subsequent plasma-induced size reduction, Macromol. Chem. Phys. 212 (2011) 1719–1734, https://doi.org/10.1002/macp.201100187.

[43] M. Moret, A. Abou Chaaya, M. Bechelany, P. Miele, Y. Robin, O. Briot, Atomic Layer Deposition of zinc oxide for solar cell applications, Superlatt. Microstruct. 75 (2014) 477–484, https://doi.org/10.1016/j.spmi.2014.07.050.

[44] I. Iatsunskyi, M. Jancelewicz, G. Nowaczyk, M. Kempiński, B. Peplińska, M. Jarek, K. Załęski, S. Jurga, V. Smyntyna, Atomic layer deposition TiO2 coated porous silicon surface: structural characterization and morphological features, Thin Solid Films. 589 (2015) 303–308, https://doi.org/10.1016/j.tsf.2015.05.056.

[45] A.A. Chaaya, R. Viter, M. Bechelany, Z. Alute, D. Erts, A. Zalesskaya, K. Kovalevskis, V. Rouessac, V. Smyntyna, P. Miele, Evolution of microstructure and related optical properties of ZnO grown by atomic layer deposition, Beilstein J. Nanotechnol. 4 (2013) 690–698, https://doi.org/10.3762/bjnano.4.78.

[46] D. Nečas, P. Klapetek, Gwyddion: an open-source software for SPM data analysis, Cent. Eur. J. Phys. 10 (2012) 181–188, https://doi.org/10.2478/s11534-011-0096-2.

[47] P. Makuła, M. Pacia, W. Macyk, How To correctly determine the band gap energy of modified semiconductor photocatalysts based on UV-Vis spectra, J. Phys. Chem. Lett. 9 (2018) 6814–6817, https://doi.org/10.1021/acs.jpclett.8b02892.

[48] E. Coy, K. Siuzdak, I. Grądzka-Kurzaj, S. Sayegh, M. Weber, M. Ziółek, M. Bechelany, I. Iatsunskyi, Exploring the effect of BN and B-N bridges on the photocatalytic performance of semiconductor heterojunctions: Enhancing carrier transfer mechanism, Appl. Mater. Today. 24 (2021) 101095, https://doi.org/10.1016/j.apmt.2021.101095.

[49] J. Idĭgoras, G. Burdzinski, J. Karolczak, J. Kubicki, G. Oskam, J.A. Anta, M. Ziółek, The impact of the electrical nature of the metal oxide on the performance in dye-sensitized solar cells: new look at old paradigms, J. Phys. Chem. c. 119 (2015) 3931–3944, https://doi.org/10.1021/jp512330f.

[50] J.C. Foster, I. Akar, M.C. Grocott, A.K. Pearce, R.T. Mathers, R.K. O'Reilly, 100th anniversary of macromolecular science viewpoint: the role of hydrophobicity in polymer phenomena, ACS Macro Lett. 9 (2020) 1700–1707, https://doi.org/10.1021/acsmacrolett.0c00645.

[51] S. Neyshtadt, J.P. Jahnke, R.J. Messinger, A. Rawal, T. Segal Peretz, D. Huppert, B.F. Chmelka, G.L. Frey, Understanding and controlling organic - Inorganic interfaces in mesostructured hybrid photovoltaic materials, J. Am. Chem. Soc. 133 (2011) 10119–10133, https://doi.org/10.1021/ja200054z.

[52] H. Hemmatpour, O. De Luca, D. Crestani, M.C.A. Stuart, A. Lasorsa, P.C.A. van der Wel, K. Loos, T. Giousis, V. Haddadi-Asl, P. Rudolf, New insights in polydopamine formation via surface adsorption, Nat. Commun. 14 (2023) 664, https://doi.org/10.1038/s41467-023-36303-8.

[53] F. Morteo-Flores, A. Roldan, The effect of pristine and hydroxylated oxide surfaces on the guaiacol HDO process: a DFT study, ChemPhysChem. 23 (2022) 1, https://doi.org/10.1002/cphc.202100583.

[54] Y. Mai, A. Eisenberg, Self-assembly of block copolymers, Chem. Soc. Rev. 41 (2012) 5969–5985, https://doi.org/10.1039/c2cs35115c.

[55] Y.O. Kim, J.M. You, H.S. Jang, S.K. Choi, B.Y. Jung, O. Kang, J.W. Kim, Y.S. Lee, Eumelanin as a support for efficient palladium nanoparticle catalyst for Suzuki coupling reaction of aryl chlorides in water, Tetrahedron Lett. 58 (2017) 2149–2152, https://doi.org/10.1016/j.tetlet.2017.04.062.

[56] T. Ami, M. Suzuki, MOCVD growth of (100)-oriented CeO2 thin films on hydrogen-terminated Si(100) substrates, Mater. Sci. Eng. b. 54 (1998) 84–91, https://doi.org/10.1016/s0921-5107(98)00133-0.

[57] Z. Tian, W. Hwang, Y.J. Kim, Mechanistic understanding of monovalent cation transport in eumelanin pigments, J. Mater. Chem. b. 7 (2019) 6355–6361, https://doi.org/10.1039/C9TB01211G.

[58] N. Rono, J.K. Kibet, B.S. Martincigh, V.O. Nyamori, A review of the current status of graphitic carbon nitride, Crit. Rev. Solid State Mater. Sci. 46 (2021) 189–217, https://doi.org/10.1080/10408436.2019.1709414.

[59] B. Gurzęda, A. Subrati, P. Florczak, Z. Kabacińska, T. Buchwald, L. Smardz, B. Peplińska, S. Jurga, P. Krawczyk, Two-step synthesis of well-ordered layered graphite oxide with high oxidation degree, Appl. Surf. Sci. 507 (2020) 145049, https://doi.org/10.1016/j.apsusc.2019.145049.

[60] A. Subrati, S. Mondal, M. Ali, A. Alhindi, R. Ghazi, A. Abdala, D. Reinalda, S. Alhassan, Developing hydrophobic graphene foam for oil spill cleanup, Ind.

Eng. Chem. Res. 56 (2017) 6945–6951, https://doi.org/10.1021/acs.iecr.7b00716.
[61] F.T. Johra, J.W. Lee, W.G. Jung, Facile and safe graphene preparation on solution based platform, J. Ind. Eng. Chem. 20 (2014) 2883–2887, https://doi.org/10.1016/j.jiec.2013.11.022.
[62] T. Qiu, J.G. Yang, X.J. Bai, Y.L. Wang, The preparation of synthetic graphite materials with hierarchical pores from lignite by one-step impregnation and their characterization as dye absorbents, RSC Adv. 9 (2019) 12737–12746, https://doi.org/10.1039/c9ra00343f.
[63] S. Sedira, B. Mendaci, Hydrothermal synthesis of spherical carbon nanoparticles (CNPs) for supercapacitor electrodes uses, Mater. Renew. Sustain Energy. 9 (2020) 1–9, https://doi.org/10.1007/s40243-019-0161-0.
[64] N. Cao, Y. Zhang, Study of reduced graphene oxide preparation by hummers' method and related characterization, J. Nanomater. 2015 (2015) 1–5, https://doi.org/10.1155/2015/168125.
[65] M. Kyotani, K. Hiratani, T. Okada, S. Matsushita, K. Akagi, Preparation of 2D carbon materials by chemical carbonization of cellulosic materials to avoid thermal decomposition, Glob. Challenges. 1 (2017) 1700061, https://doi.org/10.1002/gch2.201700061.
[66] R. Tejido-Rastrilla, G. Baldi, A.R. Boccaccini, Ag containing polydopamine coating on a melt-derived bioactive glass-ceramic: effect on surface reactivity, Ceram. Int. 44 (2018) 16083–16087, https://doi.org/10.1016/j.ceramint.2018.05.198.
[67] H. Li, J. Xi, A.G. Donaghue, J. Keum, Y. Zhao, K. An, E.R. McKenzie, F. Ren, Synthesis and catalytic performance of polydopamine supported metal nanoparticles, Sci. Rep. 10 (2020) 10416, https://doi.org/10.1038/s41598-020-67458-9.
[68] A.C. Ferrari, Raman spectroscopy of graphene and graphite: Disorder, electron-phonon coupling, doping and nonadiabatic effects, Solid State Commun. 143 (2007) 47–57, https://doi.org/10.1016/j.ssc.2007.03.052.
[69] C. Silva, F. Simon, P. Friedel, P. Pötschke, C. Zimmerer, Elucidating the chemistry behind the reduction of graphene oxide using a green approach with polydopamine, Nanomaterials. 9 (2019) 902, https://doi.org/10.3390/nano9060902.
[70] P. Venezuela, M. Lazzeri, F. Mauri, Theory of double-resonant Raman spectra in graphene: intensity and line shape of defect-induced and two-phonon bands, Phys. Rev. B - Condens. Matter Mater. Phys. 84 (2011) 035433, https://doi.org/10.1103/PhysRevB.84.035433.
[71] C. Pardanaud, G. Cartry, L. Lajaunie, R. Arenal, J.G. Buijnsters, Investigating the possible origin of raman bands in defective sp2/sp3 carbons below 900 cm−1: phonon density of states or double resonance mechanism at play? C — J. Carbon Res. 5 (2019) 79, https://doi.org/10.3390/c5040079.
[72] J. Campos-Delgado, L.G. Cançado, C.A. Achete, A. Jorio, J.P. Raskin, Raman scattering study of the phonon dispersion in twisted bilayer graphene, Nano Res. 6 (2013) 269–274, https://doi.org/10.1007/s12274-013-0304-z.
[73] D. Roy, M. Chhowalla, H. Wang, N. Sano, I. Alexandrou, T.W. Clyne, G.A. J. Amaratunga, Characterisation of carbon nano-onions using Raman spectroscopy, Chem. Phys. Lett. 373 (2003) 52–56, https://doi.org/10.1016/S0009-2614(03)00523-2.
[74] G. Perna, M. Lasalvia, V. Capozzi, Vibrational spectroscopy of synthetic and natural eumelanin, Polym. Int. 65 (2016) 1323–1330, https://doi.org/10.1002/pi.5182.
[75] J. Liebscher, R. Mrówczyński, H.A. Scheidt, C. Filip, N.D. Haìdade, R. Turcu, A. Bende, S. Beck, Structure of polydopamine: a never-ending story? Langmuir. 29 (2013) 10539–10548, https://doi.org/10.1021/la4020288.
[76] A. Alkhouzaam, H. Qiblawey, M. Khraisheh, Polydopamine functionalized graphene oxide as membrane nanofiller: Spectral and structural studies, Membranes. 11 (2021) 1–17, https://doi.org/10.3390/membranes11020086.
[77] T. Touqeer, M.W. Mumtaz, H. Mukhtar, A. Irfan, S. Akram, A. Shabbir, U. Rashid, I.A. Nehdi, T.S. Yaw Choong, Fe3O4-PDA-lipase as surface functionalized nano biocatalyst for the production of biodiesel using waste cooking oil as feedstock: characterization and process optimization, Energies. 13 (2020) 177, https://doi.org/10.3390/en13010177.
[78] H. Luo, C. Gu, W. Zheng, F. Dai, X. Wang, Z. Zheng, Facile synthesis of novel size-controlled antibacterial hybrid spheres using silver nanoparticles loaded with poly-dopamine spheres, RSC Adv. 5 (2015) 13470–13477, https://doi.org/10.1039/c4ra16469e.
[79] M. Liu, W. Jiang, Q. Chen, S. Wang, Y. Mao, X. Gong, K.C.F. Leung, J. Tian, H. Wang, S. Xuan, A facile one-step method to synthesize SiO2@polydopamine core–shell nanospheres for shear thickening fluid, RSC Adv. 6 (2016) 29279–29287, https://doi.org/10.1039/c5ra25759j.
[80] M. Massaro, V. Campisciano, C.V. Iborra, L.F. Liotta, M. Sánchez-Polo, S. Riela, M. Gruttadauria, New mussel inspired polydopamine-like silica-based material for dye adsorption, Nanomaterials. 10 (2020) 1–12, https://doi.org/10.3390/nano10071416.
[81] M. Kehrer, J. Duchoslav, A. Hinterreiter, M. Cobet, A. Mehic, T. Stehrer, D. Stifter, XPS investigation on the reactivity of surface imine groups with TFAA, Plasma Process. Polym. 16 (2019) 1800160, https://doi.org/10.1002/ppap.201800160.
[82] Q. Wei, F. Zhang, J. Li, B. Li, C. Zhao, Oxidant-induced dopamine polymerization for multifunctional coatings, Polym. Chem. 1 (2010) 1430–1433, https://doi.org/10.1039/c0py00215a.
[83] W. Shan, W. Walukiewicz, J.W. Ager, K.M. Yu, H.B. Yuan, H.P. Xin, G. Cantwell, J.J. Song, Nature of room-temperature photoluminescence in ZnO, Appl. Phys. Lett. 86 (2005) 1–3, https://doi.org/10.1063/1.1923757.
[84] A. Galdámez-Martinez, G. Santana, F. Güell, P.R. Martínez-Alanis, A. Dutt, Photoluminescence of zno nanowires: a review, Nanomaterials. 10 (2020) 857, https://doi.org/10.3390/nano10050857.
[85] A.B. Djurišić, Y.H. Leung, Optical properties of ZnO nanostructures, Small. 2 (2006) 944–961, https://doi.org/10.1002/smll.200600134.
[86] C.H. Chia, J.N. Chen, T.C. Han, J.W. Chiou, Y.C. Lin, W.L. Hsu, W.C. Chou, Size dependence of exciton-phonon coupling in sol-gel ZnMgO powders, J. Appl. Phys. 109 (2011) 063526, https://doi.org/10.1063/1.3563574.
[87] M. Xiao, M.D. Shawkey, A. Dhinojwala, Bioinspired melanin-based optically active materials, Adv. Opt. Mater. 8 (2020) 1–15, https://doi.org/10.1002/adom.202000932.
[88] F. Rahman, Zinc oxide light-emitting diodes: a review, Opt. Eng. 58 (2019) 1, https://doi.org/10.1117/1.oe.58.1.010901.
[89] T.J. Bruno, P.D.N. Svoronos, CRC Handbook of Fundamental Spectroscopic Correlation Charts (2005), https://doi.org/10.1201/9780849332500.
[90] F. Fabbri, M. Villani, A. Catellani, A. Calzolari, G. Cicero, D. Calestani, G. Calestani, A. Zappettini, B. Dierre, T. Sekiguchi, G. Salviati, Zn vacancy induced green luminescence on non-polar surfaces in ZnO nanostructures, Sci. Rep. 4 (2014) 5158, https://doi.org/10.1038/srep05158.
[91] N.H. Alvi, K. ul Hasan, O. Nur, M. Willander, The origin of the red emission in n-zno nanotubes/p-gan white light emitting diodes, Nanoscale Res. Lett. 6 (2011) 130, https://doi.org/10.1186/1556-276X-6-130.
[92] A. Janotti, C.G. Van De Walle, Native point defects in ZnO, Phys. Rev. B - Condens. Matter Mater. Phys. 76 (2007) 165202, https://doi.org/10.1103/PhysRevB.76.165202.
[93] R. Raji, K.G. Gopchandran, ZnO nanostructures with tunable visible luminescence: effects of kinetics of chemical reduction and annealing, J. Sci. Adv. Mater. Dev. 2 (2017) 51–58, https://doi.org/10.1016/j.jsamd.2017.02.002.
[94] Ü. Özgür, Y.I. Alivov, C. Liu, A. Teke, M.A. Reshchikov, S. Doğan, V. Avrutin, S. J. Cho, H. Morko, A comprehensive review of ZnO materials and devices, J. Appl. Phys. 98 (2005) 1–103, https://doi.org/10.1063/1.1992666.
[95] S.A. Studenikin, N. Golego, M. Cocivera, Fabrication of green and orange photoluminescent, undoped ZnO films using spray pyrolysis, J. Appl. Phys. 84 (1998) 2287–2294, https://doi.org/10.1063/1.368295.
[96] X. Wang, A. Kafizas, X. Li, S.J.A. Moniz, P.J.T. Reardon, J. Tang, I.P. Parkin, J. R. Durrant, Transient absorption spectroscopy of anatase and rutile: The impact of morphology and phase on photocatalytic activity, J. Phys. Chem. c. 119 (2015) 10439–10447, https://doi.org/10.1021/acs.jpcc.5b01858.
[97] Y. Tamaki, A. Furube, R. Katoh, M. Murai, K. Hara, H. Arakawa, M. Tachiya, Trapping dynamics of electrons and holes in a nanocrystalline TiO2 film revealed by femtosecond visible/near-infrared transient absorption spectroscopy, Comptes Rend. Chim. 9 (2006) 268–274, https://doi.org/10.1016/j.crci.2005.05.018.
[98] A. Furube, T. Asahi, H. Masuhara, H. Yamashita, M. Anpo, Charge carrier dynamics of standard TiO2 catalysts revealed by femtosecond diffuse reflectance spectroscopy, J. Phys. Chem. b. 103 (1999) 3120–3127, https://doi.org/10.1021/jp984162h.
[99] X. Yang, N. Tamai, How fast is interfacial hole transfer? In situ monitoring of carrier dynamics in anatase TiO2 nanoparticles by femtosecond laser spectroscopy, Phys. Chem. Chem. Phys. 3 (2001) 3393–3398, https://doi.org/10.1039/b101721g.
[100] G. Mattioli, P. Alippi, F. Filippone, R. Caminiti, A. Amore Bonapasta, Deep versus shallow behavior of intrinsic defects in rutile and anatase TiO2 polymorphs, J. Phys. Chem. c. 114 (2010) 21694–21704, https://doi.org/10.1021/jp1041316.
[101] G. Mattioli, F. Filippone, P. Alippi, A. Amore Bonapasta, Ab initio study of the electronic states induced by oxygen vacancies in rutile and anatase TiO2, Phys. Rev. B - Condens. Matter Mater. Phys. 78 (2008) 241201, https://doi.org/10.1103/PhysRevB.78.241201.
[102] W.J. Yin, B. Wen, C. Zhou, A. Selloni, L.M. Liu, Excess electrons in reduced rutile and anatase TiO2, Surf. Sci. Rep. 73 (2018) 58–82, https://doi.org/10.1016/j.surfrep.2018.02.003.
[103] C. Koral, M. Fantauzzi, C. Imparato, G.P. Papari, B. Silvestri, A. Aronne, A. Andreone, A. Rossi, Defects in the amorphous−crystalline evolution of gel-derived TiO2, J. Phys. Chem. c. 124 (2020) 23773–23783, https://doi.org/10.1021/acs.jpcc.0c07568.
[104] T. Berger, O. Diwald, E. Knözinger, M. Sterrer, J.T. Yates, UV induced local heating effects in TiO2 nanocrystals, Phys. Chem. Chem. Phys. 8 (2006) 1822–1826, https://doi.org/10.1039/b517107e.
[105] X. Wang, Z. Feng, J. Shi, G. Jia, S. Shen, J. Zhou, C. Li, Trap states and carrier dynamics of TiO2 studied by photoluminescence spectroscopy under weak excitation condition, Phys. Chem. Chem. Phys. 12 (2010) 7083–7090, https://doi.org/10.1039/b925277k.
[106] K.E. Knowles, M.D. Koch, J.L. Shelton, Three applications of ultrafast transient absorption spectroscopy of semiconductor thin films: spectroelectrochemistry, microscopy, and identification of thermal contributions, J. Mater. Chem. c. 6 (2018) 11853–11867, https://doi.org/10.1039/c8tc02977f.
[107] W. Xu, W. Yang, H. Guo, L. Ge, J. Tu, C. Zhen, Constructing a TiO2/PDA core/shell nanorod array electrode as a highly sensitive and stable photoelectrochemical glucose biosensor, RSC Adv. 10 (2020) 10017–10022, https://doi.org/10.1039/c9ra10445c.
[108] K. Mistewicz, Pyroelectric nanogenerator based on an SbSI–TiO2 nanocomposite, Sensors. 22 (2022) 69, https://doi.org/10.3390/s22010069.
[109] Z. Wang, R. Yu, X. Wang, W. Wu, Z.L. Wang, Ultrafast response p-Si/n-ZnO heterojunction ultraviolet detector based on pyro-phototronic effect, Adv. Mater. 28 (2016) 6880–6886, https://doi.org/10.1002/adma.201600884.

[110] Z. Wang, R. Yu, C. Pan, Z. Li, J. Yang, F. Yi, Z.L. Wang, Light-induced pyroelectric effect as an effective approach for ultrafast ultraviolet nanosensing, Nat. Commun. 6 (2015) 8401, https://doi.org/10.1038/ncomms9401.
[111] K. Zhao, B. Ouyang, Y. Yang, Enhancing photocurrent of radially polarized ferroelectric BaTiO3 materials by ferro-pyro-phototronic effect, Iscience. 3 (2018) 208–216, https://doi.org/10.1016/j.isci.2018.04.016.
[112] J.M. Atkin, D. Song, T.M. Shaw, E. Cartier, R.B. Laibowitz, T.F. Heinz, Photocurrent spectroscopy of low- k dielectric materials: Barrier heights and trap densities, J. Appl. Phys. 103 (2008) 094104, https://doi.org/10.1063/1.2907958.
[113] H.H. Pham, L.W. Wang, Oxygen vacancy and hole conduction in amorphous TiO2, Phys. Chem. Chem. Phys. 17 (2015) 541–550, https://doi.org/10.1039/c4cp04209c.
[114] M.J. Zhao, Z.T. Sun, Z.X. Zhang, X.P. Geng, W.Y. Wu, S.Y. Lien, W.Z. Zhu, Suppression of oxygen vacancy defects in sALD-ZnO films annealed in different conditions, Materials (basel). 13 (2020) 3910, https://doi.org/10.3390/ma13183910.
[115] N. Ahmad, X. Zhang, S. Yang, D. Zhang, J. Wang, S.U. Zafar, Y. Li, Y. Zhang, S. Hussain, Z. Cheng, A. Kumaresan, H. Zhou, Polydopamine/ZnO electron transport layers enhance charge extraction in inverted non-fullerene organic solar cells, J. Mater. Chem. c. 7 (2019) 10795–10801, https://doi.org/10.1039/c9tc02781e.
[116] Z. Wang, F. Tang, H. Fan, L. Wang, Z. Jin, Polydopamine generates hydroxyl free radicals under ultraviolet-light illumination, Langmuir. 33 (2017) 5938–5946, https://doi.org/10.1021/acs.langmuir.7b01065.
[117] C.S. Tan, Y. Zhao, R.H. Guo, W.T. Chuang, L.J. Chen, M.H. Huang, Facet-dependent surface trap states and carrier lifetimes of silicon, Nano Lett. 20 (2020) 1952–1958, https://doi.org/10.1021/acs.nanolett.9b05237.

Thesis IV - The novel approach of ex-situ transferring of the a/w-PDA films onto the semiconductor surfaces enables the formation of advanced architectures, e.g. large-scale multilayer laminar nanostructures.

Thesis IV is addressed in the Publication 6

Publication 6

The Author's individual contribution to this publication includes: Investigation, Visualization, Methodology, Conceptualization, Validation, Data curation and Writing - Original Draft, Funding Acquisition, Project Management and Manuscript Submission. Author is the Principal Investigator of the PRELUDIUM20 grant 2021/41/N/ST5/00211 which was the main funding source for this publication.

Journal: ACS Applied Materials & Interfaces
ISSN: 1944-8244
Publisher: American Chemical Society
Journal Impact Factor: 9.5
Publication Date: 13.02.2024
Number of Citations: 0

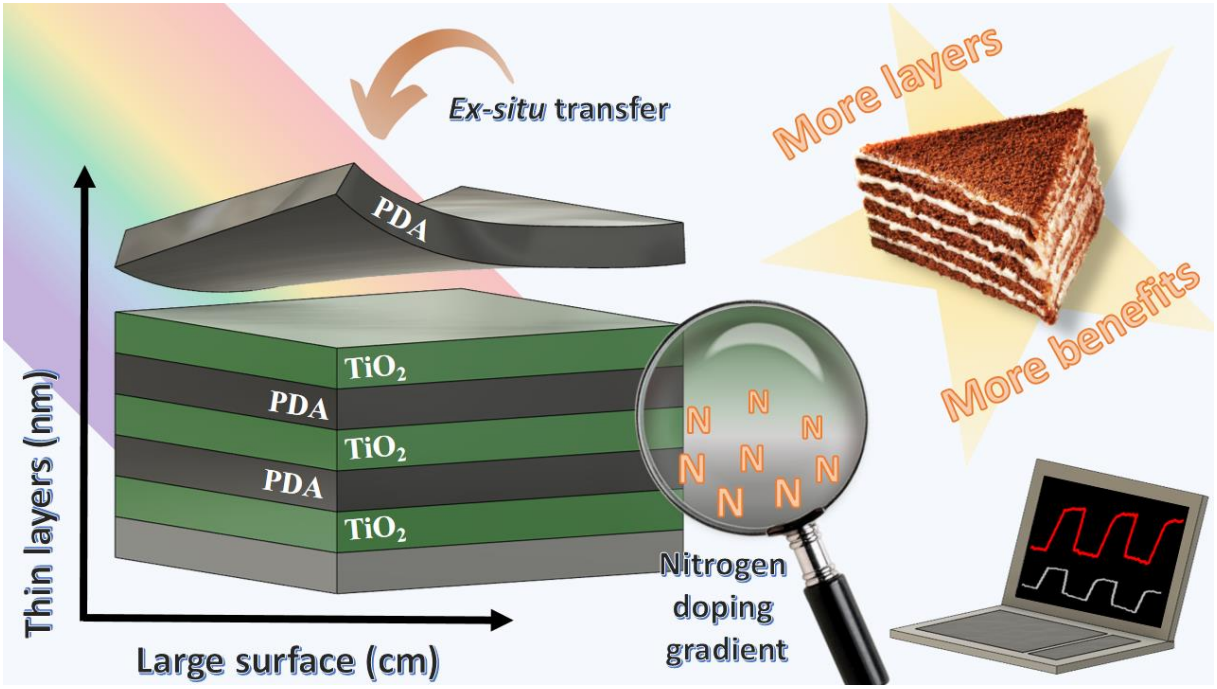

Figure 14. Graphical abstract of the P6

ACS APPLIED MATERIALS & INTERFACES

www.acsami.org

Research Article

TiO_2/PDA Multilayer Nanocomposites with Exceptionally Sharp Large-Scale Interfaces and Nitrogen Doping Gradient

Jakub Szewczyk,* Igor Iatsunskyi, Paweł Piotr Michałowski, Karol Załęski, Cassandre Lamboux, Syreina Sayegh, Elissa Makhoul, Andreu Cabot, Xingqi Chang, Mikhael Bechelany, and Emerson Coy*

Cite This: ACS Appl. Mater. Interfaces 2024, 16, 10774−10784

Read Online

ACCESS | Metrics & More | Article Recommendations | Supporting Information

ABSTRACT: The evolving field of photocatalysis requires the development of new functional materials, particularly those suitable for large-scale commercial systems. One particularly promising approach is the creation of hybrid organic/inorganic materials. Despite being extensively studied, materials such as polydopamine (PDA) and titanium oxide continue to show significant promise for use in such applications. Nitrogen-doped titanium oxide and free-standing PDA films obtained at the air/water interface are particularly interesting. This study introduces a straightforward and reproducible approach for synthesizing a novel class of large-scale multilayer nanocomposites. The method involves the alternate layering of high-quality materials at the air/water interface combined with precise atomic layer deposition techniques, resulting in a gradient nitrogen doping of titanium oxide layers with exceptionally sharp oxide/polymer interfaces. The analysis confirmed the presence of nitrogen in the interstitial and substitutional sites of the TiO_2 lattice while maintaining the 2D-like structure of the PDA films. These chemical and structural characteristics translate into a reduction of the band gap by over 0.63 eV and an increase in the photogenerated current by over 60% compared with pure amorphous TiO_2. Furthermore, the nanocomposites demonstrate excellent stability during the 1 h continuous photocurrent generation test.

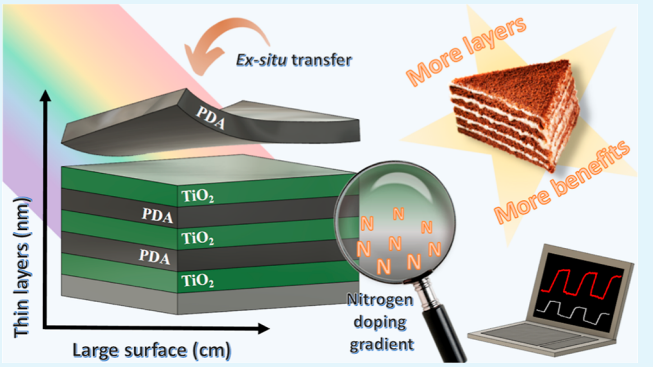

KEYWORDS: *atomic layer deposition, free-standing films, photocatalysis, bandgap, heterojunction*

1. INTRODUCTION

Heterogeneous photocatalysis shows great potential in many fields of large interest, such as water remediation,[1] air purification,[2] and renewable energy conversion and storage, e.g., water splitting and solar fuel production.[3] However, for heterogeneous photocatalysis to become widespread, cost-effective methods of production of high-performance photocatalytic materials at a commercial scale need to be developed.[4] One particularly promising class of materials is hybrid organic/inorganic composites. In particular, oxide/polymer composites combine the advantages of both inorganic materials offering proper optoelectronic properties and polymers offering ample parameter tunability, flexibility, and stretchability.[5] An additional advantage of polymers is that they can often be obtained from natural resources, i.e., biomass, or using environmentally friendly reagents. One of the most exciting polymers considered in the context of hybrid materials for photocatalysis is polydopamine (PDA), which was discovered from the inspiration of sea shells.[6] PDA has catechol and amine functional groups, which enables it to adhere strongly to virtually any surface, and at the same time exhibits the properties of an organic semiconductor, which makes it a powerful surface modification material in band structure engineering and electron transfer processes.[7] PDA has also an outstanding ability to generate photocatalytic heterojunctions with plasmonic,[8] transition metal oxide,[9,10] and sulfide[11,12] nanoparticles. PDA might seem to be a supreme candidate for obtaining large-scale layered nanocomposites serving both as an adhesive interlayer[13] and heterojunction-promoting functional coating.

We have previously shown that PDA free-standing films produced at the air/water interface (a/w-PDA) are characterized by a 2D-like laminar structure,[14] which can be obtained on a large scale (up to several cm) while maintaining homogeneity and continuity,[15] and are easily transferable to any desired substrate due to their extraordinary mechanical properties.[16] Ex situ transferred PDA is a thin layer of PDA that is free-standing on the water surface and can be transferred to another desired surface. Such nanometrically

Received: December 19, 2023
Revised: February 2, 2024
Accepted: February 5, 2024
Published: February 13, 2024

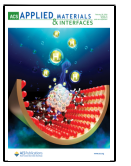

thin a/w-PDA films transferred ex situ to the surfaces of semiconductors (ZnO and TiO_2) can create efficient and stable heterojunctions useful in photocatalytic reactions.[17]

On the other hand, TiO_2 is a promising photocatalyst that constitutes the basis for the construction of novel hybrid nanomaterials with high application potential,[18−20] but simultaneously it suffers from poor efficiency due to a relatively large bandgap and fast charge recombination rate. TiO_2 nitrogen doping is one useful modification to increase the efficiency of this inorganic semiconductor by reducing the bandgap, broadening the light response, and increasing the number of photogenerated carriers.[21,22] However, there are still challenges associated with the formation and utilization of N-TiO_2. First, the exact mechanism of band gap reduction by N doping of TiO_2 is still unclear and needs further research. Also, control of the N doping concentration is essential and achieving successful optimization within various process conditions and nitrogen sources is challenging. Finally, the stability of N-TiO_2 is still questionable; therefore, it is desirable to protect the N-TiO_2 films against decomposition, e.g., passivation with a tight protection layer.[23] The production method of N-TiO_2 with superior photocatalytic activities utilizing simple facile techniques through the green routes is an emerging research topic.[24]

Atomic layer deposition (ALD) is one of the most commonly used titanium oxide (TiO_2) deposition methods due to several advantages, such as precise thickness and composition control of the obtained conformal oxide layers—particularly important aspects in the production of advanced hybrid nanoarchitectures.[25] Using mild temperatures (below 200 °C), an amorphous, high-quality thin TiO_2 film can be obtained. Additionally, it can be deposited on virtually any selected substrate, e.g., polymer, as in this experiment—on PDA. In turn, during the thermal annealing of PDA, the reported product is nitrogen-doped graphene rather than graphite or graphene.[26,27] This is because PDA, as a polymer with rich pyrrolic-N groups, serves as a nitrogen source. Profoundly, the positive correlation between the content of graphitic nitrogen, enhanced conductivity, facilitated electron transfer, and improved specific capacity was found.[27,28] Whether PDA subjected to mild temperature treatment can be an efficient nitrogen source is unknown. However, previous reports on ALD processes on polymer substrates show that precursors can penetrate and react with them.[29,30] Importantly, it was shown that the degree of this reaction can be increased by extending the precursor exposure cycle time in the ALD sequence.[29] Predictions should be made that the growth of the layer with each ALD cycle will decrease the exposure of the polymer substrate, consequently leading to gradient-like phase formation.

Bearing in mind PDA's ability to create a functional heterojunction on the surface of the inorganic semiconductor, we decided to arrange several layers alternately, thanks to which the number of interfaces obtained could be multiplied, thus the effect of heterojunction. The semiconductor chosen for modification was TiO_2 due to several key features of the TiO_2 nanofilms—a flat surface, excellent adhesion to diverse substrates' surfaces, very well described band structure, and nontoxic behavior.[31] However, another aspect was the most important, i.e., the possibility of obtaining a completely new type of heterogeneous organic/inorganic nanocomposite. We hypothesized that the ALD of TiO_2 on the PDA layer may lead to the formation of a gradient interface, i.e., PDA/N-TiO_2/TiO_2. Additionally, PDA should act as a protective layer for unstable N-TiO_2, and multiplying the number of layers will create a larger number of functional interfaces between the polymer and doped titanium oxide. Considering that amorphous TiO_2 contains more defects and disorder than crystalline TiO_2, it is predicted to be more likely to accept nitrogen.[32] Therefore, we used a low process temperature (200 °C) and an extended ALD cycle time. Ultimately, the conductive properties of PDA have not yet been well described, and it is not known whether it would ensure good electrical contact with the substrate.[33] Therefore, the first layer of the multilayer composite should be TiO_2, while the outermost layer should be PDA, which will increase the stability of the entire multilayer structure. In this way, we have developed a simple and reproducible path for obtaining a new type of multilayer composite, which we obtained on a large scale. Moreover, we present strong evidence for gradient-like nitrogen doping of TiO_2 layers, which opens up many possibilities for constructing intelligent organic/inorganic interfaces.

2. MATERIALS AND METHODS

2.1. Chemical Reagents. Materials in all synthesis procedures were used without any further purifications. Dopamine hydrochloride (CAS: 62-31-7, *s*, >98%), Trizma base (CAS: 77-86-1, *s*, >99%), hydrochloric acid (CAS: 7647-01-0, l, 25%), silicon wafer (Si 100, CAS: 7440-21-3, *s*), titanium tetrachloride (CAS: 7550-45-0), sodium sulfate (CAS: 7757-82-6, *s*), quartz (fused, thickness: 1.0 mm), and quartz/indium tin oxide (ITO) substrates (CAS: 50926-11-9) purchased from Sigma-Aldrich and ultrapure deionized water obtained from a Hydrolab Ultra UV system were used.

2.2. Synthesis of the PDA Free-Standing Films. The synthesis of PDA free-standing films was carried out in the specific conditions that we have determined in our previous work to achieve homogeneous and large-scale thin films with nanometer-scale control of the thickness and easy transfer onto the desired substrate.[15] Dopamine in the form of dopamine hydrochloride was added to a Petri dish (8 cm in diameter and 2 cm in height) containing tris buffer solution (10 mM, 45 mL) to obtain a dopamine concentration equal to 0.5 mg mL^{-1}. Stirring (300 rpm) took place on a magnetic plate throughout the synthesis time, and a glass lid covered the vessel with a small gap to allow oxygen flow and, thus, air exchange.

2.3. TiO_2 Film Deposition. TiO_2 layers were deposited by the ALD, which is described in detail elsewhere.[34−36] Briefly, process conditions were as follows: temperature: 200 °C, purge gas: Argon, TiO_2 precursors: H_2O and $TiCl_4$, number of cycles: 400, and process time: ∼12 h. The relatively long ALD time was related to longer breaks between cycles for the individual precursors. The aim was to keep the samples at a higher temperature and vacuum for longer so that the nitrogen diffusion process at the PDA/TiO_2 interface could occur. To see the thickness profile of all the obtained layers, see the Results and Discussion section. Substrates were prepared to enable different characterization methods, such as bare silicon (100) wafers for the chemical and structural characterization, quartz glass for the UV−vis transmission spectroscopy, and quartz glass covered by ITO for the photo-electrochemical tests. All substrates had dimensions of no smaller than 1 × 1 cm.

2.4. Physicochemical Characterization. Raman Spectroscopy was performed using a Renishaw instrument equipped with microscope enclosure RE04, 633 nm laser source, and Leica objective lens ×50. The number of accumulations was 3. Exposure time was set to 0.1 s with 0.1% of the power of the laser source. X-ray diffraction (XRD) characterization was executed with the use of an MRD-X'pert[3] diffractometer (PANalytical), operating at 45 kV and 40 mA with a Cu Kα radiation source (wavelength of 1.54 Å). The lamellae for high-resolution transmission electron microscopy (HRTEM) investigations were prepared by focused ion beam (FIB) JEOL, JIB-4000.

https://doi.org/10.1021/acsami.3c18935
ACS Appl. Mater. Interfaces 2024, 16, 10774−10784

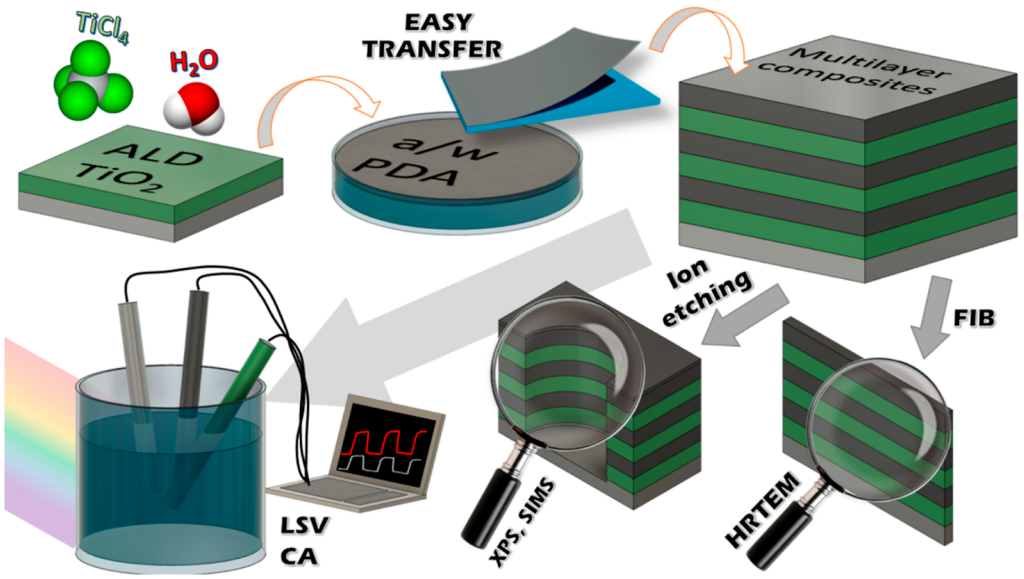

Figure 1. Scheme of the workflow—synthesis of the multilayer composites through ALD of the TiO_2 layers and transfer of the PDA film from the air/water interface alternately until three-layer composites are obtained. Then structural, chemical, and electrochemical tests were carried on.

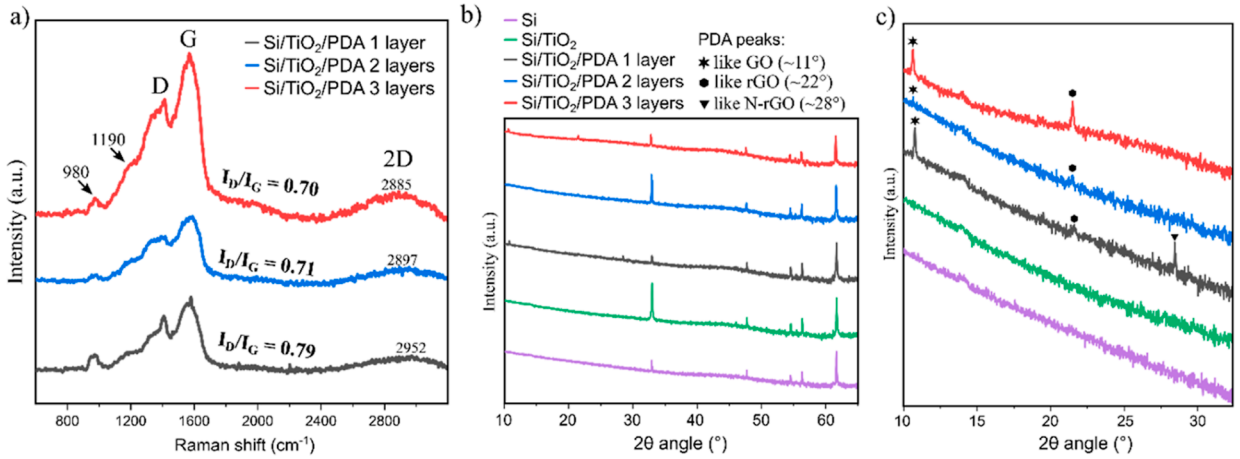

Figure 2. Raman spectra of the multilayer TiO_2/PDA nanocomposites (a) and X-ray diffractogram of the Si substrate, Si/TiO_2, and multilayer composites in the 2θ range from 10 to 65° (b) and 10 to 35° (c).

The procedure is described in detail elsewhere.[37] HRTEM was performed with a JEOL ARM 200F (200 kV). Secondary ion mass spectrometry (SIMS) measurements were performed with the CAMECA IMS SC Ultra instrument. To ensure sub-nanometer depth resolution, cesium with ultralow impact energy (100 eV) was used as primary ions, and the polarity of the detector was negative.[38] X-ray photoelectron spectroscopy (XPS) was performed using KRATOS/AXIS Ultra DLD, X-ray source: Al Kα, 1486.6 eV; fwhm resolution 0.45 eV; acquisition time 0.1 s. Stationary transmission UV—vis spectroscopy was applied to investigate the bandgap, using deuterium—halogen light source AvaLight-DHc (Avantes), AvaSpec-Mini2048CL spectrometer (Avantes) and an optical fiber capable of operating in the broad UV—vis spectrum (220—800 nm). Obtained spectra of TiO_2 (an indirect band gap semiconductor) were transformed[39] and plotted against the photon energy. To obtain the optical constants of PDA and TiO_2 films, spectroscopic ellipsometry analysis was performed using the SENTECH GmbH SER800 ellipsometer at incidence angles of θ = 60, 65, and 70°. This analysis covered the spectral range from 400 to 1000 nm with a scanning interval of 1 nm. In order to extract the refractive index and extinction coefficients of the layers, we employed the Bruggeman effective medium approximation. The TiO_2 layers in the nanolaminates were described by using the Tauc—Lorentz dispersion function, while the PDA layers were characterized by using an advanced combination layer dispersion, consisting of Tauc—Lorentz and Brendel oscillator dispersions. During the regression analysis, the optical constants of the nanolaminates were determined, with the initial thicknesses of the layers being fixed.

2.5. Photo-electrochemical Experiments. Photo-electrochemical studies were carried out using a Gamry Reference 620 potentiostat in a three-electrode system where the investigated sample was a working electrode, Pt-mesh was a counter electrode, and Ag/AgCl/0.1 M KCl was a reference electrode in 0.5 M Na_2SO_4 electrolyte solution. Linear sweep voltammetry (LSV) experiments were carried out in a potential range from 0.5 to +1 V where the linear increase of potential was equal to 10 mV/s, and the light/dark cycle length was 1 s. Chronoamperometry (CA) experiments were developed by switching potential in a step-manner from 0 to 1 V and later keeping the system at a target voltage of 1 V for stabilization during 100 and 3600 s. Open circuit photopotential (OCP) and photocurrent (OCC) measurements were executed in the following manner: 20 s dark, 40 s illumination (excitation), and 60 s dark (decay). During all photo-electrochemical experiments, the light source was a 300 W Xe arc lamp of ScienceTech's Tunable Light Source, and the used irradiation was characterized by 100 mW cm^{-2} power density and spectral range of 300—1800 nm. Additionally, a

https://doi.org/10.1021/acsami.3c18935
ACS Appl. Mater. Interfaces 2024, 16, 10774—10784

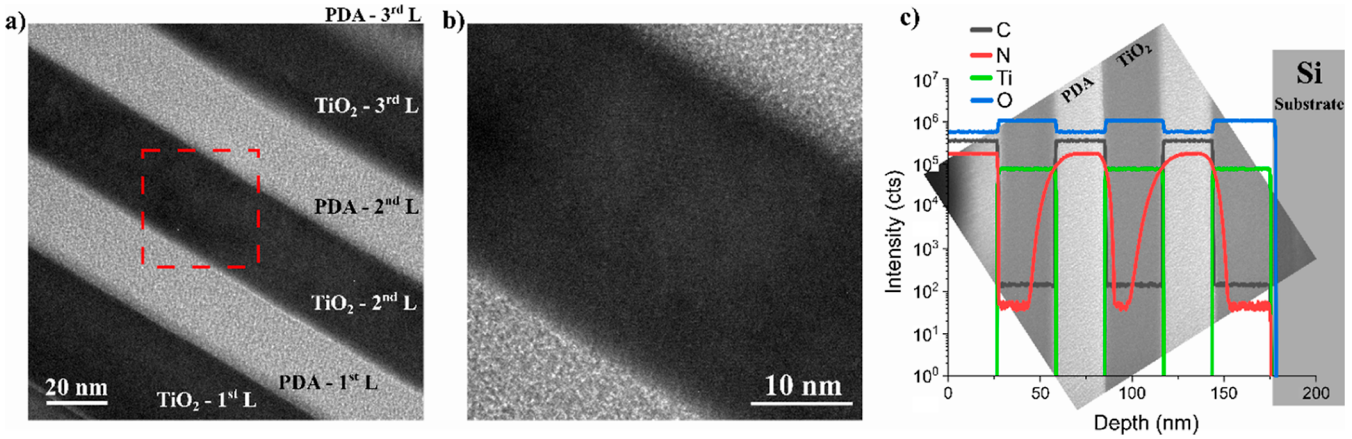

Figure 3. HRTEM image of the cross-section of the TiO_2/PDA three-layer nanocomposite (a), close-up of the interface regions (b), and SIMS depth profile of the TiO_2/PDA three-layer nanocomposite together with the HRTEM image of the cross-section in the background for better illustration of the multilayer structure (c).

filter was set—a quartz cuvette filled with distilled water to cut the infrared radiation.

3. RESULTS AND DISCUSSION

Our first goal was to obtain multilayer nanocomposites. Another goal was to generate a variable (gradient) nitrogen content in the TiO_2 layers deposited on the PDA surfaces. To the best of our knowledge, such a method of doping TiO_2 with nitrogen has not yet been described. Therefore, we conducted a series of experiments to investigate this phenomenon. First, Raman spectroscopy and XRD provided valuable information on the structural arrangement of PDA films obtained at the air/water interface and transferred ex situ to semiconductor surfaces. Then, cross sections (lamellas) of the samples were cut using the FIB. HRTEM showed the quality of the obtained interfaces and the thickness of individual layers. SIMS provided information on the element content in individual layers, allowing us to determine the gradient nature of doping and the layer interfaces. XPS was performed in the depth profiling mode, meaning that the etching of the sample surface preceded the spectrum's collection to reach deeper layers. In this way, we thoroughly examined the chemical nature of the interface between PDA and nitrogen-doped TiO_2 layers. Optical tests using UV−vis spectroscopy and ellipsometry showed a reduction in the band gap with each subsequent layer and a change in the optical properties of TiO_2 due to nitrogen doping. Finally, LSC and CA showed multilayer composites' more significant application potential than TiO_2 and single-layer composites. Schematically, the course of the experiment is presented in Figure 1.

Starting from Raman spectroscopy (Figure 2a), the band around 1190 cm^{-1} indicates an important PDA structural unit; it is NH in-plane deformation mode originating from the pyrrole rings.[16] As we presented earlier,[14,15] the occurrence of 2D, D, and G bands is typical for this type of PDA films transferred ex situ from the air/water interface. Interestingly, the increasing number of layers showed no significant shift of the D and G peaks. Their centers are around 1380 cm^{-1} (D) and 1570 cm^{-1} (G). In turn, the I_D/I_G intensity ratio, widely used to evaluate the defect density in graphene or graphite-like carbon-based materials,[40] varies. The comparison demonstrates the decreasing defect density with increasing number of layers. It has previously been described that high temperature[40] or laser annealing[41,42] of the PDA may reduce defect density. However, this result was unexpected since the low temperature used in the ALD process (for deposition of TiO_2 layers) should not lead to PDA graphitization. Notwithstanding, a dehydration reaction occurring normally in this temperature range in the PDA layer would reduce the concentration of hydroxyl groups present at the PDA surface,[43] thus converting the more GO-like structure into a more rGO-like one. Moreover, the 2D peak is shifting toward lower wavenumbers with increasing layers, further suggesting transformation into rGO-like structure.[44]

The XRD patterns are dominated by peaks originating from the Si wafer used as the substrate. In turn, the lack of clear peaks that could be assigned to crystalline TiO_2 confirms the amorphous nature of these layers (Figure 2b). Therefore, a close-up of the 2θ angle section from 10 to 30° was made and shown in Figure 2c to study a region of peaks typical for materials such as GO and rGO. The one-, two- and three-layer composites show GO-like and rGO-like peaks, but the latter is most significant in the case of the three-layer composite, which confirms the previous observations based on Raman spectroscopy. However, attention should be paid to the lack of a peak typical for N-rGO,[45,46] i.e., nitrogen-doped reduced graphene oxide, in the case of two- and three-layer composites. Once again, the relatively low temperature and generally mild conditions of the TiO_2 ALD process should not lead to the decomposition of the N-rGO.[47] Instead, we postulate that a new N-TiO_2 species may be formed at the PDA/TiO_2 interface, as further results show.

A HRTEM image of the three-layer composite cross-section is shown in Figure 3a, and a close-up is shown in Figure 3b. Unfortunately, the top layer of the PDA was significantly damaged during the FIB cutting process (see the Materials and Methods section); therefore, it is not presented in the image. However, six extremely sharp and perfectly defined layers (Si/TiO_2/PDA/TiO_2/PDA/TiO_2) can be seen; their thickness is approximately 25 nm (PDA) and 40 nm (TiO_2). The structure of the obtained laminar composite consists of alternately arranged thin, large-surface layers separated by clear sharp boundaries with no irregularities. It would be impossible to obtain such structures using the in situ PDA deposition method because the layers deposited in this way are amorphous and morphologically irregular.

https://doi.org/10.1021/acsami.3c18935
ACS Appl. Mater. Interfaces 2024, 16, 10774−10784

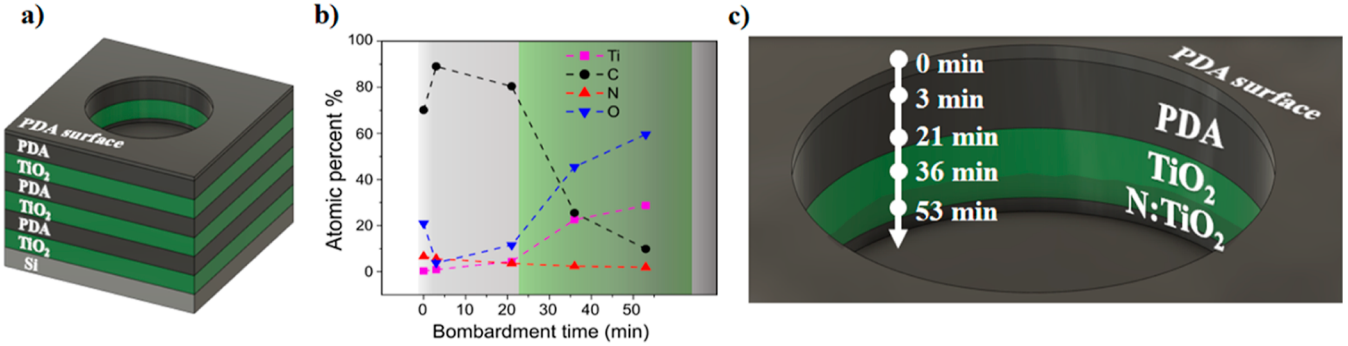

Figure 4. Scheme of the TiO_2/PDA three-layer nanocomposite structure and etching depth (a), XPS in-depth profile of the atomic percentage in the two top layers (b), and visualization of the etching depth (c).

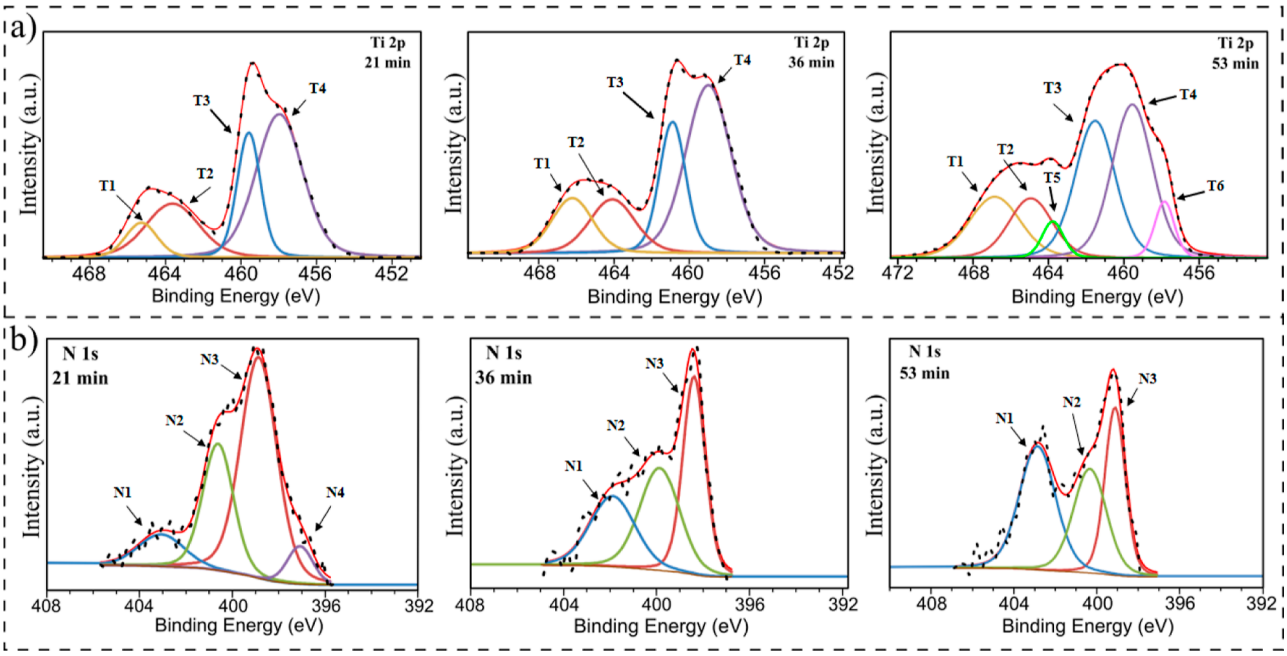

Figure 5. XPS high-resolution spectra of the Ti 2p (a) and N 1s (b) regions for etching times 21, 36, and 53 min.

Figure 3c shows the obtained SIMS depth profile of the three-layer composite sample, superimposed on the HRTEM image to better visualize the element content in individual layers. For clarity and better visualization, the depth profile starts from the top PDA layer, i.e., the one deposited last on the composite surface. Going deeper, we reach subsequent layers. The second and third TiO_2 layers (in the order in which they were obtained) were deposited on the PDA surface. The titanium spectrum can be used as a benchmark to precisely determine the interfaces between PDA and TiO_2. It is also visible that the TiO_2 layer has a higher oxygen signal intensity than PDA, further confirming sharp boundaries. The carbon signal in the TiO_2 layers is very low and is related to the presence of residual contamination, but its concentration was estimated to be in the part-per-million range. In the case of mixing of phases or carbon doping, we would note a gradient of its content in the TiO_2 layer, which we do not observe. On the other hand, a clear gradient of nitrogen content can be seen in the TiO_2 layer's growth on the PDA surfaces, starting from high content at the interface, decreasing gradually deep into the TiO_2 layer, until rapidly increasing close to the next interface with PDA deposited onto the TiO_2 surface. We postulate nitrogen migration from PDA during the TiO_2 growth process using the ALD method, where PDA acts as a polymeric nitrogen source. As a reminder, the conditions of the ALD process were as follows: temperature 200 °C, time about 12 h, and the atmosphere was a vacuum alternating with argon (for a more detailed description, see the Materials and Methods section). In the later paragraphs, we show further evidence of TiO_2 N doping via ALD with polymer nitrogen sourcing.

We used the XPS in-depth profile mode for two purposes. First, we examine the elemental content in the two top layers of the three layer sample. This helped us determine the speed of the Ar^+ ion etching process and the location where each measurement was made (Figure 4). Figure 4a schematically shows the multilayer composite with etching depth, which will be helpful when discussing the XPS spectroscopy results.

Five spectra were analyzed, for which the etching time was 0, 3, 21, 36, and 53 min. Figure 4b shows the atomic elemental content of each spot reached after a given etching time. It was possible to deduce the penetration depth using this information and the previously described results (HRTEM and SIMS). Therefore, for an etching time of 0 min, the analyzed spot is on the surfaces of the top PDA layer; for 3 min, the bulk PDA layer; for 21 min, the PDA/TiO_2 interface;

https://doi.org/10.1021/acsami.3c18935
ACS Appl. Mater. Interfaces 2024, 16, 10774−10784

for 36 min, bulk TiO_2 (low N content); and finally, for 53 min, bulk N-TiO_2 with high nitrogen content. It is schematically shown in Figure 4c.

Then, with this knowledge, we analyzed the high-resolution spectra of the key regions (Figure 5). However, bearing in mind the main drawbacks of the ion-etching method, it is preferential sputtering (e.g., oxygen in metal oxides), a mixture of nonuniform sputtering (e.g., cratering) and chemical reduction due to sputtering,[48] we mainly focus on the analysis of Ti 2p (Figure 5a) and N 1s (Figure 5b) regions. Oxygen and carbon from the first PDA layer undergo many of the effects mentioned above (etching of polymers results in their chemical degradation[49]), contaminating the TiO_2 layer and affecting the measurement. However, Supporting Information includes full XPS spectra for all samples and high-resolution spectra of the O 1s and C 1s regions (Figures S1−S5). In turn, the interactions between nitrogen and titanium should be exclusively caused by forming some new species at the interface and, therefore, nitrogen migration into the TiO_2 layers. The information about peaks in the Ti 2p and N 1s regions is also summarized in Table 1 below.

Table 1. XPS Depth Profiles—Area Percentage, Binding Energies, and FWHM Values for Ti 2p and N 1s Regions for Etching Times 21, 36, and 53 min

etching time	peak	binding energy (eV)	fwhm	area %
21 min	T1	465.27	1.95	8.0
	T2	463.63	3.32	21.1
	T3	459.58	1.46	21.5
	T4	457.97	2.92	49.4
	N1	403.06	2.31	10.1
	N2	400.62	1.55	27.0
	N3	398.86	1.85	56.2
	N4	397.08	1.28	6.7
37 min	T1	466.22	2.54	14.2
	T2	464.10	2.84	15.5
	T3	460.89	1.65	22.0
	T4	458.99	2.83	48.3
	N1	401.89	2.28	27.0
	N2	399.87	2.03	34.9
	N3	398.39	1.14	38.1
53 min	T1	466.85	3.20	16.2
	T2	464.94	2.72	13.4
	T3	463.77	1.34	4.0
	T4	461.52	2.52	28.5
	T5	459.55	2.53	32.1
	T6	457.85	1.23	5.7
	N1	402.86	2.07	39.5
	N2	400.33	1.89	30.4
	N3	399.11	1.16	30.1

Starting from fitting the Ti 2p high-resolution spectra, T1 and T3 peaks were assigned to $2p_{1/2}$ and $2p_{3/2}$ energy levels of Ti^{4+}, respectively.[50−52] Next, T2 and T4 were appointed to $2p_{1/2}$ and $2p_{3/2}$ energy levels of Ti^{3+}, respectively.[50−52] The latter suggests the formation of oxygen vacancies[53] or TiN_x species.[54] However, this can be partially or exclusively the effect of the Ar ion etching process.[55] In turn, the T5 and T6 pair is originating most probably from titanium oxynitride.[56] This observation is also supported by the decrease in the overall area of Ti^{4+} peaks, which indicates Ti−O−N formation by substituting transition metal ions.[57] The N4 peak is present only for the spectra after 21 min of etching, as described earlier (Figure 4); in this region, the PDA/TiO_2 interface is present. It most likely indicates the coordination of nitrogen to titanium atoms on the TiO_2 surface.[58,59] This is particularly reasonable because PDA adheres to surfaces via catechol and amino groups containing nitrogen. The peaks N2 and N3 cannot be assigned with certainty because they overlap with peaks typical for PDA (primary and secondary amine groups),[16] which are also visible for shorter etching times (Figures S1 and S2). However, it is visible that the intensity of N1 increases with an increasing etching time. According to the literature, it should be associated with N−Ti−O formation,[60] and it is nitrogen doping via interstitial position occupation. Therefore, we showed that TiO_2 is doped through both substitutive and interstitial nitrogen atoms and that the doping is gradient in nature (as previously shown by using SIMS). It is worth emphasizing that the multiple N doping types might induce the formation of new energy levels in the forbidden band of titanium oxide, resulting in shifting the absorption edge to lower photon energies and thus reducing the band gap of TiO_2.

Therefore, the value of the band gap was examined. Figure 6a shows the Tauc plot for bare TiO_2 and one-, two- and three-layer TiO_2/PDA composites.

It is visible that with each layer the band gap value is lowered due to the phenomena described in the previous paragraph. The difference in the obtained value between subsequent samples is ∼0.15 eV, but the exception is the difference between one and two layers (0.33 eV). This is because for two layers, nitrogen doping already introduces new energy levels in the forbidden band of TiO_2, unlike in the case of a one-layer composite where the only enhancement effect is the formation of the PDA/TiO_2 interface.

To confirm these observations, we performed ellipsometric tests. The refractive index (n) describes the speed of light propagation through the material and strongly correlates with the electrical properties. Generally, the bandgap energy and refractive index values are inversely proportional for semiconductors.[61] Moreover, it was previously shown that doping of titanium oxide can increase its refractive index.[62,63] Our model calculated the refractive index for the TiO_2 layers in each nanocomposite. For the record, two- and three-layer composites are characterized by gradient nitrogen doping of the TiO_2 layer. This is visible in Figure 6b because the n value is higher within the entire investigated spectrum (from 400 to 1000 nm). This further confirms the postulated doping mechanism and the reduction of the bandgap energy. We also determined the real part of the refractive index (Figure S6a) and extinction coefficient (Figure S6b) for PDA layers. According to our knowledge, these values were determined for the first time for this type of thin PDA film from the air/water interface, which may constitute essential reference data for other experiments. The extinction coefficient has not changed significantly, but the real part of the refractive index of PDA increases with the increasing number of layers. This is related to the XRD results, which showed that PDA in three-layer composites shows structural features more similar to rGO than in the case of one-layer and two-layer composites. It was previously shown that rGO coatings have a higher n value than GO.[64]

The band gap reduction should positively affect the photochemical properties of the obtained composites, which is why we conducted LSV under chopped light illumination and CA under chopped light illumination tests (Figure 7).

https://doi.org/10.1021/acsami.3c18935
ACS Appl. Mater. Interfaces 2024, 16, 10774−10784

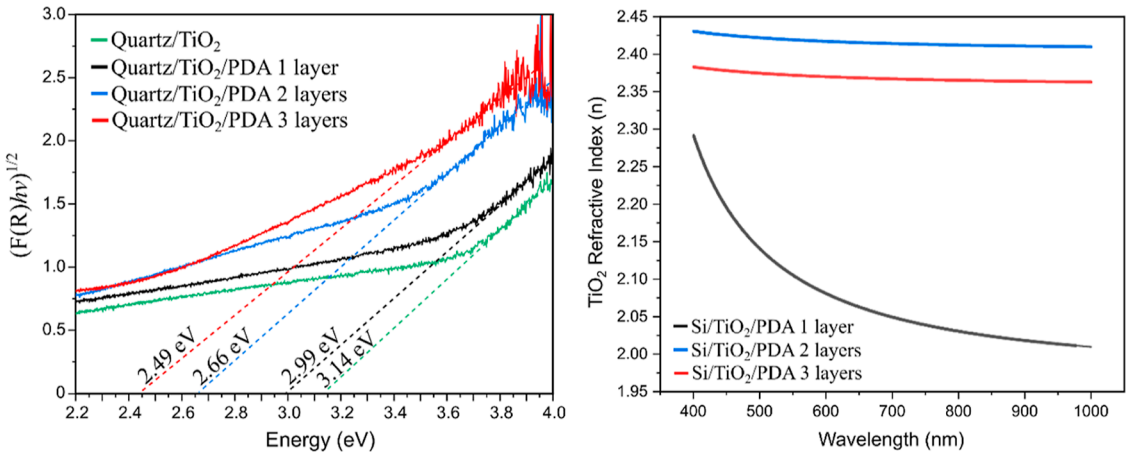

Figure 6. Tauc plot (UV−vis spectroscopy) of the quartz/TiO_2 and quartz/TiO_2/PDA multilayer composites (a) and the real part of the refractive index (n) vs wavelength graph of the TiO_2 layers in Si/TiO_2/PDA multilayer composites (b).

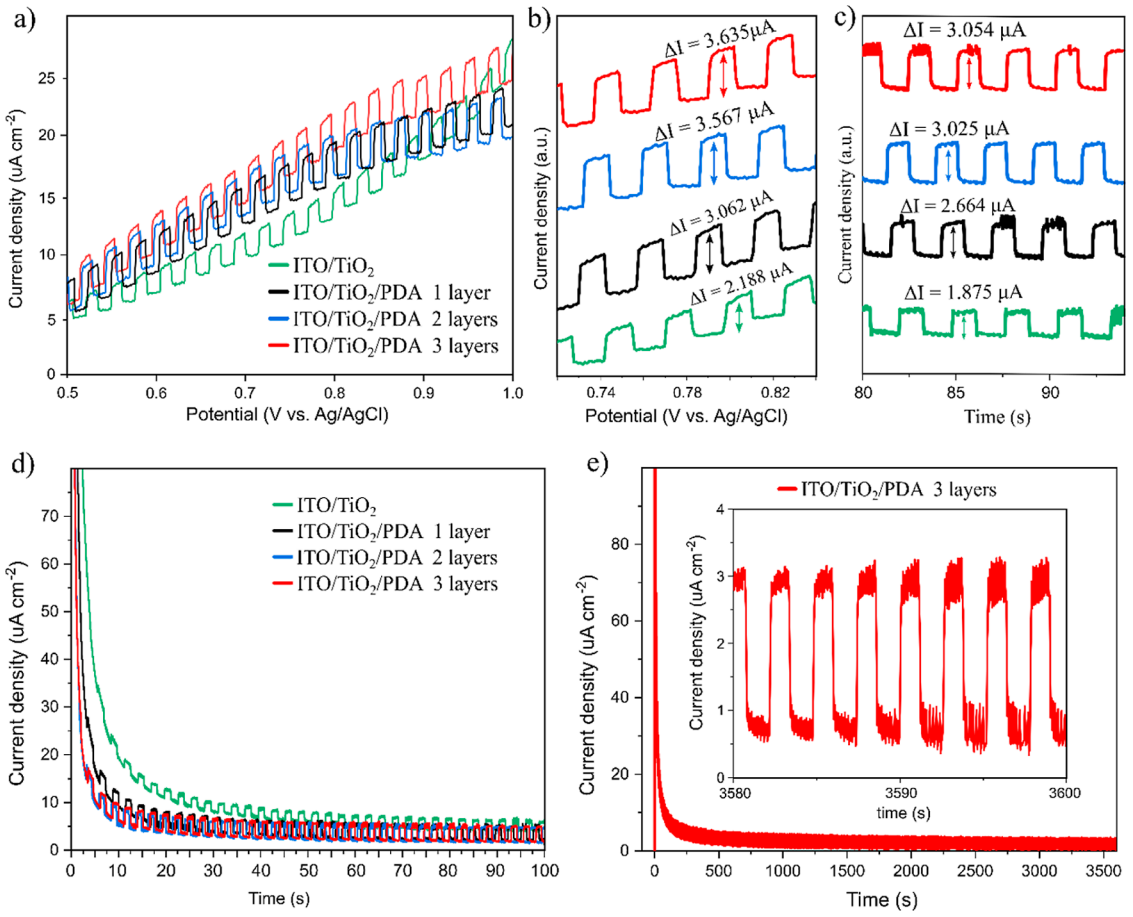

Figure 7. LSV under chopped illumination (a), close-up of the ∼0.8 V region (b), close-up of the 80−100 s region of the CA under chopped illumination (c), CA equilibrium during 100 s (d), and stability during 1 h (e).

LSV was performed in the positive potential region (0.5−1 V) under chopped UV−vis light illumination (Figure 7a) to measure the photogenerated current increase. A significant change was observed, as shown in the close-up of the ∼0.8 V region (Figure 7b). The percentage increase in photogenerated current was calculated and is presented in Table 1; as observed, there is a particularly big difference between TiO_2 vs TiO_2/PDA and between TiO_2/PDA one layer vs TiO_2/PDA two layers. As we described previously, this is related to forming a functional TiO_2/PDA interface and the nitrogen doping of the TiO_2 layer. The highest photocurrent was obtained for a three-layer composite.

The same phenomena were confirmed via the CA scan (Figure 7c). After reaching the equilibrium at the constant potential set on 1 V, the photocurrent induced again by chopped light illumination was measured. Again, there was a significant increase in the photocurrent, as presented in Table 2. The results obtained with the LSV and CA methods are very

https://doi.org/10.1021/acsami.3c18935
ACS Appl. Mater. Interfaces 2024, 16, 10774−10784

Table 2. Photogenerated Currents of the Multilayer Composites and Increases in Their Value Compared to Bare TiO_2[a]

method	LSV (at ~0.8 V)			CA (at ~80 s, 1 V)		
sample	1L	2L	3L	1L	2L	3L
photocurrent (μA)	3.062	3.567	3.635	2.664	3.025	3.054
photocurrent increase vs TiO_2 (%)	39.95	63.03	66.13	42.08	61.33	62.88

[a]1L, 2L, 3L—PDA/TiO_2 one layer, two layer, and three layer composites, respectively.

similar. A more detailed discussion of the CA results is provided in the next paragraph. The LSV photocurrent does not exhibit a significant increase as the applied potential becomes more positive. This is probably due to the lack of an efficient electron transport layer in the system and provides a perspective for future research.

In CA, the current was recorded under chopped UV−vis illumination for 100 s while the sample approached an equilibrium state after increasing the potential from 0 to 1 V (Figure 7d). After the initial rapid current increase, the current density drops exponentially due to the electrical barrier at the solid/electrolyte interface. The switching time was determined as the time for a system to reach 90% of its full current density drop. Calculated times were 0.42, 0.27, 0.14, and 0.12 s for TiO_2, one layer TiO_2/PDA, two layers, and three layers, respectively. In the course of previous tests, the three-layer composite sample showed the most outstanding performance (smallest band gap, largest photocurrent, and shortest switching time). Therefore, we decided to test its stability (Figure 7e) by applying a constant potential (1 V) while maintaining chopped illumination for 1 h (3600 s). After an initial exponential decay, the current density is stabilized at values around 1 μA cm^{-2} (light off) and 3 μA cm^{-2} (light on) and remains at this level throughout the experiment, as shown in the inset graph. This indicates the excellent stability of the multilayer composites. Lastly, we investigated the OCP and OCC of the three-layer nanocomposite, to provide data for future experiments or comparative analyses. For clarity, OCP and OCC under the dark conditions have been subtracted. In Figure S7, the typical behavior of a photocatalyst can be observed, i.e., rapid step after illumination and a noticeably slower decay after turning off the light, depending on photogenerated charge carriers' lifetimes. The maximum OCP immediately after illumination was −55 mV, while the maximum OCC was 7 nA.

4. CONCLUSIONS

Overall, this study introduced an innovative approach to nitrogen doping in amorphous TiO_2 thin films and the production of polymer/oxide nanocomposites tailored for photocatalytic applications. Central to this advancement is the utilization of a unique method for creating PDA free-standing films at the air/water interface combined with ALD of the oxide layer. This technique enhances the efficacy of the nitrogen doping process and significantly improves the structural and functional qualities of the resultant polymer/oxide nanocomposites, making them more suitable for a range of uses. We obtained TiO_2 layers with gradient nitrogen doping by ALD with polymer nitrogen sourcing at low temperature (200 °C). This approach allowed us to preserve the amorphous structure of TiO_2 (which crystallizes at higher temperatures) and the 2D-like layered structure of the PDA films from the air/water interface, which undergoes carbonization at higher temperatures. We showed with XPS depth profiling that TiO_2 is doped through both substitutive and interstitial nitrogen atoms, which is remarkably important from the point of view of applications in photocatalysis because it provides new energy levels inside the forbidden band and thus lowers the semiconductor band gap, allowing for a larger range of light absorption. Additionally, there is a synergistic effect of the previously mentioned phenomenon and PDA/TiO_2 interfaces, which are well preserved in our method, as evidenced by sharp interfaces visible in the HRTEM images and SIMS profiles. The mere presence of the PDA/TiO_2 interface contributed to reducing the bandgap energy by 0.15 eV (for the one-layer sample), while obtaining multilayer composites with nitrogen-doped titanium oxide layers resulted in a further reduction of this value by another 0.33 and 0.15 eV for the second and third layers, respectively. The total reduction for the three-layer composite compared to TiO_2 was 0.63 eV.

Furthermore, we showed that our layered nanocomposites are characterized by greater photo-electrochemical activity because in both the case of LSV and CA under chopped light illumination, the photogenerated current was increased by more than 60% for two- and three-layer composites in comparison to bare TiO_2. The stability of these materials was also proven as there was no significant reduction in the photocurrent value during the 1 h CA experiment. At the same time, we perceive much room for further improvement of the photocatalytic properties of the materials we presented. We anticipate that the critical development direction is to enrich the composite with an electron transport layer and a surface catalyst (e.g., nanoparticle decoration) to increase the photo-electrochemical activity. However, the simple, cheap, and effective method we have presented for obtaining gradient nitrogen-doped TiO_2 opens new perspectives for nanomaterials based on polymer/inorganic semiconductor heterojunctions, especially those where it is required to significantly reduce the band gap without damaging the delicate interface structure.

Finally, further studies should address optimization and design aspects of the architecture here, such as the influence of layer thickness on the total N doping migration, deposition temperature, and other postannealing effects. We also anticipate that the methodology presented here could be exploited in other N-accepting photoactive oxides and ceramic materials.

■ ASSOCIATED CONTENT

Data Availability Statement

The raw/processed data required to reproduce these findings cannot be shared at this time as the data also forms part of an ongoing study. Data might be shared upon reasonable request to the corresponding author.

Supporting Information

The Supporting Information is available free of charge at https://pubs.acs.org/doi/10.1021/acsami.3c18935.

https://doi.org/10.1021/acsami.3c18935
ACS Appl. Mater. Interfaces 2024, 16, 10774−10784

XPS atomic percentage and binding energies of the elements for etching times 0, 3, 21, 36, and 53 min; XPS area percentage, fwhm, and binding energies of high-resolution regions for etching times 0, 3, 21, 36, and 53 min; XPS full spectra and high-resolution spectra for etching times 0, 3, 21, 36, and 53 min; real part of the refractive index and the extinction coefficient for the PDA; and OCP and OCC curves for the three-layer nanocomposite (PDF)

AUTHOR INFORMATION

Corresponding Authors

Jakub Szewczyk − *NanoBioMedical Centre, Adam Mickiewicz University, 61-614 Poznan, Poland; Institut Européen des Membranes, IEM, UMR 5635, Univ Montpellier, CNRS, ENSCM Place Eugène Bataillon, 34095 Montpellier Cedex 5, France;* orcid.org/0000-0001-9149-6731; Email: jaksze3@amu.edu.pl

Emerson Coy − *NanoBioMedical Centre, Adam Mickiewicz University, 61-614 Poznan, Poland;* orcid.org/0000-0002-4149-9720; Email: coyeme@amu.edu.pl

Authors

Igor Iatsunskyi − *NanoBioMedical Centre, Adam Mickiewicz University, 61-614 Poznan, Poland*

Paweł Piotr Michałowski − *Łukasiewicz Research Network—Institute of Microelectronics and Photonics, 02-668 Warsaw, Poland;* orcid.org/0000-0002-3299-4092

Karol Załęski − *NanoBioMedical Centre, Adam Mickiewicz University, 61-614 Poznan, Poland*

Cassandre Lamboux − *Institut Européen des Membranes, IEM, UMR 5635, Univ Montpellier, CNRS, ENSCM Place Eugène Bataillon, 34095 Montpellier Cedex 5, France*

Syreina Sayegh − *Institut Européen des Membranes, IEM, UMR 5635, Univ Montpellier, CNRS, ENSCM Place Eugène Bataillon, 34095 Montpellier Cedex 5, France*

Elissa Makhoul − *Institut Européen des Membranes, IEM, UMR 5635, Univ Montpellier, CNRS, ENSCM Place Eugène Bataillon, 34095 Montpellier Cedex 5, France*

Andreu Cabot − *Advanced Materials Department, Catalonia Institute for Energy Research (IREC), 08930 Barcelona, Spain; ICREA, 08010 Barcelona, Spain;* orcid.org/0000-0002-7533-3251

Xingqi Chang − *Advanced Materials Department, Catalonia Institute for Energy Research (IREC), 08930 Barcelona, Spain*

Mikhael Bechelany − *Institut Européen des Membranes, IEM, UMR 5635, Univ Montpellier, CNRS, ENSCM Place Eugène Bataillon, 34095 Montpellier Cedex 5, France; Gulf University for Science and Technology, GUST, 32093 Hawally, Kuwait;* orcid.org/0000-0002-2913-2846

Complete contact information is available at: https://pubs.acs.org/10.1021/acsami.3c18935

Notes

The authors declare no competing financial interest.

ACKNOWLEDGMENTS

The authors acknowledge the financial support from the National Science Centre of Poland (NCN) by the OPUS grant 2019/35/B/ST5/00248. J.S. acknowledges the partial financial support from the NCN as well by the PRELUDIUM20 grant 2021/41/N/ST5/00211 for the production and deposition of the PDA free-standing films. P.P.M. was partially supported by the NCN (project no. 2018/31/D/ST5/00399) for the SIMS experiments. I.I. acknowledges the partial financial support from NCN by the OPUS grant number 2020/37/B/ST5/00576 in the ellipsometry experiments of this article. This research was supported by a French Government Scholarship. Authors acknowledge as well the financial support of project H2020-MSCA-RISE-2017, "Novel 1D photonic metal oxide nanostructures for early stage cancer detection" (project number: 778157).

REFERENCES

(1) Wang, H.; Li, X.; Zhao, X.; Li, C.; Song, X.; Zhang, P.; Huo, P.; Li, X. A Review on Heterogeneous Photocatalysis for Environmental Remediation: From Semiconductors to Modification Strategies. *Chin. J. Catal.* **2022**, *43* (2), 178−214.

(2) Zhao, W.; Adeel, M.; Zhang, P.; Zhou, P.; Huang, L.; Zhao, Y.; Ahmad, M. A.; Shakoor, N.; Lou, B.; Jiang, Y.; Lynch, I.; Rui, Y. A Critical Review on Surface-Modified Nano-Catalyst Application for the Photocatalytic Degradation of Volatile Organic Compounds. *Environ. Sci.: Nano* **2022**, *9* (1), 61−80.

(3) Wang, Z.; Li, C.; Domen, K. Recent Developments in Heterogeneous Photocatalysts for Solar-Driven Overall Water Splitting. *Chem. Soc. Rev.* **2019**, *48* (7), 2109−2125.

(4) Coy, E.; Iatsunskyi, I.; Bechelany, M. Perspectives and Current Trends on Hybrid Nanocomposite Materials for Photocatalytic Applications. *Sol. RRL* **2023**, *7* (7), 2201069.

(5) Liras, M.; Barawi, M.; de la Peña O'Shea, V. A. Hybrid Materials Based on Conjugated Polymers and Inorganic Semiconductors as Photocatalysts: From Environmental to Energy Applications. *Chem. Soc. Rev.* **2019**, *48* (22), 5454−5487.

(6) Lee, H.; Dellatore, S. M.; Miller, W. M.; Messersmith, P. B. Mussel-Inspired Surface Chemistry for Multifunctional Coatings. *Science* **2007**, *318* (5849), 426−430.

(7) Aguilar-Ferrer, D.; Szewczyk, J.; Coy, E. Recent Developments in PDA-Based Photocatalytic Nanocomposites for Energy Production: Physico-Chemical Properties and Perspectives. *Catal. Today* **2022**, *397*−*399*, 316−349.

(8) Aguilar-Ferrer, D.; Vasileiadis, T.; Iatsunskyi, I.; Ziółek, M.; Żebrowska, K.; Ivashchenko, O.; Błaszkiewicz, P.; Grześkowiak, B.; Pazos, R.; Moya, S.; Bechelany, M.; Coy, E. Understanding the Photothermal and Photocatalytic Mechanism of PDA Coated Gold Nanorods. *Adv. Funct. Mater.* **2023**, *33* (43), 2304208.

(9) Guo, Z.; Wang, G.; Fu, H.; Wang, P.; Liao, J.; Wang, A. Photocatalytic Degradation of Methylene Blue by a Cocatalytic PDA/TiO2electrode Produced by Photoelectric Polymerization. *RSC Adv.* **2020**, *10* (44), 26133−26141.

(10) Nie, N.; He, F.; Zhang, L.; Cheng, B. Direct Z-Scheme PDA-Modified ZnO Hierarchical Microspheres with Enhanced Photocatalytic CO 2 Reduction Performance. *Appl. Surf. Sci.* **2018**, *457*, 1096−1102.

(11) Kim, Y.; Coy, E.; Kim, H.; Mrówczyński, R.; Torruella, P.; Jeong, D. W.; Choi, K. S.; Jang, J. H.; Song, M. Y.; Jang, D. J.; Peiro, F.; Jurga, S.; Kim, H. J. Efficient Photocatalytic Production of Hydrogen by Exploiting the PDA-Semiconductor Interface. *Appl. Catal., B* **2021**, *280*, 119423.

(12) Arvand, M.; Sayyar, S.; Hemmati, S. Visible-Light-Driven PDA/CdS QDs Hybrid Materials with Synergistic Photocatalytic Activity. *J. Electroanal. Chem.* **2019**, *848*, 113288.

(13) Yuan, M.; Ye, X.; Song, Z.; Che, L.; Shang, S.; Yuan, M.; Wu, S.; Liu, D.; Cui, S. A Novel Mussel-Inspired Layered Montmorillonite-Based Composite Aerogel for High-Efficiency Removal of Heavy Metal Ions. *J. Water Process Eng.* **2023**, *54*, 104075.

(14) Coy, E.; Iatsunskyi, I.; Colmenares, J. C.; Kim, Y.; Mrówczyński, R. PDA Films with 2D-like Layered Structure and High Mechanical Resilience. *ACS Appl. Mater. Interfaces* **2021**, *13* (19), 23113−23120.

(15) Szewczyk, J.; Pochylski, M.; Szutkowski, K.; Kempiński, M.; Mrówczyński, R.; Iatsunskyi, I.; Gapiński, J.; Coy, E. In-Situ Thickness Control of Centimetre-Scale 2D-Like PDA Films with Large Scalability. *Mater. Today Chem.* **2022**, *24*, 100935.
(16) Szewczyk, J.; Babacic, V.; Krysztofik, A.; Ivashchenko, O.; Pochylski, M.; Pietrzak, R.; Gapiński, J.; Graczykowski, B.; Bechelany, M.; Coy, E. Control of Intermolecular Interactions toward the Production of Free-Standing Interfacial PDA Films. *ACS Appl. Mater. Interfaces* **2023**, *15* (30), 36922−36935.
(17) Szewczyk, J.; Ziółek, M.; Siuzdak, K.; Iatsunskyi, I.; Pochylski, M.; Aguilar-Ferrer, D.; Kempiński, M.; Tanos, F.; Gapiński, J.; Bechelany, M.; Coy, E. Ex-Situ Transferring of PDA Films on Semiconductor Interface: Evidence of Functional Hybrid Heterojunction. *Eur. Polym. J.* **2024**, *206*, 112781.
(18) Du, R.; Li, B.; Han, X.; Xiao, K.; Wang, X.; Zhang, C.; Arbiol, J.; Cabot, A. 2D/2D Heterojunction of TiO2 Nanoparticles and Ultrathin G-C3N4 Nanosheets for Efficient Photocatalytic Hydrogen Evolution. *Nanomaterials* **2022**, *12* (9), 1557.
(19) Xing, C.; Zhang, Z.; Zhang, Y.; Han, X.; Yang, L.; Li, J.; Wang, X.; Martinez, P.; Demir, M.; Piveteau, L.; Florian, P.; Arbiol, J.; Guo, Y.; Llorca, J.; Cabot, A. Synergistic Effect of Surface Oxygen Vacancies and Hydroxyl Groups on Cu-Doped TiO2 Photocatalyst for Hydrogen Evolution. *Mater. Today Nano* **2023**, *24*, 100435.
(20) Xing, C.; Yang, L.; He, R.; Spadaro, M. C.; Zhang, Y.; Arbiol, J.; Li, J.; Poudel, B.; Nozariasbmarz, A.; Li, W.; Lim, K. H.; Liu, Y.; Llorca, J.; Cabot, A. Brookite TiO2 Nanorods as Promising Electrochromic and Energy Storage Materials for Smart Windows. *Small* **2023**, *19* (49), 2303639.
(21) Abid, M.; Makhoul, E.; Tanos, F.; Iatsunskyi, I.; Coy, E.; Lesage, G.; Cretin, M.; Cornu, D.; Ben Haj Amara, A.; Bechelany, M. N-Doped HNT/TiO2 Nanocomposite by Electrospinning for Acetaminophen Degradation. *Membranes* **2023**, *13* (2), 204.
(22) Sudhakar, V.; Krishnamoorthy, K. Enhancing the Device Efficiency by Filling the Traps in Photoanodes. *J. Mater. Chem. C* **2019**, *7* (46), 14632−14638.
(23) Natarajan, T. S.; Mozhiarasi, V.; Tayade, R. J. Nitrogen Doped Titanium Dioxide (N-TiO2): Synopsis of Synthesis Methodologies, Doping Mechanisms, Property Evaluation and Visible Light Photocatalytic Applications. *Photochem* **2021**, *1* (3), 371−410.
(24) Ansari, S. A.; Khan, M. M.; Ansari, M. O.; Cho, M. H. Nitrogen-Doped Titanium Dioxide (N-Doped TiO2) for Visible Light Photocatalysis. *New J. Chem.* **2016**, *40* (4), 3000−3009.
(25) Kaady, E.; Habchi, R.; Bechelany, M.; Zgheib, E.; Alhussein, A. Effect of Al2O3, ZnO and TiO2 Atomic Layer Deposition Grown Thin Films on the Electrochemical and Mechanical Properties of Sputtered Al-Zr Coating. *Coatings* **2023**, *13* (1), 65.
(26) Miao, J.; Geng, W.; Alvarez, P. J. J.; Long, M. 2D N-Doped Porous Carbon Derived from PDA-Coated Graphitic Carbon Nitride for Efficient Nonradical Activation of Peroxymonosulfate. *Environ. Sci. Technol.* **2020**, *54* (13), 8473−8481.
(27) Zhou, R.; Guo, H.; Yang, Y.; Wang, Z.; Li, X.; Zhou, Y. N-Doped Carbon Layer Derived from PDA to Improve the Electrochemical Performance of Spray-Dried Si/Graphite Composite Anode Material for Lithium Ion Batteries. *J. Alloys Compd.* **2016**, *689*, 130−137.
(28) Zhang, L. L.; Ma, D.; Li, T.; Liu, J.; Ding, X. K.; Huang, Y. H.; Yang, X. L. PDA-Derived Nitrogen-Doped Carbon-Covered Na3V2(PO4)2F3 Cathode Material for High-Performance Na-Ion Batteries. *ACS Appl. Mater. Interfaces* **2018**, *10* (43), 36851−36859.
(29) Parsons, G. N.; Atanasov, S. E.; Dandley, E. C.; Devine, C. K.; Gong, B.; Jur, J. S.; Lee, K.; Oldham, C. J.; Peng, Q.; Spagnola, J. C.; Williams, P. S. Mechanisms and Reactions during Atomic Layer Deposition on Polymers. *Coord. Chem. Rev.* **2013**, *257* (23−24), 3323−3331.
(30) Casetta, J.; Ortiz, D. G.; Pochat-Bohatier, C.; Bechelany, M.; Miele, P. Atomic Layer Deposition of TiO2 on Porous Polysulfone Hollow Fibers Membranes for Water Treatment. *Sep. Purif. Technol.* **2023**, *312*, 123377.
(31) Nakata, K.; Fujishima, A. TiO2 Photocatalysis: Design and Applications. *J. Photochem. Photobiol., C* **2012**, *13* (3), 169−189.
(32) Chung, K.-H.; Kim, B.-J.; Park, Y.-K.; Kim, S.-C.; Jung, S.-C. Photocatalytic Properties of Amorphous N-Doped TiO2 Photocatalyst under Visible Light Irradiation. *Catalysts* **2021**, *11* (8), 1010.
(33) Szewczyk, J.; Aguilar-Ferrer, D.; Coy, E. PDA Films: Electrochemical Growth and Sensing Applications. *Eur. Polym. J.* **2022**, *174*, 111346.
(34) Moret, M.; Abou Chaaya, A.; Bechelany, M.; Miele, P.; Robin, Y.; Briot, O. Atomic Layer Deposition of Zinc Oxide for Solar Cell Applications. *Superlattices Microstruct.* **2014**, *75*, 477−484.
(35) Iatsunskyi, I.; Jancelewicz, M.; Nowaczyk, G.; Kempiński, M.; Peplińska, B.; Jarek, M.; Załęski, K.; Jurga, S.; Smyntyna, V. Atomic Layer Deposition TiO2 Coated Porous Silicon Surface: Structural Characterization and Morphological Features. *Thin Solid Films* **2015**, *589*, 303−308.
(36) Abou Chaaya, A.; Viter, R.; Bechelany, M.; Alute, Z.; Erts, D.; Zalesskaya, A.; Kovalevskis, K.; Rouessac, V.; Smyntyna, V.; Miele, P. Evolution of Microstructure and Related Optical Properties of ZnO Grown by Atomic Layer Deposition. *Beilstein J. Nanotechnol.* **2013**, *4* (1), 690−698.
(37) Iatsunskyi, I.; Coy, E.; Viter, R.; Nowaczyk, G.; Jancelewicz, M.; Baleviciute, I.; Załęski, K.; Jurga, S. Study on Structural, Mechanical, and Optical Properties of Al2O3-TiO2 Nanolaminates Prepared by Atomic Layer Deposition. *J. Phys. Chem. C* **2015**, *119* (35), 20591−20599.
(38) Michałowski, P. P.; Anayee, M.; Mathis, T. S.; Kozdra, S.; Wójcik, A.; Hantanasirisakul, K.; Jóźwik, I.; Piątkowska, A.; Możdżonek, M.; Malinowska, A.; Diduszko, R.; Wierzbicka, E.; Gogotsi, Y. Oxycarbide MXenes and MAX Phases Identification Using Monoatomic Layer-by-Layer Analysis with Ultralow-Energy Secondary-Ion Mass Spectrometry. *Nat. Nanotechnol.* **2022**, *17* (11), 1192−1197.
(39) Makuła, P.; Pacia, M.; Macyk, W. How To Correctly Determine the Band Gap Energy of Modified Semiconductor Photocatalysts Based on UV-Vis Spectra. *J. Phys. Chem. Lett.* **2018**, *9* (23), 6814−6817.
(40) Li, S.; Hou, X.; Lu, S.; Xu, W.; Tao, J.; Zhao, Z.; Hu, G.; Gao, F. Fabrication and Simulation of a Layered Ultrahigh Thermal Conductive Material Made of Self-Assembled Graphene and PDA on a Copper Substrate. *RSC Adv.* **2021**, *11* (55), 34676−34687.
(41) Lee, K.; Park, M.; Malollari, K. G.; Shin, J.; Winkler, S. M.; Zheng, Y.; Park, J. H.; Grigoropoulos, C. P.; Messersmith, P. B. Laser-Induced Graphitization of PDA Leads to Enhanced Mechanical Performance While Preserving Multifunctionality. *Nat. Commun.* **2020**, *11* (1), 4848.
(42) Olejnik, A.; Polaczek, K.; Szkodo, M.; Stanisławska, A.; Ryl, J.; Siuzdak, K. Laser-Induced Graphitization of PDA on Titania Nanotubes. *ACS Appl. Mater. Interfaces* **2023**, *15* (45), 52921−52938.
(43) Kafkopoulos, G.; Karakurt, E.; Duvigneau, J.; Vancso, G. J. PDA as Adhesion Promotor: The Effect of Thermal Treatment on the Performance of Poly(Lactic Acid) (PLA)-Metal Co-Molded Joints. *Macromol. Symp.* **2022**, *404* (1), 2100325.
(44) Thakur, S.; Karak, N. Green Reduction of Graphene Oxide by Aqueous Phytoextracts. *Carbon* **2012**, *50* (14), 5331−5339.
(45) Sirirak, R.; Jarulertwathana, B.; Laokawee, V.; Susingrat, W.; Sarakonsri, T. FeNi Alloy Supported on Nitrogen-Doped Graphene Catalysts by Polyol Process for Oxygen Reduction Reaction (ORR) in Proton Exchange Membrane Fuel Cell (PEMFC) Cathode. *Res. Chem. Intermed.* **2017**, *43* (5), 2905−2919.
(46) Rivera, L. M.; Fajardo, S.; Arévalo, M.; García, G.; Pastor, E. S- and N-Doped Graphene Nanomaterials for the Oxygen Reduction Reaction. *Catalysts* **2017**, *7* (9), 278.
(47) Ngidi, N. P. D.; Ollengo, M. A.; Nyamori, V. O. Effect of Doping Temperatures and Nitrogen Precursors on the Physicochemical, Optical, and Electrical Conductivity Properties of Nitrogen-Doped Reduced Graphene Oxide. *Materials* **2019**, *12* (20), 3376.
(48) Isaacs, M. A.; Davies-Jones, J.; Davies, P. R.; Guan, S.; Lee, R.; Morgan, D. J.; Palgrave, R. Advanced XPS Characterization: XPS-

https://doi.org/10.1021/acsami.3c18935
ACS Appl. Mater. Interfaces 2024, 16, 10774−10784

Based Multi-Technique Analyses for Comprehensive Understanding of Functional Materials. *Mater. Chem. Front.* **2021**, *5* (22), 7931−7963.
(49) Holländer, A.; Haupt, M.; Oehr, C. On Depth Profiling of Polymers by Argon Ion Sputtering. *Plasma Processes Polym.* **2007**, *4* (9), 773−776.
(50) Saha, N. C.; Tompkins, H. G. Titanium Nitride Oxidation Chemistry: An X-ray Photoelectron Spectroscopy Study. *J. Appl. Phys.* **1992**, *72* (7), 3072−3079.
(51) Jaeger, D.; Patscheider, J. A Complete and Self-Consistent Evaluation of XPS Spectra of TiN. *J. Electron Spectrosc. Relat. Phenom.* **2012**, *185* (11), 523−534.
(52) Greczynski, G.; Hultman, L. X-Ray Photoelectron Spectroscopy: Towards Reliable Binding Energy Referencing. *Prog. Mater. Sci.* **2020**, *107*, 100591.
(53) Bharti, B.; Kumar, S.; Kumar, R. Superhydrophilic TiO2 Thin Film by Nanometer Scale Surface Roughness and Dangling Bonds. *Appl. Surf. Sci.* **2016**, *364*, 51−60.
(54) Velasco-Velez, J. J.; Davaasuren, B.; Scherzer, M.; Cap, S.; Willinger, M.; Guo, J.-H.; Schlögl, R.; Knop-Gericke, A. Exploring the Incorporation of Nitrogen in Titanium and Its Influence on the Electrochemical Corrosion Resistance in Acidic Media. *Surf. Sci.* **2016**, *650*, 272−278.
(55) Jackman, M. J.; Thomas, A. G.; Muryn, C. Photoelectron Spectroscopy Study of Stoichiometric and Reduced Anatase TiO2(101) Surfaces: The Effect of Subsurface Defects on Water Adsorption at Near-Ambient Pressures. *J. Phys. Chem. C* **2015**, *119* (24), 13682−13690.
(56) Du, J.; Zhao, G.; Shi, Y.; HaoYang; Li, Y.; Zhu, G.; Mao, Y.; Sa, R.; Wang, W. A Facile Method for Synthesis of N-Doped TiO2 Nanooctahedra, Nanoparticles, and Nanospheres and Enhanced Photocatalytic Activity. *Appl. Surf. Sci.* **2013**, *273*, 278−286.
(57) Bharti, B.; Kumar, S.; Lee, H.-N.; Kumar, R. Formation of Oxygen Vacancies and Ti3+ State in TiO2 Thin Film and Enhanced Optical Properties by Air Plasma Treatment. *Sci. Rep.* **2016**, *6* (1), 32355.
(58) Siuzdak, K.; Szkoda, M.; Sawczak, M.; Lisowska-Oleksiak, A. Novel Nitrogen Precursors for Electrochemically Driven Doping of Titania Nanotubes Exhibiting Enhanced Photoactivity. *New J. Chem.* **2015**, *39* (4), 2741−2751.
(59) He, Z.; Que, W.; He, Y.; Hu, J.; Chen, J.; Javed, H. M. A.; Ji, Y.; Li, X.; Fei, D. Electrochemical Behavior and Photocatalytic Performance of Nitrogen-Doped TiO2 Nanotubes Arrays Powders Prepared by Combining Anodization with Solvothermal Process. *Ceram. Int.* **2013**, *39* (5), 5545−5552.
(60) Rodriguez, J. A.; Jirsak, T.; Liu, G.; Hrbek, J.; Dvorak, J.; Maiti, A. Chemistry of NO2 on Oxide Surfaces: Formation of NO3 on TiO2(110) and NO2↔O Vacancy Interactions. *J. Am. Chem. Soc.* **2001**, *123* (39), 9597−9605.
(61) Ravindra, N. M.; Ganapathy, P.; Choi, J. Energy Gap-Refractive Index Relations in Semiconductors - An Overview. *Infrared Phys. Technol.* **2007**, *50* (1), 21−29.
(62) Ben Jemaa, I.; Chaabouni, F.; Presmanes, L.; Thimont, Y.; Abaab, M.; Barnabe, A.; Tailhades, P. Structural, Optical and Electrical Investigations on Nb Doped TiO2 Radio-Frequency Sputtered Thin Films from a Powder Target. *J. Mater. Sci.: Mater. Electron.* **2016**, *27* (12), 13242−13248.
(63) Arunachalam, A.; Dhanapandian, S.; Manoharan, C. Effect of Sn Doping on the Structural, Optical and Electrical Properties of TiO2 Films Prepared by Spray Pyrolysis. *J. Mater. Sci.: Mater. Electron.* **2016**, *27* (1), 659−676.
(64) Politano, G. G.; Versace, C. Variable-Angle Spectroscopic Ellipsometry of Graphene-Based Films. *Coatings* **2021**, *11*, 462.

NOTE ADDED AFTER ASAP PUBLICATION

This paper was published ASAP on February 13, 2024 with an error in the title of the paper. The corrected version was reposted on February 14, 2024.

https://doi.org/10.1021/acsami.3c18935
ACS Appl. Mater. Interfaces 2024, 16, 10774−10784

5

Final Conclusions

The main goal of my work was to develop a novel, efficient, large-scale, laminar nanocomposite for photocatalysis based on polydopamine and selected transition metal oxides**. Based on the information presented in the Publications 1-2 and the original research results obtained in the Publications 3-6, I conclude that I have achieved the intended goal.**

This work exploits hybrid organic/inorganic nanostructures, a promising trend in photocatalysis materials. However, using a biomimetic polymer - polydopamine- allowed me to overcome the current limitations of this type of system.

The first milestone was to demonstrate that polydopamine has properties that make it suitable for constructing organic/inorganic hybrid nanolaminates with various inorganic materials. An extensive literature has provided convincing evidence that a PDA/semiconductor heterojunction can be successfully formed. Based on available data, I selected the Transition Metal Oxides as a benchmark photocatalyst for the development of a new system, i.e. large-scale nanocomposite films.

Next, I successfully controlled the synthesis of the a/w-PDA free-standing films within a centimetre scale, utilising a novel Spectroscopic Reflectometry approach. Detailed 2D maps of the thickness of the films during their formation were generated, and they show how changing synthesis conditions influenced the homogeneity of the obtained materials. Moreover, the summary of the previous approaches towards producing the a/w-PDA free-standing thin films makes it clear that obtaining layered-like large-scale a/w-PDA films during this PhD project was a breakthrough discovery.

Control of the dopamine oxidation path using boric acid allowed for obtaining ultra-thin a/w-PDA with better mechanical properties (higher Young's modulus). Chemical and structural tests have shown that in the structure of the polymer thus obtained, physical interactions between macromolecules are more important than covalent bonds. The mechanical property measurements can certainly be considered reliable because they were confirmed using two completely different techniques. Finding the data for comparison was challenging because measurements of mechanical properties for such thin, free-standing polymer films are rare. However, the study shows that both unmodified and, in particular, modified a/w-PDA have phenomenal mechanical properties. Due to the very wide scope of these studies, it was not yet possible to use boric acid-modified films (a/w-BAPDA) for the construction of large-scale organic/inorganic hybrid nanolaminate. However, as mentioned in the Future Perspectives section, we are currently conducting such experiments.

Having high-quality, large-scale a/w-PDA free-standing films at my disposal after the previous stages of the project, I started the production of the nanolaminates. Importantly, an *ex-situ* transfer of the polydopamine onto large surfaces of ZnO and TiO_2 resulted in the effective formation of functional heterojunctions. The most important conclusions from a very extensive study indicated a significant (0.14 eV) bandgap value shift toward lower photon energies in TiO_2 thin coating, quenching of the ZnO photoluminescence bands assigned to the oxygen

defect-assisted recombinations, passivating the shallow defect states (which are responsible for unfavorable recombination effects), boosting the electron transfer at the interface and lowering the local-heating effect in TiO_2 nanofilms, drop in the charge transfer resistance component at the electrode/electrolyte interface after PDA deposition. Moreover, there is a significant quenching of the pyro-phototronic effect. Finally, the remarkable efficiency enhancement in the photocatalytic degradation of the methylene blue process is 14 % after 1 h, with better stability, compared to unmodified TiO_2 films. Certainly, all this can be considered a significant improvement in the photocatalytic properties of the TMOx films.

In order to multiply the effect occurring on the interface and show the superior quality of the ultrathin layered-like large-scale a/w-PDA films, I prepared multilayer TiO_2/PDA structures. During this experiment, we discovered that a new, previously undescribed mechanism for doping TiO_2 with nitrogen occurred. The mechanism must be examined even more thoroughly in subsequent experiments (Section: Future Perspectives), but the obtained results suggest that the PDA layers on which TiO_2 layers grow provide nitrogen atoms (from amino groups) during the ALD and the thicker Oxide layer, the effect disappears. Therefore, the doping is gradient-like. In this approach, nitrogen atoms occupied both substitution and interstitial positions of the TiO_2 lattice, which contributed to introducing more than 1 new energy level and significantly reducing the band gap. Undoubtedly, this is one of the most important discoveries in this doctoral project. Moreover, we have shown through optical and photoelectrochemical studies that multilayer structures are even more interesting for applications in photocatalysis than the single-layer TiO_2/PDA laminate itself. The obtained nanocomposites can be characterized as ideal laminates where the large-scale interfaces between layers are very sharp, the thickness of the layers is uniform, and the uniformity of the nanocomposite structure over the entire surface (1 cm^2) is impressive. In addition, they are characterized by electrochemical stability because the preparation method is suitable for such real applications, unlike nanoparticles, which quickly lose their properties and are difficult to recover.

6

Future Perspectives

The real origin and extent of the observed supramolecular ordering in the a/w-PDA layered-like free-standing films is still unknown, especially at the very beginning of the film's formation. Currently, in the Hybrid Materials and Interface Group of the NanoBioMedical Center, together with collaborators from Physics Faculty of the Adam Mickiewicz University, we are investigating this issue using technologies such as cryoSEM, cryoTEM, *in-situ* Raman spectroscopy and others. In more detail, we are interested in the morphology of these films during their formation, and the question is whether the structural changes occurring as a result of oxidation, transfer and drying are of reversible character. The results are quite exciting, and we plan to share them as soon as the entire study is concluded.

Since a/w-PDA can be used to create advanced nanoarchitectures, other potential systems should also be tested. In cooperation with Southern Denmark University (SDU), we are at an advanced stage of preparing publications on a/w-PDA passivation of the active layer of Organic Photovoltaic (OPV) laminar nanocomposites. In this case, functionalization with polydopamine through standard *in-situ* deposition from solution would not be possible because the blend of conductive polymers forming the active layer (PM6:Y6), before applying the passivation layer, is not resistant to long-term stay in an aqueous environment. There are particurarly interesting signs, for which we already have partial evidence, that PDA in such a system may serve not only as a passivation layer, but also be an effective layer for transporting electron holes - which results from the developed band-alignment schemes.

Moreover, as part of cooperation with the Christian-Albrecht University (CAU) in Kiel, we are preparing publications on obtaining H:TiO_2/BAPDA nanocomposites. In this case, for the first time, we used a/w-PDA films modified with boric acid (Publication 4), which was necessary because the H:TiO_2 layers have the form of nanopillars, and the polymer film deposited onto their top surface must exhibit extremely good flexibility. In this study, we also predict that due to the more cross-linked structure of BAPDA compared to PDA, the electrochemical properties of the produced heterojunction may be even better

Concerning novel doping mechanisms within the ALD oxide layers deposition onto PDA films, a further studies are needed to address several questions like: What is the influence of different polymer substrates? Will the same effect occur for the growing crystalline phase (non-amorphous)? What about other non-metal atoms that may be sourced from (other) polymers (e.g. F, S...)? We anticipate that the methodology presented in the article could be exploited in other systems.

Finally, the increase in studies and projects in the field of PDA-based photocatalysis is foreseen. This assumption can already be partially confirmed given the increasing number of citations for publications 1-3, which is significant, especially considering their recent publication dates, in 2021 and 2022, respectively.

7

Scientific Achievements

List of Publications included in the thesis

J. Szewczyk, I. Iatsunskyi, P.P. Michałowski, K. Załęski, C.Lamboux, S. Sayegh, E. Makhoul, A. Cabot, X. Chang, M. Bechelany, E. Coy, TiO_2/PDA Multilayer Nanocomposites with Exceptionally Sharp Large-Scale Interfaces and Nitrogen Doping Gradient, *ACS Applied Materials & Interfaces 2024, XXXX, XXX, XXX-XXX* (DOI: 10.1021/acsami.3c18935)

J. Szewczyk, M. Ziółek, K. Siuzdak, I. Iatsunskyi, M. Pochylski, D. Aguilar-Ferrer, M. Kempiński, F. Tanos, J. Gapiński, M. Bechelany, E. Coy, Ex-situ transferring of polydopamine films on semiconductor interface: Evidence of functional hybrid heterojunction, *European Polymer Journal 2024, 206, 112781* (DOI: 10.1016/j.eurpolymj.2024.112781)

J. Szewczyk, V. Babacic, A. Krysztofik, O. Ivashchenko, M. Pochylski, R. Pietrzak, J. Gapiński, B. Graczykowski, M. Bechelany, E. Coy, Control of Intermolecular Interactions toward the Production of Free-Standing Interfacial Polydopamine Films, *ACS Applied Materials & Interfaces 2023, 15, 30, 36922–36935* (DOI: 10.1021/acsami.3c05236)

J. Szewczyk, M. Pochylski, K. Szutkowski, M. Kempiński, R. Mrówczyński, I. Iatsunskyi, J. Gapiński, E. Coy, In-situ thickness control of centimetre-scale 2D-Like polydopamine films with large scalability, *Materials Today Chemistry 2022, 24, 100935* (DOI: 10.1016/j.mtchem.2022.100935)

J. Szewczyk, D. Aguilar-Ferrer, E. Coy, Polydopamine films: Electrochemical growth and sensing applications, *European Polymer Journal 2022, 174, 111346* (DOI: 10.1016/j.eurpolymj.2022.111346)

D. Aguilar-Ferrer, **J. Szewczyk**, E. Coy, Recent developments in polydopamine-based photocatalytic nanocomposites for energy production: Physico-chemical properties and perspectives, *CATALYSIS TODAY 2022, 397–399, 316-349* (DOI: 10.1016/j.cattod.2021.08.016)

First author (first authors contributed equally and are listed in alphabetical order)

Total impact factor of the publication included in the thesis: 43.6

List of Publications not included in the thesis

M. Bik, **J. Szewczyk**, P. Jeleń, E. Długoń, W. Simka, M. Sowa, J. Tyczkowski, J. Balcerzak, E. Bik, K. Mroczka, M. Leśniak, M. Barańska, M. Sitarz, Optimization of the formation of coatings based on SiAlOC glasses via structural, microstructural and electrochemical studies, *Electrochimica Acta 2019, 309, 44-56* (DOI: 10.1016/j.electacta.2019.04.080)

Total impact factor of all publications: 50.2

Other achievments

Conferences

First Author of the oral presentation (1st place award) at the international conference:

- Optimization of 2D-like polydopamine thin films from the air/water interphase: morphology, hydrophobicity and electrochemical properties, *6th International Symposium on Surface Imaging/Spectroscopy at the Solid/Liquid Interface, 8th June 2021, Kraków, Poland*

First Author of the oral presentation (2nd place award) at the international conference:

- Corrosion resistance studies of aluminum doped silicon oxycarbide coatings, *XXI International Students Session on Materials and Technologies of the XXI century, 3rd May 2019, Katowice, Poland*

First Author of the oral presentations at the international conferences:

- Optimization of 2D-Like Polydopamine membranes from the Air/Water Interphase: towards morphological and hydrophilic properties improvement, *4th Conference "Nanotechnology and Innovation in the Baltic Sea Region", 4-6 August 2021, Kiel, Germany (on-line event)*

- 2D-Like Polydopamine membranes from the Air/Water Interphase: towards the improvement of their morphological properties and successful transfer on multifunctional substrates, *4th International Meeting on Materials Science for Energy Related Applications, 23th September 2021, Belgrade, Serbia (on-line event)*

- A novel, ultrathin 2D-like polydopamine membranes from the air/water interphase – tuning polymerization process towards better understanding of their nanostructure, *7th Young Polymer Scientists Conference and Short Cours*e, *27th September 2021, Łódź, Poland (on-line event)*

- Application of biomimetic polydopamine 2D-like thin films for a significant enhancement of ZnO and TiO_2 photocatalytic properties, *'Functional Materials and Nanotechnologies' and 'Nanotechnology and Innovation in the Baltic Sea region' - FM&NT – NIBS 2022, 3-6 July 2022, Riga, Latvia*

- Investigation of the novel, nature-inspired PDA/TiO_2 laminar composites-photocatalytic properties and multilayer approach, *EMRS 2022 Fall Meeting, 19 - 22 September 2022, Warsaw, Poland*

- Production of the Exceptionally Elastic and Ultra-thin Free-standing Polydopamine Films, *Nanotechnology and Innovation in the Baltic Sea Region, 3-5 July, 2023, Sønderborg, Denmark*

First Author of the poster presentations at the international conferences:

- Optimization of the morphological properties of the centimeter-scale 2D-Like Polydopamine membranes from the Air/Water Interface, *12th International Conference NanoTech Poland 2022, 1-3 Jun 2022, Poznań, Poland*

- Breakthrough Control of Intermolecular Interactions Towards the Production of Super-elastic Free-standing Polydopamine Films, *13th International Conference NanoTech Poland 2023, 14th – 16th June 2023, Poznań, Poland - distinction award*

- Super-elastic Free-standing Polydopamine Films for various applications, *2nd Symposium on Polydopamine, 11-12 October 2023, Poznań, Poland*

Author of the oral presentation (3rd place award) at the national conference

- Optimization of the process of obtaining layers from black glasses, as the key factor determining their functional properties, *55th Conference of Students Research Groups, Metallurgical Division, 11th May 2018, Kraków, AGH University of Science and Technology*

Scientific Projects

Principal Investigator in research project:

- PRELUDIUM20: Development and chemical tuning of novel 2D-like polydopamine ultrathin membranes – National Science Centre NCN (2021/41/N/ST5/00211) – NanoBioMedical Centre, Adam Mickiewicz University, Poznań, Poland

Participation in research projects:

- OPUS 18: Understanding the Interface of Polydopamine and Semiconductor Nanomaterials for Photocatalytic Water Splitting – National Science Centre NCN (2019/35/B/ST5/00248) – NanoBioMedical Centre, Adam Mickiewicz University, Poznań, Poland

- OPUS 13: Polysiloxane layers modified with carbon nanotubes on metallic substrates – National Science Centre NCN (2017/25/B/ST8/02602) - AGH University of Science and Technology, Kraków, Poland

- Diamond Grant: Black glasses as a protective coating for heat-resistant alloys under high-temperature corrosion - Polish Ministry of Science and Higher Education (DI2016 004046) - AGH University of Science and Technology, Kraków, Poland

Awards

- Scholarship for Doctoral Students of the AMU Foundation (2022)
    - For scientific achievements during doctoral studies

- French Government Scholarship (2021)
    - For participation in a double PhD cotutelle program

- Scholarship of the Minister of Science and Higher Education for Students (2019)
    - For scientific achievements in the academic year 2018/2019

- Scholarship of the AGH UST Rector
    - For scientific achievements in the academic year 2017/2018 and 2018/2019

- Finalist of the ABB Competition for the Best Thesis (2020)
    - For a master's thesis that stands out for its high-quality

Research internships abroad

- European Institute for the Membranes, University of Montpellier, France (12 months, Febuary – June 2022, 2023 and 2024)
    - Thin free-standing polymeric films production and transferring methods
    - Atomic Layer Deposition of ZnO, TiO_2 thin films. Principles of operation and rector maintenance

- Catalonia Institute for Energy Research (IREC), Barcelona, Spain (1 week, May 2023)
    - Electrochemical performance tests (e.g. specific capacitance measurement) of the multilayer organic/inorganic composite materials

- Technical Faculty of Christian Albrecht University, Kiel, Germany (2 weeks, September 2023)
    - Reactive Magnetron Sputtering of highly crystalline TiO_2 films
    - Principles of operation of the Chemical Vapor Deposition
    - Photocatalytic activity performance tests towards water remediation, degradation of dyes

8

Literature

[1] J. Barber, P.D. Tran, From natural to artificial photosynthesis, J. R. Soc. Interface. 10 (2013) 20120984. https://doi.org/10.1098/rsif.2012.0984.

[2] S. Ghosh, R. Yadav, Future of photovoltaic technologies: A comprehensive review, Sustain. Energy Technol. Assessments. 47 (2021) 101410. https://doi.org/10.1016/j.seta.2021.101410.

[3] M. Dada, P. Popoola, Recent advances in solar photovoltaic materials and systems for energy storage applications: a review, Beni-Suef Univ. J. Basic Appl. Sci. 12 (2023) 66. https://doi.org/10.1186/s43088-023-00405-5.

[4] L.S.F. Frowijn, W.G.J.H.M. van Sark, Analysis of photon-driven solar-to-hydrogen production methods in the Netherlands, Sustain. Energy Technol. Assessments. 48 (2021) 101631. https://doi.org/10.1016/j.seta.2021.101631.

[5] T. Yu, W. He, Q. Zhang, D. Ma, Advanced Nanomaterials and Characterization Techniques for Photovoltaic and Photocatalysis Applications, Accounts Mater. Res. 4 (2023) 507–521. https://doi.org/10.1021/accountsmr.3c00012.

[6] H. Ali, M. Masar, M. Yasir, M. Machovsky, O.C. Monteiro, I. Kuritka, Current trends in environmental and energy photocatalysis and ISO standardization, J. Environ. Chem. Eng. 11 (2023) 111541. https://doi.org/10.1016/j.jece.2023.111541.

[7] X. Yang, D. Wang, Photocatalysis: From Fundamental Principles to Materials and Applications, ACS Appl. Energy Mater. 1 (2018) 6657–6693. https://doi.org/10.1021/acsaem.8b01345.

[8] M.A. Hassaan, M.A. El-Nemr, M.R. Elkatory, S. Ragab, V.-C. Niculescu, A. El Nemr, Principles of Photocatalysts and Their Different Applications: A Review, Top. Curr. Chem. 381 (2023) 31. https://doi.org/10.1007/s41061-023-00444-7.

[9] X. Li, Y. Chen, Y. Tao, L. Shen, Z. Xu, Z. Bian, H. Li, Challenges of photocatalysis and their coping strategies, Chem Catal. 2 (2022) 1315–1345. https://doi.org/10.1016/j.checat.2022.04.007.

[10] L. Yang, D. Fan, Z. Li, Y. Cheng, X. Yang, T. Zhang, A Review on the Bioinspired Photocatalysts and Photocatalytic Systems, Adv. Sustain. Syst. 6 (2022) 2100477. https://doi.org/10.1002/adsu.202100477.

[11] J.-M. Herrmann, Heterogeneous photocatalysis: fundamentals and applications to the removal of various types of aqueous pollutants, Catal. Today. 53 (1999) 115–129. https://doi.org/10.1016/S0920-5861(99)00107-8.

[12] R. Qian, H. Zong, J. Schneider, G. Zhou, T. Zhao, Y. Li, J. Yang, D.W. Bahnemann, J.H. Pan, Charge carrier trapping, recombination and transfer during TiO2 photocatalysis: An overview, Catal. Today. 335 (2019) 78–90. https://doi.org/10.1016/j.cattod.2018.10.053.

[13] Ștefan Neațu, J.A. Maciá-Agulló, H. Garcia, Solar Light Photocatalytic CO2 Reduction: General Considerations and Selected Bench-Mark Photocatalysts, Int. J. Mol. Sci. 15 (2014) 5246–5262. https://doi.org/10.3390/ijms15045246.

[14] N. Goodarzi, Z. Ashrafi-Peyman, E. Khani, A.Z. Moshfegh, Recent Progress on Semiconductor Heterogeneous Photocatalysts in Clean Energy Production and Environmental Remediation, Catalysts. 13 (2023) 1102. https://doi.org/10.3390/catal13071102.

[15] H.L. Tan, F.F. Abdi, Y.H. Ng, Heterogeneous photocatalysts: an overview of classic and modern approaches for optical, electronic, and charge dynamics evaluation, Chem. Soc. Rev. 48 (2019) 1255–1271. https://doi.org/10.1039/C8CS00882E.

[16] S. Singh, H. Chen, S. Shahrokhi, L.P. Wang, C.-H. Lin, L. Hu, X. Guan, A. Tricoli, Z.J. Xu, T. Wu, Hybrid Organic–Inorganic Materials and Composites for Photoelectrochemical Water Splitting, ACS Energy Lett. 5 (2020) 1487–1497. https://doi.org/10.1021/acsenergylett.0c00327.

[17] F. Fresno, R. Portela, S. Suárez, J.M. Coronado, Photocatalytic materials: recent achievements and near future trends, J. Mater. Chem. A. 2 (2014) 2863–2884. https://doi.org/10.1039/C3TA13793G.

[18] D.D. Thongam, H. Chaturvedi, Advances in nanomaterials for heterogeneous photocatalysis, Nano Express. 2 (2021) 012005. https://doi.org/10.1088/2632-959X/abeb8d.

[19] A. V Emeline, V.N. Kuznetsov, V.K. Ryabchuk, N. Serpone, On the way to the creation of next generation photoactive materials, Environ. Sci. Pollut. Res. 19 (2012) 3666–3675. https://doi.org/10.1007/s11356-011-0665-3.

[20] N. Serpone, A. V Emeline, Semiconductor Photocatalysis — Past, Present, and Future Outlook, J. Phys. Chem. Lett. 3 (2012) 673–677. https://doi.org/10.1021/jz300071j.

[21] A. Krishnan, A. Swarnalal, D. Das, M. Krishnan, V.S. Saji, S.M.A. Shibli, A review on transition metal oxides based photocatalysts for degradation of synthetic organic pollutants, J. Environ. Sci. 139 (2024) 389–417. https://doi.org/10.1016/j.jes.2023.02.051.

[22] A. Pattnaik, J.N. Sahu, A.K. Poonia, P. Ghosh, Current perspective of nano-engineered metal oxide based photocatalysts in advanced oxidation processes for degradation of organic pollutants in wastewater, Chem. Eng. Res. Des. 190 (2023) 667–686. https://doi.org/10.1016/j.cherd.2023.01.014.

[23] S. Chandrasekaran, L. Yao, L. Deng, C. Bowen, Y. Zhang, S. Chen, Z. Lin, F. Peng, P. Zhang, Recent advances in metal sulfides: from controlled fabrication to electrocatalytic, photocatalytic and photoelectrochemical water splitting and beyond, Chem. Soc. Rev. 48 (2019) 4178–4280. https://doi.org/10.1039/C8CS00664D.

[24] H. Hao, X. Lang, Metal sulfide photocatalysis: visible-light-induced organic transformations, ChemCatChem. 11 (2019) 1378–1393. https://doi.org/10.1002/cctc.201801773.

[25] K. Ren, S. Yue, C. Li, Z. Fang, K.A.M. Gasem, J. Leszczynski, S. Qu, Z. Wang, M. Fan, Metal halide perovskites for photocatalysis applications, J. Mater. Chem. A. 10 (2022) 407–429. https://doi.org/10.1039/D1TA09148D.

[26] K. Wei, Y. Faraj, G. Yao, R. Xie, B. Lai, Strategies for improving perovskite photocatalysts reactivity for organic pollutants degradation: A review on recent progress, Chem. Eng. J. 414 (2021) 128783. https://doi.org/10.1016/j.cej.2021.128783.

[27] H. Li, B. Cheng, J. Xu, J. Yu, S. Cao, Crystalline carbon nitrides for photocatalysis, EES Catal. 2 (2024) 411-447. https://doi.org/10.1039/D3EY00302G.

[28] K. Chen, J. Xiao, T. Hisatomi, K. Domen, Transition-metal (oxy)nitride photocatalysts for water splitting, Chem. Sci. 14 (2023) 9248–9257. https://doi.org/10.1039/D3SC03198E.

[29] S. Kumar, K.R. Reddy, C.V. Reddy, N.P. Shetti, V. Sadhu, M. V Shankar, V.G. Reddy, A. V Raghu, T.M. Aminabhavi, Metal Nitrides and Graphitic Carbon Nitrides as Novel Photocatalysts for Hydrogen Production and Environmental Remediation BT - Nanostructured Materials for Environmental Applications, in: S. Balakumar, V. Keller, M. V Shankar (Eds.), Springer International Publishing (2021) 485–519. https://doi.org/10.1007/978-3-030-72076-6_19.

[30] L. Liu, X. Zhang, L. Yang, L. Ren, D. Wang, J. Ye, Metal nanoparticles induced photocatalysis, Natl. Sci. Rev. 4 (2017) 761–780. https://doi.org/10.1093/nsr/nwx019.

[31] M.J. Kale, T. Avanesian, P. Christopher, Direct photocatalysis by plasmonic nanostructures, ACS Catal. 4 (2014) 116–128. https://doi.org/10.1021/cs400993w.

[32] J.L. Lopes, M.J. Martins, H.I.S. Nogueira, A.C. Estrada, T. Trindade, Carbon-based heterogeneous photocatalysts for water cleaning technologies: a review, Environ. Chem. Lett. 19 (2021) 643–668. https://doi.org/10.1007/s10311-020-01092-9.

[33] H. Li, L. Wang, G. Yu, Covalent organic frameworks: Design, synthesis, and performance for photocatalytic applications, Nano Today. 40 (2021) 101247. https://doi.org/10.1016/j.nantod.2021.101247.

[34] V. García-Salcido, P. Mercado-Oliva, J.L. Guzmán-Mar, B.I. Kharisov, L. Hinojosa-Reyes, MOF-based composites for visible-light-driven heterogeneous photocatalysis: Synthesis, characterization and environmental application studies, J. Solid State Chem. 307 (2022) 122801. https://doi.org/10.1016/j.jssc.2021.122801.

[35] Z. Kuspanov, B. Bakbolat, A. Baimenov, A. Issadykov, M. Yeleuov, C. Daulbayev, Photocatalysts for a sustainable future: Innovations in large-scale environmental and energy applications, Sci. Total Environ. 885 (2023) 163914. https://doi.org/10.1016/j.scitotenv.2023.163914.

[36] K. Hashimoto, H. Irie, A. Fujishima, TiO2 Photocatalysis: A Historical Overview and Future Prospects, Jpn. J. Appl. Phys. 44 (2005) 8269. https://doi.org/10.1143/JJAP.44.8269.

[37] E.S. Araújo, M.F.G. Pereira, G.M.G. da Silva, G.F. Tavares, C.Y.B. Oliveira, P.M. Faia, A Review on the Use of Metal Oxide-Based Nanocomposites for the Remediation of Organics-Contaminated Water via Photocatalysis: Fundamentals, Bibliometric Study and Recent Advances, Toxics. 11 (2023) 658. https://doi.org/10.3390/toxics11080658.

[38] R.S.R. Mohd Zaki, R. Jusoh, I. Chanakaewsomboon, H.D. Setiabudi, Recent advances in metal oxide photocatalysts for photocatalytic degradation of organic pollutants: A review on photocatalysts modification strategies, Mater. Today Proc. (2023). https://doi.org/10.1016/j.matpr.2023.07.102.

[39] A. Khlyustova, N. Sirotkin, T. Kusova, A. Kraev, V. Titov, A. Agafonov, Doped TiO2: the effect of doping elements on photocatalytic activity, Mater. Adv. 1 (2020) 1193–1201. https://doi.org/10.1039/D0MA00171F.

[40] X. Hou, C.-W. Wang, W.-D. Zhu, X.-Q. Wang, Y. Li, J. Wang, J.-B. Chen, T. Gan, H.-Y. Hu, F. Zhou, Preparation of nitrogen-doped anatase TiO2 nanoworm/nanotube hierarchical structures and its photocatalytic effect, Solid State Sci. 29 (2014) 27–33. https://doi.org/10.1016/j.solidstatesciences.2014.01.007.

[41] S. Ali, J. Abdul Nasir, R. Nasir Dara, Z. Rehman, Modification strategies of metal oxide photocatalysts for clean energy and environmental applications: A review, Inorg. Chem. Commun. 145 (2022) 110011. https://doi.org/10.1016/j.inoche.2022.110011.

[42] X. Zong, C. Sun, H. Yu, Z.G. Chen, Z. Xing, D. Ye, G.Q. (Max) Lu, X. Li, L. Wang, Activation of Photocatalytic Water Oxidation on N-Doped ZnO Bundle-like Nanoparticles under Visible Light, J. Phys. Chem. C. 117 (2013) 4937–4942. https://doi.org/10.1021/jp311729b.

[43] J. Lin, D. Ma, Y. Li, P. Zhang, H. Mi, L. Deng, L. Sun, X. Ren, In situ nitrogen doping of TiO2 by plasma enhanced atomic layer deposition for enhanced sodium storage performance, Dalt. Trans. 46 (2017) 13101–13107. https://doi.org/10.1039/C7DT03303F.

[44] M.-L. Kääriäinen, D.C. Cameron, Nitrogen doping in atomic layer deposition grown titanium dioxide films by using ammonium hydroxide, Thin Solid Films. 526 (2012) 212–217. https://doi.org/10.1016/j.tsf.2012.11.005.

[45] H.M. Yates, M.G. Nolan, D.W. Sheel, M.E. Pemble, The role of nitrogen doping on the development of visible light-induced photocatalytic activity in thin TiO2 films grown on glass by chemical vapour deposition, J. Photochem. Photobiol. A Chem. 179 (2006) 213–223. https://doi.org/10.1016/j.jphotochem.2005.08.018.

[46] O. Diwald, T.L. Thompson, E.G. Goralski, S.D. Walck, J.T. Yates, The Effect of Nitrogen Ion Implantation on the Photoactivity of TiO2 Rutile Single Crystals, J. Phys. Chem. B. 108 (2004) 52–57. https://doi.org/10.1021/jp030529t.

[47] M. Batzill, E.H. Morales, U. Diebold, Influence of Nitrogen Doping on the Defect Formation and Surface Properties of TiO2 Rutile and Anatase, Phys. Rev. Lett. 96 (2006) 26103. https://doi.org/10.1103/PhysRevLett.96.026103.

[48] J.M. Mwabora, T. Lindgren, E. Avendaño, T.F. Jaramillo, J. Lu, S.-E. Lindquist, C.-G. Granqvist, Structure, Composition, and Morphology of Photoelectrochemically Active TiO2-xNx Thin Films Deposited by Reactive DC Magnetron Sputtering, J. Phys. Chem. B. 108 (2004) 20193–20198. https://doi.org/10.1021/jp0368987.

[49] Y. Nakano, T. Morikawa, T. Ohwaki, Y. Taga, Deep-level optical spectroscopy investigation of N-doped TiO2 films, Appl. Phys. Lett. 86 (2005) 132104. https://doi.org/10.1063/1.1896450.

[50] J. Cao, T. Hasegawa, Y. Asakura, P. Sun, S. Yang, B. Li, W. Cao, S. Yin, Synthesis and color tuning of titanium oxide inorganic pigment by phase control and mixed-anion co-doping, Adv. Powder Technol. 33 (2022) 103576. https://doi.org/10.1016/j.apt.2022.103576.

[51] C. Wang, H. Ni, J. Dai, T. Liu, Z. Wu, X. Chen, Z. Dong, J. Qian, Z. Wu, Comparison of highly active Type-I and Type-II heterojunction photocatalytic composites synthesized by electrospinning for humic acid degradation, Chem. Phys. Lett. 803 (2022) 139815. https://doi.org/10.1016/j.cplett.2022.139815.

[52] J. Low, J. Yu, M. Jaroniec, S. Wageh, A.A. Al-Ghamdi, Heterojunction Photocatalysts, Adv. Mater. 29 (2017) 1601694. https://doi.org/10.1002/adma.201601694.

[53] A. Balapure, J. Ray Dutta, R. Ganesan, Recent advances in semiconductor heterojunctions: a detailed review of the fundamentals of photocatalysis, charge transfer mechanism and materials, RSC Appl. Interfaces. 1 (2024) 43–69. https://doi.org/10.1039/D3LF00126A.

[54] D. Wang, P. Ye, K. Li, H. Zeng, Y.-C. Nie, F. Dong, Q.-J. Xing, J.-P. Zou, Highly durable isotypic heterojunction generated by covalent cross-linking with organic linkers for improving visible-light-driven photocatalytic performance, Appl. Catal. B Environ. 260 (2020) 118182. https://doi.org/10.1016/j.apcatb.2019.118182.

[55] D. Walter, J. Peng, K. Weber, K.R. Catchpole, T.P. White, Performance limitations imposed by the TCO heterojunction in high efficiency perovskite solar cells, Energy Environ. Sci. 15 (2022) 5202–5216. https://doi.org/10.1039/D2EE01742C.

[56] V. Melinte, L. Stroea, A.L. Chibac-Scutaru, Polymer nanocomposites for photocatalytic applications, Catalysts. 9 (2019) 986. https://doi.org/10.3390/catal9120986.

[57] E. Coy, I. Iatsunskyi, M. Bechelany, Perspectives and Current Trends on Hybrid Nanocomposite Materials for Photocatalytic Applications, Sol. RRL. 7 (2023) 2201069. https://doi.org/10.1002/solr.202201069.

[58] Z. Han, J. Fei, J. Li, Y. Deng, M. Lv, J. Zhao, C. Wang, X. Zhao, Enhanced dye-sensitized photocatalysis for water purification by an alveoli-like bilayer Janus membrane, Chem. Eng. J. 407 (2021) 127214. https://doi.org/10.1016/j.cej.2020.127214.

[59] M. Liras, M. Barawi, V.A. de la Peña O'Shea, Hybrid materials based on conjugated polymers and inorganic semiconductors as photocatalysts: from environmental to energy applications, Chem. Soc. Rev. 48 (2019) 5454–5487. https://doi.org/10.1039/C9CS00377K.

[60] J. You, Y. Zhao, L. Wang, W. Bao, Recent developments in the photocatalytic applications of covalent organic frameworks: A review, J. Clean. Prod. 291 (2021) 125822. https://doi.org/10.1016/j.jclepro.2021.125822.

[61] F. Gao, X. Hou, A. Wang, G. Chu, W. Wu, J. Chen, H. Zou, Preparation of polypyrrole/TiO2 nanocomposites with enhanced photocatalytic performance, Particuology. 26 (2016) 73–78. https://doi.org/10.1016/j.partic.2015.07.003.

[62] N.M. Dimitrijevic, S. Tepavcevic, Y. Liu, T. Rajh, S.C. Silver, D.M. Tiede, Nanostructured TiO2/Polypyrrole for Visible Light Photocatalysis, J. Phys. Chem. C. 117 (2013) 15540–15544. https://doi.org/10.1021/jp405562b.

[63] B. Yan, Y. Wang, X. Jiang, K. Liu, L. Guo, Flexible Photocatalytic Composite Film of ZnO-Microrods/Polypyrrole, ACS Appl. Mater. Interfaces. 9 (2017) 29113–29119. https://doi.org/10.1021/acsami.7b08462.

[64] Z. Katančić, W.-T. Chen, G.I.N. Waterhouse, H. Kušić, A. Lončarić Božić, Z. Hrnjak-Murgić, J. Travas-Sejdic, Solar-active photocatalysts based on TiO2 and conductive polymer PEDOT for the removal of bisphenol A, J. Photochem. Photobiol. A Chem. 396 (2020) 112546. https://doi.org/10.1016/j.jphotochem.2020.112546.

[65] A. Sulowska, A. Fiszka Borzyszkowska, K. Cysewska, K. Siwińska-Ciesielczyk, K. Nikiforow, G. Trykowski, A. Zielińska-Jurek, The effect of PEDOT morphology on hexavalent chromium reduction over 2D TiO2/PEDOT photocatalyst under UV–vis light, Mater. Chem. Phys. 299 (2023) 127430. https://doi.org/10.1016/j.matchemphys.2023.127430.

[66] D.S. Vavilapalli, J. Rosen, S. Singh, Immobilization of a TiO2–PEDOT:PSS hybrid heterojunction photocatalyst for degradation of organic effluents, RSC Adv. 13 (2023) 3095–3101. https://doi.org/10.1039/D2RA06729C.

[67] S. Khan, A.K. Narula, Synthesis of the ternary photocatalyst based on ZnO sensitized graphene quantum dot reinforced with conducting polymer exhibiting photocatalytic activity, J. Mater. Sci. Mater. Electron. 29 (2018) 6337–6349. https://doi.org/10.1007/s10854-018-8613-3.

[68] S.S. Sambaza, A. Maity, K. Pillay, Polyaniline-Coated TiO2 Nanorods for Photocatalytic Degradation of Bisphenol A in Water, ACS Omega. 5 (2020) 29642–29656. https://doi.org/10.1021/acsomega.0c00628.

[69] X. Chen, H. Li, H. Wu, Y. Wu, Y. Shang, J. Pan, X. Xiong, Fabrication of TiO2@PANI nanobelts with the enhanced absorption and photocatalytic performance under visible light, Mater. Lett. 172 (2016) 52–55. https://doi.org/10.1016/j.matlet.2016.02.134.

[70] V. Gilja, I. Vrban, V. Mandić, M. Žic, Z. Hrnjak-Murgić, Preparation of a PANI/ZnO Composite for Efficient Photocatalytic Degradation of Acid Blue, Polymers (Basel). 10 (2018) 940. https://doi.org/10.3390/polym10090940.

[71] H. Zhang, R. Zong, Y. Zhu, Photocorrosion Inhibition and Photoactivity Enhancement for Zinc Oxide via Hybridization with Monolayer Polyaniline, J. Phys. Chem. C. 113 (2009) 4605–4611. https://doi.org/10.1021/jp810748u.

[72] J. Li, Q. Xiao, L. Li, J. Shen, D. Hu, Novel ternary composites: Preparation, performance and application of ZnFe2O4/TiO2/polyaniline, Appl. Surf. Sci. 331 (2015) 108–114. https://doi.org/10.1016/j.apsusc.2015.01.001.

[73] J. Feng, Y. Hou, X. Wang, W. Quan, J. Zhang, Y. Wang, L. Li, In-depth study on adsorption and photocatalytic performance of novel reduced graphene oxide-ZnFe2O4-polyaniline composites, J. Alloys Compd. 681 (2016) 157–166. https://doi.org/10.1016/j.jallcom.2016.04.146.

[74] A.M. Mohammed, S.S. Mohtar, F. Aziz, M. Aziz, A. Ul-Hamid, Cu2O/ZnO-PANI ternary nanocomposite as an efficient photocatalyst for the photodegradation of Congo Red dye, J. Environ. Chem. Eng. 9 (2021) 105065. https://doi.org/10.1016/j.jece.2021.105065.

[75] R. Kumar, M.O. Ansari, N. Parveen, M. Oves, M.A. Barakat, A. Alshahri, M.Y. Khan, M.H. Cho, Facile route to a conducting ternary polyaniline@TiO2/GN nanocomposite for environmentally benign applications: photocatalytic degradation of pollutants and biological activity, RSC Adv. 6 (2016) 111308–111317. https://doi.org/10.1039/C6RA24079H.

[76] Y. Park, A. Numan, N. Ponomarev, J. Iqbal, M. Khalid, Enhanced photocatalytic performance of PANI-rGO-MnO2 ternary composite for degradation of organic contaminants under visible light, J. Environ. Chem. Eng. 9 (2021) 106006. https://doi.org/10.1016/j.jece.2021.106006.

[77] M.A. Alenizi, R. Kumar, M. Aslam, F.A. Alseroury, M.A. Barakat, Construction of a ternary g-C3N4/TiO2@polyaniline nanocomposite for the enhanced photocatalytic activity under solar light, Sci. Rep. 9 (2019) 12091. https://doi.org/10.1038/s41598-019-48516-3.

[78] K.T. Karthikeyan, A. Nithya, K. Jothivenkatachalam, Photocatalytic and antimicrobial activities of chitosan-TiO2 nanocomposite, Int. J. Biol. Macromol. 104 (2017) 1762–1773. https://doi.org/10.1016/j.ijbiomac.2017.03.121.

[79] G. Madhan, A.A. Begam, L.V. Varsha, R. Ranjithkumar, D. Bharathi, Facile synthesis and characterization of chitosan/zinc oxide nanocomposite for enhanced antibacterial and photocatalytic activity, Int. J. Biol. Macromol. 190 (2021) 259–269. https://doi.org/10.1016/j.ijbiomac.2021.08.100.

[80] T. Kamal, M. Ul-Islam, S.B. Khan, A.M. Asiri, Adsorption and photocatalyst assisted dye removal and bactericidal performance of ZnO/chitosan coating layer, Int. J. Biol. Macromol. 81 (2015) 584–590. https://doi.org/10.1016/j.ijbiomac.2015.08.060.

[81] H. Zhu, R. Jiang, L. Xiao, Y. Chang, Y. Guan, X. Li, G. Zeng, Photocatalytic decolorization and degradation of Congo Red on innovative crosslinked chitosan/nano-CdS composite catalyst under visible light irradiation, J. Hazard. Mater. 169 (2009) 933–940. https://doi.org/10.1016/j.jhazmat.2009.04.037.

[82] S. Zhang, Saeeda, A. Khan, N. Ali, S. Malik, H. Khan, N. Ali, H.M.N. Iqbal, M. Bilal, Designing, characterization, and evaluation of chitosan-zinc selenide nanoparticles for visible-light-induced degradation of tartrazine and sunset yellow dyes, Environ. Res. 213 (2022) 113722. https://doi.org/10.1016/j.envres.2022.113722.

[83] Y. Li, J. Ma, D. Jin, G. Jiao, X. Yang, K. Liu, J. Zhou, R. Sun, Copper oxide functionalized chitosan hybrid hydrogels for highly efficient photocatalytic-reforming of biomass-based monosaccharides to lactic acid, Appl. Catal. B Environ. 291 (2021) 120123. https://doi.org/10.1016/j.apcatb.2021.120123.

[84] M.A. Alcudia-Ramos, M.O. Fuentez-Torres, F. Ortiz-Chi, C.G. Espinosa-González, N. Hernández-Como, D.S. García-Zaleta, M.K. Kesarla, J.G. Torres-Torres, V. Collins-Martínez, S. Godavarthi, Fabrication of g-C3N4/TiO2 heterojunction composite for enhanced photocatalytic hydrogen production, Ceram. Int. 46 (2020) 38–45. https://doi.org/10.1016/j.ceramint.2019.08.228.

[85] X. Wu, H. Zhao, M.A. Khan, P. Maity, T. Al-Attas, S. Larter, Q. Yong, O.F. Mohammed, M.G. Kibria, J. Hu, Sunlight-Driven Biomass Photorefinery for Coproduction of Sustainable Hydrogen and Value-Added Biochemicals, ACS Sustain. Chem. Eng. 8 (2020) 15772–15781. https://doi.org/10.1021/acssuschemeng.0c06282.

[86] B. Zhu, H. Tan, J. Fan, B. Cheng, J. Yu, W. Ho, Tuning the strength of built-in electric field in 2D/2D g-C3N4/SnS2 and g-C3N4/ZrS2 S-scheme heterojunctions by nonmetal doping, J. Mater. 7 (2021) 988–997. https://doi.org/10.1016/j.jmat.2021.02.015.

[87] D. Wang, Z. Lin, C. Miao, W. Jiang, H. Li, C. Liu, G. Che, An S-scheme photocatalyst constructed by modifying Ni-doped Sn3O4 micro-flowers on g-C3N4 nanosheets for enhanced visible-light-driven hydrogen evolution, J. Ind. Eng. Chem. 113 (2022) 380–388. https://doi.org/10.1016/j.jiec.2022.06.013.

[88] B. Dai, Y. Li, J. Xu, C. Sun, S. Li, W. Zhao, Photocatalytic oxidation of tetracycline, reduction of hexavalent chromium and hydrogen evolution by Cu2O/g-C3N4 S-scheme photocatalyst: Performance and mechanism insight, Appl. Surf. Sci. 592 (2022) 153309. https://doi.org/10.1016/j.apsusc.2022.153309.

[89] G. Nagaraju, K. Manjunath, S. Sarkar, E. Gunter, S.R. Teixeira, J. Dupont, TiO2–RGO hybrid nanomaterials for enhanced water splitting reaction, Int. J. Hydrogen Energy. 40 (2015) 12209–12216. https://doi.org/10.1016/j.ijhydene.2015.07.094.

[90] Q.-P. Luo, X.-Y. Yu, B.-X. Lei, H.-Y. Chen, D.-B. Kuang, C.-Y. Su, Reduced Graphene Oxide-Hierarchical ZnO Hollow Sphere Composites with Enhanced Photocurrent and Photocatalytic Activity, J. Phys. Chem. C. 116 (2012) 8111–8117. https://doi.org/10.1021/jp2113329.

[91] P. Zeng, Q. Zhang, T. Peng, X. Zhang, One-pot synthesis of reduced graphene oxide–cadmium sulfide nanocomposite and its photocatalytic hydrogen production, Phys. Chem. Chem. Phys. 13 (2011) 21496–21502. https://doi.org/10.1039/C1CP22059D.

[92] Y. Zhao, X. Zhang, C. Wang, Y. Zhao, H. Zhou, J. Li, H. Jin, The synthesis of hierarchical nanostructured MoS2/Graphene composites with enhanced visible-light photo-degradation property, Appl. Surf. Sci. 412 (2017) 207–213. https://doi.org/10.1016/j.apsusc.2017.03.181.

[93] B. Ye, W. Wang, L. Wang, H. Tang, J. Hu, Q. Liu, Organic-inorganic heterojunction photocatalysts: From organic molecules to frameworks, Mater. Sci. Semicond. Process. 164 (2023) 107623. https://doi.org/10.1016/j.mssp.2023.107623.

[94] J. Low, S. Cao, J. Yu, S. Wageh, Two-dimensional layered composite photocatalysts, Chem. Commun. 50 (2014) 10768–10777. https://doi.org/10.1039/C4CC02553A.

[95] R. Shwetharani, H.R. Chandan, M. Sakar, G.R. Balakrishna, K.R. Reddy, A. V Raghu, Photocatalytic semiconductor thin films for hydrogen production and environmental applications, Int. J. Hydrogen Energy. 45 (2020) 18289–18308. https://doi.org/10.1016/j.ijhydene.2019.03.149.

[96] R.S. Pedanekar, S.K. Shaikh, K.Y. Rajpure, Thin film photocatalysis for environmental remediation: A status review, Curr. Appl. Phys. 20 (2020) 931–952. https://doi.org/10.1016/j.cap.2020.04.006.

[97] Z. Tian, C. Xu, J. Li, G. Zhu, J. Wu, Z. Shi, Y. Wang, A facile preparation route for highly conductive borate cross-linked reduced graphene oxide paper, New J. Chem. 39 (2015) 6907–6913. https://doi.org/10.1039/C5NJ00906E.

[98] Y. Guo, X. Hu, R. Sun, X. Wang, B. Tan, Covalent Triazine Framework Films through In-Situ Growth for Photocatalytic Hydrogen Evolution, ChemSusChem. 16 (2023) e202300759. https://doi.org/10.1002/cssc.202300759.

[99] G. Luna-Sanguino, A. Ruíz-Delgado, A. Tolosana-Moranchel, L. Pascual, S. Malato, A. Bahamonde, M. Faraldos, Solar photocatalytic degradation of pesticides over TiO2-rGO nanocomposites at pilot plant scale, Sci. Total Environ. 737 (2020) 140286. https://doi.org/10.1016/j.scitotenv.2020.140286.

[100] M. Samy, M.G. Ibrahim, M. Fujii, K.E. Diab, M. ElKady, M. Gar Alalm, CNTs/MOF-808 painted plates for extended treatment of pharmaceutical and agrochemical wastewaters in a novel photocatalytic reactor, Chem. Eng. J. 406 (2021) 127152. https://doi.org/10.1016/j.cej.2020.127152.

[101] A. Surenjan, T. Pradeep, L. Philip, Application and performance evaluation of a cost-effective vis- LED based fluidized bed reactor for the treatment of emerging contaminants, Chemosphere. 228 (2019) 629–639. https://doi.org/10.1016/j.chemosphere.2019.04.179.

[102] Z. Fang, Y. Hu, J. Cheng, Y. Chen, Continuous removal of trace bisphenol A from water by high efficacy TiO2 nanotube pillared graphene-based macrostructures in a photocatalytically fluidized bed, Chem. Eng. J. 372 (2019) 581–589. https://doi.org/10.1016/j.cej.2019.04.129.

[103] O. Sacco, D. Sannino, V. Vaiano, Packed Bed Photoreactor for the Removal of Water Pollutants Using Visible Light Emitting Diodes, Appl. Sci. 9 (2019) 472. https://doi.org/10.3390/app9030472.

[104] M. Schröder, K. Kailasam, J. Borgmeyer, M. Neumann, A. Thomas, R. Schomäcker, M. Schwarze, Hydrogen Evolution Reaction in a Large-Scale Reactor using a Carbon Nitride Photocatalyst under Natural Sunlight Irradiation, Energy Technol. 3 (2015) 1014–1017. https://doi.org/10.1002/ente.201500142.

[105] X. Wang, P. Xu, R. Han, J. Ren, L. Li, N. Han, F. Xing, J. Zhu, A review on the mechanical properties for thin film and block structure characterised by using nanoscratch test, Nanotechnol. Rev. 8 (2019) 628–644. https://doi.org/10.1515/ntrev-2019-0055.

[106] M. G, P. Ghosh, Pile-up response of polymer thin films to static and dynamic loading, Thin Solid Films. 677 (2019) 1–12. https://doi.org/10.1016/j.tsf.2019.01.040.

[107] S. Zhang, L.A. Galuska, X. Gu, Water-assisted mechanical testing of polymeric thin-films, J. Polym. Sci. 60 (2022) 1108–1129. https://doi.org/10.1002/pol.20210281.

[108] H. Lee, S.M. Dellatore, W.M. Miller, P.B. Messersmith, Mussel-inspired surface chemistry for multifunctional coatings, Science. 318 (2007) 426–430. https://doi.org/10.1126/science.1147241.

[109] S.A. Pawar, A.N. Chand, A.V. Kumar, Polydopamine: An Amine Oxidase Mimicking Sustainable Catalyst for the Synthesis of Nitrogen Heterocycles under Aqueous Conditions, ACS Sustain. Chem. Eng. 7 (2019) 8274–8286. https://doi.org/10.1021/acssuschemeng.8b06677.

[110] W.X. Mao, X.J. Lin, W. Zhang, Z.X. Chi, R.W. Lyu, A.M. Cao, L.J. Wan, Core-shell structured TiO2@polydopamine for highly active visible-light photocatalysis, Chem. Commun. 52 (2016) 7122–7125. https://doi.org/10.1039/c6cc02041k.

[111] D. Damberga, V. Fedorenko, K. Grundšteins, Ş. Altundal, A. Šutka, A. Ramanavičius, E. Coy, R. Mrówczyński, I. Iatsunskyi, R. Viter, Influence of pda coating on the structural, optical and surface properties of zno nanostructures, Nanomaterials. 10 (2020) 1–11. https://doi.org/10.3390/nano10122438.

[112] Y. Kim, E. Coy, H. Kim, R. Mrówczyński, P. Torruella, D.W. Jeong, K.S. Choi, J.H. Jang, M.Y. Song, D.J. Jang, F. Peiro, S. Jurga, H.J. Kim, Efficient photocatalytic production of hydrogen by exploiting the polydopamine-semiconductor interface, Appl. Catal. B Environ. 280 (2021) 119423. https://doi.org/10.1016/j.apcatb.2020.119423.

[113] M. Ruan, D. Guo, Q. Jia, A uniformly decorated and photostable polydopamine–organic semiconductor to boost the photoelectrochemical water splitting performance of CdS photoanodes, Dalt. Trans. 50 (2021) 1913–1922. https://doi.org/10.1039/d0dt04056h.

[114] J.H. Ryu, P.B. Messersmith, H. Lee, Polydopamine Surface Chemistry: A Decade of Discovery, ACS Appl. Mater. Interfaces. 10 (2018) 7523–7540. https://doi.org/10.1021/acsami.7b19865.

[115] E. Coy, I. Iatsunskyi, J.C. Colmenares, Y. Kim, R. Mrówczyński, Polydopamine Films with 2D-like Layered Structure and High Mechanical Resilience, ACS Appl. Mater. Interfaces. 13 (2021) 23113–23120. https://doi.org/10.1021/acsami.1c02483.

[116] F. Ponzio, P. Payamyar, A. Schneider, M. Winterhalter, J. Bour, F. Addiego, M.P. Krafft, J. Hemmerle, V. Ball, Polydopamine films from the forgotten Air/water interface, J. Phys. Chem. Lett. 5 (2014) 3436–3440. https://doi.org/10.1021/jz501842r.

[117] Z. Wang, F. Tang, H. Fan, L. Wang, Z. Jin, Polydopamine Generates Hydroxyl Free Radicals under Ultraviolet-Light Illumination, Langmuir. 33 (2017) 5938–5946. https://doi.org/10.1021/acs.langmuir.7b01065.